

NO-A179 489

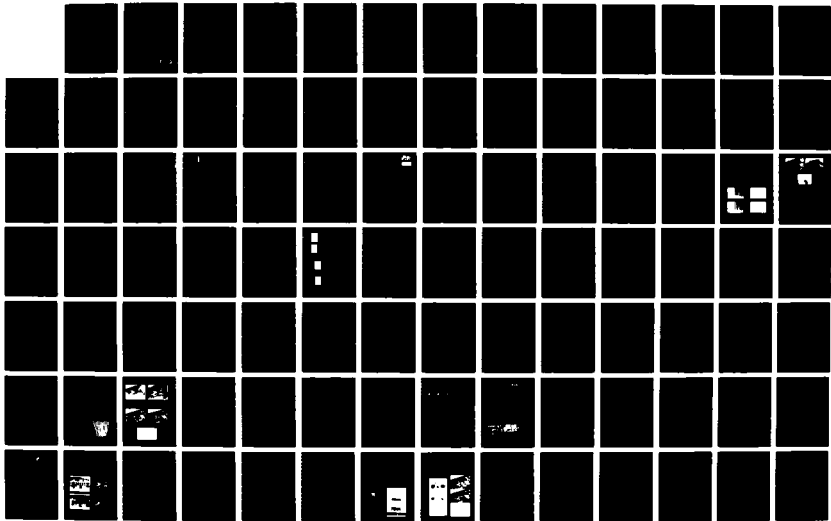
WHITE-LIGHT OPTICAL INFORMATION PROCESSING AND
HOLOGRAPHY(U) PENNSYLVANIA STATE UNIV UNIVERSITY PARK
DEPT OF ELECTRICAL ENGINEERING F T YU 23 JAN 87
AFOSR-TR-87-0456 AFOSR-83-0148

1/4
6

UNCLASSIFIED

F/B 20/6

ML





MI

DTIC FILE COPY

AFOSR-TN- 87-0456

White-light Optical Information Processing and Holography

(2)

AD-A179 489

by:

Approved for public release;
distribution unlimited.

F. T. S. Yu
(Principal Investigator)

Electrical Engineering Department
The Pennsylvania State University
University Park, Pennsylvania 16802

Prepared for:

AFOSR/NE

Building 410
Bolling Air Force Base
Washington, D.C. 20332

Attention: Dr. C. Lee Giles

AFOSR Final Report on
Contracts AFOSR-81-0148 and
AFOSR-83-0140

Period Covered (February 15, 1981 - May 14, 1986)

Date: December 16, 1986

AIR FORCE OFFICE OF SCIENTIFIC RESEARCH (AFSC)
NOTICE OF RESEARCH TO DTIC
This technical report has been reviewed and is
approved for public release (AFR 190-12).
Distribution is unlimited.
MATTHEW J. L. ELLIOTT
Chief, Technical Information Division

DTIC
ELECTE
APR 24 1987
S D

Unclassified

SECURITY CLASSIFICATION OF THIS PAGE

REPORT DOCUMENTATION PAGE

1a. REPORT SECURITY CLASSIFICATION Unclassified			1b. RESTRICTIVE MARKINGS A179489		
2a. SECURITY CLASSIFICATION AUTHORITY			3. DISTRIBUTION / AVAILABILITY OF REPORT Unlimited		
2b. DECLASSIFICATION / DOWNGRADING SCHEDULE					
4. PERFORMING ORGANIZATION REPORT NUMBER(S)			5. MONITORING ORGANIZATION REPORT NUMBER(S) AFOSR-TR- 87-0456		
6a. NAME OF PERFORMING ORGANIZATION Electrical Engineering Dept. Pennsylvania State University		6b. OFFICE SYMBOL (If applicable) NE		7a. NAME OF MONITORING ORGANIZATION Dr. Lee Giles AFOSR	
6c. ADDRESS (City, State, and ZIP Code) University Park, PA 16802			7b. ADDRESS (City, State, and ZIP Code) Building 410 Bolling Air Force Base Washington, D.C. 20332		
8a. NAME OF FUNDING / SPONSORING ORGANIZATION AFOSR/NE		8b. OFFICE SYMBOL (If applicable) NE		9. PROCUREMENT INSTRUMENT IDENTIFICATION NUMBER AFOSR-83-0140 / AFOSR-81-0148	
8c. ADDRESS (City, State, and ZIP Code) Building 410 Bolling Air Force Base Washington, D.C. 20332			10. SOURCE OF FUNDING NUMBERS		
			PROGRAM ELEMENT NO. 61102F	PROJECT NO. 2305	TASK NO. B1
11. TITLE (Include Security Classification) WHITE LIGHT OPTICAL PROCESSING AND HOLOGRAPHY					
12. PERSONAL AUTHOR(S) Yu, Francis T.S.					
13a. TYPE OF REPORT Final Report		13b. TIME COVERED FROM 2/15/81 TO 5/14/86		14. DATE OF REPORT (Year, Month, Day) 1987, January 23	
15. PAGE COUNT 302					
16. SUPPLEMENTARY NOTATION					
17. COSATI CODES			18. SUBJECT TERMS (Continue on reverse if necessary and identify by block number)		
FIELD	GROUP	SUB-GROUP			
			WHITE-LIGHT OPTICAL INFORMATION PROCESSING AND HOLOGRAPHY		
19. ABSTRACT (Continue on reverse if necessary and identify by block number)					
<p>Since its invention as a strong coherent source, the laser has become an indispensable light source for many applications, particularly with regard to optical information processing holography. However coherent systems are plagued with coherent noise, which frequently limits their processing capability. We have in recent years developed a white-light processing technique which is able to alleviate this disadvantage. The basic advantage of white-light processing can be summarized as: (1) it is capable of suppressing coherent noise, (2) white light source is inexpensive, (3) environmental factors for processing are rather relaxed, (4) white-light systems are economical and easy to operate, and (5) it is very suitable for color image processing. In the following, we shall highlight some of the major results accomplished with this research supported by AFOSR Grants 81-0148 and 83-0140.</p> <p>The application of white-light optical processing to photographic image deblurring was first demonstrated in this research program. Since the white-light source emanates all the visible light, we have extended the image deblurring technique to smeared color image</p>					
20. DISTRIBUTION / AVAILABILITY OF ABSTRACT <input checked="" type="checkbox"/> UNCLASSIFIED/UNLIMITED <input type="checkbox"/> SAME AS RPT <input type="checkbox"/> DTIC USERS			21. ABSTRACT SECURITY CLASSIFICATION Unclassified		
22a. NAME OF RESPONSIBLE INDIVIDUAL Dr. Lee Giles			22b. TELEPHONE (Include Area Code) (202) 767-4931		22c. OFFICE SYMBOL AFOSR / NE

restoration.

We have in this research developed a source encoding and signal sampling concept, such that the optical signal processing can be carried out in complex amplitude, with an incoherent white-light source. In this connection a new technique for image subtraction was developed for white-light illumination. We have extended the source encoding technique for broad spectral bandwidth. Notice that, the digital counterpart is not able to perform the color image restoration at the present time.

In this research, we have quantitatively evaluated the coherence requirement for the white-light optical processor. The spatial and temporal coherence requirements have been evaluated for a dispersive white-light system. The requirements for image deblurring, subtraction, and correlation have been thoroughly calculated.

We have, in this research, evaluated the apparent transfer function for the white-light processor. The MTF of the white-light processor is depending on the degree of temporal and spatial coherence. The calculated MTF is rather general, which can be applied to any partially coherent optical processor.

One of the interesting results was the development of a density pseudocolor encoder with white-light. This white-light pseudocolor encoder is a high resolution system and it is very cost effective as compared with the digital counterpart. We have applied the pseudocolor encoder for medical diagnostic imaging, Landsat data falsed-color composites, as well as color image retrievals.

In white-light holography research, we have evaluated the primary aberrations and bandwidth requirement for rainbow holographic process. The conditions for the removal of the primary aberrations have been calculated. We have also developed a technique of generating a broadband white-light Fourier hologram. The technique utilizes a source encoding principle. This broadband Fourier hologram is vitally important, for the generation of a wide band spatial filter as applied to complex signal detection with white-light. In addition, we have also developed a dual-beam encoding technique for color hologram construction with white-light. This encoding technique utilizes no reference beam.

Another interesting demonstration must be the optical signal processing with sun light. The advantage of sun-light processing is that the optical system does not carry its own light source, which is very suitable for spaceborne application.

Noise performance and measurement have been quantitatively analyzed in this research. We have shown that the white-light system offers coherent artifact noise immunity, which is the primary advantage over the coherent counterpart.

We have also in this research, applied various spatial light modulators (SLM) (for examples, Magneto-optic, Liquid Crystal TV, Liquid Crystal light valve, etc) to white-light optical signal processing. The

programmability of the SLM have been exploited and interesting colorful results have been obtained.

Furthermore, the application of white-light processing to spectrogram generation, Talbat interferometer, phase object visualization, and many others have been carried out in various phases of this research. The results, in part, can be found in this report.

Final remarks, the net effects of this study is to emphasize the reality of a white-light optical processor and its capability of performing complex amplitude processing, which would offers many colorful applications, that in part, have been documented in the list of publications.

White-light Optical Information Processing and Holography

by:

F. T. S. Yu
(Principal Investigator)

Electrical Engineering Department
The Pennsylvania State University
University Park, Pennsylvania 16802

Prepared for:

AFOSR/NE

Building 410
Bolling Air Force Base
Washington, D.C. 20332

Attention: Dr. C. Lee Giles

AFOSR Final Report on
Contracts AFOSR-81-0148 and
AFOSR-83-0140

Period Covered (February 15, 1981 - May 14, 1986)

Date: December 16, 1986

Table of Contents

Abstract	
I. Introduction	1
II. Summary and Overview	1
2.1 Smeared Image Deblurring	1
2.2 Image Subtraction	2
2.3 Visualization of Phase Object	3
2.4 Coherence Requirement	3
2.5 Apparent Transfer Function	4
2.6 Source Encoding and Signal Sampling	6
2.7 Broadband Image Deblurring	6
2.8 Color Image Subtraction	7
2.9 Rainbow Holographic Aberrations	8
2.10 Pseudocolor Encoding with Three Primary Colors	8
2.11 Partial Coherent Measurement	9
2.12 Restoration of Out-of-Focused Color Image	9
2.13 Solar Light Optical Signal Processing	9
2.14 White-light Processing with Magneto-Optic Device	9
2.15 Measurement of Noise Performance	10
2.16 White-Light Fourier Holography	10
2.17 Optical Generation of Speech Spectrogram with White-Light Source	11
2.18 Progress on Archival Color Film Storage	11
2.19 Generating False-Color Composites for Landsat data	11
2.20 Developed a Low-Cost White-Light Processor	12
2.21 White-Light Talbot Interferometer	13
2.22 Analysis of Cross-Spectral Density Function for White-Light Processing	13
2.23 Computer Generated Filters in White-Light Processor	13
2.24 Holographic Tomography for 3-D Object Field	14
2.25 Medical Imaging with White-Light	15
2.26 Dual-Aperture Sampling with Partially Coherent Light	15
2.27 Application of LCTV	15
2.28 Computer Generated Tricolor Sampling and Application	16
2.29 References	17
III. Smeared-Photographic Image Deblurring	20
IV. Image Subtraction with Incoherent Source	24
V. Visualization of Phase Object	35
VI. Coherence Requirement	40
VII. Apparent Transfer Function	50
VIII. Source Encoding and Signal Sampling	59
IX. Broad Spectral Band Color Image Deblurring	72
X. Color Image Subtraction	79



A-1

y Codes
nd/or
dial

XI.	Rainbow Holographic Aberrations	85
XII.	Pseudocolor Color Encoding with Primary Colors	92
XIII.	Partial Coherence Measurement	97
XIV.	Restoration of Out-of-Focused Color Image	106
XV.	Solar-Light Optical Processing	113
XVI.	White-Light Processing with Magneto-Optic Device	118
XVII.	Measurement of Noise Performance	124
XVIII.	White-Light Fourier Holography	131
XIV.	Optical Generation of Speech Spectrogram	137
XX.	Progress on Archival Color Film Storage	144
XXI.	Falsed-Color Composites for Landsat Data	152
XXII.	Low-cost White-Light Processor	158
XXIII.	White-Light Talbot Interferometer	166
XXIV.	Cross Spectral Density Analysis	177
XXV.	Computer Generated Filter in White-Light Processor	210
XXVI.	Holographic Tomography	258
XXVII.	Medical Imaging with White-Light	267
XXVIII.	Dual-Aperture Sampling with White-Light	272
XXIX.	LCTV Processing with White-Light	280
XXX.	Computer Generated Tricolor Sampling	284
XXXI.	Concluding Remarks	294
XXXII.	List of Publications Resulting from AFOSR Support	298

I. Introduction

We have, in the period covered from February 15, 1981 to May 14, 1986, completed the major research programs in the area on white-light signal processing and holography. The performance of our tasks done were very consistent with proposed research programs supported by the Air Force Office of Scientific Research Grant AFOSR-81-0148 and Nos. AFOSR-83-0140. The research finds have been published in various open technical journals and in part, have been presented in scientific conferences on various occasions. Sample copies of these papers are included in this final report in the subsequent sections, to provide a concise documentation of our research accomplishment. In the following sections, we shall give an overview of the overall research done, that cover the entire period of this research. We shall detail some of those accomplished works in the following sections. A list of publications resulting from this support is also included at the end of this report.

II. Summary and Overview

2.1 Smeared Image Deblurring

One of the earliest research done on "White-Light Optical Signal Processing and Holography", must be the smeared-photographic-image deblurring with white-light [7]. A simple technique of synthesizing a complex deblurring spatial filter is given. Experimental demonstrations of smeared-image deblurring with a white-light processing technique are provided. Compared with the coherent-processing technique, the white-light technique offers artifact-noise suppression, and the processing system is simple, versatile, and economical. We note that the white-light-processing technique is suitable for smeared-color-image restoration

We have also extended this image deblurring technique to color photographic image deblurring [2]. Since white-light processing technique is suitable for image processing, the color image deblurring can be achieved with narrow red and green color deblurring filters. Experimental demonstrations for smeared-color image were obtained. The extension to the entire spectral band of a white-light source will be given in Section IX.

2.2 Image Subtraction (Section IV)

We have in this research investigated the possibility of using a white-light source for image subtraction. Since optical image subtraction is a one-dimensional processing operation, instead of using a point source of light, a line source can be utilized. However the image subtraction operates upon the one-to-one image points, a strictly broad coherence requirement is not needed. It is therefore possible to encode an extended incoherence source to obtain a point-pair coherence function for the image subtraction operation [3,5].

A technique of encoding an extended incoherent source for image subtraction is developed. The source encoding is obtained from the coherence requirement for image subtraction operation. Since the coherence requirement is a point-pair concept for image subtraction the encoding can take place by spatial sampling an extended incoherent source with narrow slit apertures. The basic advantage of the source encoding is to increase the available light power for the processing operation, so that the inherent difficulty of obtaining a very small incoherent source can be alleviated. Experimental results obtained with this encoded incoherent source are given. Comparisons with the results obtained by coherent processing technique are also provided. We have concluded that the

incoherent processing technique offers a better artifact noise suppression and better image quality.

2.3 Visualization of Phase Object (Section V)

We have extended the source encoding concept for the application to visualization of color coded phase variation with white-light processing. This technique utilized a dual color optical processor with encoded extended white-light sources. The color coded phase visualization enable one to observe fine detail phase variation between fringes, which includes both the positive and negative phase changes. Excellent experimental demonstrations of the phase visualization technique are provided [6].

2.4 Coherence Requirement (Section VI)

Our research has included the evaluation of the coherent requirement for white-light optical signal processing [7]. The mutual intensity function for a partially coherent light is used to develop an expression for the output intensity distribution for a broadband optical information processor. The coherence requirement for smeared image deblurring and image subtraction is then determined using the intensity distribution.

We have shown that the temporal and spatial coherence requirements for some partially coherent optical processing operations, namely, image deblurring and image subtraction, can be determined in terms of the output intensity distribution. For image deblurring the temporal coherence requirement depends on the ratio of the deblurring width to the smeared length of the blurred image. To obtain a higher degree of deblurring a narrower spectral width of the light source is required. For example, if the deblurring ratio $\Delta w/w$ is 0.1, the spectral width, $\Delta\lambda$, should be < 640 A.

For the spatial coherence requirement the image deblurring depends on both the deblurring ratio $\Delta w/w$ and the smeared length w . If the deblurring ratio $\Delta w/w = 1/10$ and $w = 1\text{mm}$, a slit source $< 0.26\text{ mm}$ should be used. For a smeared image deblurring operation the constraints of the temporal and spatial coherence requirements are not critical, which can be achieved in practice.

For image subtraction, the temporal coherence requirement is determined by the highest spatial frequency and the separation of the input object transparencies. If the separation and spatial frequency of the input transparencies are high, a narrower spatial bandwidth of the light source is required.

For spatial coherence requirement, the modulation transfer function, which determines the contrast of the subtracted image, depends on the ratio of the slit width to the spatial period of the encoding mask, i.e., d/D . If the ratio d/D is low, a higher contrast subtracted image can be obtained. For example, with $d/C = 0.05$, a relatively higher $\text{MTF} = 0.85$ can be obtained. Compared with the image deblurring operations, the coherence requirements are more stringent for the subtraction process.

Finally, we have concluded that, the solution to the coherence requirement for partially coherent processing is not restricted to the application of the deblurring and subtraction operation, but may also be applied to any other optical processing operation.

2.5 Apparent Transfer Function (Section VII).

We have in this research evaluated an apparent transfer function for our white-light optical signal processing system [8].

The nonlinear behavior of the partially coherent optical processor, when considering either intensity or amplitude distribution input signals,

necessitates the use of the apparent transfer function to accurately predict the system response. We have derived the general formulas for MTF in terms of the theory of partially coherent light. These derivations indicate the dependence of MTF upon the degree of spatial coherence (i.e., the source size) as well as the degree of temporal coherence (i.e., the source spectral bandwidth). MTF has been shown to be less dependent upon the spatial coherence requirement as compared to its relationship with the temporal coherence requirement.

It has been noted that the spatial bandwidth of our optical processor is primarily dependent upon the size of the filter Δx , where the filter is placed in the Fourier plane. The transfer systems bandwidth may be increased by using a larger spatial filter Δx . However, the size of the filter is selected such that $\Delta x = p_0 f \Delta \lambda$, which is linearly related to the spatial frequency of the grating, the focal length of the transform lens and the spectral width of the light source. A narrow spectral band $\Delta \lambda$ is necessary for most partially coherent optical information processing operations. In order to achieve the required $\Delta \lambda$ for a wide strip of spatial filter Δx in the spatial frequency plane, a diffraction grating of sufficiently high frequency p_0 at the input plane is needed. For example, for partially coherent processing with a white light source, a set of narrow spectral band filters, each with a spectral bandwidth $\delta \lambda$, can be used in the spatial frequency plane.

Finally, we conclude that the apparent transfer function which we have obtained is rather general and may be applied to any partially coherent optical processing system.

2.6 Source Encoding and Signal Sampling (Section VIII)

We have developed a concept of source encoding and signal sampling for our white-light signal processor [4]. We have shown that the advantage of source encoding is to provide an appropriate spatial coherence function at the input plane so that the signal processing can be carried out by extended incoherent source. The effect of the signal sampling is to achieve the temporal coherence requirement at the Fourier plane so that the signal can be processed in complex amplitude. If the filtering operation is two-dimensional, a multi-spectral-band 2-D filter should be utilized. If the filtering operation is one-dimensional, a fan-shape filter can be used.

In short, one should carry out the processing requirements backward for a white-light processor. With these processing requirements (e.g., operation, temporal and spatial coherence requirements), multi-spectral-band or broad-band filter, signal sampling function, and source encoding mask can be synthesized. Thus the signal processing can be carried out in complex amplitude over the whole-spectral band of the white-light source [9].

2.7 Broadband Image Deblurring (Section IX)

In this research, we have shown a broadband color image deblurring technique utilizing a white-light source [10]. This broad spatial band deblurring technique utilized a grating base method to obtain a dispersed smeared image spectra in the Fourier plane so that the deblurring operation can be taken place in complex amplitude deblurring for the entire visible wavelengths. To perform this complex amplitude deblurring for the entire spectral band of the light source, we have shown that a fan-type deblurring filter to compensate the scale variation of the smeared signal spectra due

to wavelength dispersion can be utilized. To alleviate the low transmission efficiency of the deblurring filter, we synthesized the deblurring filter with the combination of a broadband phase filter and a fan-shaped amplitude filter. The broad spectral band phase filter is synthesized by optical coating techniques, while the fan-shaped amplitude filter is obtained by a 1-D coherent processing technique.

By comparison of results obtained by the broadband image deblurring with the narrow spectral band and coherent techniques, we have seen that the results obtained by the broadband deblurring offer a higher image quality. We have also shown that the broadband deblurring technique is very suitable for color image deblurring. We have provided several color image deblurring results obtained by the broadband deblurring technique. From these color deblurred images we have seen that the fidelity of the color reproduction is very high and the quality of deblurred image is rather good. Although there is some degree of color blur due to chromatic aberration of the transform lenses, it can be eliminated by utilizing higher-quality achromatic transform lenses. Further improvements of the deblurring can also be obtained by utilizing a blazed grating to achieve a higher smeared spectral diffraction efficiency so that a wider spatial band deblurring filter can be used to achieve a higher degree of deblurring.

2.8 Color Image Subtraction (Section X)

We have also accomplished a research project on color image subtraction with extended incoherent sources [11]. We have introduced a source encoding technique to obtain a point-pair spatial coherence function for the subtraction operation. The basic advantage of source encoding is to increase the available light power for the image subtraction operation, so that the inherent difficulty of obtaining incoherent point sources can

be alleviated. Since the technique uses incoherent sources, the annoying coherent artifact noise can be suppressed. We would see that the concept of color image subtraction may also be extended to the use of white-light source, for which a program is currently under investigation. In experimental demonstrations, we have shown that color subtracted images can be easily obtained by this incoherent subtraction technique. Since virtually all images of natural objects are color, the technique may offer a wide range of practical applications.

2.9 Rainbow Holographic Aberrations (Section XI)

We have also theoretically evaluated the primary aberrations and the bandwidth requirements for rainbow holographic processes [12]. The results obtained for the rainbow holographic process are rather general, for which the conventional holographic image resolution, aberrations, and bandwidth requirements, can be derived. The conditions for the elimination of the five primary rainbow holographic aberrations are also given. These conditions may be useful for the application of obtaining a high quality rainbow hologram image. In terms of bandwidth requirements, we have shown that the bandwidth requirement for a rainbow holographic construction is usually several orders lower than that of a conventional holographic process. Therefore, a lower-resolution recording medium has generally been used for most of the rainbow holographic constructions.

2.10 Pseudocolor Encoding with Three Primary Colors (Section XII)

We have also developed a white-light density pseudocolor encoder for three primary colors [13]. The advantages of this technique are; it is very cost effective and offers a high image resolution, as compared with the digital technique.

2.11 Partial Coherent Measurement (Section XIII)

We have accomplished a coherent measurement for our white-light optical signal processor [14]. The results show that the degree of coherence in this Fourier plane increases as the spatial frequency of the sampling grating increases. However, the improvement in coherence is somewhat more effective in the direction perpendicular to light dispersion. Since the white-light processor is capable of processing complex signal with entire spectral band of the light source, it is suitable for color signal processing.

2.12 Restoration of Out-of Focused Color Image (Section XIV)

We have also extended the color image deblurring to 2-D out-of-focused color photographic images [15]. Final results of this restoration technique have been obtained.

2.13 Solar-Light Optical Signal Processing (Section XV)

We have performed an experiment of optical signal processing with natural solar light [16]. We have shown that a white-light processor can be easily implemented with natural solar light for optical signal processing. The basic advantage of the solar optical processing is that the processing system does not require to carry an artificial light source, which is very suitable for spaceborne optical processing application. In addition to the simplicity, versatility, polychromaticity, and noise immunity of the white-light processing system, the solar processor is very durable and the operation is very cost effective.

2.14 White-Light Processing with Magneto-Optic Device (Section XVI)

We have also performed an application of a magneto-optic spatial light modulator with white-light processing [17]. We have shown that the magneto-optic device responds to the polarized white light, in which a wide

range of color object patterns can be generated. Since the magneto-optic device is a transmitted type spatial light modulator, it is very suitable for real-time programmable spatial filter synthesis and object pattern generation for optical signal processings.

2.15 Measurement of Noise Performance (Section XVII)

A measurement technique for the noise performance of a white-light optical signal processor is also performed in this period [18]. The technique utilizes a scanning photometer to trace out the output noise intensity fluctuation of the optical system. The effect of noise performance due to noise perturbation at the input and Fourier planes is measured. The experimental results, except for amplitude noise at the input plane, show the claims for better noise immunity, if the optical system is operating in the partially coherent regime. We have also measured the noise performance due to perturbation along the optical axis of the system. The experimental results show that the resulting output SNR improves considerably by increasing the bandwidth and source size of the illuminator. The optimum noise immunity occurs for phase noise at the input and output planes. For amplitude noise, the optimum SNR occurs at the Fourier plane. In brief, the experimental results confirm the analytical results that we recently evaluated.

2.16 White-Light Fourier Holography (Section XVIII)

In this research, we have also developed a technique for generating broad spectral band Fourier holograms with an encoded white light source [19]. Since this technique utilizes primary white-light construction and reconstruction process, it is quite suitable for color Fourier hologram image reconstruction.

2.17 Optical Generation of Speech Spectrogram with White-Light Source (Section XIX)

We have also developed a technique of generating speech spectrogram with a white-light optical processor [20]. Since the technique utilizes a white-light source, the speech spectrograms thus generated are frequency color-coded resulting in easier visual discrimination. The temporal-to-spatial conversion of speech signal is accomplished by means of density modulation with a CRT scanner. The scaling procedure of the speech spectrogram as well as the frequency resolution limit of the system are discussed.

2.18 Progress on Archival Color Film Storage (Section XIX)

In the research, we have completed an investigation of archival storage of color films with white-light optical processing technique [21]. We have developed a spatial encoding technique such that the moire fringe pattern inherently existing with the retrieved color image can be avoided. To improve the diffraction efficiency of the film, we have introduced a bleaching process so that the step of obtaining a positive encoded transparency can be eliminated. Instead of restricting the encoding processing in the linear region of the T-E curve, we would allow the encoding in the linear region of the D-E curve, so that a broader range of encoding exposure can be utilized. Experimental results indicate that excellent color fidelity, high signal to noise ratio, and good resolution of the reproduced color images can be obtained.

2.19 Generating False-Color Composites for Landsat Data (Section XXI).

We have developed a technique of false-color compositing by encoding multispectral remote sensing data with a low-cost white-light optical processor. Spatial encodings are made with various multispectral band

image transparencies, and false-coloring is obtained by color filtering the smeared Fourier spectra. In contrast to the low-resolution digital image, the white-light method generates a high-quality color-coded product. This image is free from coherent artifact noise because coherent light sources are not used. This simple and versatile technique may offer a wide range of applications. Three bands of multispectral Landsat data were processed using 70 mm black-and-white film negatives. These false-color encoded images allowed for discrimination of various Earth surface features. Forests, agricultural lands, water, urban areas, and strip mines could be shown on the images as each of these thematic classes were displayed as a different color.

2.20 Developed a Low-Cost White-Light Processor (Section XXII)

We have developed a white-light optical signal processor which can be coupled with a relatively unsophisticated system featuring low cost, portability, and high processing power-to-cost ratio [23]. The low-cost white-light optical processor (LCP) offers educators and businesses a powerful teaching aid while providing a system capable of optical processing usually associated with complex optical systems. Experimental results are provided for four processing techniques applied to the system. The methods applied are: scanning optical correlation and convolution, color schlieren optical processing, processing of bubble chamber event photographs, and density pseudocolor encoding. A full list of system equipment and details of the system construction are included. Emphasis is on the processing power available for low cost, making this a tool to be utilized in undergraduate optics laboratory courses.

2.21 White-Light Talbot Interferometer (Section XXIII)

In this research, we have developed a method for real-time color-coding of depth using a white-light Talbot interferometer [24]. Based on the fact that the Talbot planes of a grating are formed at different distances for different colors, the topographical structure of a surface can be color-coded in real-time. Experimental results are provided to verify the proposed method.

We have also in this phase of research developed a method of color visualization of a phase object based on Talbot effect [25]. If a grating is illuminated with a collimated white-light, the distance of the Talbot image will differ for different color. By placing an identical grating at a certain distance of negative or positive Talbot image, a single color output is extracted. A color visualization of a phase object placed between two gratings can be performed by a first-order spatial filtering. The hue is related to the first derivative of the phase distribution.

2.22 Analysis of Cross-Spectral Density Function for White-light

Processing (Section XXIV)

In this phase of research, we have analyzed a white-light optical processing system based on the cross-spectral density function. A plane-by-plane analysis is given, which includes the effects of source size and grating frequency. The degree of coherence in the Fourier plane is examined in detail, and an explanation of the fan-shaped deblurring filter based on this analysis is also provided [26].

2.23 Computer Generated Filters in White-light Processor (Section XXV)

We have also investigated the effects of computer generated filters as applied in a dispersed white-light processing system. Experimental results of computer-generated hologram (CGH) spatial filters applied to the

deblurring of color images are given. Significant performance can be achieved with moderate resolution images and 1-D processing operations. Color smear and multi-band filter/signal spectrum size mismatch limit applications involving large space-band-width images and/or 2-D processing operations with the dispersed system configuration. The flexibility of the CGH spatial filter fabrication technique, combined with the added processing dimension of wavelength and the inherent ability to reduce coherent artifact noise, make this processing scheme attractive for many image processing applications [27].

2.24 Holographic Tomography for 3-D Object Field (Section XXVI)

We have developed a holographic tomography concept by which a 3-D complex field may be studied and reconstructed from 2-D projected data [28]. A particular case of some opaque objects in a 3-D field is discussed as a preliminary application of this concept. The holographic multiplexing technique provides a series of projected data for tomographic reconstruction. With the algorithm used in computer post-processing, the image of a chosen slice in the studied field can be reconstructed from its one-dimensional projected data. The relative locations and the shapes of the objects inside the field are well defined by the reconstructed image. It is noted in this particular case, the principle used in the algorithm is much more suitable for convex object fields. This limitation arises from the fact that the projected data are the silhouettes of opaque objects. However, the ultimate objective is the study of 3-D complex fields. Hopefully, with the aid of holographic concept, some advantages such as reduction in computational procedures, may be achieved as compared with conventional tomographic techniques.

2.25 Medical Imaging with White-Light (Section XXVII)

Color enhancement of medical images has been shown to be effective in increasing the perceived dynamic range of the images and thereby the diagnostic value of those images. An analog pseudocoloring technique based upon Fourier optics has been developed in our laboratory to encode images obtained from such modalities as conventional X-ray, Ultrasound and CT. Emphasis is placed on the production of pseudocolored images mapped into the "heated-object" scale by way of primary intensity functions which are based on color matching principles and realized by film non-linearity properties. A final phase relief transparency contains the information required to produce the color scale when used as the input signal to the white-light optical processor [29].

2.26 Dual-Aperture Sampling with Partially Coherent Light (Section XXVIII)

We have also analyzed the effect on fringe visibility of a dual-aperture imaging system under partially coherent illumination [30]. The problem formulation is developed from the partial coherence theory of Wolf. The results show that the fringe visibility is affected by the spectral bandwidth, source size, sampling aperture size, as well as the defocused distance of the imaging system. These results are quite consistent with the Thompson's predictions of Young's experiment.

2.27 Application of LCTV to White-Light Processing (Section XXIX)

The applications of a low-cost commercially available flat screen transmission type LCTV to real-time elementary optical signal processing using white light sources have been studied. Although the picture is displayed on the LCTV based on a scanning process, the sufficiently long relaxation time of the pixels provide a partially spatially coherent input image. Thus, real-time optical signal processing can be carried out using

the LCTV instead of other extremely expensive light modulators. However, the LCTV has some drawbacks which are low resolution, low contrast and phase distortion. We like to stress that the LCTV is low cost, and that with further improvements, the LCTV should be very useful to both coherent and white-light optical signal processing [31].

2.28 Computer Generated Tricolor Sampling and Application (Section XXX)

We have also developed one-step method for recording color information on a monochrome transparency using a linear tricolor sampling pattern [32]. It was shown that the method avoids color-cross-talk, moire fringes, and marginal resolution loss. The linear tricolor sampling pattern is described in detail as well as a method for computer generating the tricolor grating. Color images retrieved using the grating show that the method is a viable alternative to previous three step encoding methods.

2.29 References

1. S. L. Zhuang, T. H. Chao and F. T. S. Yu, "Smeared Photographic Image Image Restoration with White-Light Optical Processing," Opt. Lett., 6, 109 (1981).
2. F. T. S. Yu, S. L. Zhuang and T. H. Chao, "Color-Photographic-Image Deblurring by White-Light Processing Technique," J. of Opt., 13, 57 (1982).
3. F. T. S. Yu, S. L. Zhunag and S. T. Wu, "Source Encoding for Partially Coherent Optical Processing," Appl. Phy., B27, 99 (1982).
4. S. T. Wu and F. T. S. Yu, "Source Encoding for Image Subtraction," Opt. Lett., 6, 452 (1981).
5. S. T. Wu and F. T. S. Yu, "Image Subtraction with Encoded Extended Incoherent Source," App. Opt., 20, 4082 (1981).
6. S. T. Wu and F. T. S. Yu, "Visualization of color Coded Phase Object Variation with Incoherent Optical Processing Technique," J. Opt., 13, 111 (1982).
7. S. L. Zhuang and F. T. S. Yu, "Coherence Requirement for Partially Coherent Optical Information Processing," Appl. Opt., 21, 2187 (1982).
8. S. L. Zhuang and F. T. S. Yu, "Apparent Transfer Function for Partially Coherent Optical Information Processing," Appl. Phy., B28, 359 (1982).
9. F. T. S. Yu, "Source Encoding, Signal Sampling, and Spectral Band Filtering For Partially Coherent Optical Signal Processing", J. Opt., 14, 173 (1983).
10. T. H. Chao, S. L. Zhuang, S. Z. Mao and F. T. S. Yu, "Broad Spectral Band Color Image Deblurring," Appl. Opt., 22, 1439 (1983).
11. F. T. S. Yu and S. T. Wu, "Color Image Subtraction with Encoded Extended Incoherent Source," Journal of Optics, 13, 183 (1982).
12. Y. W. Zhang, W. G. Zhu, and F. T. S. Yu, "Rainbow Holographic Aberrations and Bandwidth Requirements," Applied Optics, 22, 164 (1983).
13. F. T. S. Yu, X. X. Chen and T. H. Chao, "White-Light Density Pseudocolor Encoding with Three Primary Colors," J. Opt., 15, 55 (1984).
14. F. T. S. Yu, F. K. Hsu and T. H. Chao, "Coherence Measurement of a Grating-Based White-Light Optical Signal Processor," Appl Opt., 23, 333 (1984).
15. S. J. Lu and F. T. S. Yu, "Restoration of Out-of-Focused Color Photographic Images," Opt. Commun., 46, 278 (1983).

16. F. T. S. Yu and X. X. Chen, "Solar Optical Processing," Opt. Commun. 51, 377 (1984).
17. F. T. S. Yu, X. J. Lu and M. F. Cao, "Application of a Magneto-Optic Spatial Light Modulator to White-Light Optical Processing," Appl. Opt., 23, 4100 (1984).
18. F. T. S. Yu, L. N. Zheng and F. K. Hsu, "Measurement of Noise Performance for a White-Light Optical Signal Processor," Appl. Opt., 24, 173 (1985).
19. F. T. S. Yu and F. K. Hsu, "White-Light Fourier Holography," Opt. Commun., 52, 384 (1985).
20. F. T. S. Yu, T. W. Lin and K. B. Xu, "White-Light Optical Speech Spectrogram Generation," Appl. Opt., 24 836 (1985).
21. F. T. S. Yu, X. X. Chen and S. L. Zhuang, "Progress Report on Archival Storage of Color Films Utilizing a White-Light Processing Technique," J. Opt., 16, 59 (1985).
22. F. T. S. Yu and G. W. Peterson, "Generating False-Color Composites with a White-Light Optical Processor", Photogramm. Eng. and REMote Sensing, 52, 367 (1980).
23. F. T. S. Yu and H. M. Mueller, "A Low-Cost White-Light Optical Processor for the Undergraduate Optics Laboratory", IEEE Tran. Ed., E-28, 131 (1985).
24. S. Jutamulia, T. W. Lin and F. T. S. Yu, "Real-Time Color-Coding for Depth using a White-Light Talbot Interferometer", Opt. Commun., 58, 78 (1986).
25. S. Jutamulia, T. W. Lin and F. T. S. Yu, "Color Visualization of Phase Object Using Talbot Interferometer", J. Opt., 17, 129 (1986).
26. X. J. Lu and F. T. S. Yu, "Analysis of White-Light Processing Systems Based on Cross-Spectral Density Function", Submitted to J. Opt. Soc. Am.
27. M. S. Dymek and F. T. S. Yu, "Color Image processing with CGH Filters in a White-Light Optical System", Appl. Opt. (in press)
28. F. T. S. Yu, L. N. Zheng and T. W. Lin, "Holographic Tomography in Determining the Structure of Three Dimensional Object Fields", J. Opt., 17, 97 (1986).
29. P. M. Palmer, K. K. Shung and F. T. S. Yu, " Pseudocolor Encoding of Medical Images with White Light", IEEE Proc. 12th Annual Northeast Bioeng. Conf. 83 (1986).
30. F. T. S. Yu and Y. W. Zhang, "Fringe Visibility of Dual-Aperture Sampling with Partially Coherent Illumination", 25, 3191 (1986).

31. F. T. S. Yu, S. Jutamulia and X. L. Huang, "Experimental Application of Low-Cost Liquid Crystal TV to White Light Optical Signal Processing", Appl. Opt. 25, 3324 (1986).
32. F. T. S. Yu, X. X. Chin and K. E. McClure, "Computer Generated Linear Tricolor Sampling Pattern and its Application", J. Opt., 17, (1987).

SECTION III

Smeared-Photographic Image Deblurring

Smeared-photographic-image deblurring utilizing white-light-processing technique

S. L. Zhuang,* T. H. Chao, and F. T. S. Yu

Department of Electrical Engineering, The Pennsylvania State University, University Park, Pennsylvania 16802

Received September 22, 1980

A white-light-processing technique for smeared-photographic-image restoration is described. A simple technique of synthesizing a complex deblurring spatial filter is also given. Experimental demonstrations of smeared-image deblurring with a white-light-processing technique are provided. Compared with the coherent-processing technique, the white-light technique offers artifact-noise suppression, and the processing system is simple, versatile, and economical. We note that the white-light-processing technique is suitable for smeared-color-image restoration.

An interesting application of coherent optical information processing is restoration of smeared photographic images.¹⁻¹⁰ However, the unavoidable coherent artifact noise in the coherent optical-processing system frequently degrades the quality of the restored image. Thus, if a smeared photographic image can be restored with a white-light (i.e., incoherent) source, then coherent artifact noise may be avoided, and a higher quality of restored image can be obtained. Attempts to reduce the temporal-coherence requirement in optical information processing have been reported by several investigators.¹¹⁻¹³ One that uses incoherent instead of coherent optics has been pursued by Loventhal and Chavel,¹¹ and the other, which reduces the coherent requirement while still operating in complex amplitude, has been pursued by Leith and Roth.¹³

We have described¹⁴⁻¹⁸ white-light optical processing utilizing a diffraction-grating technique. We proposed that this technique be applied to complex signal detection,¹⁴ restoration of smeared photographic images,¹⁵ and image addition and subtraction.¹⁶ Recently we applied this white-light-processing technique to multi-image regeneration,¹⁹ archival storage of color films,²⁰ pseudocolor encoding,^{21,22} color restoration of faded color films,²³ and color image processing.^{24,25} We have shown that the white-light optical-processing system offers the advantage of artifact-noise suppression and that the system is simple and economical. The use of the diffraction-grating concept in coherent optical information processing for multiple-image storage was first reported by Mueller.²⁶ He also applied the same concept for color image retrieval.²⁷ Goedgebuer and Gazeu²⁸ recently employed light dispersion with a pair of prism dispersers to obtain spatial coherence for 1-D signal correlation.

In this Letter we demonstrate experimentally that a linear smeared image can be corrected with the white-light-processing technique. Since the essential part of optical processing is the synthesis of a deblurring complex filter,^{2,7,29,30} we will briefly describe a technique of deblurring filter synthesis.

First we describe the white-light-processing technique for smeared-image deblurring.

As is shown in Fig. 1, we place a smeared-image transparency in contact with a sinusoidal phase grating at the input plane P_1 . The complex light distribution, for a given wavelength λ , in the spatial frequency plane would be^{13,14}

$$E(\alpha, \beta; \lambda) = C_1 S(\alpha, \beta) + C_2 S\left(\alpha - \frac{\lambda f}{2\pi} p_0, \beta\right) + C_3 S\left(\alpha + \frac{\lambda f}{2\pi} p_0, \beta\right), \quad (1)$$

where $S(\alpha, \beta)$ is the Fourier spectrum of the smeared-image transparency $S(x, y)$, p_0 is the spatial frequency of the diffraction grating, f is the focal length of the achromatic transform lens, (α, β) is the spatial-coordinate system of the Fourier plane P_2 , and C 's are the complex constants. For simplicity, we assume that the input transparency is spatial frequency limited and that the smearing is in the y direction of the input spatial plane. We further assume that a narrow-band (i.e., band-limited) deblurring filter, for a given wavelength λ_0 , is provided, as is shown in Figs. 2 and 3 of Ref. 15.

If we insert the deblurring filter of $H(\beta)$ over a narrow spectral band of the smeared-signal spectra $S[\alpha - (\lambda f/2\pi)p_0, \beta]$ at $\lambda = \lambda_0$, then the complex light field at the output plane P_3 , for a given wavelength λ over the deblurring filter, can be evaluated by the following integral equation:

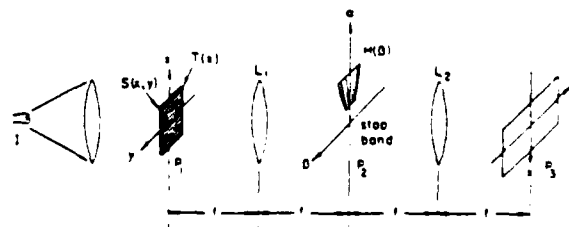


Fig. 1. A white-light optical information processor. 1, white-light point source; $S(x, y)$, smeared-image transparency; $T(x)$, diffraction grating; L_1 and L_2 , achromatic transform lenses; $H(\beta)$, deblurring spatial filter.

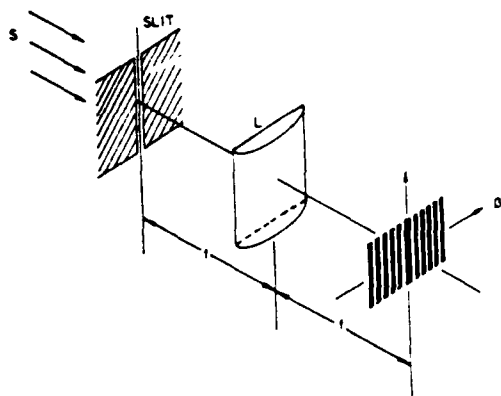


Fig. 2. Generation of amplitude filter. S, monochromatic plane wave; L, cylindrical transform lens.

$$g(x,y;\lambda) = C \int_{-\infty}^{\infty} \int_{\alpha_1}^{\alpha_2} S\left(\alpha - \frac{\lambda f}{2\pi p_0} \beta\right) H(\beta) \times \exp\left[\frac{2\pi}{\lambda f}(\alpha x + \beta y)\right] d\alpha d\beta, \quad (2)$$

where C is a complex constant and $H(\beta)$ is the deblurring filter. The corresponding output-light intensity distribution can be approximated by

$$I(x,y) \approx \int_{\Delta\lambda} |g(x,y;\lambda)|^2 d\lambda \approx K \Delta\lambda |S(x,y) \exp(ip_0 x) * h(y)|^2, \quad (3)$$

where $\Delta\lambda \approx \lambda_0 (4\Delta p/p_0)$ is the narrow spectral band of light over the deblurring filter, $h(y)$ is the spatial impulse response of $H(\beta)$, $*$ denotes the convolution operation, and K is a proportionality constant. From the above equation, we see that the filtered image is diffracted around the optical axis at the output-image plane P_3 .

We now describe a simple technique of synthesizing a deblurring filter in which the complex filter is synthesized as the product of an amplitude and a phase filter. The amplitude filter can be generated by recording a 1-D signal spectrum of a slit aperture on a photographic plate. The width of the slit corresponds to the smearing length of the blurred image.^{1,15} A 1-D cylindrical transform lens can be used to obtain an appropriate 1-D Fourier spectrum, as shown in Fig. 2. To obtain the required amplitude-transmittance function, we control the film gamma⁶ of the recorded film equal to 1.

In the generation of a deblurring phase filter, a black-and-white bar pattern on a high-contrast film, as shown in Fig. 3, is recorded. The width of the bar pattern is determined by the wavelength and the smearing length of the image.^{1,15} We also add a transparent reference point in an area near the recorded bar pattern. The recorded binary bar pattern is used as a mask to reproduce a number of gray-level bar patterns on a low-contrast photographic plate. If the recorded photographic plate is bleached, then a set of spatial phase filters can be obtained. To search for an appropriate π -phase filter, we used a Ronchi-type grating as an input object in a coherent optical processor and

placed a bleached reference point over the zero-order spectrum at the spatial-frequency plane, as shown in Fig. 4. If a contrast-reversed image is observed at the output plane, then the corresponding bleached bar pattern must be a π -phase filter with respect to the wavelength of the coherent source.

In an experimental demonstration, we first simulated a linear smeared photographic image. The simulation was accomplished by recording a linear object motion on a photographic film and then contact printing to obtain a positive smeared-image transparency. To ensure linearity in amplitude transmittance, we controlled the overall film gamma to about 2. The white-light source that we used for our experiments was a 75-W xenon-arc lamp with a 100- μ m pinhole, which acted as a point source. Since we used a white-light source, index-matching liquid gates were not used in our experiments. The spectral width of the deblurring complex filter used was about 100 Å, the center wavelength λ_0 was 5154 Å, and spatial bandwidth of the filter contained five main lobes. The results of the first experiments are shown in Fig. 5. A slit aperture of 0.5-mm width was used as a linear blurred object, as shown in Fig. 5(a). Figure 5(b) shows the deblurring image obtained with the white-light optical-processing technique. For comparison we also provide the deblurring image obtained with a coherent optical-pro-

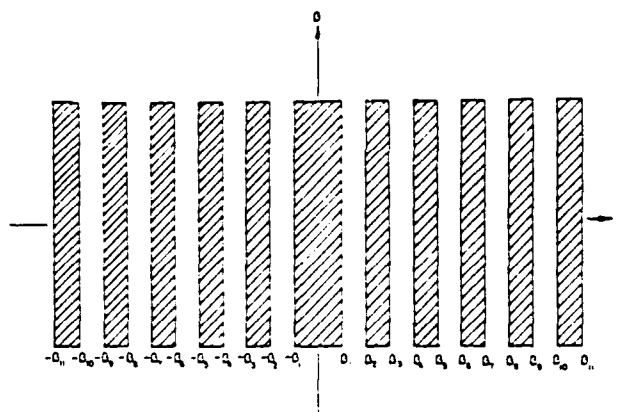


Fig. 3. Phase-filter mask.

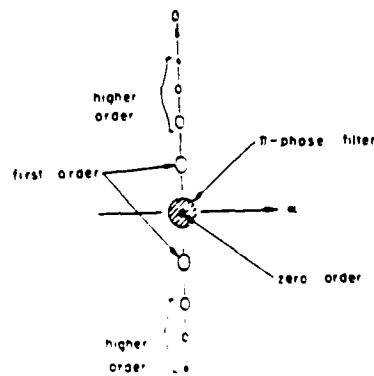


Fig. 4. A technique of determining a π -phase filter through contrast reversal.

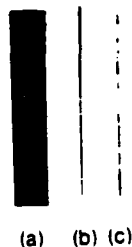


Fig. 5. Smeared-image restoration of a slit. (a) Original slit aperture, (b) deblurred with white-light processing, (c) deblurred with coherent processing.



Fig. 6. Smeared-image restoration of the word *optics*. (a) Original smeared image, (b) deblurred with white-light technique, (c) deblurred with coherent technique.

cessing technique, as shown in Fig. 5(c). From Fig. 5, we see that the coherent artifact noise was substantially suppressed with the white-light-processing technique. Compared with the original slit width, the deblurring ratio obtained with the white-light-processing technique is about 17 to 1.

As a second experimental result, Fig. 6(a) shows a linear smeared photographic image of a word *optics* as a blurred object. Figure 6(b) shows the deblurred image obtained with the white-light-processing technique, and Fig. 6(c) shows the result obtained with the coherent-processing technique. In our experiments, an argon laser emitting a wavelength of 5154 Å of green light was used. Again, from the results shown in Fig. 6, we see that the artifact noise was substantially reduced with the white-light-processing technique. The deblurred image obtained with the coherent technique appears to be sharper than the one obtained with the white-light technique because of the high spatial coherence of the light source. However, the drawback can be overcome if one uses a smaller white-light source (i.e., a pinhole) and a broad-spectral-band deblurring filter to cover the entire smeared-signal spectrum. In other words, a fan-shaped filter can be used to compensate for the changing size of the signal spectrum. Design of such a fan-shaped filter is under investigation. We believe that such a filter can be synthesized with an optical-coating or computer technique.

In conclusion, we point out that linear smeared-image restoration can be easily achieved with a white-light-processing technique. Compared with the deblurred images obtained with a coherent-processing technique, those obtained by white-light techniques exhibit lower coherent artifact noise. The white-light-processing technique described in this Letter possesses the advantages of both coherent and incoherent processing. For example, it is capable of processing the signal in complex amplitude like a coherent processor, and at the same time it suppresses the coherent noise like an incoherent processor. Moreover, the white-light de-

blurring technique is simple and economical. To compensate for the scaling of the signal spectrum, which is linearly proportional to wavelength, a fan-shaped filter can be used. Finally, we note that the white-light deblurring technique is also suitable for smeared-color-image restoration, which is currently being investigated.

We acknowledge the partial support of the National Science Foundation (grant Eng. 78-06864).

* Visiting scholar from Shanghai Optical Instrument Research Institute, Shanghai, China.

References

1. J. Tsujiuchi, "Correction of optical image by compensation of aberration and spatial frequency filtering," in *Progress in Optics*, Vol. 2 (North-Holland, Amsterdam, 1963).
2. G. W. Stroke and R. G. Zech, *Phys. Lett.* **25A**, 89 (1967).
3. G. W. Stroke, F. Furrer, and D. R. Lamberty, *Opt. Commun.* **1**, 141 (1969).
4. F. T. S. Yu, *Appl. Opt.* **8**, 53 (1969).
5. J. L. Horner, *J. Opt. Soc. Am.* **59**, 553 (1969).
6. J. L. Horner, *Appl. Opt.* **9**, 167 (1970).
7. J. Tsujiuchi, T. Honda, and T. Fukaya, *Opt. Commun.* **1**, 379 (1970).
8. F. T. S. Yu, *Introduction to Diffraction, Information Processing, and Holography* (MIT Press, Cambridge, Mass., 1973), Chap. 9.
9. F. T. S. Yu, *Optics and Information Theory* (Wiley-Interscience, New York, 1976), Chap. 7.
10. E. N. Leith, *Opt. Lett.* **5**, 70 (1980).
11. S. Lowenthal and P. Chavel in *Proceedings of the ICO Jerusalem 1976 Conference on Holography and Optical Processing*, R. Wiener and J. Shamir, ed. (Plenum, New York, 1977).
12. A. Lohmann, *Appl. Opt.* **16**, 261 (1977).
13. E. N. Leith and J. Roth, *Appl. Opt.* **16**, 2565 (1977).
14. F. T. S. Yu, *Opt. Commun.* **27**, 23 (1978).
15. F. T. S. Yu, *Appl. Opt.* **17**, 3571 (1978).
16. F. T. S. Yu and A. Tai, *Appl. Opt.* **18**, 2705 (1979).
17. F. T. S. Yu, in *Proceedings of the SPIE International Optical Computing Conference*, W. T. Rhodes, ed. (Society for Photo-Optical Instrumentation Engineers, Bellingham, Wash., 1980).
18. F. T. S. Yu and T. H. Chao, *Optik* **56**, 423 (1980).
19. F. T. S. Yu, S. L. Zhuang, and T. H. Chao, *Opt. Commun.* **34**, 11 (1980).
20. F. T. S. Yu, *Appl. Opt.* **19**, 2457 (1980).
21. T. H. Chao, S. L. Zhuang, and F. T. S. Yu, *Opt. Lett.* **5**, 230 (1980).
22. F. T. S. Yu *et al.*, *Appl. Opt.* **19**, 2986 (1980).
23. F. T. S. Yu and M. S. Dymek, *Appl. Opt.* (to be published).
24. F. T. S. Yu, T. H. Chao, and S. L. Zhuang, *Appl. Opt.* **19**, 1887 (1980).
25. F. T. S. Yu, G. G. Mu, and S. L. Zhuang, *Opt. Lett.* (to be published).
26. P. E. Mueller, *Appl. Opt.* **8**, 267 (1969).
27. P. E. Mueller, *Appl. Opt.* **8**, 2051 (1969).
28. I. P. Goedgebuer and R. Gazeu, *Opt. Commun.* **27**, 53 (1978).
29. A. W. Lohmann and D. P. Paris, *Appl. Opt.* **7**, 651 (1968).
30. R. M. Vasu and G. L. Rogers, *Appl. Opt.* **19**, 469 (1980).

SECTION IV

Image Subtraction with Incoherent Source

Source encoding for image subtraction

S. T. Wu* and F. T. S. Yu

Department of Electrical Engineering, The Pennsylvania State University, University Park, Pennsylvania 16802

Received March 27, 1981

A technique of source encoding of an extended incoherent source for image subtraction is presented. The source-encoding constraints are obtained from the coherence requirement for the subtraction operation. Source encoding increases the available light power for the processing operation, as a small incoherent source is no longer required. An experimental result obtained with the encoded incoherent-source technique is given. A similar result obtained by using a coherent technique is included for comparison.

Optical image subtraction with complex amplitude was described by Gabor *et al.*¹ more than a decade ago. The technique involves successive recordings of two or more complex diffraction patterns on a holographic plate and the subsequent reproduction of the composite hologram images. A few years later, Bromley *et al.*² described a holographic Fourier subtraction technique with which a real-time image and a previously recorded hologram image can be subtracted. Although Bromley *et al.* achieved good image subtraction in their experiments it appears that the illumination for the hologram image reconstruction must be arranged carefully. In a more recent paper, Lee *et al.*³ proposed a method whereby image subtraction and addition can also be achieved by a diffraction-grating technique. This technique involves the insertion of a diffraction grating in the spatial-frequency domain of the coherent optical processor.

However, most of the image subtraction techniques⁴ require a coherent source. Such sources introduce coherent artifact noise which limits their processing capabilities. In previous papers^{5,6} we have proposed a technique of image subtraction that requires an incoherent point source. However, a small incoherent source is difficult to obtain in practice. Nevertheless, this difficulty can be removed with the source-encoding technique that is discussed in this Letter.

Optical image subtraction with the diffraction-grating technique developed by Lee *et al.*³ is basically a one-dimensional processing operation. Instead of using a point source of light, one can use a line source perpendicular to the separation of the two input object transparencies. Since the image subtraction operates upon the corresponding image points to be subtracted, a strictly broad spatial-coherence requirement is not needed. Thus it is possible to encode an extended source in order to obtain a reduced point-pair spatial coherence for the image-subtraction operation.

In evaluating the spatial-coherence requirement for subtraction, we apply partially coherent imaging theory⁷ at the spatial-frequency plane P_3 of an optical processor, as shown in Fig. 1. The mutual coherence function is

$$\mu_3(x_3, x'_3) = \iint \mu_2(x_2, x'_2) f(x_2) f^*(x'_2) \times (\lambda f) [K_2(x_2, x'_2) f^*(x'_2) + O_2(x_2) O_1^*(x'_2)] dx_2 dx'_2 \quad (1)$$

where the integration is over the input plane P_2 , x_2 and x'_2 are the spatial-coordinate systems of P_2 and P_3 , $\mu_2(x_2, x'_2)$ is the complex coherence function at the input plane P_2 , $f(x_2)$ is the input object function at P_2 and can be expressed as $f(x_2) = O_1(x_2 - h_0) + O_2(x_2 + h_0)$; $O_1(x_2)$ and $O_2(x_2)$ are the two input object transparencies, and

$$K_2(x_2, x'_2) = \exp \left(i 2 \pi \frac{x_2 x'_2}{\lambda f} \right) \quad (2)$$

is the transmittance function between planes P_2 and P_3 , λ is the wavelength of the light source, and f is the focal length of the transform lens L_2 .

Thus the mutual coherence function immediately after the diffraction grating G , with a spatial period $d = (\lambda f)/h_0$, can be shown to be

$$\mu_3(x_3, x'_3) = \left[\exp \left(i 2 \pi \frac{h_0}{\lambda f} x_3 \right) - \exp \left(-i 2 \pi \frac{h_0}{\lambda f} x_3 \right) \right] \left[\exp \left(-i 2 \pi \frac{h_0}{\lambda f} x'_3 \right) - \exp \left(i 2 \pi \frac{h_0}{\lambda f} x'_3 \right) \right] \mu_3(x_3, x'_3) \quad (3)$$

where we ignored the dc term of the diffraction grating and $G = 1/2 [1 + \cos \{ 2 \pi (h_0/\lambda f) x_3 \}]$ is a cosine grating. We note that for complex image addition of sine grating should be used. The image intensity at the output plane P_4 is

$$I(x_4) = \iint \mu_3(x_3, x'_3) \exp \left(i 2 \pi \frac{x_3 - x'_3}{\lambda f} x_4 \right) dx_3 dx'_3 \quad (4)$$

where the integration is over the spatial-frequency plane and x_4 is the output spatial coordinate system.

Let us substitute Eqs. (2) and (3) into Eq. (4) and integrate over the spatial-frequency plane. Considering only the image terms around the origin of the output plane P_4 , we have

$$I_0(x_4) = [\mu_2(2h_0/\lambda f)] [O_1(x_4) - O_2(x_4)]^2 - (1 - [\mu_2(2h_0/\lambda f)] [O_1(x_4)]^2 - [O_2(x_4)]^2) \quad (5)$$

From Eq. (5) we see that the first term is proportional to the intensity of the subtracted image and the second term is proportional to the sum of the image irradiances.

where $|\mu(2h_0)|$ is the degree of spatial coherence. If the degree of coherence $|\mu(2h_0)|$ is high, i.e., if $|\mu(2h_0)| \approx 1$, then Eq. (5) reduces to

$$I_0(-x_4) \approx |O_1(x_4) - O_2(x_4)|^2, \quad |\mu_2(2h_0)| \approx 1. \quad (6)$$

Thus we see that spatial coherence is required for every pair of subtracted image points. In other words, only a point-pair spatial-coherence requirement $|\mu_2(x_2 - x'_2)| \approx 1$ for $|x_2 - x'_2| = 2h_0$ is needed for the subtraction operation.

In source-encoding, we let the intensity transmittance of the encoding mask be

$$S(x_1) = \sum_{n=1}^N \text{rect} \left(\frac{x_1 - nd}{s} \right), \quad (7)$$

a multiple-slit source, where N is the number of encoded slits, s is the slit width, and d is the spacing between slits of the encoding mask. We note that d is also the spatial period of the grating G . At the input plane P_2 , the spatial coherence function can be shown,⁷

$$\mu_2(x_2 - x'_2) = \frac{\sin \left(N\pi \frac{x_2 - x'_2}{h_0} \right)}{N \sin \left(\pi \frac{x_2 - x'_2}{h_0} \right)} \times \text{sinc} \left[\pi \frac{s}{dh_0} (x_2 - x'_2) \right], \quad (8)$$

where $d = \lambda f/h_0$. From this equation we see that the last sinc factor is identical with the single-slit case, which represents a broad spread of coherence over $(x_2 - x'_2)$. However, the first factor, for large values of N , converges to a sequence of narrow pulses. The locations of the pulses (i.e., the peaks) occur at every $x = x_2 - x'_2 = n\lambda f/d$, which yields a spatial-coherence discrimination of $n(\lambda f/d)$ over the input plane P_2 . Thus the multislit source encoding not only provides the point-pair coherence needed for image subtraction but also provides a higher available light power for the operation. In other words, the multislit encoding utilizes the light source more effectively so that the inherent difficulty of acquiring a small incoherent source can be removed.

In our experiment a mercury-arc lamp with a green filter was used as an extended incoherent source. A multislit mask was used to encode the light source. The

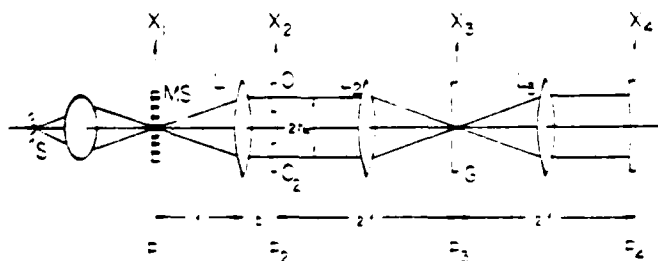


Fig. 1. Image subtraction with encoded extended incoherent source. S, mercury-arc lamp; MS, multislit mask; O_1 and O_2 , object transparencies; G, diffraction grating; L, transform lens.

APPLIED OPTICS

(a)

PP E
I

(b)

A L I D OPT CS

(c)

A L I D OPT CS

(d)

Fig. 2. Image subtraction. (a), (b) Input object transparencies, (c) subtracted image obtained with incoherent technique, (d) subtracted image obtained with coherent technique.

slit width s was $2.5 \mu\text{m}$, the spacing between slits was $25 \mu\text{m}$, and the overall size of the mask, which contained about 100 slits, was about $2.5 \text{ mm} \times 2.5 \text{ mm}$. The focal lengths of the transform lenses were 300 mm. A liquid gate, which contained the two object transparencies of size $6 \text{ mm} \times 8 \text{ mm}$ was inserted immediately behind the collimator. A sinusoidal phase grating with a period of $25 \mu\text{m}$ was used in the spatial-frequency plane P_3 . The separation between the two input images to P_2 was 13.2 mm.

In our experiments, a set of binary images as shown in Figs. 2(a) and 2(b) was used as input objects. Figure 2(c) shows the subtracted image obtained with this source-encoding technique. For comparison the subtracted image obtained with the conventional coherent processing technique is shown in Fig. 2(d). As can be seen, we obtained better artifact-noise suppression by using the incoherent technique, which results in a better subtracted image.

We have introduced a source-encoding technique for image subtraction. We stress that the concept of source encoding may be extended to other information processing operations. We also note that image subtraction with the encoded extended incoherent-source technique is generally simple, versatile, and economical to operate. It may offer a wide range of practical applications. In addition, the technique is also capable of operating in a real-time mode.

The authors wish to acknowledge the assistance of H. Shoemaker and J. R. Monkowski and his students of the Solid State Laboratory, The Pennsylvania State University in the preparation of the encoding masks. We also wish to thank S. L. Zhuang for his valuable comments and suggestions. This work has been supported by U.S. Air Force Office of Scientific Research under grant no. AFSOR-81-0145.

S. T. Wu is a visiting scholar from Shanghai Institute of Optics and Fine Mechanics, Academia Sinica, China.

References

1. J. Gao, G. W. Stroke, R. Barakat, A. Fung, J. Lee, and J. Brumm, *Proc. SPIE* 18, 114 (1977).

2. K. Bromley, M. A. Monahan, J. F. Bryant, and B. J. Thompson, *Appl. Phys. Lett.* **14**, 67 (1969).
3. S. H. Lee, S. K. Yao, and A. G. Milnes, *J. Opt. Soc. Am.* **60**, 1037 (1970).
4. J. F. Ebersole, *Opt. Eng.* **14**, 436 (1975).
5. F. T. S. Yu and A. Tai, *Appl. Opt.* **18**, 2705 (1979).
6. F. T. S. Yu, *Proc. Soc. Photo-Opt. Instrum. Eng.* **232**, 9 (1980).
7. M. Born and E. Wolf, *Principles of Optics*, 2nd ed. (Pergamon, New York, 1964).

Image subtraction with an encoded extended incoherent source

S. T. Wu and F. T. S. Yu

A technique of encoding an extended incoherent source for image subtraction is presented. The source encoding is obtained from the coherence requirement for image subtraction operation. Since the coherence requirement is a point-pair concept for image subtraction the encoding can take place by spatial sampling an extended incoherent source with narrow slit apertures. The basic advantage of the source encoding is to increase the available light power for the processing operation, so that the inherent difficulty of obtaining a very small incoherent source can be alleviated. Experimental results obtained with this encoded incoherent source are given. Comparisons with the results obtained by processing technique are also provided.

1. Introduction

One most interesting and important application of optical information processing must be image subtraction. The applications may be of value in urban development, earth resource studies, meteorology, highway planning, land use, inspection, automatic tracking and surveillance, etc. Optical image subtraction may also apply to electrical and video communications as a means of bandwidth compression. For example, it is only necessary to transmit the differences between the code words or images in successive cycles rather than the whole code word or the entire image in each cycle (e.g., TV).

In 1965, optical image synthesis by complex amplitude subtraction was first described by Gabor *et al.*¹ The technique involves successive recordings of two or more complex diffraction patterns on a holographic plate and the subsequent reproduction of the composite hologram images. A few years later, Bromley *et al.*² described a holographic Fourier subtraction technique, for which a real-time image and a previously recorded hologram image can be subtracted. Although good image subtraction by their experiments had been reported, it appears that the illumination for the hologram image reconstruction must be arranged carefully. In 1970, Lee *et al.*³ proposed a technique so that image subtraction and addition can also be achieved by a diffraction grating technique. This technique involves

insertion of a diffraction grating in the spatial frequency domain of the coherent optical processor. Good results by the diffraction grating technique were also reported in their article. In a more recent article, Zhao *et al.*⁴ also proposed a technique of image subtraction utilizing a halftone screen method. However, their technique cannot be implemented in real time.

There are several other techniques available for image subtraction which can be found in a review paper by Ebersole.⁵ However, most of the optical information processing techniques require a coherent source to carry out the subtraction operation. But coherent optical processing systems are plagued with coherent artifact noise, which frequently limits their processing capabilities.

We have in previous papers^{6,7} proposed a technique of optical processing with an incoherent source for complex signal detection and image debiurring.^{8,9} We have also extended the technique for possible application to image subtraction.^{10,11} However, to obtain a spatial coherence requirement for subtraction operation a very small source size is needed, but a small incoherent source is difficult to obtain in practice. Nevertheless, this difficulty may be alleviated with a source encoding (i.e., spatial sampling) technique, so that the extended incoherent source can be used. We have briefly discussed in a recent communication that image subtraction can indeed obtain with an encoded extended source.¹² The basic objective of source encoding is to utilize the light power more effectively so that image subtraction can be carried out with an extended incoherent source. Moreover, with the use of an incoherent source, coherent artifact noise can be avoided. We stress that this image subtraction system is capable of operating in the real-time mode, and it is generally simple, versatile, and economical.

The authors are with Pennsylvania State University, Electrical Engineering Department, University Park, Pennsylvania 16802.

Received 25 March 1981.

0003-6935/81/254082-07\$01.50/0

© 1981 Optical Society of America

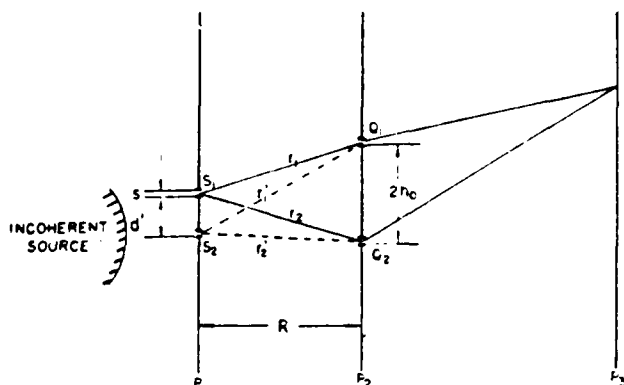


Fig. 1. Young's experiments with an extended source.

Basically, the optical image subtraction is a 1-D processing operation. Instead of utilizing a point source of light, a line source of light can be used for the subtraction operation. Since the spatial coherence requirement for subtraction operation is a point-pair concept, a strictly coherence requirement is not needed. In other words, it is possible to encode an extended incoherent source to obtain a point-pair coherence requirement for image subtraction operation.

II. Young's Experiment with Extended Source

We will now illustrate the concept of Young's experiment for the source encoding. Let us consider first a narrow slit of light source S_1 situated in plane P_1 to Fig. 1. To maintain a high degree of spatial coherence between apertures Q_1 and Q_2 , the source S_1 should be very narrow. In other words, if the separation between the two open apertures is larger, the narrower incoherent source S_1 is required. It can be shown that, to maintain a high degree of coherence, the slit size can be approximated by^{13,14}

$$S \approx [\lambda / (2h_0)] R, \quad (1)$$

where R is the distance between planes P_1 and P_2 .

We now consider two narrow slits of light sources S_1 and S_2 , as shown in Fig. 1. If the separation d between the two sources S_1 and S_2 satisfies the relation

$$r_1 - r_2 = (r_1 - r_2) + m\lambda, \quad (2)$$

where the r 's are the distances from sources S_1 and S_2 to the open apertures Q_1 and Q_2 as shown in the figure, m is an arbitrary integer, and λ is the wavelength of the light source, the interference fringes due to each slit source are in-phase, and a brighter fringe pattern can be observed at plane P_3 . With the application of Eq. (2), we can employ many narrow slit sources since we wish to obtain a coherent fringe pattern at the output plane P_3 . We note that the separations between any of the two slit sources should satisfy the fringe (i.e., spatial coherence) condition of Eq. (2). If the separation R between planes P_1 and P_2 is large, i.e., $R \gg d$, and $R \gg 2h_0$, the coherent condition of Eq. (2) becomes

$$d = \pm [2h_0 / \lambda]. \quad (3)$$

From this equation we see that equal spacing slits can be used so that a brighter fringe pattern can be observed. We note that the intensity of the fringe pattern increases linearly as the number of slits increases. Thus on one hand the source encoding preserves the coherence requirement, and on the other hand it increases the overall intensity of illumination. Therefore, with appropriate source encoding, an extended source may be efficiently utilized.

III. Spatial Coherence Requirement

We will now adopt the concept of source encoding in evaluating the spatial coherence requirement for image subtraction operation. With reference to the incoherent optical processor of Fig. 2, we see that the processor is similar to that of a coherent optical processor except with an extended incoherent source and an encoding mask. Since image subtraction is a 1-D operation, we will adopt a 1-D notation for our analysis.

In evaluating the spatial coherence requirement, we use partially coherent imaging theory.^{13,14} The mutual coherence function at the spatial frequency plane P_3 is

$$\mu_3(x_3, x_3) = \iint \mu_2(x_2, x_2) f(x_2) f^*(x_2) K_2(x_2, x_3) \times K_2^*(x_2, x_3) dx_2 dx_2, \quad (4)$$

where the integration is over the input plane P_2 ; x_2 , x_2 , x_3 , and x_3 are the position coordinates of P_2 and P_3 , respectively, $\mu_2(x_2, x_2)$ is the complex coherence function at the input plane P_2 ; $f(x_2)$ is the input function at P_2 , which can be expressed as

$$f(x_2) = O_1(x_2 - h_0) + O_2(x_2 + h_0), \quad (5)$$

where $O_1(x_2)$ and $O_2(x_2)$ are the two input object transparencies and

$$K_2(x_2, x_3) = \exp\left(i2\pi \frac{x_2 x_3}{\lambda f}\right) \quad (6)$$

is the transmittance function between planes P_2 and P_3 , λ is the wavelength of the light source, and f is the focal

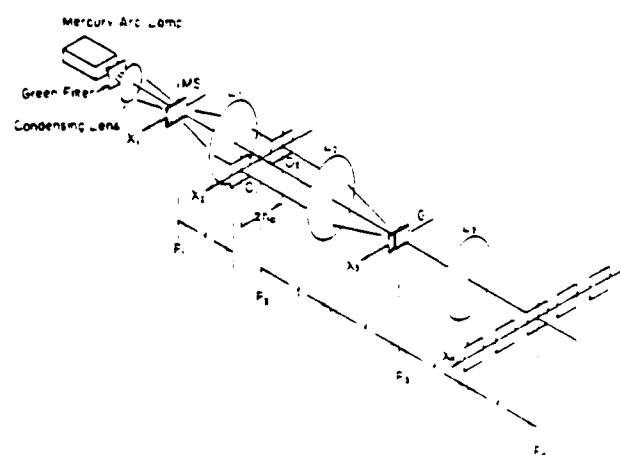


Fig. 2. Image subtraction with an encoded extended incoherent source: S, mercury arc lamp; MS, multislit mask; O_1 and O_2 , object transparencies; G, diffraction grating; L, transform lens.

length of the transform lens L_2 . Equation (4) can also be written

$$\begin{aligned} \mu_3(x_3, x_3') &= \iint \mu_2(x_2, x_2') [O_1(x_2 - h_0) + O_2(x_2 + h_0)] \\ &\quad \times [O_1^*(x_2' - h_0) + O_2^*(x_2' + h_0)] \\ &\quad \times \exp\left(i2\pi \frac{x_3 x_2 - x_3' x_2'}{\lambda f}\right) dx_2 dx_2', \end{aligned} \quad (7)$$

where superscript * denotes the complex conjugate.

It is clear that the mutual coherence function immediately behind the diffraction grating G , with a spacing period $d = (\lambda f)/h_0$, is

$$\begin{aligned} \mu_3(x_3, x_3') &= \left[\exp\left(i2\pi \frac{h_0}{\lambda f} x_3\right) - \exp\left(-i2\pi \frac{h_0}{\lambda f} x_3\right) \right] \\ &\quad \times \left[\exp\left(-i2\pi \frac{h_0}{\lambda f} x_3'\right) - \exp\left(i2\pi \frac{h_0}{\lambda f} x_3'\right) \right] \mu_3(x_3, x_3'), \end{aligned} \quad (8)$$

where we ignore the dc term of the diffraction grating. The image intensity at the output plane P_4 is

$$I(x_4) = \iint \mu_3(x_3, x_3') \exp\left(i2\pi \frac{x_4 - x_4'}{\lambda f} x_3\right) dx_3 dx_3', \quad (9)$$

where the integration is over the spatial frequency plane, and x_4 is the output spatial coordinate system.

By substituting Eqs. (7) and (8) into Eq. (9) and integrating over the spatial frequency plane, we have

$$\begin{aligned} I(x_4) &= \iint \mu_2(x_2, x_2') [O_1(x_2 - h_0) + O_2(x_2 + h_0)] [O_1^*(x_2' - h_0) + O_2^*(x_2' + h_0)] \\ &\quad \times [\delta(x_2 + x_4 + h_0)\delta(x_2' + x_4 + h_0) + \delta(x_2 + x_4 - h_0)\delta(x_2' + x_4 - h_0) \\ &\quad - \delta(x_2 + x_4 + h_0)\delta(x_2' + x_4 - h_0) - \delta(x_2 + x_4 - h_0)\delta(x_2' + x_4 + h_0)] dx_2 dx_2', \end{aligned} \quad (10)$$

where $\delta(x)$ is the Dirac delta function. Let us assume that $\mu(x_2, x_2')$ takes the form $\mu(x_2 - x_2')$ and $\mu(x) = \mu^*(-x)$. If we evaluate Eq. (10) termwise and note that the input images are spatially limited, we have

$$\begin{aligned} I(x_4) &= \mu(0) [|O_1(-x_4)|^2 + |O_2(-x_4)|^2] - \mu(2h_0) O_1(-x_4) O_2^*(-x_4) \\ &\quad - \mu^*(2h_0) O_1^*(-x_4) O_2(-x_4) + \mu(0) [O_1(-x_4 - 2h_0)|^2 \\ &\quad + |O_2(-x_4 + 2h_0)|^2], \end{aligned} \quad (11)$$

where $\mu(2h_0) = |\mu(2h_0)| \exp(i\phi)$ is a complex quantity. We stress that phase factor ϕ can be avoided by adjusting the grating position G .

We now consider only the image terms around the origin of the output plane P_4 .

$$\begin{aligned} I_0(-x_4) &= |\mu(2h_0)| [O_1(x_4) - O_2(x_4)]^2 \\ &\quad + [1 - |\mu(2h_0)|] [|O_1(x_4)|^2 + |O_2(x_4)|^2], \quad \text{for } c = 0. \end{aligned} \quad (12)$$

From Eq. (12) we see that the first term is proportional to the intensity of the subtracted image, and the second term is proportional to the sum of the image irradiances, where $|\mu(2h_0)|$ is the degree of spatial coherence. If the degree of coherence $|\mu(2h_0)|$ is high, i.e., $\mu(2h_0) \approx 1$, Eq. (12) reduces to

$$I_0(-x_4) \approx |O_1(x_4) - O_2(x_4)|^2, \quad \text{for } |\mu(2h_0)| \approx 1. \quad (13)$$

Thus we see that the spatial coherence is only needed for every pair of points $(x_2 - x_2') = 2h_0$. In other words, only a point-pair spatial coherence is required for subtraction operation.

IV. Source Encoding

We will now search a source encoding so that point-pair spatial coherence can be established. We will adopt the concept of Young's experiment that we described in a previous section. Now we insert a mask transparency for the source encoding at the front focal plane P_1 of the collimator L_1 as shown in Fig. 2. The spatial coherent function $\mu(x_2, x_2')$ over the input plane P_2 can be written¹³

$$\mu(x_2, x_2') = \int S(x_1) K_1(x_1, x_2) K_1^*(x_1, x_2') dx_1, \quad (14)$$

where $S(x_1)$ is the intensity transmittance function of the mask, and $K_1(x_1, x_2)$ is the transmittance function between planes P_1 and P_2 . We assume that the mask is located within an isoplanatic patch, and $K_1(x_1, x_2)$ can be written¹³

$$K_1(x_1, x_2) = \exp\left[i2\pi \frac{x_1 x_2}{\lambda f} + \epsilon\left(x_2 - x_1 \frac{b}{f}\right)\right], \quad (15)$$

where $\epsilon(x)$ is the wave aberration of the collimator, and b is the distance between the collimator and the input plane P_2 .

We note that if b is sufficiently small, i.e., $(b/f)x_{1\max} \ll x_2$, the transmittance function of Eq. (15) can reduce to

$$K_1(x_1, x_2) \approx \exp\left[i2\pi \frac{x_1 x_2}{\lambda f} + \epsilon(x_2)\right]. \quad (16)$$

By substituting Eq. (16) into Eq. (14), the spatial coherence function becomes

$$\begin{aligned} \mu(x_2, x_2') &= \exp[i\epsilon(x_2) - \epsilon(x_2')] \\ &\quad \times \int S(x_1) \exp\left[i2\pi \frac{x_1}{\lambda f} (x_2 - x_2')\right] dx_1. \end{aligned} \quad (17)$$

From the above equation we see that the spatial coherence function is the Fourier transform of the mask transmittance function modulated by a phase (wave aberration) factor. However, the phase aberration will not affect the degree of mutual coherence $|\mu(x_2, x_2')|$. In the remaining analysis, we shall ignore the phase aberration and assume that $\mu(x_2, x_2')$ takes the form $\mu(x_2 - x_2')$.

Now we evaluate the degree of coherence $|\mu(2h_0)|$ for two different cases. We will first evaluate a single-slit encoding, i.e.,

$$S(x_1) = \text{rect}(x_1/s), \quad (18)$$

where s is the slit width. By substituting Eq. (18) into Eq. (17), we have

$$\mu(x_2 - x_2') = \text{sinc} \frac{\pi s}{\lambda f} (x_2 - x_2'), \quad (19)$$

where the phase factor was ignored. Since the spacing

Table I. Spatial Coherence Requirement for Single-Slit Mask

s/d	1/2	1/5	1/10	1/20
$\mu(2h_0)$	0	0.756	0.936	0.988

period of the grating $G, d = (f\lambda)/h_0$, if we let $x_2 - x'_2 = 2h_0 = (2f\lambda)/d$, Eq. (19) can be written

$$\mu(2h_0) = \text{sinc}\left(2\pi \frac{s}{d}\right). \quad (20)$$

Thus we see that the degree of spatial coherence $|\mu(2h_0)|$ depends upon the ratio of the slit width s to the spacing d .

To gain a feeling of magnitude, we provide several values of $\mu(2h_0)$ in Table I, from which we can see that a high degree of spatial coherence can be attained only through a very narrow slit. For example, if the spacing of the grating $d = 25 \mu\text{m}$, to achieve a high degree of spatial coherence a slit width $s \leq 2.5 \mu\text{m}$ should be used. Thus it makes the source too weak for a practical processing operation.

As noted in the previous section, the spatial coherence requirement for image subtraction is a point-pair problem. It is possible to encode the extended source with N number of narrow slits. Thus with a multislit source encoding, an N -fold light power can be used for the image subtraction operation.

We will now let the intensity transmittance of the encoding mask be

$$S(x_1) = \sum_{n=1}^N \text{rect}\left(\frac{x - nd'}{s}\right), \quad (21)$$

where s is the slit width, and d' is the spacing between slits.

By substituting Eq. (21) into Eq. (17), the spatial coherence function becomes

$$\mu(x) = \frac{\sin\left(N\pi \frac{d'x}{\lambda f}\right)}{N \sin\left(\pi \frac{d'x}{\lambda f}\right)} \text{sinc}\left(\frac{\pi s}{\lambda f} x\right), \quad (22)$$

where $x = x_2 - x'_2$. From the above equation we see that the last sinc factor is identical to the single-slit case of Eq. (19), which represents a broad spread of coherence over x . However, the first factor for large values of N converges to a sequence of narrow pulses. The locations of the pulses (i.e., the peaks) occur at every $x = x_2 - x'_2 = n(\lambda f/d')$. Thus this factor yields the fine spatial coherence discrimination at every point-pair separated at distance $(\lambda f/d')$ over the input plane P_2 .

If we let the spacing of d' equal the spacing d of the diffraction grating G (i.e., $d' = d$), the spatial coherence of Eq. (22) becomes

$$\mu(x) = \frac{\sin\left(N\pi \frac{x}{h_0}\right)}{N \sin\left(\pi \frac{x}{h_0}\right)} \text{sinc}\left(\pi \frac{sx}{\lambda h_0}\right), \quad (23)$$

where we substitute $d = (\lambda f)/h_0$. From Eq. (23), we see that a sequence of narrow pulses occurs at $x = x_2 - x'_2 = nh_0$, where n is an integer, and their peak values are

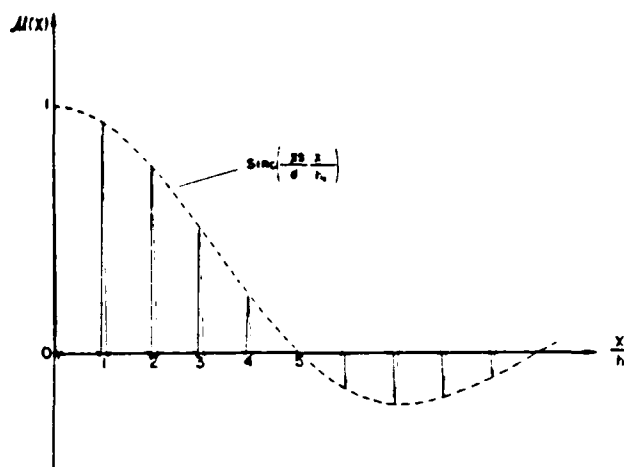


Fig. 3. Coherence function obtained with multislit source encoding, where $x = |x_2 - x'_2|$ and $s/d = 1.5$.

weighed by a broader sinc factor, as shown in Fig. 3. It can be shown that the width of the pulses is inversely proportional to the number of slits N . Thus the multislit source encoding not only provides a point-pair coherence requirement for image subtraction but also a higher available light power for the operation. In other words, the multislit encoding utilizes the light source more efficiently, so that the inherent difficulty of acquiring a small incoherent source can be alleviated.

V. Temporal Coherence Requirement

So far we have considered only the quasi-monochromatic light, but the effect of the temporal coherence has not been discussed. Since the scale of Fourier spectrum varies with wavelength, there is a temporal coherence requirement for every processing operation. With this consideration, we must limit the temporal bandwidth $\Delta\lambda$ of the source so that the dispersed Fourier spectra will not spread beyond the allowable limit. In the image subtraction operation, we should limit the spectrum spread within a very small fraction of the grating spacing d , i.e.,

$$[p_m(f\Delta\lambda)/(2\pi)] \ll d, \quad (24)$$

where p_m is the highest angular spatial frequency of the input objects, f is the focal length of the transform lens, and $\Delta\lambda$ is the spatial bandwidth of the source. Therefore, the temporal bandwidth of the source should be limited by the following inequality:

$$\frac{\Delta\lambda}{\lambda} \ll \frac{2\pi}{f_0 p_m}, \quad (25)$$

where λ is the center wavelength of the light source, and $2h_0$ is the separation of the input images.

To gain a practical feeling, we let $h_0 = 6.6 \text{ mm}$, $\lambda = 5461 \text{ Å}$ and take a factor of 10 of Eq. (25). The temporal bandwidth requirements $\Delta\lambda$ for various values of spatial frequencies p_m are tabulated in Table II. We see that, if the spatial frequency of the input objects is low, a broader temporal bandwidth of the light source can be

Table II. Temporal Coherence Requirements

$\frac{P_m}{2\tau}$ (lines/mm)	0.5	1	5	20	100
$\Delta\lambda(\text{\AA})$	166	83	16.5	4.1	0.8

used. In other words, the higher the spatial frequency of the input objects, the narrower the temporal bandwidth required. We assumed that all the lenses are achromatic.

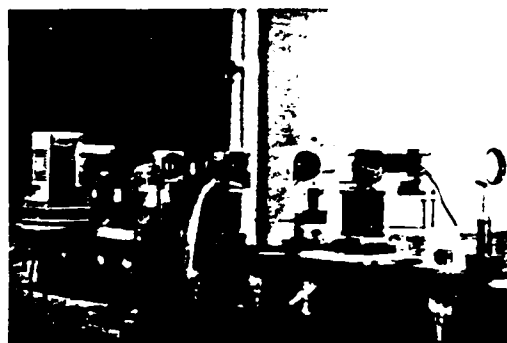
VI. Experimental Results

In our experiments, a mercury arc lamp with a green filter was used as an extended incoherent source. A multislit mask was used to encode the light source. The slit width s was $2.5\ \mu\text{m}$, the spacing of slits d' was $25\ \mu\text{m}$, and the overall size of the mask was $\sim 2.5 \times 2.5\ \text{mm}^2$, which contained ~ 100 slits. The focal length of the transform lenses was $300\ \text{mm}$. A liquid gate containing two object transparencies of $\sim 6 \times 8\text{-mm}^2$ size was inserted immediately behind the collimator. A sinusoidal phase grating with a spacing period of $25\ \mu\text{m}$ was used in the spatial frequency plane P_3 of Fig. 2. The separation between the two input images to P_2 was $13.2\ \text{mm}$. We evaluated the coherence area at the input plane P_2 as $\sim 75 \times 75\ \mu\text{m}^2$. We note that the coherence area is rather small and the spacing of the diffraction grating should be accurately matched with the spacing of the slits.

For our first demonstration, we provide two continuous tone images as input object transparencies as shown in Figs. 4(a) and (b). By comparing these two figures, we see that a liquid gate was withdrawn from the optical bench in Fig. 4(b). Figure 4(c) shows the subtracted image obtained with this incoherent processing technique, while Fig. 4(d) is obtained with the coherent processing technique. From the result obtained with the incoherent technique, a profile of a subtracted liquid gate can be seen. While from the result obtained with the coherent technique, the subtracted image is severely damaged by the coherent artifact noise. Thus we see that the incoherent technique offers a better image quality and contains virtually no coherent artifact noise.

Although a liquid gate was used in the experiment, however, the phase fluctuation created by the density fluctuation of the photographic film cannot be completely compensated. As Chavel and Lowenthal^{16,17} have shown, incoherent processing can indeed suppress the phase noise effectively, which can be seen from Fig. 4(c).

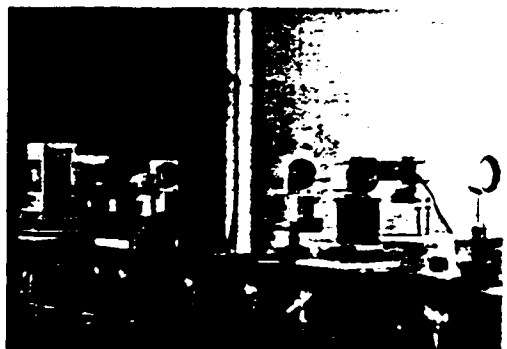
For our second demonstration, we again provide two continuous tone objects of a parking lot as input object transparencies, as shown in Figs. 5(a) and (b). From these two input object transparencies, we see that a dark gray small passenger car in a parking lot as shown in Fig. 5(a) is missing in Fig. 5(b). Figure 5(c) is the result of a subtracted image obtained from the incoherent image subtraction technique as described in this paper. In



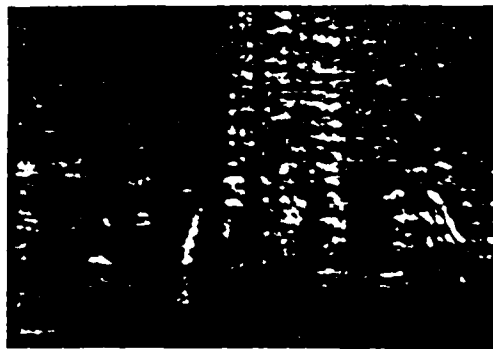
(a)



(b)



(c)



(d)

Fig. 4 Image subtraction: continuous tone objects (a) and (b) input object transparencies; (c) subtracted image obtained with an incoherent technique; (d) subtracted image obtained with a coherent technique.

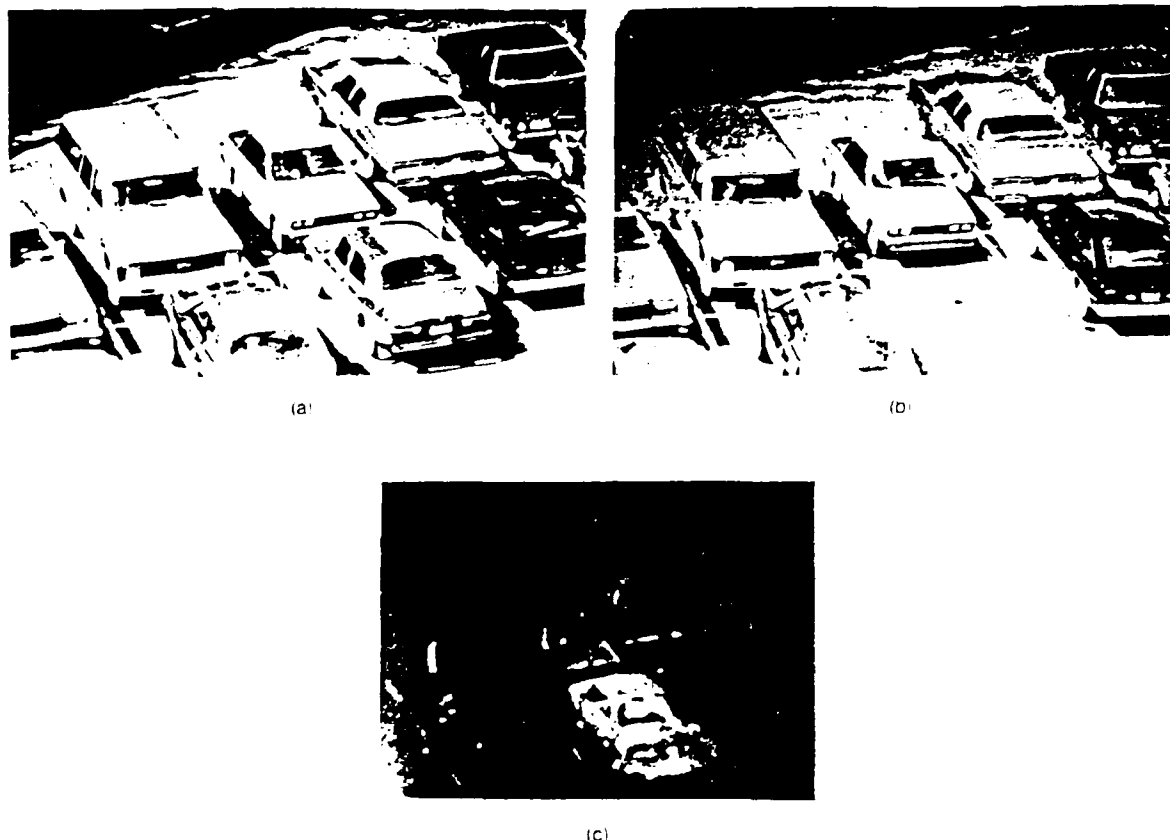


Fig. 5. Image subtraction: parking lot: (a), (b) input object transparencies; (c) subtracted image obtained with an incoherent technique

this figure, the profile of the missing passenger car can readily be seen at the output image plane P_4 . It is also interesting to note that the parking line on the right side of the missing passenger car and the shadow can clearly be seen in the subtracted image of Fig. 5(c).

VII. Summary

We have introduced a source encoding technique for image subtraction. The source encoded function was evaluated from a specific coherence requirement for image subtraction operation. Since the image subtraction is a point-pair problem, and the processing is essentially a 1-D operation, it is possible to obtain a required coherence function by encoding an extended source with a set of narrow slits. In other words, the slit width, the spacing of the slits, and the number of slits determine the spatial coherence requirement.

The basic advantage of the source encoding is to increase the available light power for the processing operation, so that the inherent difficulty of acquiring a very small incoherent source can be alleviated. We stress that the concept of source encoding may be extended to other incoherent information processing operations.

Aside from the spatial coherence requirement, there is, however, a temporal coherence requirement for the

image subtraction operation. If the spatial frequency requirement for the image subtraction is high, a higher temporal coherence (i.e., a narrower spectral width) of the light source is required.

In experimental demonstrations, we have shown both the results obtained with the incoherent processing and coherent processing techniques. By comparing these results, we conclude that the incoherent processing technique offers a better artifact noise suppression and better image quality.

Finally, we also stress that the incoherent image subtraction technique is generally very simple, versatile, and economical to operate. It may offer a wide range of practical applications. In addition, the technique is also capable of operating in a real-time mode.

The authors wish to acknowledge H. Shoemaker, J. R. Monkowski, and their students of the Solid State Laboratory for their assistance in preparing the encoding masks. Many thanks go to S. L. Zhuang for his valuable comments and suggestions. The authors also wish to acknowledge the support by the U.S. Air Force Office of Scientific Research grant AFSOR-81-0148.

S. T. Wu is a visiting scholar from the Shanghai Institute of Optics & Fine Mechanics, Academia Sinica, China.

References

1. D. Gabor, G. W. Stroke, R. Restrick, A. Funkhouser, and D. Brumm, *Phys. Lett.* **18**, 123 (1965).
2. K. Bromley, M. A. Monahan, J. F. Bryant, and B. J. Thompson, *Appl. Phys. Lett.* **14**, 67 (1969).
3. S. H. Lee, S. K. Yao, and A. G. Milnes, *J. Opt. Soc. Am.* **60**, 1037 (1970).
4. D. Z. Zhao, C. K. Chiang, and H. K. Lin, *Opt. Lett.* **6**, 490 (1981).
5. J. F. Ebersole, *Opt. Eng.* **14**, 436 (1975).
6. F. T. S. Yu, *Opt. Commun.* **27**, 23 (1978).
7. F. T. S. Yu, *Appl. Opt.* **17**, 3571 (1978).
8. S. L. Zhuang, T. H. Chao, and F. T. S. Yu, *Opt. Lett.* **6**, 109 (1981).
9. F. T. S. Yu, S. L. Zhuang, and T. H. Chao, *J. Opt.* (in press).
10. F. T. S. Yu and A. M. Tai, *Appl. Opt.* **18**, 2705 (1979).
11. F. T. S. Yu, *Proc. Soc. Photo-Opt. Instrum. Eng.* **232**, 9 (1980).
12. S. T. Wu and F. T. S. Yu, *Opt. Lett.* **6**, 452 (1981).
13. M. Born and E. Wolf, *Principle of Optics* (Pergamon, New York, 1964).
14. F. T. S. Yu, *Introduction to Diffraction, Information Processing, and Holography* (MIT Press, Cambridge, 1973).
15. M. J. Beran and G. B. Parrent, Jr., *Theory of Partial Coherence* (Prentice-Hall, Englewood Cliffs, N.J., 1964).
16. P. Chavel and S. Lowenthal, *J. Opt. Soc. Am.* **68**, 559 (1978).
17. P. Chavel and S. Lowenthal, *J. Opt. Soc. Am.* **68**, 721 (1978).

SECTION V

Visualization of Phase Object

ELECTRICAL ENGINEERING DEPARTMENT
THE PENNSYLVANIA STATE UNIVERSITY

University Park, PA 16802 (U.S.A.)

VISUALIZATION OF COLOR CODED PHASE VARIATION WITH AN INCOHERENT OPTICAL PROCESSING TECHNIQUE

S. T. WU (*), F. T. S. YU

MOTS CLÉS :

Traitement des images en lumière incohérente
Objets de phase

KEY WORDS :

Incoherent optical processing
Phase objects

Observation des variations de phases codées en couleur

SUMMARY : An object phase color encoding technique which uses a dual color optical processor with encoded extended incoherent sources is presented. This technique provides fine detail of the object phase variation between fringes, including both the positive and negative phase variations. Experimental demonstrations of this color encoding technique are given.

RÉSUMÉ : On présente un processeur optique permettant de coder en couleurs un objet de phase. Cette technique permet de mettre en évidence les petits détails de l'objet.

1. — INTRODUCTION

The study of phase objects has generally depended upon interferometric techniques [1, 2]. For slowly changing object phase variation the measurement could be very accurate by measured with those interferometric techniques [3]. However, for phase objects such as living cells which contain fine structure, interpretation with the interferometric technique is usually difficult, if not impossible. Frequently in the study of phase objects of this type it is necessary to produce an image irradiance which is related to the phase of the object.

The Schlieren technique [4, 5] and differential shearing interference microscopy [6, 7] both produce an image irradiance that is proportional to the derivative of the object phase. Although the differential techniques provide visualization of shapes and sizes of the phase objects, they are not able to detect the detailed phase variation between fringes. Nevertheless, the total shearing interference microscope is capable of producing fringe patterns superimposed on a phase object, but the application is limited to evaluation of simple isolated phase structures and it is difficult to apply for the more general case of phase variation.

One technique available for detecting the phase object whose image irradiance is proportional to the phase variation [8, 9] is limited to very small phase variation in the order of a fraction of a wavelength.

The concept of detecting large phase variation by differentiating and integrating to obtain an image irradiance proportional to phase variation was proposed by DeVelis and Reynolds [10] and was subsequently carried out by Sprague and Thompson [11] with a coherent optical processing technique. They have been successful in obtaining an image irradiance which is proportional to a large object phase variation. However the technique is rather elaborate and the phase detection is not a real-time operation. Moreover, since the system utilizes a coherent source, the annoying coherent artifact noise cannot be avoided. Although the multi-beam interferometric technique [2] is able to produce sharper fringe patterns, the technique cannot display the phase variation between the fringes with a single monotone fringe pattern. The phase variation between the fringes is capable of being detected by simultaneously changing the viewing angle, reference beam, or wavelength of the

(*) Visiting scholar from Shanghai Institute of Optics and Fine Mechanics, Academia Sinica (China).

light source. In a recent paper [12], Roblin and Sherif described an electronic scanning technique, based on phase modulation interferometry, for detecting phase variation between the fringes. But this scanning technique requires complicated electronic circuitry and the operation is rather cumbersome.

In a recent paper we have proposed a technique of encoding an extended incoherent source for image subtraction [13]. We will extend the same basic optical processing concept to the detection of object phase variation with a pseudocolor encoding technique. Since this technique utilizes incoherent sources, high quality color-coded phase variation patterns can be visualized. We stress that this incoherent processing technique may alleviate certain drawbacks of the previous techniques, and the processing system is rather simple and economical to operate.

II. — OBJECT PHASE DETECTION

We will now describe an incoherent optical processing technique for object phase detection, as depicted in figure 1. From this figure, we see that two encoded extended incoherent sources, each for a different color of light (i.e., red and green) are used for the processing. The purpose of using a source encoding mask to achieve a point-pair spatial coherence requirement for the image subtraction operation was discussed in our previous articles [13, 14].

In pseudocolor encoding, we insert a phase object $\exp[i\phi(x, y)]$ in one of the open apertures in the input plane P_2 and two sinusoidal gratings, G_1 and G_2 , in the spatial frequency plane P_3 which are described by

$$(1) \quad G_1 = 1 + \sin(h_0 p_r + \theta),$$

and

$$(2) \quad G_2 = 1 + \sin(h_0 p_g)$$

where $2h_0$ is the separation of the O_1 and O_2 , $p_r = (2\pi x)/\lambda_r f$ and $p_g = (2\pi x)/\lambda_g f$ are the spatial frequencies of the gratings, λ_r and λ_g are the red and green color wavelengths, x denotes the spatial coordinate in the same direction of p , f is the focal length of the achromatic transform lens, and θ is a phase factor that we introduced. We note that θ will play an important factor in the color encoding process.

By a straight forward but rather tedious computation, the irradiance near the origin of the output image plane P_3 can be written [13],

$$(3) \quad I(x, y) = I_r(x, y) + I_g(x, y) \\ = K \{ 1 - \cos[\phi_r(x, y) + \theta] \} + \\ + K \{ 1 - \cos[\phi_g(x, y)] \},$$

where I_r and I_g denote the red and green color image irradiances, $\phi(x, y)$ is the phase distribution of the object, θ is a constant phase factor that we have introduced (by shifting one of the gratings), and K is a proportional constant. We note that the phase distributions $\phi_r(x, y)$ and $\phi_g(x, y)$ are slightly different because of the different wavelength illuminations. From Eq. (3), we see that a broad range color coded phase fringe pattern can be visualized.

In color mixing analysis, we would use I_r and I_g to form a 2-D orthogonal coordinate system, as shown in figure 2. The values of color mixing irradiance as a function of object phase variation ϕ for $\theta = 0^\circ$, 180° and $\theta = 90^\circ$, -90° are plotted in figures 2(a) and 2(b) respectively. Since different wavelengths (i.e., red and green) were used in the color encoding, the color mixing curve as a function of ϕ would not

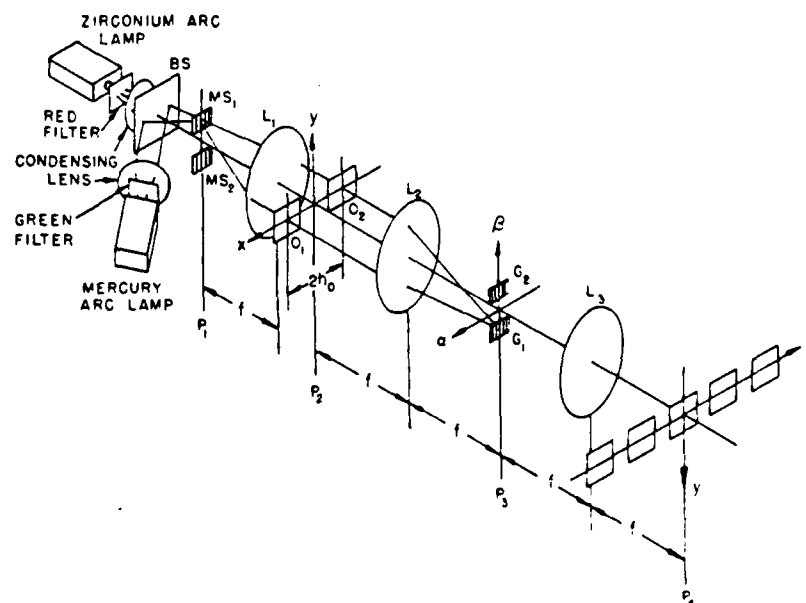


FIG. 1. — A multicolor incoherent processing system for detecting object phase variation. BS, Beam Splitter, MS, Source Encoding Mask, L, Achromatic Transform Lens, G, Diffraction Grating.

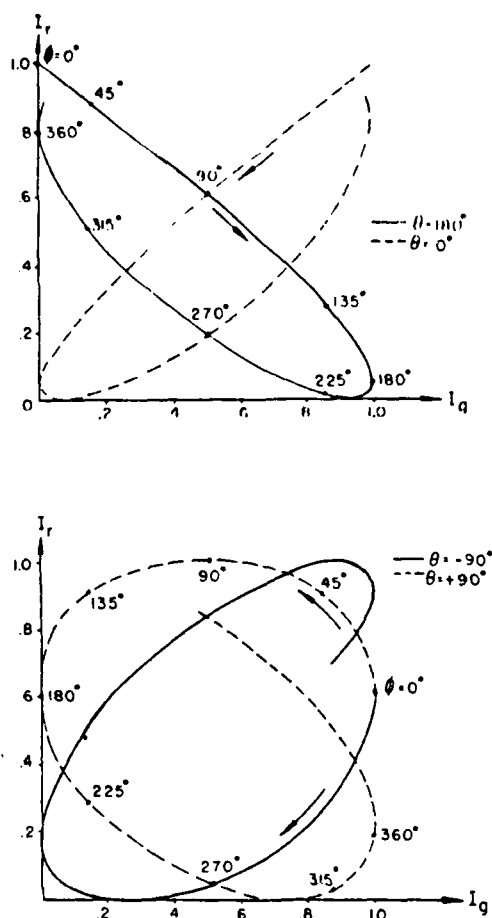


FIG. 2. — Color encoding mixing curves. (a) $\theta = 0^\circ, 180^\circ$. (b) $\theta = \pm 90^\circ$.

generally be closed for every 2π cycle, as shown in the figures. In other words, the phase detection is more accurate within $-\pi \leq \varphi \leq \pi$.

We would now consider a few cases of the color mixing procedure. For example, if $\theta = 0$, the locus of the color mixing curve lies near the 45° degree angle of (I_r, I_q) coordinates as shown in figure 2(a). There is no significant color change in this region to distinguish the object phase variation. On the other hand, if $\theta = 180^\circ$, the locus of the color mixing curve lies near the -45° degree region (i.e., $I_r = 1 - I_q$) of the (I_r, I_q) coordinate system, yielding a broad range of color variation. However, in this region it is difficult to distinguish a positive from a negative phase variation (i.e., $\pm \varphi$). If we let $\theta = 90^\circ$, the locus of the color mixing curve extends outward around the edges of the (I_r, I_q) coordinate system, as shown in figure 2(b). Thus it provides not only a broad range of color coded phase variation, but it also provides two different sequences of color coded bands, so that the positive and negative phase variations can be detected. In other words, this color encoded technique is capable of displaying finer detail of phase variations, including both the positive and negative phases.

III. — EXPERIMENTAL RESULT

In our experiments, a mercury arc lamp with a green filter (5461 Å) and a Zirconium arc lamp with a red filter (6328 Å) were used for the color light sources. The intensity ratio of these two color lights was adjusted to unity with a variable beam splitter.

Figure 3(a) shows a monotone fringe pattern of a phase object obtained with this incoherent processing technique. From this figure we see that detailed phase variation between the fringes cannot be perceived. Figure 3(b) was obtained with the multi-color technique as described earlier. The phase factor θ between the diffraction gratings G_1 and G_2 was set to approximately 90° . From this figure, we see that a multicolor phase fringe pattern is formed so that considerably more detail of the phase variation between the fringes can be observed. For example, between the two yellow color bands, there is a color variation from yellow-to-red-dim yellow-green-and back to yellow again. The phase angle between these two color bands is 360° . If we refer to the color mixing curve of figure 2(b), then the phase variations corresponding to the color bands shown in figure 3(b) are $0^\circ \rightarrow 180^\circ \rightarrow 225^\circ \rightarrow 315^\circ \rightarrow 360^\circ$. Therefore we see that there is a positive increasing phase variation from the upper yellow band to the lower band.

Figure 4(a) shows another monotone phase fringe pattern of a phase object obtained with this technique, in which detail of the phase variation between the fringes cannot be determined. For example, if we take the cross section along the line A-A of the phase object between the two arrows, as shown in the figure, then there are four possible phase variations that may be interpreted, as shown in figure 5. With a monotone fringe pattern it may not be possible to retrieve the actual object phase variation. However, with the multicolor phase fringe pattern of figure 4(b), we are able to identify the detailed phase variation between the fringes. To illustrate, if we take the same cross section A-A, then a sequence of color bands from left to right, i.e., green-dim yellow-red-yellow-red, can be observed. Referring to the color mixing curve of figure 1(b), this sequence of color bands represents a sequence of phase angles of $315^\circ \rightarrow 250^\circ \rightarrow 180^\circ \rightarrow 90^\circ \rightarrow 180^\circ$. Thus this region represents a phase depression object, which corresponds to the case of figure 5(a).

IV. — CONCLUSION

In concluding this paper, we would note that, object phase variation can be visually studied by a color coded incoherent processing technique which utilizes a modified complex image subtraction scheme. The object phase distribution within the range $-\pi \leq \varphi \leq \pi$ can be detected with less ambiguity using this multi-color coding scheme than by using a monochromatic scheme. This technique offers the capability of detecting finer detail of the object phase as compared with the other interferometric techniques. Since inexpensive incoherent sources are used, the multicolor technique may offer a wider range of applications. In the case of microscopic phase

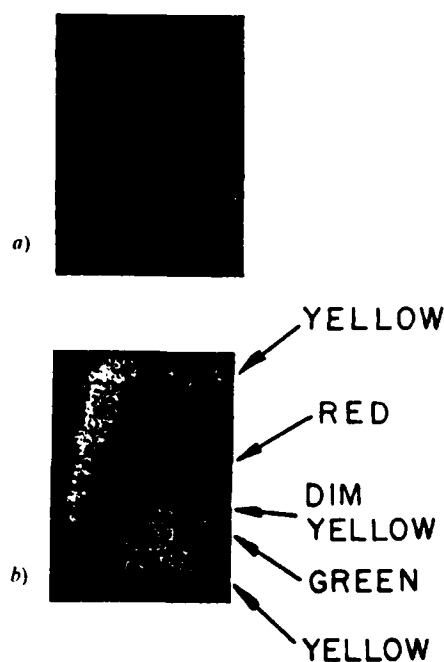


FIG. 3. — A color-coded object phase variation. (a) Monotone phase fringe pattern. (b) Color-coded fringe pattern.

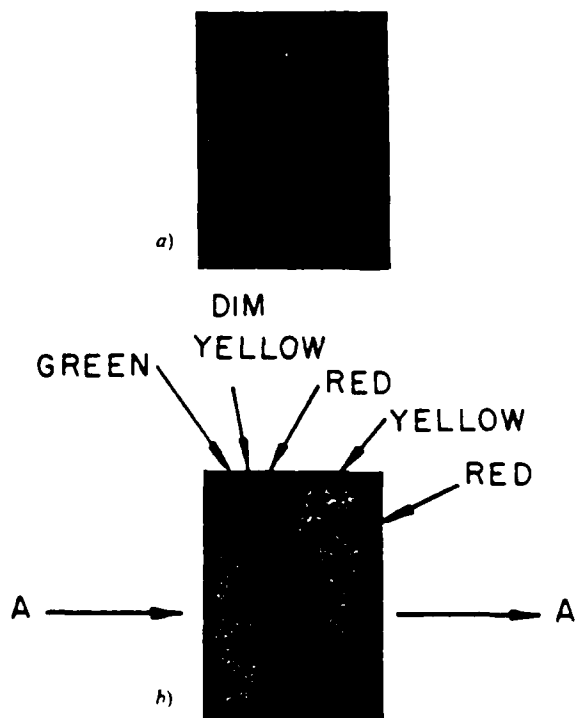


FIG. 4. — A color-coded phase object. (a) Monotone fringe pattern. (b) Color-coded fringe pattern.

object observation, the system can be designed to fit within a microscope system. In addition, the technique may not be restricted only to phase object visual-

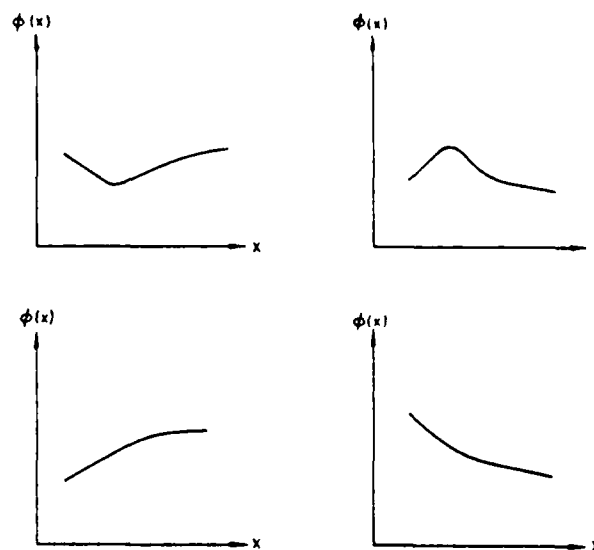


FIG. 5. — Four possible object phase variations for figure 4(a).

ization — it may be used in other fields as well : study of birefringence and interference figures in polarizing microscopy and crystallography; distinction between compressed and stretched photoelastic areas; analysis of the aerodynamic pressure variations examined inside a wind tunnel by the stereoscopic technique; analysis of wavefronts to test the aberrations of optical system; and others.

We wish to acknowledge the support of the U.S. Air Force Office of Scientific Research grant AFOSR-81-0148.

* * *

REFERENCES

- [1] BORN (M.), WOLF (E.). — Principles of Optics (2nd rev. ed.), Pergamon Press, New York, 1964.
- [2] MALACARA (D.). — Optical Shop Testing, John Wiley, New York, 1978.
- [3] STEEL (W. H.). — Interferometry, Cambridge University Press, London, 1967.
- [4] DEVELIS (J. B.), REYNOLDS (G. O.). — Theory and Application of Holography, Addison-Wesley, Reading (Mass.), 1967, pp. 166-8.
- [5] WADDELL (J. W.), WADDELL (J. W.). — IBM Res. Develop., 1970, 21, 30.
- [6] FRANCON (M.). — Progress in Microscopy, Pergamon Press, New York, 1961.
- [7] MARTIN (L. C.). — The Theory of the Microscope, American Elsevier, New York, 1966.
- [8] BENNETT (A.), JUPINK (H.), OSTERBERG (H.), RICHARDS (O.). — Phase Microscopy, John Wiley, New York, 1951.
- [9] PAYNE (B. O.), IBM Res. Develop., 1963, 21, 47.
- [10] DEVELIS (J. B.), REYNOLDS (G. O.). — Theory and Applications of Holography, Addison-Wesley, Reading (Mass.), 1967, pp. 161-2.
- [11] SPRAGUE (R. A.), THOMPSON (B. J.). — Appl. Opt., 1972, 11, 1969.
- [12] ROBLIN (G.), SHERIF (M. E.). — Appl. Opt., 1980, 19, 4247.
- [13] WU (S. T.), YU (F. T. S.). — Opt. Letters, 1981, 6, 452.
- [14] YU (F. T. S.), ZHUANG (S. L.), WU (S. T.). — Appl. Phys., 1982, B 27, 99.

(Manuscript received in June 1, 1981)

SECTION VI

Coherence Requirement

Coherence requirements for partially coherent optical processing

S. L. Zhuann and F. T. S. Yu

The mutual intensity function for a partially coherent light is used to develop an expression for the output intensity distribution for a broadband optical information processor. The coherence requirement for smeared image deblurring and image subtraction is then determined using the intensity distribution. We also quantitatively show the dependence of coherence criteria on the spectral bandwidth, the source size, deblurring width, spatial frequency, and the separation of input object transparencies.

I. Introduction

Optical systems perform myriad sophisticated information processing operations using coherent light.¹⁻³ However, coherent systems are susceptible to coherent artifacts and noise, which frequently limits their processing capability. The use of incoherent light alleviates the noise problem,⁴⁻⁷ usually at the cost of a lowered signal-to-noise ratio due to dc bias. Various workers have studied optical systems which employ (a) a totally incoherent source^{8,9} or (b) a broadband source with reduced coherence.¹⁰ The question to be addressed in the paper is, to what degree can we relax the coherence requirement without sacrificing the overall results of the processing system? We use Wolf's¹¹ theory of partially coherent light to develop the necessary coherence criteria for an optical processor. The results are used to discuss the temporal and spatial coherence requirements for the specific problems of image deblurring and image subtraction.

The nature of optical processing operations governs the spatial and temporal coherence requirements necessary to obtain satisfactory results. As system configuration varies from one application to the other it is desirable to develop a generalized function for the system output intensity expressed as a function of the spectral and spatial bandwidths.

Consider the partially coherent optical processing system¹²⁻¹⁴ in Fig. 1. Let the source plane P_0 be that of an incoherent spatially extended light source (i.e.,

white-light source) with an intensity distribution $\gamma(x_0, y_0)$. The input plane P_1 contains the signal transparency and also a coding mask (e.g., a sinusoidal grating) if needed.¹²⁻¹⁴ Let the complex amplitude transmittance at this plane be $t(u, v)$. Its spectrum may then be processed in complex amplitude by placing a complex spatial filter $f(x, y)$ in the Fourier plane. The theory of partially coherent light can be used now to write the output intensity distribution.^{11,16}

$$I(u', v') = \int_{\lambda_0 - \Delta\lambda/2}^{\lambda_0 + \Delta\lambda/2} \iint_{-\infty}^{\infty} \gamma(x_0, y_0) S(\lambda) C(\lambda) \times \left| \iint_{-\infty}^{\infty} T(x + x_0, y + y_0; \lambda) f(x, y) \times \exp\left[-j \frac{2\pi}{\lambda f} (xu' + yv')\right] dx dy \right|^2 dx dy d\lambda, \quad (1)$$

where $S(\lambda)$ and $C(\lambda)$ are defined to be the relative spectral intensity of the light source and the relative spectral response sensitivity of the detector, respectively. $T(x, y; \lambda)$ is the Fourier spectrum of the input transparency for wavelength λ of the light source. The integration is performed over the spectral bandwidth $\Delta\lambda$ of the light source, λ_0 being its center wavelength.

In the following sections we shall use the output intensity distribution given by Eq. (1) to evaluate the coherence requirement for image deblurring and image subtraction of a partially coherent optical information processor.

II. Coherence Requirement for Image Deblurring

A photographic image deblurring technique employing a white-light source has been described in previous papers.^{15,16} We had briefly stated that the coherence requirements depend on the smeared length of the object and the size and spectral bandwidth of the light source.¹⁷ We shall now discuss the temporal and spatial coherence requirements for image deblurring separately.

The authors are with Pennsylvania State University, Electrical Engineering Department, University Park, Pennsylvania 16802.

Received 5 March 1982

0001-6960/82/142587-09\$01.00/0

© 1982 Optical Society of America

A. Temporal Coherence Requirement

We consider a spectrally broadband point source for which the intensity distribution can be expressed by a Dirac δ function, i.e., $\gamma(x_0, y_0) = \delta(x_0, y_0)$. The spectral distribution is uniform over the bandwidth $[\lambda(\lambda) = k, \text{ a constant}]$. If the smeared length W is known *a priori*, the output deblurred image irradiance can be derived from Eq. (1) as

$$I(u', v') = \int_{\lambda_l}^{\lambda_h} |A(u', v'; \lambda)|^2 d\lambda, \quad (2)$$

where λ_l and λ_h are the extreme lower and upper wavelengths of the light source;

$$A(u', v'; \lambda) = \int_{-\infty}^{\infty} T(x, y; \lambda) f(x, y) \exp\left[-j \frac{2\pi}{\lambda f} (xu' + yv')\right] dx dy \quad (3)$$

is the output complex light distribution of the deblurred image due to wavelength λ ; $T(x, y; \lambda)$ is the Fourier spectrum of the input blurred transparency $t(u, v)$ due to λ ; and $f(x, y)$ is the deblurring filter.

We note that, if the input blurred image is superimposed with a sinusoidal phase grating, the blurred image spectrum will disperse into rainbow colors in the Fourier plane thus allowing a stripwise design of deblurring filter for each narrow spatial band in the Fourier plane. It is evident that the temporal coherence requirement is limited by the narrow spectral band (i.e., narrow strip) of the deblurring filter. If the input object is a linear smeared image, a fan-shaped deblurring filter can be used to compensate the wavelength variation.^{13,15} Since each of the narrow strip deblurring filters is spatial frequency-limited over a narrow spectral band, the coherence requirement for each narrow strip filter can be equivalently analyzed as the case without the input phase grating (i.e., the coding mask).

Since the image deblurring takes place at every image point the linear blurred image transparency may be represented as

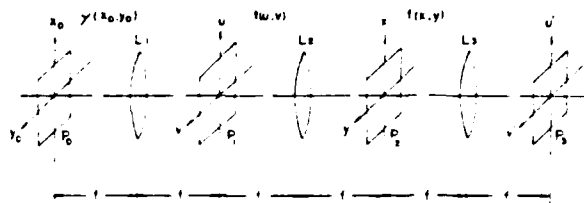


Fig. 1. Partially coherent optical processing system: P_0 , source plane; P_1 , input plane; P_2 , Fourier plane; P_3 , output plane; L , achromatic lenses.

$$t(u, v) = \text{rect}(u/W), \quad (4)$$

$$T(x, y; \lambda) = \mathcal{F}[t(u, v)] = \text{sinc}\left(\frac{W}{\lambda f} x\right), \quad (5)$$

where f is the focal length of the achromatic transform lenses, and

$$\text{rect}(u/W) = \begin{cases} 1 & |u| \leq W/2, \\ 0 & \text{otherwise.} \end{cases} \quad (6)$$

The deblurring filter is thus

$$f(x; \lambda_0) = \frac{1}{T(x; \lambda_0)} = \frac{1}{\text{sinc}\left(\frac{W}{\lambda_0 f} x\right)}, \quad (7)$$

where λ_0 is the center wavelength of the light source, and for simplicity we have adopted a 1-D notation. The corresponding deblurred image is given by

$$A(u'; \lambda) = \int_{-\infty}^{\infty} T(x; \lambda) f(x; \lambda_0) \exp\left[-j \frac{2\pi}{\lambda f} xu'\right] dx \\ = \text{rect}(u'/W) * \int_{-\infty}^{\infty} \frac{1}{\text{sinc}\left(\frac{W}{\lambda_0 f} x\right)} \exp\left[-j \frac{2\pi}{\lambda f} xu'\right] dx, \quad (8)$$

where $*$ denotes the convolution operation. By a straightforward but tedious calculation, illustrated in the Appendix, the deblurred image of Eq. (8) can be shown to be

$$A(u'; \lambda) = \begin{cases} \frac{4\lambda_0 f}{\pi} \sum_{n=1}^{\infty} \frac{(-1)^n \sin \frac{\pi n \lambda_0}{\lambda} \sin \frac{2\pi n \lambda_0}{\lambda W} u' \cdot \text{sgn}(u'), & \text{for } |u'| > W/2, \\ -\frac{4\lambda_0 f}{\pi} \sum_{n=1}^{\infty} \frac{(-1)^n \cos \frac{\pi n \lambda_0}{\lambda} \cos \frac{2\pi n \lambda_0}{\lambda W} u', & \text{for } |u'| \leq W/2. \end{cases} \quad (9)$$

where the series converges for $2m \gg 1$. In the final result it can be shown that the output image irradiance is given by

$$I^{(1)}(u', \Delta\lambda) = \frac{2\lambda_0^2 f^2}{\pi^2} \sum_n \sum_{n'} \frac{1}{n n'} (-1)^{n+n'} \{3[\lambda_0^{-2} \cos[c'_{nn'}(u')\lambda_0] \\ - \lambda_0^{-2} \cos[c'_{nn'}(u')\lambda_0] - 6[c'_{nn'}(u')]^2 \lambda_0^{-2} \sin[c'_{nn'}(u')\lambda_0] \\ - \lambda_0^{-2} \sin[c'_{nn'}(u')\lambda_0] - 6[c'_{nn'}(u')]^2 \lambda_0^{-2} \cos[c'_{nn'}(u')\lambda_0] \\ - \lambda_0^{-2} \cos[c'_{nn'}(u')\lambda_0] - 6[c'_{nn'}(u')]^2 [\text{Si}(\lambda_0) - \text{Si}(\lambda_0)]\}, \quad \text{for } |u'| > W/2, \quad (10)$$

$$I^{(2)}(u', \Delta\lambda) = \frac{2\lambda_0^2 f^2}{\pi^2} \sum_n \sum_{n'} \frac{1}{n n'} (-1)^{n+n'} \{6[c'_{nn'}(u')]^2 [\text{Si}(\lambda_0) - \text{Si}(\lambda_0)] \\ + 6[c'_{nn'}(u')]^2 \lambda_0^{-2} \cos[c'_{nn'}(u')\lambda_0] - \lambda_0^{-2} \cos[c'_{nn'}(u')\lambda_0] \\ + 6[c'_{nn'}(u')]^2 \lambda_0^{-2} \sin[c'_{nn'}(u')\lambda_0] - \lambda_0^{-2} \sin[c'_{nn'}(u')\lambda_0] \\ - 3\lambda_0^{-2} \sin[c'_{nn'}(u')\lambda_0] - \lambda_0^{-2} \cos[c'_{nn'}(u')\lambda_0]\}, \quad \text{for } |u'| \leq W/2. \quad (11)$$

For these equations, note that

$$\lambda_0 = \lambda_0 / (\lambda_0 - \Delta\lambda), \quad (12)$$

$$\lambda_0 = \lambda_0 / (\lambda_0 + \Delta\lambda), \quad (13)$$

$$\text{Si}(x) \triangleq \int_0^x \frac{\sin y}{y} dy, \quad (14)$$

$$\begin{aligned} a_{nn}^{(1)}(u') &= \pi(n - n')(1 - 2u'/W), \\ a_{nn}^{(3)}(u') &= \pi(n - n')(1 + 2u'/W), \\ a_{nn}^{(5)}(u') &= \pi(n + n')(1 - 2u'/W), \\ a_{nn}^{(7)}(u') &= \pi(n + n')(1 + 2u'/W), \end{aligned} \quad (15)$$

and

$$\begin{aligned} a_{nn}^{(2)}(u') &= \pi[n(1 - 2u'/W) - n'(1 + 2u'/W)], \\ a_{nn}^{(4)}(u') &= \pi[n(1 + 2u'/W) - n'(1 - 2u'/W)], \\ a_{nn}^{(6)}(u') &= \pi[n(1 - 2u'/W) + n'(1 + 2u'/W)], \\ a_{nn}^{(8)}(u') &= \pi[n(1 + 2u'/W) + n'(1 - 2u'/W)]. \end{aligned} \quad (16)$$

Equations (10)–(16) provide the mathematical basis for the evaluation of the temporal coherence requirement of a smeared image deblurring process. Plots of the normalized deblurred image irradiance, defined as a function of u' and the bandwidth $\Delta\lambda$, are shown in Fig. 2. $\lambda_0 = 5461 \text{ \AA}$ was used for the calculation. It is evident that if the light source is strictly coherent (i.e., $\Delta\lambda = 0$), the deblurred point image is infinitesimal. Also note that the degree of deblurring decreases as the temporal coherence of the light source reduces. The deblurred length ΔW represents the spread of the deblurred image irradiance. It is formally defined as the separation between the 10% points of $I(u')$. The deblurred length ΔW can be shown to decrease monotonically with $\Delta\lambda$. Plots of ΔW as a function of the spectral bandwidth $\Delta\lambda$ for various values of smeared length W are shown in Fig. 3. It may be shown that the deblurred length ΔW is linearly proportional to the smear length W for a given value of $\Delta\lambda$. The greater the smear, the more difficult the deblurring process. In principle this may be corrected by decreasing the spectral bandwidth of the light source. Table I numerically summarizes the preceding analysis. The value of $\Delta\lambda$ can be regarded as the temporal coherence requirement for the deblurring process.

E. Spatial Coherence Requirement

The relationship between the source size and the image intensity distribution is the key factor in the calculation of the degree of spatial coherence requirement for a particular image deblurring system. The following analysis assumes a 1-D processor for simplicity.

Assume the intensity distribution of the light source is given by

$$I(x_0) = \text{rect}(x_0/\Delta s), \quad (17)$$

If an extended monochromatic light source is used, the output intensity distribution of Eq. (1) becomes

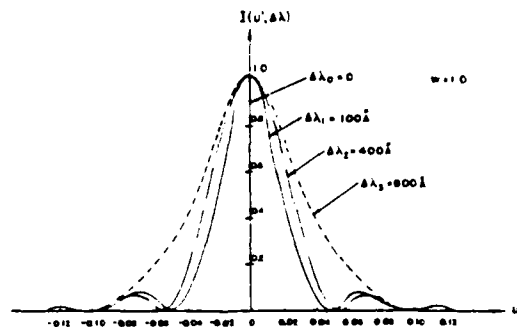


Fig. 2. Output intensity distribution of the deblurred image. $\Delta\lambda$, spectral bandwidth of the light source; W , smeared length.

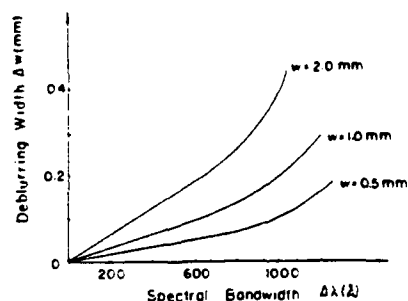


Fig. 3. Plots of the deblurring width ΔW as a function of the spectral bandwidth of the light source $\Delta\lambda$ for various values of smeared light W .

Table I. Effect of Temporal Coherence Requirement

$\Delta W/W$	1/20	1/15	1/10	1/8	1/5
$\Delta\lambda(\text{\AA})$	270	400	640	750	990

$$I(u') = \int_{-\infty}^{\infty} \text{rect}(x_0/\Delta s) |A(u', x_0; \lambda)|^2 dx_0, \quad (18)$$

where

$$\begin{aligned} A(u', x_0; \lambda) &= \int_{-\infty}^{\infty} \text{sinc}\left[\frac{W}{\lambda'}(x - x_0)\right] \exp\left(-j\frac{2\pi}{\lambda'}xu'\right) dx \\ &= \int_{-\infty}^{\infty} \frac{1}{\text{sinc}\left[\frac{W}{\lambda'}x\right]} \exp\left(-j\frac{2\pi}{\lambda'}xu'\right) dx, \end{aligned} \quad (19)$$

and $*$ denotes the convolution operation.

Equation (19) can be reduced to the form of

$$A(u', x_0; \lambda) = \begin{cases} \frac{2f\lambda_0}{\pi} \sum_{n=1}^{\infty} (-1)^n n \exp(j2\pi\alpha u'/W) \left[\exp\left(j\frac{2\pi n}{W} u'\right) \text{sinc}(\alpha + n) - \exp\left(-j\frac{2\pi n}{W} u'\right) \text{sinc}(\alpha - n) \right], & \text{for } |u'| > W/2, \\ \frac{2f\lambda_0}{\pi} \sum_{n=1}^{\infty} (-1)^n n \exp(j2\pi\alpha u'/W) \left(\frac{1}{\alpha - n} [1 - \exp[j2\pi(\alpha - n)u'/W] \cos\pi(\alpha - n)] \right) \\ + \frac{1}{\alpha + n} [1 - \exp[j2\pi(\alpha + n)u'/W] \cos\pi(\alpha + n)], & \text{for } |u'| \leq W/2, \end{cases} \quad (20)$$

where $\alpha = x_0 W/(\lambda f)$.

By substituting Eq. (20) into Eq. (2) and performing the required mathematical evaluation, the deblurred image irradiance is found to be (a) for $|u'| > W/2$:

$$I^{(1)}(u', \Delta s) = \frac{16f^3\lambda_0^3}{W^2\pi^2} \sum_n \sum_{n'} |\Phi_{nn'}^{(1)}(\Delta s) \cos[2\pi(n - n')u'/W] + \Phi_{nn'}^{(2)}(\Delta s) \cos[2\pi(n + n')u'/W]|. \quad (21)$$

Note that, in this equation, the following parameters may be defined:

$$S_j(m, \Delta s) = S_j[2\pi|\bar{\alpha}(\Delta s) - m|] - S_j[2\pi|-\bar{\alpha}(\Delta s) - m|]. \quad (22)$$

In addition define

$$C_j(m, \Delta s) = C_j[2\pi|\bar{\alpha}(\Delta s) + m|] - C_j[2\pi|\bar{\alpha}(\Delta s) - m|], \quad (23)$$

where

$$\begin{aligned} S_i(x) &= \int_0^x \frac{\sin\beta}{\beta} d\beta, \\ C_i(x) &= \int_x^\infty \frac{\cos\beta}{\beta} d\beta, \\ \bar{\alpha}(\Delta s) &= \Delta s W/(2\lambda f), \end{aligned} \quad (24)$$

and

$$\begin{aligned} \Phi_{nn'}^{(1)}(\Delta s) &= \frac{nn'}{n' - n} \left\{ \left| n \frac{n + \bar{\alpha}(\Delta s)}{n - \bar{\alpha}(\Delta s)} \right| \right. \\ &\quad \left. - [(-1)^n C_j(n, \Delta s) - (-1)^{n'} C_j(n', \Delta s)] \right\}, \\ \Phi_{nn'}^{(2)}(\Delta s) &= \frac{nn'}{n' + n} \left\{ \left| n \frac{n - \bar{\alpha}(\Delta s)}{n + \bar{\alpha}(\Delta s)} \right| \right. \\ &\quad \left. - [(-1)^n C_j(n, \Delta s) - (-1)^{n'} C_j(n', \Delta s)] \right\}. \end{aligned} \quad (25)$$

(b) for $|u'| \leq W/2$ we may similarly show

$$\begin{aligned} I^{(2)}(u', \Delta s) &= \frac{16f^3\lambda_0^3}{W^2\pi^2} \sum_n \sum_{n'} |\Phi_{nn'}^{(3)}(\Delta s) - \Phi_{nn'}^{(4)}(\Delta s) \sin[2\pi(n' - n)u'/W] \\ &\quad + \Phi_{nn'}^{(5)}(\Delta s) \cos[2\pi(n' - n)u'/W] - \Phi_{nn'}^{(6)}(\Delta s) \cos[2\pi(n - n')u'/W]|, \end{aligned} \quad (26)$$

where

$$\begin{aligned} \Phi_{nn'}^{(3)}(\Delta s) &= (-1)^n \frac{2n}{n^2 - n'^2} \left| n \frac{n - \bar{\alpha}(\Delta s)}{n + \bar{\alpha}(\Delta s)} \right| \\ &\quad - (-1)^{n'} \frac{n}{n^2 - n'^2} [C_j(n, \Delta s) - C_j(n', \Delta s)], \\ \Phi_{nn'}^{(4)}(\Delta s) &= \frac{n'}{n^2 - n'^2} [S_j(n, \Delta s) - S_j(n', \Delta s)], \\ \Phi_{nn'}^{(5)}(\Delta s) &= (-1)^{n-1} \frac{n'}{n^2 - n'^2} [C_j(n, \Delta s) - C_j(n', \Delta s)] \\ &\quad - \frac{2}{n - n'} \left\{ \left| n \frac{n - \bar{\alpha}(\Delta s)}{n + \bar{\alpha}(\Delta s)} \right| - [C_j(n, \Delta s) - C_j(n', \Delta s)] \right\}, \\ \Phi_{nn'}^{(6)}(\Delta s) &= \frac{1}{n - n'} \left\{ \left| n \frac{n - \bar{\alpha}(\Delta s)}{n + \bar{\alpha}(\Delta s)} \right| - [C_j(n, \Delta s) - C_j(n', \Delta s)] \right\}. \end{aligned} \quad (27)$$

and

$$\begin{aligned} S_j^*(m, \Delta s) &= S_j[\pi(2u'/W \pm 1)|\bar{\alpha}(\Delta s) + m|] \\ &\quad - S_j[\pi(2u'/W \pm 1)|-\bar{\alpha}(\Delta s) + m|], \\ C_j^*(m, \Delta s) &= C_j[\pi|2u'/W \pm 1||\bar{\alpha}(\Delta s) + m|] \\ &\quad - C_j[\pi|2u'/W \pm 1||-\bar{\alpha}(\Delta s) + m|]. \end{aligned} \quad (28)$$

Thus the spatial coherence requirement of an image deblurring process may be evaluated by using Eqs. (21) and (26). The output intensity distribution of this process is plotted in Fig. 4.

Recall the definition of the deblurred length ΔW stated to be the separation between the 10% points of the image irradiance $I(u')$. Figure 5 shows the plots of ΔW as a function of the source size Δs and the smear length W . From this figure it can be seen that when the spatial width of the light source increases beyond a critical size Δs_c , the deblurred length becomes inde-

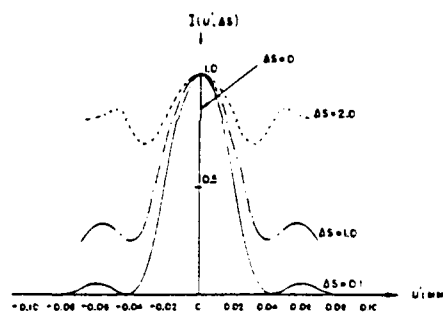


Fig. 4. Output intensity distribution of the deblurred image for various values of the source size Δs .

pendent of Δs and equal to W . Table II provides a brief numerical summary of the key parameters for the determination of the spatial coherence in image deblurring. From this table it is evident that the spatial coherence requirement is inversely proportional to the smear length W . That is, the longer the smearing length, the smaller the source size is required.

III. Coherence Requirement for Image Subtraction

Wu and Yu¹⁸ have reported an image subtraction procedure employing an extended incoherent source and a source encoded mask. Here, we shall discuss the temporal and spatial coherence requirements of the image subtraction process and show that they depend on the size and spectral bandwidth of the light source.

The output intensity distribution can be derived by calculating the propagation of the mutual coherence function through an optical system that utilizes an encoded extended source. With reference to Fig. 6 the encoded source intensity distribution may be described by

$$\gamma(x_0, y_0) = \text{rect}(x_0/d) * \sum_{n=-N}^N \delta(x_0 - nD), \quad (29)$$

where $*$ denotes the convolution operation, D is the spacing of the $2N + 1$ encoding slits, and d is the width of each slit. Image subtraction is essentially a 1-D processing operation and will be analyzed as such.

The encoded mutual coherence function at the input plane P_1 can be written

$$J(u_1 - u_2; \lambda) = \int_{-\infty}^{\infty} \gamma(x_0, y_0) \exp\left[-j \frac{2\pi}{\lambda f} (u_1 - u_2)x_0\right] dx_0, \quad (30)$$

or, in regard to Eq. (29),

$$J(u_1 - u_2; \lambda) = \sum_{n=-N}^N \text{sinc} \frac{d(u_1 - u_2)}{\lambda f} \exp\left[-j \frac{2\pi}{\lambda f} (u_1 - u_2)nD\right]. \quad (31)$$

As shown in Fig. 6 two object transparencies, $A(u)$ and $B(u)$, are placed at the input plane P_1 . These can be represented by

$$t(u) = A(u - H) + B(u + H), \quad (32)$$

where the separation between transparencies is $2H$. The mutual coherence function in the P_2 plane is simply the Fourier transform of $J_0(u_1 - u_2; \lambda)$ convolved with the spectrum of the amplitude transmittance function $t(u)$. The image subtraction process requires that a sinusoidal grating of spatial frequency ω_0 be placed in the Fourier plane. Thus the mutual coherence function behind this grating is given by

$$J(x_1, x_2; \lambda) = \tilde{J}(u_1 - u_2; \lambda) t(u_1) t^*(u_2) (1 - C \sin 2\pi \omega_0 x_1) \times (1 - C \sin 2\pi \omega_0 x_2), \quad (33)$$

A final Fourier transform operation due to wavelength λ will give the intensity distribution at the output plane P_3 :

$$I(u, \lambda) = \iint_{-\infty}^{\infty} J(x_1, x_2; \lambda) \exp\left[-j \frac{2\pi}{\lambda f} (x_1 - x_2)u\right] dx_1 dx_2. \quad (34)$$

or

Table II. Effect of Spatial Coherence Requirement

Δs mm W	$\frac{\Delta W}{W}$	1/20	1/15	1/10	1/5
0.5 mm		0.2	0.38	0.6	0.92
1 mm		0.1	0.18	0.26	0.40
2 mm		0.05	0.08	0.12	0.18

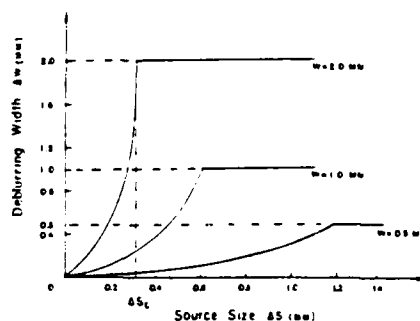


Fig. 5. Plots of the deblurring width as a function of the source size for various values of the smear length W .

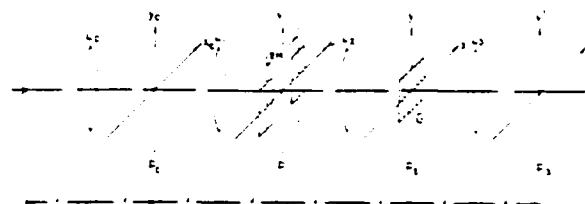


Fig. 6. Partially coherent optical processing system for image subtraction. S_0 , light source; P_0 , encoded extended source plane; P_1 , input plane; P_2 , Fourier plane; P_3 , output plane; L , achromatic lens.

$$I(u'; \lambda) = N[|A(u' - H)|^2 + |B(u' + H)|^2] + \frac{NC^2}{4} [2 \sin(2d\omega_0) \times \text{Re}[A(u' - H + \lambda f \omega_0)B(u' + H - \lambda f \omega_0)] - |A(u' - H + \lambda f \omega_0)|^2 - |B(u' + H - \lambda f \omega_0)|^2 - |A(u' - H - \lambda f \omega_0)|^2 - |B(u' + H + \lambda f \omega_0)|^2], \quad (35)$$

where Re denotes the real part of $\{\}$. From the above equation we see that there are six diffracted image terms at the output plane. If we only consider the diffracted images around the optical axis of the output plane, from Eq. (35) we have

$$I^{(0)}(u'; \lambda) = |A(u' - H + \lambda f \omega_0)|^2 - 2 \text{sinc}(2d\omega_0) \times \text{Re}[A(u' - H + \lambda f \omega_0)B(u' + H - \lambda f \omega_0)] + |B(u' + H - \lambda f \omega_0)|^2, \quad (36)$$

where $\omega_0 = H/\lambda f$.

If the slit size d equals zero, the analysis reduces to the case of strictly spatial coherence with the intensity distribution given by

$$I^{(0)}(u'; \lambda)|_{d=0} = |A(u') - B(u')|^2. \quad (37)$$

Equations (36) and (37) show that a high-contrast subtracted image requires a strictly spatial coherent system, and that the image quality will decrease as the slit width d increases.

To analyze the case of partial coherence assume the light source has a uniform spectral bandwidth and that the spectral response of the detector is also uniform [i.e., $s(\lambda) = k$; $C(\lambda) = k$]. Then the image intensity distribution at the output plane may be given by

$$I^{(0)}(u') = \int_{-\Delta\lambda/2}^{\Delta\lambda/2} [|A(u' + \lambda' f \omega_0)|^2 - 2 \text{sinc}(2d\omega_0) \times \text{Re}[A(u' + \lambda' f \omega_0) \times B(u' - \lambda' f \omega_0)] + |B(u' - \lambda' f \omega_0)|^2] d\lambda', \quad (38)$$

where $\lambda' = \lambda - \lambda_0$, λ_0 is the center frequency, and $\Delta\lambda$ is the spectral bandwidth of the source; ω_0 is the spatial frequency of the grating. Equation (38) may be simplified by using a Taylor series expansion for the input object functions. Thus for

$$A(u' + \lambda' f \omega_0) \approx A(u') + \sum_{m=1}^{\infty} \frac{1}{m!} A^{(m)}(u') (\lambda' f \omega_0)^m, \\ B(u' - \lambda' f \omega_0) \approx B(u') - \sum_{m=1}^{\infty} \frac{1}{m!} B^{(m)}(u') (\lambda' f \omega_0)^m, \quad (39)$$

where

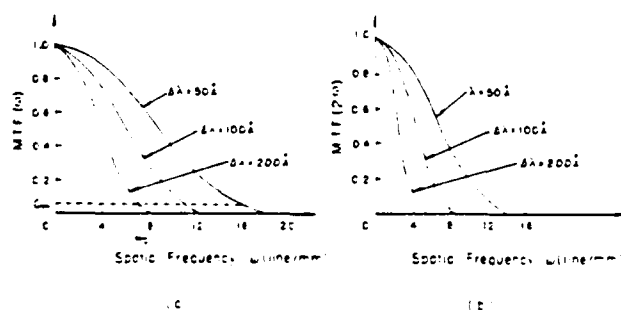


Fig. 7. Apparent modulation transfer function for a partially coherent image subtraction: (a) basic frequency, (b) second harmonic.

$$A^{(m)}(u') = d^m A(u')/du'^m, \\ B^{(m)}(u') = d^m B(u')/du'^m. \quad (40)$$

we find that

$$I^{(0)}(u') = [|A(u')|^2 - 2 \text{sinc}(2d\omega_0) A(u')B(u') + |B(u')|^2] \Delta\lambda \\ + \sum_{\substack{m, m' \text{ even} \\ m \neq 0}} \frac{1}{2^{m-1}(m+1)!} (f\omega_0)^m [A^{(m)}(u') \\ - \text{sinc}(2d\omega_0) B^{(m)}(u')] \\ \times [A(u') + B(u')] (\Delta\lambda)^{m+1} \\ + \sum_{\substack{m, m' \\ m+m' \text{ even} \\ m \neq 0 \\ m' \neq 0}} \frac{1}{2^{m+m'-1}(m+m'+1)m!m'!} \\ \times (f\omega_0)^{m+m'} [A^{(m)}(u')A^{(m')}(u') \\ - (-1)^m \text{sinc}(2d\omega_0) A^{(m)}(u')B^{(m')}(u') \\ + (-1)^{m+m'} B^{(m)}(u')B^{(m')}(u')] (\Delta\lambda)^{m+m'+1}. \quad (41)$$

This equation shows that a high-contrast subtracted image can be obtained with object transparencies of moderately low spatial frequency content. In addition this equation may be used to compute the spectral requirement of the light source.

An example analysis will be presented to develop the modulation transfer function (MTF) equations. These will be used to determine the temporal and spatial coherence requirements of the image subtraction process. Assume that the input object transparencies are given by

$$A(u) = 1, \quad B(u) = \frac{1}{2} [1 - C_0 \cos(2\pi\omega u)], \quad (42)$$

where C_0 is the contrast of the sinusoidal grating.

In the case of strictly coherence (i.e., $\Delta\lambda = d = 0$) the subtracted image produces a contrast reversed image with intensity distribution

$$I_0(u') = [A(u') - B(u')]^2. \quad (43)$$

or

$$I_0(u') = \frac{1}{4} - \frac{C_0^2}{8} - \frac{C_0}{2} \cos(2\pi\omega u') - \frac{C_0^2}{8} \cos(2\pi(2\omega)u'). \quad (44)$$

For a partially coherent case due to Eq. (38), the intensity of the subtracted image can be shown to be

$$I_0(u') = \left[\frac{1}{4} - \frac{C_0^2}{8} - \text{sinc}(2d\omega_0) \Delta\lambda - C_0 \frac{1}{2} \cos(2\pi\omega u') \right. \\ \times \text{sinc}(f\omega_0 \Delta\lambda) \Delta\lambda \cos(2\pi\omega u') \\ \left. - \frac{C_0^2}{8} \text{sinc}(2^2\omega_0 \Delta\lambda) \Delta\lambda \cos(2\pi(2\omega)u') \right]. \quad (45)$$

Note the addition of a second harmonic term $[\cos(2\pi(2\omega)u')]$ to the basic frequency. The MTF is defined as the ratio of the contrasts of the input and output sinusoidal objects. These are given by

$$MTF(\omega) = \frac{[1 - 2 \operatorname{sinc}(2d\omega_0)](2 - C_0^2) \operatorname{sinc}(\omega\omega_0\Delta\lambda)}{10 - C_0^2 - 8 \operatorname{sinc}(2d\omega_0)} \quad (46)$$

$$MTF(2\omega) = \frac{(2 - C_0^2) \operatorname{sinc}(2\omega\omega_0\Delta\lambda)}{10 - C_0^2 - 8 \operatorname{sinc}(2d\omega_0)} \quad (47)$$

As previously stated Eqs. (46) and (47) will allow the evaluation of the temporal and spatial coherent requirements for image subtraction.

A. Temporal Coherence Requirement

The case of strictly spatial coherence will be discussed first. This requires that the slit width d approach zero. Equations (46) and (47) will then become

$$MTF(\omega) = \operatorname{sinc}(\omega\omega_0\Delta\lambda), \quad (48)$$

$$MTF(2\omega) = \operatorname{sinc}(2\omega\omega_0\Delta\lambda). \quad (49)$$

The normalized MTF curves of the basic and harmonic frequencies are shown in Fig. 7. It is obvious that the contrast of the subtracted image decreases monotonically as a function of the object spatial frequency. However, the MTF of the subtracted image decreases as the spectral bandwidth of the light source increases. In other words the quality of the subtracted image improves as the spectral bandwidth of light source and the spatial frequency of the object decrease.

Let ω_c be the cutoff spatial frequency where the MTF decreases to a minimum value C_m as shown in Fig. 7. The value C_m depends on the maximum resolution of the output recording material. Figure 8 shows the functional relationship of the cutoff frequency ω_c and the spectral width $\Delta\lambda$ for various values of C_m . It is possible to determine the spectral bandwidth requirement $\Delta\lambda$ from this figure. The relationship between the cutoff frequency ω_c , the spectral width $\Delta\lambda$, and the separation between two input transparencies H is shown in Fig. 9. Note that the spectral bandwidth required for a given cutoff frequency decreases with increasing separation H . Table III illustrates the dependence of $\Delta\lambda$ on ω_c and H . The focal length of the Fourier transform lens selected is $f = 300$ mm for calculation. It is clear from the table that, as the spatial frequency and object separation increase, the spectral bandwidth of the light source must decrease.

B. Spatial Coherence Requirement

Consider the case of perfect temporal coherence (i.e., $\Delta\lambda = 0$) and partially spatial coherence, where Eqs. (46) and (47) are of the form

$$MTF_1 = \frac{(2 - C_0^2)[1 - 2 \operatorname{sinc}(2d\omega_0)]}{10 - C_0^2 - 8 \operatorname{sinc}(2d\omega_0)} \quad (50)$$

$$MTF_2 = \frac{2 - C_0^2}{10 - C_0^2 - 8 \operatorname{sinc}(2d\omega_0)} \quad (51)$$

Note that the MTFs are independent of the object's spatial bandwidth. The above equations are, however, dependent on the slit width d . This requires that the grating be precisely designed to match the separation of the object transparencies, i.e.,

$$d = H/\lambda_0 \quad (52)$$

The plots of the MTF vs the separation H for Eqs. (50)

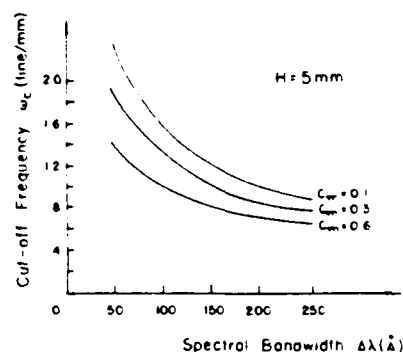


Fig. 8. Relationship between the cutoff frequency ω_c and the spectral bandwidth of the light source $\Delta\lambda$ for different minimum desirable contrasts C_m .

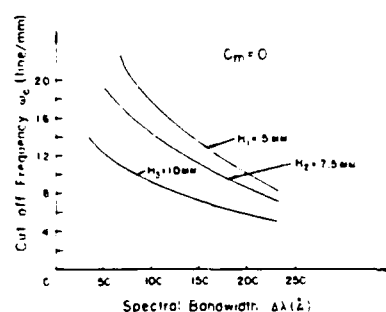


Fig. 9. Relationship between the cutoff frequency and the spectral bandwidth of the light source $\Delta\lambda$ for various values of separation H . $2H$ is the main separation between the input object transparencies.

Table III. Temporal Coherence Requirement for Different ω_c and H .

$\Delta\lambda(\text{\AA})$ $H(\text{mm})$	$\omega_c(\text{mm}^{-1})$	4	8	12	16	18
5.0		240	135	92	67	52
7.5		176	92	62	45	32
10.0		130	70	47	32	22

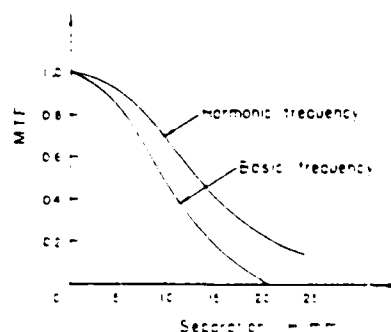


Fig. 10. Apparent modulation transfer function vs the separation H for different desirable contrasts.

and (51) are shown in Fig. 10. It is obvious that to obtain a high-contrast subtraction image the separation H must be reduced. However, decreasing the separation between the object transparencies limits the size of input objects to be processed. The relationship between the MTF, the object transparency separation H , and the slit width d is numerically presented in Table IV, where the focal length of the Fourier transform lens was assumed to be 300 mm.

Note that this table indicates the necessity of a very narrow source size to achieve an adequate MTF. However, to obtain a high-intensity narrow source size is difficult to achieve in practice. The problem can be solved considerably if source encoding techniques for image subtracting are used.^{17,18}

A multislit source encoding mask is used for this illustration. The spatial period of the encoding mask should be precisely equal to that of the diffraction grating G (i.e., $D = 1/\omega_0$). The spatial coherence requirement, although independent of the slit size, is governed by the ratio of the slit width to the spatial period of the encoding mask, i.e., d/D . The ratio d/D must be relatively small to achieve a high degree of spatial coherence. The dependence of the MTF on d/D is shown in Fig. 11. It is obvious that the subtraction effect ceases when the MTF approaches zero, i.e., $d/D = 0.3$. A few numerical examples are presented in Table V.

IV. Summary

We have shown that the temporal and spatial coherence requirements for some partially coherent optical processing operations, namely, image deblurring and image subtraction, can be determined in terms of the output intensity distribution. For image deblurring the temporal coherence requirement depends on the ratio of the deblurring width to the smeared length of the blurred image. To obtain a higher degree of deblurring a narrower spectral width of the light source is required. For example, if the deblurring ratio $\Delta w/w$ is 0.1, the spectral width, $\Delta\lambda$, should be $<640 \text{ \AA}$.

For the spatial coherence requirement the image deblurring depends on both the deblurring ratio $\Delta w/w$ and the smeared length w . If the deblurring ratio $\Delta w/w = 1/10$ and $w = 1 \text{ mm}$, a slit source $<0.26 \text{ mm}$ should be used. For a smeared image deblurring operation the constraints of the temporal and spatial coherence requirements are not critical, which can be achieved in practice.

For image subtraction, the temporal coherence requirement is determined by the highest spatial frequency and the separation of the input object transparencies. If the separation and spatial frequency of the input transparencies are high, a narrower spatial bandwidth of the light source is required.

For spatial coherence requirement, the modulation transfer function, which determines the contrast of the subtracted image, depends on the ratio of the slit width to the spatial period of the encoding mask, i.e., d/D . If the ratio d/D is low, a higher contrast subtracted image can be obtained. For example, with $d/D = 0.05$, a rel-

Table IV. Source Size for Image Subtraction Under Different MTS and Separation H

$d(\text{mm})$	$H(\text{mm})$	5.0	7.5	10.0
MTF				
0.1		0.0076	0.005	0.0036
0.3		0.0052	0.0035	0.0026
0.6		0.0031	0.0021	0.0015

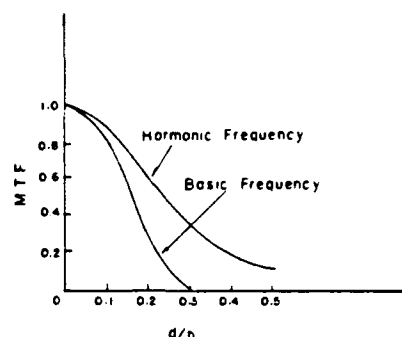


Fig. 11. Relationship between MTF (ω), MTF (2ω), and the ratio of the slit width to spatial period d/D .

Table V. Spatial Coherence Requirement for Various d/D

d/D	0.05	0.10	0.20	0.30
MTF	0.85	0.57	0.18	0.006

atively higher MTF = 0.85 can be obtained. Compared with the image deblurring operations, the coherence requirements are more stringent for the subtraction process.

Finally, the solution to the coherence requirement for partially coherent processing is not restricted to the application of the deblurring and subtraction operation, but may also be applied to any other optical processing operation.

We wish to acknowledge the support by the U.S. Air Force Office of Scientific Research grant AFOSR-81-0148.

Appendix

To prove the following relationship:

$$\int_{-\infty}^{\infty} \frac{1}{\text{sinc}\left(\frac{Wx}{\lambda_0'}\right)} \exp\left(-j \frac{2\pi}{\lambda_f'} x u'\right) dx = -\left\{ \frac{4\pi\lambda_f'}{W} \sum_{n=1}^{\infty} (-1)^n \times \sin \frac{2\pi n \lambda_f'}{\lambda W} u' \right\} \text{sinc}(u'). \quad (A1)$$

we let $x/\lambda_f' = f_z$ and $\lambda/\lambda_0' W = l$.

The problem then reduces to finding the solution for

$$\lambda/l \int \frac{\pi/x}{\sin(\pi/lx)} \exp(j2\pi/x u') dx. \quad (A2)$$

Since there are an infinite number of poles in the real domain, i.e.,

$$fx = n/l, \quad n = 1, 2, \dots \quad (A3)$$

Equation (A1) will be evaluated for the cases of $u' > 0$ and $u' \leq 0$. The contour integration, which is taken over the upper half of the complex plane (see Fig. 12), is given by

$$\left\{ \int_{-\infty}^{\infty} - \sum \int_{-\infty}^{\infty} + \int_R \right\} \frac{\pi/x}{\sin(\pi/lx)} \exp(-j2\pi/x u') dx = 0, \quad (A4)$$

where x is the radius of the small half-circles around the poles, and R is the radius of the larger contour half-circle. Denote

$$z = R \exp(j\theta), \quad dz = j\theta R \exp(j\theta) d\theta. \quad (A5)$$

The last term of Eq. (A4) may then be written

$$\begin{aligned} \int_R \frac{\pi/x}{\sin(\pi/lx)} \exp(j2\pi/x u') dx &= \int \frac{\pi z}{\sin(\pi/lz)} \exp(j2\pi z u') dz \\ &= \int_R \frac{-2\pi R^2 \exp(j2\pi R u' \cos\theta) \exp(-2\pi R \sin\theta u') \theta \exp(2j\theta)}{\exp[j\pi l R (\cos\theta + j \sin\theta)] - \exp[-j\pi l R (\cos\theta + j \sin\theta)]} d\theta, \end{aligned} \quad (A6)$$

so that

$$\lim_{R \rightarrow \infty} \int_R \frac{\pi/z}{\sin(\pi/lz)} \exp(j2\pi/z u') dz = 0. \quad (A7)$$

But from Eq. (A4) it is easily shown that as R approaches infinity

$$\int_{-\infty}^{\infty} \frac{\pi/z}{\sin(\pi/lz)} \exp(j2\pi/z u') dz = -2\pi j \sum_{n=-\infty}^{\infty} R_n, \quad (A8)$$

where

$$R_n = \lim_{z \rightarrow \frac{n}{l}} \left(z - \frac{n}{l} \right) \frac{\pi z \exp(j2\pi z u')}{\sin(\pi/lz)} = \frac{(-1)^n \exp(j2\pi n u'/l)}{\pi l^2}. \quad (A9)$$

Therefore,

$$\int_{-\infty}^{\infty} \frac{\pi/z}{\sin(\pi/lz)} \exp(j2\pi/z u') dz = \frac{4}{l^2} \sum_{n=-\infty}^{\infty} (-1)^n n \sin \frac{2\pi n}{l} u', \quad \text{for } u' > 0. \quad (A10)$$

The contour integral taken over the lower half of the plane as shown in Fig. 13 is similarly given by

$$\int_{-\infty}^{\infty} \frac{\pi/z}{\sin(\pi/lz)} \exp(j2\pi/z u') dz = -\frac{4}{l^2} \sum_{n=-\infty}^{\infty} (-1)^n n \sin \frac{2\pi n}{l} u', \quad \text{for } u' < 0. \quad (A11)$$

The results of Eqs. (A10) and (A11) thus prove that the equality of Eq. (A1) holds true.

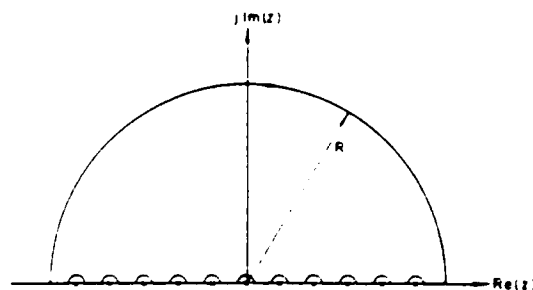


Fig. 12.

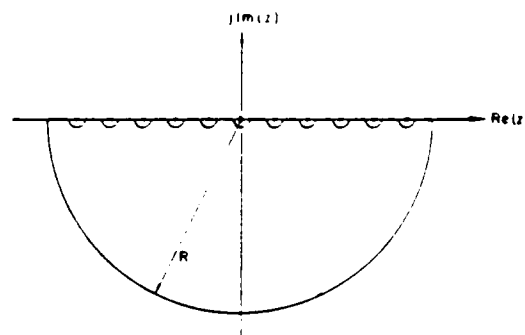


Fig. 13.

References

1. J. W. Goodman, *Introduction to Fourier Optics* (McGraw-Hill, New York, 1968).
2. F. T. S. Yu, *Introduction to Diffraction Information Processing and Holography* (MIT Press, Cambridge, 1973).
3. A. Vander Lugt, *IEEE Proc.* 62, 1300 (1974).
4. G. L. Rogers, *Opt. Laser Technol.* 7, 153 (1975).
5. M. A. Monahan, K. Bromley, and R. P. Bocker, *Proc. IEEE* 65, 121 (1977).
6. K. Bromley, *Opt. Acta* 21, 35 (1974).
7. G. L. Rogers, *Noncoherent Optical Processing* (Wiley, New York, 1977).
8. S. Lowenthal and P. Chavel, in *Proceedings, ICO Jerusalem 1976 Conference on Holography and Optical Processing*, E. Marom, A. Friesem, and E. Wiener-Avneer, Eds. (Pergamon, New York, 1977).
9. A. Lohmann, *Appl. Opt.* 16, 261 (1977).
10. E. N. Leith and J. Roth, *Appl. Opt.* 16, 2565 (1977).
11. M. Born and E. Wolf, *Principles of Optics* (Pergamon, New York, 1970).
12. F. T. S. Yu, *Opt. Comm.* 27, 23 (1978).
13. F. T. S. Yu, *Appl. Opt.* 17, 3571 (1978).
14. F. T. S. Yu, *Proc. Soc. Photo-Opt. Instrum. Eng.* 232, 9 (1980).
15. S. L. Zhuang, T. H. Chao, and F. T. S. Yu, *Opt. Lett.* 6, 102 (1981).
16. K. Dutta and J. W. Goodman, *J. Opt. Soc. Am.* 67, 796 (1977).
17. F. T. S. Yu, S. L. Zhuang, and S. T. Wu, *Appl. Phys.* 22, 99 (1981).
18. S. T. Wu and F. T. S. Yu, *Appl. Opt.* 20, 431 (1981).

SECTION VII

Apparent Transfer Function

Apparent Transfer Function for Partially Coherent Optical Information Processing

S. L. Zhuang* and F. T. S. Yu

Electrical Engineering Department, The Pennsylvania State University
University Park, PA 16802, USA

Received 5 March 1982/Accepted 3 April 1982

Abstract. In this paper, the general formulations of the apparent transfer function for the partially coherent optical processor will be derived. Although these formulas show that the apparent transfer function is dependent upon the degree of spatial and temporal coherence, there is actually more variability in the spatial coherence. We note that the obtained formulas may also be used as a criterion in the selection of source size and spectral bandwidth of an incoherent light source. Thus a specific optical information processing operation can be carried out with an incoherent source.

PACS: 42.30, 42.80

The description of a transfer-function for a linear spatially invariant optical system is an important concept in image evaluation. The techniques of using amplitude and intensely sinusoidal objects as input signals to determine the transfer characteristic of a coherent and an incoherent optical system has been investigated previously [1, 2]. In the past, the concept of system transfer function has been used as a criterion to evaluate the image quality of an optical system. However, a strict coherent or incoherent optical field is a mathematical idealization. An optical field that occurs in practice consists of a very limited degree of coherence, because the electromagnetic radiation from a real physical source is never strictly monochromatic. In reality, a physical source cannot be a point, but rather a finite extension which consists of many elementary radiators.

The optical system under the partially coherent regime has been studied by Becherer and Parrent [3], and Swing and Clay [4]. They have shown that there are difficulties in applying the linear system theory to the evaluation of imagery at high spatial frequencies. These difficulties are primarily due to the inapplicability of the linear system theory under partially

coherence regime. Nevertheless, using a sinusoidal analysis, an apparent transfer function for a partially coherent optical system was obtained. The result is appreciably different from those that would have been obtained from a linear system concept, either in intensity or in complex amplitude. In a more recent paper, Dutta and Goodman [5] described a procedure for sampling the mutual intensity function so that the image of a partially coherent object can be reconstructed.

In this paper, we shall show that an apparent transfer function for an optical information processing system can be derived from a partially coherent illuminator. We shall show that the apparent transfer function of a partially coherent optical processor is dependent upon the temporal and spatial coherence of the light source. We shall also show that the concept of transfer function is a valuable one that can be used as a criterion for selecting an appropriate incoherent light source for a specific information processing operation.

1. Apparent Transfer Function for Temporal Coherence

In a recent paper [6], we have evaluated the coherence requirement for a partially coherent optical information processing system. We have shown that the temporal and spatial coherence requirements are, re-

* Visiting scientist from Shanghai Optical Instrument Research Institute, Shanghai, China

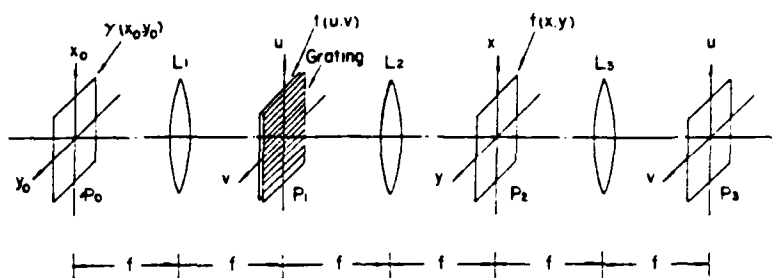


Fig. 1. A partially coherent optical information processor. (L: achromatic transform lens; p_0 : source plane; p_1 : input plane; p_2 : spatial frequency plane; p_3 : output plane)

spectively, dependent upon the spectral bandwidth and the source size of the light source. In the analysis of the temporal coherence requirement, we have assumed an infinitely small light source with finite spectral width. And for the evaluation of the spatial coherence requirement, we let monochromatic source with finite extent. In the evaluation of the apparent transfer for a partially coherent processing system, we shall also use these basic approaches.

We shall now evaluate the relationship between the apparent transfer function of an optical system and the spectral bandwidth of a light source. Let us now refer to the partially coherent optical information system of Fig. 1. We note that a diffraction grating is used at the input signal plane (u, v). The purpose of using a diffraction grating at the input plane is to disperse the input signal in the spatial frequency plane (x, y) so that a high spatial coherence can be achieved in the Fourier domain [7]. Thus the input signal can be processed in a complex amplitude, rather than in intensity, with a broad-band incoherent or white-light source. By using the partial coherent theory [8], we have computed a general output intensity distribution for the partially coherent processor, as shown in the following [7]:

$$I(u', v') = \int_{\lambda_0 - \Delta\lambda/2}^{\lambda_0 + \Delta\lambda/2} \int_{-\alpha}^{\alpha} \gamma(x_0, y_0) s(\lambda) c(\lambda) \times \left| \int_{-\alpha}^{\alpha} \int_{-\alpha}^{\alpha} T(x_0 + x - \lambda f p_0, y_0 + y) f(x, y) e^{-j \frac{2\pi}{\lambda f} (x u' - y v')} dx dy \right|^2 \cdot dx_0 dy_0 d\lambda, \quad (1)$$

where λ_0 and $\Delta\lambda$ are the central wavelength and spectral width of the light source, $\gamma(x_0, y_0)$ is the source intensity distribution, $s(\lambda)$ and $c(\lambda)$ are the source spectral distribution and the spectral sensitivity of the recording material, respectively, $f(x, y)$ is the filter function at the Fourier plane, $T(x, y)$ is the Fourier spectrum of the input signal and p_0 is the spatial frequency of this diffraction grating. For simplicity, we assume that both $s(\lambda)$ and $c(\lambda)$ are constants which can be ignored in (1). We now use a sinusoidal input object transparency to evaluate the apparent transfer function of the optical processing system. The overall input signal transmittance, that includes the diffraction grat-

ing, can be written as:

$$t(u) = (1 + c \cos 2\pi\omega u)(1 + \cos 2\pi p_0 u), \quad (2)$$

where ω is the spatial frequency of sinusoidal signal and c is the contrast. For simplicity, we use a one dimension analysis. Thus, the output intensity distribution of Eq. (1) can be reduced to:

$$I(u', \Delta\lambda) = \int_{\lambda_0 - \Delta\lambda/2}^{\lambda_0 + \Delta\lambda/2} \int_{-\alpha}^{\alpha} \gamma(x_0) |A(x_0, u'; \lambda)|^2 dx_0 d\lambda, \quad (3)$$

where

$$A(x_0, u'; \lambda) = \int_{-\alpha}^{\alpha} T(x_0, x; \lambda) f(x) e^{-j \frac{2\pi}{\lambda f} x u'} dx, \quad (4)$$

is a complex amplitude function.

In order to achieve a higher temporal coherence requirement for the complex filtering process, we limit the spatial filter $f(x, y)$ to a finite extension in the x direction, i.e.,

$$f(x) = \text{rect} \left\{ \frac{x - \lambda f p_0}{\Delta x} \right\}, \quad (5)$$

where Δx is the spatial width of the filter, and the filter is centered at $x = \lambda f p_0$ in the spatial frequency plane.

Since the Fourier spectrum of the input signal at the spatial frequency plane p_2 is:

$$T(x_0, x; \lambda) = \int_{-\alpha}^{\alpha} (1 - c \cos 2\pi\omega u) \cdot (1 - \cos 2\pi p_0 u) e^{-j \frac{2\pi}{\lambda f} u (x_0 - x)} du \quad (6)$$

we obtain:

$$\begin{aligned} T(x_0, x; \lambda) = & \delta \left(\frac{x_0 - x}{\lambda f} \right) - \frac{c}{2} \delta \left(\frac{x_0 - x}{\lambda f} - \omega \right) \\ & - \frac{c}{2} \delta \left(\frac{x_0 - x}{\lambda f} + \omega \right) \\ & - \frac{1}{2} \delta \left(\frac{x_0 - x}{\lambda f} - p_0 \right) - \frac{1}{2} \delta \left(\frac{x_0 - x}{\lambda f} + p_0 \right) \\ & - \frac{c}{2} \delta \left(\frac{x_0 - x}{\lambda f} - (\omega - p_0) \right) \\ & - \frac{c}{2} \delta \left(\frac{x_0 - x}{\lambda f} - (\omega + p_0) \right) \end{aligned}$$

$$\begin{aligned}
& + \frac{c}{4} \delta \left(\frac{x_0 + x}{\lambda f} - (p_0 - \omega) \right) \\
& + \frac{c}{4} \delta \left(\frac{x_0 + x}{\lambda f} + (p_0 + \omega) \right)
\end{aligned} \quad (7)$$

where $p_0 \gg \omega$.

In optical signal processing we focus only the first-order terms of (7) in the following

$$\begin{aligned}
T(x_0, x; \lambda) = & \frac{1}{2} \delta \left(\frac{x_0 + x}{\lambda f} - p_0 \right) + \frac{c}{4} \delta \left(\frac{x_0 + x}{\lambda f} - (p_0 - \omega) \right) \\
& + \frac{c}{4} \delta \left(\frac{x_0 + x}{\lambda f} - (p_0 + \omega) \right).
\end{aligned} \quad (8)$$

By substituting (5) and (8) into (4), we have:

$$\begin{aligned}
A(x_0, u'; \lambda) = & \int_{-\infty}^{\infty} \text{rect} \left\{ \frac{x - \lambda f p_0}{\Delta x} \right\} e^{-j \frac{2\pi}{\lambda f} x u'} dx \\
& * \int_{-\infty}^{\infty} \frac{1}{2} \delta \left(\frac{x_0 + x}{\lambda f} + p_0 \right) e^{-j \frac{2\pi}{\lambda f} x u'} dx \\
& + \int_{-\infty}^{\infty} \text{rect} \left\{ \frac{x - \lambda f p_0}{\Delta x} \right\} e^{-j \frac{2\pi}{\lambda f} x u'} dx \\
& * \int_{-\infty}^{\infty} \frac{c}{4} \delta \left(\frac{x_0 + x}{\lambda f} + p_0 - \omega \right) e^{-j \frac{2\pi}{\lambda f} x u'} dx \\
& + \int_{-\infty}^{\infty} \text{rect} \left\{ \frac{x - \lambda f p_0}{\Delta x} \right\} e^{-j \frac{2\pi}{\lambda f} x u'} dx \\
& * \int_{-\infty}^{\infty} \frac{c}{4} \delta \left(\frac{x_0 + x}{\lambda f} + p_0 + \omega \right) e^{-j \frac{2\pi}{\lambda f} x u'} dx \\
= & \left(\frac{1}{2} e^{j \frac{2\pi}{\lambda f} x_0 u'} \text{rect} \left\{ \frac{x_0}{\Delta x} \right\} \right. \\
& - \frac{c}{4} e^{j 2\pi \left(\frac{x_0}{\lambda f} - \omega \right) u'} \text{rect} \left\{ \frac{x_0 + \lambda f \omega}{\Delta x} \right\} \\
& \left. - \frac{c}{4} e^{j 2\pi \left(\frac{x_0}{\lambda f} + \omega \right) u'} \text{rect} \left\{ \frac{x_0 - \lambda f \omega}{\Delta x} \right\} \right) e^{-j 2\pi p_0 u'}
\end{aligned} \quad (9)$$

where * denotes the convolution operation.

We now consider the effect due to temporal coherence. Let us now assume that the incoherent source is a point source, i.e., $\gamma(x_0) = \delta(x_0)$, thus (3) becomes

$$\begin{aligned}
I(u', \Delta \lambda) = & \int_{\lambda_c - \Delta \lambda/2}^{\lambda_c + \Delta \lambda/2} A(u'; \lambda) A^*(u'; \lambda) d\lambda \\
= & \int_{\lambda_c - \Delta \lambda/2}^{\lambda_c + \Delta \lambda/2} \left[\frac{1}{2} - \frac{c^2}{8} \text{rect} \left\{ \frac{\lambda f \omega}{\Delta x} \right\} \right. \\
& - \frac{c}{2} \cos(2\pi \omega u') \text{rect} \left\{ \frac{\lambda f \omega}{\Delta x} \right\} \\
& \left. - \frac{c^2}{8} \cos(2\pi 2\omega u') \text{rect} \left\{ \frac{\lambda f \omega}{\Delta x} \right\} \right] d\lambda,
\end{aligned} \quad (10)$$

where $\Delta \lambda$ is the spatial bandwidth of the light source. In the following, we shall attempt to evaluate the output intensity distribution of (10) in the following separated cases:

(i) for $\omega < \frac{\Delta x}{(2\lambda_c + \Delta \lambda)f}$, the output intensity distribution of Eq. (10) becomes

$$\begin{aligned}
I^{(1)}(u', \Delta \lambda) = & \left[\frac{1}{4} + \frac{c^2}{8} + \frac{c}{2} \cos(2\pi \omega u') + \frac{c^2}{8} \cos(2\pi 2\omega u') \right] \Delta \lambda,
\end{aligned} \quad (11)$$

where the image contrast for both basic and second harmonic frequencies are

$$\gamma_1^{(1)}(\omega) = \frac{4c}{2 + c^2}, \quad (12a)$$

and

$$\gamma_2^{(1)}(\omega) = \frac{c^2}{2 + c^2}; \quad (12b)$$

(ii) for $\frac{\Delta x}{f(2\lambda_c + \Delta \lambda)} < \omega < \frac{\Delta x}{f(2\lambda_c - \Delta \lambda)}$, we obtain

$$\begin{aligned}
I^{(2)}(u', \Delta \lambda) = & \frac{1}{4} \Delta \lambda + \frac{c^2}{8} \left(\frac{\Delta x}{2f\omega} - \lambda_c + \frac{\Delta \lambda}{2} \right) \\
& + \frac{c}{2} \cos(2\pi \omega u') \left(\frac{\Delta x}{2f\omega} - \lambda_c + \frac{\Delta \lambda}{2} \right) \\
& + \frac{c^2}{8} \cos(2\pi 2\omega u') \left(\frac{\Delta x}{2f\omega} - \lambda_c + \frac{\Delta \lambda}{2} \right),
\end{aligned} \quad (13)$$

and

$$\gamma_1^{(2)}(\omega) = \frac{4c(\Delta x - 2f\omega\lambda_c - f\omega\Delta \lambda)}{4f\omega\Delta \lambda - c^2(\Delta x - 2f\omega\lambda_c - f\omega\Delta \lambda)}, \quad (14a)$$

$$\gamma_2^{(2)}(\omega) = \frac{c^2(\Delta x - 2f\omega\lambda_c - f\omega\Delta \lambda)}{4f\omega\Delta \lambda - c^2(\Delta x - 2f\omega\lambda_c - f\omega\Delta \lambda)}; \quad (14b)$$

(iii) for $\omega > \frac{\Delta x}{f(2\lambda_c - \Delta \lambda)}$, (10) becomes

$$I^{(3)}(u', \Delta \lambda) = \frac{1}{2} \Delta \lambda, \quad (15)$$

and

$$\gamma_1^{(3)}(\omega) = \gamma_2^{(3)}(\omega) = 0. \quad (16)$$

We also note that for the case of monochromatic point source, the output irradiance distribution is

$$I(u) = 1 - \frac{c^2}{2} - 2c \cos(2\pi \omega u) - \frac{c^2}{2} \cos(2\pi 2\omega u), \quad (17)$$

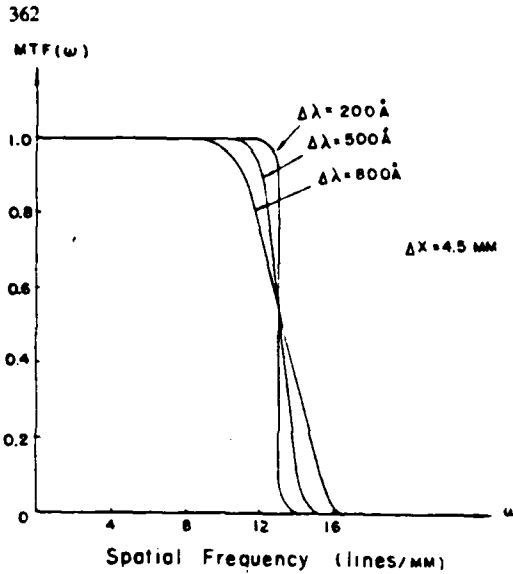


Fig. 2. Temporal coherence apparent transfer function as a function of input signal frequency ω , for various values of spectral width $\Delta\lambda$.

where

$$\gamma_1^{(0)} = \frac{4c}{2+c^2}, \quad (18a)$$

and

$$\gamma_2^{(0)} = \frac{c^2}{2+c^2}. \quad (18b)$$

Because the apparent transfer function can be obtained by the ratio of the contrast of the output basic frequency signal to the contrast of the input signal, we have

$$MTF(\omega) = \begin{cases} 1 & \text{for } \omega < \frac{\Delta x}{f(2\lambda_0 + \Delta\lambda)} \\ \frac{(2+c^2)(\Delta x - 2f\omega\lambda_0 + f\omega\Delta\lambda)}{4f\omega\Delta\lambda - c^2(\Delta x - 2f\omega\lambda_0 + f\omega\Delta\lambda)} & \text{for } \frac{\Delta x}{f(2\lambda_0 + \Delta\lambda)} \leq \omega < \frac{\Delta x}{f(2\lambda_0 - \Delta\lambda)} \\ 0 & \text{for } \omega \geq \frac{\Delta x}{f(2\lambda_0 - \Delta\lambda)} \end{cases} \quad (19)$$

which is depending upon the spatial frequency of the diffraction grating p_0 , the spatial width of the filter Δx , and the spectral bandwidth of the light source $\Delta\lambda$.

We note that the width of the filter Δx should be chosen to coincide with the product of the spatial frequency p_0 of the diffraction grating, the focal length of the achromatic transform lens, and the spectral width $\Delta\lambda$ of the light source, i.e.,

$$\Delta x = p_0 f \Delta\lambda. \quad (20)$$

By substituting this relationship of (20) into (19), we have

$$MFT(\omega) = \begin{cases} 1 & \text{for } \omega < \frac{p_0 \Delta\lambda}{2\lambda_0 - \Delta\lambda} \\ \frac{(2-c^2)(p_0 \Delta\lambda - 2\omega\lambda_0 - \omega\Delta\lambda)}{4\omega\Delta\lambda - c^2(p_0 \Delta\lambda - 2\omega\lambda_0 - \omega\Delta\lambda)} & \text{for } \frac{p_0 \Delta\lambda}{2\lambda_0 - \Delta\lambda} \leq \omega < \frac{p_0 \Delta\lambda}{2\lambda_0 + \Delta\lambda} \\ 0 & \text{for } \omega \geq \frac{p_0 \Delta\lambda}{2\lambda_0 + \Delta\lambda} \end{cases} \quad (21)$$

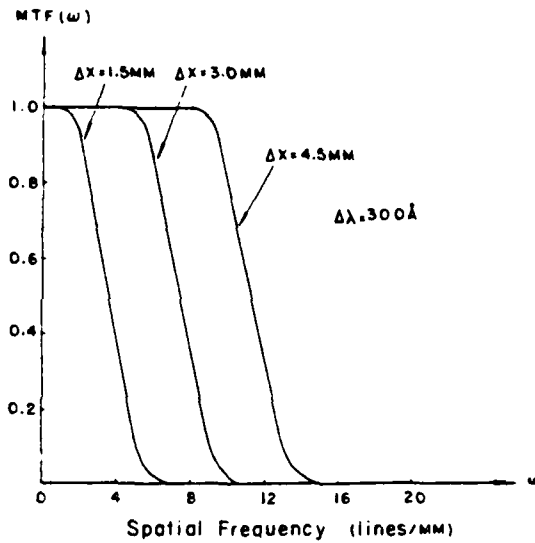


Fig. 3. Temporal coherence apparent transfer function as a function of ω , for various of spatial width of filter Δx .

Which apparent transfer function reduces to a function of p_0 and $\Delta\lambda$.

We now illustrate the dependency of the apparent transfer function upon the spectral width of the light source $\Delta\lambda$, the spatial width of the filter Δx , and the spatial frequency of the grating p_0 . Figure 2 shows the plots of the apparent transfer function (MTF) as a function of the input signal frequency ω for various values of spectral bandwidth $\Delta\lambda$. From this figure we

notice that the MTF is not appreciably affected by the spectral bandwidth $\Delta\lambda$ of the light source, except for some slight changes in frequency response. For example, an $\Delta\lambda$ becomes broader, a slight reduction in lower frequency response is expected. However, the system bandwidth is somewhat slightly broader. Figure 3 shows the variation of MTF as a function of ω for various values of spatial width Δx of the filter and a

Apparent Transfer Function

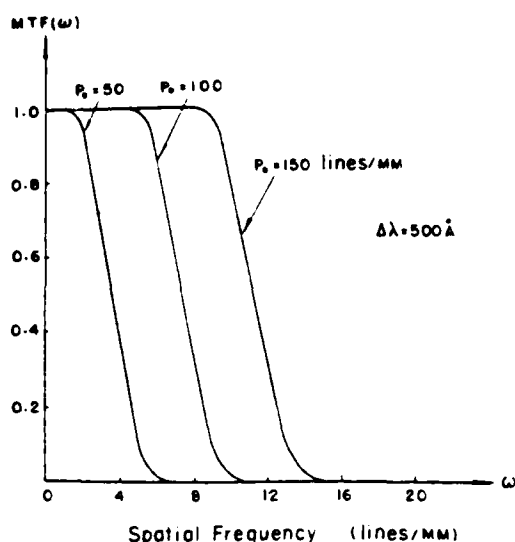


Fig. 4. Temporal coherence apparent transfer function as a function of ω , for various values of grating spatial frequency p_0 .

given $\Delta\lambda$. From this figure we see that the system bandwidth is linearly related to that of the spatial width of the filter. In other words, the larger the spatial width of the filter used, the wider the system bandwidth which may result. Figure 4 also shows the dependent of the MTF upon the spatial frequency of the grating p_0 . Again, we see that the system bandwidth is linearly proportional to p_0 , as expected from the relationship of (20). In other words, a higher frequency grating has the advantage of achieving finer image resolution. However, this advantage of using a higher spatial frequency grating is somewhat compensated with the use of a larger achromatic transform lens, to which is generally more expensive.

2. Apparent Transfer Function for Spatial Coherence

Now we shall determine the dependent of the apparent transfer function upon the source size Δs . To simplify our analysis, we assume that the light source is monochromatic but with finite extent. The output intensity distribution of (3) can therefore be written as:

$$I(u', \Delta s) = \int_{-\infty}^{\infty} \gamma(x_0) A(u', x_0)^2 dx_0. \quad (22)$$

For simplicity, we assume that a uniform irradiance distribution of the extended light source exists, i.e.,

$$\gamma(x_0) = \text{rect} \left\{ \frac{x_0}{\Delta s} \right\}. \quad (23)$$

where Δs is the extended source size with reference to (4), we see that

$$\begin{aligned} A(u', x_0) A^*(u', x_0) &= \frac{1}{4} \text{rect} \left\{ \frac{x_0}{\Delta x} \right\} \\ &+ \frac{c^2}{16} \left(\text{rect} \left\{ \frac{x_0 + \lambda_0 f \omega}{\Delta x} \right\} + \text{rect} \left\{ \frac{x_0 - \lambda_0 f \omega}{\Delta x} \right\} \right) \\ &+ \frac{c}{4} \cos(2\pi \omega u') \left(\text{rect} \left\{ \frac{x_0 + \frac{1}{2} \lambda_0 f \omega}{\Delta x - \lambda_0 f \omega} \right\} \right. \\ &\left. + \text{rect} \left\{ \frac{x_0 - \frac{1}{2} \lambda_0 f \omega}{\Delta x - \lambda_0 f \omega} \right\} \right) \\ &+ \frac{c^2}{8} \cos(2\pi \omega u') \text{rect} \left\{ \frac{x_0}{\Delta x - 2\lambda_0 f \omega} \right\}, \end{aligned} \quad (24)$$

where we have used the following relationship

$$\text{rect} \left\{ \frac{x}{a} \right\} \text{rect} \left\{ \frac{x+b}{a} \right\} = \text{rect} \left\{ \frac{x+b/2}{a+b} \right\}. \quad (25)$$

By properly shifting the coordinate axis, (24) can be written as

$$\begin{aligned} A(u', x_0) A^*(u', x_0) &= \frac{1}{4} \text{rect} \left\{ \frac{x_0}{\Delta x} \right\} \\ &+ \frac{c^2}{16} \left(\text{rect} \left\{ \frac{x_0}{\Delta x + 2\lambda_0 f \omega} \right\} + \text{rect} \left\{ \frac{x_0}{\Delta x - 2\lambda_0 f \omega} \right\} \right) \\ &+ \frac{c}{4} \cos(2\pi \omega u') \left(\text{rect} \left\{ \frac{x_0}{\Delta x} \right\} + \text{rect} \left\{ \frac{x_0}{\Delta x - 2\lambda_0 f \omega} \right\} \right) \\ &+ \frac{c^2}{8} \cos(2\pi \omega u') \text{rect} \left\{ \frac{x_0}{\Delta x - 2\lambda_0 f \omega} \right\}. \end{aligned} \quad (26)$$

By substituting (23) and (26) into (22), we obtained the following output intensity distribution and the basic and second harmonic frequencies

(i) for $0 < \Delta s < \Delta x - 2\lambda_0 f \omega$, we have:

$$\begin{aligned} I^{(1)}(u', \Delta s) &= \left[\left(\frac{1}{4} - \frac{c^2}{8} \right) - \frac{c}{2} \cos(2\pi \omega u') \right. \\ &\left. - \frac{c^2}{8} \cos(2\pi \omega u') \right] \Delta s, \end{aligned} \quad (27)$$

and

$$\gamma_1^{(1)}(\omega) = \frac{4c}{2 - c^2}. \quad (28a)$$

$$\gamma_2^{(1)}(\omega) = \frac{c^2}{2 - c^2}. \quad (28b)$$

(ii) for $\Delta x - 2\lambda_0 f \omega < \Delta s < \Delta x$, we obtain

$$\begin{aligned} I^{(2)}(u', \Delta s) &= \left[\left(\frac{1}{2} - \frac{c^2}{16} \right) \Delta s - \frac{c^2}{16} (\Delta x - 2\lambda_0 f \omega) \right] \\ &- \frac{c}{2} (\Delta s - \Delta x + 2\lambda_0 f \omega) \cos(2\pi \omega u') \\ &- \frac{c^2}{8} (\Delta x - 2\lambda_0 f \omega) \cos(2\pi \omega u'). \end{aligned} \quad (29)$$

364

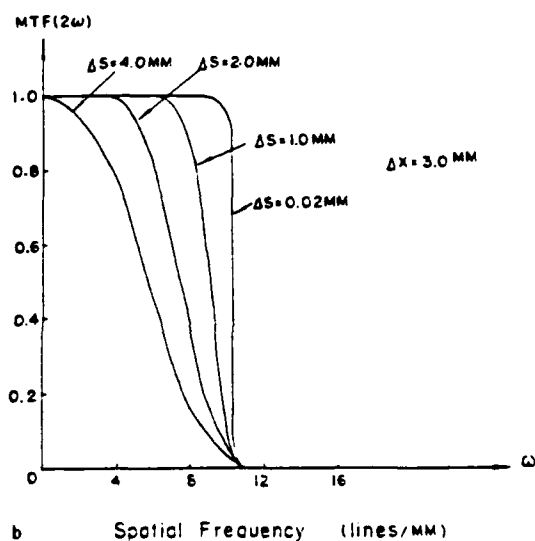
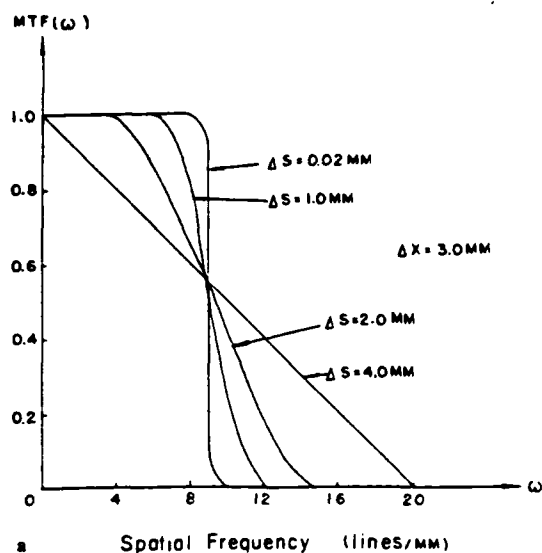


Fig. 5a and b. Spatial coherence apparent transfer function as a function of input signal frequency ω , for various values of source size Δs . (a) Basic MTF. (b) Second-harmonic MTF

and

$$T_1^{(2)}(\omega) = \frac{4c(\Delta s - \Delta x - 2\lambda_0 f \omega)}{4\Delta s + c^2(\Delta s - \Delta x - 2\lambda_0 f \omega)} \quad (30a)$$

$$T_2^{(2)}(\omega) = \frac{2c^2(\Delta x - 2\lambda_0 f \omega)}{4\Delta s - c^2(\Delta s - \Delta x - 2\lambda_0 f \omega)} \quad (30b)$$

(iii) for $\Delta x < \Delta s < \Delta x - 2\lambda_0 f \omega$, (26) becomes

$$T^{(3)}(u', \Delta s) = \left(\frac{1}{2} - \frac{c^2}{16} \right) \Delta x - \frac{c^2}{16} (\Delta s - 2\lambda_0 f \omega) - \frac{c}{2} (\Delta x - \lambda_0 f \omega) \cos(2\pi \omega u') - \frac{c^2}{8} (\Delta x - 2\lambda_0 f \omega) \cos(2\pi 2\omega u'). \quad (31)$$

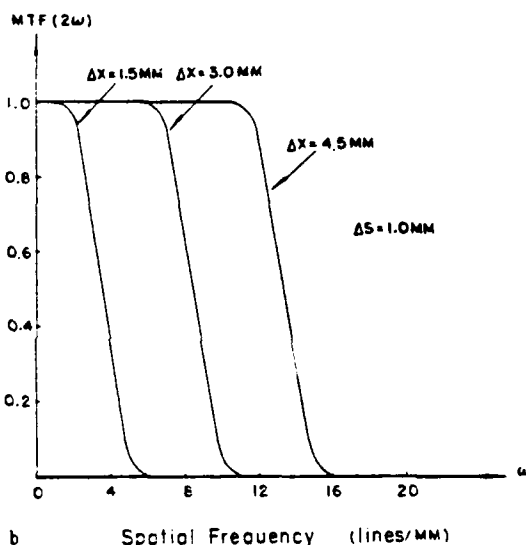
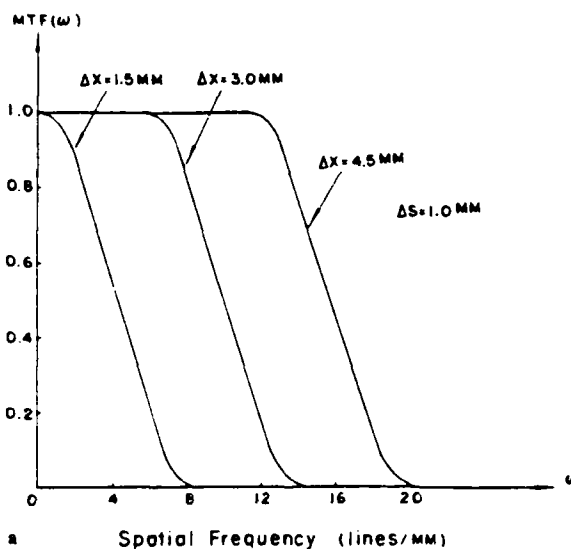


Fig. 6a and b. Spatial coherence apparent transfer function as a function of input signal frequency ω , for various values of filter width Δx . (a) Basic MTF. (b) Second harmonic MTF

$$T_1^{(3)}(\omega) = \frac{8c(\Delta x - \lambda_0 f \omega)}{4\Delta x - c^2(\Delta s - \Delta x - 2\lambda_0 f \omega)} \quad (32a)$$

and

$$T_2^{(3)}(\omega) = \frac{2c^2(\Delta x - 2\lambda_0 f \omega)}{4\Delta x - c^2(\Delta s - \Delta x - 2\lambda_0 f \omega)} \quad (32b)$$

for $\Delta s > \Delta x - 2\lambda_0 f \omega$, we have:

$$T^{(4)}(u', \Delta s) = \left(\frac{1}{2} - \frac{c^2}{8} \right) \Delta x - \frac{c}{2} (\Delta x - \lambda_0 f \omega) \cos(2\pi \omega u') - \frac{c^2}{8} (\Delta x - 2\lambda_0 f \omega) \cos(2\pi 2\omega u') \quad (33)$$

$$T_1^{(4)}(\omega) = \frac{4c(\Delta x - \lambda_0 f \omega)}{2 - c^2 \Delta x} \quad (34a)$$

and

$$\gamma_2^{(4)}(\omega) = \frac{c^2(\Delta x - 2\lambda_0 f \omega)}{(2 + c^2)\Delta x}; \quad (34b)$$

(v) for $\Delta x < \omega\lambda_0 f$, we again obtain

$$I^{(5)}(u', \Delta s) = \text{constant}, \quad (35)$$

and

$$\gamma_1^{(5)}(\omega) = \gamma_2^{(5)}(\omega) = 0. \quad (36)$$

Notice that where this cut-off frequency of the optical system is $\omega_{\max} = \Delta x / \lambda_0 f$. Thus the apparent transfer function of the optical processing system, for both the basic and second harmonic frequencies are

$$\text{MTF}(\omega) = \begin{cases} 1 & \text{for } 0 \leq \Delta s < \Delta x - 2\lambda_0 f \omega \\ \frac{(2 + c^2)(\Delta s + \Delta x - 2\lambda_0 f \omega)}{4\Delta s + c^2(\Delta s + \Delta x - 2\lambda_0 f \omega)} & \text{for } \Delta x - 2\lambda_0 f \omega \leq \Delta s < \Delta x \\ \frac{2(2 + c^2)(\Delta x - \lambda_0 f \omega)}{4\Delta x + c^2(\Delta s + \Delta x - 2\lambda_0 f \omega)} & \text{for } \Delta x \leq \Delta s \leq \Delta x + 2\lambda_0 f \omega \\ \frac{\Delta x - \lambda_0 f \omega}{\Delta x} & \text{for } \Delta x + 2\lambda_0 f \omega \leq \Delta s \\ 0 & \text{for } \Delta x \leq \omega\lambda_0 f \end{cases} \quad (37)$$

and similarly:

$$\text{MTF}(2\omega) = \begin{cases} 1 & \text{for } 0 \leq \Delta s < \Delta x - 2\lambda_0 f \omega \\ \frac{2(2 + c^2)(\Delta x - 2\lambda_0 f \omega)}{4\Delta s + c^2(\Delta s + \Delta x - 2\lambda_0 f \omega)} & \text{for } \Delta x - 2\lambda_0 f \omega \leq \Delta s < \Delta x \\ \frac{2(2 + c^2)(\Delta x - 2\lambda_0 f \omega)}{4\Delta x + c^2(\Delta s + \Delta x - 2\lambda_0 f \omega)} & \text{for } \Delta x \leq \Delta s < \Delta x + 2\lambda_0 f \omega \\ \frac{\Delta x - 2\lambda_0 f \omega}{\Delta x} & \text{for } \Delta x + 2\lambda_0 f \omega \leq \Delta s \\ 0 & \text{for } \Delta x \leq \lambda_0 f \omega. \end{cases} \quad (38)$$

From the above equations, one may see that MTF, either for the fundamental or for the second-harmonic frequency, decreases rather rapidly as the source size Δs increases. Figure 5a shows MTF as a function of input spatial frequency ω , for various values of source size Δs . From this figure, we discover that the frequency response (i.e., MTF) decreases quite rapidly as the source size increases. In other words, for a fixed filter size, the smaller the source size used, the better the system frequency response. We also see that, where the source size is adequately small (e.g., $\Delta s \leq 0.02 \text{ mm}$) the MTF approaches the strict coherent MTF, on the other hand, if the source size is significantly large (e.g., $\Delta s \geq 4 \text{ mm}$) the MTF approaches that of the incoherent case. Figure 5b shows the second-harmonic MTF as a function of input spatial frequency ω . From the figure, we see that frequency response decreases even faster as

the source size increases. Unlike the first harmonic MTF of Fig. 5a, the cut-off frequency tends to stay at the same values, although the higher frequency response decreases rather rapidly.

Figures 6a and 6b show the basic and the second-harmonic MTF as a function of input spatial frequency ω , for various sizes of spatial filters Δx , for a given Δs . From these two figures, again we see that the transfer system bandwidth is linearly related to the size of the spatial filter. Thus MTF is obviously limited by the filter bandwidth of the optical processor. The increase of filter bandwidth also causes a reduction in temporal coherence, which in turn reduces the processing capability. Nevertheless, an optimum processing capability

can be obtained with the appropriate MTF for certain optical processing operations.

3. Conclusion

The nonlinear behavior of the partially coherent optical processor, when considering either intensity or amplitude distribution input signals, necessitates the use of the apparent transfer function to accurately predict the system response. We have derived the general formulas for MTF in terms of the theory of partially coherent light. These derivations indicate the dependence of MTF upon the degree of spatial coherence (i.e., the source size) as well as the degree of temporal coherence (i.e., the source spectral bandwidth). MTF has been shown to be less dependent

upon the spatial coherence requirement as compared to its relationship with the temporal coherence requirement.

It has been noted that the spatial bandwidth of our optical processor is primarily dependent upon the size of the filter Δx , where the filter is placed in the Fourier plane. The transfer systems bandwidth may be increased by using a larger spatial filter Δx . However, the size of the filter is selected such that $\Delta x = p_0 f \Delta \lambda$, which is linearly related to the spatial frequency of grating, the focal length of the transform lens and the spectral width of the light source. A narrow spectral band $\Delta \lambda$ is necessary for most partially coherent optical information processing operations. In order to achieve the required $\Delta \lambda$ for a wide strip of spatial filter Δx in the spatial frequency plane, a diffraction grating of sufficiently high frequency p_0 at the input plane is needed. For example, for partially coherent processing with a white light source, a set of narrow spectral band filters, each with a spectral bandwidth $\Delta \lambda$, can be used in the

spatial frequency plane. Finally, we stress that the apparent transfer function which we have obtained is rather general and may be applied to any partially coherent optical processing system.

Acknowledgement. This work is supported by U.S. Air Force Office of Scientific Research under grant no. AFOSR-81-0148.

References

1. E.L. O'Neill: *Introduction to Statistical Optics* (Addison-Wesley, Reading, MA 1963)
2. J.W. Goodman: *Introduction to Fourier Optics* (McGraw-Hill, New York, NY 1968)
3. R.J. Becherer, G.B. Parrent: *J. Opt. Soc. Am.* **57**, 1479-1486 (1967)
4. R.E. Swing, J.R. Clay: *J. Opt. Soc. Am.* **57**, 1180-1189 (1967)
5. K. Dutta, J.W. Goodman: *J. Opt. Soc. Am.* **67**, 796-802 (1977)
6. F.T.S. Yu: *Opt. Commun.* **27**, 23-26 (1978)
7. S.L. Zhuang, F.T.S. Yu: "Coherence Requirement for Partially Coherent Optical Processing", *Appl. Opt.* (to be published)
8. M. Born, E. Wolf: *Principles of Optics*, 4th ed. (Pergamon Press, New York, NY 1970)

SECTION VIII

Source Encoding and Signal Sampling

ELECTRICAL ENGINEERING DEPARTMENT
THE PENNSYLVANIA STATE UNIVERSITY

University Park, Pennsylvania 16802

SOURCE ENCODING, SIGNAL SAMPLING AND SPECTRAL BAND FILTERING FOR PARTIALLY COHERENT OPTICAL SIGNAL PROCESSING

F. T. S. YU

MOTS CLÉS

Traitement optique
Cohérence

KEY WORDS

Optical processing
Coherence

Traitement optique en éclairage partiellement cohérent en modulant la source et le signal et en filtrant le spectre du signal

SUMMARY : Relations between coherence requirement, spectral filtering, signal sampling, and source encoding are discussed. Since the spatial coherence requirement is determined by the signal processing operation, a strict spatial coherence is usually not required. The advantage of the source encoding is to relax the constraints of a physical light source so that the signal processing can be carried out with an extended incoherent source. The effect of signal sampling is to improve the temporal coherence requirement at the Fourier plane so that the spatial filtering can be carried out with partially coherence mode. The objective of broad spectral band filtering is to carry out the signal processing over the entire spectral band of the light source so that the coherent noise can be eliminated. Since the partially coherent optical processor utilizes a broad spectral band white-light source, it is particularly suitable for color signal processing. Experimental demonstrations for the source encoding, signal sampling and spectral band filtering are included.

RÉSUMÉ : On discute des relations entre la cohérence, le filtrage, l'échantillonnage du signal et la modulation de la source. Puisque le degré de cohérence spatiale est déterminé par le traitement de l'image, une parfaite cohérence spatiale n'est, en général, pas nécessaire. L'avantage de moduler la source est de permettre de traiter l'image avec une source étendue incohérente. L'effet d'échantillonner l'image est d'améliorer la cohérence temporelle dans le plan de Fourier de façon que le filtrage puisse s'effectuer en lumière partiellement cohérente temporellement. L'utilisation d'un domaine spectral large a pour but de réduire le bruit dû à la cohérence spatiale de l'éclairage. Enfin, puisque un dispositif de traitement d'image en lumière partiellement cohérente utilise une source de lumière blanche, il paraît particulièrement bien adapté au traitement des images en couleurs. On présente des expériences montrant l'avantage de moduler la source et d'échantillonner l'image lorsqu'on utilise une source étendue de lumière blanche.

INTRODUCTION

Since the invention of laser (i.e., a strong coherent source) laser has become a fashionable tool for many scientific applications particularly as applied to coherent optical signal processing. However coherent optical signal processing systems are plagued with coherent noises, which frequently limit their processing capability. As noted by the late Gabor, the Nobel prize winner in physics in 1970 for his invention of holography, the coherent noise is the number one enemy of the Modern Optical Signal Processing [1]. Aside the coherent noise, the coherent sources are usually expensive, and the coherent processing envi-

ronments are very stringent. For example, heavy optical benches and dust free environments are generally required.

Recently, we have looked at the optical processing from a different standpoint. A question arises, is it necessarily true that all optical signal processing required a coherent source? The answer to this question is that there are many optical signal processes that can be carried out by a white-light source [2]. The advantages of the proposed white-light signal processing technique are: 1. It is capable of suppressing the coherent noise; 2. White-light sources are usually inexpensive; 3. The processing environments are not critical; 4. The white-light sys-

tem is relatively easy and economical to maintain; and 5. The white-light processor is particularly suitable for color image processing.

One question that the reader may ask, since the white-light system offers all these glamorous merits, why it has been ignored for so long? The answer to this question is that, it was a general acceptance that an incoherent source cannot process the signal in complex amplitude. However, none of the practical sources are strictly incoherent, even a white-light source. In fact, we were able to utilize the partial coherence of a white-light source to perform the complex amplitude processing. The proposed white-light processor, on one hand it is capable of suppressing the coherent noise like an incoherent processor, on the other hand it is capable of processing the signal in complex amplitude like a coherent processor.

There is however a basic different approach toward a coherent and a white-light processor. In coherent processing, virtually no one seems to care about the coherence requirements, since the laser provides a strong coherent source. However, in white-light processing, the knowledge of the coherence requirement is usually needed.

In white-light processing we would approach the problem backward. First, we should know what is the processing operation we wish to perform: Is it a 1-D or 2-D processing? Is the signal filtering a point or point-pair concept? What is the spatial bandwidth of the signal? etc. Then with these knowledges, we would be able to evaluate the coherence requirements at the Fourier and at the input planes. From the evaluated results, we would be able to design a signal sampling function and a source encoding function to obtain these requirements. The objective of using a signal sampling function is to achieve a high degree of temporal coherence in Fourier plane so that the signal can be processing in complex amplitude, for the entire spectral band of a white-light source. And for the source encoding is to alleviate the constraint of an extended white-light source.

In the following sections, we shall discuss in detail the source encoding, signal sampling and spatial band filtering as applied to a partially coherent optical (e.g., white-light) signal processing.

PARTIALLY COHERENT OPTICAL SIGNAL PROCESSING

We shall now describe an optical signal processing technique that can be carried out by a broad band white-light source, as illustrated in figure 1. The white-light signal processing system is similar to that of a coherent system, except the use of a white-light source, source encoding mask, signal sampling grating, multispectral filters and achromatic transform lenses. For example, if we place a signal transparency $s(x, y)$ in contact with a sampling phase grating, the complex light field for every wavelength λ behind the achromatic transform lens L_1 would be

$$E(p, q; \lambda) = \iint s(x, y) \exp(i p_0 x) \times \exp[-i(p x + q y)] dx dy = S(p - p_0, q), \quad (1)$$

where the integral is over the spatial domain of the input plane P_1 , (p, q) denotes the angular spatial frequency coordinate system, p_0 is the angular spatial frequency of the sampling phase grating, and $S(p, q)$ is the Fourier spectrum of $s(x, y)$. If we write Eq. (1) in the form of linear spatial coordinate system (α, β) , we have

$$E(\alpha, \beta; \lambda) = S\left(\alpha - \frac{\lambda f}{2\pi} p_0, \beta\right), \quad (2)$$

where $p \triangleq (2\pi/\lambda f)\alpha$, $q \triangleq (2\pi/\lambda f)\beta$, and f is the focal length of the achromatic transform lens. Thus, we see that the Fourier spectra would disperse into rainbow color along the α axis, and each Fourier spectrum for a given wavelength λ is centered at $\alpha \pm (\lambda f/2\pi)p_0$.

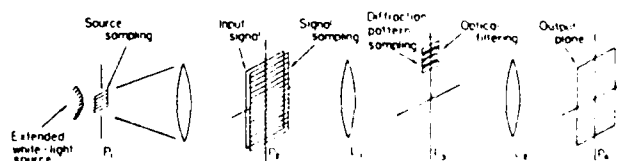


FIG. 1. — A white-light optical signal processor

In signal filtering, we assume that a sequence of complex spatial filters for various λ_n are available, i.e., $H(p_n, q_n)$, where $p_n = (2\pi/\lambda_n f)\alpha$, $q_n = (2\pi/\lambda_n f)\beta$. In practice, all the processing signals are spatial frequency limited, the spatial bandwidth of each spectral band filter $H(p_n, q_n)$ is also bandlimited, such as

$$H(p_n, q_n) = \begin{cases} H(p_n, q_n), & \alpha_1 < \alpha < \alpha_2, \\ 0, & \text{otherwise.} \end{cases} \quad (3)$$

where $\alpha_1 \triangleq (\lambda_n f/2\pi)(p_0 + \Delta p)$ and $\alpha_2 = (\lambda_n f/2\pi)(p_0 - \Delta p)$ are the upper and the lower spatial limits of $H(p_n, q_n)$, and Δp is the spatial bandwidth of the input signal $s(x, y)$.

The limiting wavelengths of each $H(p_n, q_n)$ can be written as

$$\lambda_l = \lambda_n \frac{p_0 + \Delta p}{p_0 - \Delta p}, \quad \text{and} \quad \lambda_h = \lambda_n \frac{p_0 - \Delta p}{p_0 + \Delta p}. \quad (4)$$

The spectral bandwidth of $H(p_n, q_n)$ is therefore,

$$\Delta\lambda_n = \lambda_n \frac{4 p_0 \Delta p}{p^2 - (\Delta p)^2} \approx \frac{4 \Delta p}{p_0} \lambda_n. \quad (5)$$

If we place this set of spectral band filters side-by-side positioned over the smeared Fourier spectra, then the intensity distribution of the output light field can be shown as,

$$I(x, y) \approx \sum_{n=1}^N \Delta\lambda_n |s(x, y; \lambda_n) \cdot h(x, y; \lambda_n)|^2, \quad (6)$$

where $h(x, y; \lambda)$ is the spatial impulse response of

$H(p_n, q_n)$ and $*$ denotes the convolution operation. Thus, the proposed white-light signal processor is capable of processing the signal in complex amplitude. Since the output intensity is the sum of the mutually incoherent narrow band irradiances, the annoying coherent noise can be eliminated. Furthermore, the white-light source contains all the color wavelengths, the proposed system is particularly suitable for color signal processing.

SPECTRAL BAND FILTERING, SIGNAL SAMPLING AND SOURCE ENCODING

We have mentioned earlier for white-light or partially coherent processing, we would approach the problem in backward manner. For example, if signal filtering is two-dimensional (e.g., 2-D correlation operation), we would synthesize a set of narrow spectral band filters for each λ_n for the entire smeared Fourier spectra, as illustrated in figure 2(a). On the other hand, if the signal filtering is one-dimensional (e.g., deblurring due to linear motion), a broadband fan-shape spatial filter, to accommodate the scale variation due to wavelength, can be utilized as illustrated in figure 2(b). Since the filtering is taken place with the

entire spectral band of the light source, the coherent noise can be suppressed and the white-light processing technique is very suitable for colour image processing.

There is, however, a temporal coherence requirement imposed upon the signal filtering in Fourier plane. Since the scale of the Fourier spectrum varies with wavelength, a temporal coherence requirement should be imposed on each spatial filter at the Fourier plane. Thus, the spectral spread over each filter $H(p_n, q_n)$ is imposed by the temporal coherence requirement, i.e.,

$$\frac{\Delta \lambda_n}{\lambda_n} = \frac{4 \Delta \rho}{P_0} \ll 1. \quad (7)$$

From this requirement, a high degree of temporal coherence is achievable in the Fourier plane by simply increasing the spatial frequency of the sampling grating. Needless to say that the same temporal coherence requirement of Eq. (7) can also be applied for a broadband fan-shape filter.

There is also a spatial coherence requirement imposed at the input plane of the white-light processor. With reference to the Wolf's [3] partial coherence theory [3], the spatial coherence function at the input plane can be shown [4],

$$\Gamma(\mathbf{x} - \mathbf{x}') = \iint \gamma(\mathbf{x}_0) \exp \left[i 2 \pi \frac{\mathbf{x}_0}{\lambda f} (\mathbf{x} - \mathbf{x}') \right] d\mathbf{x}_0, \quad (8)$$

where $\gamma(\mathbf{x}_0)$ denotes the intensity distribution of the source encoding function.

From the above equation, we see that the spatial coherence and source encoding functions form a Fourier transform pair, i.e.,

$$\gamma(\mathbf{x}_0) = \mathcal{F}[\Gamma(\mathbf{x} - \mathbf{x}')], \quad (9)$$

and

$$\Gamma(\mathbf{x} - \mathbf{x}') = \mathcal{F}^{-1}[\gamma(\mathbf{x}_0)], \quad (10)$$

where \mathcal{F} denotes the Fourier transformation. This Fourier transform pair implies that if a spatial coherence function is given then the source encoding function can be evaluated through the Fourier transformation and vice versa. We note that source encoding function can consist of apertures of any shape or complicated gray scale transparency. However the source encoding function is only limited to a positive real quantity which is restricted by the following physical realizability condition :

$$0 \leq \gamma(\mathbf{x}_0) \leq 1. \quad (11)$$

In white-light processing, we would search for a reduced spatial coherence requirement for the processing operation. With reference to this reduced spatial coherence function, a source encoding function that satisfied the physical realizability condition can be obtained. One of the basic objectives of the source encoding is to alleviate the constraint of a white-light source. Furthermore the source encoding also improves the utilization of the light power such that the optical processing can be carried out by an extended source.

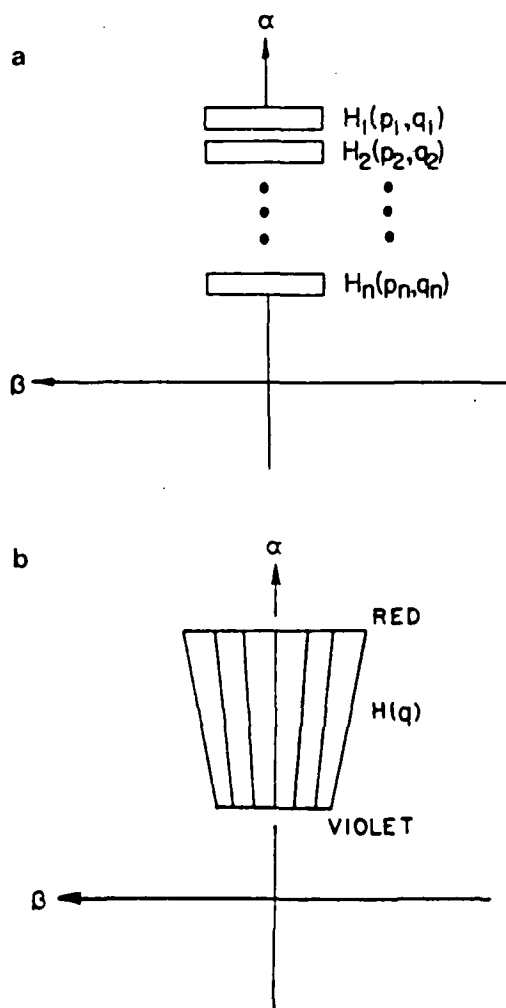


Fig. 2. (a) A multi spectral-band filter. (b) A fan-shape filter.

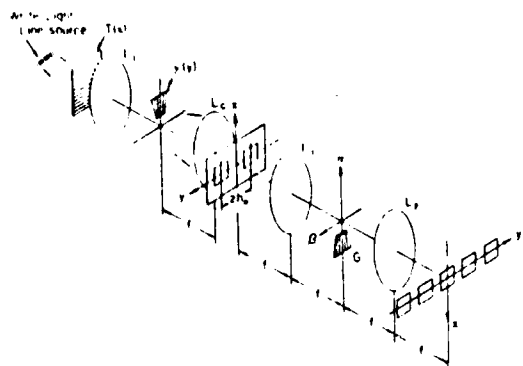


FIG. 3. A white-light image subtraction processor. TG: phase grating, L_1 : image lens, L_2 : collimated lens, L_3 and L_4 : achromatic transform lenses, $\gamma(y)$: source encoding mask, G: fan-shape diffraction grating.

We shall now illustrate an application of the source encoding, signal sampling and filtering for a white-light signal processing. Let us now consider a polychromatic image subtraction [5]. The image subtraction of Lee [6] that we would consider is essentially a one-dimensional processing operation, in which a 1-D fan-shape diffraction grating should be utilized, as illustrated in figure 3. We note that the fan-shape grating (i.e., filter) is imposed by the temporal coherence condition of Eq. (7). Since the image subtraction is a point-pair processing operation, a strictly broad spatial coherence function at the input plane is not required. In other words, if one maintains the spatial coherence between the corresponding image points to be subtracted at the input plane, then the subtraction operation can be carried out at the output image plane. Thus instead of using a strictly broad spatial coherence function, a reduced spatial coherence function may be utilized, such as

$$\Gamma(y - y') = \delta(y - y' - h_0) + \delta(y' - y' + h_0), \quad (12)$$

where $2h_0$ is the main separation between the two input color transparencies. The source encoding function can therefore be evaluated by through the Fourier transform of Eq. (9), such as

$$\gamma(y_0) = 2 \cos\left(\frac{2\pi h_0}{\lambda f} y_0\right). \quad (13)$$

Unfortunately Eq. (13) is a bipolar function which is not physically realizable. To ensure a physically realizable source encoding function, we let a reduced spatial coherence function with the required point-pair coherence characteristic be [7].

$$\begin{aligned} \Gamma(|y - y'|) &= \\ &= \frac{\sin\left(\frac{N\pi}{h_0} |y - y'|\right)}{N \sin\left(\frac{\pi}{h_0} |y - y'|\right)} \operatorname{sinc}\left(\frac{\pi w}{h_0 d} |y - y'|\right), \quad (14) \end{aligned}$$

where $N \gg 1$ a positive integer, and $w \ll d$. Eq. (14) represents a sequence of narrow pulses which occur at every $|y - y'| = nh_0$, where n is a positive integer, and their peak values are weighted by a broader sine factor, as shown in figure 4(a). Thus, a high degree of spatial coherence can be achieved at every point-pair between the two input color transparencies. By taking the Fourier transformation of the reduced spatial coherence function of Eq. (14), the corresponding source encoding function is

$$\gamma(|y|) = \sum_{n=1}^N \operatorname{rect} \frac{|y - nd|}{w}, \quad (15)$$

where w is the slit width, $d = (\lambda/fh_0)$ is the separation between the slits, and N is the number of the slits. Since $\gamma(|y|)$ is a positive real function which satisfies the constraint of Eq. (11), the proposed source encoding function of Eq. (15) is physically realizable.

In view of Eq. (15), we also note that, the separation of slit d is linearly proportional of the λ . The source encoding is a fan-shape type function, as shown in figure 4(b). To obtain lines of rainbow color spectral light source for the signal processing, we would utilize a linear extended white-light source with a dispersive phase grating, as illustrated in figure 3. Thus with

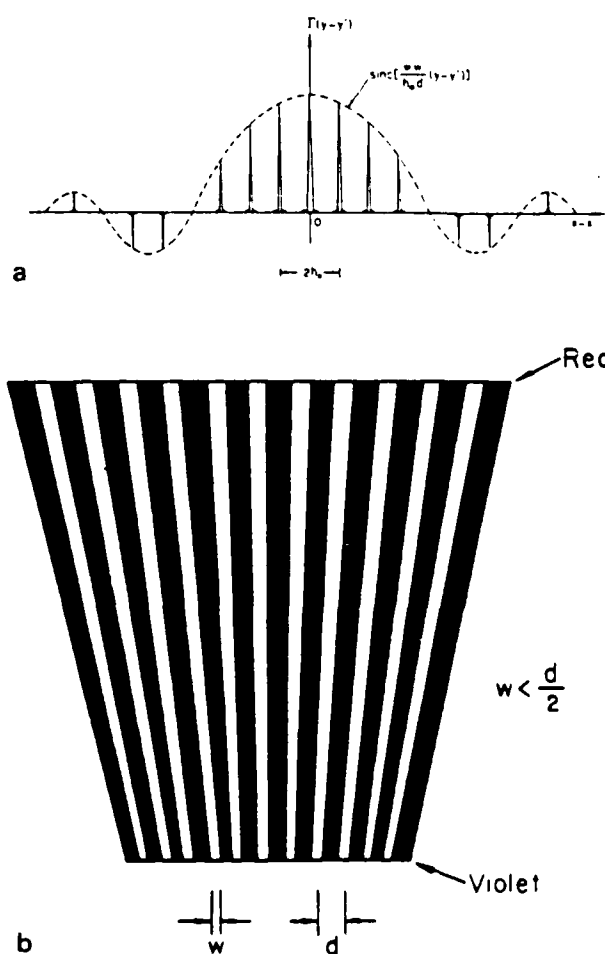
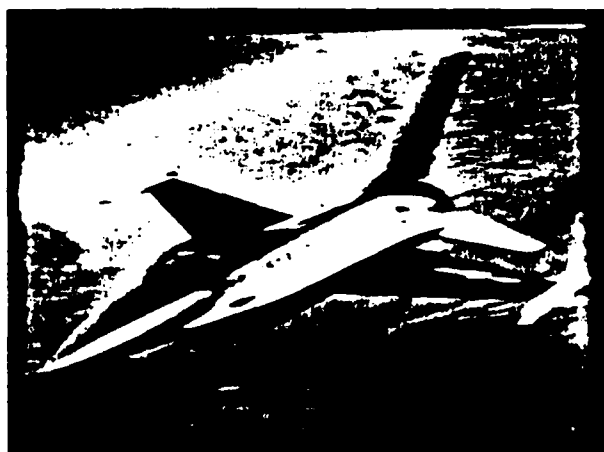
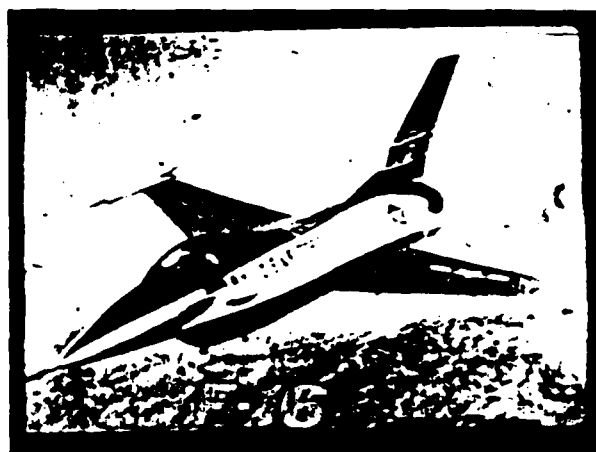


FIG. 4. - (a) A spatial coherence function. (b) A source encoding mask.



a



b

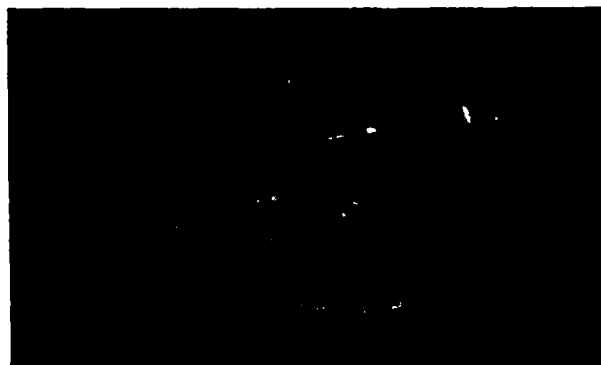
FIG. 5. - (a) A blurred color image, (b) A deblurred color image.



a



b



c

FIG. 6. - (a) and (b), Pictures of the input color objects, (c) The subtracted color image

appropriate source encoding, signal sampling and filtering, color image subtraction operation can be obtained at the output plane. We stress again, the basic advantage of source encoding is to alleviate the constraint of strict spatial coherence requirement imposed upon the optical signal processor. The source encoding also offers the advantage of efficient utilization of the light power.

EXPERIMENTAL DEMONSTRATIONS

We shall now provide a couple of experimental results obtained with the source encoding, signal sampling and spectral band filtering technique for white-light and extended incoherent sources. We shall first show the result obtained for color image deblurring due to linear motion with the white-light processing technique. Since linear motion deblurring is a 1-D processing operation and the inverse filtering is a point-by-point filtering concept such that the operation is taking place on the smearing length of the blurred image. Thus the deblurring filter (i.e., inverse filter) is a fan-shape type spatial filter [8] and the temporal coherence requirement is imposed by Eq. (7). The spatial coherence requirement is dependent upon the smearing length. A source encoding function of a narrow slit width (dependent upon the smearing) perpendicular to the smearing length is utilized. Figure 5(a) shows a color picture of a blurred image due to linear motion of a F-16 fighter plane. The body of this fighter plane is painted in navy blue-and-white colors, the wings are mostly painted in red, the tail is navy blue-and-white, and the ground terrain is generally bluish color. From this figure, we see that the plane is badly blurred. Figure 5(b) shows the color image deblurring result that we obtained with the proposed white-light deblurring technique. From this deblurred result, the letters and overall shape of the entire airplane are more distinctive than the blurred one. Furthermore the river, the highways, and the forestry of the ground terrain are far more visible. We note that the color reproduction of the deblurred image is spectacularly faithful, and coherent artifact noise is virtually non-existent. There is, however, some degree of color blur and color deviation, which are primarily due to the chromatic aberration and the anti-reflection coating of the transform lenses. Nevertheless, these drawbacks can be overcome by utilizing good quality achromatic transform lenses.

Let us now provide a color image subtraction utilized by the source encoding technique with extended incoherent sources as described in previous sections. Figure 6(a) and 6(b) show two color image transparencies of a parking lot as input color objects. Figure 6(c) shows the color subtracted

image obtained by the source encoding technique with extended incoherent source. In this figure, the profile of a (red) subcompact car can be seen at the output image plane. The shadow and the parking line (in yellow color) can also be readily identified. We however note that, this color image subtraction result is obtained by two narrow band extended incoherent sources. Extension toward the entire spectral band of a white-light source is currently under investigation.

CONCLUSION

In conclusion we would point out that the advantage of source encoding is to provide an appropriate spatial coherence function at the input plane so that the signal processing can be carried out by an extended incoherent source. The effect of the signal sampling is to achieve the temporal coherence requirement at the Fourier plane so that the signal can be processed in complex amplitude. If the filtering operation is two-dimensional, a multi-spectral-band 2-D filters should be utilized. If the filtering operation is one-dimensional, a fan-shape filter can be used.

In short, one should carry out the processing requirements backward for a partially coherent or white-light processing. With these processing requirements (e.g., operation, temporal and spatial coherence requirements), multi-spectral-band or fan-shape filter, signal sampling function, and source encoding mask can be synthesized. Thus the signal processing can be carried out in complex amplitude over the whole-spectral band of an extended white-light source.

We acknowledge the support of the U.S. Air Force Office of Scientific Research Grant AFOSR-81-0148.

* * *

REFERENCES

- [1] GABOR (D.) — IBM, J. Res. Develop. 1970, 14, 509.
- [2] YU (F. T. S.) — Optical Information Processing, Wiley-Interscience, NY, 1983.
- [3] BORN (M.) and WOLF (E.) — Principles of Optics, 2nd rev. ed., Pergamon Press, New York, 1964.
- [4] YU (F. T. S.), ZHUANG (S. L.) and WU (S. T.) — Appl. Phys., 1982, B27, 99.
- [5] YU (F. T. S.) and WU (S. T.) — J. Opt., 1982, 13, 183.
- [6] LI (S. H.), YAO (S. K.) and MIEN (A. C.) — J. Opt. Soc. Am., 1970, 60, 1037.
- [7] WU (S. T.) and YU (F. T. S.) — Appl. Opt., 1981, 20, 4082.
- [8] CHAO (T. H.), ZHUANG (S. L.), MAO (S. Z.) and YU (F. T. S.) — Appl. Opt., 1983, 22, 1439.

(Manuscript received in March, 7, 1983.)

Source Encoding for Partially Coherent Optical Processing

F. T. S. Yu, S. L. Zhuang*, and S. T. Wu**

Electrical Engineering Department, The Pennsylvania State University, University Park,
PA 16802, USA

Received 10 September 1981/Accepted 2 October 1981

Abstract. A relation between spatial coherence function and source encoding intensity transmittance function is presented. Since the spatial coherence is depending upon the information processing operation, a strictly broad spatial coherence function may not be required for the processing. The advantage of the source encoding is to relax the constraints of strict coherence requirement, so that the processing operation can be carried out with an extended incoherent source. Emphasis of the source encodings and experimental demonstrations are given. The constraint of temporal coherence requirement is also discussed.

PACS: 42.30, 42.80

The use of coherent light enables optical processing systems to carry out many sophisticated information processing operations [1, 2]. However, coherent optical processing systems are contaminated with coherent artifact noise, which frequently limits their processing capabilities. Recently, attempts of using an incoherent source to carry out complex information processing operations had been pursued by several investigators [3-6]. The basic limitations of using incoherent source for partially coherent processing is the extended source size. To achieve a broad spatial coherence function at the input plane of an optical information processor, a very small source size is required. However, such a small light source is difficult to obtain in practice. We have, nevertheless, shown in recent published papers [7-10] that there are information processing operations which can be carried out with incoherent source. In other words, a strictly broad coherence requirement may not be needed for some optical information processing operations.

In this paper, we shall describe a linear transformation relationship between spatial coherence function and

source encoding intensity transmittance function. Since the spatial coherence requirement is depending upon the information processing operation, a more relaxed coherence function may be used for a specific processing operation. By Fourier transforming this coherence function, a source encoding intensity transmittance function may be found.

The purpose of source encoding is to reduce the coherent requirement, so that an extended incoherent source can be used for the processing. In other words, the source encoding technique is capable of generating an appropriate coherence function for a specific information processing operation and at the same time it utilizes the available light power more effectively. We shall illustrate examples that complex information processing operation can actually be carried out by an encoded extended incoherent source. Experimental illustrations with this source encoding technique are also included.

Source Encoding with Spatial Coherence

We shall begin our discussion with the Young's experiment under extended incoherent source illumination, as shown in Fig. 1. First, we assume that a narrow slit is placed at plane P_1 behind an extended source. To maintain a high degree of spatial coherence between

* Visiting scholar from Shanghai Optical Instrument Research Institute, Shanghai, China

** Visiting scholar from Shanghai Institute of Optics and Fine Mechanics, Academia Sinica, China

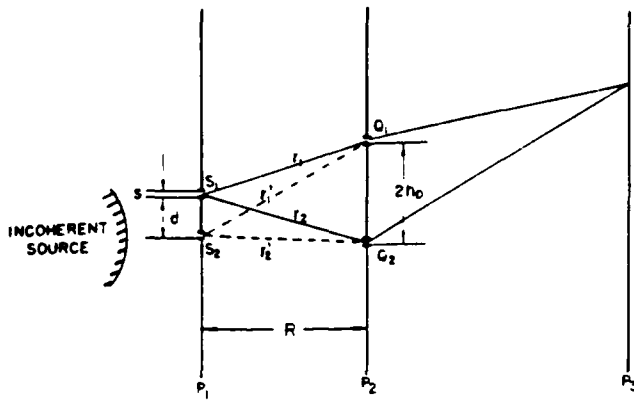


Fig. 1. Young's experiment with extended source illumination

the slits Q_1 and Q_2 at P_2 , it is known that the source size should be very narrow. If the separation between Q_1 and Q_2 is large, then a narrower slit size S_1 is required. Thus, to maintain a high degree of spatial coherence between Q_1 and Q_2 , the slit width should be [11]

$$w \leq \frac{\lambda R}{2h_0}, \quad (1)$$

where R is the distance between planes P_1 and P_2 , and $2h_0$ is the separation between Q_1 and Q_2 (Fig. 1).

Let us now consider two narrow slits of S_1 and S_2 located in source plane P_1 . We assume that the separation between S_1 and S_2 satisfied the following path length relation:

$$r_1 - r_2 = (r_1 - r_2) + m\lambda, \quad (2)$$

where the r 's are the respective distances from S_1 and S_2 to Q_1 and Q_2 , as shown in the figure. m is an arbitrary integer, and λ is the wavelength of the extended source. Then the interference fringes due to each of the two source slits S_1 and S_2 would be in phase. A brighter fringe pattern can be seen at plane P_2 . To further increase the intensity of the fringe pattern, one would simply increase the number of source slits in appropriate locations in the source plane P_1 such that every separation between slits satisfied the coherence or fringe condition of (2). If separation R is

large, i.e., $R \gg d$ and $R \gg 2h_0$, then the spacing d between the source slits becomes,

$$d = m \frac{\lambda R}{2h_0}. \quad (3)$$

From the above illustration, we see that by properly encoding an extended source, it is possible to maintain the spatial coherence between Q_1 and Q_2 , and at the same time it increases the intensity of illumination. Thus, with a specific source encoding technique for a given information processing operation may result a better utilization of an extended source.

To encode an extended source, we would first search for a spatial coherence function for an information processing operation. With reference to an extended source optical processor of Fig. 2, the spatial coherence function at input plane P_2 can be written [11]

$$\Gamma(x_2, x'_2) = \iint S(x_1) K_1(x_1, x_2) K_1(x_1, x'_2) dx_1, \quad (4)$$

where the integration is over the source plane P_1 . $S(x_1)$ is the intensity transmittance function of a source encoding mask, and $K_1(x_1, x_2)$ is the transmittance function between source Plane P_1 the input plane P_2 , which can be written

$$K_1(x_1, x_2) \approx \exp \left[i \left(2\pi \frac{x_1 x_2}{\lambda f} \right) \right]. \quad (5)$$

By substituting $K_1(x_1, x_2)$ into (4), we have

$$\Gamma(x_2 - x'_2) = \iint s(x_1) \exp \left[i 2\pi \frac{x_1}{\lambda f} (x_2 - x'_2) \right] dx_1. \quad (6)$$

From the above equation, we see that the spatial coherence function and source encoding intensity transmittance function forms a Fourier transform pair

$$s(x_1) = \mathcal{F}[\Gamma(x_2 - x'_2)], \quad (7)$$

and

$$\Gamma(x_2 - x'_2) = \mathcal{F}^{-1}[s(x_1)]. \quad (8)$$

where \mathcal{F} denotes the Fourier transformation operation. If a spatial coherence function for an information processing operation is provided, then the source encoding intensity transmittance function can

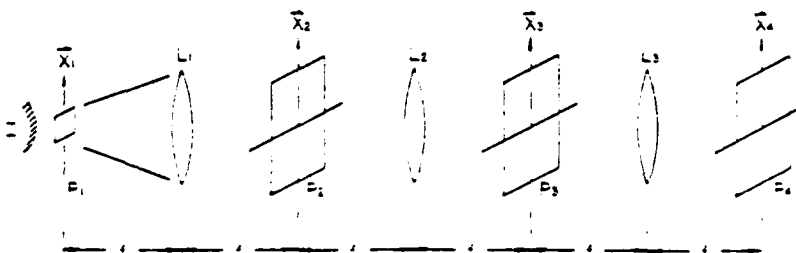


Fig. 2. Partially coherent optical processing with encoder: extended incoherent source (1), extended incoherent source, L_1 : collimation lens, L_2 and L_3 : transform lenses.

be determined through Fourier transformation of (7). We note that the source encoding function $S(x_1)$ can consist of apertures or slits of any shape. We further note that in practice $S(x_1)$ should be a positive real function which satisfies the following physical realizable condition:

$$0 \leq S(x_1) \leq 1. \quad (9)$$

For example, if a spatial coherence function for an information processing operation is

$$\Gamma(x_2 - x'_2) = \text{rect} \left\{ \frac{|x_2 - x'_2|}{A} \right\}, \quad (10)$$

where A is an arbitrary positive constant, and

$$\text{rect} \left\{ \frac{x}{A} \right\} = \begin{cases} 1, & |x| \leq A, \\ 0, & \text{otherwise.} \end{cases}$$

then the source encoding intensity transmittance would be

$$S(x_1) = \text{sinc} \left(\frac{\pi A x_1}{\lambda f} \right). \quad (11)$$

Since $S(x_1)$ is a bipolar function, therefore it is not physically realizable.

Temporal Coherence Requirement

There is, however, a temporal coherence requirement for incoherent source. In optical information processing operation, the scale of the Fourier spectrum varies with wavelength of the light source. Therefore, a temporal coherence requirement should be imposed on every processing operation. If we restrict the Fourier spectra, due to wavelength spread, within a small fraction of the fringe spacing d of a complex spatial filter (e.g., deblurring filter), then we have,

$$\frac{P_m f \Delta \lambda}{2\pi} \ll d, \quad (12)$$

where $1/d$ is the highest spatial frequency of the filter, P_m is the angular spatial frequency limit of the input object transparency, f is the focal length of the transform lens, and $\Delta \lambda$ is the spectral bandwidth of the light source. The spectral width or the temporal coherence requirement of the light source is, therefore,

$$\frac{\Delta \lambda}{\lambda} \ll \frac{\pi}{h_0 P_m}, \quad (13)$$

where λ is the center wavelength of the light source, $2h_0$ is the size of the input object transparency, and $2h_0 = (\lambda f) d$.

In order to gain some feeling of magnitude, we provide a numerical example. Let us assume that the size of the

Table 1. Source spectral requirement

$\frac{P_m}{2\pi}$ [lines/mm]	0.5	1	5	20	100
$\Delta \lambda$ [Å]	218.4	109.2	21.8	5.46	1.09

object is $2h_0 = 5$ mm, the wavelength of the light source is $\lambda = 5461$ Å, and we take a factor 10 for (13) for consideration, that is

$$\Delta \lambda = \frac{10\pi\lambda}{h_0 P_m}. \quad (14)$$

Several values of spectral width requirement $\Delta \lambda$ for various spatial frequency P_m are tabulated in Table 1.

From Table 1, we see that, if the spatial frequency of the input object transparency is low, a broader spectral width of light source can be used. In other words, if higher spatial frequency is required for an information processing operation, then a narrower spectral width of light source is needed.

Examples of Source Encoding

We shall now illustrate examples of source encoding for partially coherent processing operations. We would first consider the correlation detection operation [12].

In correlation detection, the spatial coherence requirement is determined by the size of the detecting object (i.e., signal). To insure a physically realizable encoded source transmittance function, we assume a spatial coherence function over the input plane P_2 is

$$\Gamma(x_2 - x'_2) = \frac{J_1 \left(\frac{\pi}{h_0} |x_2 - x'_2| \right)}{\frac{\pi}{h_0} |x_2 - x'_2|}, \quad (15)$$

where J_1 is a first-order Bessel function of first kind, and h_0 is the size of the detecting signal. A sketch of the spatial coherence as a function of $|x_2 - x'_2|$ is shown in Fig. 3a. By taking the Fourier transform of (15), we obtain the following source encoding intensity transmittance function,

$$S(x_1) = \text{cir} \left\{ \frac{|x_1|}{w} \right\}, \quad (16)$$

where $w = (\lambda f) h_0$ is the diameter of a circular aperture as shown in Fig. 3a.

$$\text{cir} \left\{ \frac{|x_1|}{w} \right\} = \begin{cases} 1, & 0 \leq |x_1| \leq w, \\ 0, & \text{otherwise.} \end{cases}$$

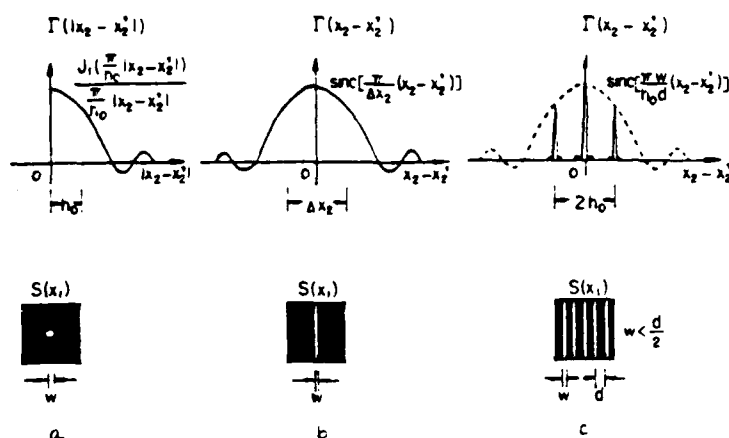


Fig. 3a-c. Examples of spatial coherence requirements and source encodings. $\Gamma(x_2 - x_2')$: spatial coherence function. $S(x_1)$: source encoding transmittance. (a) For correlation detection, (b) for smeared image deblurring, and (c) for image subtraction

f is the focal length of the collimating lens and λ is the wavelength of the extended source. As a numerical example, we assume that the signal size is $h_0 = 5$ mm, the wavelength is $\lambda = 5461$ Å, focal length is $f = 300$ mm, then the diameter w of the source encoding aperture should be about $32.8 \mu\text{m}$ or smaller.

We now consider smeared image deblurring [13] operation as our second example. We note that the smeared image deblurring is a 1-D processing operation and the inverse filtering is a point-by-point processing concept such that the operation is taking place on the smearing length of the blurred object. Thus, the spatial coherence requirement is depending upon the smearing length of the blurred object. To obtain a physically realizable source encoding function, we let the spatial coherence function at the input plane P_2 be

$$\Gamma(x_2 - x_2') = \text{sinc}\left(\frac{\pi}{\Delta x_2} |x_2 - x_2'|\right), \quad (17)$$

where Δx_2 is the smearing length. A sketch of (17) is shown in Fig. 3b. By taking the Fourier Transform of (17), we obtain

$$S(x_1) = \text{rect}\left\{\frac{|x_1|}{w}\right\}, \quad (18)$$

where $w = (f/\lambda)(\Delta x_2)$ is the slit width of the source encoding aperture, as shown in Fig. 3b, and

$$\text{rect}\left\{\frac{|x_1|}{w}\right\} = \begin{cases} 1, & 0 \leq |x_1| \leq w, \\ 0, & \text{otherwise.} \end{cases}$$

For a numerical illustration if the smearing length is $\Delta x_2 = 1$ mm, the wavelength is $\lambda = 5461$ Å, and the focal length is $f = 300$ mm, then the slit width w should be about $163.8 \mu\text{m}$ or smaller.

We would now consider image subtraction [14] for our third illustration. Since the image subtraction is a 1-D processing operation and the spatial coherence

requirement is depending upon the corresponding point-pair of the images, thus a strictly broad spatial coherence function is not required. In other words, if one can maintain the spatial coherence between the corresponding image points to be subtracted, then the subtraction operation can take place at the output image plane. Therefore, instead of utilizing a strictly broad coherence function over the input plane P_2 , we would use a point-pair spatial coherence function. Again, to insure a physically realizable source-encoding transmittance, we would let the point-pair spatial coherence function be [10]

$$\begin{aligned} \Gamma(x_2 - x_2') &= \frac{\sin\left(\frac{N\pi}{h_0} |x_2 - x_2'|\right)}{N \sin\left(\frac{\pi}{h_0} |x_2 - x_2'|\right)} \text{sinc}\left(\frac{\pi w}{h_0 d} |x_2 - x_2'|\right), \end{aligned} \quad (19)$$

where $2h_0$ is the main separation of the two input object transparencies at plane P_2 , $N \gg 1$ a positive integer, and we note that $w \ll d$. Equation (19) represents a sequence of narrow pulses which occur at $|x_2 - x_2'| = nh_0$, where n is a positive integer, and their peak values are weighted by a broader sinc factor, as shown in Fig. 3c. Thus, we see that a high degree of spatial coherence is maintained at every point-pair between the two input object transparencies. By taking the Fourier transformation of (19), we obtain the following source encoding intensity transmittance

$$S(x_1) = \sum_{n=1}^N \text{rect}\left\{\frac{|x_1 - nd|}{w}\right\}, \quad (20)$$

where w is the slit width, and $d = (\lambda/f)h_0$ is the separation between the slits. It is clear that (20) represents N number of narrow slits with equal spacing d , as shown in Fig. 3c. As a numerical example, we let the separation of the input objects $h_0 = 10$ mm, the wavelength $\lambda = 5461$ Å, the focal length of the col-

limator $f = 300$ mm, then the spacing d between the slits is $16.4 \mu\text{m}$. The slit width w should be smaller than $d/2$, or about $1.5 \mu\text{m}$. If the size of the encoding mask is 2 mm square, then the number of slits N is about 122. Thus we see that with the source encoding it is possible to increase the intensity of the illumination N fold, and at the same time it maintains the point-pair spatial coherence requirement for image subtraction operation.

Experimental Results

In this section, we would illustrate two examples as obtained from the source encoding technique. The first experimental illustration is the result obtained for smeared photographic image deblurring with encoded incoherent source as shown in Fig. 4. In this experiment a Xenon arc lamp with a green interference filter was used as extended incoherent source. A single slit mask of about $100 \mu\text{m}$ was used as a source encoding mask. The smeared length of the blurred image was about 1 mm.

Figure 5 shows an experimental result obtained from image subtraction operation with encoded incoherent source. In this experiment, a mercury arc lamp with a green filter was used as an extended incoherent source. A multislit mask was used to encode the light source. The slit width w is $2.5 \mu\text{m}$ and the spacing between slits was $25 \mu\text{m}$. The overall size of the source encoding mask was about $2.5 \times 2.5 \text{ mm}^2$. The mask contains about 100 slits.

From these experimental results, we see that the constraint of strictly broad spatial coherence requirement may be alleviated with source encoding techniques so that it allows the optical information processing operation can be carried out with extended incoherent source.

OPTICS

a

OPTICS

b

Fig 4a and b. Photographic image deblurring with encoded extended incoherent source. (a) Input blurred object and (b) deblurred image

Conclusion

We have derived a Fourier transform relationship between the spatial coherence function and the source encoding intensity transmittance function. Since the coherence requirement is depending upon the nature of a specific information processing operation, a strictly broad coherence requirement may not be needed in practice. The basic advantage of the source encoding technique is to alleviate the constraints of the strict coherence requirement imposed upon the optical information processing system, so that the information processing can be carried out with encoded extended incoherent source. The use of incoherent source to carry out the optical processing operation has the advantage of suppressing the coherent artifact noise. In addition, the incoherent processing system is usually simple and economical to operate. Finally, we would stress that the source encoding technique may be extended to white-light optical processing operation, a program is currently under investigation.

Acknowledgement: We wish to acknowledge the support of the U.S. Air Force Office of Scientific Research Grant AFOSR-81-0148.

APPLIED A L I D
OPTICS OPT CS
PP E
I

a

Fig 5a and b. Image subtraction with encoded extended incoherent source. (a) Input object transparencies and (b) subtracted image

References

1. A. VanderLugt: Proc. IEEE 62, 1300 (1974)
2. F.T.S. Yu: *Introduction to Diffraction, Information Processing, and Holography* (MIT Press, Cambridge, MA 1973) Chap. 7
3. A. Lohmann: Appl. Opt. 16, 261 (1977)
4. E. N. Leith, J. Roth: Appl. Opt. 16, 2565 (1977)
5. F.T.S. Yu: Opt. Commun. 27, 23 (1978)
6. F.T.S. Yu: Appl. Opt. 17, 3571 (1978)
7. F.T.S. Yu: Proc. SPIE 232, 9 (1980)
8. F.T.S. Yu, S.L. Zhuang, T.H. Chao, M.S. Dymek: Appl. Opt. 19, 2986 (1980)
9. S.L. Zhuang, T.H. Chao, F.T.S. Yu: Opt. Lett. 6, 102 (1981)
10. S.T. Wu, F.T.S. Yu: Opt. Lett. 6, 452 (1981)
11. M. Born, E. Wolf: *Principle of Optics*, 2nd ed. (Pergamon Press, New York 1964)
12. A. VanderLugt: IEEE Trans. IT-10, 139 (1964)
13. G.W. Stroke, R.G. Zech: Phys. Lett. 25A, 89 (1967)
14. S.H. Lee, S.K. Yao, A.G. Milnes: J. Opt. Soc. Am. 60, 1037 (1970)

SECTION IX

Broad Spectral Band Color Image Deblurring

Broad spectral band color image deblurring

T. H. Chao, S. L. Zhuang, S. Z. Mao, and F. T. S. Yu

A broadband white-light processing technique for smeared color photographic image deblurring is described. The technique utilizes a diffraction grating method to disperse the smeared image spectra in the Fourier plane so that the entire spectral band of the white-light source can be utilized for the deblurring. In this paper the technique of synthesizing a fan-shape type complex deblurring filter to accommodate wavelength variation is presented. Experimental results showed that this broad spectral band processing technique offers an excellent coherent artifact noise suppression, and the technique is particularly suitable for color image deblurring. Experimental demonstrations and comparisons with the narrowband and coherent deblurring are also provided.

I. Introduction

Restoration of smeared photographic images has long been an interesting and important application in optical processing.¹⁻⁷ In image deblurring much of the effort has been devoted to applying inverse filtering concepts to the image restoration. As those works evolved, two problems are still of intense interest; namely, the coherent artifact reduction and color image deblurring. Although Wiener filters had been applied in coherent processors by several investigations¹⁻⁶ for noise reduction, they do not suppress the inherent coherent artifact noise in the processing system. Recently, Yang and Leith⁷ proposed a spatial domain deconvolution technique for image deblurring. They used an extended incoherent line source for deblurring, and the coherent noise was remarkably reduced. However, their technique is only suitable for processing monochrome blurred images. In previous papers⁸⁻¹⁰ we presented a white-light processing technique for linearly smeared image deblurring. We have shown that the white-light image deblurring technique is capable of eliminating the coherent artifact noise and is suitable for color image deblurring. However, the results that we obtained were primarily restricted to the narrow spectral band deblurring concept.

In this paper we shall extend the image deblurring technique to the entire broad spectral band of the

white-light source. To obtain the broadband deblurring effect, a fan-shaped spatial filter to compensate the scale of the Fourier spectra should be utilized at the Fourier plane. The technique of synthesizing the fan-shaped broadband deblurring filter is given. The coherence requirements for the white-light image deblurring are illustrated. Experimental demonstrations with the comparison of narrowband deblurring and coherent technique are provided.

II. Broadband Image Deblurring

We shall now discuss a broadband image deblurring technique utilizing the entire spectral band of a white-light source. Let this linear smeared image be given, i.e.,

$$\hat{s}(x,y) = s(x,y) * \text{rect}\left(\frac{y}{W}\right), \quad (1)$$

where $\hat{s}(x,y)$ and $s(x,y)$ are the smeared and unsmeared images,

$$\text{rect}\left(\frac{y}{W}\right) \triangleq \begin{cases} 1, & |y| \leq \frac{W}{2} \\ 0, & \text{otherwise,} \end{cases} \quad (2)$$

and W is the smeared length.

Let us insert the smeared image transparency of Eq. (1) into the input plane P_1 of a white-light optical processor as shown in Fig. 1. The complex light distribution for every wavelength λ at the back focal length of the transform lens would be

$$E(\alpha,\beta;\lambda) = C \iint \hat{s}(x,y,\lambda) \exp(ip_0\alpha) \\ \times \exp\left[-i\frac{2\pi}{\lambda}(\alpha x + \beta y)\right] dx dy, \quad (3)$$

where p_0 is the angular spatial frequency of the phase grating, $\alpha = [(\lambda f)/2\pi]p$ and $\beta = [(\lambda f)/2\pi]q$ represent the

The authors are with Pennsylvania State University, Electrical Engineering Department, University Park, Pennsylvania 16802.

Received 13 October 1982.

0003-6935/83/101439-06\$01.00/0.

© 1983 Optical Society of America.

spatial coordinate system of Fourier plane P_2 , (p, q) is the corresponding angular spatial frequency coordinate system, f is the focal length of the achromatic transform lens, and C is an appropriate complex constant. Thus, Eq. (3) can be written as

$$E(\alpha, \beta; \lambda) = C S \left(\alpha - \frac{\lambda f}{2\pi} p_0, \beta \right), \quad (4)$$

where

$$S \left[\alpha - \left(\frac{\lambda f}{2\pi} \right) p_0, \beta \right] = S \left[\alpha - \left(\frac{\lambda f}{2\pi} \right) p_0, \beta \right] \text{sinc} \left(\frac{\pi W}{\lambda f} \beta \right) \quad (5)$$

is the linear smeared image spectrum.

Since scale of the signal spectrum is proportional to the wavelength of the light source, the corresponding signal spectra would smear into a fan-shaped rainbow color as can be seen from Eq. (5). In other words, the top (i.e., the wider region) of the smeared spectra is in red and the bottom is in violet.

Let us assume that a fan-shaped broad spectral band deblurring filter (i.e., a broadband inverse filter) to accommodate the variation of the scale of the signal spectra is available. This fan-shaped filter is described in the following equation:

$$H(\alpha, \beta; \lambda) = \delta \left(\alpha - \frac{\lambda f}{2\pi} p_0, \beta \right) \left\{ \int \text{rect} \left(\frac{y}{W} \right) \exp \left(-i \frac{2\pi}{\lambda f} \beta y \right) dy \right\}^{-1} \\ = \delta \left(\alpha - \frac{\lambda f}{2\pi} p_0, \beta \right) \left[\text{sinc} \left(\frac{\pi W}{\lambda f} \beta \right) \right]^{-1}. \quad (6)$$

In image deblurring we would insert this deblurring filter of Eq. (5) in the spatial frequency plane of P_2 . The complex light distribution for every λ at the output image plane P_3 can be written as

$$g(x, y; \lambda) = F^{-1} \left[S \left(\alpha - \frac{\lambda f}{2\pi} p_0, \beta \right) H(\alpha, \beta; \lambda) \right]. \quad (7)$$

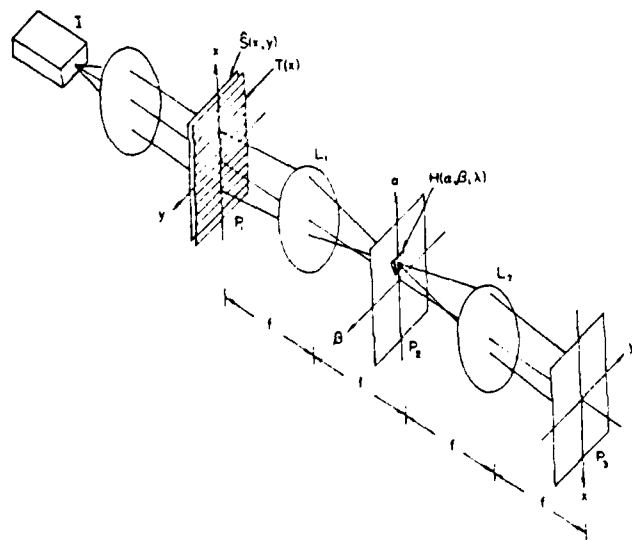


Fig. 1. White-light processor for smeared color image deblurring: I , white-light point source; $S(x, y)$, smeared color image transparency; $T(x)$, diffraction grating; L_1 and L_2 , achromatic transform lenses; $H(\alpha, \beta, \lambda)$, broad spectral band deblurring filter.

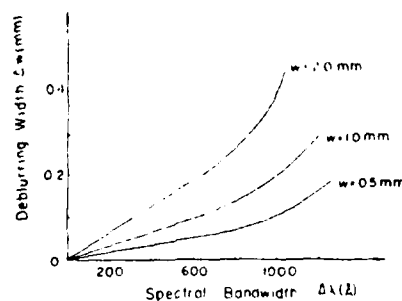


Fig. 2. Plots of the deblurring width ΔW as a function of the spectral bandwidth of the light source $\Delta \lambda$ for various values of smeared length W .

where F^{-1} denotes the inverse Fourier transform; by substituting Eqs. (5) and (6) into Eq. (7), we have

$$g(x, y; \lambda) = s(x, y) \exp(ip_0 x), \quad (8)$$

which is independent of the wavelength of the light source. The resultant output intensity distribution can be shown as

$$I(x, y) = \int_{\Delta \lambda} |g(x, y; \lambda)|^2 d\lambda \approx \Delta \lambda |s(x, y)|^2, \quad (9)$$

which is proportional to the entire spectral bandwidth $\Delta \lambda$ of the white-light source. Thus we see that this proposed white-light deblurring technique is capable of processing the information with the entire visible spectral band, and it is very suitable for the application to color-image deblurring. Since the integration of Eq. (9) is taken from the entire spectral band of the white-light source, the coherent artifact noise in principle can be eliminated.

III. Coherence Requirement

Although this proposed deblurring technique utilizes a white-light source, the processing is operated in a partially coherent mode. It is, therefore, our aim in this section to discuss the basic coherence requirement for this proposed color image deblurring technique.

In a previous paper¹¹ we obtained the coherence requirements for a partially coherent optical processor. Several of those fruitful results can be applied to our proposed white-light image deblurring system.

We shall first discuss the temporal coherence requirement for the image deblurring. We shall use the results obtained in our previous article as shown in Fig. 2. This figure shows the plots of the spectral width $\Delta \lambda$ requirement of the light source (i.e., equivalent to the narrow spectral width of the deblurring filter) as a function of deblurred length (ΔW) for various values of smeared length W . The wavelength spread across a narrow spectral band filter centered at wavelength λ_0 ^{8,9} is

$$\Delta \lambda = \lambda_0 [4 \Delta p / p_0], \quad p_0 \gg \Delta p, \quad (10)$$

or

$$\frac{\Delta p}{p_0} = \frac{\Delta \lambda}{4 \lambda_0}, \quad (11)$$

where Δp is the angular spatial frequency limit of the

Table I. Temporal Coherence Requirement for $\lambda_0 = 5461 \text{ \AA}$

$\Delta p/p_0$	0.012	0.018	0.029	0.034	0.045
$\Delta\lambda (\text{\AA})$	270	400	610	750	990
$\Delta W/W$	1/20	1/15	1/10	1/8	1/5

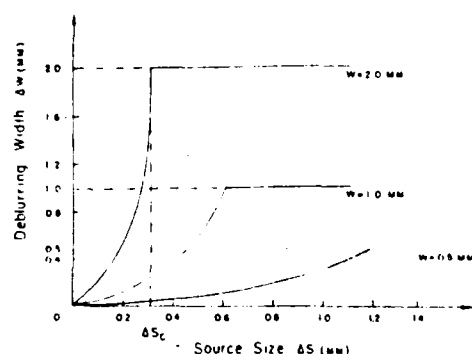
Fig. 3. Plots of the deblurring width as a function of the source size for various values of the smeared length W .

Table II. Effect of Spatial Coherence Requirement

$\frac{\Delta W}{W}$	$\frac{\Delta S}{W}$	1/20	1/15	1/10	1/5
0.5 mm		0.2	0.38	0.6	0.92
1 mm		0.1	0.18	0.26	0.40
2 mm		0.05	0.08	0.12	0.18

input blurred object transparency, and p_0 is the angular spatial frequency of the phase grating. The temporal coherence requirement for a narrow spectral band deblurring filter for wavelength 5461 \AA is tabulated in Table I.

Although the temporal requirement is based on a narrow spectral band analysis, it can be extended to a broad spectral band operation. For example, a broad spectral band filter (e.g., fan-shaped deblurring filter) can be considered as a summation of a sequence of narrowband spatial filters of various wavelengths. The deblurred image is the result of the superposition of the mutually incoherent light fields derived from the narrowband filters. Thus, the temporal coherence requirement shown in Table I can also be applied to a broad spectral band filtering. As an example, if $(\Delta p)/p_0 = 0.012$ and the spectral bandwidth of the light source is 3000 \AA , the broad spectral band deblurring filter is approximately equal to the sum of eleven narrow spectral band filters. The mean spectral bandwidth $\Delta\lambda$ of those filters is 270 \AA , and the deblurring ratio $(\Delta W)/W$ is $1/20$. In other words, it is possible to synthesize a fan-shaped type spatial filter to compensate with the scale variation of the smeared Fourier spectra in the spatial frequency plane so that the deblurring takes place with the entire spectral band of the white-light source. Since the broadband deblurring utilizes the whole visible spectrum of the light source, it is particularly suitable for color image deblurring.

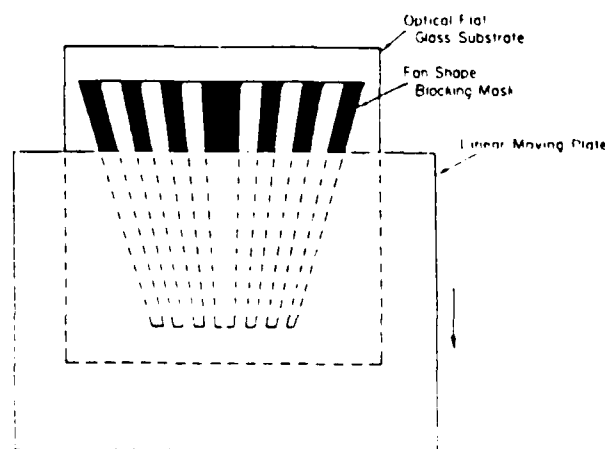
We shall now discuss the spatial coherence requirement. Since the deblurring operation acts on the smeared length, the coherence requirement is dependent on the width of the light source. Let us now use the plots of deblurring width as a function of the source size as shown in Fig. 3. From this figure we see that the deblurring effect (i.e., ΔW) ceases when the source width ΔS reaches a critical width ΔS_c . We shall now summarize the results of the spatial coherence requirement in Table II. From this table we see that the higher the degree of deblurring (i.e., smaller ΔW), the more critical the spatial coherence (i.e., smaller the ΔS) is required. It is, therefore, one of the prices we paid for a higher degree of deblurring.

IV. Broadband Deblurring Filter Synthesis

We shall now briefly describe the synthesis of a fan-shaped (i.e., broad spectral band) deblurring filter. The synthesis is a combination of an absorptive-amplitude filter and a phase filter. A fan-shaped phase filter is composed of several slanted bar-type phase objects as illustrated in Fig. 4. Each phase bar would give rise to specific π phase retardation for a prescribed dispersion of rainbow color wavelength. We note that the height of deblurring filter is, of course, dependent on the grating frequency p_0 at the input plane. The periodicity of the deblurred filter is certainly determined by the smeared length of the blurred object, and the width of the filter defines the degree of deblurring.¹² In constructing a broad spectral band phase deblurring filter, we utilize a vacuum deposition technique. It can be accomplished by depositing the magnesium fluoride (MgF_2) on this surface of an optical flat glass substrate. In this technique, a blocking mask of a fan-shaped bar pattern as shown in Fig. 4 is used for the vacuum deposition. The MgF_2 vapor is deposited through this blocking mask, together with a linear moving covering plate, from top to bottom as illustrated in Fig. 4.

The thickness of the deposited coating can be determined by the following equation:

$$d = \frac{\lambda}{2(n-1)} \quad (12)$$

Fig. 4. Phase filter mask for MgF_2 vapor deposition.

where n is the refractive index of the coating material. This coating thickness is linearly proportional to the dispersion of the illuminating wavelength. We note that a strictly linear control of coating thicknesses is very essential. The advantage of this phase type filter is to improve the transmission efficiency, since the overall deblurring filter is, in general, highly absorptive.

In principle, it is a straightforward method to synthesize a fan-shaped amplitude filter. The synthesis can be accomplished by inserting a slit aperture of a slit width equal to the smeared length of the blurred image at the input plane P_1 of the white-light optical processor shown in Fig. 1. The size of the white-light source should be adequately small under the spatial coherence regime to obtain a smeared sinc factor (i.e., smeared Fourier spectra of the slit aperture) in the Fourier plane. An amplitude filter can then be synthesized by simply recording this smeared sinc factor on a photographic plate. If the film-gamma of the recorded plate is controlled to about unity (i.e., $\gamma = 1$), the amplitude transmittance of the recorded plate is equivalent to that of the desired fan-shaped amplitude filter. However, in practice, a fan-shaped type amplitude filter is not that easy to synthesize due to three primary reasons. First, if a very small source size is required for the filter synthesis, it usually takes a longer exposure time, for example, if Kodak 649F plate (a low-speed film) is used. Second, the spectral response of the recording plate is generally not uniform for all visible wavelengths. The recorded filter would produce uneven transmittance in the direction of the smeared color spectra. The effect of the transmittance variation of the filter would affect the fidelity of color reproduction and the degree of restoration. Third, it is difficult to synthesize a side-band amplitude filter, since the dynamic range of the photographic film is very limited.

There is an alternative technique of generating a fan-shaped amplitude filter with coherent illumination as shown in Fig. 5. The purpose of using a curved-slit aperture is to accommodate the scale variation of the amplitude filter. The expression of the curved-slit aperture can be written

$$d(x, y; \lambda) = \text{rect} \left(\frac{y}{W \lambda_0 / \lambda} \right) \delta \left(x - \frac{\lambda f}{2\pi} p_0 \right), \quad (13)$$

where λ_0 is the wavelength of the coherence source, W is the smeared length of the blurred image, f is the focal length of the cylindrical transform lens, and λ is the wavelength of the white-light source.

The corresponding Fourier transformation of the curved-slit aperture can be shown as

$$D(u, v; \lambda) = \text{sinc} \left(\frac{\pi W}{\lambda f} v \right) \cdot \delta \left(u - \frac{\lambda f}{2\pi} p_0 \right), \quad (14)$$

where \cdot denotes the convolution operation.

It is clear now that a photographic recording of the spectra shown in Eq. (14) would produce a desirable fan-shaped amplitude filter for deblurring. In synthesis of this broadband amplitude filter, a He-Ne laser, with a rotating ground glass to reduce the artifact noise, is

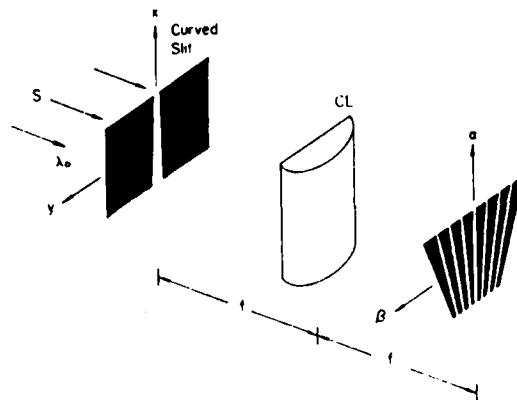


Fig. 5. Generation of amplitude filter S from monochromatic plane wave; CL, cylindrical transform lens.

used as a coherent source. Kodak 131 plate is used for the recording plate, and a 6-min developing time in a POTA developer at 24°C is used to control the film gamma to about unity. The spectral wavelength limits are chosen from 4000 to 7000 Å. Within the dynamic range of the recording film, five sidelobes of ~ 300 –1 dynamic range (or a density range of 2.5) are recorded with good accuracy. The fan-shaped amplitude filter obtained is tested with satisfactory results.

V. Experimental Results

In this section we shall provide a few experimental results of image deblurring utilizing a broadband white-light source. In our experiments, a 75-W xenon arc lamp with a 200- μ m pinhole is used as a broadband white-light source. A phase grating of 130 lines/mm with 25% diffraction efficiency at each first-order diffraction is used at the input plane. An $f/8$ transform lens with 300-mm focal length is used for image Fourier transformation.

We shall first demonstrate the effect of the broadband deblurring as compared with the narrowband and the result obtained with coherent source. For simplicity of illustrations, we use a set of linear blurred alphabets as input objects as shown in Fig. 6(a). The smeared length is ~ 0.5 mm. Figure 6(b) shows the deblurred image obtained with this broadband deblurring technique, and the spectral bandwidth is ~ 3000 Å under white-light illumination. Figure 6(c) is the result obtained with a narrow spectral band deblurring filter of $\sim \Delta\lambda = 100$ Å centered at 6328 Å. Figure 6(d) is the deblurred image obtained with a He-Ne coherent source. In the comparison of these results, we see that the results obtained with a broad spectral band white-light source offers a higher deblurred image quality; for example, the coherent artifact noise is substantially suppressed, and the deblurred image appears to be sharper than the one obtained with a narrowband case.

We shall now experimentally demonstrate the capability of the white-light technique for color images. Figure 7(a) shows a black-and-white color blurred image of a building due to linear motion as an input color

**PENN
STATE**

(a)

**PENN
STATE**

(b)

**PENN
STATE**

(c)

**PENN
STATE**

(d)

Fig. 6. Smeared image restoration of the words PENN STATE: (a) smeared image, (b) deblurred image obtained with broadband white-light source, (c) deblurred image obtained with narrow spectral band white-light source, and (d) deblurred image obtained with coherent source.



(a)

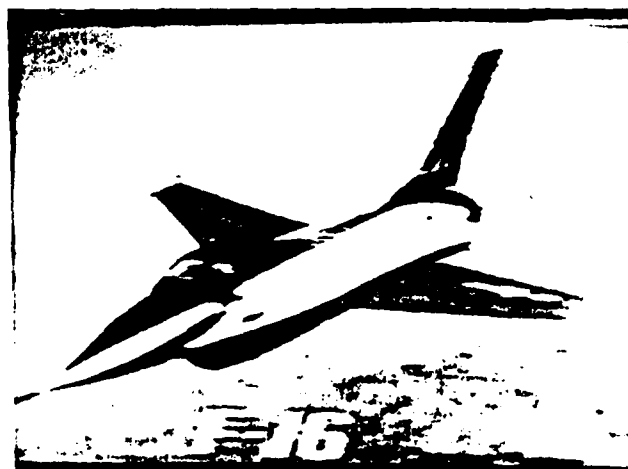


(b)

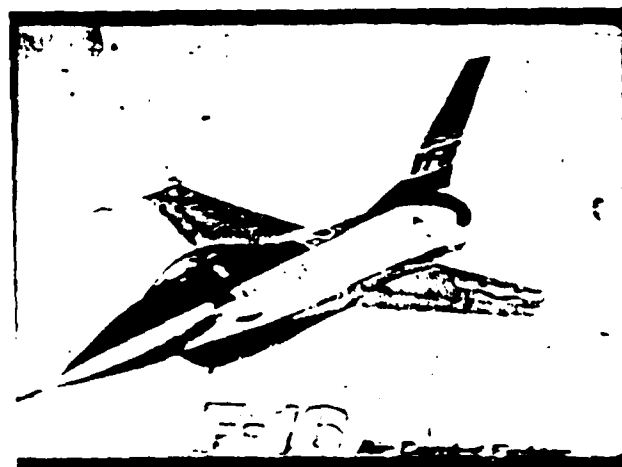
Fig. 7. Continuous-tone color image deblurring: (a) a black-and-white picture of a smeared color photograph of a building, (b) a black-and-white picture of the deblurred color image.

object. From this figure we see that the white window frames, the front doors, bushes, two white beams, trees, etc. are severely smeared. Figure 7(b) shows the deblurring result that we have obtained with this white-light processing technique. From this figure, we have seen that the color reproduction is rather faithful and the deblurred effect is spectacularly good; for example, the window frames, the bushes, the beams, the front doors, the trees, etc. can be clearly identified.

We would now provide another more striking example of the color image deblurring with this white-light processing technique. Figure 8(a) shows a black-and-white linear-motion blurred picture of an F-16 fighter plane. The body of this fighter plane is painted in blue-and-white colors, the wings are mostly painted red, the tail is blue-and-white, and the ground terrain is generally a bluish color. From this figure we see that the letters on the body on one of the wings and on this side of the tail are smeared beyond recognition. The details of the missiles at the tips of the wings are lost.



(a)



(b)

Fig. 8. Color image deblurring: (a) a black-and-white picture of a smeared color image of an F-16 fighter plane, (b) a black-and-white picture of the deblurred color image.

The star symbols at the tail end of the body and on the top of the wings are badly distorted. The features of ground terrain are obscured. Figure 8(b) shows the color image deblurring result that we have obtained from Fig. 8(a) with the proposed white-light deblurring technique. From this deblurred result, the letters USAF on the wing and YF-16 on the side of the tail can be clearly seen. The words U.S. AIR FORCE may be recognized. The star symbol on the wing can be clearly identified; however, the one on the body is rather obscured. Undoubtedly, the missiles at the tips of the wings can be seen, and the pilot in the cockpit is quite visible. The overall shape of the entire airplane is more distinctive than the blurred one. Moreover the river, the highways, and the forestry of the ground terrain are far more recognizable in this deblurred image. The color reproduction of the deblurred image is spectacularly faithful, and coherent artifact noise is virtually nonexistent. There is, however, some degree of color deviation inherently existing in the deblurred image. These are primarily due to chromatic aberration and the antireflectance coating of the transform lenses. Nevertheless, these two drawbacks can be overcome by utilizing good-quality achromatic transform lenses. A research program is currently underway to investigate this effect. Further improvement of the deblurring can also be accomplished by utilizing a blazed grating for high diffraction efficiency and a broader spatial bandwidth of the deblurred filter for a higher degree of deblurring. These two problems are also under current research.

VI. Summary

We have shown a broadband color image deblurring technique utilizing a white-light source. This broad spatial band deblurring technique utilized a grating base method to obtain a dispersed smeared image spectra in the Fourier plane so that the deblurring operation can be taken placed in complex amplitude for the entire visible wavelengths. To perform this complex amplitude deblurring for the entire spectral band of the light source, we have shown that a fan-type deblurring filter to compensate the scale variation of the smeared signal spectra due to wavelength dispersion can be utilized. To alleviate the low transmission efficiency of the deblurring filter, we synthesized the deblurring filter with the combination of a broadband phase filter and a fan-shaped amplitude filter. The broad spectral band

phase filter is synthesized by optical coating techniques, while the fan-shaped amplitude filter is obtained by a 1-D coherent processing technique.

By comparison of the results obtained by the broadband image deblurring with the narrow spectral band and coherent techniques, we have seen that the results obtained by the broadband deblurring offer a higher image quality. We have also shown that the broadband deblurring technique is very suitable for color image deblurring. We have provided several color image deblurring results obtained by the broadband deblurring technique. From these color deblurred images we have seen that the fidelity of the color reproduction is very high and the quality of deblurred image is rather good. Although there is some degree of color blur due to chromatic aberration of the transform lenses, it can be eliminated by utilizing higher-quality achromatic transform lenses.

Further improvements of the deblurring can also be obtained by utilizing a blazed grating to achieve a higher smeared spectral diffraction efficiency so that a wider spatial band deblurring filter can be used to achieve a higher degree of deblurring. Finally, we would like to point out that the utilization of higher-quality achromatic transform lenses and a blazed grating for the broadband image deblurring technique is currently under investigation.

We acknowledge the support of the U.S. Air Force Office of Scientific Research grant AFOSR-81-0148.

References

1. J. Tsujiuchi, *Prog. Opt.* **2**, 133 (1963).
2. G. W. Stroke and R. G. Zech, *Phys. Lett. A* **25**, 89 (1967).
3. J. Tsujiuchi, T. Honda, and T. Fukaya, *Opt. Commun.* **1**, 379 (1970).
4. J. L. Horner, *J. Opt. Soc. Am.* **59**, 553 (1969).
5. J. L. Horner, *Appl. Opt.* **9**, 167 (1970).
6. R. M. Vasu and G. L. Rogers, *Appl. Opt.* **19**, 469 (1980).
7. G. G. Yang and E. N. Leith, *Opt. Commun.* **36**, 101 (1981).
8. F. T. S. Yu, *Appl. Opt.* **17**, 3571 (1978).
9. S. L. Zhuang, T. H. Chao, and F. T. S. Yu, *Opt. Lett.* **6**, 102 (1981).
10. F. T. S. Yu, S. L. Zhuang, and T. H. Chao, *J. Opt. (Paris)* **13**, 57 (1982).
11. S. L. Zhuang and F. T. S. Yu, *Appl. Opt.* **21**, 2587 (1982).
12. F. T. S. Yu, *Introduction to Diffraction, Information Processing, and Holography* (MIT Press, Cambridge, Mass., 1973), pp. 206-212.

SECTION X

Color Image Subtraction

ELECTRICAL ENGINEERING DEPARTMENT
THE PENNSYLVANIA STATE UNIVERSITY

University Park, PA 16802 (U.S.A.)

COLOR IMAGE SUBTRACTION WITH EXTENDED INCOHERENT SOURCES

F. T. S. YU, S. T. WU (*)

MOTS CLÉS :

Soustraction d'images en couleur
Sources incohérentes codées

KEY WORDS :

Color image subtraction
Coded incoherent sources

Soustraction d'images en couleur utilisant des sources étendues incohérentes

SUMMARY : A technique of color image subtraction with encoded extended incoherent sources is presented. The objective of the source encoding is to obtain a reduced coherence requirement for the image subtraction so that the inherent difficulty of obtaining an incoherent point source can be alleviated. Experimental results for the color image subtraction obtained with the incoherent processing technique are given. Since most images are multi-colored, this color image subtraction technique may offer a broad range of applications.

RÉSUMÉ : Nous présentons une méthode de soustraction d'images en couleur utilisant des sources incohérentes codées. Le but du codage est d'obtenir la cohérence nécessaire pour notre expérience avec une source relativement grande. Nous donnons des résultats expérimentaux. La plupart des images étant des images en couleur, cette technique de soustraction peut avoir des applications diverses.

I. — INTRODUCTION

One of the most interesting segments of optical information processing must be the image subtraction. The applications may be of value in earth resource studies, urban development, highway planning, land use, surveillance, automatic tracking, and many others. The image subtraction may also be applied to video communications as a means of bandwidth compression. For example it is only necessary to transmit the differences between the two images in successive cycles, rather than the entire image in each cycle.

There are several techniques available for image subtraction which can be found in a review paper by Ebersole [1]. However most of the optical image subtraction techniques have relied on a coherent source to carry out the subtraction operation. But a coherent optical processing system is plagued with coherent noise, which frequently limits its processing capabilities.

We have in a recent paper [2] demonstrated a technique of image subtraction utilizing an extended incoherent source. Since the image subtraction is a one-dimensional processing operation and the spatial coherence requirement for the subtraction operation is a point-pair coherence requirement, it is, therefore, possible to encode an extended source to obtain the required spatial coherence. In a previous paper [3] we have shown a Fourier transform relationship between the spatial coherence and source intensity distribution. In principle, it is possible to encode an extended source to obtain an appropriate spatial coherence for specific information processing operations.

Strictly speaking, all images in the visible wavelengths, which includes the black-and-white images, are color images. Therefore it is of interest for us, in this paper, to extend this incoherent processing technique for color image subtraction.

II. — COLOR IMAGE SUBTRACTION

We will now describe a color image subtraction operation with an encoded extended incoherent source, as depicted in figure 1. For simplicity, two

(*) Visiting scholar from Shanghai Institute of Optics and Fine Mechanics, Academia Sinica (China).

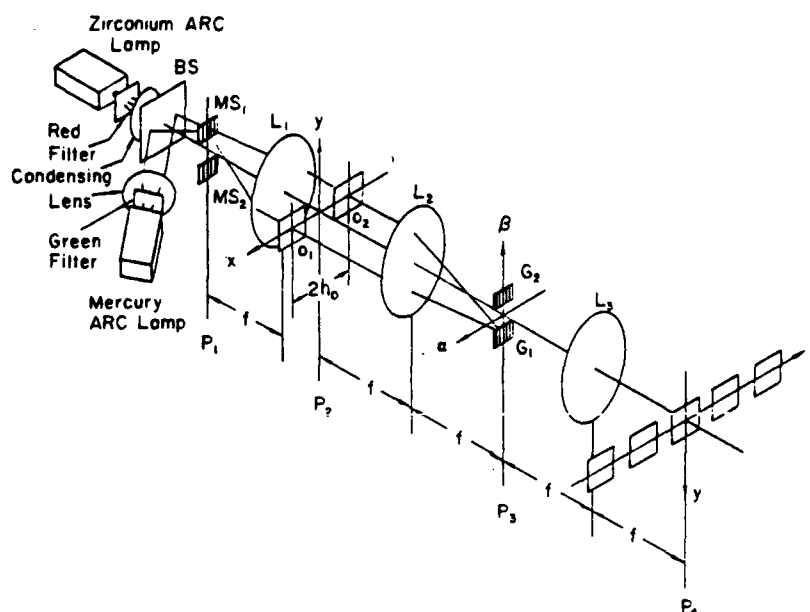


FIG. 1. — Color Image Subtraction with Encoded Extended Incoherent Sources. BS: Beam Splitter, MS: Source Encoding Mask, L: Achromatic Transform Lens, G: Diffraction Gratings.

incoherent light sources, each for a different color of light (i.e., red and green), are used for the subtraction operation. For the detailed analysis of image subtraction with an encoded extended source we refer the reader to our previous paper [2].

In color image subtraction, we insert the color image transparencies $O_1(x, y)$ and $O_2(x, y)$ in the open apertures of the input plane P_2 , which can be described as

$$(1) \quad f(x, y) = O_1(x - h_0, y) - O_2(x - h_0, y),$$

where $2h_0$ is the separation between the two input transparencies O_1 and O_2 . Two sinusoidal gratings G_1 and G_2 designed for the red and the green wavelengths respectively are inserted in the spatial frequency plane P_3 , and can be written as

$$(2) \quad G_1 = \frac{1}{2} [1 - \sin(h_0 p_r)],$$

and

$$(3) \quad G_2 = \frac{1}{2} [1 - \sin(h_0 p_g)],$$

where $p_r = (2\pi x)/(\lambda_r f)$ and $p_g = (2\pi x)/(\lambda_g f)$ are the spatial frequencies of the gratings. λ_r and λ_g are the red and green color wavelengths. x denotes the spatial coordinate in the same direction as p , and f is the focal length of the achromatic transform lens L_2 . By a straight-forward but rather cumbersome evaluation, the irradiance around the origin of the output image plane P_4 can be shown [2],

$$(4) \quad I(x, y) = I_r(x, y) - I_g(x, y) \\ = K [O_1(x, y) - O_2(x, y)]^2 - \\ - K [O_1(x, y) + O_2(x, y)]^2,$$

where $I_r(x, y)$ and $I_g(x, y)$ denote the red and green subtracted color image irradiances, O_{1r} , O_{2r} , O_{1g} and O_{2g} are the corresponding red and green color input objects. From Eq. (4) we see that the subtracted color image can be obtained at the output image plane. Since the color image subtraction is obtained with extended incoherent sources, the coherent artifact noise can be suppressed.

III. — SOURCE ENCODING FOR IMAGE SUBTRACTION

We would now consider a source encoding technique for image subtraction. As we have pointed out earlier, the image subtraction is a $1 - D$ processing operation and the spatial coherence requirement is dependent upon corresponding image points to be subtracted. Therefore, instead of utilizing a strictly broad spatial coherence function, a point-pair spatial coherence is sufficient. To insure a physically realizable source intensity distribution, we let the point-pair spatial coherence be [2, 3]

$$(5) \quad \Gamma(x - x') = \frac{\sin\left(\frac{N\pi}{h_c} (x - x')\right)}{N \sin\left(\frac{\pi}{h_c} (x - x')\right)} \\ \times \text{sinc}\left(\frac{\pi v}{h_c a} (x - x')\right),$$

where $2h_c$ is the separation between the image points, $N \gg 1$ a positive integer, and $v \ll a$. The first factor of Eq. (5) represents a sequence of narrow pulses present at every $x - x' = nh_c$, where n is a positive

integer, and the peak values of the pulses are weighted by a broader sinc factor, as shown in figure 2(a). From this figure, we see that there exists a high degree of spatial coherence between every point-pair of the two input objects O_1 and O_2 . By taking the Fourier transformation of Eq. (5), we obtain the following intensity distribution [3]

$$(6) \quad S(|x|) = \sum_{n=1}^N \text{rect}\left(\frac{|x - nd|}{w}\right),$$

where w is the slit width, $d = (\lambda f)/h_0$ is the separation between the slits of the source coding apertures, λ is the wavelength of the light source, and f is the focal length of the collimating lens. Thus the intensity distribution of Eq. (6) represents N number of narrow slit apertures with equal spacing d , as shown in figure 2(b). From this result, it is possible to encode an extended source to obtain a spatial coherence function at the input plane for the subtraction operation.

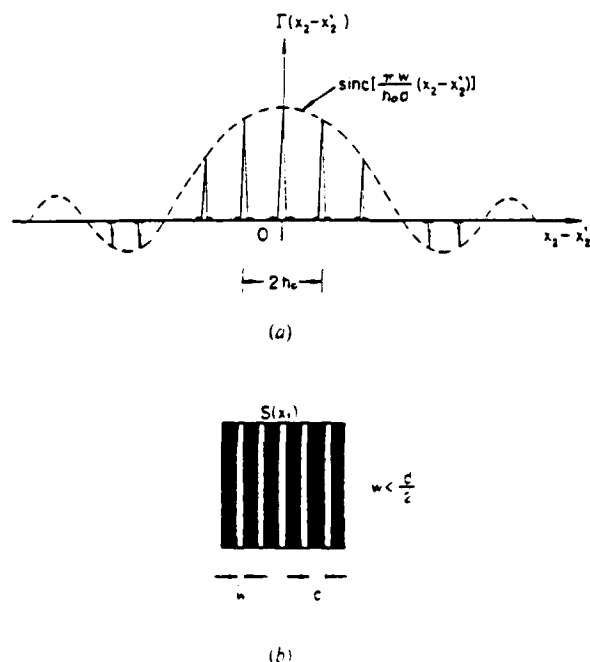


FIG. 2 — (a) A Point-pair Spatial Coherence Function. (b) Source Encoding Mask.

Since the scale of the Fourier spectrum varies with the wavelength of the light source, a temporal coherence requirement should also be imposed on every processing operation. In other words, the spectral width (i.e., temporal coherence) of the light source should be restricted by the following inequality [3],

$$(7) \quad \frac{\Delta\lambda}{\lambda} < \frac{1}{h_0 f_p},$$

where λ is the center wavelength of the light source and f_p is the highest angular spatial frequency required for the image subtraction. Consequently, if the

spatial frequency requirement is high, then a narrow spectral width of the light source is required.

IV. — EXPERIMENTAL DEMONSTRATION

Strictly speaking, light sources emitting all primary colors (i.e., red, green, and blue) should be used for the color images subtraction. For simplicity of experimental demonstration, a mercury arc lamp with a green filter (5461 Å) and a zirconium arc lamp with a red filter (6328 Å) were used for the color light sources. The intensity ratio of the two resulting light sources was adjusted to about unity with a variable beam splitter.

The slit widths for the source encoding masks were about 2.5 μ and the spacings of the slits were 25 μ for the green wavelength and 29 μ for the red wavelength. The overall size of the source encoding masks was about 3 × 3 mm² which contained about 120 and 100 slits respectively. The focal length of the transform lenses was 300 mm. A liquid gate containing two color image transparencies about 6 × 8 mm² each and with a separation of about 13.2 mm was placed behind the collimator. Two sinusoidal gratings with spatial frequencies of 1/(25 μ) and 1/(29 μ) were used for the green and red color image subtraction operation, as shown in figure 1.

In our first experimental demonstration, we provide in figures 3(a) and 3(b) two sets of different colored

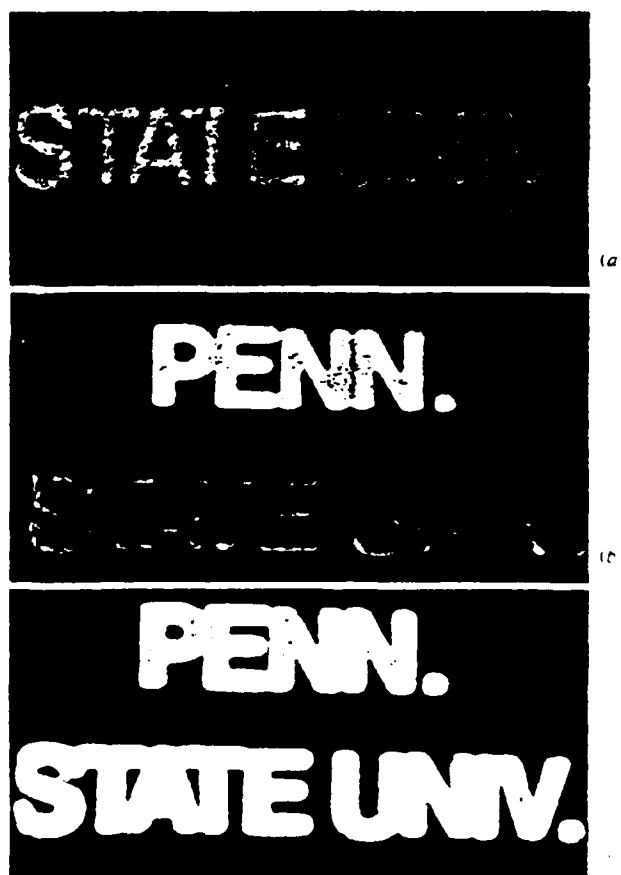


FIG. 3 — (a) Original Subtraction Image. (b) Color Image Subtraction Result Image.

English words as input objects. *Figure 3(c)* shows the subtracted color image obtained with the color subtraction technique. The input words *STATE* *UNIV.* are red and green respectively in one set but they are green and red respectively in the other set, while in the subtracted image, as shown in *figure 3(c)*, both words are in yellow color, which is consistent with the result we expected. In other words, the subtracted image of red and green produces yellow color since the red and green wavelengths are incoherent and therefore add incoherently to produce a yellow color.

For a second demonstration, we provide two continuous tone color images of two sets of fruit, as shown in *figures 4(a)* and *4(b)*. By comparing these two figures, we see that a dark green cucumber and a red tomato are missing in *figure 4(b)*. *Figure 4(c)* shows the subtracted color image obtained with this incoherent color image subtraction technique. In this result,

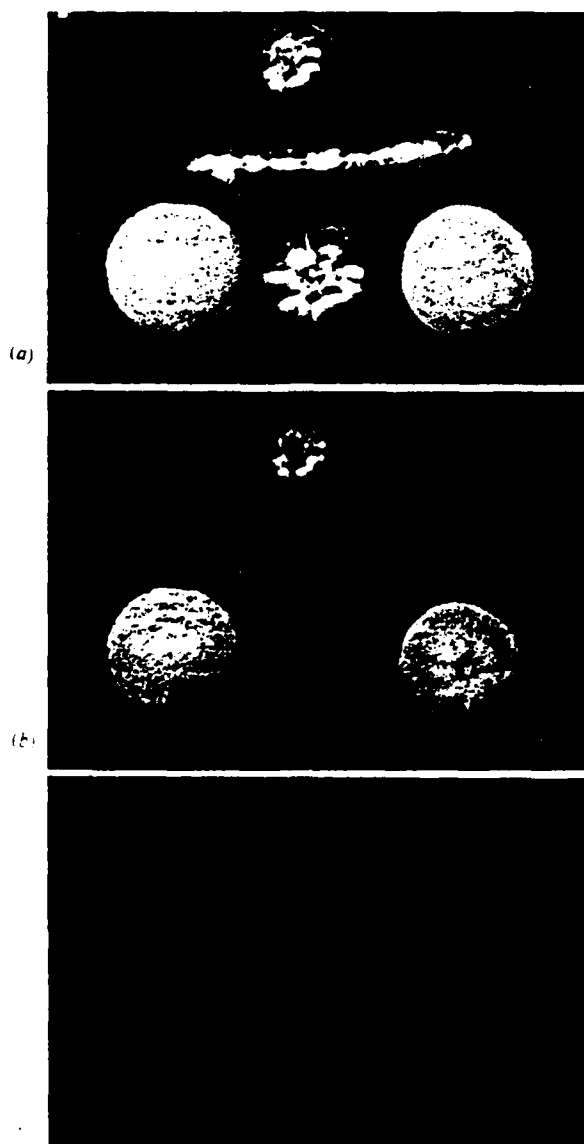


FIG. 4 — Color Image Subtraction. Continuous Tone Objects: (a) et (b) Input Color Object Transparencies; Subtracted Color Image.

the profiles of a cucumber and a tomato can be seen at the output image plane.

For the final demonstration, we again provide two continuous tone color images of a parking lot as input color object transparencies, as shown in *figures 5(a)* and *5(b)*. From these input transparencies, we see that a red color passenger car shown in the parking lot in *figure 5(a)* is missing in *figure 5(b)*. *Figure 5(c)* is the color subtracted image obtained from the incoherent color image subtraction technique as previously described. In this figure, a red passenger car can clearly be seen at the output image plane. It is also interesting to point out that the parking line (in yellow color) on the right side of the red car can readily be seen with the subtracted image.

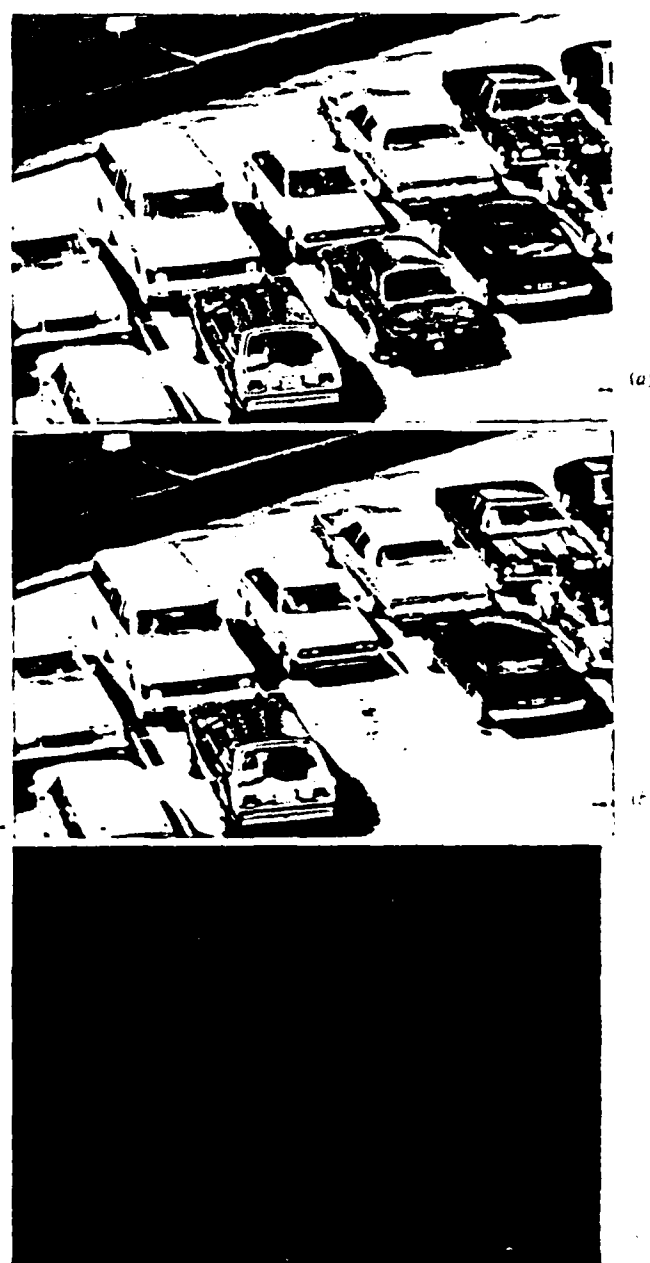


FIG. 5 — Color Image Subtraction. Parking Lot Image: (a) Input Color Transparencies; (c) Subtracted Color Image.

V. — CONCLUSION

We have introduced a color image subtraction technique with encoded incoherent sources. The basic advantage of source encoding is to increase the available light power for the image subtraction operation, so that the inherent difficulty of obtaining incoherent point sources can be alleviated. Since the technique uses incoherent sources, the annoying coherent artifact noise can be suppressed. We would see that the concept of color image subtraction may also be extended to the use of white-light source, for which a program is currently under investigation. In experimental demonstrations, we have shown that color subtracted images can be easily obtained by this

incoherent subtraction technique. Since virtually all images of natural objects are color, the technique may offer a wide range of practical applications.

REFERENCES

- [1] EBERSOLE (J. F.). — *Opt. Eng.*, 1975, 14, 436.
- [2] WU (S. T.), YU (F. T. S.). — *Appl. Opt.* (to be published).
- [3] YU (F. T. S.), ZHUANG (S. L.), WU (S. T.). — *Appl. Phys.* (to be published).

The authors wish to acknowledge the support by U.S. Air Force Office of Scientific Research Grant AFSOR-81-0148.

(Manuscript received in August 3, 1981)



SECTION XI

Rainbow Holographic Aberrations

Rainbow holographic aberrations and the bandwidth requirements

Y. W. Zhang, W. G. Zhu, and F. T. S. Yu

Rainbow holographic image resolution, primary aberrations, and bandwidth requirements are presented. The results obtained for the rainbow holographic process are rather general, for which the conventional holographic image resolution, aberrations, and bandwidth requirements can be derived. The conditions for the elimination of the five primary rainbow holographic aberrations are also given. These conditions may be useful for the application of obtaining a high-quality rainbow hologram image. In terms of bandwidth requirements, we have shown that the bandwidth requirement for a rainbow holographic construction is usually several orders lower than that of a conventional holographic process. Therefore, a lower-resolution recording medium can generally be used for most of the rainbow holographic constructions.

I. Introduction

The rainbow holographic process of Benton¹ involves two recording steps. First, a primary hologram is made from a real object with the conventional off-axis holographic techniques, and second, the rainbow hologram is recorded from the real hologram image from the primary hologram. The relaxation of the coherence requirement on the reconstructing process arises from the placement of a narrow slit behind the primary hologram in the second-step holographic recording. However, the two-step holographic recording process is cumbersome and requires a separate optical setup for each step. It is usually a major undertaking for laboratories with limited optical components. An alternative method of obtaining a rainbow hologram is the one-step process of Chen *et al.*²⁻⁵ They had shown that the one-step technique offers certain flexibilities, and the optical arrangement is simpler than the conventional two-step process. We also note that the color blur of the Benton type rainbow hologram has been subsequently analyzed by Wyant,⁶ Chen,⁷ and Tamura.⁸ Recently, Zhuang *et al.*⁹ investigated the image resolution and color blur for a one-step rainbow holographic process utilizing diffraction optics.

In this paper, we shall evaluate the primary aberrations and bandwidth requirement for a rainbow holographic process. The correlations for the elimination of the rainbow holographic aberrations are presented.

Since the effective aperture of a rainbow hologram is generally smaller than that of a conventional hologram, the spatial bandwidth requirement is generally somewhat lower for the rainbow holographic process. Therefore, it is usually possible to construct a rainbow hologram utilizing a lower-resolution film.

II. Rainbow Holographic Resolution

In a recent paper,⁶ the resolution limit and color blur of a rainbow hologram were analyzed from diffraction optics. However, in practice, the slit used in a rainbow holographic process is many orders larger than the light wavelength. Therefore, the rainbow holographic process can also be approached from slightly different configurations as depicted in Fig. 1. For simplicity, both the recording and the reconstruction processes are drawn in a composite diagram, where H_1 represents the primary hologram which is in contact with a narrow-slit aperture SL . H_2 represents the constructing rainbow hologram, $O(x_0, y_0)$ is the object image point, $I(x_i, y_i)$ is the rainbow hologram image point, and $R(x_r, y_r)$ and $C(x_c, y_c)$ are the reference and the reconstruction point sources, respectively. We note that if O and SL represent the object and slit images due to an imaging lens, the same diagram of Fig. 1 can also be used for the analysis of a one-step rainbow holographic process.

With reference to Fig. 1, it is evident that the coordinate points P_{11} and P_{12} are the marginal extensions of the rainbow holographic recording region, which can be written as

$$P_{11} = \left(1 - \frac{d}{f} \right) x_0 - \frac{c_0}{-f} \quad (1)$$

$$P_{12} = \left(1 - \frac{d}{f} \right) x_0 - \frac{c_0}{-f}$$

where $d = z_0 - z_c$

The authors are with Pennsylvania State University Electrical Engineering Department, University Park, Pennsylvania 16802.

Received 26 August 1982.

0003-6995/83/010164-05\$01.00/0

© 1983 Optical Society of America

Thus, the complex light-amplitude distribution due to the object image point O at the rainbow holographic recording plate H_2 is

$$U_1(x; k_1) = A_1 \exp[-ik_1[d^2 + (x - x_0)^2]^{1/2}], \quad (3)$$

and the corresponding complex light distribution due to the reference and reconstructing (called illuminating) beams are

$$U_2(x; k_1) = A_2 \exp[-ik_1[L_1^2 + (x - x_r)^2]^{1/2}], \quad (4)$$

$$U_3(x; k_2) = A_3 \exp[-ik_2[L_2^2 + (x - x_c)^2]^{1/2}], \quad (5)$$

respectively, where the spatial impulse response is

$$h_1(\alpha - x; k_2) = A_4 \exp[ik_2[l^2 + (\alpha - x)^2]^{1/2}], \quad (6)$$

A_i is a complex constant, $k = 2\pi/\lambda$, and λ_1 and λ_2 are the wavelengths for the rainbow hologram construction and the reconstructing processing, respectively.

The corresponding complex light field of the rainbow hologram image point I is

$$B_1(\alpha; k_2) = C_1 \int_{P_{12}}^{P_{11}} U_1 U_2^* U_3 h_1 dx = C_2 \operatorname{sinc} \left[\frac{dW}{\lambda_2 g l_1} (\alpha + \alpha_i) \right], \quad (7)$$

where

$$l_1 = \frac{dL_1 L_2}{\mu L_1 L_2 + dL_1 - \mu dL_2}, \quad (8)$$

$$\alpha_i = l_1 \left(-\mu \frac{x_0}{d} - \frac{x_c}{L_2} + \mu \frac{x_r}{L_1} \right), \quad (9)$$

(l_1, α_i) identifies the position of the rainbow hologram image point I , and $\mu \triangleq \lambda_2/\lambda_1$.

The magnification of the hologram image can then be written as

$$M_i = \frac{\alpha_i}{x_0} = \frac{\mu l_1}{d} = \left(1 - \frac{d}{L_1} + \frac{d}{\mu L_2} \right)^{-1}, \quad (10)$$

and the resolution limit of the rainbow holographic process is

$$\Delta H_i = \frac{\lambda_2 l_1 \left(1 + \frac{s}{d} \right)}{W} = \frac{\lambda_2 L_1 L_2 (d + s)}{(\mu L_1 L_2 - L_1 d - \mu L_2 d) W}, \quad (11)$$

where W is the slit width. If both the reference and the reconstruction beams are plane waves, the resolution limit becomes

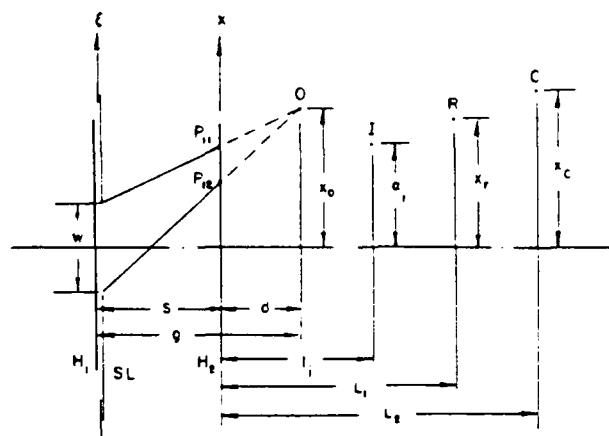


Fig. 1. A composite rainbow holographic construction and reconstruction process for the evaluation of the hologram image resolution and the primary aberrations: H_1 , primary hologram; SL , slit aperture; W , slit width; H_2 , rainbow holographic plate; O , object image point; I , rainbow hologram image point; R , convergent reference point source; C , white-light reconstruction point source.

$$\Delta H_i = \frac{\lambda_1 (d + s)}{W}. \quad (12)$$

We note that these results are identical to the results we obtained previously by Zhuang *et al.*¹⁰ It is evident that this partial geometrics approach simplifies the rainbow holographic analysis.

III. Rainbow Holographic Aberrations

In evaluating the rainbow holographic aberration, we expand the exponent of Eq. (7) in binomial expansion such as

$$\phi(x, k) = k[L^2 + (x - a)^2]^{1/2} = k \left[1 + \frac{(x - a)^2}{2L} - \frac{(x - a)^4}{8L^3} + \dots \right]. \quad (13)$$

Thus, by retaining the first three terms of Eq. (13), the third-order primary aberrations of a rainbow holographic process can be obtained.

To evaluate the third-order primary aberrations, the phase factor of the real rainbow hologram image can be written as

$$\phi_i = k_2 \mu [L_1^2 + (x - x_0)^2]^{1/2} - (x - x_0)^2]^{1/2} - \mu d^2 - (x - x_0)^2 - (x - x_0)^2]^{1/2} - [L_2^2 + (x - x_c)^2 - (x - x_c)^2]^{1/2} - [L_1^2 + (x - x_r)^2 - (x - x_r)^2]^{1/2}. \quad (14)$$

With reference to the binomial expansion of Eq. (13), Eq. (14) can be written as a configuration of the order terms, i.e.,

$$\phi_i = \phi_0 + \phi_1 + \phi_2 + \phi_3, \quad (15)$$

where ϕ_0 , ϕ_1 , and ϕ_2 are the first-, second-, and higher-order terms, which shall be ignored in our evaluation. The third-order term, ϕ_3 , is written as

$$\phi_3 = \frac{k_2 \mu}{8} \left[\frac{(x - x_0)^4}{L_1^3} - \frac{(x - x_0)^4}{L_2^3} - \frac{(x - x_r)^4}{L_1^3} \right]$$

Table 1. Rainbow Holographic Aberrations and the Conditions for Elimination

Name	Formula	Condition of eliminating aberration
Spherical	$S = \frac{\mu}{L_1^3} - \frac{\mu}{d^3} + \frac{1}{l_1^3} - \frac{1}{L_2^3}$	$\mu = 1; d = l_1; L_1 = L_2$
Coma	$C_x = \frac{\mu}{L_1^3} x_r - \frac{\mu}{d^3} x_0 + \frac{\alpha_1}{l_1^3} - \frac{x_c}{L_2^3}$	$\mu = 1; d = l_1; L_1 = L_2 = \infty,$
	$C_y = \frac{\mu}{L_1^3} y_r - \frac{\mu}{d^3} y_0 + \frac{\beta_1}{l_1^3} - \frac{y_c}{L_2^3}$	but, $\frac{x_r}{L_1}, \frac{y_r}{L_1}, \frac{x_c}{L_2}, \frac{y_c}{L_2}$ are finite
Astigmatism	$A_x = \frac{\mu x_r^2}{L_1^3} - \frac{\mu x_0^2}{d^3} + \frac{\alpha_1^2}{l_1^3} - \frac{x_c^2}{L_2^3}$	$\mu = 1; d = l_1; L_1 = L_2 = \infty,$
	$A_{xy} = \frac{\mu x_r y_r}{L_1^3} - \frac{\mu x_0 y_0}{d^3} + \frac{\alpha_1 \beta_1}{l_1^3} - \frac{x_c y_c}{L_2^3}$	but, $\frac{x_r}{L_1}, \frac{y_r}{L_1}, \frac{x_c}{L_2}, \frac{y_c}{L_2}$ are finite
	$A_y = \frac{\mu y_r^2}{L_1^3} - \frac{\mu y_0^2}{d^3} + \frac{\beta_1^2}{l_1^3} - \frac{y_c^2}{L_2^3}$	
Curvature of field	$F = \frac{\mu}{L_1^3} (x_r^2 + y_r^2) - \frac{\mu}{d^3} (x_0^2 + y_0^2)$	$\mu = 1; d = l_1; L_1 = L_2 = \infty,$
	$+ \frac{1}{l_1^3} (\alpha_1^2 + \beta_1^2) - \frac{1}{L_2^3} (x_c^2 + y_c^2)$	but, $\frac{x_r}{L_1}, \frac{y_r}{L_1}, \frac{x_c}{L_2}, \frac{y_c}{L_2}$ are finite
Distortion	$D_x = \frac{\mu}{L_1^3} x_r^3 - \frac{\mu}{d^3} x_0^3 + \frac{\alpha_1^3}{l_1^3} - \frac{x_c^3}{L_2^3}$	$\mu = 1; \frac{x_r}{L_1} = \frac{x_c}{L_2}; \frac{y_r}{L_1} = \frac{y_c}{L_2}$
	$D_y = \frac{\mu}{L_1^3} y_r^3 - \frac{\mu}{d^3} y_0^3 + \frac{\beta_1^3}{l_1^3} - \frac{y_c^3}{L_2^3}$	

By substituting the relation of $x = r \cos \theta$ and $y = r \sin \theta$ into Eq. (16), the third-order phase factor can be shown as

$$\begin{aligned} \phi_r = k_2 \left[\frac{1}{18} \left(\frac{\mu}{d^3} - \frac{\mu}{L_1^3} - \frac{1}{L_1^3} - \frac{1}{L_2^3} \right) r^4 - \frac{1}{2} \left[\left(\frac{\mu}{d^3} x_c - \frac{\mu}{L_1^3} x_r \right. \right. \right. \\ \left. \left. - \frac{1}{L_1^3} \right) \cos^2 \theta - \left(\frac{\mu}{d^3} y_c - \frac{\mu}{L_1^3} y_r - \frac{1}{L_1^3} - \frac{\beta_1^2}{L_2^3} \right) \sin^2 \theta \right] r^2 \\ - \frac{1}{4} \left[\left(\frac{\mu}{d^3} (x_c^2 - y_c^2) - \frac{\mu}{L_1^3} (x_r^2 - y_r^2) - \frac{1}{L_1^3} (x_c^2 - y_c^2) \right. \right. \\ \left. \left. - \frac{1}{L_1^3} (\alpha_1^2 - \beta_1^2) \right) r^2 - \frac{1}{2} \left[\left(\frac{\mu}{d^3} x_c^2 - \frac{\mu}{L_1^3} x_r^2 - \frac{1}{L_1^3} - \frac{\alpha_1^2}{L_2^3} \right) \cos^2 \theta \right. \right. \\ \left. \left. - \left(\frac{\mu}{d^3} y_c^2 - \frac{\mu}{L_1^3} y_r^2 - \frac{1}{L_1^3} - \frac{\beta_1^2}{L_2^3} \right) \sin^2 \theta - \left(\frac{\mu}{d^3} x_c y_c \right. \right. \right. \\ \left. \left. - \frac{\mu}{L_1^3} x_r y_r - \frac{1}{L_1^3} \alpha_1 \beta_1 \sin^2 \theta \cos^2 \theta \right) r^2 \right. \\ \left. \left. - \frac{1}{4} \left[\left(\frac{\mu}{d^3} x_c^3 - \frac{\mu}{L_1^3} x_r^3 - \frac{1}{L_1^3} \alpha_1^3 \right) \cos^3 \theta - \left(\frac{\mu}{d^3} y_c^3 \right. \right. \right. \right. \\ \left. \left. - \frac{\mu}{L_1^3} y_r^3 - \frac{1}{L_1^3} \beta_1^3 \right) \sin^3 \theta \right] \right] \end{aligned} \quad (17)$$

Thus ϕ_r can be written as a function of the five primary aberrations, such as

$$\begin{aligned} \phi_r = k_2 \left[-\frac{r^4}{8} S + \frac{r^3}{2} (C_x \cos \theta + C_y \sin \theta) - \frac{r^2}{4} F \right. \\ \left. - \frac{r^2}{2} (A_x \cos^2 \theta - 2A_{xy} \sin \theta \cos \theta + A_y \sin^2 \theta) \right. \\ \left. + \frac{r}{2} (D_x \cos \theta + D_y \sin \theta) \right] \quad (18) \end{aligned}$$

where S represents the spherical aberrations, C_x and C_y represent the meridian and tangential coma, A_x , A_{xy} , and A_y are the astigmatisms, F is the curvature of field, and D_x and D_y are the horizontal and vertical distortions. By comparing this equation with Eq. (17), the equations for the five primary rainbow holographic aberrations can be obtained as tabulated in Table 1.

In this table, the conditions for the elimination of the primary aberrations are given. It is evident that all the primary aberrations can be eliminated if both the reference and the reconstruction beams are plane waves and $\mu = 1$. It is interesting to note that, if the slit width W is equal to the size of the primary hologram, by letting $S = 0$, the primary aberrations reduce to the conventional off-axis holographic aberrations as obtained by Meier.¹¹

Since the rainbow holographic imaging is generally produced from a point source, the aberrations are

affected by the wavelength spread $\Delta\lambda_2$ during the reconstruction process. We note that this wavelength spread $\Delta\lambda_2$ is limited by observer eye through the slit image. Thus, the effect of aberration variation due to $\Delta\lambda_2$ can be determined as shown in the following, for simplicity as a 1-D notation:

$$\Delta S = \left(1 - \frac{\Delta\lambda_2}{\lambda_2}\right) \left[S - \frac{\Delta\lambda_2}{\lambda_1} \left(\frac{1}{L_1^3} - \frac{1}{d^3} \right) + \frac{\partial}{\partial \lambda_2} \left(\frac{1}{L_1^3} \right) \Delta\lambda_2 \right] - S$$

$$\approx -\frac{\Delta\lambda_2}{\lambda_2} S + \frac{\Delta\lambda_2}{\lambda_1} \left[\left(\frac{1}{L_1^3} - \frac{1}{d^3} \right) + \frac{L_2(L_1 - d)(\mu L_1 L_2 + L_1 d - \mu L_2 d)^2}{(d L_1 L_2)^3} \right] \quad (19)$$

$$\Delta C_s = \left(1 - \frac{\Delta\lambda_2}{\lambda_2}\right) \left[C_s - \left(\frac{x_0}{d^3} - \frac{x_r}{L_1^3} \right) \frac{\Delta\lambda_2}{\lambda_1} - \frac{\Delta\lambda_2}{\lambda_1} \left[\frac{1}{L_1^3} \left(\frac{x_0}{d} - \frac{x_r}{L_1} \right) + \frac{2L_2(L_1 - d)}{L_1^2(\mu L_1 L_2 + L_1 d - \mu L_2 d)} \left(\mu \frac{x_0}{d} + \frac{x_r}{L_2} - \mu \frac{x_r}{L_1} \right) \right] \right] - C_s$$

$$\approx -\frac{\Delta\lambda_2}{\lambda_2} C_s + \frac{\Delta\lambda_2}{\lambda_1} \left[\left(\frac{x_r}{L_1^3} - \frac{x_0}{d^3} \right) - \frac{1}{L_1^3} \left(\frac{x_0}{d} - \frac{x_r}{L_1} \right) + \frac{2L_2(L_1 - d)}{(\mu L_1 L_2 + L_1 d - \mu L_2 d)} \left(\mu \frac{x_0}{d} + \frac{x_r}{L_2} - \mu \frac{x_r}{L_1} \right) \right] \quad (20)$$

$$\Delta F = \Delta A_s = \left(1 - \frac{\Delta\lambda_2}{\lambda_2}\right) \left[F + \left(\frac{x_0^2}{d^3} - \frac{x_r^2}{L_1^3} \right) \frac{\Delta\lambda_2}{\lambda_1} + \frac{\Delta\lambda_2}{\lambda_1 d L_1 L_2} \left[L_2(L_1 - d) \left(\mu \frac{x_0}{d} + \frac{x_r}{L_2} - \mu \frac{x_r}{L_1} \right)^2 + 2(\mu L_1 L_2 + L_1 d - \mu L_2 d) \left(\mu \frac{x_0}{d} + \frac{x_r}{L_2} - \mu \frac{x_r}{L_1} \right) \left(\frac{x_0}{d} - \frac{x_r}{L_1} \right) \right] \right] - F$$

$$\approx -\frac{\Delta\lambda_2}{\lambda_2} F + \frac{\Delta\lambda_2}{\lambda_1} \left[\left(\frac{x_0^2}{d^3} - \frac{x_r^2}{L_1^3} \right) + \frac{L_2(L_1 - d)}{d L_1 L_2} \left[L_2(L_1 - d) \left(\mu \frac{x_0}{d} + \frac{x_r}{L_2} - \mu \frac{x_r}{L_1} \right)^2 + 2 \left(\frac{x_0}{d} - \frac{x_r}{L_1} \right) (\mu L_1 L_2 + L_1 d - \mu L_2 d) \right] \right] \quad (21)$$

$$\Delta D_s = \left(1 - \frac{\Delta\lambda_2}{\lambda_2}\right) \left[D_s - \left[\left(\frac{x_0^2}{d^3} - \frac{x_r^2}{L_1^3} \right) - 3 \left(\mu \frac{x_0}{d} + \frac{x_r}{L_2} - \mu \frac{x_r}{L_1} \right) \left(\frac{x_0}{d} - \frac{x_r}{L_1} \right) \right] \frac{\Delta\lambda_2}{\lambda_1} \right] - D_s$$

$$\approx -\frac{\Delta\lambda_2}{\lambda_2} D_s + \frac{\Delta\lambda_2}{\lambda_1} \left[\left(\frac{x_0^2}{d^3} - \frac{x_r^2}{L_1^3} \right) + 3 \left(\mu \frac{x_0}{d} + \frac{x_r}{L_2} - \mu \frac{x_r}{L_1} \right) \left(\frac{x_0}{d} - \frac{x_r}{L_1} \right) \right] \quad (22)$$

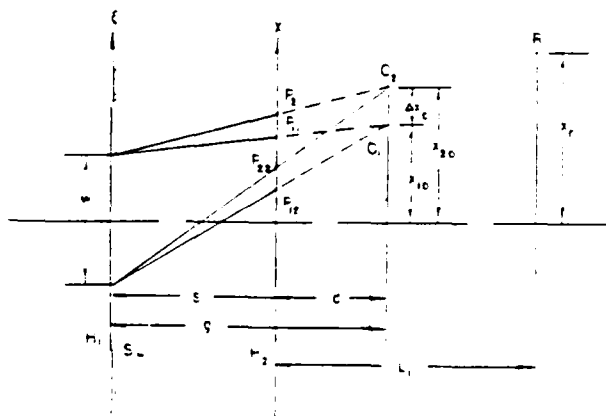


Fig. 2. A composite rainbow holographic construction and reconstruction process for determining the bandwidth requirements. H_1 , primary hologram; SL, slit aperture; W, slit width; H_2 , rainbow holographic plate; O_1, O_2 , extended hologram object image; S , coherent reference point source.

From Eq. (21) we see that the variation of the astigmatism is identical to that of the variation of curvature of field. In ending this section, we point out that the above equations have useful applications for evaluating the rainbow hologram image quality.

IV. Bandwidth Requirements

Since the effective aperture of a rainbow hologram is generally smaller than that of a conventional hologram, it is possible that a lower-resolution film can be utilized. Therefore, it is our aim in this section to discuss the bandwidth requirements of a rainbow holographic process.

We shall investigate for the case in which the slit and the object image are located at opposite sides of the rainbow holographic plate H_2 as shown in Fig. 2, where O_1 and O_2 are the two external points of an extended object image reconstructed from a primary hologram H_1 . Thus, from Fig. 2, we see that

$$r_1 = \frac{d}{\lambda_1} \left(\frac{x_0}{d} - \frac{x_r}{L_1} \right)$$

$$r_2 = \frac{d}{\lambda_2} \left(\frac{x_0}{d} - \frac{x_r}{L_1} \right)$$

$$r_1 = \frac{d}{\lambda_1} \left(\frac{x_0}{d} - \frac{x_r}{L_1} \right)$$

$$r_2 = \frac{d}{\lambda_2} \left(\frac{x_0}{d} - \frac{x_r}{L_1} \right)$$

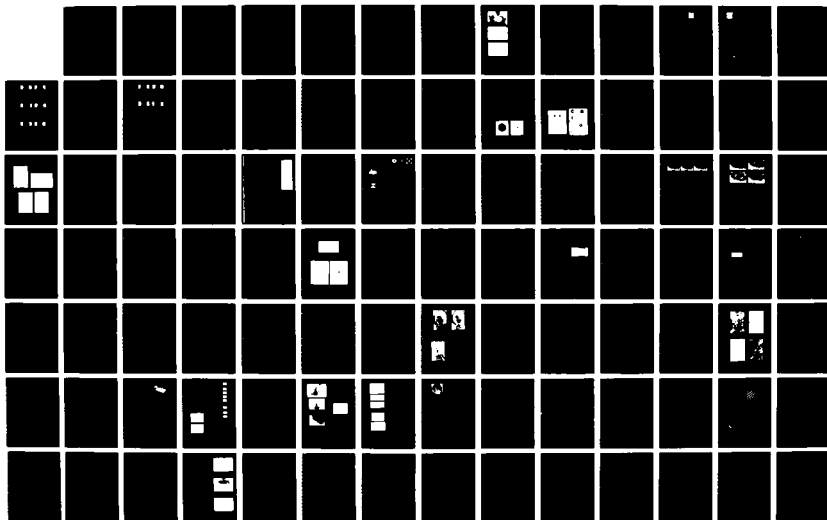
AD-A179 489

WHITE-LIGHT OPTICAL INFORMATION PROCESSING AND
HOLOGRAPHY(U) PENNSYLVANIA STATE UNIV UNIVERSITY PARK
DEPT OF ELECTRICAL ENGINEERING F T YU 23 JAN 87
AFOSR-TR-87-0456 AFOSR-83-0140 F/G 20/6

24

UNCLASSIFIED

NL





MI
N

Similar to what we did in previous sections, the complex light fields U_1 , U_2 , and U_3 due to the object image points O_1 and O_2 and the reference beam R can be formulated. The terms contributing to the rainbow holographic reconstruction process are

$$U_1 U_3^* + U_3 U_1^* = 2|A_1||A_3| \cos \left\{ k_1 \left[L_1 - d - \frac{(x - x_{01})^2}{2d} + \frac{(x - x_r)^2}{2L_1} \right] + \theta_1 \right\}, \quad (24)$$

$$U_2 U_3^* + U_3 U_2^* = 2|A_2||A_3| \cos \left\{ k_1 \left[L_1 - d - \frac{(x - x_{02})^2}{2d} + \frac{(x - x_r)^2}{2L_1} \right] + \theta_2 \right\}, \quad (25)$$

where A_1 , A_2 , and A_3 are the complex constants, and θ_1 and θ_2 are the constant phase factors. The phase shifts due to the U_1 , U_2 , and U_3 are

$$\varphi_{31} = k_1 \left[L_1 - d - \frac{(x - x_{01})^2}{2d} + \frac{(x - x_r)^2}{2L_1} \right] + \theta_1, \quad (26)$$

$$\varphi_{32} = k_1 \left[L_1 - d - \frac{(x - x_{02})^2}{2d} + \frac{(x - x_r)^2}{2L_1} \right] + \theta_2, \quad (27)$$

respectively.

The derivatives of φ_{31} and φ_{32} represent the angular spatial frequency along the x direction. Thus, the corresponding linear spatial frequencies are

$$\nu_{31} = \frac{1}{2\pi} \frac{d\varphi_{31}}{dx} = \frac{1}{\lambda_1} \left[\left(\frac{1}{L_1} - \frac{1}{d} \right) x + \frac{x_{01}}{d} - \frac{x_r}{L_1} \right], \quad (28)$$

$$\nu_{32} = \frac{1}{2\pi} \frac{d\varphi_{32}}{dx} = \frac{1}{\lambda_1} \left[\left(\frac{1}{L_1} - \frac{1}{d} \right) x + \frac{x_{02}}{d} - \frac{x_r}{L_1} \right], \quad (29)$$

where ν denotes the spatial frequency. Therefore, the spatial frequency bandwidth of the rainbow hologram can be shown as

$$\Delta\nu = \nu_{32}|_{x=P_{22}} - \nu_{31}|_{x=P_{11}} = \frac{1}{\lambda_1 L_1 g} [(L_1 + s)\Delta x_0 + (L_1 - d)W], \quad (30)$$

where $g = s + d$ and $\Delta x_0 = x_{02} - x_{01}$. If we let

$$\Delta\nu_1 = \frac{1}{\lambda_1 g} \left(1 + \frac{s}{L_1} \right) \Delta x_0, \quad (31)$$

$$\Delta\nu_2 = \frac{1}{\lambda_1 g} \left(1 - \frac{d}{L_1} \right) W, \quad (32)$$

Eq. (30) reduces to

$$\Delta\nu = \Delta\nu_1 + \Delta\nu_2, \quad (33)$$

where $\Delta\nu_1$ and $\Delta\nu_2$ are the spatial frequency bandwidths due to the size of object image and the slit of the rainbow holographic construction, respectively. Moreover, Eq. (30) can also be written as

$$\Delta\nu = \frac{1}{\lambda_1 g} \left[\Delta x_0 + W + (s\Delta x_0 - dW) \frac{1}{L_1} \right]. \quad (34)$$

From this equation, we see that if $(\Delta x_0)/W > d/s$, increasing L_1 can compress the spatial frequency bandwidth of the rainbow hologram. On the other hand, if $(\Delta x_0)/W < d/s$, decreasing L_1 can also compress the spatial frequency bandwidth of the rainbow hologram. However, for the case $(\Delta x_0)/W = d/s$, the L_1 is independent of $\Delta\nu$.

Table II shows the spatial frequency bandwidth requirements for various rainbow holographic recording

Table II. Rainbow Holographic Bandwidth Requirements

L_1	Reference waveform	$\Delta\nu$
$L_1 = \infty$	plane wave	$\frac{1}{\lambda_1 g} (\Delta x_0 + W)$
$d < L_1 < \infty$	convergent	$\frac{1}{\lambda_1 g} \left[\left(1 + \frac{s}{L_1} \right) \Delta x_0 + \left(1 - \frac{d}{L_1} \right) W \right]$
$L_1 = d$	convergent	$\frac{1}{\lambda_1 g} \Delta x_0$
$P < L_1 < d$	convergent	$\frac{1}{\lambda_1 g} \left[\left(1 - \frac{s}{L_1} \right) \Delta x_0 - \left(1 - \frac{d}{L_1} \right) W \right]$
$-\infty < L_1 < -P$	divergent	$\frac{1}{\lambda_1 g} \left[\left(\frac{s}{ L_1 } - 1 \right) \Delta x_0 - \left(1 - \frac{d}{ L_1 } \right) W \right]$
$L_1 = -s$	divergent	$\frac{1}{\lambda_1 g} W$
$-\infty < L_1 < -s$	divergent	$\frac{1}{\lambda_1 g} \left[\left(1 - \frac{s}{ L_1 } \right) \Delta x_0 - \left(1 - \frac{d}{ L_1 } \right) W \right]$
$L_1 = -\infty$	plane wave	$\frac{1}{\lambda_1 g} \Delta x_0 - W$

conditions. In this table, the notation p denotes the distance from rainbow holographic plate H_2 with respect to the reference beam R , where the paraxial approximation holds.

We note that, for a 2-D case, the general formulas for spatial frequency bandwidth requirements for a rainbow holographic process can be written as

$$\begin{aligned}\Delta\nu_x &= \frac{1}{\lambda_1 d} \left[\left| 1 + \frac{s}{L_1} \right| \Delta x_0 + \left| 1 - \frac{d}{L_1} \right| W \right], \\ \Delta\nu_y &= \frac{1}{\lambda_1 d} \left[\left| 1 + \frac{s}{L_1} \right| \Delta y_0 + \left| 1 - \frac{d}{L_1} \right| L \right],\end{aligned}\quad (35)$$

where $\Delta\nu_x$ and $\Delta\nu_y$ are the corresponding spatial frequency bandwidths in the x and y directions, respectively, for $\Delta x_0 > 0$, $\Delta y_0 > 0$, and $s > 0$. It is interesting to note that if $s = 0$, $W = L_x$, and $L = L_y$, which correspond to the recording conditions of a conventional hologram, Eq. (35) reduces to the results obtained by Yu,¹² i.e.,

$$\begin{aligned}\Delta\nu'_x &= \frac{1}{\lambda_1 d} \left[\Delta x_0 + \left| 1 - \frac{d}{L_1} \right| L_x \right], \\ \Delta\nu'_y &= \frac{1}{\lambda_1 d} \left[\Delta y_0 + \left| 1 - \frac{d}{L_1} \right| L_y \right].\end{aligned}\quad (36)$$

To have some feeling of magnitude, we would provide two numerical examples as given in the following:

(1) For conventional holograph construction process; we let $L_x = L_y = 100$ mm, $\Delta x_0 = \Delta y_0 = 60$ mm, $d = 200$ mm, $L_1 \rightarrow \infty$, and $\lambda_1 = 5 \times 10^{-4}$ mm. By substituting these data into Eq. (36), we obtain the following bandwidth requirements: $\Delta\nu'_x = \Delta\nu'_y = 1600$ lines/mm.

(2) For rainbow holographic construction process, we let $W = 7$ mm, $L = 100$ mm, $s = 830$ mm, $d = 40$ mm, $L_1 = 1000$ mm, $\lambda_1 = 5 \times 10^{-4}$ mm, and $\Delta x_0 = \Delta y_0 = 6$ mm. By substituting these data into Eq. (35), we obtain the following rainbow holographic bandwidth requirements for the x and y directions: $\Delta\nu_x = 40$ lines/mm, and $\Delta\nu_y = 246$ lines/mm. In comparison with these two numerical examples, we see that the bandwidth requirements for the rainbow holographic construction are somewhat lower than those of the conventional holographic process. Thus, in practice, a lower-resolution film can be utilized for rainbow hologram recording.

V. Conclusion

The image resolution and third-order primary aberrations of a rainbow holographic process were derived. The results that we have obtained are rather general, for which the resolution limits and the aberrations of a conventional holographic process can be derived from these results. The conditions for the elimination of the rainbow holographic aberrations were also presented. These conditions are very useful for controlling the rainbow holographic image quality.

The bandwidth requirement of a rainbow holographic process was also evaluated. As compared with the conventional holographic process, the bandwidth requirement for a rainbow holographic process is usually several orders lower than that of a conventional holographic process. Thus, in practice, a lower-resolution film can be utilized for most rainbow holographic constructions.

We wish to acknowledge S. L. Zhuang for his valuable comments and suggestions and the support of the U.S. Air Force Office of Scientific Research grant AFOSR-81-0148.

References

1. S. A. Benton, *J. Opt. Soc. Am.* **59**, 1545A (1969).
2. H. Chen and F. T. S. Yu, *Opt. Lett.* **2**, 85 (1978).
3. F. T. S. Yu and H. Chen, *Opt. Commun.* **25**, 173 (1978).
4. A. M. Tai, F. T. S. Yu, and H. Chen, *Appl. Opt.* **18**, 61 (1979).
5. F. T. S. Yu, A. M. Tai, and H. Chen, *Opt. Eng.* **19**, 666 (1980).
6. J. C. Wyant, *Opt. Lett.* **1**, 130 (1977).
7. H. Chen, *Appl. Opt.* **17**, 3290 (1978).
8. P. N. Tamura, *Appl. Opt.* **17**, 3343 (1978).
9. S. L. Zhuang, P. H. Ruterbusch, Y. W. Zhang, and F. T. S. Yu, *Appl. Opt.* **20**, 872 (1981).
10. M. Born and E. Wolf, Eds., *Principles of Optics* (Pergamon, New York, 1964).
11. R. W. Meier, *J. Opt. Soc. Am.* **55**, 989 (1965).
12. F. T. S. Yu, *Introduction to Diffraction Information Processing and Holography* (MIT Press, Cambridge, 1973).

SECTION XII

Pseudocolor Color Encoding with Primary Colors

ELECTRICAL ENGINEERING DEPARTMENT
THE PENNSYLVANIA STATE UNIVERSITY

University Park, PA 16802

WHITE-LIGHT DENSITY PSEUDOCOLOR ENCODING WITH THREE PRIMARY COLORS

F. T. S. YU, X. X. CHEN, T. H. CHAO

MOIS CLÉS :

Traitement des images
Pseudocouleurs

KEY WORDS :

Optical processing
Pseudocolors

SUMMARY : A technique of generating density pseudocolor encoding with three primary colors using a white-light optical processor is described. Spatial encodings are made with positive, negative, and product of positive and negative photographic-image transparencies, and the pseudocoloring is obtained by color filtering of the smeared Fourier spectra. The technique is simple, versatile, and economical to operate that may offer a wide range of applications. Since coherent sources are not utilized, the color coded image is free from coherent artifact noise. Experimental demonstrations of this density pseudocolor encoder are provided.

Images codées par trois couleurs primaires

RÉSUMÉ : On décrit une méthode de codage pseudocoloré avec trois couleurs primaires en utilisant un processeur optique en lumière blanche. Le codage pseudocoloré est fait en filtrant par des écrans colorés les spectres de transparents photographiques.

Le procédé est simple et il permet des applications variées dans de nombreux domaines. L'éclairage étant incohérent, on évite les défauts bien connus des images en lumière cohérente.

Quelques exemples montrent l'efficacité de la méthode.

Most of the optical images obtained in various scientific applications and usually gray-level density images. For example, scanning electron microscopic images, multispectral band aerial photographic images, x-ray transparencies, etc. However, humans can perceive in color better than gray-level variations. In other words, a color coded image can provide a greater ability in visual discrimination.

In current practice, most of the pseudocolorings are performed by digital computer technique [1]. If the images are initially digitized, the computer technique may be a logical choice. However, for continuous tone images, optical color encoding technique [2] would be more advantageous for at least three major reasons: first, the technique in principle can preserve the spatial frequency resolution of the image to be color coded; second, the optical system is generally easy and economical to operate; third, the cost of an optical pseudocolor encoder is generally less expensive as compared with the digital counterpart.

Density pseudocolor encoding by halftone screen implementation with a coherent optical processor was first reported by Liu and Goodman [3], and later with a white-light processor by Tai, Yu and Chen [4]. Although good results have been subsequently report-

ed, however there is a spatial resolution loss with the half-tone technique and number of discrete lines due to sampling are generally present in the color-coded image. A technique of density pseudocoloring through contrast reversal was recently reported by Santamaria *et al.* [5]. Although this technique offers the advantage over the halftone technique, the optical system is more elaborate and it requires both incoherent and coherence sources. Since the coherence source is utilized, the coherence artifact noise is unavoidable.

More recently a density pseudocolor encoding using a white-light processing technique was reported by Chao, Zhuang and Yu [6]. This technique offers the advantages of coherence noise reduction, no apparent resolution loss, versatility and simplicity of system operation, and low cost of pseudocoloring. Although excellent results have been reported by this technique, however pseudocolor encoding is primarily obtained by means two primary colors. We shall, in this paper, extend this white-light pseudocolor encoding technique for three primary colors. There is however one disadvantage of this proposed technique, it is still not a real-time pseudocolor encoding technique.

We shall now describe a simple white-light density

pseudocolor encoding technique for three primary colors. We assume that a x-ray transparency (called a positive image) is provided for pseudocoloring. By contact printing process, a negative x-ray image transparency is made. Let us now describe a spatial encoding technique to obtain a three-gray-level-image encoding transparency for the pseudocoloring. The spatial encoding is performed by respectively sampling the positive, negative, and the combination of both (i.e., the product of positive and negative) transparencies onto a black-and-white photographic film, with specific sampling grating frequencies oriented at specific azimuthal directions. To avoid the Moire fringe pattern, we shall sample these three images in orthogonal direction with different specific sampling frequencies, as proposed in figure 1. As an

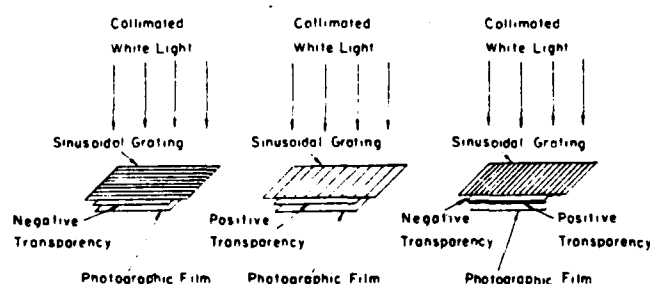


FIG. 1 — Spatial encoding.

illustration, the intensity transmittance of the encoded film can be written as

$$(1) \quad T(x, y) = K \{ T_1(x, y) [1 + \operatorname{sgn}(\cos p_1 y)] + T_2(x, y) [1 + \operatorname{sgn}(\cos p_2 x)] + T_3(x, y) [1 + \operatorname{sgn}(\cos p_3 x)] \}^{-\gamma},$$

where K is an appropriate proportionality constant, T_1 , T_2 , and T_3 are the positive, the negative, and the product image exposures, p_1 , p_2 , and p_3 are the respective carrier spatial frequencies, (x, y) is the spatial frequency coordinate system of the encoded film, γ is the film gamma, and

$$(2) \quad \operatorname{sgn}(\cos x) \triangleq \begin{cases} 1, & \cos x \geq 0, \\ -1, & \cos x < 0. \end{cases}$$

We shall now bleach the encoded transparency to obtain a surface relief phase object [7, 8]. We assume that the bleached transparency is encoded in the linear region of the diffraction efficiency D versus log-exposure E curve [8]. Thus, the amplitude transmittance of the bleached transparency can be written as

$$(3) \quad t(x, y) = \exp[i\phi(x, y)],$$

where $\phi(x, y)$ represents the phase delay distribution, which is proportional to the exposure of the encoded film [9], such as

$$(4) \quad \phi(x, y) = M \{ T_1(x, y) [1 + \operatorname{sgn}(\cos p_1 y)] + T_2(x, y) [1 + \operatorname{sgn}(\cos p_2 x)] + T_3(x, y) [1 + \operatorname{sgn}(\cos p_3 x)] \},$$

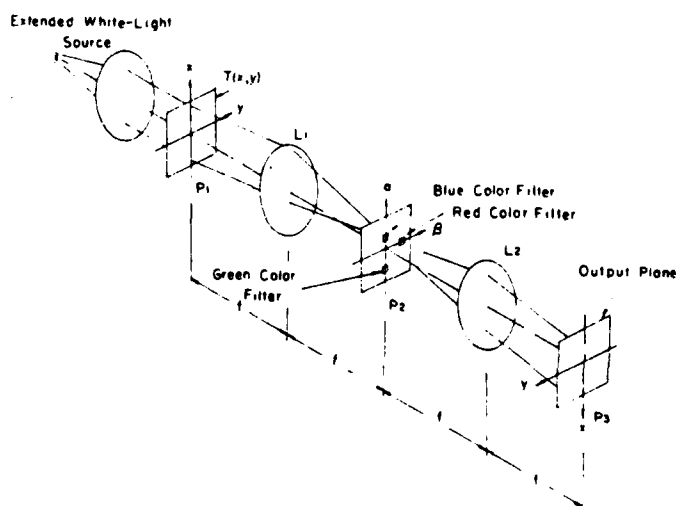


FIG. 2. — A white-light pseudocolor encoder.

where M is an appropriate proportionality constant. If we place this bleached encoded film at the input plane P_1 of a white-light optical processor, as illustrated in figure 2 then the complex light distribution due to $t(x, y)$, for every λ , at the spatial frequency plane P_2 can be determined by the following Fourier transformation :

$$(5) \quad S(\alpha, \beta; \lambda) = \iint t(x, y) \exp\left[-i \frac{2\pi}{\lambda f} (\alpha x + \beta y)\right] dx dy = \iint \exp[i\phi(x, y)] \exp\left[-i \frac{2\pi}{\lambda f} (\alpha x + \beta y)\right] dx dy.$$

By expanding $t(x, y)$ into an exponential series, Eq. (5) can be written as

$$(6) \quad S(\alpha, \beta; \lambda) = \iint \left\{ 1 + i\phi(x, y) + \frac{1}{2} [i\phi(x, y)]^2 + \dots \right\} \exp\left[-i \frac{2\pi}{\lambda f} (\alpha x + \beta y)\right] dx dy.$$

By substituting Eq. (4) into Eq. (6) and retaining the first-order terms and the first-order convolution terms, we have :

$$\begin{aligned}
 (7) \quad S'(\alpha, \beta; \lambda) = & \hat{T}_1\left(\alpha, \beta \pm \frac{\lambda l}{2\pi} p_1\right) + \hat{T}_2\left(\alpha \pm \frac{\lambda l}{2\pi} p_2, \beta\right) \\
 & + \hat{T}_3\left(\alpha \pm \frac{\lambda f}{2\pi} p_3, \beta\right) + \hat{T}_1\left(\alpha, \beta \pm \frac{\lambda f}{2\pi} p_1\right) * \hat{T}_2\left(\alpha \pm \frac{\lambda f}{2\pi} p_2, \beta\right) \\
 & + \hat{T}_1\left(\alpha, \beta \pm \frac{\lambda f}{2\pi} p_1\right) * \hat{T}_3\left(\alpha \pm \frac{\lambda f}{2\pi} p_3, \beta\right) \\
 & + \hat{T}_2\left(\alpha \pm \frac{\lambda f}{2\pi} p_2, \beta\right) * \hat{T}_3\left(\alpha \pm \frac{\lambda f}{2\pi} p_3, \beta\right),
 \end{aligned}$$

where \hat{T}_1 , \hat{T}_2 and \hat{T}_3 are the Fourier transforms of T_1 , T_2 and T_3 respectively. * denotes the convolution operation, and the proportional constants have been neglected for simplicity. We note that, the last cross product term of Eq. (7) would introduce a Moire fringe pattern, which in the same sampling direction of p_2 and p_3 . Nevertheless, all of these cross product terms can be properly masked out at the Fourier plane. Thus by proper color filtering the first-order smeared Fourier spectra, as shown in figure 3, a Moire free pseudocolor coded image can be obtained at the output plane P_3 . The corresponding complex light field immediately behind the Fourier plane would be

$$(8) \quad S(\alpha, \beta) = \hat{T}_1\left(\alpha, \beta - \frac{\lambda_r f}{2\pi} p_1\right) + \hat{T}_2\left(\alpha - \frac{\lambda_b f}{2\pi} p_2, \beta\right) + \hat{T}_3\left(\alpha + \frac{\lambda_g f}{2\pi} p_3, \beta\right),$$

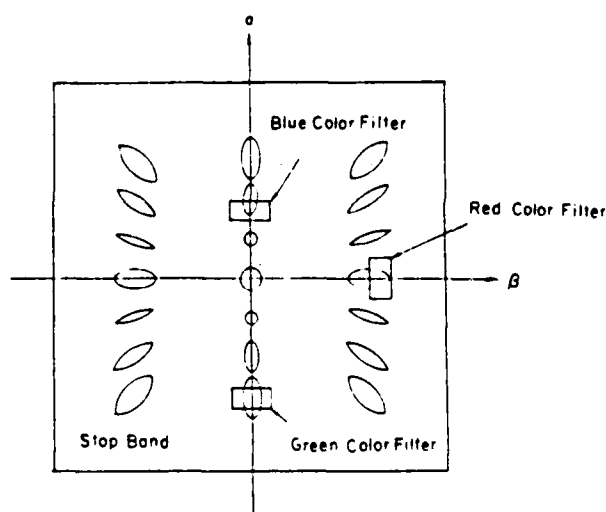


FIG. 3. — Fourier plane color filtering.

where λ_r , λ_b and λ_g are the respective red, blue, and green color wavelengths. At the output image plane, the pseudocolor coded image irradiance is therefore,

$$(9) \quad I(x, y) = T_{1r}^2(x, y) + T_{2b}^2(x, y) + T_{3g}^2(x, y),$$

which is a superposition of three primary color encoded images, where T_{1r} , T_{2b} , and T_{3g} are the red, blue, and green amplitude distributions of the three spatially encoded images. Thus a Moire free color coded image can be obtained at the output plane.

In our experiment, we utilized two sinusoidal sampling gratings, one is 26.7 lines/mm and the other is 40 lines/mm for the spatial encodings. The encoding transparency was made by Kodak technical pan film 2415. The advantage of using Kodak

2415 film is that it is a low contrast film with a relatively flat spectral response. The plot of diffraction efficiency versus log-exposure for Kodak 2415 film at 40 lines/mm sampling frequency is shown in figure 4. From this figure, we see that the bleached encoded films offer a higher diffraction efficiency, the optimum value occurs at exposures 8.50×10^{-3} mcs. With reference to this optimum exposure, it is possible to optimize the encoding process in the following: first, preexposing the film beyond the shoulder region; second, subdividing the remaining exposure into three regions by taking the account of the transient exposures of the three encoded images.

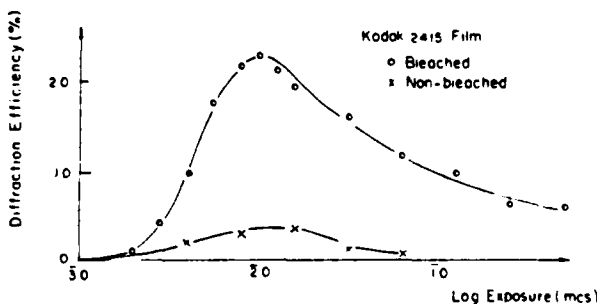


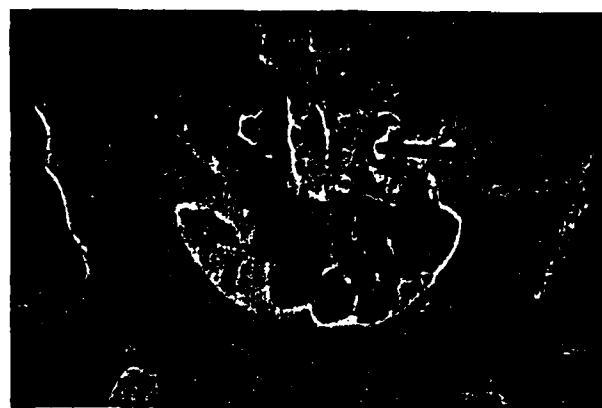
FIG. 4 — Diffraction efficiency versus log exposure plot of a typical spatially encoded film

In pseudocoloring, we utilize the Kodak primary color filters of No. 25, 47B and 58 in the Fourier plane, as shown in figure 3. A xenon-arc lamp is used as extended white-light source for pseudocolor encoded of figure 2.

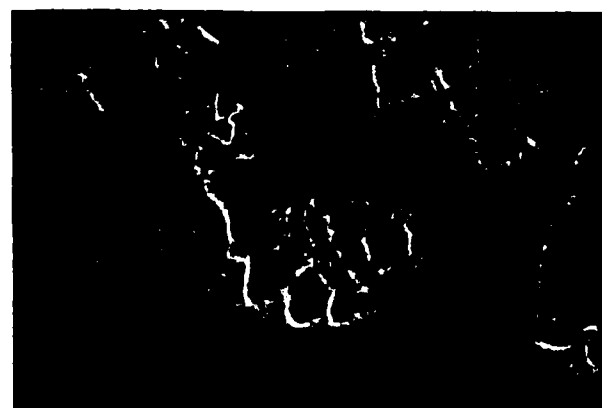
For experimental demonstrations, we would first provide a gray-level x-ray picture of a front view female pelvis, as shown in figure 5(a). Figure 5(b) shows the color encoded image obtained by the white-light pseudocolor encoder. In this color coded



(a)



(b)



(c)

FIG. 5. (a) A gray-level x-ray picture (b) A density pseudocolor coded picture. Positive image is coded in red, negative image is coded in blue, and the product image is coded in green (c) A reversal color coded image of figure 5 (b). Positive image is coded in blue, negative image is coded in red, and the product image is again coded in green

image, the positive image is encoded in red, the negative image is encoded in blue, and the product transmittance of the positive and negative images is encoded in green. From this figure, we see that a broad range of pseudocolor encoded density can be perceived, and the color-coded image appears free from coherent artifact noise and Moiré fringes. The patient of the x-ray picture appears to have suffered from a surgical operation, where the bore and point hardwares can be seen. A section of the bone, between the sacroiliac joint and spinal column, has been removed.

It may also be interesting to note that a reversal of the color encoding can be easily obtained by this white-light pseudocolor encoding technique, as shown in figure 5(c). In this figure, the positive image is encoded in blue, the negative image is encoded in red, and the product transmittance is encoded in green. From this figure, again we see that a broad range density pseudocolor encoded image with different color textures can be obtained. For example the air pockets in the colon of the patient in figure 5(c) is much easier to be identified. In concluding this paper, we note that a wide variety of pseudocolor encoded images can easily be obtained by simply alternating the color filters in the Fourier plane of the white-light processor. The proposed white-light pseudocolor encoder is economical and easy to operate, which may offer many practical applications. There is, however, one disadvantage of this technique, it requires a spatial encoding process. Therefore, it is not a real-time pseudocolor encoding method.

We acknowledge the support of the U.S. Air Force Office of Scientific Research Grant AFOSR-81-0148.

REFERENCES

- [1] ANDREWS (H. C.), TESCHER (A. B.) and KRUGER (R. P.). — *IEEE Spectrum*, 9, 20 (1972).
- [2] YU (F. T. S.) — *Optical Information Processing*, Wiley-Interscience Publishing Co., New York, 1982.
- [3] LIU (H. K.) and GOODMAN (J. W.). — *Nouv. Rev. Opt.*, 7, 285 (1976).
- [4] TAI (A.), YU (F. T. S.) and CHEN (H.). — *Opt. Lett.*, 3, 190 (1978).
- [5] SANTAMARIA (J.), GIL (M.) and BISCOX (J.). — *J. Opt.*, 10, 15 (1979).
- [6] CHAO (T. H.), ZHUANG (S. L.) and YU (F. T. S.). — *Opt. Lett.*, 5, 230 (1980).
- [7] UPATNIEKS (J.) and LEONARD (C.). — *Appl. Opt.*, 8, 85 (1969).
- [8] CHIANG (B. J.) and WISICK (K.). — *SPIE*, 215, 172 (1980).
- [9] SMITH (H. M.). — «Basic Holographic Principles», Ed. : H. M. Smith, Holographic Recording Materials, Springer-Verlag, New York, 1977.

Manuscript received in October 10, 1983.

SECTION XIII

Partial Coherence Measurement

Coherence measurement of a grating-based white-light optical signal processor

F. T. S. Yu, F. K. Hsu, and T. H. Chao

A two-beam interference technique for coherence measurement in the Fourier plane of a grating-based white-light optical signal processor is presented. The visibility measurement is obtained with a scanning photometer at the output plane of the processor. The degree of coherence as a function of slit separation, due to source size, input object size, and the spatial frequency of the sampling grating, is plotted. The results show that the degree of coherence increases as the spatial frequency of the sampling grating increases. However, this improvement of coherence is somewhat more effective in the direction perpendicular to the light dispersion. Thus, this white-light signal processing technique is more effective in one dimension. Since this white-light processor is capable of processing the signal with the entire spectral band of the light source, it is very suitable for color image processing.

I. Introduction

In the 1930s, work by Van Cittert¹ and later by Zernike² drew attention to the study of partial coherence. They have shown that the spatial coherence and the intensity distribution of the light source form a Fourier transform relationship. More recently, the work of Thompson³⁻⁵ has demonstrated a two-beam interference technique to measure the degree of partial coherence. He has shown that, under quasi-monochromatic illumination, the degree of spatial coherence is dependent on the source size and the distance between two arbitrary points. The degree of temporal coherence is however dependent on the spectral bandwidth of the light source. He has also illustrated several coherence measurements that are consistent with the Van Cittert mode in the Fourier predictions.

We recently proposed a grating-based white-light optical signal processor.⁶⁻⁸ We have shown that the white-light processor is capable of processing the information in complex amplitude like a coherent processor, and at the same time it suppresses the coherent artifact noise like an incoherent processor. In other words, this white-light processor is operating in a par-

tially coherent mode in the Fourier plane as a partially coherent processor instead of an incoherent processor.

In this paper we shall describe a dual-beam technique for coherence measurement in the Fourier plane. We shall show that a high degree of coherence can be obtained in the spatial frequency plane such that the signal can be processed in complex amplitude for the entire spectral band of the white-light source.

II. White-Light Optical Processing Technique

With reference to the schematic diagram of Fig. 1, the white-light optical processor is similar to that of a coherent optical processing system, except for the use of an extended white-light source, source encoding mask, signal sampling grating, and achromatic transform lenses. By the Wolf partial coherence theory,⁹ the output intensity distribution can be obtained by the following integrating equations¹⁰:

$$I(x', y') = \int_{\lambda_l}^{\lambda_h} \iint_{-\infty}^{\infty} \gamma(x_0, y_0) \cdot \left| \iint_{-\infty}^{\infty} S\left(x_0 + \alpha - \frac{\lambda f}{2\pi} p_0 y_0 + \beta\right) H(\alpha, \beta) \times \exp\left[-i \frac{2\pi}{\lambda f} (x' \alpha + y' \beta)\right] \cdot d\alpha d\beta \right|^2 dx_0 dy_0 d\lambda, \quad (1)$$

where $\gamma(x_0, y_0)$ is the intensity distribution of the source encoder at the source plane (x_0, y_0) , $S(\alpha, \beta)$ is the Fourier spectrum of the input signal $s(x, y)$, p_0 is the angular spatial frequency of the grating, f is the focal length of the achromatic transform lenses, $H(\alpha, \beta)$ is the complex spatial filter in the Fourier plane, λ_l, λ_h are the lower

T. H. Chao is with University of Utah, Department of Electrical Engineering, Salt Lake City, Utah 84111; the other authors are with Pennsylvania State University, Electrical Engineering Department, University Park, Pennsylvania 16802.

Received 5 July 1983.

0003-6935/84/020333-08\$02.00/0

© 1984 Optical Society of America.

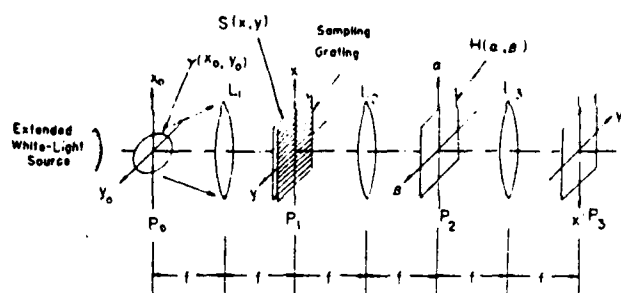


Fig. 1. Grating-based white-light optical signal processor: $\gamma(x_0, y_0)$, source encoding mask; L , achromatic transform lenses.

and upper wavelength limits of the light source, and (α, β) is the spatial coordinate system of the Fourier plane.

In optical signal processing, a set of N narrow discrete spectral band filters $H_n(\alpha_n, \beta_n)$ over the rainbow color of Fourier spectra are used in the Fourier plane. Each of the spectral band filters is limited by a finite spectral bandwidth that can be approximated by the following equation^{7,8}:

$$\Delta\lambda \approx \frac{4\Delta p}{p_0} \lambda_n, p_0 \gg \Delta p. \quad (2)$$

where Δp is the angular spatial frequency limit of the input signal in the x direction, p_0 is the angular spatial frequency of the sampling grating, and λ_n is the center wavelength of the filter $H_n(\alpha_n, \beta_n)$. Since the narrow spectral band filtered signals are mutually incoherent, the output intensity distribution of Eq. (1) can be written as

$$I(x', y') \approx \sum_{n=1}^N I_n(x', y') \approx \sum_{n=1}^N \int_{\lambda_n - \Delta\lambda/2}^{\lambda_n + \Delta\lambda/2} \iint_{-\infty}^{\infty} \gamma(x_0, y_0) \cdot \left| \iint_{-\infty}^{\infty} S\left(x_0 + \alpha - \frac{\lambda'}{2\pi} p_0, y_0 + \beta\right) H_n(\alpha_n, \beta_n) \times \exp\left[-i \frac{2\pi}{\lambda'} (x' \alpha + y' \beta)\right] d\alpha d\beta \right|^2 dx_0 dy_0 d\lambda. \quad (3)$$

With reference to Eq. (1) or (3), we see that the white-light signal processor is indeed capable of processing the signal in complex amplitude for the entire spectral band of the light source, and it is very suitable for color image processing. From these two equations, we also see that the degree of coherence is governed by the source encoding mask $\gamma(x_0, y_0)$, the spatial frequency of the sampling grating p_0 , and the spatial frequency limit of the input signal Δp . In other words, the source encoding function is to improve the degree of spatial coherence at the input plane and the signal sampling grating is to increase the degree of temporal coherence in the Fourier plane, so that the signal processing can be carried out in complex amplitude at each narrow spectral band filter.

It is not hard to see from Fig. 1 that the signal spectrum is dispersed into rainbow color along the α axis in the Fourier plane. The improvement of the degree of coherence is expected to be more effective in the β direction than in the α direction. In devising a coherence measurement scheme for this white-light optical pro-

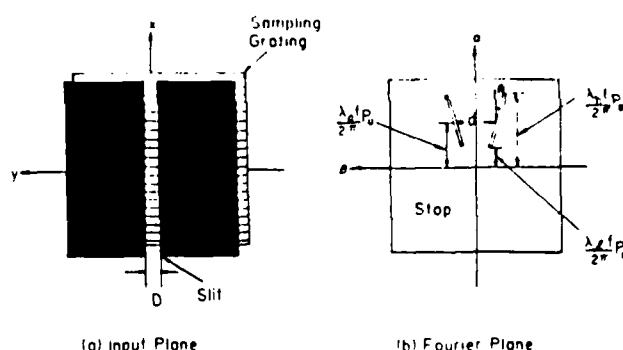


Fig. 2. Visibility measurement along the β directions: D , input slit width; d , mean slit separation; λ_0 , mean wavelength of the light source; p_0 , angular spatial frequency of the sampling grating.

cessor, we propose a dual-beam interference technique for coherence measurement in the Fourier plane. For simplicity, we would however measure the degree of coherence in the β and in the α axes independently.

III. Coherence Measurement Technique

We shall now describe a visibility measurement technique to determine the degree of coherence in the β direction in the Fourier plane. For simplicity, we shall utilize a narrow slit as a 1-D object at the input plane as shown in Fig. 2(a). The complex light distribution in the Fourier plane would be

$$E(\alpha, \beta; \lambda) = C \left[\text{sinc} \left(\frac{\pi D}{\lambda'} \beta \right) \right] * \delta \left(\alpha - \frac{\lambda'}{2\pi} p_0, \beta \right), \quad (4)$$

where C represents an appropriate complex constant, D is the slit width, f is the focal length of the achromatic transform lens, p_0 is the angular spatial frequency of the phase sampling grating, and $*$ denotes the convolution operation.

It is clear that Eq. 4 describes a fan-shaped smeared Fourier spectrum of the input slit, for which the scale of the sinc factor increases as a function of the wavelength λ of the light source and decreases as the size of the object D (i.e., slit width) increases. To increase the efficiency of the coherence measurement along the β direction, we would use a pair of slanted narrow slits at the smeared Fourier spectra, as illustrated in Fig. 2(b). The angle of inclination of this pair of slits should be adjusted with the separation of the slits, such as,

$$\theta = \tan^{-1} \frac{\pi d}{\lambda_0 / p_0}, \quad (5)$$

where d is the mean separation of the slits, λ_0 is the mean wavelength of the light source, and p_0 is the angular spatial frequency of the sampling grating. The filtering function of this pair of slanted slits can be written as

$$H(\alpha, \beta) = \left[\delta \left(\beta - \frac{d\lambda}{2\lambda_0} \right) + \delta \left(\beta + \frac{d\lambda}{2\lambda_0} \right) \right] * \delta \left(\alpha - \frac{\lambda'}{2\pi} p_0, \beta \right). \quad (6)$$

The output intensity distribution can be shown as

$$I(x', y') = K [1 + \cos(2\pi d x')], \quad (7)$$

where K is an appropriate proportionality constant.

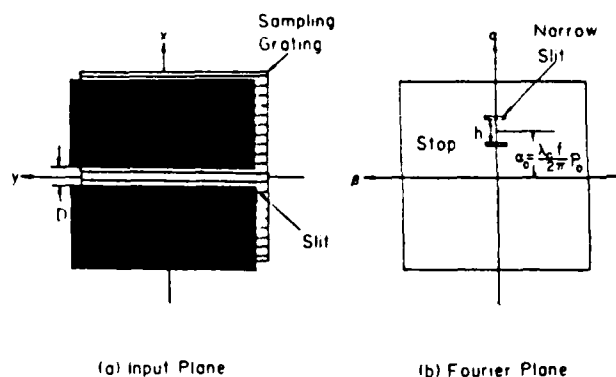


Fig. 3. Visibility measurement along the α direction: D , input slit width; h , slit separation; α_0 , center location of the pair of narrow slits; λ_0 , mean wavelength of the light source; p_0 , angular spatial frequency of the sampling grating.

Equation (7) represents an achromatic fringe pattern due to this entire spectral band of the light source.

Strictly speaking, all practical white-light sources are extended sources. For simplicity of illustration, we assume that an extended square source is used in this white-light optical processor. Thus the output intensity distribution can be written as

$$I(x', y') = \int_{\lambda_1}^{\lambda_2} \iint_{-\infty}^{\infty} \text{rect}\left(\frac{x_0}{a}\right) \cdot \text{rect}\left(\frac{y_0}{a}\right) \cdot \left| \iint_{-\infty}^{\infty} \text{sinc}\left[\frac{\pi D}{\lambda f}(\beta + y_0)\right] \cdot \delta\left(\alpha + x_0 - \frac{\lambda f}{2\pi} p_0, \beta\right) \cdot H(\alpha, \beta) \exp\left[-i \frac{2\pi}{\lambda f}(x'\alpha + y'\beta)\right] d\alpha d\beta \right|^2 dx_0 dy_0 d\lambda, \quad (8)$$

where $H(\alpha, \beta)$ is given by Eq. (6),

$$\text{rect}\left(\frac{x_0}{a}\right) \triangleq \begin{cases} 1, & |x_0| \leq a/2, \\ 0, & |x_0| > a/2, \end{cases}$$

and a is the dimension of the extended light source. From the above equation we see that the visibility (i.e., degree of coherence) is dependent on the source size a , the object size D (i.e., slit width), and the angular spatial frequency p_0 of the sampling grating.

To investigate the degree of coherence variation in the α direction, again we insert a narrow slit aperture as an input object but parallel to the sampling direction of the sampling grating, as shown in Fig. 3(a). The smeared Fourier spectra can be shown as

$$E(\alpha, \beta; \lambda) = \text{sinc}\left(\frac{\pi D}{\lambda f} \alpha\right) \cdot \delta\left(\alpha - \frac{\lambda f}{2\pi} p_0, \beta\right), \quad (9)$$

which describes a narrow smeared rainbow color spectra along the α axis. For the visibility measurement, a pair of narrow slits is inserted at the Fourier plane perpendicular to the α axis and centered at $\alpha = \lambda_0 / p_0 / (2\pi)$, as shown in Fig. 3(b), where λ_0 is the center wavelength of the light source and f is the focal length. The filtering function of this pair of slits can be written as

$$H(\alpha, \beta) = \delta\left(\alpha - \frac{h}{2} - \frac{\lambda_0 f}{2\pi} p_0, \beta\right) + \delta\left(\alpha + \frac{h}{2} - \frac{\lambda_0 f}{2\pi} p_0, \beta\right), \quad (10)$$

where h is the separation between the slits. Again with the assumption of a square light source, the output intensity distribution can be shown as

$$I(x', y') = \int_{\lambda_1}^{\lambda_2} \iint_{-\infty}^{\infty} \text{rect}\left(\frac{x_0}{a}\right) \text{rect}\left(\frac{y_0}{a}\right) \cdot \left| \iint_{-\infty}^{\infty} \text{sinc}\left[\frac{\pi D}{\lambda f}(\alpha + x_0)\right] \cdot \delta\left(\alpha - \frac{\lambda f}{2\pi} p_0, \beta + y_0\right) \cdot H(\alpha, \beta) \exp\left[-i \frac{2\pi}{\lambda f}(x'\alpha + y'\beta)\right] d\alpha d\beta \right|^2 dx_0 dy_0 d\lambda, \quad (11)$$

where $H(\alpha, \beta)$ is defined in Eq. (10). From this equation, again we see that the degree of coherence in the α direction is dependent on the source size a , the object size D , and the angular spatial frequency p_0 of the sampling grating.

IV. Experimental Results

The optical setup for the measurement of the degree of coherence in the Fourier plane of a grating-based white-light optical processor is shown in Fig. 4. This setup utilizes the principle of a dual-beam interference

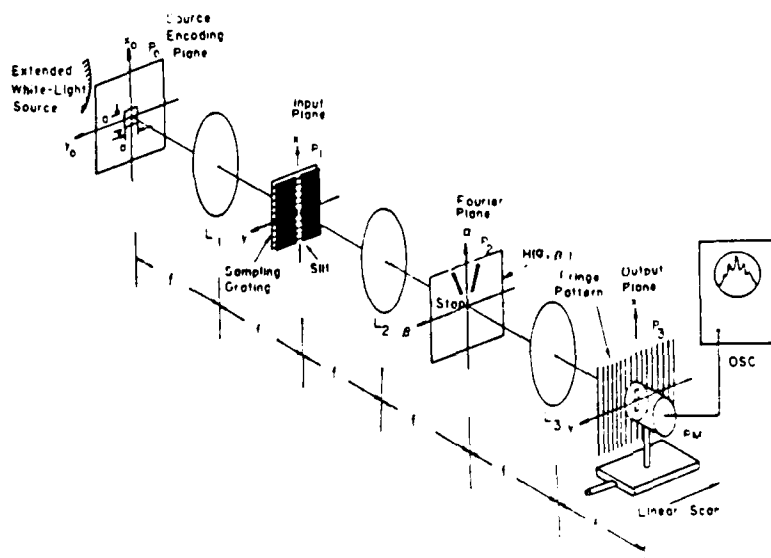


Fig. 4. Optical setup for the coherence measurement along the β direction: a , source size; D , input slit size; L , achromatic transform lenses; $H(\alpha, \beta)$, pair of slant slits; PM , photometer; OSC , oscilloscope.

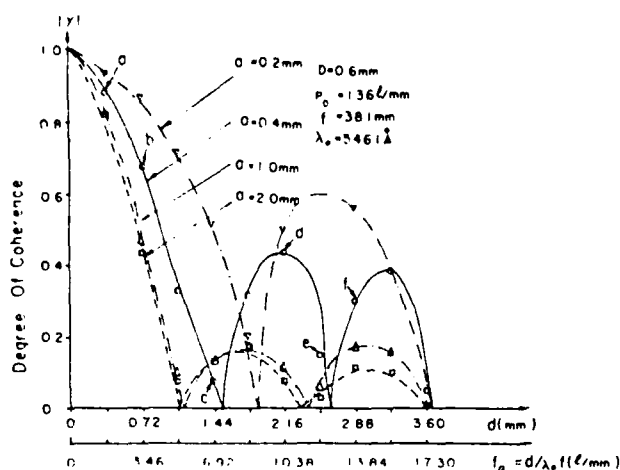


Fig. 5. Plots of degree of coherence along the β direction as a function of mean slit separation d for various values of source size a . $f_d = d/(\lambda_0 f)$, the mean slit separation in spatial frequency.

technique for coherence measurement. The output interference fringe pattern can be traced by a linear scanning photometer and displayed on an oscilloscope for the visibility measurement. In the experiment, the photometer is made by mounting a photomultiplier on the top of a motor-driven linear translator. Since it is a 1-D fringe pattern, a narrow slit can be utilized at the input end of the photomultiplier for the visibility measurement, i.e.,

$$V = \frac{I_{\max} - I_{\min}}{I_{\max} + I_{\min}} \quad (12)$$

where I_{\max} and I_{\min} are the maximum and minimum intensities of the fringes. Needless to say that the visibility of the fringes is in fact a measure of the degree of coherence measurement,^{8,9} i.e., $V = |\gamma|$, where γ is the complex degree of coherence.

In the following we shall illustrate the visibility (i.e., coherence) measurement in the β and α directions in the Fourier plane.

A. Case I: Coherence Measurement in the β Direction

We shall now describe the coherence measurement in the β direction as illustrated in Fig. 4. We shall show that the visibility varies as functions of mean separation d of the pair of slanted slits, source size a , object size D (i.e., slit width), and spatial frequencies of the sampling grating. Figure 5 shows the variation of the degree of coherence as a function of mean separation d for various values of source sizes a . From this figure we see that the degree of coherence decreases as the separation d increases. Further increase in d increases the reappearance of the coherence. Still further increase in d causes the repeated fluctuation of visibility. In this figure, we also see that the degree of coherence increases as the source size a decreases. There is an interesting phenomenon in this coherence measurement. We see that as the source size a decreases further, the reap-

pearance of the visibility is higher. However the overall intensity of the smeared Fourier spectra decreases. This phenomenon is primarily due to the finite object size under a uniform source size illumination. Furthermore, if the source size a is further increased, for example, exceeding 1.0 mm in Fig. 5, the decrease in coherence due to the source size is not apparent. This is primarily due to a comparable broader object size D (e.g., $D = 0.6$ mm) compared to a narrower sinc factor derived from source size a . Nevertheless, if the input slit size further decreases, the changes in degree of coherence for large source sizes can be seen.

We shall now provide a set of output fringe patterns with a set of normalized scanned photometer traces as shown in Fig. 6. The fringe patterns of Figs. 6(a)–(c) were taken at visibilities of 0.88, 0.68, and 0.08 that correspond to the mean separations $d = 0.36$, 0.72, and 1.44 mm at points a , b , and c indicated on the main lobe of the plot $a = 0.4$ mm in Fig. 5. Figures 6(d) and (e) were taken on the second lobe of the visibility reappearance that correspond to points d and e in Fig. 5. The degrees of coherence at these two points are 0.42 and 0.15, respectively. And the corresponding mean slit separations are 2.16 and 2.52 mm. Figure 6(f) was taken on the third lobe visibility at point f . The degree of coherence is 0.3 and the mean slit separation is 2.88 mm.

Let us now investigate the degree of coherence as a function of mean separation d for various input object sizes D (i.e., slit width) as plotted in Fig. 7. Again, we see that the degree of coherence decreases as d increases. Further increase in d also causes side lobes to reappear. In this figure we also see that the degree of coherence increases as object size D decreases. Finally, Fig. 8 shows the visibility measure as a function of mean separation d for two values of sampling grating frequencies. From this figure we see that the degree of coherence is dramatically improved in the Fourier plane by the insertion of the sampling grating.

B. Case II: Coherence Measurement in the α Direction

At this stage we shall now measure the degree of coherence in the α direction in the Fourier plane. The measurement technique is essentially identical to that of Fig. 4, except the input object is replaced by a pair of horizontal slits as shown in Fig. 3. In coherence measurement, we centered the pair of slits at the center of the smeared Fourier spectra corresponding to $\lambda = 5461$ Å.

Figure 9 shows plots of degree of coherence as a function of slit separation h for various values of source sizes a . From this figure we see that the degree of coherence decreases as h increases. Further increase in h again causes the reappearance of the visibility side lobes. However, the degree of coherence is generally not affected by the variation of the source size a . Figure 10 shows a set of the visibility fringe patterns that we have obtained in the output image plane. This set of pictures was taken at points a , b , c , and d as shown in Fig. 9. The corresponding degrees of coherence are

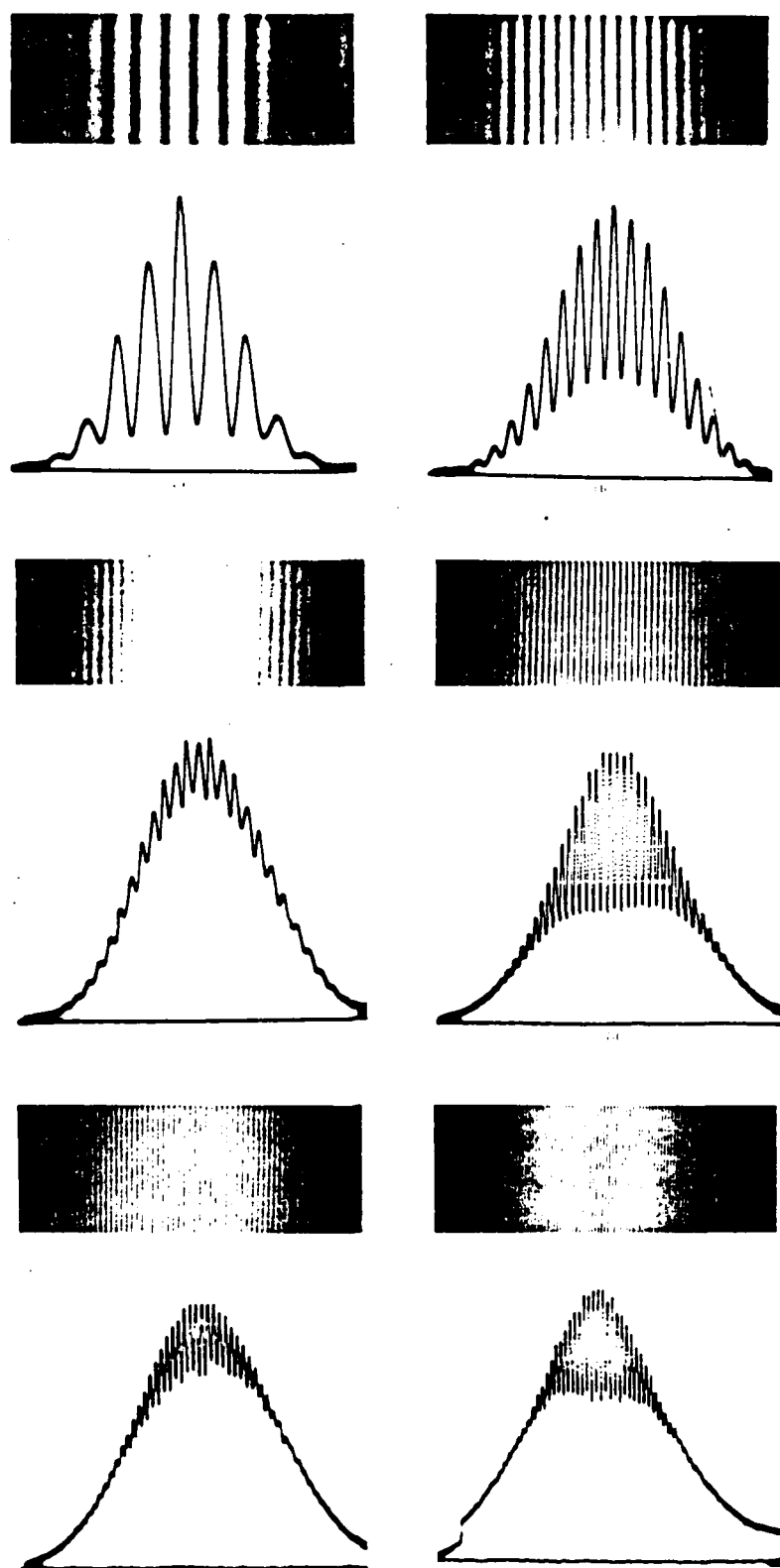


Fig. 6. Samples of fringe visibility patterns at the output plane. The upper portion of (a)-(f) shows the fringe visibility patterns. The lower portion shows the corresponding photometer traces. In these experiments, the fringe visibility and the spatial frequency were varied by changing the mean separation distance d between the two slanted slits. (a)-(c) were obtained at points a , b , and c on the first lobe of Fig. 5. These figures show the decrease in fringe visibility and corresponding increase in spatial frequency as the separation d increases. (d) and (e) were obtained at points d and e on the second lobe of Fig. 5. These two figures also show the increase of spatial frequency as d further increases. (f) was obtained at point f on the third lobe of Fig. 5.

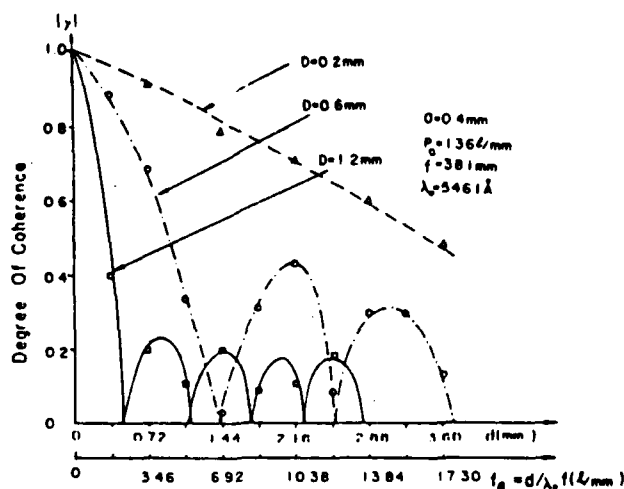


Fig. 7. Plots of degree of coherence along the β direction as a function of mean slit separation d for various values of input slit width D .

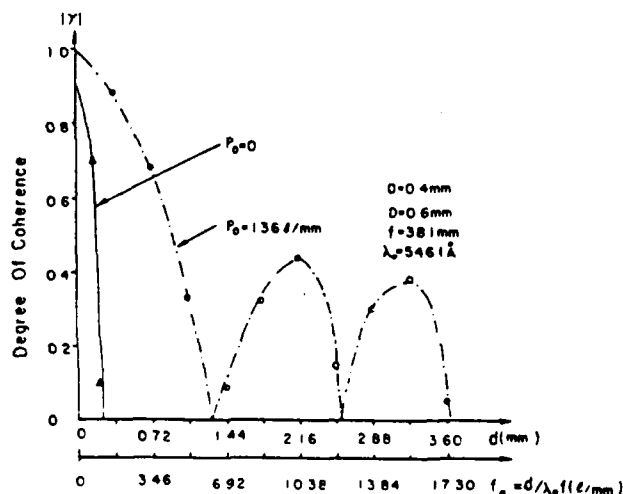


Fig. 8. Plots of degree of coherence along the β direction as a function of mean slit separation d for two values of sampling grating frequency p_0 .

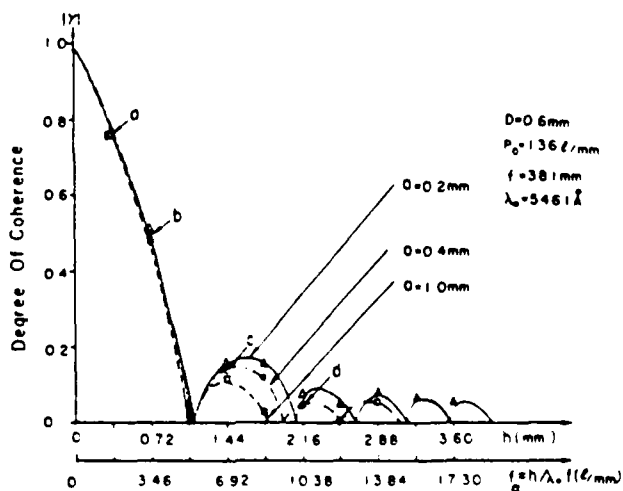


Fig. 9. Plots of degree of coherence along the α direction as a function of slit separation h for various values of source size a . $f_0 = h/(\lambda_0 f)$, the corresponding slit separation in spatial frequency.

0.76, 0.50, 0.14, and 0.05. The respective separations are $h = 0.36, 0.72, 1.44,$ and 2.16 mm.

We shall now plot the degree of coherence as a function of h for various values of object sizes D (i.e., slit widths D) as shown in Fig. 11. From these plots we see that the degree of coherence decreases as the object size D increases. Figure 12 shows the variation of coherence due to spatial frequency of the sampling grating as a function of slit separation h . From this figure we see that higher degree of coherence is achievable with the insertion of a high spatial frequency grating in the input plane.

We shall now briefly discuss the overall effect of coherence in the (α, β) spatial frequency plane. By comparing the visibility measurement of Figs. 5 and 9, we see that the degree of coherence substantially increases in the β direction as the source size decreases. There is, however, no significant improvement in the α direction for smaller source sizes. Although both cases show the increase in coherence for smaller object sizes, however, the increase in coherence is higher in the β direction compared with the α direction, as shown in Figs. 7 and 11. With reference to the plots of Figs. 8 and 12, both cases show significant improvement in the degree of coherence with the insertion of a sampling grating. However the improvement in coherence in the β direction is somewhat higher than in the α direction, due primarily to overlapping of the smeared rainbow Fourier spectra.

To summarize these observations, we stress that the grating-based white-light optical signal processor does improve the degree of coherence in the Fourier plane. Although the higher degree of coherence is obtainable in both spatial frequency directions, the coherence improvement in the β direction is generally higher. Thus, the white-light optical signal processing technique is generally more effective in the β direction than in the α direction. We note that this effect can be seen in a recent paper on linear motion color image deblurring.¹¹

V. Conclusion

We have devised a dual-beam interference technique to measure the degree of coherence in the Fourier plane of a grating-based white-light optical signal processor. The effect of coherence variation due to source size, input object size, and the spatial frequency of the sampling grating is plotted as a function of distance in the β and α directions of the Fourier plane. We have shown that the degree of coherence increases as the spatial frequency of the sampling grating increases. Although the improvement in degree of coherence in the Fourier plane is quite evident, the improvement in the β direction (i.e., the direction perpendicular to the light dispersion) is somewhat more effective than in the α direction. The results indicate that this white-light optical signal processing technique is somewhat more effective in the β direction than in the α direction. Nevertheless the existence of the high degree of coherence in the Fourier plane allows us to process the in-

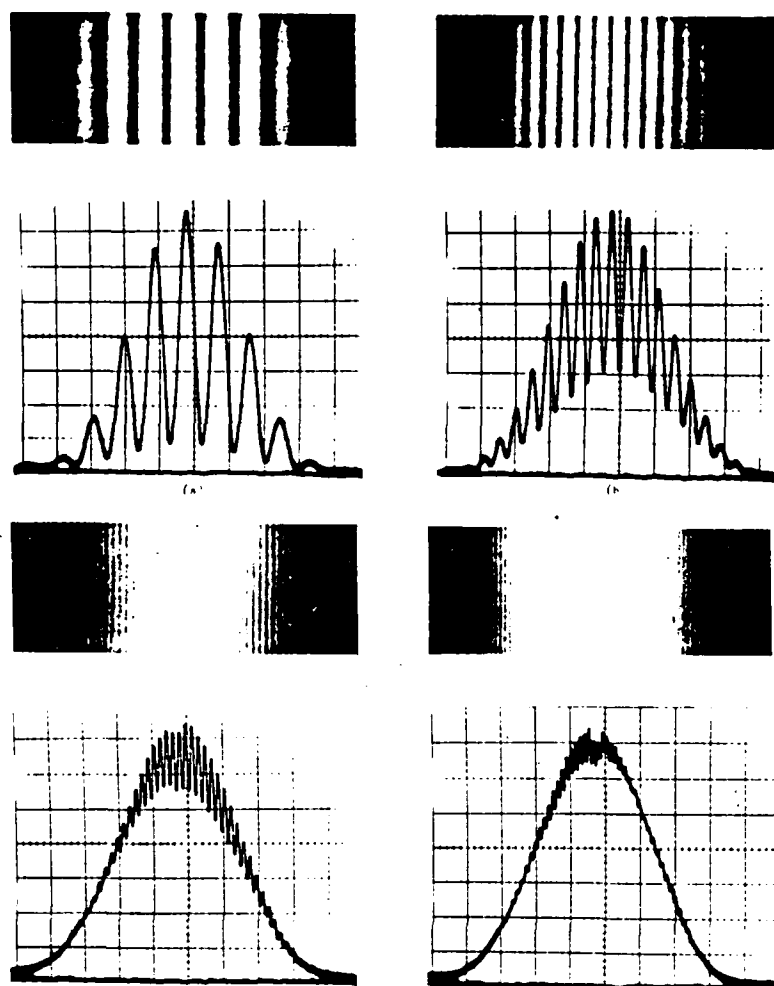


Fig. 10. Samples of fringe visibility patterns. The upper portion of (a)-(d) shows fringe visibility patterns; the lower portion shows the corresponding intensity profiles. (a) and (b) were obtained at points *a* and *b* on the first lobe of Fig. 9. (c) was obtained at point *c* on the second lobe of Fig. 9, and (d) was obtained at point *d* on the third lobe of Fig. 9.

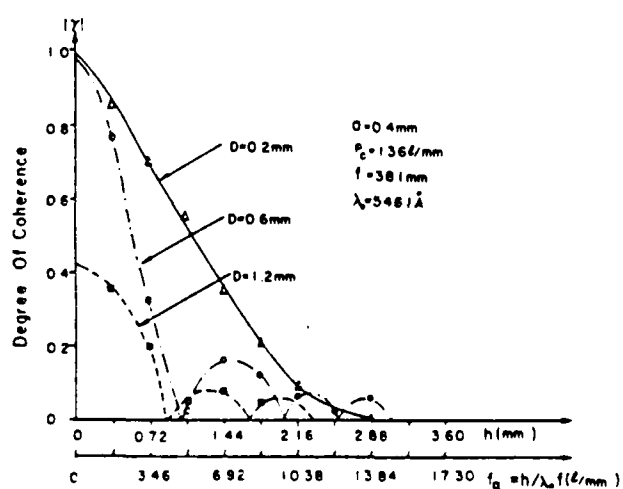


Fig. 11. Plots of degree of coherence along the α direction as a function of slit separation h for various values of object size D .

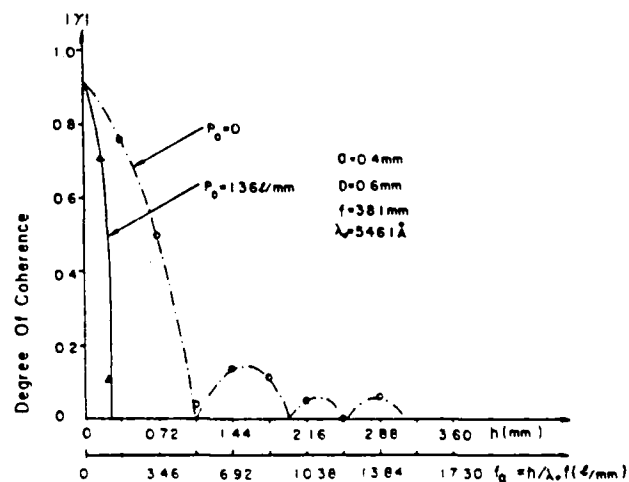


Fig. 12. Plots of degree of coherence along the α direction as a function of slit separation h for two values of sampling grating frequency p_0 .

formation in complex amplitude rather than in intensity. And the white-light processing technique is very suitable for color signal processing.

We acknowledge the support of the U.S. Air Force Office of Scientific Research grant AFOSR-81-0148.

References

1. P. H. Van Cittert, *Physica* 1, 201 (1934).
 2. F. Zernike, *Physica* 5, 785 (1938).
 3. B. J. Thompson, *J. Opt. Soc. Am.* 48, 95 (1958).
 4. B. J. Thompson and E. Wolf, *J. Opt. Soc. Am.* 47, 895 (1957).
 5. B. J. Thompson, *Proc. Soc. Photo-Opt. Instrum. Eng.* 4, 7 (1965).
 6. F. T. S. Yu, *Opt. Commun.* 27, 23 (1978).
 7. F. T. S. Yu, *Proc. Soc. Photo-Opt. Instrum. Eng.* 232, 9 (1980).
 8. F. T. S. Yu, *Optical Information Processing* (Wiley-Interscience, New York, 1983).
 9. M. Born and E. Wolf, *Principles of Optics* (Pergamon, New York, 1980).
 10. S. L. Zhuang, and F. T. S. Yu, *Appl. Opt.* 21, 2587 (1982).
 11. T. H. Chao, S. L. Zhuang, S. Z. Mao, and F. T. S. Yu, *Appl. Opt.* 22, 1439 (1983).
-

SECTION XIV

Restoration of Out-of-Focused Color Image

RESTORATION OF OUT-OF-FOCUSED COLOR PHOTOGRAPHIC IMAGES

X.J. LU and F.T.S. YU

*Electrical Engineering Department, The Pennsylvania State University,
University Park, PA 16802, USA*

Received 14 March 1983

A method of deconvoluting the defocused color photographic images utilizing a white-light processing is described. In the white-light processing, a diffraction grating is used to provide three primary color light sources for the color image restoration. Three complex inverse filters, for each primary color, are used in the Fourier transform plane. Experimental demonstrations of the color image restoration of defocused photographic images are given.

1. Introduction

Restoration of blurred photographic images has long been an interesting application in optical signal processing [1-8]. We have in previous papers [9-12] presented a white-light processing technique for linearly smeared image deblurring. We have shown that the white-light image deblurring technique is capable of suppressing the coherent artifact noise and is suitable for color image deblurring. However the results that we had obtained were primarily restricted to blurred due to linear motion.

In this paper, we shall extend the white-light image restoration technique to two-dimensional image deblurring. We shall utilize a white-light source for the restoration of the out-of-focused color photograph images. The proposed color image restoration technique includes three primary color sensitive inverse filters, as shown in fig. 1. In this figure, a high diffraction efficient grating is used at plane P_{01} to produce three orders of smeared color spectra at the back focal plane P_{02} . Three pinholes (one with a blue filter) are properly placed over this set of spectral lights, to produce three primary color point sources (i.e., spatially small) at plane P_{02} . In the Fourier transform plane P_2 , three color sensitive inverse filters are used for the restoration, and the deblurred color images can be seen at the output plane of the optical processor.

2. Defocused color image restoration

With reference to the optical processor of fig. 1, there are three primary color point sources derived from a white-light source. The intensity distribution of these three primary color point sources can be represented by the following equation

$$I(\alpha, \beta; \lambda) = K_B \text{cir}\{(\alpha^2 + \beta^2)^{1/2}/d_B\} \\ + K_R \text{cir}\{((\alpha + \lambda_R f p_0)^2 + \beta^2)^{1/2}/d_R\} \\ + K_G \text{cir}\{((\alpha - \lambda_G f p_0)^2 + \beta^2)^{1/2}/d_G\}, \quad (1)$$

where $\text{cir}[X] \doteq 1, |X| \leq 1$, and 0 otherwise; (α, β) is the spatial coordinate system of plane P_{02} , p_0 is the spatial frequency of the diffraction grating, $T(x), f$ is the focal length of the achromatic transform lens, K_B, K_R, K_G are the proportional constants, d_B, d_R, d_G are diameters of the pinholes, and $\lambda_B, \lambda_R, \lambda_G$ are the center wavelengths of the blue, red, green spectral bands of the light sources, respectively. For red and green point sources, the center wavelength of each spectral band would be

$$\lambda = \alpha/fp_0, \quad (2)$$

which is determined by the position of the pinhole at α axis. The corresponding spectral bandwidth $\Delta\lambda$ of the point sources can be written as

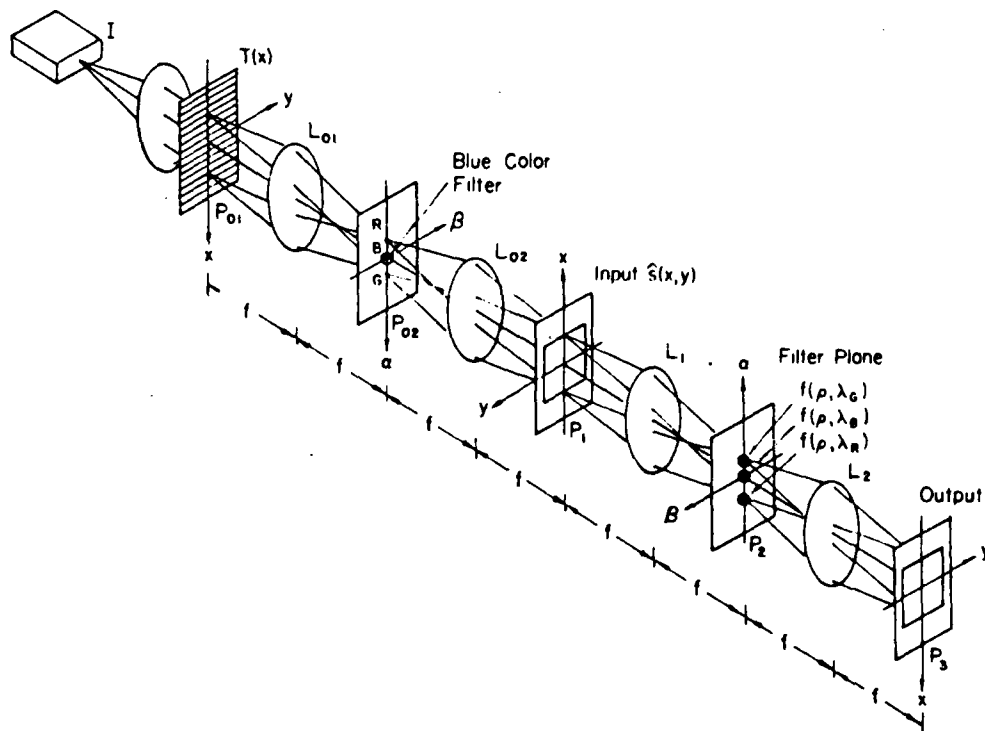


Fig. 1. A white-light optical processor for out-of-focused color image deblurring. I: white-light source, $T(x)$: diffraction grating, R, B, G: red, blue, and green color sources, $S(x,y)$: out-of-focused color image, L: achromatic transform lenses, $f(\rho, \lambda_G)$, $f(\rho, \lambda_B)$, $f(\rho, \lambda_R)$: inverse filters for green, blue, red light.

$$\Delta\lambda = \Delta\alpha/fp_0 = d/fp_0, \quad (3)$$

where d is the diameter of the pinholes.

We note that the complex degree of coherence produced by the color point sources at the input plane P_1 of the processor is [13]

$$\mu_n = \frac{2J_1(\pi d_n r_n)}{\pi d_n r_n} \exp(i2\pi\phi_n x), \quad n = R, G, B, \quad (4)$$

where J_1 is the first-order Bessel function, $r_n = (1/\lambda_n f)(x^2 + y^2)^{1/2}$, and $\phi_n = 0$, $-\lambda_R p_0$, and $\lambda_G p_0$ for the blue, red, and green color point sources, respectively. Since the transform lens L_{02} is achromatic, the spatial coherence length produced by a circular point source would be

$$R = Kf\lambda/d, \quad (5)$$

where K is a proportionality constant, and $K = 1.22$ if the spatial coherence length R is defined as the dis-

tance in which the degree of coherence μ drops from unit to first zero value. If R is defined from a drop of 12% from the unit degree of coherence, then $K = 0.32$. With reference to eqs. (3) and (5), we note that

$$R = K\lambda/\Delta\lambda p_0. \quad (6)$$

Thus to maintain the same spatial coherence length and the same spectral bandwidth, different spatial frequency p_0 of the grating should be used. However, with the use of multi-grating frequency, it would reduce to available power of the light source for the processing. Nevertheless this problem can be alleviated by using a single diffraction grating at P_{01} and different sizes of pinholes at P_{02} plane. In this manner the same spatial coherence length can be obtained by simply varying the size of the pinholes of the primary color sources. As a numerical example, we tabulate the requirement of the size of the pinholes, spatial coherence lengths, and the spectral bandwidths of the

Table 1
Relationship of size, spectral bandwidth and spatial coherence length of three color sources.

λ (Å)	d (μm)	$\Delta\lambda$ (Å)	K	R (mm)
6300 red	400	290	0.32	0.18
			1.22	0.67
	200	140	0.32	0.35
			1.22	1.35
5500 green	400	290	0.32	0.15
			1.22	0.59
	170	120	0.32	0.36
			1.22	1.38
4300 blue	400	500	0.32	0.12
			1.22	0.46
	140	500	0.32	0.34
			1.22	1.31

Note: $\Delta\lambda = 500$ Å for blue wavelength $\lambda = 4300$ Å is limited by Kodak 47B filter.

sources, in table 1. If the pinholes for red and green sources are of the same diameter, e.g., $d_R = d_G = 400$ μm, the spectral bandwidths would be $\Delta\lambda = 290$ Å. On the other hand, if the three pinhole diameters are different, e.g., $d_R = 200$ μm, $d_G = 170$ μm, and $d_B = 140$ μm, coherence lengths obtained would be similar, i.e., 1.35 mm (red), 1.38 mm (green), and 1.31 mm (blue).

In filter synthesis, we note that the inverse filter function for the restoration of out-of-focus image, for each primary color wavelength, should be

$$f(\rho, \lambda) = \begin{cases} \frac{\pi a \rho}{2J_1(\pi a \rho)} \frac{1}{m}, & |f(\rho, \lambda)| \leq 1, \\ \pm 1, & \text{otherwise,} \end{cases} \quad (7)$$

where a is the diameter of the defocused point spread function, $\rho = (1/\lambda\sqrt{\alpha^2 + \beta^2})^{1/2}$, and m is a constant of the order of 10 to 10^2 . The meaning of m is that the finite filter in dynamic range can be made in physical sense because $J_1(\pi a \rho)$ has an infinite number of zeros [1]. Needless to say that eq. (7) can also be written as

$$f(\rho, \lambda) = |f(\rho, \lambda)| e^{i\theta}.$$

Thus an inverse filter can be synthesized by the combination of an amplitude and a phase filter. The amplitude filter can be synthesized by recording an am-

plitude spectrum of a circular aperture of a given diameter using a He-Ne laser. Since the scale of the spectrum is proportional to the wavelength, the diameter of the circular aperture should be properly fitted with the color wavelength. In other words, the diameter for the red amplitude filter should be smaller than the green amplitude filter, and the diameter for the green filter should be smaller than the blue. For example, if the diameter of the circular aperture for red light is taken equal to 0.5 mm, then the diameter of the aperture for the green should be 0.58 mm, and the diameter for the blue light should be 0.74 mm. In amplitude filter synthesis, it is necessary to control the gamma of the recording plate equal to 1 to obtain the required amplitude transmittance.

In phase filter synthesis, we see that, the filter is primarily composed of a set of π -phase circular concentric rings, as shown in fig. 2. The diameters of the rings are determined by the primary color wavelength and the size of the defocused point spread function. A simple technique of producing the phase filter is a bleaching method [14]. A black-and-white ring pattern, corresponding to the π -phase zone of the phase filter, is recorded on a high-contrast film. The recorded binary ring pattern is used as a mask to reproduce a number of gray-level rings on a low-contrast photographic plate. If the recorded plate is bleached, a set of deblurring phase filters can be obtained. To search for a π -phase filter for a given wavelength, one can

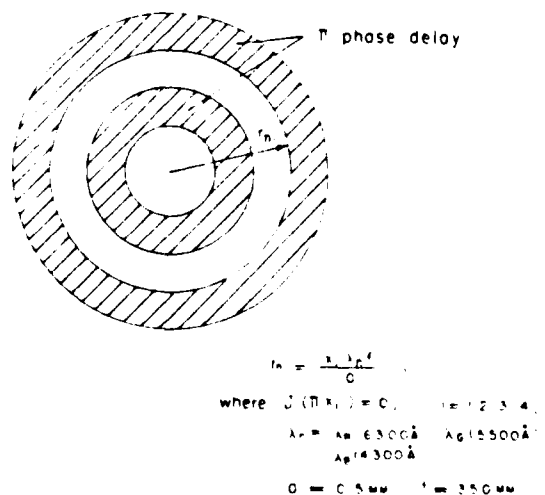


Fig. 2. A π -phase concentric rings for a deblurring phase filter

utilize the contrast-reverse method or by observing the intensity ratio of the main peak and the second peak of a processed point spread function.

In this manner, a set of deblurring filters suitable for the three primary color wavelengths can be obtained. The primary color inverse filter functions can be described as

$$f(\rho_n, \lambda) = \frac{\pi a \rho_n}{2J_1(\pi a \rho_n)} \frac{1}{m}, \quad n = R, G, B, \quad (8)$$

where

$$\rho_n = (1/\lambda_R f)((\alpha + \lambda_R f p_0)^2 + \beta^2)^{1/2}, \quad \text{for } \lambda_R,$$

$$(1/\lambda_G f)((\alpha - \lambda_G f p_0)^2 + \beta^2)^{1/2}, \quad \text{for } \lambda_G,$$

$$(1/\lambda_B f)(\alpha^2 + \beta^2)^{1/2}, \quad \text{for } \lambda_B.$$

The three inverse filters are placed in the Fourier plane P_2 of the processor, their positions should be adjusted properly, such that $\alpha = -\lambda_R f p_0, \beta = 0$ for red sensitive inverse filter, $\alpha = \lambda_G f p_0, \beta = 0$ for green, and $\alpha = 0, \beta = 0$ for blue.

3. Experimental results

In our experiment, a 75 W xenon arc lamp with a 500 μm pinhole is used as the white-light source I. A phase grating of 40 ℓ/mm is placed at plane P_{01} ,

and three pinholes of 200 μm , 170 μm , and 150 μm , for the red, green, and blue spectral bands are used at plane P_{02} . The center wavelength for the red spectral band is 6300 \AA , 5500 \AA for the green, and 4300 \AA for the blue. Since we utilize the zero-order spectra for the blue color source, a Kodak 47B blue color filter is used to cover the pinhole. The spectral bandwidths of these primary color sources are: 140 \AA for the red, 120 \AA for the green, and 500 \AA for the blue. Needless to say that the intensities of these three primary color sources can be adjusted by a set of neutral density filters for color balance.

For the first experimental demonstration, we used a circular aperture of about 0.5 mm in diameter as a defocused point spread function, as shown in fig. 3a. Fig. 3b shows the restored image of fig. 3a obtained with this polychromatic restoration technique. From this figure, we see that, the deblurred point spread function mainly consists of a high intensity center peak, as the deblurred image, and a weak circular ring image, which is primarily due to the finite extent of the deblurring filters. In our experiment the deblurring filters are limited to about four lobes, and the greatest density of the amplitude filter is about 2 to 2.5 D.

From the result of fig. 3b, we also see that there is a slight color dispersion at two edges of the center restored peak image. We note that, the dispersion is

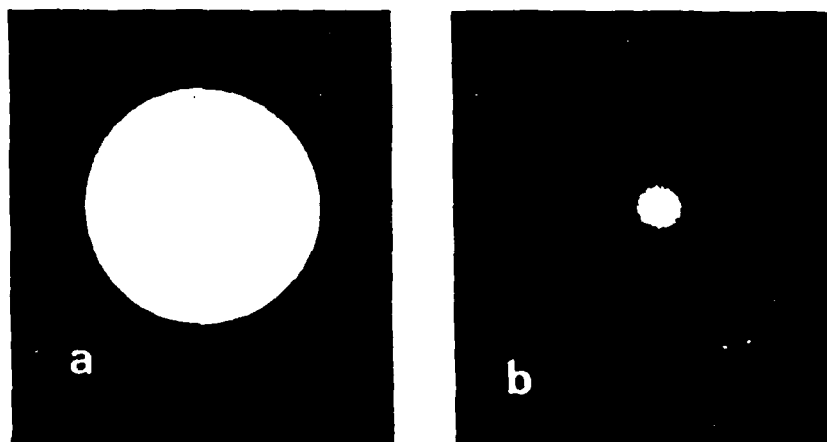


Fig. 3. Restoration of a defocused point spread function. a) A transparent circular disk as a defocused point spread function. b) A black-and-white picture of the deblurred point spread-function.

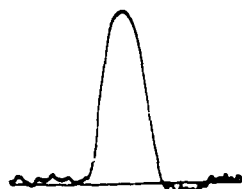


Fig. 4. A electronic scanned image of fig. 3b.

primarily due to the chromatic aberration of the transform lenses, which can be eliminated by using higher quality achromatic transform lenses. Fig. 4 shows an electronic scanned image of the result of fig. 3b. From this figure, we see that the intensity of the center peak is much higher than that of the first-order ring.

We now provide a second experimental demonstration for three overlapping primary color disks, as shown in fig. 5a. The size of these primary color disks

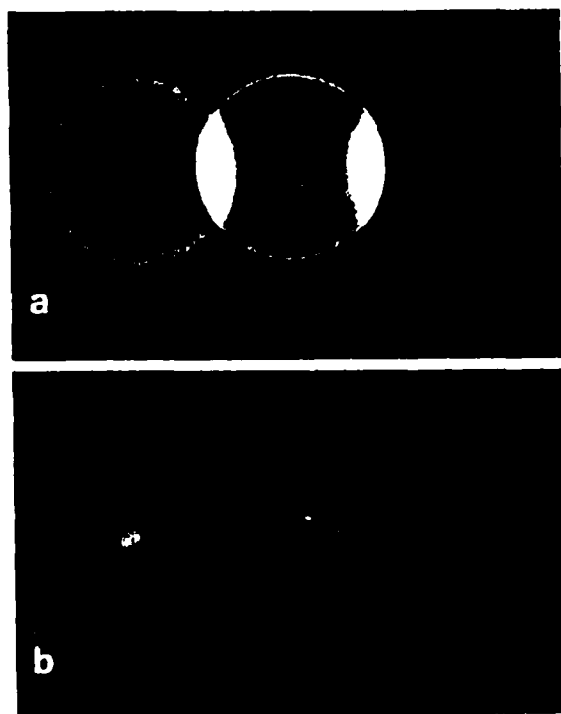


Fig. 5. Restoration of three defocused color point spread functions. a) A black-and-white photograph of three overlapping primary color disks as the color defocused point spread functions. b) A black-and-white photograph of the corresponding deblurred point spread functions.

are about 0.5 mm in diameter. If the color transparency of fig. 5a is inserted at the input plane of the proposed deblurring processor of fig. 1, the restored color point images can be obtained, as shown in fig. 5b. From this figure we see that the color of the restored images are very faithful. However there is a slight replacement of the deblurred color point image, which is primarily due to the chromatic aberration of the transform lenses.

As a final experimental result, fig. 6a shows two blurred color words (i.e., "Color Image") as an input blurred image. The corresponding deblurred color image obtained with this deblurring technique is shown in fig. 6b. From this deblurred color image, again we see that the color reproduction is rather faithful and the quality of the deblurred image is quite impressive. Since the color image deblurring is obtained with three

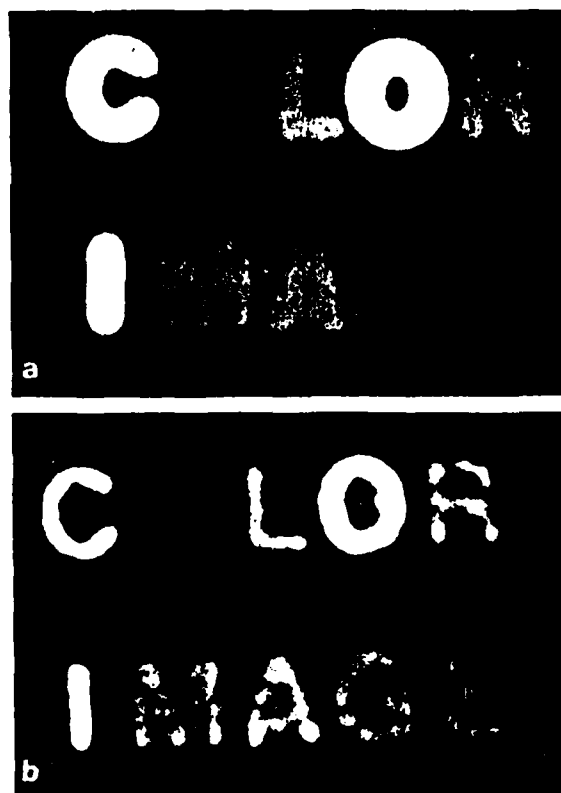


Fig. 6. Color image restoration of defocused color words "Color Image". a) A black-and-white photograph of the defocused color words. b) A black-and-white photograph of the corresponding deblurred color image.

relatively temporally broad and spatially large primary color light sources, the finger print like structure coherent artifact noise is eliminated, as can be seen from figs. 3b, 5b, and 6b.

4. Summary

We have shown that the color image restoration for out-of-focused photographic images can be obtained by a white-light processing technique. This technique uses a diffraction grating to generate three diffraction orders, so that three relatively spectrally broad and spatially large primary color sources can be derived from these diffractions. Since the temporal and spatial coherence requirements for the image deblurring are determined by the spectral bandwidth and the spatial size of the primary color sources, the three primary color partially coherent sources can be obtained by this proposed technique. The advantage of the technique is that one can adjust the degree of the temporal and spatial coherence of each primary color source by simply changing its diameter. By utilizing these primary color sources, an out-of-focused blurred color photographic image can be restored by a set of color sensitive inverse filters. And good deblurred color images have been obtained with pinhole sizes as large as $400\ \mu\text{m}$. To alleviate the low diffraction efficiency of the holographic inverse filters, the filter synthesis are obtained by the combination of non-absorptive phase filters and absorptive amplitude filters. The phase filters are obtained with a bleaching technique, while the amplitude filters are obtained by intensity exposure.

In view of the experimental results, we see that the resolved color images offer a reasonably good deblurred image quality and the colors are faithfully reproduced. Since the primary color light sources are spectrally and spatially broad, the coherent artifact noise is substantially suppressed. Although there is some degree of chromatic aberration, it can be alleviated by utilizing higher quality achromatic transform lenses.

We acknowledge the support of the U.S. Air Force Office of Scientific Research Grant AFOSR-81-0148.

References

- [1] J. Tsujiuchi, Correction of optical image by compensation of aberration and spatial frequency filtering, in: *Progress in Optics*, Vol. II, ed. E. Wolf (North-Holland Publishing Company, Amsterdam, 1963) p. 133.
- [2] G.W. Stroke and R.G. Zech, *Phys. Lett. A25* (1967) 89.
- [3] J. Tsujiuchi, T. Honda and T. Fukaya, *Optics Comm.* 1 (1970) 379.
- [4] J.L. Horner, *J. Opt. Soc. Am.* 59 (1969) 553.
- [5] J.L. Horner, *Appl. Optics* 9 (1970) 167.
- [6] X.J. Lu, *Optics and Fine Mechanics* 10 (1977) 302, (chinese journal).
- [7] R.M. Vasu and G.L. Rogers, *Appl. Optics* 19 (1980) 469.
- [8] G.G. Yang and E.N. Leith, *Optics Comm.* 36 (1981) 101.
- [9] F.T.S. Yu, *Appl. Optics* 17 (1978) 3571.
- [10] S.L. Zhuang, T.H. Chao and F.T.S. Yu, *Optics Lett.* 6 (1981) 102.
- [11] F.T.S. Yu, S.L. Zhuang and T.H. Chao, *J. Optics (Paris)* 13 (1982) 57.
- [12] T.H. Chao, S.L. Zhuang, S.Z. Mao and F.T.S. Yu, *Appl. Optics*, to be published.
- [13] M. Born and E. Wolf, *Principles of optics*, 2nd rev. ed. (Pergamon Press, New York, 1964) chapter 10.
- [14] S.L. Zhuang and F.T.S. Yu, *Appl. Optics* 21 (1982) 2587.

SECTION XV

Solar-Light Optical Processing

SOLAR OPTICAL PROCESSING

F.T.S. YU and X.X. CHEN

*Electrical Engineering Department, The Pennsylvania State University,
University Park, PA 16802, USA*

Received 27 March 1984

We will show that a white-light processor can be easily implemented with natural solar light for optical signal processing. The basic advantage of the solar optical processing is that the processing system does not require to carry an artificial light source, which is very suitable for spaceborne optical processing application. In addition to the simplicity, versatility, polychromaticity, and noise immunity of the white-light processing system, the solar processor is very durable and the operation is very cost effective. Several elementary experimental demonstrations obtained with the solar light processing are given.

1. Introduction

Since the discovery of laser in the earlier 60's, the laser has become an indispensable light source for most of the optical signal processings [1-4]. Aside from the disadvantage of inherent artifact noise, the lasers are generally expensive and in some cases the maintenance of a coherent source could be a problem. Recently we have developed a grating based optical signal processing technique, which can be easily carried out with a broad band white-light source [5]. The major advantages of the white-light processing, as in contrast with the coherent counterpart, are the simplicity, versatility, polychromaticity, cost efficiency and artifact noise immunity.

We will, however, in this paper experimentally demonstrate that several elementary optical image processings can be carried out by solar or sun-light illumination. Since the solar light contains all the visible wavelength, the experimental results that we will show would be in colour images.

2. Color image retrieval

Let us briefly describe a color image retrieval utilizing the solar light. Let us assume that a spatially encoded transmittance of a color object transparency be [6]

$$t(x, y) \approx \exp[iM\{T_r(x, y)[1 + \operatorname{sgn}(\cos p_r y)] + T_b(x, y)[1 + \operatorname{sgn}(\cos p_b x)] + T_g(x, y)[1 + \operatorname{sgn}(\cos p_g x)]\}], \quad (1)$$

where M is an arbitrary constant, T_r , T_b , and T_g are the red, blue, and green image irradiances of the color object, p_r , p_b , and p_g are the respective carrier spatial frequencies, (x, y) is the spatial coordinate system of the encoded film, and

$$\operatorname{sgn}(\cos x) \equiv \begin{cases} 1, & \cos x \geq 0, \\ -1, & \cos x \leq 0. \end{cases}$$

If we place the encoded film of eq. (1) at the input plane of a solar optical processor of fig. 1, then the first-order complex wave field at the Fourier plane, for every λ , would be

$$\begin{aligned} S(\alpha, \beta; \lambda) \approx & \dot{T}_r\left(\alpha, \beta \pm \frac{\lambda f}{2\pi} p_r\right) + \dot{T}_b\left(\alpha \pm \frac{\lambda f}{2\pi} p_b, \beta\right) \\ & + \dot{T}_g\left(\alpha \pm \frac{\lambda f}{2\pi} p_g, \beta\right) + \dot{T}_r\left(\alpha, \beta \pm \frac{\lambda f}{2\pi} p_r\right) \cdot \dot{T}_b\left(\alpha \pm \frac{\lambda f}{2\pi} p_b, \beta\right) \\ & + \dot{T}_r\left(\alpha, \beta \pm \frac{\lambda f}{2\pi} p_r\right) \cdot \dot{T}_g\left(\alpha \pm \frac{\lambda f}{2\pi} p_g, \beta\right) \\ & + \dot{T}_b\left(\alpha \pm \frac{\lambda f}{2\pi} p_b, \beta\right) \cdot \dot{T}_g\left(\alpha \pm \frac{\lambda f}{2\pi} p_g, \beta\right), \quad (2) \end{aligned}$$

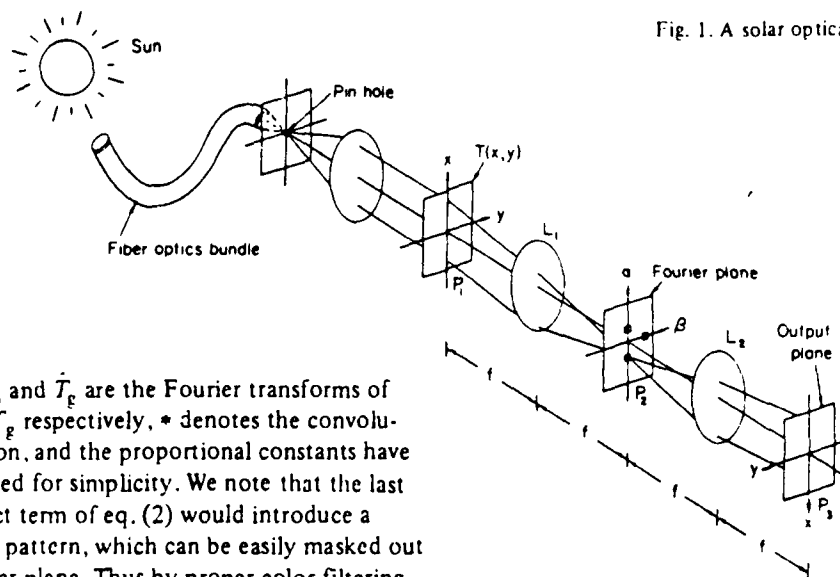


Fig. 1. A solar optical processor.

where \hat{T}_r , \hat{T}_b and \hat{T}_g are the Fourier transforms of T_r , T_b and T_g respectively, $*$ denotes the convolution operation, and the proportional constants have been neglected for simplicity. We note that the last cross product term of eq. (2) would introduce a moiré fringe pattern, which can be easily masked out at the Fourier plane. Thus by proper color filtering the smeared Fourier spectra as illustrated in fig. 1, a true color image can be retrieved at the output image plane p_3 . The corresponding output image irradiance would be

$$I(x, y) = T_r^2(x, y) + T_b^2(x, y) + T_g^2(x, y), \quad (3)$$

which is a superposition of three primary encoded color images. Thus we see that a moiré free color image can be retrieved from a natural solar light.

For experimental demonstration, we show a retrieved color image of fig. 2 obtained from the solar light optical processing. In view of the retrieved color image, we see that the reproduced color image is spectacularly faithful with respect to the original color object and the image contains virtually no coherent artifact noise.

3. Pseudocolor encoding

Most of the optical images obtained in various scientific applications are gray-level density images. For example, scanning electron microscopic images, multispectral band aerial photographic images, X-ray transparencies, infra-red scanning images, etc. However, humans can perceive in color better than gray-level variations. Therefore a color coded image can provide a greater ability in visual discrimination.

Let a three-level (i.e., positive, negative and intermediate level) spatially encoding transparency be

$$t(x, y) \approx \exp[iM\{T_1(x, y)[1 + \text{sgn}(\cos p_1 x)] + T_2(x, y)[1 + \text{sgn}(\cos p_2 x)] + T_3(x, y)[1 + \text{sgn}(\cos p_3 x)]\}], \quad (4)$$

where M is an arbitrary constant, T_1 , T_2 , and T_3 are the positive, the negative, and the negative and positive product image exposures, p_1 , p_2 , and p_3 are the respective carrier spatial frequencies.

Again by the insertion of the encoded transparency of eq. (4) at the input plane p_1 of the solar light processor of fig. 1, and by various color filtering of the smeared Fourier spectra in the Fourier plane, a density color coded image can be obtained at the output plane, such as

$$I(x, y) = T_{1r}^2(x, y) + T_{2b}^2(x, y) + T_{3g}^2(x, y),$$

where T_{1r}^2 , T_{2b}^2 , and T_{3g}^2 are the red, blue, and green color intensity distributions of the three spatially encoded images. Thus we see that a density color coded image can be easily obtained with the solar light.

Fig. 3 shows a density pseudocolor encoded X-ray image of a woman's pelvis, obtained with the solar processor of fig. 1. In this color encoded image, the positive image is encoded in red, the negative image is encoded in blue, while the product image is encoded in green. By comparing the pseudocolor coded image with the original X-ray picture, it appears that the soft tissues can be better differentiated by the color coded image.



Fig. 2. A retrieved color image.



Fig. 3. A density pseudocolor encoded X-ray image.

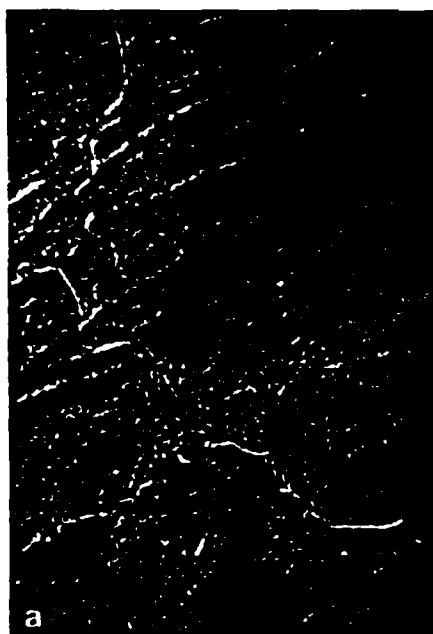


Fig. 4. Samples of false-color Landsat images. (a) Band 4 is encoded in green while band 5 is encoded in red. (b) Band 4 is encoded in green, band 5 is encoded red, and band 7 is encoded blue.

4. As apply to multispectral Landsat images

False-color encoded Landsat images would allow us for the discrimination of various earth surface features. For example, forests agricultural lands, water, urban areas, and strip mines can be shown on the color coded images if each of the thematic image were displayed in a different color. With reference to the spatial encoding method as described previously, a N -spectral band encoded transparency may be described as

$$t(x, y) \approx \exp \left[iM \left(\sum_{n=2k+1}^{N/2} T_n(x, y) [1 + \operatorname{sgn}(\cos p_n y)] \right. \right. \\ \left. \left. + \sum_{n=2k}^{N/2} T_n(x, y) [1 + \operatorname{sgn}(\cos p_n x)] \right) \right], \quad k = 1, 2, \dots, \quad (5)$$

where T_n are the multispectral band image irradiances. We note that the use of the orthogonal samplings (i.e., spatial encoding directions) is to avoid the moiré fringes of the output image. Needless to say that if the encoded film of eq. (5) is inserted at the input plane of the solar optical processor, then false-color encoding can be taken place in Fourier plane. The output false-color coded image irradiances can be shown as

$$I(x, y) = \sum_{n=1}^N T_n^2(x, y; \lambda_n), \quad (6)$$

where T_n^2 represents the irradiance of n th spectral band image and λ_n denotes the corresponding coded color. Thus we see that a false-color coded multispectral image can be easily obtained with the solar light processing.

For simplicity, three bands of multispectral scanner Landsat data were processed for pseudocoloring. These bands were from the blue-green (band 4: 0.5–0.6 μm), red (band 5: 0.6–0.7 μm), and reflected infrared (band 7: 0.8–1.1 μm) spectral regimes. The scene is a 78 X 107 km subsample of Landsat scene showing a section of Susquehanna River Valley in Southeastern Pennsylvania. Fig. 4 shows the results of the false-color coded Landsat data obtained with the solar optical processor of fig. 1. In fig. 4(a) where band 4 is encoded green and band 5 is encoded red, the Susquehanna River and small bodies of water are delineated as deep red. The islands in the Susquehanna River are easily distinguished. Strip mines are dark red, urban areas (Harrisburg) are medium red, and

agricultural lands are light red, orange, and yellow. Forested areas are green. In fig. 4(b), where band 4 is encoded green, band 5 is encoded red, and band 7 is encoded blue, the Susquehanna River appears as violet, and the other bodies of water as shades of blue. The surface mines and urban areas are dark red. The agricultural valleys are orange and the forested regions are green. Thus again we see that false-color coded images can be easily obtained with a solar optical processor.

5. Conclusion

We have demonstrated that a white-light optical processor can also utilize natural solar light for image processing. One of the obvious advantages of the solar light optical processing is that the system does not require to carry its own light source. Thus the proposed solar optical processor is very suitable for spaceborne or satellite optical processing applications. One can image that if an orbiting spaceborne satellite optical processor is required to carry its own light source, for example a powerful laser, then, aside the heavier payload, the question is that how long the light source will last? If one used the natural solar light, we can easily perceive that the optical system would continue to function for a great number of years, possibly beyond the present civilization. Although the development of the solar optical processing is still in the infancy stage however it is not difficult to predict that it would offer many useful applications, particularly to the space communication and signal processing needs.

We wish to acknowledge the support of the US Air Force Office of Scientific Research grant AFOSR-83-0140.

References

- [1] L.J. Cutrona, E.N. Leith, C.J. Paterno and L.J. Porcello, *IRE Trans. Inform. Theory*, IT-6 (1960) 386.
- [2] A. Vander Lugt, *IEEE Trans. Inform. Theory*, IT-10 (1964) 139.
- [3] A. Vander Lugt, *IEEE Proceedings* 62 (1974) 1300.
- [4] F.T.S. Yu, *Optical information processing* (Wiley-Interscience, New York, 1983).
- [5] F.T.S. Yu, *Optics Comm.* 27 (1978) 23.
- [6] F.T.S. Yu, X.X. Chen and S.L. Zhuang, *Appl. Optics*, to be published.
- [7] F.T.S. Yu, X.X. Chen and T.H. Chao, *J. Optics*, to be published.

SECTION XVI

White-Light processing with Magneto-Optic Device

Application of a magneto-optic spatial light modulator to white-light optical processing

Francis T. S. Yu, Xiaojing Lu, and Miaofu Cao

The application of a programmable magneto-optic spatial light modulator to white-light optical signal processing is presented. We have shown that the magneto-optic device responds to the polarized white light, in which a wide range of color object patterns can be generated. Since the magneto-optic device is a transmitted type spatial light modulator, it is very suitable for real-time programmable spatial filter synthesis and object pattern generation for optical signal processing. Experimental demonstrations of some of the elementary spatial filter syntheses and pseudocolor encodings are provided.

I. Introduction

The recent development of magneto-optic spatial light modulator (also called Light-Mod) has stimulated potential applications to the real-time optical signal processing.^{1,2} The Light-Mod consists of a layer of magnetic iron-garnet thin film deposited on a transparent nonmagnetic substrate. The magnetic thin film is, however, formed into a 2-D array of separated magnetically bistable mesas or pixels. As a plane polarized light transmits through the array of the mesas, the polarization of the mesas can be spatially modulated by magnetically switching through the Faraday effect. Since the Light-Mod is a transparent type device unlike the other spatial light modulators,^{3,4} the device is very suitable for the applications to real-time object pattern generation and spatial filter synthesis.

Because of the cross-array formation of the mesas, the device has a 2-D mesh structure for which the array of mesas or pixels can be switched on and off with an x - y matrix addressed of currents. Thus each pixel of the Light-Mod would take one of the only two possible states, which depends on the direction in which the pixel is magnetized. Thus we see that the Light-Mod is essentially a binary type spatial light modulator (SLM) in contrast with the other SLM.

Since the Light-Mod can be electrically switched, an object pattern can be written on the device with a computer; thus the Light-Mod is also a programmable

spatial light modulator, which is particularly attractive to the application to programmable optical processing.

In this paper we will, however, illustrate some applications of this magneto-optics device to a white-light optical signal processor. We will show that the device is capable of generating various elementary spatial filters and object patterns for optical processings. Since the device would be used in a white-light optical processor, we will first demonstrate the effect of the device under the polarized white-light illumination. We will show that the device responds to a wide range of polarized light, and it is suitable for generating color-coded spatial filters and color-coded object patterns.

II. Effect under White-Light Illumination

We shall first illustrate the effect of spectra distribution under white-light illumination. Since the device is essentially an $n \times m$ array of transparent pixels (or mesas), the Fourier spectra of the device would have a similar distribution to that of a 2-D cross grating. If we insert the Light-Mod in the input plane of a white-light processor, we would expect a set of smeared rainbow color Fourier spectra distributed at the spatial frequency plane. Since the current Light-Mod under test would not respond to wavelengths shorter than the green light, their Fourier spectra would, therefore, only smear from red to green. Nevertheless, this range of spectral lines would provide us with a wide variety of colors for the polychromatic processing.

To simplify our discussion on the effect under the white-light illumination, we provide three simple object patterns of the device, as illustrated in the left-hand column of Fig. 1. The center column is a set of equations to represent the Fourier transforms of these object patterns, where $1/l$ is the spatial frequency of the inherent grating structure of the device, a is the pixel size,

The authors are with Pennsylvania State University, Department of Electrical Engineering, University Park, Pennsylvania 16802.

Received 28 April 1984.

0003-6935/84/224100-05\$02.00/0.

© 1984 Optical Society of America.

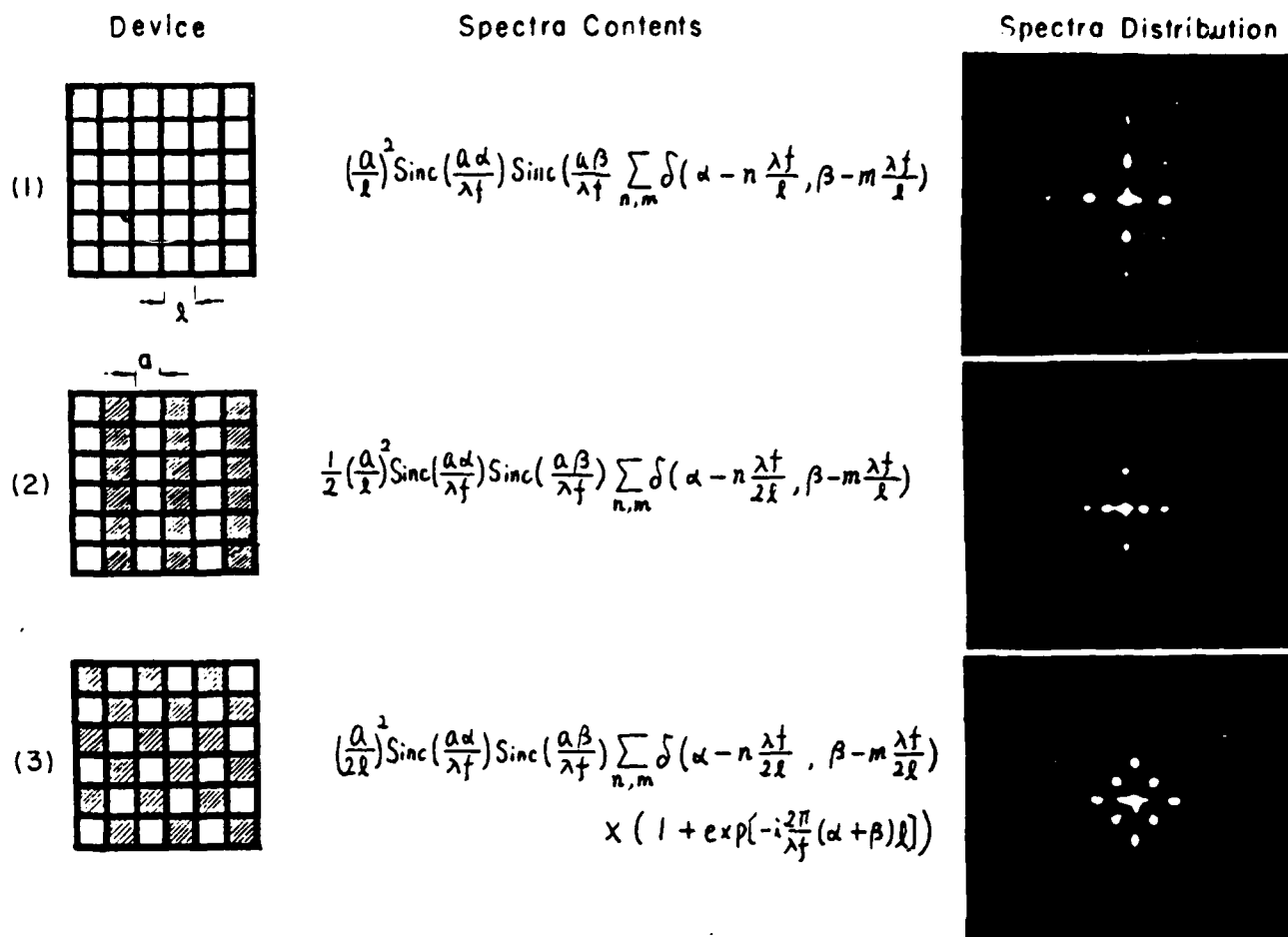


Fig. 1. Elementary patterns of the device and the corresponding smeared Fourier spectra.

λ is the wavelength of illumination, and f is the focal length of the transform lens. The corresponding smeared Fourier spectra distributions are also shown in the right-hand column of the same figure.

Let us now discuss the effect of the device under the polarized white-light illumination. We assume that an object pattern, used either as a spatial filter or as an input object, is generated by the device with a programmable computer. If the device is illuminated by a polarized white-light, one would see the color of the object pattern changes as the direction of the polarization changes. Since the device responds to a broad spectral bandwidth of light from red to green, a wide variety of color object patterns can be generated in which the color characterization of the device is shown in Fig. 2. In this figure the outer region represents the magnetized pixels (i.e., object pattern), and the inner region represents the unmagnetized pixels (i.e., background). For example, if the polarizer is set at $\sim 88^\circ$ angle relative to the vertical axis of the device, the object pattern would be in yellow color, which has the greatest transmittance, while the background would be in black, as can be seen in Fig. 2. If the polarizer is turned slightly counterclockwise, one would see that the object pattern remains in yellow color while the background changes to dark green color (or red color, if the polarizer

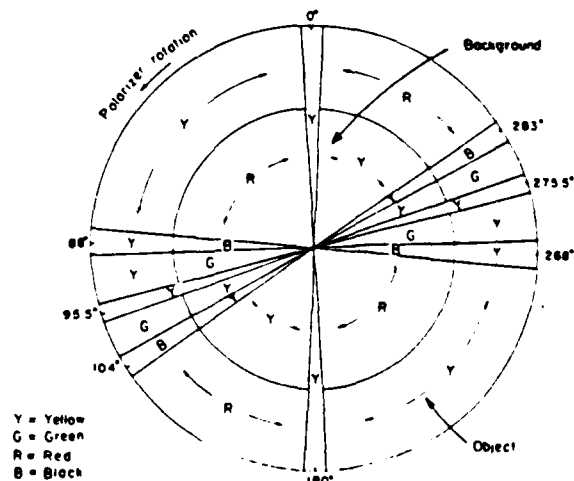


Fig. 2. Color transmittant characteristic of the magnetooptic device under polarized white-light illumination.

is rotated slightly clockwise). If further advancing counterclockwise, the background would become light green while the object pattern still remains in yellow. We further note that, if the polarizer is set at $\sim 104^\circ$, a contrast reverse of the color object pattern appears. If the polarizer is set between 180 and 95.5° , the entire

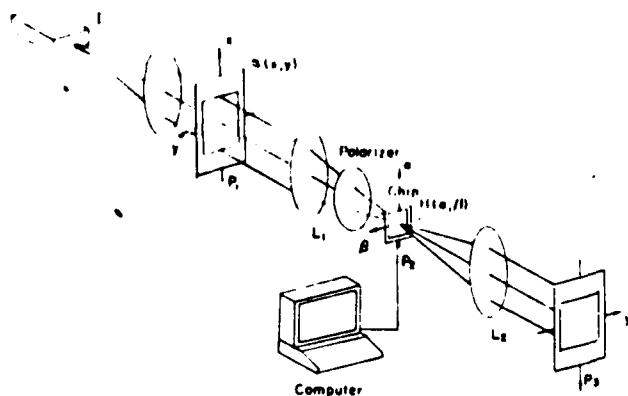


Fig. 3. White-light optical signal processing utilizing a programmable spatial filter: *I*, white-light source; *H*(α, β), spatial filter generated by the device; *L*, transform lens.

device would become yellowish, a contrast reverse color pattern would take place for further turning of the polarizer. Moreover, from Fig. 2 we see that the color characterizations of the device are repeated for every rotation of the polarizer. Thus a wide range of color object patterns can be generated for polychromatic signal processing.

III. Elementary Spatial Filtering

We shall now discuss the utilization of the Light-Mod as a programmable spatial filter for a white-light optical processing as shown in Fig. 3. We note that the device is driven by a computer to generate elementary binary spatial filters (e.g., high-pass and wedge filters).

Since the inherent grating structure of the device produces higher-order diffractions (as shown in Fig. 1), the separation of these higher-order signals is depending on the sampling frequency (i.e., the grating structure) of the device, and the spatial frequency content of the arriving complex wave field. In other words, it depends on the pixel size of the device, the frequency content of the object spectra, and the focal length of the transform lens.

We shall now investigate the effect of the output image irradiance due to the device used as a programmable spatial filter. With reference to Fig. 3, the intensity distribution at the output plane can be written as⁵

$$\begin{aligned} \mathcal{F}^{-1}[S(\alpha, \beta; \lambda)H(\alpha, \beta)] &= s(x, y) * h(x, y; \lambda); \\ &= s(x, y) * \sum_{n, m} \left(\frac{a}{l}\right)^2 \text{sinc}\left(\frac{a}{\lambda f}x\right) \text{sinc}\left(\frac{a}{\lambda f}y\right) \delta\left(x - n\frac{\lambda f}{l}, y - m\frac{\lambda f}{l}\right) \\ &= \left(\frac{a}{l}\right)^2 \sum_{n, m} \text{sinc}\left(n\frac{a}{l}\right) \text{sinc}\left(m\frac{a}{l}\right) s\left(x - n\frac{\lambda f}{l}, y - m\frac{\lambda f}{l}\right), \end{aligned} \quad (1)$$

where \mathcal{F}^{-1} denotes the inverse Fourier transformation, $*$ represents the convolution operation, $S(\alpha, \beta; \lambda)$ is the Fourier spectrum of the input signal $s(x, y)$, $H(\alpha, \beta)$ is the amplitude transmittance of the device used as a spatial filter, $h(x, y; \lambda)$ is the corresponding impulse response, δ is the Dirac delta function, and (x, y) and (α, β) are the spatial coordinate systems. From this equation we see

that the input signal is carried out by an $(n \times m)$ array of smeared delta functions which are located at

$$\left(n\frac{\lambda f}{l}, m\frac{\lambda f}{l}\right)$$

in the output plane P_3 . We also note that the intensity of the multiple array of output signals (or images) is proportional to magnitude square of the sinc factors in Eq. (1), i.e.,

$$I_{n, m}(x, y) \propto \left|\text{sinc}\left(n\frac{a}{l}\right)\right|^2 \left|\text{sinc}\left(m\frac{a}{l}\right)\right|^2. \quad (2)$$

Thus the intensity of the higher-order images decreases rapidly as n and m increase. We would, however, treat the zero order (i.e., $m = n = 0$) as the signal and the rest of the diffracted orders as noise. Thus to improve the output SNR, one would make the ratio a/l (where $a \leq l$) approached to unity. However, to make the size of the pixel approach the size of the mesh cell of the device is equivalent to saying that making the x - y drive lines very thin is very difficult to achieve in practice. Nevertheless, if the mesh cell of device l is made smaller and the focal length of transform lens f is made longer, the separation of the output signal with respect to the unwanted noise (i.e., higher-order diffractions) can be obtained. As a numerical example: given $l = 0.127$ mm for a 48×48 -array Light-Mod and $f = 1000$ mm, the mean separation of the output smeared signals would be $\lambda f/l = 4.3$ mm for $\lambda = 5500$ Å. If $l = 0.02$ mm, the mean separation of smeared signals would be ~ 27.5 mm for the same focal length. Thus the input signal size could be as large as 14 mm.

IV. Experimental Results

In our experiments, we show that a piece of 48×48 -array magneto-optics light-mod is used to generate elementary spatial filter in the Fourier plane of a white-light optical processor as depicted in Fig. 3. The pixel size of the device is ~ 0.127 mm, and the size of the light-mod is $\sim 1/4$ in. square. Needless to say that elementary spatial filters can be generated by the device with a programmable computer. Now if we assume a high-pass filter as shown in Fig. 4(a) is being generated in the Fourier plane, an edge-enhanced image can be obtained at the output plane of the processor. Since the magneto-optic device responds to a broad band of light waves (i.e., from red to green), it is, therefore, a simple matter of utilizing the device to generate a color coded high-pass spatial filter. In example, if the polarizer is set at an angle between 95.5 and 104° of Fig. 2, a high-pass color-coded filter of Fig. 4(a) can be generated (i.e., low-pass region is in dark green, while high-pass region is in yellow). And it is apparent that a color-coded edge-enhanced image can be observed at the output plane.

For experimental demonstration, Fig. 4(b) shows a gray scale black-and-white input object. Figure 4(c) is a black-and-white picture of the corresponding color-coded edge-enhanced image obtained with the programmable spatial filter with white-light processing. In the original color image, the edges of the building are

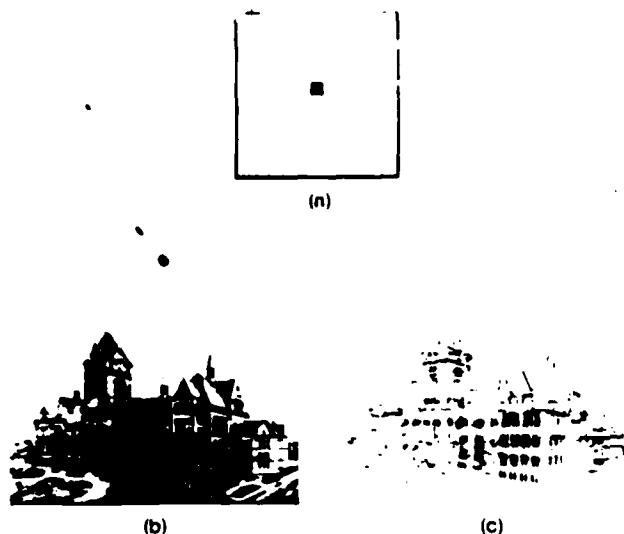


Fig. 4. Edge enhancement: (a) black-and-white picture of a color-coded high-pass filter generated by the device; in reality, the low-pass region is green, and the high-pass region is yellow; (b) input object transparency; (c) black-and-white color-coded edge-enhanced image. In reality, the edges of the building are yellow-white, and the rest of the picture is greenish.

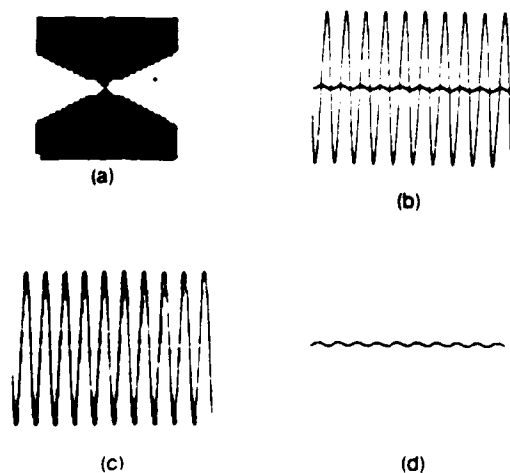


Fig. 5. Directional filtering: (a) black-and-white picture of a wedge filter; (b) input signal; (c) extraction of the larger signal; (d) extraction of the smaller signal.

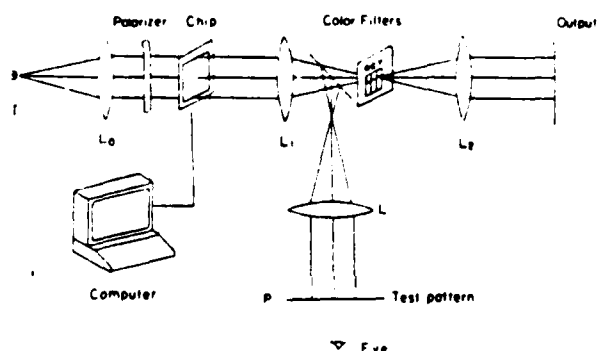


Fig. 6. White-light processor with a programmable input object for pseudocolor encoding: *I*, white-light source; *L*, transform lens.

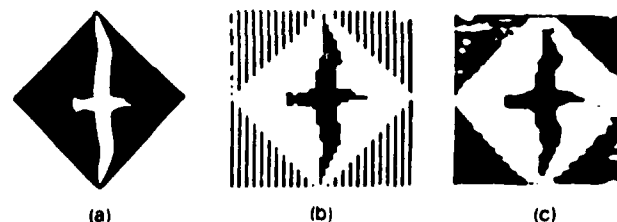


Fig. 7. Pseudocolor encoding: (a) Input object; (b) object pattern generated by the device; (c) a black-and-white color-coded image. In color the bird is yellow, the square region is in green, and the outer region is reddish.

mostly coded in yellow, while the rest of the picture is greenish color. Needless to say that, if the polarizer is set at a different angle, a different shade of color-coded edge-enhanced image can be obtained.

We shall now show a second experimental result obtained with a directional or wedge filter^{6,7} of Fig. 5. Figure 5(a) shows a two-shade radial spectral filter generated by the device. Figure 5(b) shows a black-and-white input object of two sinusoidal waves taken from an oscilloscope. Although these two sinusoidal waveforms are of the same frequency, however, the slopes of these two waveforms are very distinctive. Thus these two sinusoids of different amplitudes can be exclusively extracted with a wedge filter. Figures 5(c) and (d) show a set of the results obtained by the wedge filter of Fig. 5(a), with two sequential settings of the polarizer: Fig. 5(c) is obtained when the vertical region of the wedge filter is coded in black, while the horizontal region is coded in yellow. Figure 5(d) is obtained with a contrast reversed filter of Fig. 5(a).

We shall now demonstrate a theta modulation⁸ pseudocolor encoding technique with this device as shown in Fig. 6. First, a binary black-and-white input object of Fig. 7(a) is placed at the observation plane *P*. Then a pattern of input object can be generated by the Light-Mod with a programmable computer as shown in Fig. 6. The object pattern of the device consists of three distinctive spatially modulated regions as shown in Fig. 7(b). The inner region (i.e., the bird) is modulated with a uniform cross-grating frequency in both directions, while the intermediate region is not modulated, and the outer region is modulated at a lower grating frequency in the horizontal direction. Thus the corresponding smeared object pattern spectra would be spatially separated along the horizontal axis in Fourier plane. In pseudocolor encoding, we allow the zero-order (i.e., the intermediate region) and two first-order (i.e., the bird and the outer region) Fourier spectra to pass through three preselected color filters, (e.g., red, green, and yellow), respectively, at the spatial frequency plane of Fig. 6. Then a pseudocolor-coded image can be obtained at the output plane as shown in a black-and-white picture of Fig. 7(c). Needless to say, different shades of pseudocolor encoded images can also be obtained with different sets of the color filters and different settings of the polarizer orientations. Thus a wide range of pseudocolor images can be obtained with the theta modulation technique.

V. Conclusion

In conclusion, we have incorporated a programmable magneto-optic spatial light modulator with a white-light optical signal processor. We have shown that the device responded to polarized white light, in which it offers the advantage of color-coded spatial filters synthesis and the generation of pseudocolor object image. The device can be used as an input programmable object and also as a programmable spatial filter for real-time optical signal processing. Even though the resolution of this device is rather limited, however, we have shown some the interesting applications with the white-light illumination. Nevertheless, one of the important assets of the device must be the programmability, which, in principle, would offer a wide range of real-time processing capabilities. If the resolution of the device is further improved, the device would have significant impact to the application of modern optical signal processing.

We acknowledge the Litton Data Systems for support of the Light-Mod investigation and the support of U.S. Air Force Office of Scientific Research grant AFOSR-83-0140.

References

1. W. E. Ross, D. Psaltis, and R. H. Anderson, "Two-Dimensional Magneto-Optic Spatial Light Modulator for Signal Processing," *Proc. Soc. Photo-Opt. Instrum. Eng.* 341, 191 (1982).
2. W. E. Ross, D. Psaltis, and R. H. Anderson, "Two-Dimensional Magneto-Optic Spatial Light Modulator for Signal Processing," *Opt. Eng.* 22, 485 (1983).
3. W. P. Bleha *et al.*, "Application of Liquid Crystal Light Valve to Real Time Optical Data Processing," *Opt. Eng.* 17, 371 (1978).
4. C. Warde *et al.*, "Microchannel Spatial Light Modulator," *Opt. Lett.* 3, 196 (1978).
5. F. T. S. Yu, *Optical Information Processing* (Wiley, New York, 1983).
6. F. T. S. Yu, A. Tai, and H. Chen, "Spatial Filtered Pseudocolor Holographic Imaging," *J. Opt.* 9, 269 (1978).
7. X. J. Lu, "Pseudocolor Encoding with a White-Light Processing System," *Opt. Commun.* 48, 13 (1983).
8. J. D. Armitage and A. W. Lohmann, "Theta Modulation in Optics," *Appl. Opt.* 4, 399 (1965).

SECTION XVII

Measurement of Noise Performance

Measurement of noise performance for a white-light optical signal processor

Francis T. S. Yu, Le-Nian Zheng, and Fu-Kuo Hsu

A measurement technique for the noise performance of a white-light optical signal processor is presented. The technique utilizes a scanning photometer to trace out the output noise intensity fluctuation of the optical system. The effect of noise performance due to noise perturbation at the input and Fourier planes is measured. The experimental results, except for amplitude noise at the input plane, show the claims for better noise immunity, if the optical system is operating in the partially coherent regime. We have also measured the noise performance due to perturbation along the optical axis of the system. The experimental results show that the resulting output SNR improves considerably by increasing the bandwidth and source size of the illuminator. The optimum noise immunity occurs for phase noise at the input and output planes. For amplitude noise, the optimum SNR occurs at the Fourier plane. In brief, the experimental results confirm the analytical results that we recently evaluated.

I. Introduction

White-light optical processors are known to perform better in noisy conditions compared with coherent optical processors, because the artifact noise in the coherent optical system is unavoidable. The analysis of noise performance under coherent and partial coherent regimes has been quantitatively studied by Chavel and Lowenthal¹ and Chavel.² They show that noise fluctuations caused by the pupil plane can be drastically reduced under broadband illumination. They have also pointed out that the noise at the object plane due to defects other than the phase deviations cannot be suppressed under partially coherent illumination.

Recently, Leith and Roth³ studied the noise performance of an achromatic coherent optical processor. They demonstrated that such a system shows considerable noise immunity if a broad spectral band source is employed. More recently, we analyzed the performance of a white-light optical processor under noisy environment.^{4,5}

We have shown that except for the case when the amplitude noise is present at the input plane, the resulting output SNR improves considerably by in-

creasing the number of filter channels (or equivalently the spectral bandwidth) and the size of the light source employed.

In this paper, we shall experimentally measure the noise performance of a white-light optical processor. We shall show that the measured results confirm the analytical predictions.^{4,5} Aside from the noise effects at the input and Fourier planes, we have also measured the noise performance due to thin noise effects along the longitudinal direction (i.e., Z axis) of a white-light optical system.

II. Noise Measurement

The white-light optical signal processor to be studied here is described in Fig. 1. The processor is similar to that of a coherent optical processor, except for the use of an extended white-light source, source encoding mask, sampling phase grating, and achromatic Fourier transform lenses. The output light intensity distribution due to the n th narrow spectral band spatial filter in the Fourier plane can be determined by the following integral equation⁴⁻⁶:

$$I(x', y') = \int_{\lambda_{ln}}^{\lambda_{hn}} \iint_{-\infty}^{\infty} \gamma(x_0, y_0) \cdot \left| \iint_{-\infty}^{\infty} S(x_0 + \alpha - \lambda f_{00}, y_0 + \beta) H_n(\alpha, \beta) \cdot \exp \left[-i \frac{2\pi}{\lambda f} (x' \alpha + y' \beta) \right] d\alpha d\beta \right|^2 dx_0 dy_0 d\lambda, \quad (1)$$

where $\gamma(x_0, y_0)$ represents the intensity distribution of the light source at P_0 , λ_{hn} and λ_{ln} are the longest and shortest limiting wavelengths of the n th spectral band filter $H_n(\alpha, \beta)$, $S(x_0 + \alpha - \lambda f_{00}, y_0 + \beta)$ is the smeared

The authors are with Pennsylvania State University, Electrical Engineering Department, University Park, Pennsylvania 16802.

Received 3 July 1984.

0003-6935/85/020173-06\$02.00/0.

© 1985 Optical Society of America.

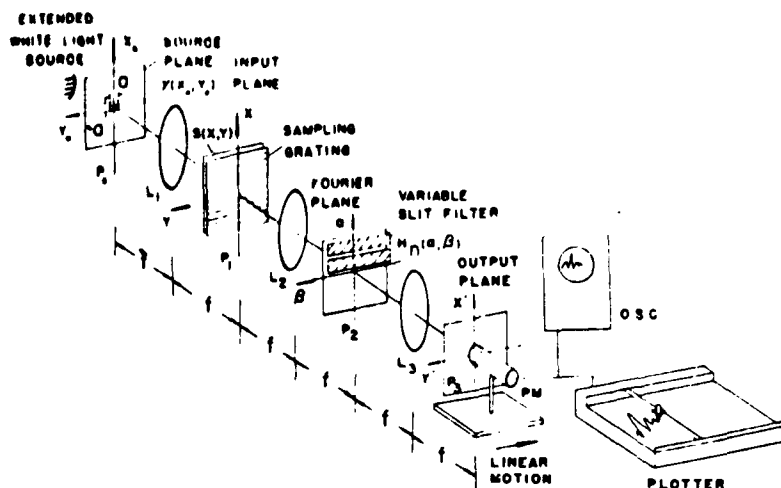


Fig. 1. Grating-based white-light optical processor: $\gamma(x_0, y_0)$, source intensity distributions; P_0 , source plane; P_1 , input plane; P_2 , Fourier plane; P_3 , output plane; $s(x, y)$, object transparency; $H_n(\alpha, \beta)$, slit filter; PM , photometer; OSC , oscilloscope; L , achromatic transform lenses.

Fourier spectra of the input object $s(x, y)$, $H_n(\alpha, \beta)$ is the n th spectral band spatial filter corresponding to the n th channel in the system, f is the focal length of the achromatic Fourier transform lens, and ν_0 is the spatial frequency of the sampling phase grating, which can be written as

$$T(x) = \exp(i2\pi\nu_0 x). \quad (2)$$

We shall first investigate the noise performance of the proposed white-light processor under the spatially coherent illumination, i.e., the effects due to source size. For convenience, we assume that the source irradiance is uniform over a square aperture at source plane P_0 , which can be written as

$$\gamma(x_0, y_0) = \text{rect}\left(\frac{x_0}{a}\right) \text{rect}\left(\frac{y_0}{a}\right), \quad (3)$$

where

$$\text{rect}\left(\frac{x_0}{a}\right) \triangleq \begin{cases} 1, & |x_0| \leq \frac{a}{2} \\ 0, & |x_0| > \frac{a}{2} \end{cases}.$$

For simplicity, we assume that the input signal is a 1-D object independent of the y axis. The Fourier spectrum would also be 1-D in the β axis but smeared into rainbow colors along the α direction. Let the width of the n th narrow spectral band filter be $\Delta\alpha_n$. If the filter is placed in the smeared Fourier spectra, the spectral bandwidth of the filter can be written as

$$\Delta\lambda_n = \lambda_{nH} - \lambda_{nL} \approx \frac{\Delta\alpha_n}{\nu_0 f}. \quad (4)$$

The total number of filter channels can be determined,

$$N \triangleq \frac{\Delta\lambda}{\Delta\lambda_n} \approx \frac{\Delta\lambda \nu_0 f}{\Delta\alpha_n}, \quad (5)$$

where $\Delta\lambda$ is the spectral bandwidth of the white-light source. Thus, we see that the degree of temporal coherence at the Fourier plane increases as spatial frequency of the sampling grating ν_0 increases.

For the noise measurement under temporally coherent illumination, we would use a variable slit representing a broad spectral filter in the Fourier plane. The output noise fluctuation can be traced out with a linearly scanned photometer, as illustrated in Fig. 1. It is therefore apparent that the output noise fluctuation due to spectral bandwidth of the slit filter and due to the source size can then be separately determined. We shall adopt the definition of output signal-to-noise ratio (SNR), as proposed in a previous paper,⁴ for the measurement of the noise performance, i.e.,

$$\text{SNR}_n(y') \triangleq E[I_n(y')]/\sigma_n^2(y'), \quad (6)$$

where $I_n(y')$ is the output irradiance due to the n th channel, $E[\cdot]$ denotes the ensemble average, and $\sigma_n^2(y')$ is the variance of the output noise fluctuation, i.e.,

$$\sigma_n^2(y') \triangleq E[I_n^2(y')] - [E[I_n(y')]]^2. \quad (7)$$

Evidently the output intensity fluctuation $I_n(y')$ can be traced out by a linearly scanned photometer. The dc component of the output traces is obviously the output signal irradiance (i.e., $E[I_n]$), and the mean square fluctuation of the traces is the variance of the output noise (i.e., σ_n^2). Thus we see that the effect of the output SNR due to spectral bandwidth (i.e., temporal coherence) and source size (i.e., spatial coherence) can readily be obtained with the proposed measurement technique.

III. Experimental Results

In our experiments, a 75-W xenon arc lamp is used as the white-light source. The spatial frequency of the sampling phase grating used is ~ 50 lines/mm, the focal length of the achromatic transform lenses is ~ 380 mm. Both the amplitude and the phase noise plates used in the experiments are generated by photographing a laser speckle pattern, and the phase plate is obtained with a surface relieving technique through an R-10 bleaching process.⁷ Shower glass, for strong phase perturbation, is also utilized in the experiments. We shall first demonstrate the noise performance due to perturbation



Fig. 2. Effect on output image (with a section of photometer traces) due to phase noise at the input plane for different spectral bandwidths. The source size used is 0.7 mm square (i.e., $a = 0.7$ mm): (a) $\Delta\lambda_n = 1500$ Å; (b) $\Delta\lambda_n = 1000$ Å; (c) $\Delta\lambda_n = 500$ Å.

at the input plane. For the amplitude noise at the input plane, the experiments have shown that there is no apparent improvement in noise performance under partially coherent illumination. The result is quite conclusive with the previous prediction.^{3,4} However for the phase noise at the input plane, the noise performance of the system is largely improved with a partially coherent illumination. We shall first utilize a weak phase model (obtained by laser speckle and a photographic bleaching process described earlier) as the input noise. Now we consider the situation of an input object transparency superimposing with the phase noise at the input plane. The effect of the noise performance of the optical system can then be obtained by varying the source size and the spectral bandwidth of the slit filter, as described in Fig. 1. Figure 2 shows a set of output photographic images together with sections of corresponding photometer traces to illustrate the effect due to spectral bandwidth of the slit filter. From these pictures we see that the noise performance (i.e., SNR) improves as the spectral bandwidth (i.e., temporal coherence) of the slit filter increases.

Quantitative measurements of the noise performance due to phase noise at the input plane are plotted in Figs. 3 and 4. From these two figures we see that the output SNR increases monotonically as the spectral bandwidth $\Delta\lambda_n$ of the slit filter increases and it linearly increases as the source size enlarges. Thus the noise performance for a partially coherent optical system improves as the degree of coherence (i.e., temporal and spatial coherence) relaxes. In other words, to improve the output SNR of the white-light (i.e., partially coherent) processor, one can either relax the spatial coherence (i.e., the source size) or the temporal coherence (i.e., the spectral bandwidth of the filter) or both in the optical processing system. We stress that the experimental results are quite compatible with the results obtained in our recent analysis.^{4,5}

Let us now demonstrate the effect of the noise performance due to strong phase noise. In the experiments, a conventional shower glass is used as the input phase noise. Figure 5 shows a set of results we obtained

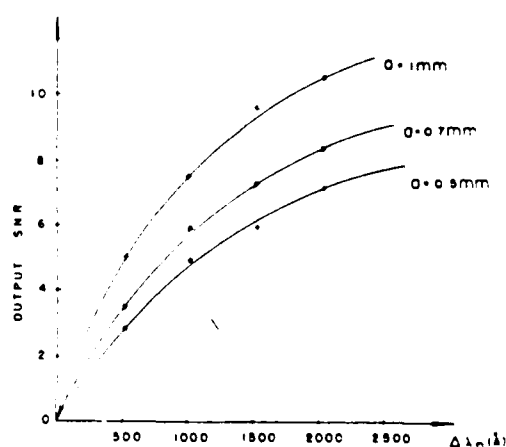


Fig. 3. Output SNR for phase noise at the input plane as a function of spectral bandwidth of the slit filter for various values of source sizes.

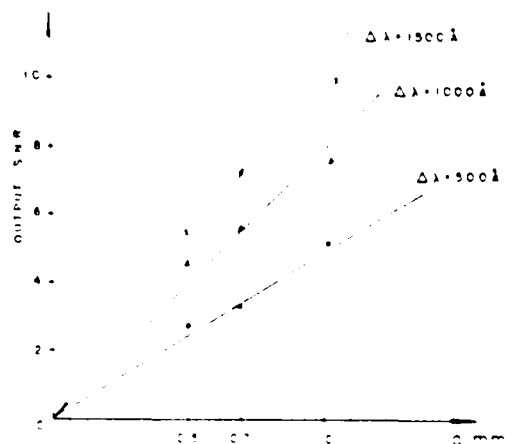


Fig. 4. Output SNR for phase noise at the input plane as a function of source size for various values of spectral bandwidths.



Fig. 5. Effect of output image due to strong phase perturbation at the input plane ($a = 0.7$ mm): (a) $\Delta\lambda_n = 3000$ Å; (b) $\Delta\lambda_n = 1500$ Å; (c) $\Delta\lambda_n = 500$ Å; (d) obtained with a He-Ne laser.

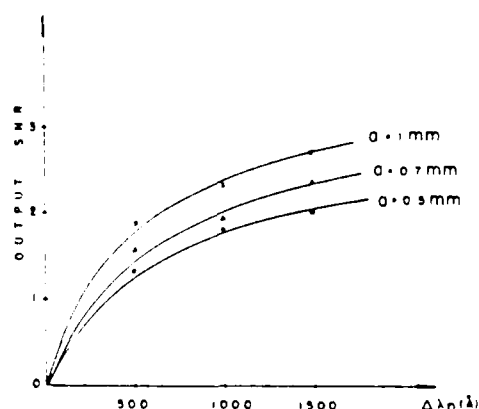


Fig. 6. Output SNR for amplitude noise at the Fourier plane as a function of spectral bandwidth for various source sizes.

under various spectral bandwidth illuminations. Figure 5(a) shows an output result obtained under entire broadband white-light illumination. Although this image is somewhat aberrated due to the thick phase perturbation, the image is relatively immune from random noise fluctuation. Compared with the results obtained from Figs. 5(a)–(d), we see that the output SNR decreases rather rapidly as the spectral bandwidth of the slit filter decreases. Furthermore, Fig. 5(d) shows a result obtained with a narrowband coherent source (i.e., a He-Ne laser). Aside from the poor noise per-

formance, we have noted that the output image is also severely corrupted by coherent artifact noise.

We shall now demonstrate the noise performance of a white-light optical processing system due to noise at the Fourier plane. With reference to the same measurement technique as proposed in Fig. 1, the effects of amplitude noise at the Fourier plane are plotted in Fig. 6. In contrast with the amplitude noise at the input plane, we see that the output SNR increases monotonically as the spectral bandwidth of the slit filter increases. The output SNR also improves as the source size enlarges. Thus, for amplitude noise at the Fourier plane, the noise performance of a white-light optical processor improves as the degree of temporal and spatial coherence decreases.

Figure 7 shows the noise performance of a white-light processor for phase noise at the Fourier plane. From this figure, once again we see that the output SNR is a monotonic increasing function of spectral bandwidth $\Delta\lambda_n$. The SNR also increases as the source size increases. However, compared with the case of phase noise at the input plane of Fig. 2, the improvement of the noise performance is somewhat less effective compared with the phase noise at the input plane. Once again we see that the experimental results are compatible with the analytical results that we obtained in our previous papers.^{4,5}

We shall now provide the result of noise performance due to thin phase noise along the optical axis (i.e., Z

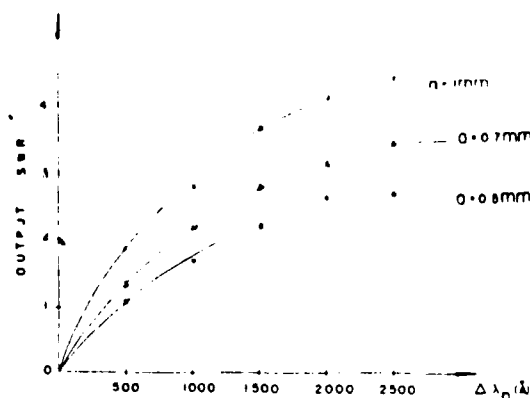


Fig. 7. Output SNR for phase noise at the Fourier plane as a function of source size for various values of spectral bandwidths.

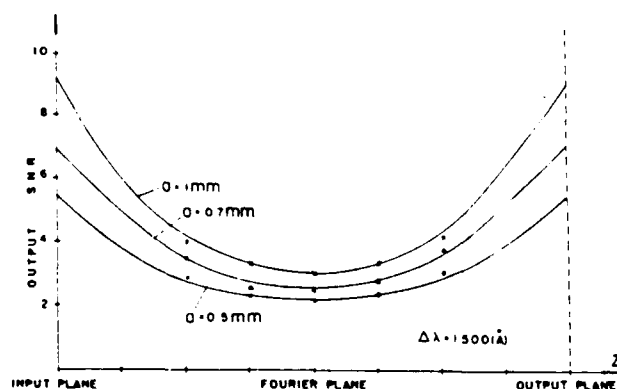


Fig. 8. Variation of the output SNR due to thin phase noise as a function of the Z direction for various source sizes.

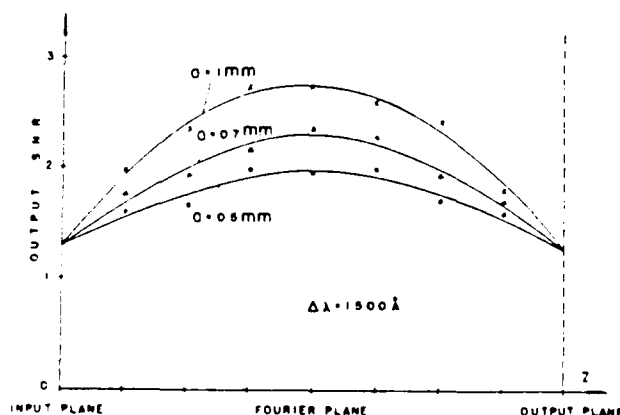


Fig. 9. Variation of the output SNR due to thin amplitude noise as a function of the Z direction for various source sizes.

axis) of the optical system. Figure 8 shows the variation of output SNR due to phase noise inserted in various planes of the optical system. From this figure we see that the output SNR improves drastically for phase noise inserted at the input and output planes under temporal and spatial partially coherent illumination. The noise performance is somewhat less effective for the phase noise at the Fourier plane, even under partially

coherent illumination. Nonetheless, the phase noise at the Fourier plane can, in principle, be totally eliminated under very broadband illumination, if each of the noise channels is uncorrelated. We have also noted that the output SNR is somewhat lower for higher spatial coherent illumination (i.e., smaller source size). In other words, the output SNR can also be improved with extended source illumination.

The noise performance, due to amplitude noise along the Z axis of the proposed optical processor, is plotted in Fig. 9. From this figure we see that the output SNR improves as the noise perturbation moved away from the input and output planes and where the optimum SNR occurs at the Fourier plane. Again, we see that the output SNR is somewhat higher for larger source sizes (i.e., lower degree of spatial coherence). However we stress that the noise performance cannot be improved with partially coherent illumination, if the amplitude noise is placed at the input or at the output plane.

IV. Summary and Conclusion

We have devised a technique for measuring the noise performance of a white-light (i.e., partially coherent) optical signal processor. We have utilized a scanning photometer method to obtain the output intensity traces of a partially coherent system operating in noisy conditions. The effects of output SNR due to the amplitude and the phase noise at the input and Fourier planes were quantitatively studied. The experimental results show that there has been no improvement in noise performance due to amplitude noise at the input plane. However the output SNR improves drastically for the phase noise at the input plane with a partially coherent (i.e., temporal and spatial coherence) illumination. For very strong input phase disturbance, the experiments show that the output noise can essentially be eliminated, if it is under very broadband illumination.

As for the performance due to noise at the Fourier plane, the experimental results show that the output SNR improves for both the amplitude and phase noise under a partially coherent regime. However the overall improvement is somewhat lower than the effect due to phase noise at the input plane, under the same partially coherent (i.e., temporal and spatial coherence) illumination.

We have also measured the noise performance due to thin noise effects along the Z axis of the optical processing system. The experimental results show that optimum noise immunity occurs for phase noise at the input and output planes, and optimum output SNR occurs for amplitude noise at the Fourier plane. The results also indicate that a higher output SNR can in fact be obtained for more relaxed temporal and spatial coherence constraints.

In concluding this paper we stress that the experimental results are quite compatible with the analytical results that we recently evaluated.^{4,5}

We acknowledge the support of the U.S. Air Force Office of Scientific Research grant AFOSR-83-1040.

References

1. P. Chavel and S. Lowenthal, "Noise and Coherence in Optical Image Processing. II: Noise Fluctuations," *J. Opt. Soc. Am.* **64**, 721 (1978).
2. P. Chavel, "Optical Noise and Temporal Coherence," *J. Opt. Soc. Am.* **70**, 935 (1980).
3. E. N. Leith and J. A. Roth, "Noise Performance of an Achromatic Coherent Optical System," *Appl. Opt.* **18**, 2803 (1979).
4. F. T. S. Yu, K. S. Shaik, and S. L. Zhuang, "Noise Performance of a White-Light Optical Signal Processor. I: Temporally Partially Coherent Illumination," *J. Opt. Soc. Am. A* **1**, 489 (1984).
5. F. T. S. Yu, K. S. Shaik, and S. L. Zhuang, "Noise Performance of a White-Light Optical Signal Processor. II: Spatially Partially Coherent Illumination," *Appl. Phys.* **B36**, 1 (1985).
6. M. Born and E. Wolf, *Principles of Optics* (Pergamon, New York, 1964).
7. B. J. Chang and K. Winick, "Silver-Halide Gelatin Holograms," *Proc. Soc. Photo-Opt. Instrum. Eng.* **215**, 172 (1980).

SECTION XVIII

White-Light Fourier Holography

WHITE-LIGHT FOURIER HOLOGRAPHY

F.T.S. YU and F.K. HSU

*Electrical Engineering Department, The Pennsylvania State University,
University Park, PA 16802, USA*

Received 17 August 1984

This paper describes a technique for generating broad spectral band Fourier holograms with an encoded white light source. Since this technique utilizes primary white-light construction and reconstruction process, it is quite suitable for color Fourier hologram image reconstruction. Experimental results are also given.

1. Introduction

The construction of Fourier transform hologram for a two-dimensional object transparency with coherent optics was first introduced by Vander Lugt in 1964 in the application to complex signal detection [1]. Since then efforts have been made to develop techniques for making Fourier holograms with incoherent light.

Recently, Courjon and Bulabois [2-4] had demonstrated a technique of producing Fourier holograms with a spatially incoherent source. They utilized an interference filter and a holographic transparency to achieve a high degree of coherence illumination for the Fourier hologram construction and the hologram image reconstruction was obtained with narrow spectral band illumination. Although good experimental results have been reported, however the technique is limited to monochrome hologram image reconstruction. Ferriere et al. [5] have also demonstrated a technique of generating Fourier holograms with an incoherent source. They utilized dispersive prisms and a slit filter to achieve a high temporal coherence (i.e., narrow band illumination) for Fourier hologram generation. Although positive results have been reported in their article, however the image quality is rather poor. The major drawback of this technique must be due to low-light construction process, in which results with poor noise performance.

In this paper we shall describe a technique of pro-

ducing a broad band Fourier hologram with a white-light source. The technique utilizes a high efficient dispersive grating and a source encoding mask for the Fourier hologram generation. Since the hologram construction utilizes all colors of visible light, this technique is suitable for color Fourier hologram image reconstruction.

2. Construction and reconstruction process

We shall now describe a technique of generating a broad spectral band Fourier hologram with a white-light processing technique [6], as schematized in fig. 1. A high diffraction efficient phase grating is used to disperse the spectral content of the light source into rainbow color at the back focal plane of the achromatic lens L_0 . To alleviate the constraint of recording medium due to limited dynamic range, we shall spatially sample the smeared optical light source with periodic pinholes such that a sequence of partially coherent sources for various spectral colors can be obtained at the source plane P_0 . The intensity distribution of these encoded sources, for various λ_n , would be

$$\gamma(x_0, y_0) = K \sum_{n=1}^N \text{cir}_n [|x_0, y_0 - f_0 \lambda_n| / \Delta \gamma_n] \quad (1)$$

where K is a proportionality constant,

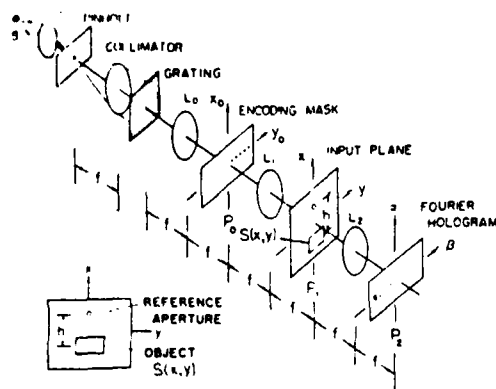


Fig. 1. A technique of generating a broad spectral band Fourier hologram with a white-light source. S, white-light source.

$$\text{cir}_n[r/\Delta r_n] = 1, \quad 0 \leq r \leq \Delta r_n, \\ = 0, \quad \text{otherwise,}$$

Δr_n is the radius of the n th sampling pinholes, f is the focal length of the achromatic lens, ν_0 is the spatial frequency of the phase grating, λ_n is the main wavelength within the n th sampled source, and (x_0, y_0) is the spatial coordinate system of the source plane P_0 . To achieve the required spatial coherence at the input plane P_1 , it is apparent that the size of the sampling pinholes should be small compared with the overall input object, such as

$$\Delta r_n < f\lambda_n/h. \quad (2)$$

where h denotes the separation between the reference point and the input object $s(x, y)$ as shown in fig. 1.

To maintain a high temporal coherence for Fourier hologram construction, it is required that the wavelength spread $\Delta\lambda_n$ over the n th sampling aperture should satisfy the following inequality

$$\Delta\lambda_n/\lambda_n \ll \Delta\nu/\nu_0, \quad (3)$$

where $\Delta\nu$ is the spatial frequency bandwidth of the input object $s(x, y)$ and ν_0 is the spatial frequency of the phase grating.

Thus we see that a sequence of encoded partially coherent sources are illuminating the input plane P_1 . Since the source encoding mask is covered over a wide spectral content of the smeared white-light source, it is apparent that N discrete Fourier holograms, for dif-

ferent wavelengths, can be synthesized. Let us now assume that the input plane contains an object transparency and a reference pinhole, as described in the following equation:

$$f(x, y) = s(x + h/2, y) + \delta(x - h/2, y), \quad (4)$$

where $s(x, y)$ denotes an input object function, $\delta(x, y)$ denotes the Dirac delta function, and h is the main separation between the target and the reference pinholes. It is therefore apparent that a broad band Fourier hologram can be interferometrically generated in the Fourier plane P_2 . If we assume that the holographic construction is in the linear region of the recording emulsion, the amplitude transmittance distribution of the recorded Fourier hologram would be

$$H(\alpha, \beta) = \sum_{\substack{n=-N \\ n \neq 0}}^N \{K_1 |S(\alpha, \beta + f\nu_0\lambda_n)|^2 \\ + K_2 |S(\alpha, \beta + f\nu_0\lambda_n)| \\ \times \cos[(2\pi h/\lambda_n f)\alpha + \phi(\alpha, \beta + f\nu_0\lambda_n)]\}, \quad (5)$$

where K_1 and K_2 are arbitrarily proportional constants, $S(\alpha, \beta; \lambda_n)$ is the Fourier spectrum of input object function $s(x, y; \lambda_n)$, (α, β) is the spatial coordinate system of the Fourier plane, λ_n is the main wavelength of the n th quasi monochromatic coherent source, f is the focal length of the achromatic transform lens L_2 , and ν_0 is the spatial frequency of the grating.

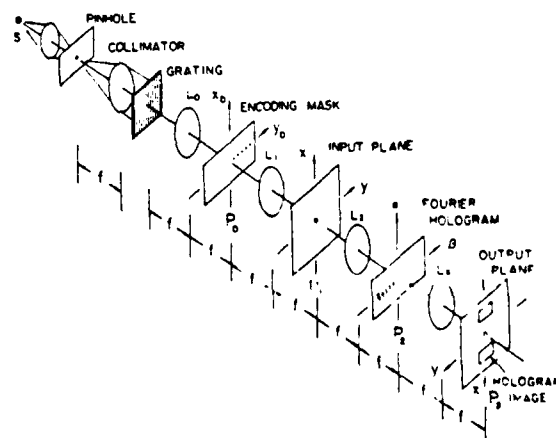


Fig. 2. Fourier hologram image reconstruction with white-light processing.

It is interesting to note that if the broad band hologram $H(\alpha, \beta)$ is illuminated by a beam of encoded white-light source (shown in fig. 2) such as

$$E(\alpha, \beta; \lambda) = C \sum_{\substack{n=-N \\ n \neq 0}}^N \text{cir}_n(\alpha, \beta + f\nu_0\lambda_n; \lambda), \quad (6)$$

where C is a complex proportionality constant, then the complex light field at the output plane would be

$$g(x, y; \lambda) = \iint E(\alpha, \beta; \lambda) H(\alpha, \beta) \times \exp[-i(2\pi/\lambda f)(\alpha x + \beta y)] d\alpha d\beta. \quad (7)$$

By substituting eqs. (5) and (6) into eq. (7), we have

$$g(x, y; \lambda) = \sum_{n=1}^N C_1 \delta(x, y; \lambda) * s(x, y; \lambda_n) * s^*(-x, -y; \lambda_n) + \sum_{n=1}^N C_2 \delta(x, y; \lambda) * [s(x+h, y; \lambda_n) + s^*(-x+h, -y; \lambda_n)], \quad (8)$$

where C_1 and C_2 are complex constants, $*$ denotes the convolution operation and the superscript $*$ represents the complex conjugation. The corresponding output irradiance can be shown as

$$I(x, y) = \int_{\Delta\lambda_n} |g(x, y; \lambda)|^2 d\lambda, \quad \text{for } n = 1, 2, \dots, N, \quad (9)$$

which is approximated by

$$I(x, y) \approx \Delta\lambda_n \sum_{n=1}^N \{K_1 s(x, y; \lambda_n) * s^*(x, y; \lambda_n) + K_2 [|s(x+h, y; \lambda_n)|^2 + |s(x-h, y; \lambda_n)|^2]\}, \quad (10)$$

where K_1 and K_2 are proportionality constants, $*$ denotes the correlation operation. From this equation we see that two hologram images of $s(x, y)$ would be diffracted around $x = \pm h$ at the output image plane of fig. 2.

3. Experimental result

We would now provide a couple of experimental results obtained with the proposed white-light Fourier holographic process. In our experiments, a 75-W xenon arc lamp with a 1 mm square pinhole is used as a white-light source. A sinusoidal phase grating of about 110 lines/mm, with 25% diffraction efficiency for the first-order diffraction, is used to disperse the spectral content of the light source. The achromatic transform lenses used are about 750 cm focal length. The source encoding mask composes a set of periodic circular pinholes of about 40 μm and their spacing is about 2.5 mm. The separation between the reference aperture and the input target object is about 8 mm. The size of the reference aperture is roughly about 300 μm .

We shall now show a couple of Fourier hologram images obtained with this white-light processing technique. Fig. 3(a) shows a gray scale object, with a reference pinhole, used as an input transparency. A broad-band Fourier hologram is generated as shown in the enlarged photograph of fig. 3(b). Fig. 3(c) shows a pair of twine holographic images obtained with this technique. As compared with the original object, the feature of the hologram image can readily be seen, although the image quality is still needed to improve.

One of the features of the white-light Fourier holography must be the color image reconstruction. Fig. 4(a) shows a set of binary color English characters, with a reference pinhole, used as input object to generate a broad-band color Fourier hologram. Fig. 4(b) shows a pair of color holographic images obtained with this technique. Although the image quality of this result is still somewhat poor, however as compared with the original transparency, the color reproduction is rather faithful. Nevertheless, this result may be the first white-light colour Fourier hologram image that is ever reconstructed.

4. Conclusion

We have described a technique of generating a broad spectral band (i.e., white-light) Fourier hologram. The technique utilizes light dispersion and source sampling method to obtain a set of narrow-band partially coherent sources for the hologram construction process. Since the technique utilizes

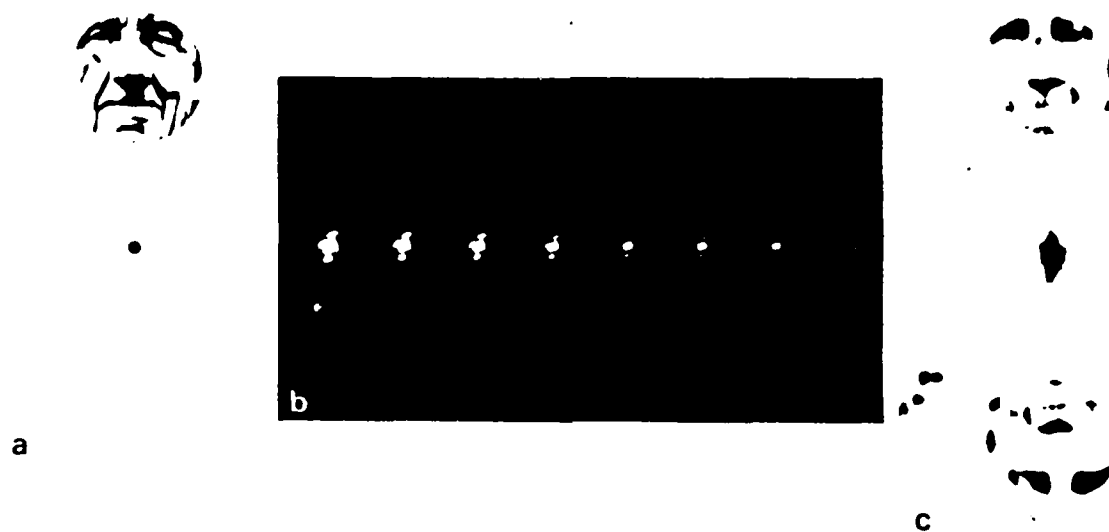


Fig. 3. Fourier hologram image reconstruction. (a) Input object with a reference pinhole. (b) A broad band Fourier hologram. (c) Fourier hologram images.

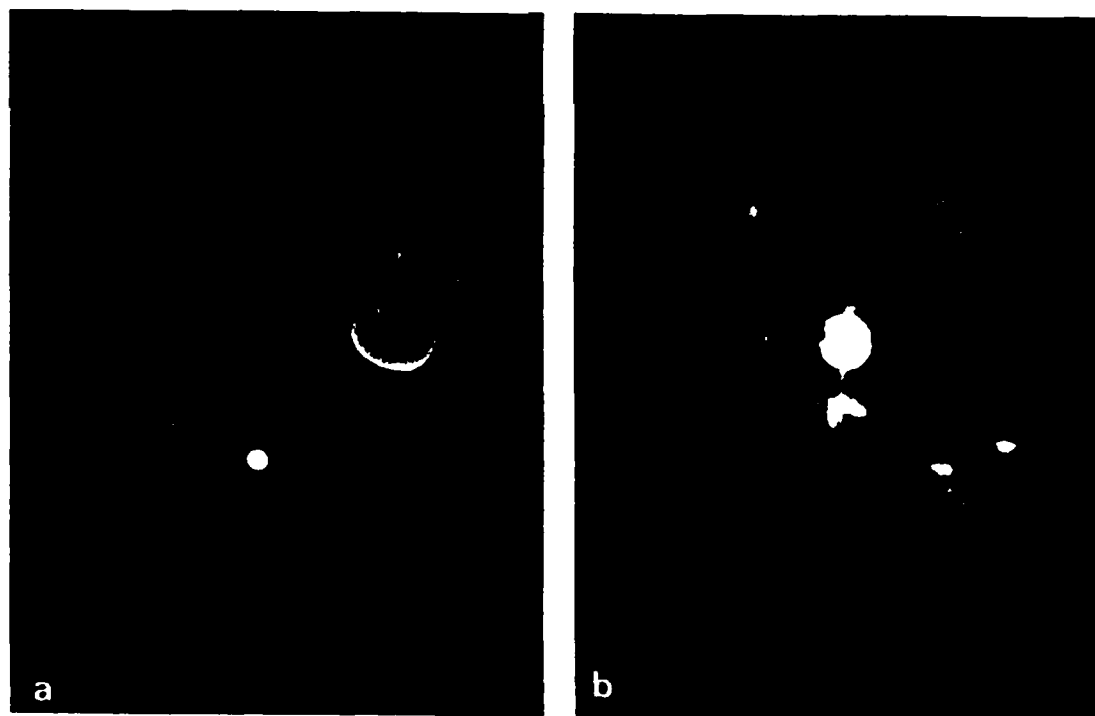


Fig. 4. Color hologram image. (a) Input object with reference pinhole. (b) Color Fourier hologram images.

white-light illumination, it is quite suitable for color Fourier holographic imaging.

Acknowledgement

We acknowledge the support of the U.S. Air Force Office of Scientific Research AFOSR Grant 83-0140.

References

- [1] A. Vander Lugt, I.I.E. Trans. Inform. Theory 11-10 (1964) 139.
- [2] D. Courjon and J. Bulabois, Optics Comm. 21 (1977) 96.
- [3] D. Courjon and J. Bulabois, Optics Comm. 31 (1979) 270.
- [4] D. Courjon and J. Bulabois, SPIE 194 (1979) 129.
- [5] R. Ferrière, J.P. Goedgebuer and J.C. Vienot, Optics Comm. 31 (1979) 285.
- [6] F.T.S. Yu, Optical information processing (Wiley-Interscience, New York, 1983).

SECTION XIV

Optical Generation of Speech Spectrogram

White-light optical speech spectrogram generation

F. T. S. Yu, T. W. Lin, and K. B. Xu

A white-light optical processing technique of generating speech spectrogram is presented. The speech spectrograms thus generated are frequency color-coded resulting in easier visual discrimination. The temporal-to-spatial conversion of speech signal is accomplished by means of density modulation with a CRT scanner. The scaling procedure of the speech spectrogram as well as the frequency resolution limit of the system is discussed. Experimental demonstrations of the proposed frequency color coded speech spectrograms generated by the proposed white-light optical processing technique are given.

I. Introduction

Since development of the first electronic sound spectrograph by Bell Telephone Laboratories nearly four decades ago,¹ great strides have been made in the field of speech analysis. The electronically generated sound spectrograph has been widely used for various applications including such areas as linguistics, phonetics, speech synthesis, and speech recognition. However, an optical system utilizing the Fourier transform properties of the positive lens offers a viable alternative to the electronic counterpart. The multichannel optical processor suggested by Cutrona *et al.*² was found to be able to utilize efficiently the 2-D nature of an optical system. Moreover, by sacrificing the multichannel capability of such a processor, Thomas³ pointed out the feasibility of generating a near real time spectrum analysis for large space-bandwidth signal. Later Yu⁴ reinforced Thomas's concept in the synthesis of a coherent optical sound spectrograph. He pointed out that a near real time optical sound spectrograph can be designed and constructed at a competitively low cost.⁵

In this paper, we will describe a technique of generating multicolor speech spectrograms with a white-light optical processor. This technique utilizes a cathode ray tube (CRT) scanner density modulator to convert a temporal signal to a spatial signal that is suitable for white-light signal processing. To obtain a color-coded speech spectrogram, a dispersive element such as a

grating (or prism) can be used at the input plane of the processor. In frequency color encoding, a narrow slit is placed over the smeared color signal spectra at the Fourier plane so that a frequency color encoded spectrogram can be recorded. In the following, we shall describe the basic performance of this white-light optical spectrum analyzer as applied to speech signals. The frequency resolution limit of the system as well as the frequency scaling of the spectrogram will be given. Experimental demonstrations of the color-coded speech spectrograms, obtained with the white-light processing technique, will be provided.

II. Temporal-Spatial Signal Conversion

It is well known that an optical processor is capable of performing 2-D spatial Fourier transformation. However, the processing of time signals by optical means necessitates the transformation of the signals to a 2-D spatial format. Generally speaking, there are two ways of performing this conversion, namely, the density and the area modulation techniques.⁶ Nevertheless, the density modulation method is the simplest and most commonly used technique in practice.⁷ We shall use a density modulation technique for temporal-to-spatial signal conversion and also show that the temporal-spatial formats obtained from this technique are very suitable for color-coded spectrogram generation with a white-light source.

The conversion can be obtained by displaying the time signal with a CRT scanner and then recorded on a moving photographic film. In other words, the time signal is first applied to the Z axis of a high-resolution CRT scanner to produce an intensity modulated electron beam so that the fluorescence light intensity varies linearly with the input signal voltage. Since the signal voltage is usually a bipolar function and the light intensity is a positive real quantity, an appropriate bias should be added with the time signal to produce a density modulated signal. To ensure a linear density

The authors are with Pennsylvania State University, Electrical Engineering Department, University Park, Pennsylvania.

Received 10 September 1984.

0003-6935/85/060836-06\$02.00/0.

© 1985 Optical Society of America.

modulated signal, the input signal should be scaled down within the linear region of the CRT scanner. Furthermore, a ramp function is fed into the Y axis of the CRT scanner to produce the vertical sweep. To maintain the uniformity of sweep intensity, the scan rate should be set considerably higher than the maximum frequency content of the input signal. Thus the signal would be displayed on the CRT screen as a uniform intensity scan at each vertical sweep. Consequently, a spatially recorded format, whose amplitude transmittance is linearly proportional to the intensity of CRT display, can be produced by imaging the CRT display onto a moving photographic film. Figure 1(a) shows the schematic diagram of the conversion process. The recorded format, as typified in Fig. 1(b), can then be inserted into the input plane of the optical processor for spectrogram generation.

In the time-spatial conversion recording, the speed of the recording film limits the highest-frequency content of the signal to be recorded. For example, if the highest frequency content of the signal is ν cps, the speed of the film motion should be

$$v \geq \nu/R, \quad (1)$$

where R is the spatial frequency limit of the film. Thus it is apparent that to resolve the highest frequency content of the recorded format, the speed of the recording film should be so adjusted higher than the ratio of ν/R . Unfortunately, the finite optical processing window would set the speed limit of the recording film. A higher speed of the recording film would result in a lower frequency resolution of the spectrogram generation, thus corresponding to a wideband spectrogram analysis.⁸ However, this drawback may be alleviated by utilizing a higher-resolution CRT scanner. Nevertheless, in practice, a higher-resolution CRT tends to be more expensive. Moreover, the frequency resolution of the optical processor is also limited by the source size as well as the point spread function of the imaging lens and, of course, the width of the optical window in the processor. Thus the speed of recording film should be restricted by the following inequality:

$$v \leq W\nu_l, \quad (2)$$

where W is the width of the optical window of the processor and ν_l is the lowest frequency limit.

III. System Analysis

Let us now discuss a white-light optical spectrum analyzer as depicted in Fig. 2, where L_1 , L_2 , and L_3 are achromatic Fourier transform lenses. If the recorded format of a time-spatial signal, as described in Sec. II, is loaded in a linear motion film transport at the input plane of the processor, a slanted set of rainbow smeared Fourier spectra in the Fourier plane can be observed. We note that the effect of the phase grating at the input plane is to disperse the signal spectra in a direction perpendicular to the recorded input format (i.e., direction of the film motion), so that a set of nonoverlapping slanted (or fan-shaped) rainbow color smear spectra can be displayed at the Fourier plane. It is now

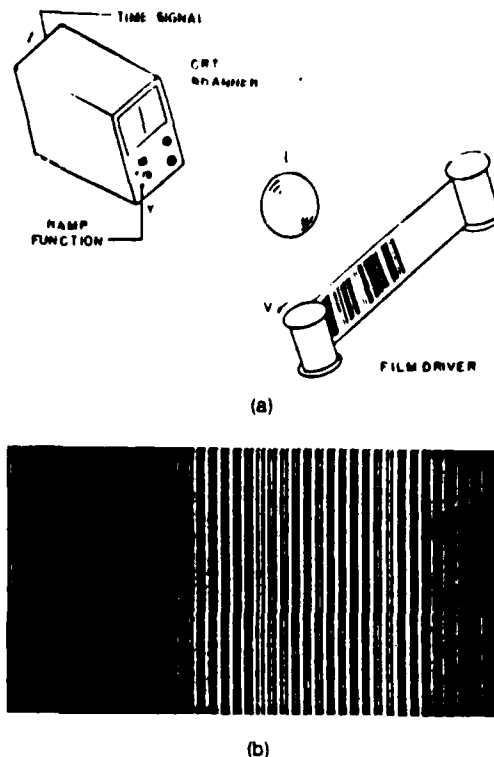


Fig. 1. (a) Temporal-to-spatial signal conversion. L , imaging lens. (b) Segment of recorded format.

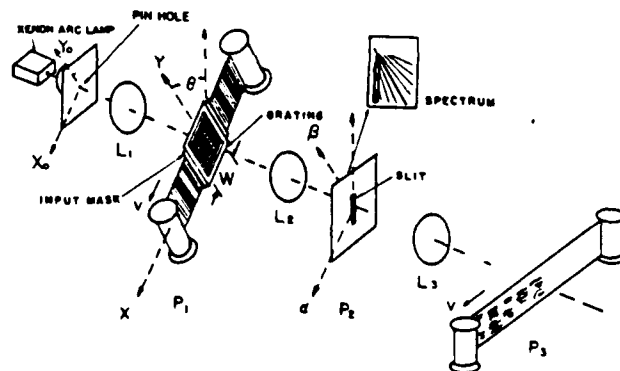


Fig. 2. White-light optical sound spectrograph. L , achromatic transform lens.

apparent that, if a slanted narrow slit is properly utilized at the Fourier plane, as illustrated in the figure, a frequency color-coded spectrogram can be recorded at the output plane, with a moving color film. The color-coded spectrographic signal can also be picked up by a color TV camera for displaying, storage, transmission, and further processing by electronic or digital system. We further note that, by simply varying the width of the input optical window, one would expect to obtain the so-called wideband and narrowband spectrograms. In other words, if a broader optical window is utilized for the spectrogram generation, a high spectral resolution, corresponding to a narrowband spectrogram, can be obtained.

However, by increasing the spectral resolution of the spectrogram, we would expect to lose the spatial (i.e., time) resolution. Conversely, if the optical window is narrower, which corresponds to a wideband analysis, a loss of spectral resolution is expected. However, loss of the spectral resolution improves the time resolution of the spectrogram. This time-bandwidth relationship is in fact the consequence of the Heisenberg's uncertainty relation in quantum mechanics.⁹

For simplicity in analysis, we let the light source be a square white-light source. The source irradiance may be written as

$$\gamma(x_0, y_0; \lambda) = S(\lambda) \operatorname{rect}\left(\frac{x_0}{b}\right) \operatorname{rect}\left(\frac{y_0}{b}\right), \quad (3)$$

where $S(\lambda)$ is the spectral distribution of the light source, b denotes the size of the square source, and

$$\operatorname{rect}\left(\frac{x}{b}\right) = \begin{cases} 1, & |x| \leq b, \\ 0, & \text{otherwise.} \end{cases}$$

With reference to Wolf's partial coherence theory¹⁰ the mutual coherence function at the input plane P_1 of the spectrum analyzer of Fig. 2 would be

$$\begin{aligned} \Gamma(x_1, y_1; x_2, y_2; \lambda) &= \iint \gamma(x_0, y_0; \lambda) \\ &\cdot \exp\left\{-i \frac{2\pi}{\lambda f} [x_0(x_1 - x_2) \right. \\ &\quad \left. + y_0(y_1 - y_2)]\right\} dx_0 dy_0, \end{aligned} \quad (4)$$

where the integration is over the source irradiance. By carrying out the integration, the mutual coherence function at plane P_1 becomes

$$\begin{aligned} \Gamma(x_1, y_1; x_2, y_2; \lambda) &= KS(\lambda) \operatorname{sinc}\left[\frac{\pi b(x_1 - x_2)}{\lambda f}\right] \\ &\cdot \operatorname{sinc}\left[\frac{\pi b(y_1 - y_2)}{\lambda f}\right], \end{aligned} \quad (5)$$

where

$$\operatorname{sinc}(\pi\chi) \triangleq \frac{\sin(\pi\chi)}{\pi\chi},$$

and K is an appropriate constant.

Now, if the time-spatial signal format is inserted at the input plane P_1 of the processor, the mutual coherence function behind the input plane would be

$$\begin{aligned} \Gamma'(x_1, y_1; x_2, y_2; \lambda) &= \Gamma(x_1, y_1; x_2, y_2; \lambda) \exp[iq_0(y_1 - y_2)] \\ &\cdot t(x_1)t^*(x_2) \operatorname{rect}\left(\frac{x_1}{W}\right) \operatorname{rect}\left(\frac{x_2}{W}\right), \end{aligned} \quad (6)$$

where the exponential factor represents the phase transform of the 1-D phase grating, q_0 is the angular spatial frequency of the grating, $t(x)$ is the amplitude transmittance function of the recorded format, and W is the width of the input optical window as shown in the figure. Thus it is apparent that the mutual coherence function arriving at the Fourier plane P_2 would be

$$\begin{aligned} \Gamma(p_1, q_1; p_2, q_2; \lambda) &= \iiint \Gamma'(x_1, y_1; x_2, y_2; \lambda) \\ &\cdot \exp[-i(x_1 p_1 + y_1 q_1 - x_2 p_2 - y_2 q_2)] \\ &\cdot dx_1 dy_1 dx_2 dy_2, \end{aligned} \quad (7)$$

where the proportional constant is ignored for convenience, and (p, q) is the angular spatial frequency coordinate system which can be written as $p \triangleq 2\pi\alpha/\lambda f$, $q \triangleq 2\pi\beta/\lambda f$, and (x, y) is the spatial coordinate system of the Fourier plane P_2 .

By properly substituting Eq. (6) into Eq. (7) and integrating over the y_1 and y_2 variables, we have

$$\begin{aligned} \Gamma(p_1, q_1; p_2, q_2; \lambda) &= S(\lambda) \operatorname{rect}\left[\frac{\lambda f\left(\frac{q_1}{2} + \frac{q_2}{2} - q_0\right)}{2\pi b}\right] \cdot \delta(q_1 - q_2) \\ &\cdot \iint \operatorname{sinc}\left[\frac{\pi b(x_1 - x_2)}{\lambda f}\right] t(x_1)t^*(x_2) \\ &\cdot \operatorname{rect}\left(\frac{x_1}{W}\right) \operatorname{rect}\left(\frac{x_2}{W}\right) \\ &\cdot \exp[-i(x_1 p_1 - x_2 p_2)] dx_1 dx_2 \end{aligned} \quad (8)$$

For simplicity of illustration, we assume that the input format is a single sinusoidal signal, i.e.,

$$t(x) = 1 + \cos(p_0 x) \quad \text{for all } x, \quad (9)$$

where p_0 is the spatial frequency of the sinusoid. Since the cosine function of Eq. (9) can be written into two exponential functions, we focus our attention merely to one of the diffraction order, that is,

$$t(x_1)t^*(x_2) = \exp[ip_0(x_1 - x_2)]. \quad (10)$$

By substituting Eq. (10) into Eq. (8), we obtain

$$\begin{aligned} \Gamma(p_1, q_1; p_2, q_2; \lambda) &= S(\lambda) \operatorname{rect}\left[\frac{\lambda f\left(\frac{q_1}{2} + \frac{q_2}{2} - q_0\right)}{2\pi b}\right] \cdot \delta(q_1 - q_2) \\ &\cdot \iint \operatorname{sinc}\left[\frac{\pi b(x_1 - x_2)}{\lambda f}\right] \exp[ip_0(x_1 - x_2)] \\ &\cdot \operatorname{rect}\left(\frac{x_1}{W}\right) \operatorname{rect}\left(\frac{x_2}{W}\right) \exp[-i(x_1 p_1 - x_2 p_2)] dx_1 dx_2. \end{aligned} \quad (11)$$

Since the interest is centered at the output irradiance, by letting $p_1 = p_2 = p$ and $q_1 = q_2 = q$, the irradiance at the Fourier plane would be

$$I(p, q; \lambda) = S(\lambda) \operatorname{rect}\left[\frac{\lambda f(q - q_0)}{2\pi b}\right] I(p), \quad (12)$$

where

$$\begin{aligned} I(p) &\triangleq \iint \operatorname{sinc}\left[\frac{\pi b(x_1 - x_2)}{\lambda f}\right] \exp[ip_0(x_1 - x_2)] \\ &\cdot \operatorname{rect}\left(\frac{x_1}{W}\right) \operatorname{rect}\left(\frac{x_2}{W}\right) \exp[-i(x_1 - x_2)p] dx_1 dx_2 \end{aligned} \quad (13)$$

To investigate the variation of the output irradiance due to the width of the input optical window, Fig. 3 shows a plot of the normalized intensity variation of Eq. (13) for two values of W . From this figure we see that a narrower spread of output irradiance corresponds to a broader optical window W at the input plane. Thus a narrowband spectrogram can be generated in this manner. On the contrary, if a narrower optical window is utilized, a broader spread of the output irradiance is

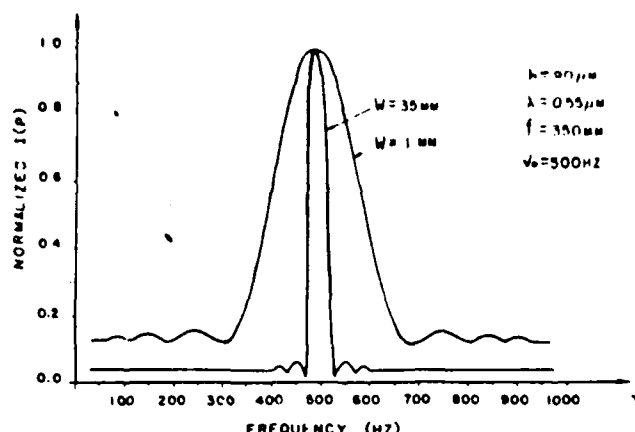


Fig. 3. Normalized output spectral distribution as a function of input frequency for two sizes of optical windows.

expected. Thus a wideband spectrogram may be generated with a narrow optical window.

To have a better understanding of Eq. (12), two extreme cases of the light source will be discussed in the following:

(a) If we assume that the broadband light source is vanishingly small (i.e., $b \rightarrow 0$), then

$$\lim_{b \rightarrow 0} \text{sinc} \left[\frac{\pi b(x_1 - x_2)}{\lambda f} \right] = 1,$$

and Eq. (12) takes the form

$$I(p, q; \lambda) = S(\lambda) \text{rect} \left[\frac{\lambda f(q - q_0)}{2\pi b} \right] \cdot W^2 \text{sinc}^2[\pi W(p - p_0)]. \quad (14)$$

This result describes a completely spatially coherent illumination.

(b) On the other hand, if the light source becomes infinitely large (i.e., $b \rightarrow \infty$), then

$$\lim_{b \rightarrow \infty} \text{sinc} \left[\frac{\pi b(x_1 - x_2)}{\lambda f} \right] = K \delta(x_1 - x_2),$$

where K is an appropriate constant, and Eq. (12) becomes

$$I(p, q; \lambda) = S(\lambda) \text{rect} \left[\frac{\lambda f(q - q_0)}{2\pi b} \right] W^2. \quad (15)$$

This result corresponds to a completely spatially incoherent illumination. Nevertheless, the proposed white-light spectrum analyzer, as can be seen, is operating in a partially coherent mode.

IV. Frequency Calibration and Resolution

We shall now discuss the frequency calibration of the proposed white-light optical speech spectrogram. The accuracy of the frequency measurement depends on the width of the input optical window as well as the width of the sampling slit at the Fourier plane. By adjusting these parameters, a properly calibrated speech spectrogram can be generated at the output plane.

Let us assume that the transform lenses are achromatic (i.e., $\partial f / \partial \lambda = 0$) and the angular spatial frequency of the input phase grating is q_0 . Thus we see that the

Fourier spectrum of the phase grating would be diffracted at

$$\beta = (\lambda / 2\pi) q_0, \quad (16)$$

where f is the focal length of the achromatic transform lens. Since Eq. (16) is linearly proportional to the wavelength of the light source, a rainbow color of smeared spectra can be observed along the β axis in the Fourier plane P_2 . For simplicity, we assume that input format is a single sinusoid of spatial frequency p_0 ; then the Fourier spectra points are located at

$$\alpha = \pm \frac{\lambda f}{2\pi} p_0. \quad (17)$$

For convenience, we use the positive value of Eq. (17) in our discussion. By taking the ratio of Eqs. (16) and (17), we have

$$\alpha = \frac{p_0}{q_0} \beta, \quad (18)$$

where we assume that $p_0 \ll q_0$, and q_0 is the spatial frequency of the phase grating. Thus we see that the frequency locus of the input signal can be properly traced out in the Fourier plane. In view of Eqs. (16) and (17), and the fact that $q_0 \gg p_0$, we further see that the spectrum of the input signal would disperse into a rainbow color at a slanted angle in the Fourier plane. It is, therefore, apparent that, if a narrow masking slit is properly utilized in the Fourier plane, a frequency color-coded spectrogram can be obtained at the output plane.

Now let us suppose that the masking slit can be described as

$$\beta = \frac{\lambda_0 f}{2\pi} q_0 + \alpha \tan \gamma, \quad (19)$$

where λ_0 denotes the upper or lower limit of the source wavelength depending on the slit orientation, and $\tan \gamma$ is the slope of the slit. By substituting Eqs. (16) and (17) into Eq. (19), we have

$$p_0 = \frac{q_0(\lambda - \lambda_0)}{\lambda \tan \gamma},$$

which can be written as

$$\nu = \frac{p_0 v}{2\pi} = \frac{q_0(\lambda - \lambda_0)v}{2\pi \lambda \tan \gamma}, \quad (20)$$

where ν is the time frequency of the input signal. Thus we see that the temporal frequency of the input signal and the spectral wavelength of the light source form a nonlinear function, as plotted in Fig. 4(a). Figure 4(b) shows the experimental result to confirm this relationship. Nevertheless this nonlinearity of frequency-spectral wavelength relationship can be linearized by using an appropriate curve slit instead of a linear one in the Fourier plane.

We shall now discuss the frequency resolution of the proposed system. We note that the frequency resolution is primarily limited by the width of the input optical window, the source size, and the width of the sampling slit in the Fourier plane. To investigate these effects, we assume that the size of the white-light source

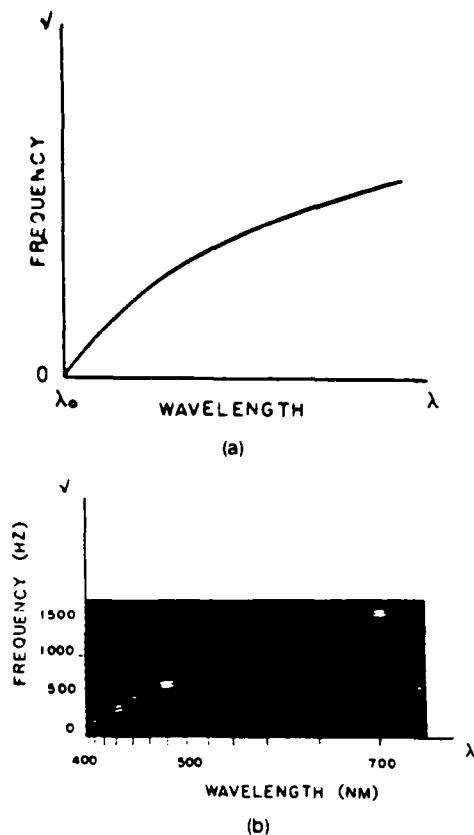


Fig. 4. Variation of input frequency vs spectral wavelength of the light source: (a) calculated result; (b) experimental result.

is b . Then the size of a point spread image would be

$$b' = b/f', \quad (21)$$

where f' and f are the focal lengths of collimating and achromatic Fourier transform lenses, respectively. Thus the width of the point spread image at the spatial frequency plane would be

$$\Delta\nu_1 = \frac{b'}{\lambda f'} v = \frac{bv}{\lambda f'}. \quad (22)$$

Since the width of input optical window affects the spectral resolution of the processor, the width of the spectral lines in hertz for a point source is

$$\Delta\nu_2 = v/W, \quad (23)$$

where v is the speed of the film motion, and W is the width of the input optical window.

For simplicity, we shall treat these two factors (i.e., source size and width of optical window) independently. It is apparent that the spread of the smeared spectral line (i.e., frequency resolution) of the system can be approximated by the following equation:

$$\Delta\nu = [(\Delta\nu_1)^2 + (\Delta\nu_2)^2]^{1/2} = v \left[\left(\frac{b}{\lambda f'} \right)^2 + \left(\frac{1}{W} \right)^2 \right]^{1/2}. \quad (24)$$

As an example, if we let $v = 195$ mm/sec, $b = 90$ μ m, $\lambda = 0.55$ μ m, $W = 35$ mm, and $f' = 762$ mm, the frequency spread of the proposed optical spectrum analyzer is $\Delta\nu = 42$ Hz, which corresponds to a narrowband analysis

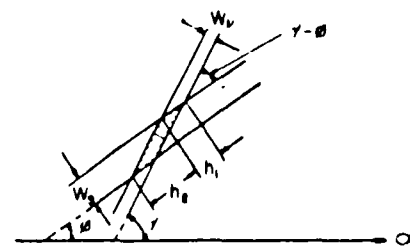


Fig. 5. Determination of the output spectral resolution.

(e.g., narrowband speech spectrogram). However, we see that the overall output resolution of the spectral spread is determined by the width and orientation of the sampling slit at the Fourier plane, as illustrated in Fig. 5. Thus the effective output frequency resolution can be shown as

$$\Delta\nu_r = \epsilon(h_1 + h_2) = \left[\frac{W_s}{\sin(\gamma - \phi)} + \frac{W_s}{\tan(\gamma - \phi)} \right], \quad (25)$$

where W_ν and W_s are the width of the smeared frequency spectral line and the width of the sampling slit, ϵ is an appropriate conversion factor, and γ and ϕ are defined in the figure.

From this equation we see that the effective output frequency resolution is proportional to the diagonal region of the spectral line that intersects the sampling slit, as shown in the shaded area. Therefore, the overall output frequency resolution is somewhat lower than the width of the smeared spectral line, i.e.,

$$\Delta\nu_r \geq \Delta\nu. \quad (26)$$

This is the price of the color encoding. Nevertheless the price we paid is considered small compared with the advantages we gained from the white-light processing.

V. Experimental Demonstrations

In our experiments, a 75-W xenon arc lamp with a 90- μ m pinhole was used as a white-light source. A phase grating of 80 lines/mm was used as a dispersive element at the input plane. A narrow slit of ~ 70 μ m is inserted in the Fourier plane for color encoding. The focal length of the achromatic transform lens was ~ 350 mm.

In the experimental demonstration, we show two sets of color-coded speech spectrograms obtained with this technique, as depicted in Figs. 6 and 7. The frequency contents of these spectrograms are encoded in rainbow color from red to blue for upper to lower frequencies. These spectrograms were produced by a sequence of English words, testing, one, two, three, four, spoken by a male and a female voice, respectively. Figure 6 shows a set of narrowband speech spectrograms representing a 45-Hz bandwidth resolution. Figure 7 illustrates a set of wideband speech spectrograms with a 300-Hz bandwidth analysis. From these sets of spectrograms, we see that the basic structure of the spectrographic contents is preserved. The characterization of the formant variation can readily be identified. Since Fig. 6(a) is produced by a low-pitched voice (i.e., male), the

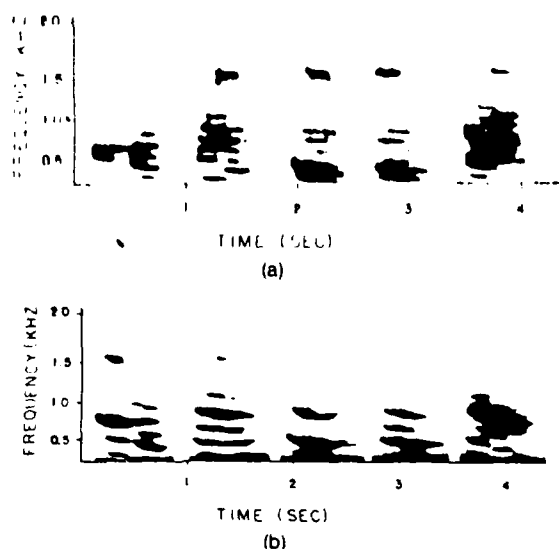


Fig. 6. Black-and-white photographs of narrowband color-coded speech spectrograms (~ 45 -Hz bandwidth): (a) obtained with a male voice; (b) obtained with a female voice.

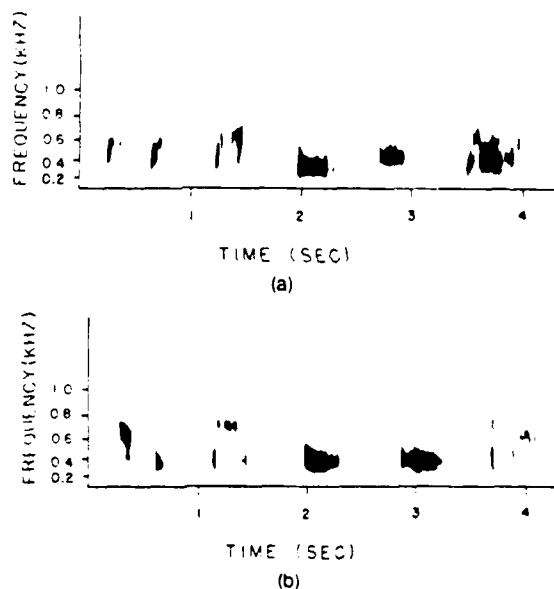


Fig. 7. Black-and-white pictures of wideband color-coded speech spectrograms (~ 300 -Hz bandwidth): (a) generated by a male voice; (b) generated by a female voice.

spectrogram shows more abundant harmonics as compared with the high-pitched voice in Fig. 6(b).

It is worthwhile to mention that although the narrowband spectrogram is capable of resolving the spectral contents of a speech, it loses the time striation, as can be seen in Fig. 6. On the other hand, the wideband

spectrogram of Fig. 7 are capable of resolving the time resolution, but it fails to resolve the spectral lines. We note that the trading of time and frequency resolutions between the wide and narrow spectrograms is essentially the well-known $\Delta\nu\Delta t$ concept in the communication theory (i.e., $\Delta\nu\Delta t \geq 1$), which is related to the famous Heisenberg's uncertainty principle⁹ in quantum mechanics.

VI. Conclusion

In this paper, we have presented a method of generating a continuous frequency color-coded speech spectrogram with a white-light processing technique. The proposed system not only offers a low-cost alternative but also eliminates the coherent artifact noise. Moreover, the multicolor display of the spectrogram is adapted to the natural sensitivity of human eyes and thereby provides improved visual discrimination. Nevertheless, we want to stress that due to the very limited resolution of the CRT scanner used in our experiments, the results that we obtained only extended to 1.6 kHz. This limitation is more pronounced for a wideband spectrographic analysis, which is primarily due to low-light performance of narrower optical window used at the object plane. However, to our experience, if a higher-resolution CRT scanner is utilized, the frequency range can easily push up to 4 kHz. This frequency range is commonly used for most telephonic systems.

References

1. W. Koenig, H. K. Dunn, and L. Y. Lacy, "The Sound Spectrograph," *J. Acoust. Soc. Am.* 18, 19 (1946).
2. L. J. Cutrona, E. Leith, C. Palermo, and J. Porcello, "Optical Data Processing and Filtering Systems," *IRE Trans. Inf. Theory* IT-6, 386 (1960).
3. C. E. Thomas, "Optical Spectrum Analysis of Large Space Bandwidth Signals," *Appl. Opt.* 5, 1782 (1966).
4. F. T. S. Yu, "Synthesis of an Optical-Sound Spectrograph," *J. Acoust. Soc. Am.* 51, 433 (1972).
5. F. T. S. Yu, "Generating Speech Spectrograms Optically," *IEEE Spectrum*, 12, (Feb. 1975).
6. E. B. Felstead, "Optical Fourier Transformation of Area-Modulated Spatial Functions," *Appl. Opt.* 10, 2468 (1971).
7. K. R. Hessel, "Some Theoretical Limitations of the Optical Power Spectrum Analyzer," *Appl. Opt.* 13, 1023 (1974).
8. F. T. S. Yu, "Information Content of a Sound Spectrogram," *J. Audio Eng. Soc.* 15, 407 (1967).
9. F. T. S. Yu, *Optics and Information Theory* (Wiley-Interscience, New York, 1976).
10. M. Born and E. Wolf, *Principles of Optics* (Pergamon, New York, 1980).

We acknowledge the support of U.S. Air Force Office of Scientific Research grant AFOSR-83-0140.

SECTION XX

Progress on Archival Color Film Storage

ELECTRICAL ENGINEERING DEPARTMENT, THE PENNSYLVANIA STATE UNIVERSITY

University Park, Pennsylvania 16802 (USA)

PROGRESS REPORT ON ARCHIVAL STORAGE OF COLOR FILMS UTILIZING A WHITE-LIGHT PROCESSING TECHNIQUE

F. T. S. YU, X. X. CHEN and S. L. ZHUANG

MOTS CLÉS :

Traitement d'image
Codage couleur

KEY WORDS :

Image processing
Color encoding

SUMMARY : In this paper, we report a spatially encoding technique such that the moiré fringe pattern inherently existing with the retrieved image can be avoided. To improve the diffraction efficiency of the film, we have introduced a bleaching process so that the step of obtaining a positive encoded transparency can be eliminated. Instead of restricting the encoding processing in the linear region of the $T-E$ curve, we would allow the encoding in the linear region of the $D-E$ curve, so that a broader range of encoding exposure can be utilized. Experimental results indicate that excellent color fidelity, high signal to noise ratio, and good resolution of the reproduced color images can be obtained.

Amélioration d'une technique de traitement en lumière blanche pour l'archivage de films en couleurs

RÉSUMÉ : Dans cet article nous décrivons une technique de codage spatial qui évite les effets de moiré dans l'image restituée. Pour améliorer l'efficacité du réseau de diffraction formé par le film, nous avons introduit une technique de blanchiment qui élimine le tirage d'un positif. Au lieu de restreindre le codage dans la partie linéaire de la courbe transmission-éclairage, il est possible de coder sur la partie linéaire de la courbe efficacité de diffraction-éclairage, ce qui élargit la gamme d'expositions. Les résultats expérimentaux montrent une excellente fidélité des couleurs, un grand rapport signal sur bruit et une bonne résolution dans la restitution des images en couleurs.

INTRODUCTION

Archival storage of color films has long been an unresolved problem for the film industry. The major reason is that the organic dyes used in color films are usually unstable under prolonged storage, often causing gradual color fading. Although there are several available techniques for preserving the color images, all of them possess certain definite drawbacks. One of the most commonly used techniques involves repetitive application of primary color filters, so that the color images can be preserved, in three separate rolls of black-and-white film. To retrieve the color image, a system with three primary color projectors are used. These films should be projected in perfect unison so that the primary color images will be precisely recorded on a fresh roll of color film. However, this technique has two major drawbacks : first, the storage volume for each film is tripled. Second, the reproduction system is rather elaborate and expensive.

The use of monochrome transparencies to retrieve

color images was first reported by Ives [1] in 1906. He introduced a slide viewer that produced color images by a diffraction phenomenon. Grating either of different spatial frequencies or of azimuthal orientations were used. More recently, Mueller [2] described a similar technique, employing a tricolor grid screen for image encoding. In decoding, he used three quasi-monochromatic sources for color image retrieval. Since then, similar work on color image retrieval has been reported by Macovski [3], Grousson and Kinany [4], and Yu [5]. However, those techniques suffer a major drawback : namely, the moiré fringes in the retrieval color image will not be avoided.

We will, in this paper, report a spatially encoding and decoding process such that the moiré fringe pattern can be avoided by spatial filtering. To improve the diffraction efficiency, we have introduced a bleaching processing for the encoded film in which the step of generating a positive transparency can be eliminated. We have also experimentally demonstrated that the spatially encoding process should not be restricted to the linear region of the $H-D$ curve.

Instead, it is recommended to encode in the linear region of the diffraction efficiency *versus* exposure curve (called *D-E* curve). Detail experimental procedure of this archival storage technique is presented. Preliminary results of retrieval color images are provided. Comparisons with original color transparency are also given.

SPATIAL ENCODING AND DECODING

We shall now describe a spatial encoding technique utilizing a white-light source. A color transparency is used as an object to be encoded, by sequentially exposing with primary color of lights, onto a black-and-white film, as illustrated in *figure 1*. The encoding is taken place by spatial sampling; the primary color images of the color transparency, with a specific sampling frequency and a predescribed direction onto a monochrome film. In order to avoid the moire fringe pattern in the retrieval color image, we propose to sample one of the primary color images in one independent spatial coordinate, and the remaining two primary color images in the other independent spatial coordinate, as shown in *figure 2*. Since any mixture of red with green or with blue colors produces a wide range of intermediate colors, we propose to encode the red color image in one independent spatial coordinate direction, and the blue and green color images in the other remaining independent coordinate direction. Thus a small amount of color spread (i.e., color crosstalk) from blue to green (but not from green to blue) may not be avoided. However this small amount of color spread will not cause significant adverse effect in the retrieved color image, for primarily two reasons: first, a slight mixture of blue into green will not produce significant color changes. Second, strictly speaking all the color transparencies are not natural colors, thus a small amount of color deviation would not be noticeable by human perception.

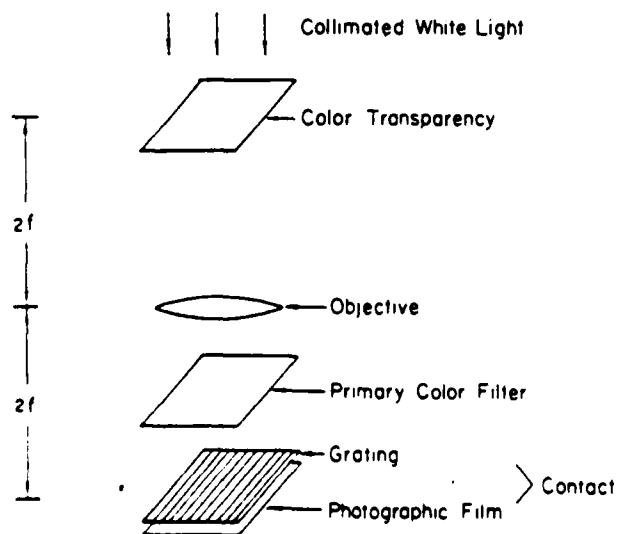


FIG. 1. — Sequential spatial color encodings

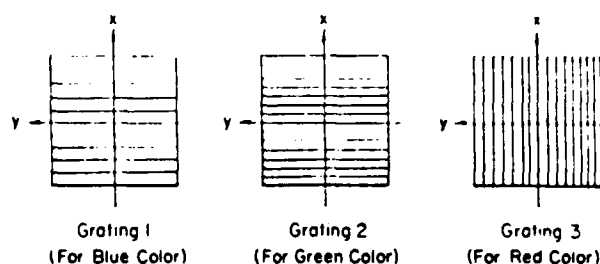


FIG. 2. — Positions of the three spatial samplings.

We shall now demonstrate that the moire fringes can be avoided with the proposed encoding-decoding technique. Let this intensity transmittance of the encoded films be [5]

$$T_n(x, y) = K \{ T_r(x, y) [1 + \text{sgn}(\cos p_r y)] + T_b(x, y) [1 + \text{sgn}(\cos p_b x)] + T_g(x, y) [1 + \text{sgn}(\cos p_g x)] \}^{-\gamma}, \quad (1)$$

where $T_n(x, y)$ is the encoded black-and-white negative transparency, K is an appropriate proportionality constant, T_r , T_b and T_g are the red, blue, and green color image exposures, p_r , p_b , and p_g are the respective carrier spatial frequencies, (x, y) is the spatial frequency coordinate system of the encoded film, γ is the film gamma [6], and

$$\text{sgn}(\cos x) \triangleq \begin{cases} 1, & \cos x \geq 0, \\ -1, & \cos x < 0. \end{cases} \quad (2)$$

Instead of obtained a positive image transparency, through a contact printing process of Eq. (2) as proposed in a previous paper [5], we shall bleach the encoded negative-image film to obtain a phase object transparency [7, 8]. Let us assume that the bleached transparency is encoded in the linear region of the diffraction efficiency *D* *versus* exposure *E* (e.g., as shown in *fig. 6*). The amplitude transmittance of the bleached transparency can be written

$$t(x, y) = \exp[i\phi(x, y)], \quad (3)$$

where $\phi(x, y)$ represents the phase delay distribution, which is proportional to the exposure of the encoded film [9], such as

$$\phi(x, y) = M \{ T_r(x, y) [1 + \text{sgn}(\cos p_r y)] + T_b(x, y) [1 + \text{sgn}(\cos p_b x)] + T_g(x, y) [1 + \text{sgn}(\cos p_g x)] \}, \quad (4)$$

where M is an appropriate proportionality constant. If we place this bleached encoded film at the input plane P_1 of a white-light optical processor, as illustrated in *figure 3*, then the complex light distribution due to $t(x, y)$, for every λ , at the spatial frequency plane P_2 can be determined by the following Fourier

transformation :

$$\begin{aligned} S(\alpha, \beta; \lambda) &= \iint T(x, y) \exp \left[-i \frac{\lambda}{2f} (\alpha x + \beta y) \right] dx dy \\ &= \iint \exp[i\phi(x, y)] \exp \left[-i \frac{\lambda}{2f} (\alpha x + \beta y) \right] dx dy. \end{aligned} \quad (5)$$

By expanding $T(x, y)$ into exponential series, Eq. (5) can be written

$$S(\alpha, \beta; \lambda) = \iint \left\{ 1 + i\phi(x, y) + \frac{1}{2} [i\phi(x, y)]^2 + \dots \right\} \exp \left[-i \frac{\lambda}{2f} (\alpha x + \beta y) \right] dx dy. \quad (6)$$

By substituting Eq. (4) into Eq. (6) and retaining the first-order and the first-order convolution terms we have :

$$\begin{aligned} S'(\alpha, \beta; \lambda) &= \hat{T}_r \left(\alpha, \beta \pm \frac{\lambda_r}{2\pi} p_r \right) + \hat{T}_b \left(\alpha \pm \frac{\lambda_b}{2\pi} p_b, \beta \right) \\ &\quad + \hat{T}_u \left(\alpha \pm \frac{\lambda_u}{2\pi} p_u, \beta \right) + \hat{T}_r \left(\alpha, \beta \pm \frac{\lambda_r}{2\pi} p_r \right) * \hat{T}_b \left(\alpha \pm \frac{\lambda_b}{2\pi} p_b, \beta \right) \\ &\quad + \hat{T}_r \left(\alpha, \beta \pm \frac{\lambda_r}{2\pi} p_r \right) * \hat{T}_u \left(\alpha \pm \frac{\lambda_u}{2\pi} p_u, \beta \right) + \hat{T}_b \left(\alpha \pm \frac{\lambda_b}{2\pi} p_b, \beta \right) * \hat{T}_u \left(\alpha \pm \frac{\lambda_u}{2\pi} p_u, \beta \right). \end{aligned} \quad (7)$$

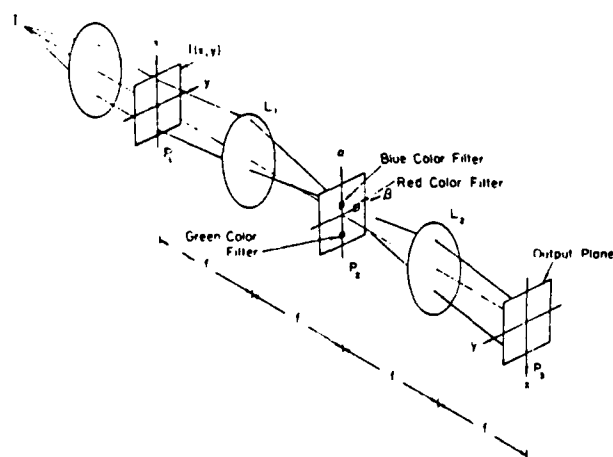


FIG. 3. White light processor for spatial color decoding. 1, extended white light source; L_1 , transform lens; $T(x, y)$, bleached encoded transparency.

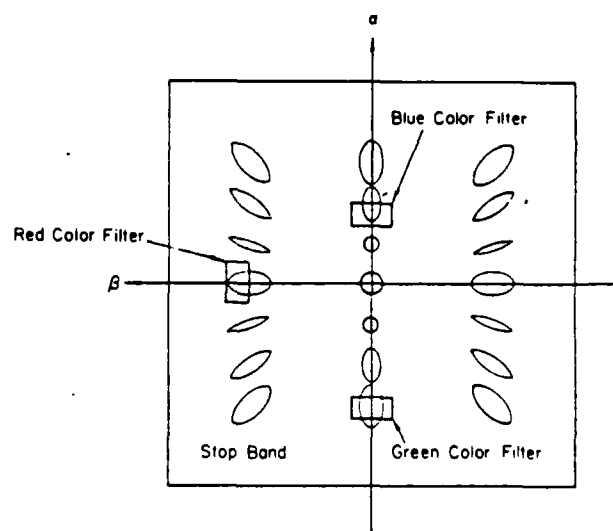


FIG. 4. Color spatial filtering at the spatial frequency plane.

where \hat{T}_r , \hat{T}_b and \hat{T}_u are the Fourier transforms of T_r , T_b and T_u respectively. * denotes the convolution operation, and the proportional constants have been neglected for simplicity. We note that, the last cross product term of Eq. (7) would introduce a moiré fringe pattern, parallel to encoding gratings of blue and green, in the retrieved color image. Nevertheless, all of those cross product terms can be properly masked out at the Fourier plane. Thus by proper color filtering those first-order smeared Fourier spectra, as shown in figure 4, a moiré free true color image can be retrieved at the output image plane P_3 . The corresponding complex light field immediately behind

the Fourier plane would be

$$\begin{aligned} S(\alpha, \beta) &= \hat{T}_r \left(\alpha, \beta - \frac{\lambda_r}{2\pi} p_r \right) \\ &\quad + \hat{T}_b \left(\alpha - \frac{\lambda_b}{2\pi} p_b, \beta \right) + \hat{T}_u \left(\alpha + \frac{\lambda_u}{2\pi} p_u, \beta \right) \end{aligned} \quad (8)$$

where λ_r , λ_b and λ_u are the respective red, blue, and green color wavelengths. At the output image plane, the complex light distribution is

$$\begin{aligned} s(x, y) &= T_r(x, y) \exp(i p_r x) + T_b(x, y) \exp(i p_b x) + \\ &\quad + T_u(x, y) \exp(-i p_u x). \end{aligned} \quad (9)$$

The output image irradiance is therefore

$$I(x, y) = I_r^2(x, y) + I_g^2(x, y) + I_b^2(x, y), \quad (10)$$

which is a superposition of three primary encoded color images. Thus we see that a moire free color image can indeed be obtained.

We shall now discuss the effect of moire fringe pattern in more detail. It is well known that a moire pattern is produced by the overlaying of two or more gratings [10, 11]. When two gratings of spacing a and b are superimposed with an obliquity angle of θ , the moire fringe spacing d can be written as :

$$d = \frac{hab}{\sqrt{a^2 + b^2 - 2ab \cos \theta}} \quad (11)$$

and this slope of the moire fringe is

$$\tan \phi = \frac{h \sin \theta}{a - b \cos \theta}, \quad (12)$$

where h is the index of moire pattern ($h = 0, \pm 1, \pm 2, \dots$) which represents the resultant moire fringes as an indexed family of curves (see ref. 11). If these two gratings are perpendicularly superimposed at an angle $\theta = 90^\circ$, then they form a cross grating pattern, without moire fringes [11].

On the other hand, if two gratings are parallel-superimposed on the top of the other (i.e., $\theta = 0^\circ$), then a beating frequency parallel to those gratings would occur. The corresponding fringe spacing is

$$d = \frac{hab}{|a - b|}, \quad (13)$$

and the relevant (i.e., moire) spatial frequency is

$$p_m = \frac{2\pi}{d} = |p_a - p_b|, \quad (14)$$

where $p_a = 2\pi/a$ and $p_b = 2\pi/b$ are the spatial frequencies of the two gratings.

We shall now investigate the moire fringe effects due the spatial encoding of figure 2. Since grating no. 3 is perpendicularly superimposed with grating

nos. 1 and 2, it will not generate any undesirable moire fringes except a cross grid between gratings 3 and 1, and 3 and 2. Whereas gratings 1 and 2 are parallel-superimposed, it produces a moire fringe pattern of spatial frequency $p_m = |p_b - p_g|$ in the same direction of gratings 1 and 2.

Since the last term of Eq. (7) represents the Fourier transform of this moire fringe pattern, the resolution of the retrieved encoded color image (blue or green) is limited by the size of the color spatial filters, as illustrated in figure 4. Therefore, the spatial frequency requirements of the gratings 1 and 2 can be determined by the following equation

$$p_g = \frac{1}{2}(p_g + 2p_b) = \frac{3}{2}p_b. \quad (15)$$

The resolution limit of retrieved color image is

$$p = |p_g - p_b| = \frac{1}{2}p_b, \quad (16)$$

and the spatial frequency of the moire fringe pattern is

$$p_m = |p_g - p_b| = \frac{1}{2}p_b. \quad (17)$$

Thus, by proper selection of desirable grating frequencies, which depends upon the resolution limit of the object transparency, the spatial frequency content of the moire pattern can be determined. With appropriate color filtering, the encoded Fourier spectra as illustrated in figure 4, a moire free color image can be obtained.

EXPERIMENTAL DEMONSTRATION

In our experiment, we utilized three Kodak primary color filters of No. 25, 47B and 58 for the encoding and decoding process. The characterizations of these filters, illuminated by standard A illuminant [12, 13], are specified by the C.I.E. diagram, as shown in figure 5. The corresponding trichromatic coefficients of these filters are tabulated in the following :

No. 25 - R^* : $\lambda = 6150 \text{ \AA}$	$x_R = 0.680$	$y_R = 0.320$	$z_R = 0$
No. 58 - G^* : $\lambda = 5500 \text{ \AA}$	$x_g = 0.302$	$y_g = 0.692$	$z_g = 0.006$
No. 47B - B^* : $\lambda = 4300 \text{ \AA}$	$x_b = 0.169$	$y_b = 0.007$	$z_b = 0.824$
and W_A^* :	$x_w = 0.448$	$y_w = 0.408$	$z_w = 0.144$

(18)

where R^* , G^* , B^* and W_A^* denote the red, green, blue and white colors, respectively, $x + y + z = 1$, and x , y , and z are the trichromatic coefficients obtained from the chromaticity coordinates of the C.I.E. chromaticity diagram [12, 13]. Grating frequency of 40 lines/mm is used for red and green color image encodings, and grating frequency of 26.7 lines/mm is used for blue color image encoding. A xenon arc lamp is used for the white-light processing, and the color

decoding filters are the same type of color filters used for the encoding. The trichromatic coefficients are expected to be the same as those in Eq. (18), except for the white color, that is

$$W_c^* : x_w = 0.310, \quad y_w = 0.316, \quad z_w = 0.374. \quad (19)$$

We shall now illustrate that any choice of color can be reproduced by a simple transformation from C.I.E.

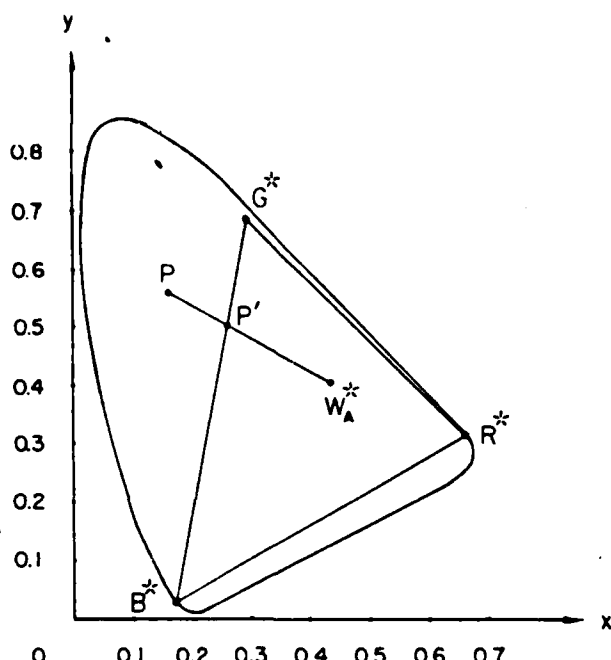


FIG. 5. — Chromaticity coordinates in C.I.E.

to $R^*G^*B^*$ as described in the following equation [14, 15].

$$\begin{aligned} R &= K_1 X + K_2 Y + K_3 Z, \\ G &= K_4 X + K_5 Y + K_6 Z, \end{aligned} \quad (20)$$

$$\text{and } B = K_7 X + K_8 Y + K_9 Z,$$

where R , G , and B are the red, green, and blue color tristimulus values, and X , Y , and Z are the C.I.E. tristimulus values, and the K 's are arbitrary constants. We note that these tristimulus values can be expressed as [14, 15]:

$$\begin{aligned} R &= y_W \begin{vmatrix} X & x_G & x_B \\ Y & y_G & y_B \\ Z & z_G & z_B \end{vmatrix} \\ &= y_W \begin{vmatrix} x_W & x_G & x_B \\ y_W & y_G & y_B \\ z_W & z_G & z_B \end{vmatrix}, \\ G &= y_W \begin{vmatrix} x_R & X & x_B \\ y_R & Y & y_B \\ z_R & Z & z_B \end{vmatrix} \\ &= y_W \begin{vmatrix} x_R & x_W & x_B \\ y_R & y_W & y_B \\ z_R & z_W & z_B \end{vmatrix}, \quad (21) \\ B &= y_W \begin{vmatrix} x_R & x_G & X \\ y_R & y_G & Y \\ z_R & z_G & Z \end{vmatrix} \\ &= y_W \begin{vmatrix} x_R & x_G & x_W \\ y_R & y_G & y_W \\ z_R & z_G & z_W \end{vmatrix} \end{aligned}$$

and

where the x 's and y 's are the trichromatic coefficients. By substituting the trichromatic coefficients of Eq. (18) into Eq. (21), we have

$$\begin{aligned} R &= 1.688 X - 0.734 Y - 0.340 Z, \\ G &= -0.915 X + 1.944 Y + 0.171 Z, \end{aligned} \quad (22)$$

$$\text{and } B = 0.014 X - 0.031 Y + 2.810 Z.$$

The chromaticity coordinates can be determined in the following definitions:

$$r \triangleq \frac{R}{R+G+B} = \frac{1.688 X - 0.734 Y - 0.340 Z}{0.787 X + 1.179 Y + 2.641 Z},$$

$$g \triangleq \frac{G}{R+G+B} = \frac{-0.915 X + 1.944 Y + 0.171 Z}{0.787 X + 1.179 Y + 2.641 Z}, \quad (23)$$

and

$$b \triangleq \frac{B}{R+G+B} = \frac{0.014 X - 0.031 Y + 2.810 Z}{0.787 X + 1.179 Y + 2.641 Z},$$

where r , g , and b are the chromaticity coordinates. Thus, any choice of color can be one-to-one homologically reproduced with this color transformation.

Although the color retrieval is evaluated within the triangle defined by $R^*G^*B^*$ of figure 5, any color point outside the triangle can be replaced by the nearness neighboring point on the boundary of the triangle, for example, p can be replaced by p' . Since the hue is generally keeping it up, it will not introduce significant adverse effect by human perception. In practice, we need only to control the exposure ratio of the encodings such that white color object can be retrieved by a white-light processor. With reference to these available exposure ratios, a broad dynamic range of encodings onto a typical photographic plate can then be achieved, as shown in figure 6.

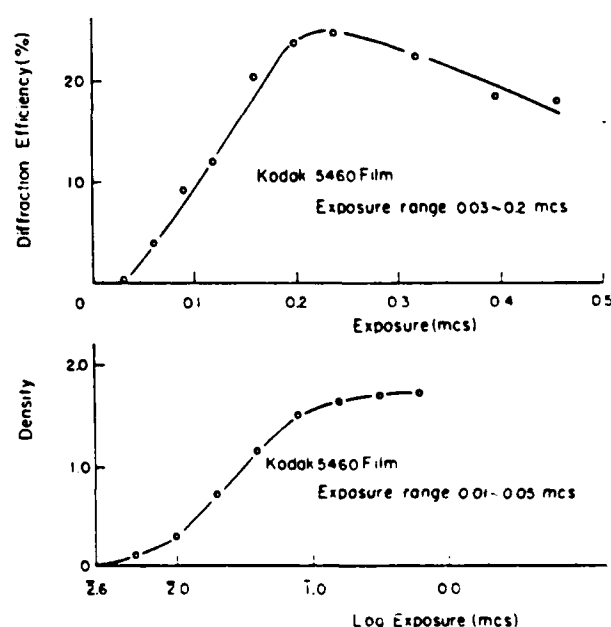


FIG. 6. — A broad exposure range of encodings

In our experiment, the encoding transparencies are made by Kodak technical pan film 2415 and Kodak Microfilm 5460. The advantage of using Kodak film 2415 is that it is a low contrast film with a relatively flat spectral response, as shown in figure 7. The disadvantage is that this film is coated with a thin layer of dyed-gel backing, for which it introduces additional noise through the bleaching process. Although the microfilm used is a clear base film, however, it is a high gamma film and the spectral response decreases somewhat in the red color region, as shown in figure 7. In order to compensate this low spectral response, one would encode the red wavelength with a higher exposure. Needless to say that, the resolution and contrast of the retrieval color image are also affected by this developing process of the film.

It should emphasize that, to avoid the shoulder region of the *D-E* curve, the film should be preexposed. Otherwise, it would introduce low exposure nonlinear effect which causes color unbalance in the retrieval image. The plots of diffraction efficiency versus exposure for Kodak 2415 and 5460 films with 40 lines/mm sampling frequency, are plotted in figure 8. From the figure, we see that the bleached encoded films offer a higher diffraction efficiency, the optimum value occurs at exposures 8.50×10^{-3} mcs and 1.95×10^{-1} mcs, respectively for Kodak films 2415 and 5460. With these optimum exposures, it is possible to optimize the encoding process in the following: first, by preexposing the film beyond the toe region. Second, by subdividing the remaining exposure, taken the account of the film spectral response, into three parts for the red, green, and blue color images.

For experimental demonstrations, we would like to provide two results obtained by Kodak 2415 and Kodak 5460 encoding films, as shown respectively in figures 9a and 9b. From these figures we see that the moiré free color images can indeed be obtained. We also see that the retrieved color image, obtained by this Kodak Microfilm 5460, provides a higher image quality (i.e., higher resolution and lower noise level). The primary reason is that, commercially available, Kodak 2415 is coated with a thin layer of dyed-gel backing. Accordingly, this thin layer of dyed-gel backing causes additional noise level through bleaching process. For comparison, we also provide

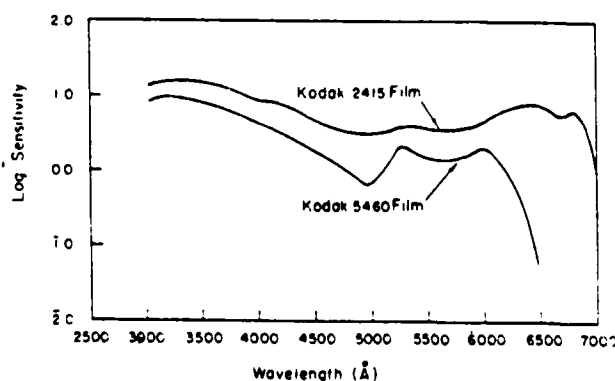


FIG. 7. — Spectral responses of Kodak films 2415 and 5460.

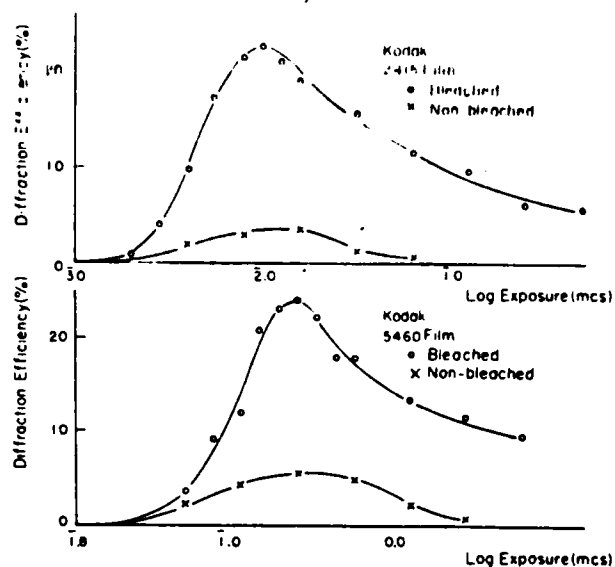


FIG. 8. — The plots of diffraction efficiency versus exposure for Kodak film 2415 and 5460 for a 40 lines/mm sampling.

the original color transparency as shown in figure 10. By comparing the results of figure 9 with figure 10, we see that the retrieval color images are spectacularly faithful, with virtually no color cross-talk. Although the resolution and contrast are still far below the acceptable stage for applications, however these drawbacks may be overcome by utilizing a more suitable film, for which a research program is currently under investigation. We are confident that better results would be obtained from our future research in this program.

CONCLUSION

In conclusion, we would like to point out that, a technique of spatial encoding for archival storage of color films utilizing a white-light processing is presented. The encoding is taken place with red color image on one independent coordinate, and blue and green color images on another independent coordinate, so that the moiré free color image can be retrieved at the output plane. We have also introduced a bleaching process to convert a negative encoded image into a phase object encoded transparency, in which the step of generating a positive encoded transparency can be avoided. Experimental results show that spectacularly faithful color images can be obtained with the technique. Although the resolution and contrast are still below the general acceptable stage for practical application, however by using a more suitable encoding film these drawbacks may be eliminated.

We acknowledge the support of the U.S. Air Force Office of Scientific Research grant AFOSR-81-0148.



a)



b)

FIG. 9. — Color pictures reproduced by this technique.

(a) obtained by Kodak 2415;

(b) obtained by Kodak 5460.



FIG. 10. — Color picture of the original color image.

REFERENCES

- [1] IVES (H. E.). — *Br. J. Photog.*, 609 (1906).
- [2] MUELLER (P. Y.). — *Appl. Opt.*, 8, 2051 (1969).
- [3] MACOVSKI (A.). — *Appl. Opt.*, 11, 416 (1972).
- [4] GROSSON (R.), KINANY (R. J.). — *J. Opt.*, 9, 333 (1978).
- [5] YU (F. T. S.). — *Appl. Opt.*, 19, 2457 (1980).
- [6] YU (F. T. S.). — *Optical Information Processing*, Wiley-Interscience Publishing Co., New York, 1982.
- [7] UPATNIEKS (J.), LEONARD (C.). — *Appl. Opt.*, 8, 85 (1969).
- [8] CHANG (B. J.), WINICK (K.). — *SPIE*, 215, 172 (1980).
- [9] SMITH (H. M.). — « Basic Holographic Principles », Ed. : H. M. Smith, *Holographic Recording Materials*, Springer-Verlag, New York, 1977.
- [10] GUILD (J.). — *The Interference System of Crossed Diffraction Gratings*, Oxford University Press, London, 1956.
- [11] OSTER (G.). — *Symposium in Quasi-Optics*, Polytechnic Press, Brooklyn, NY, 1964.
- [12] *Kodak Filters for Scientific and Technical Use*, Eastman Kodak Company, 1st ed., NY, 1970, p. 18.
- [13] COMPTON (K. T.). — *Handbook of Colorimetry*, MIT Press, Cambridge, 1936.
- [14] *The Science of Color*, published by Optical Society of America, 1963.
- [15] FINK (D. G.) — Ed., *Color Television Standards*, McGraw-Hill Book Company, NY, 1955.

(Manuscript received in May 15, 1984)

SECTION XXI

Falsed-Color Composites for Landsat Data

Generating False-Color Composites with a White-Light Optical Processor

F. T. S. Yu

Department of Electrical Engineering, The Pennsylvania State University, University Park, PA 16802

G. W. Petersen

Department of Agronomy and Office for Remote Sensing of Earth Resources, The Pennsylvania State University, University Park, PA 16802

ABSTRACT: A technique of false-color compositing by encoding multispectral remote sensing data with a low-cost white-light optical processor is described. Spatial encodings are made with various multispectral band image transparencies, and false-coloring is obtained by color filtering the smeared Fourier spectra. In contrast to the low-resolution digital image, the white-light method generates a high-quality color-coded product. This image is free from coherent artifact noise because coherent light sources are not used. This simple and versatile technique may offer a wide range of applications. Three bands of multispectral Landsat data were processed using 70-mm black-and-white film negatives. These false-color encoded images allowed for discrimination of various Earth surface features. Forests, agricultural lands, water, urban areas, and strip mines could be shown on the images as each of these thematic classes were displayed as a different color.

INTRODUCTION

MOST OPTICAL IMAGES used in scientific applications are gray-level density images, such as scanning electron microscopic images and x-ray transparencies. However, as has been shown for multispectral scanner images from satellites, color provides far greater visual discrimination.

In current practice, most false-color images are generated using digital computer techniques (Andrews *et al.*, 1972). Unfortunately, this method has three major drawbacks: (1) the equipment to generate these images is usually very expensive, (2) the technique is generally elaborate, and (3) image resolution is limited by the finite sample points of the system. A white-light false-color compositing technique that alleviates these three problems is described in this paper. The advantages of this new technique are (1) the cost of the equipment is substantially lower than for the digital process, (2) the encoder is relatively easy and economical to operate, and (3) the results of the optical technique can, in principle, match the resolution of the multispectral images.

In an earlier paper, the technique of false-color compositing with a white-light processing technique was described (Chao *et al.*, 1980). Although excellent results were reported using this method, false-color composites were obtained using only two primary colors. In this paper we shall extend the white-light false-color compositing technique to the multicolor case. For simplicity, we shall describe the case for three primary colors.

MATERIALS AND METHODS

Three bands of multispectral scanner Landsat data were processed for false-coloring using 70-mm black-and-white film negative transparencies. The bands were from the blue-green (Band 4: 0.5 to 0.6 μm), red (Band 5: 0.6 to 0.7 μm), and reflected infrared (Band 7: 0.8 to 1.1 μm) spectral regions. The scene is a 78 by 107 km subsample of Landsat scene 1440-15172 showing southeastern Pennsylvania (Figure 1). A multispectral-band image-encoding transparency was obtained by spatially sampling each of these three images onto black-and-white photographic film, with specific sampling grating frequencies oriented at specific azimuthal directions. To avoid the Moiré fringe pattern, these three images were sampled in orthogonal directions with different specific sampling frequencies, as shown in Figure 2. The intensity transmittance of the encoded film can be written as

$$T(x,y) = K\{T_1(x,y) [1 - \text{sgn}(\cos W_1 y)] + T_2(x,y) [1 - \text{sgn}(\cos W_2 x)] + T_3(x,y) [1 + \text{sgn}(\cos W_3 x)]\}^{-\gamma} \quad (1)$$

where K is an appropriate proportionality constant; T_1 , T_2 , and T_3 are the multispectral band transparencies, bands 4, 5, and 7, respectively; W_1 , W_2 , and W_3 are the respective carrier spatial frequencies; (x,y) is the spatial coordinate system of the encoded film; γ is the film gamma, and

$$\text{sgn}(\cos x) \triangleq \begin{cases} 1, & \cos x \geq 0 \\ -1, & \cos x < 0 \end{cases} \quad (2)$$

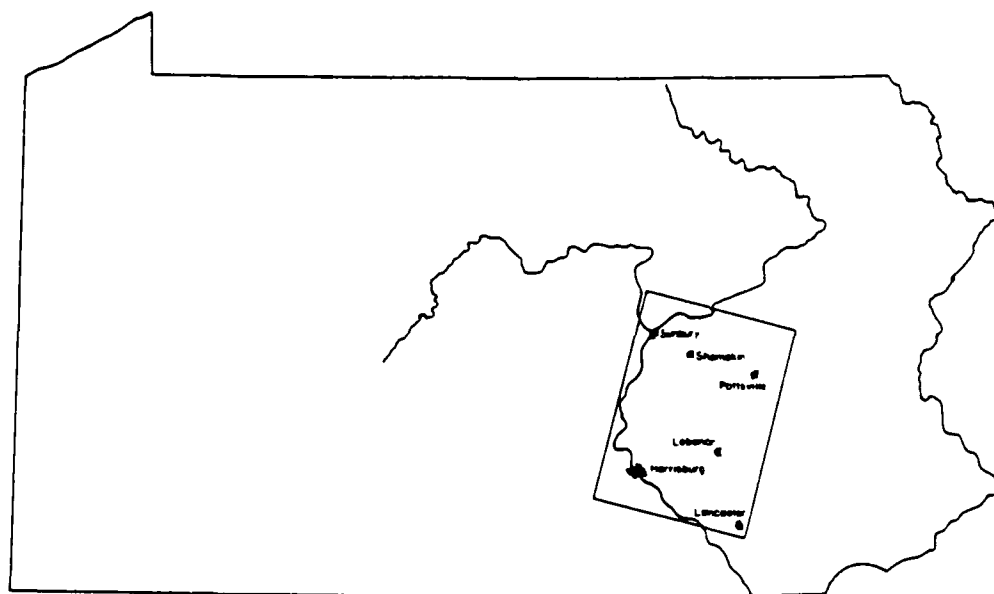


FIG. 1. Location map of the study site.

The encoded transparency was then bleached to obtain a surface relief phase object (Upatnick and Leonard, 1969; Chang and Winick, 1980). We assume that the bleached transparency is encoded in the linear region of the diffraction efficiency versus the log exposure curve (Figure 3) (Chang and Winick, 1980). Thus, the amplitude transmittance of the bleached transparency can be written as

$$t(x,y) = \exp[i\phi(x,y)] \quad (3)$$

where $\phi(x,y)$ represents the phase delay distribution, which is proportional to the exposure of the encoded film (Smith, 1977), such that

$$\begin{aligned} \phi(x,y) = M \{ & T_1(x,y) [1 - \operatorname{sgn}(\cos W_1 x)] \\ & - T_2(x,y) [1 + \operatorname{sgn}(\cos W_2 x)] \\ & + T_3(x,y) [1 + \operatorname{sgn}(\cos W_3 x)] \} \end{aligned} \quad (4)$$

where M is an appropriate proportionality constant. If we place this bleached encoded film at the input plane P_1 of a white-light optical processor (Yu, 1983), as illustrated in Figure 4, then the complex light distribution due to $t(x,y)$, for every λ , at the spatial frequency plane P_2 , can be determined by the following Fourier transformation:

$$\begin{aligned} S(\alpha, \beta; \lambda) = \iint t(x,y) \\ \exp \left[-i \frac{2\pi}{\lambda f} (\alpha x - \beta y) \right] dx dy \\ = \iint \exp [i\phi(x,y)] \\ \exp \left[-i \frac{2\pi}{\lambda f} (\alpha x - \beta y) \right] dx dy \end{aligned} \quad (5)$$

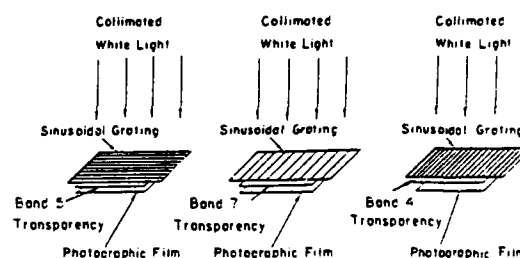


FIG. 2. Spatial encoding.

By expanding $t(x,y)$ into an exponential series, Equation 5 can be written as

$$\begin{aligned} S(\alpha, \beta; \lambda) = \iint \{ 1 + i\phi(x,y) + \frac{1}{2} [i\phi(x,y)]^2 \\ + \dots \} \exp \left[-i \frac{2\pi}{\lambda f} (\alpha x - \beta y) \right] dx dy \end{aligned} \quad (6)$$

By substituting Equation 4 into Equation 6 and retaining the first-order terms and the first-order convolution terms, we have

$$\begin{aligned} S'(\alpha, \beta; \lambda) = \hat{T}_1(\alpha, \beta = \frac{\lambda'}{2\pi} W_1) \\ + \hat{T}_2(\alpha = \frac{\lambda'}{2\pi} W_2, \beta) - \hat{T}_3(\alpha = \frac{\lambda'}{2\pi} W_3, \beta) \\ - \hat{T}_1(\alpha, \beta = \frac{\lambda'}{2\pi} W_1) \cdot \hat{T}_2(\alpha = \frac{\lambda'}{2\pi} W_2, \beta) \end{aligned} \quad (7)$$

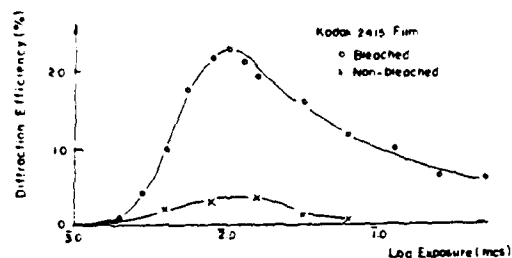


FIG. 3. Diffraction efficiency versus log exposure plot of a typical spatially-encoded film.

$$\begin{aligned}
 &+ \hat{T}_1(\alpha, \beta = \frac{\lambda f}{2\pi} W_1) * \hat{T}_3(\alpha + \frac{\lambda f}{2\pi} W_3, \beta) \\
 &+ \hat{T}_2(\alpha = \frac{\lambda f}{2\pi} W_2, \beta) * \hat{T}_3(\alpha = \frac{\lambda f}{2\pi} W_3, \beta)
 \end{aligned}$$

where \hat{T}_1 , \hat{T}_2 , and \hat{T}_3 are the Fourier transforms of T_1 , T_2 , and T_3 respectively; $*$ denotes the convolution operation; and the proportional constants have been neglected for simplicity. We note that the last cross product term of Equation 7 would introduce a Moiré fringe pattern, which is in the same sampling direction of W_2 and W_3 . Nevertheless, all of these cross product terms can be properly masked out at the Fourier plane. Thus, by proper color-filtering of the first-order smeared Fourier spectra, as shown in Figure 5, a Moiré-free false-color coded image can be obtained at the output plane P_3 . The corresponding complex light field immediately behind the Fourier plane would be

$$\begin{aligned}
 S(\alpha, \beta) = & \hat{T}_1(\alpha, \beta - \frac{\lambda_r f}{2\pi} W_1) \\
 & + \hat{T}_2(\alpha - \frac{\lambda_b f}{2\pi} W_2, \beta) \\
 & + \hat{T}_3(\alpha + \frac{\lambda_g f}{2\pi} W_3, \beta)
 \end{aligned} \quad (8)$$

where λ_r , λ_b , and λ_g are the respective red, blue, and green color wavelengths. At the output image plane, the false-color coded image irradiance is, therefore,

$$I(x, y) = T_1^2(x, y) + T_2^2(x, y) + T_3^2(x, y) \quad (9)$$

which is a superposition of three primary color encoded images, where T_1 , T_2 , and T_3 are the red, blue, and green amplitude distributions, respectively, of the three spatially encoded images. Thus, a Moiré-free color-coded image can be obtained at the output plane.

In our experiment, we used two sinusoidal sampling gratings for the spatial encodings, one with 26.7 lines/mm and the other with 40 lines/mm. The encoding transparency was made by Kodak Technical Pan Film 2415. The advantage of using this film is that it is a high resolution film and has a relatively flat spectral response. The plot of diffraction efficiency versus log exposure for Kodak 2415 film at 40 lines/mm sampling frequency is shown in Figure 3. From this figure, we see that bleached encoded films offer a higher diffraction efficiency — the optimum value occurs at exposures of 8.50×10^{-3} mcs. With this optimum exposure, it is possible to optimize the encoding process by first pre-ex-

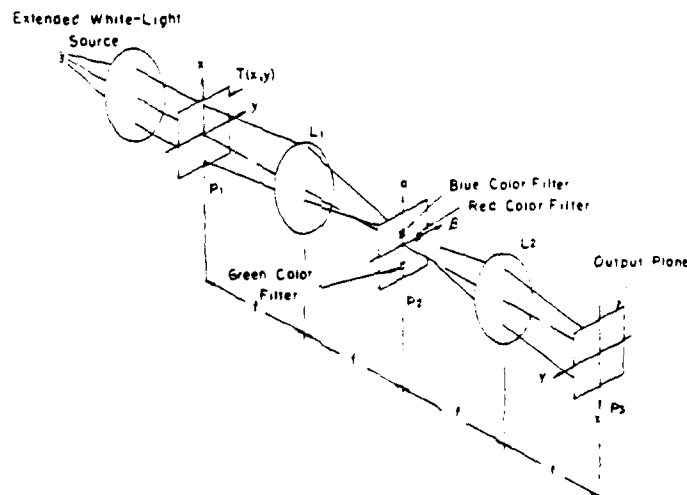


FIG. 4. A white-light false-color encoder.

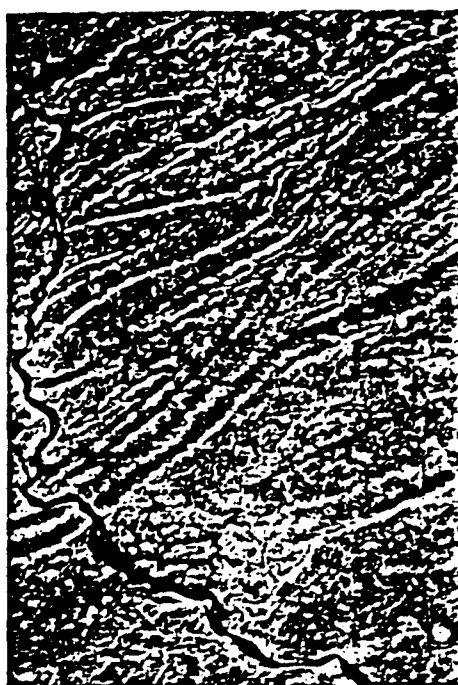


PLATE 1. Multispectral Landsat data with band 4 encoded green and band 5 encoded red.

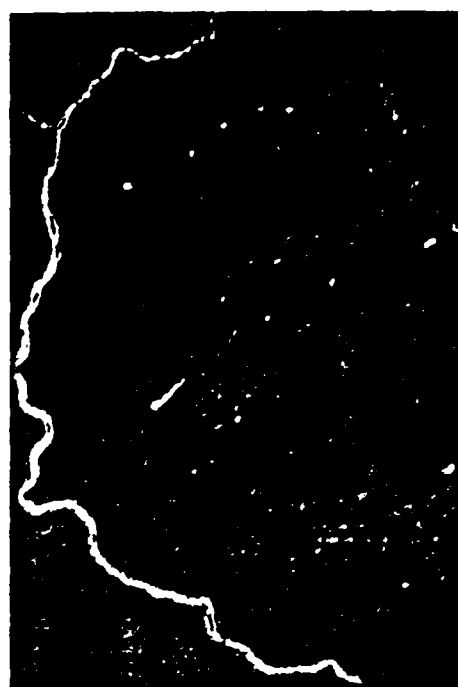


PLATE 2. Multispectral Landsat data with band 5 encoded red and band 7 encoded blue.



PLATE 3. Multispectral Landsat data with band 4 encoded green and band 7 encoded blue.



PLATE 4. Multispectral Landsat data with band 4 encoded green, band 5 encoded red, and band 7 encoded blue.

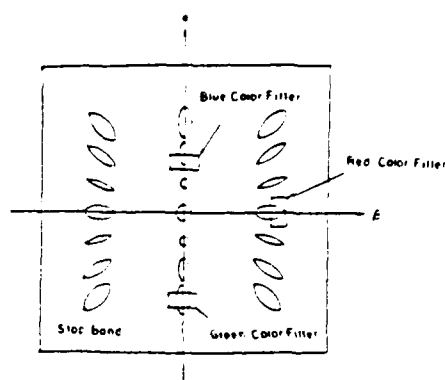


FIG. 5. Fourier plane color filtering.

posing the film beyond the toe region of the diffraction efficiency versus log exposure curve. Then the remaining exposure is subdivided into three regions, by taking into account the linear transmittant exposures of the three encoded images.

In false-color compositing, we use Kodak primary color filters 25, 47B, and 56 in the Fourier plane, as shown in Figure 5. A xenon-arc lamp is used as the extended white-light source for the false-color encoding technique shown in Figure 4.

RESULTS OF FALSE-COLOR ENCODING

The results of the false-color encoding of the Landsat multispectral scanner data are shown in Plates 1 through 4. In Plate 1, where band 4 is encoded green and band 5 is encoded red, the Susquehanna River and small bodies of water are delineated as deep red. The islands in the Susquehanna River are easily distinguished. Strip mines are dark red, urban areas (Harrisburg) are medium red, and agricultural lands are light red, orange, and yellow. Forested areas are green.

When red-encoded band 5 is combined with blue-encoded band 7 (Plate 2), the Susquehanna River is shown as a violet color. Small lakes and reservoirs appear as bluish hues. Some of the surface-mined areas appear as a light violet color, along with some of the bare fields in the agricultural valleys. The forested regions are dark blue and the agricultural areas are red. Urban areas are not delineated.

Water appears as several shades of blue when band 4 is encoded green, and band 7 is encoded blue (Plate 3). Northeast-southwest trending streams are also evident near the center of the image. Surface-mined areas are a much darker blue, and can be easily distinguished from water. Forested areas are most clearly distinguished on this image product as light green. The dark green areas are agri-

cultural regions. Urban areas and strip development along major highways appear as dark blue to black in color.

When all three bands of the Landsat data are encoded (Plate 4), the Susquehanna River appears as violet, and the other bodies of water as shades of blue. The surface mines and urban areas are dark red. The agricultural valleys are orange and the forested regions are green.

The images presented in Plates 1 through 4 show the results of false-color encoding using a white-light optical processor. Six bands would be the practical limit for encoding. This approach for generating false-color composites has great potential. The white-light system is a high resolution color encoder. In principle, the resolution of the color encoded image can be as high as the original monochrome transparency. The white-light encoder is easy to construct and can be assembled for costs of less than \$5,000. Once constructed, the system is also easy to operate. Therefore, this system offers a new and inexpensive approach to the development of false-color composites.

ACKNOWLEDGMENTS

Paper No. 6888 of the Journal Series of the Pennsylvania Agricultural Experiment Station. The authors would like to gratefully acknowledge the financial assistance of the Office of Scientific Research, U. S. Air Force, and the Office of Health and Environmental Research, U. S. Department of Energy.

REFERENCES

- Andrews, H. C., A. B. Tescher, and R. P. Kruger: 1972, Image Processing by Digital Computer *IEEE Spectrum* 9:20-32.
- Chang, B. J., and K. Winick: 1980, Silver-halide gelatin hologram, *Society of Photo-optical Instrumentation Engineers* 215:172-177.
- Chao, T. H., S. L. Zhuang, and F. T. S. Yu: 1980, White-light Pseudocolor Density Encoding Through Contrast Reversal, *Optical Letters* 5:226-228.
- Smuth, H. M.: 1977, Basic Holographic Principles, Chapter 1 in *Holographic Recording Materials* (H. M. Smuth, Ed.) Springer-Verlag, NY.
- Upatueks, J., and C. Leonard: 1966, Diffraction Efficiency of Bleached, Photographically Recorded Interference Patterns, *Applied Optics* 5:83-89.
- Yu, F. T. S.: 1983, *Optical Information Processing*, Wiley-Interscience Publishing Co., NY.

(Received 26 April 1984; accepted 25 September 1985; revised 5 November 1985)

SECTION XXII

Low-Cost White-Light Processor

A Low-Cost White-Light Optical Processor for the Undergraduate Optics Laboratory

FRANCIS T. S. YU, SENIOR MEMBER, IEEE, AND H. M. MUELLER

Abstract—Techniques of white-light optical signal processing are coupled with a relatively unsophisticated system featuring low cost, portability, and high processing power-to-cost ratio. The low-cost white-light optical processor (LCP) offers educators and businesses a powerful teaching aid while providing a system capable of optical processing usually associated with complex optical systems. Experimental results are provided for four processing techniques applied to the system. The methods applied are: scanning optical correlation and convolution, color schlieren optical processing, processing of bubble chamber event photographs, and density pseudocolor encoding. A full list of system equipment and details of the system construction are included. Emphasis is on the processing power available for low cost, making this a tool to be utilized in undergraduate optics laboratory courses.

I. INTRODUCTION

UNDERGRADUATE optics laboratory courses are often restricted in class size due to the high cost of optical systems. Modern optical processing systems are most often a complex array of equipment. A simple optical processor offers distinct advantages over complex systems for some processing techniques. Such a simple system is of immense interest to educators and businesses if it can be offered at a low cost.

Development of coherent optical processing techniques (those using a coherent light source) has taken great strides since the invention of the laser. This has tended to obscure a parallel development of noncoherent optical processing techniques. In fact, much of optical processing predates the laser and is thus based on incoherent processing techniques which are based on the use of an incoherent or "white-light" source. Rogers [1] presents a review of early incoherent processing methods. Some of these early techniques are still used today.

Coherent optical processing is conceptually simple. Its basis is the ability to operate on the complex amplitude light distribution formed by a coherent source, but most authors agree that the major problem with coherent optical processing is the accompanying artifact noise [2]–[4].

In contrast to the use of a coherent light source is the utilization of an incoherent or white-light source. The white-light source can be made to appear more coherent at the input plane of the optical processor by the independent manipulation of the temporal coherence and spatial

coherence of a wide-band or white-light source, where the desired degree of coherence is specified by the requirements of the particular process of interest. Thus, the white-light processor can operate in both an incoherent mode or a partially coherent mode, and can therefore process signals in complex amplitude [3] such as the coherent processor. The white-light processor is of primary interest herein, and its advantages are worth repeating.

The coherent source is most often quite expensive. The white-light source is much less so and can even be an inexpensive slide projector, as in this system. The alignment and operation of a coherent system is generally complex and sensitive to vibration and other environmental factors. The white-light processor is not as sensitive and thus lends itself better to use in a less strictly controlled laboratory environment.

The foremost advantage of the white-light processor, without question, is its ability to suppress the noise normally associated with coherent optical processing. Yet by using the white-light processor in a partially coherent mode, it can process in complex amplitude, as a coherent optical processor, thus showing a simultaneous combination of the attributes of a coherent system and an incoherent system.

The white-light processor is also immensely better suited for color optical processing because of its wide-band spectral content. Coherent optical processing in color requires the use of multiple coherent sources thereby doubling or tripling the cost of the system source.

II. MOTIVATION

To demonstrate the abilities of simple optical processing systems and their application to undergraduate optics labs, the low-cost white-light optical processor, herein after referred to as the LCP, has been developed. The motivation to develop such a low-cost processor may be suspect to some now that high technology and sophisticated equipment are visible in nearly all of our lives. Yet to the educator who requires optical equipment for an undergraduate level optics lab, or to the young engineering firm, a less sophisticated (i.e., less expensive) but adequate optical processing system is attractive.

The LCP is thus based on the philosophy of seeing how much can be done with how little. There is an elegance in turning to the basic tools that the early researchers in optical processing used and applying more recently developed techniques to them.

Manuscript received June 8, 1984; revised October 15, 1984. This work was supported by the U.S. Airforce Office of Scientific Research under Grant AFOSR-83-0140.

The authors are with the Department of Electrical Engineering, the Pennsylvania State University, University Park, PA 16802.

III. CONSTRUCTION

The LCP is built on a base of $\frac{3}{4}$ in plywood. The lenses are held in wooden mounts that are slotted to allow adjustments along the wooden rails attached to the base. Each rail is faced on one side with a metal strip to allow a screw in each lens mount to tighten on the rail, fixing the mount in place. Object transparencies and filters for experiments are held in mounts which are similar to the lens mounts in their operation. Translators were fabricated in a machine shop and run on a simple uncalibrated machine screw. The entire base is mounted on height-adjustable bolts serving as legs at each corner. The complete LCP is shown in Fig. 1. Normally, for good vibration isolation, the slide projector is placed on an adjacent stand. A complete list of equipment is shown below.

Equipment	Quantity	Model
1) Lens and mount	2	Wollensak 209 mm f/4.5 Raptar Copy Lens
2) Slide projector	1	Kodak 600H with 300 W Lamp
3) Transparency mount	3	
4) LCP base with rails	1	
5) Translators	2	
6) Vibrating mirror	1	General Scanning, Inc. Model G330
7) Photodetector	1	
8) Signal generator	1	
9) Oscilloscope	1	

The design of the LCP is by no means optimal. Substitution of materials and equipment could easily be affected in later investigations. It is, however, a simple system.

The copy lenses are not achromatic, so some chromatic aberration of color image is inherent, although not limiting. The photodetector is a photodiode powered by self-contained batteries [5], but any detector available is suitable. The vibrating mirror is mounted on a 60 Hz solenoid, driven by a sine wave generator. The signal generator and oscilloscope used in this system were not low cost, as is the other equipment, but low-cost versions of these two items do exist.

Three of the four optical processing techniques investigated required only items 1-4 of the equipment list. Thus, the LCP is truly a low-cost, simple, and portable white-light optical processor.

IV. EXPERIMENTAL RESULTS

Four optical information processing techniques were used with the LCP. The first showed the LCP as an optical scanner correlator. Second, the LCP was used as a color schlieren optical system. Third, the LCP was used to process bubble chamber photographs with several different spatial frequency filtering techniques. Finally, the LCP

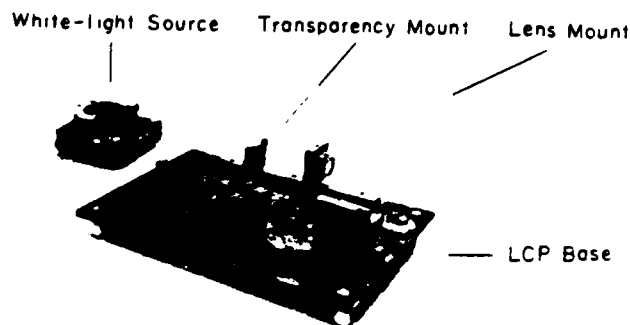


Fig. 1. A photograph of the low-cost white-light optical processor (LCP).

demonstrated density pseudocolor processing abilities. These techniques demonstrate the wide range of the applications with which the LCP can be used to aid in teaching optics and optical processing. Many additional optics experiments can be performed using the LCP.

A. Scanner Optical Correlator

The LCP is configured as an optical correlator [5] to demonstrate the principles of correlation and convolution as shown in Fig. 2. Distances between components are in terms of focal lengths. The pinhole is a slide placed in the slide projector. $L1$ and $L2$ are nearly identical lenses—the angle between them is not critical. The photodetector is at the focus of $L2$. The signal generator drives the vibrating mirror to scan the image of $f(x, y)$ across the transparency $g(x, y)$. By simply reversing $f(x, y)$ to form $f(x, -y)$, the convolution of the two functions can be observed.

The signal transparencies $f(x, y)$ and $g(x, y)$ are shown in Fig. 3(a) along with a calculated result for the correlation and convolution of these transparencies. The output irradiance of the optical correlator is shown in Fig. 3(b). The output shows the result of the correlation of the two transparencies and their convolution. Slight differences which occur between the calculated results and the scan profiles must be attributed to the photodetector. It is clear that the LCP can effectively demonstrate correlation and convolution in one dimension for a simple slit pattern.

A more complex problem is the correlation of transparencies in both the x and y directions. To demonstrate, the second transparency $g(x, y)$ was mounted on a translator to allow adjustment in the x direction. The maximum output of the photodetector was found by manually adjusting the translator in the x direction. That position then represented the highest level of correlation in the x and y directions of the two transparencies. Fig. 4 shows the signal transparencies and the results of this two-dimensional correlation. Note that although the triangle and star shape can be circumscribed inside the circle, the autocorrelation function is higher in amplitude than any of the cross correlations with the other shapes.

A problem related to correlation is the performance of correlation of color transparencies. In this case, we consider not only a spatial correlation but a frequency or spectral correlation as well.

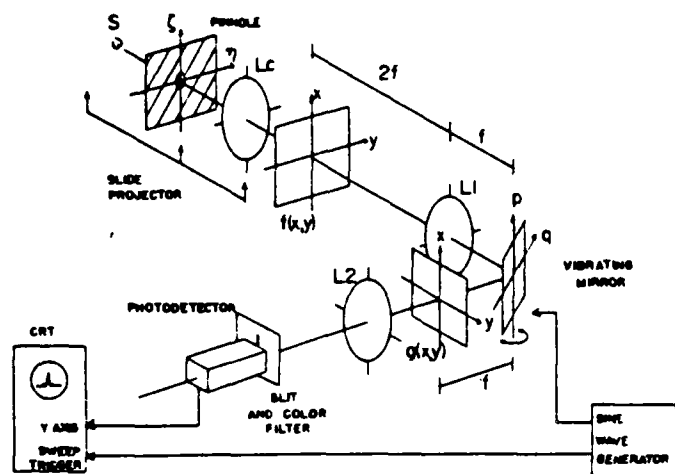


Fig. 2. Schematic diagram of a scanner optical correlator.

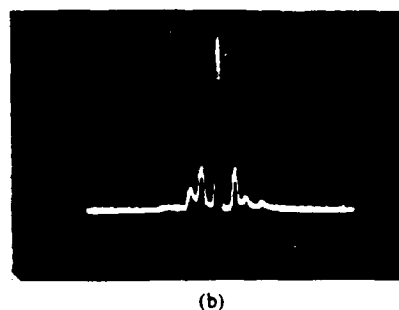
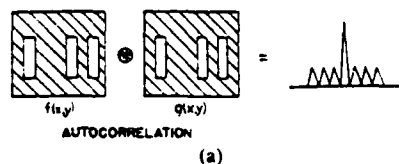
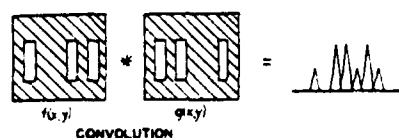


Fig. 3. (a) Calculated result for convolution autocorrelation of a three-slit transparency. (b) Output intensity distributions of the convolution and the autocorrelation obtained from the LCP.

The response of the photodetector was made nearly panchromatic by placing a blue-green color filter at the input of the detector. The transmittance of the first transparency was controlled by matching a neutral density filter with the red and green color filters as shown in Fig. 5.

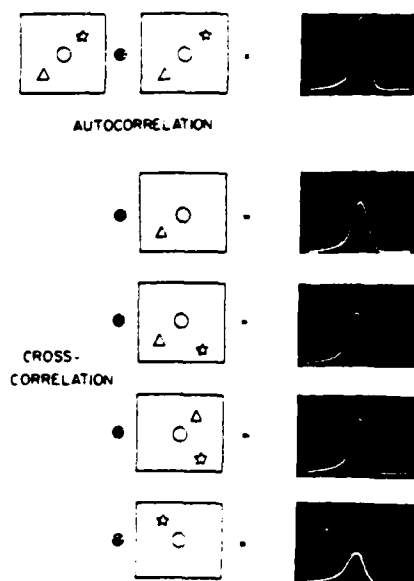


Fig. 4. Output photometer traces of a two-dimensional correlation for various signal transparencies.

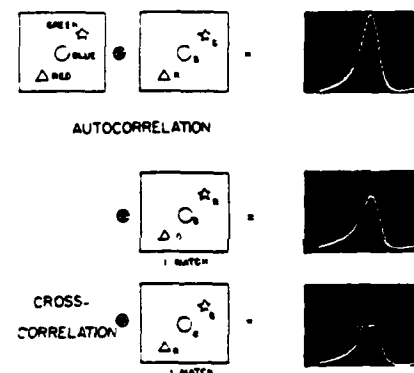


Fig. 5. Spectral correlation of two transparencies.

The results of the correlation of these transparencies, seen in Fig. 5, are expanded to show a single sweep of the correlator. The relative heights of the outputs show that although a high degree of spatial correlation exists in the two transparencies (in fact they are identical), the degree of spectral correlation causes a difference in the correlation of the two transparencies.

It is clear, in each case, that the LCP can be used as a low-cost method of demonstrating and teaching the principles of correlation and convolution. The fact that even more complex problems in correlation of two-dimensional and color transparencies can be shown is a bonus.

B. Color Schlieren Optical Processing

The German word "schlieren" has come to mean, in a transparent medium, a local inhomogeneity which causes a diffraction of light [6]. The schlieren method is used extensively in visualization of flow in aerodynamic and thermodynamic research, but the technique can be applied to many flow visualization problems.

The schlieren method is an incoherent processing tech-

nique and the processor is therefore linear in irradiance. The diffraction of the light passing through the transparent object is proportional to the derivative of the object phase [4] which, in a fluid, is dependent on the change in refractive index [8].

In color schlieren optical processing [6]–[9], the LCP is configured as shown in Fig. 6. The transparent object is located at $P1$. Distances are in terms of focal lengths. Again $L1$ and $L2$ are nearly identical lenses. The source encoding masks used in the system are shown in Fig. 7(a), and the corresponding filters used are shown in Fig. 7(b). The filters were placed in uncalibrated translators to allow for adjustment in the p and q directions.

To further demonstrate the ability of the color schlieren processing technique to provide information about a transparent object, a stationary three-dimensional object was presented at the input plane $P1$ in the form of a water drop. The water drop can be considered as a transparent object which refracts light due to a gradient in the thickness of the water drop.

From Fig. 8(a), it is clear that some difficulty exists in the interpretation of a schlieren photograph without color. The light and dark areas do impart some information concerning the contours of the water drop, but do not clearly indicate the direction of the inhomogeneities. In the photo of a color schlieren image, Fig. 8(b) (costs for color printing prohibit showing the color image—color prints are available from the authors), the direction and slope of the contours are much more clearly indicated. The colors are very vivid and their blending indicates the direction of the contours in two dimensions.

Fig. 8 also shows two of the limitations of the LCP. The dark areas of the photo indicate light which is diffracted past $L1$, the transform lens of the white-light system. With larger lenses, these dark areas of the output image would contain information about the input object. Normally, in flow visualization problems, this limitation would not be as severe as it is here. Second, light appears outside the boundary of the water drop. Since the lenses are not achromatic these inconsistencies are attributable to the quality of the lenses. These are merely distractions, however, since they do not obstruct the object image.

Finally, after demonstrating the directional qualities and informational advantages of color in Fig. 8, Fig. 9 is a black-and-white reproduction of a color photo which shows the flow of heated air from a soldering iron placed at $P1$, the input plane of the system. The color in the photo changes from blue to green to red depending on the direction of the heated air flow. There are subtle color changes as the flow changes direction. Although no quantitative data are presented, the value of the visualization of such a flow of a gas is obvious and the applications numerous. The ability to use the LCP in such a situation makes it a valuable low-cost analytical tool.

C. Optical Processing of Bubble Chamber Event Photographs

Processing the immense number of bubble chamber photographs gained from a single high-energy experiment

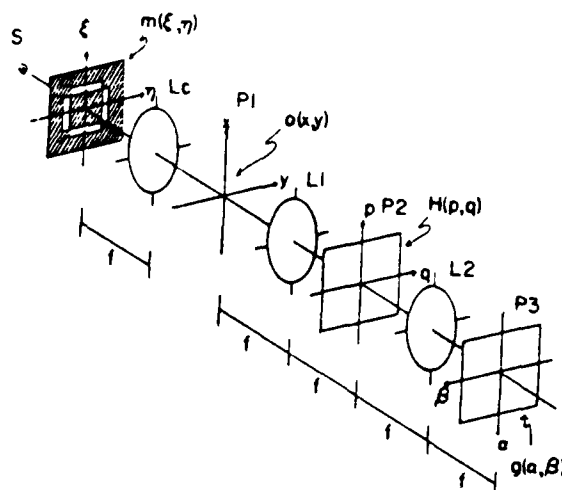


Fig. 6. Schematic diagram of color schlieren optical processor. $m(\xi, \eta)$ is the source encoding mask. $H(p, q)$ is the spatial frequency filters.

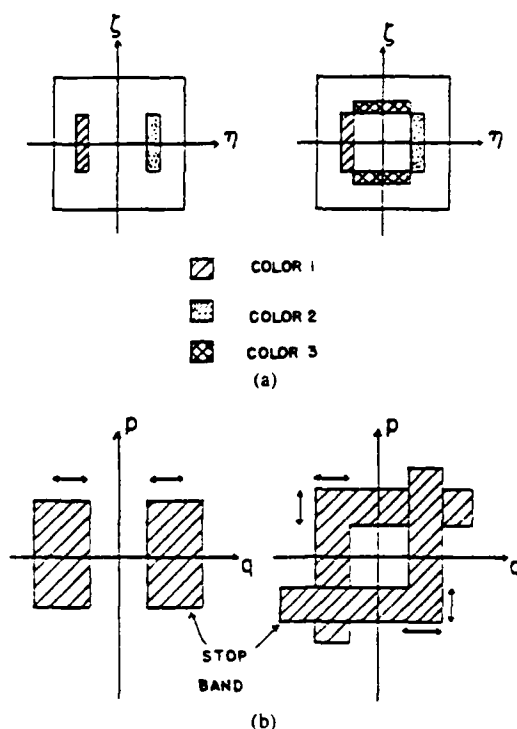


Fig. 7. (a) Source encoding masks for color schlieren optical processing. (b) Spatial frequency filters.

has emerged as a major, labor-intensive task [10]. An optical technique to obtain the necessary data is attractive in terms of labor saved and in additional features that the optical processing offers over standard hand processing.

The principles of spatial frequency filtering used in the optical processing of these photographs can be traced to experiments done by Abbe (1873) and Porter (1906) [11]. These principles are the basis of much of optical processing, and this technique is a good demonstration of those principles. In order to process bubble chamber event photographs [10], the LCP is configured as the standard white-light optical processor as shown in Fig. 10. The input to the system, placed at plane $P1$, is shown in Fig. 11 and represents a "draftsman's version" of a bubble chamber event. The horizontal lines are called "beam tracks" and



(a)



(b)

Fig. 8. (a) One-dimensional schlieren optical processing. Source mask had no color. (b) Black-and-white picture of a two-dimensional color schlieren optical processing.



Fig. 9. Black-and-white picture of a color schlieren optical processing showing flow of heated air from tip of soldering iron.

are normally of no interest. The angled "event tracks" are the signals of interest, so their enhancement is the objective of the processing.

Four different filtering schemes were used at plane P_2 . The performance of each filter is presented to show the range of processing possible with the LCP.

The first filtering scheme used was a stop-band filter shown in Fig. 12(a). The corresponding output of the LCP is seen in Fig. 13(a). Note that ideally the beam tracks are totally suppressed, but in practice there is usually just a marked contrast difference between them and the event tracks. Normally, the enhancement of the event tracks, as shown, is the effect required.

The second filter is a directional high-pass filter as shown in Fig. 12(b) oriented in the direction of the event tracks' spatial frequency diffraction. The corresponding

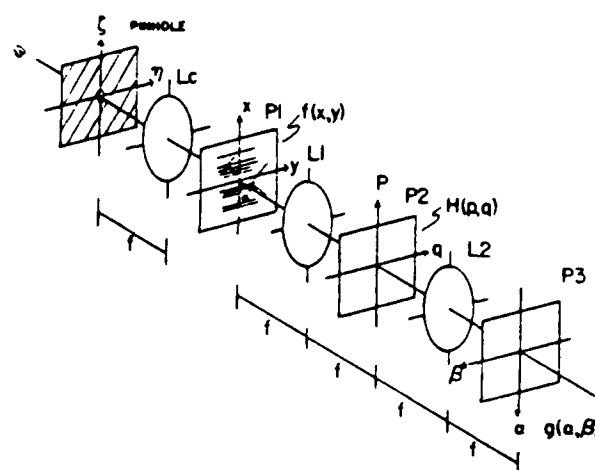


Fig. 10. Schematic diagram for optical processing of bubble chamber event photographs.

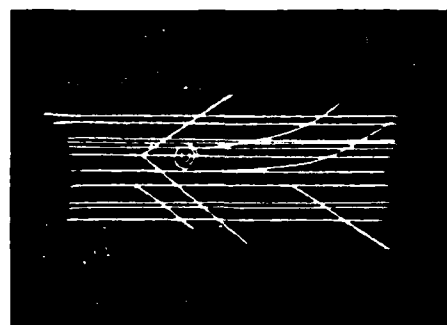


Fig. 11. A bubble chamber event photograph.

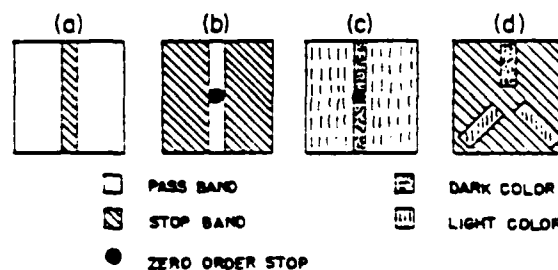


Fig. 12. Spatial frequency filters used for processing bubble chamber event photographs. (a) Stop-band filter. (b) Directional high-pass filter. (c) Color filter with zero-order stop. (d) Color directional high-pass filter.

ideal output of the LCP is seen in Fig. 13(b). Usually the beam tracks are almost completely suppressed and only those event tracks at the proper scattering angle are shown. This is most useful in measuring these angles. Note that a two-slit filter should be made which would show both directions of the event tracks, allowing the angle between the two event tracks to be found.

The third filter brings in the dimension of color as shown in Fig. 12(c). Rather than suppress the beam tracks, a color contrast is produced in the tracks as seen in Fig. 14(a) which is a black-and-white reproduction of a color photo. The beam tracks are blue and the event tracks are red.

The fourth filter is shown in Fig. 12(d). This method is least accurate in portraying the scattering angles, yet provides the clearest color coding and is seen in the black-

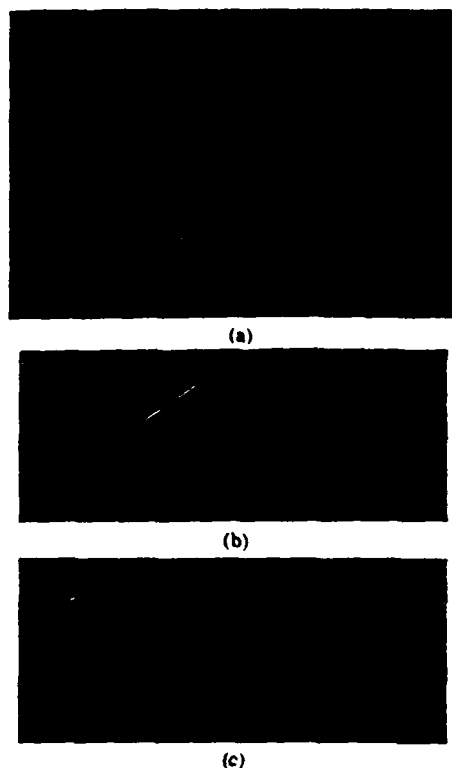


Fig. 13. (a) Output of LCP using stop-band filter to suppress beam tracks. (b) and (c) Output of LCP using directional high-pass filter to show only event tracks in a particular direction.

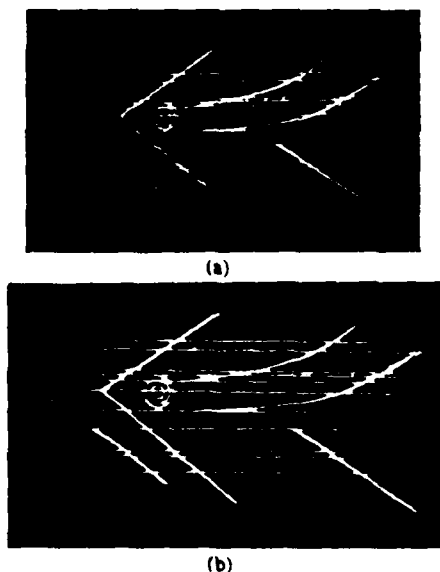


Fig. 14. (a) Black-and-white picture of a color output of LCP using color filter with zero-order stop. Beam tracks are blue and event tracks are red. (b) Black-and-white picture of a color output of LCP using color directional high-pass filter. Beam tracks are yellow and event tracks are red.

and-white photo Fig. 14(b). The beam tracks are bright yellow and the event tracks are red. The addition of color clearly delineates the areas of interest.

As stated before, these filtering methods generalize to any object wherein a regular pattern may obscure a point of interest having a different directional orientation. A scratch on an integrated circuit mask could easily be detected using the LCP in this optical processing mode.

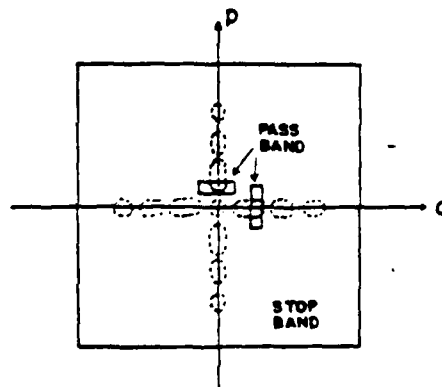


Fig. 15. Spatial frequency filter for pseudocolor encoding.

D. Density Encoded Pseudocolor Optical Processing

For pseudocolor optical processing through contrast reversal [4], the LCP is configured as a standard white light optical processor, as in Fig. 10, with a different object image at plane P_1 and a different filter at plane P_2 . The filter used at the spatial frequency plane P_2 is seen in Fig. 15. The color filters shown in the figure are used during only part of the process.

The object image was contact printed to yield both the positive and negative images of the object. These two images were sequentially recorded on a third sheet of film and encoded by the use of a 40 lines/mm Ronchi grating. Since the sampling theorem states that we must sample at twice the highest frequency that we wish to encode, the highest spatial frequency encoded properly is 20 lines/mm. This is also nearly the limit of accuracy in hand alignment of the positive and negative images during the encoding process. The recorded image was then chemically bleached during the film processing to yield a transparent phase object with a high diffraction efficiency.

Since, in pseudocolor processing, we are most interested in the quality of the color output of the processor, Fig. 16 shows a black-and-white photo of a pseudocolor image of an X-ray. The more dense parts of the hand are green while the least dense parts appear in red. Smaller bones and tissues are more easily seen in color rather than in a conventional black-and-white X-ray transparency. The colors are very rich and provide better visual discrimination than a simple black-and-white image.

V. CONCLUSION

The LCP, a low-cost white-light optical processor, has been demonstrated. The system is simple and portable, yet it is capable of performing many complex optical processing techniques. The versatility of the processor and its low cost make it especially suitable for educational instruction.

Four techniques of optical processing were demonstrated using the LCP. Correlation and convolution of two signal transparencies and the correlation of the spectral content of two transparencies were demonstrated. The LCP was shown to be able to perform schlieren optical



Fig. 16. Black-and-white picture of a pseudocolor output of LCP. More-dense parts of the X-ray picture appear in green while least-dense parts are red.

processing for several different transparent input objects. Optical processing of bubble chamber event photographs showed the spatial frequency filtering capabilities of the LCP to simplify a very tedious, labor-intensive job. Finally, a demonstration of density pseudocolor processing was presented.

Considering these processes, the message is clear—a low-cost optical processor such as the LCP is able to aid in teaching complex techniques of optical processing that are normally associated with specialized, sophisticated optical systems. There is an elegance in the fact that some of the optical processing techniques demonstrated herein were pioneered over a century ago. For the next 100 years, they were researched, refined, and applied in increasingly accurate and complex optical systems, yet now are finding renewed interest when applied to a system more akin to those early processors.

REFERENCES

- [1] G. L. Rogers, *Noncoherent Optical Processing*. New York: Wiley, 1977.
- [2] W. T. Rhodes and A. A. Sawchuck, "Incoherent optical processing," in *Optical Processing Fundamentals*, S. H. Lee, Ed. New York: Springer-Verlag, 1981.
- [3] S. H. Lee et al., "Coherent optical processing," in *Optical Processing Fundamentals*. Berlin, Germany: Springer-Verlag, 1981.
- [4] F. T. S. Yu, *Optical Information Processing*. New York: Wiley, 1983.
- [5] R. E. Haskell, "Fourier analysis using coherent light," *IEEE Trans. Educ.*, vol. E-14, p. 880, 1971.
- [6] W. Merzkirch, *Flow Visualization*. New York: Academic, 1974.
- [7] G. S. Settles, "Color schlieren optics—A review of techniques and applications," in *Flow Visualization II*, W. Merzkirch, Ed. New York: Hemisphere Publications, 1982.
- [8] D. W. Holder and R. J. North, *Schlieren Methods*. London, England: Her Majesty's Stationary Office, 1963.
- [9] G. S. Settles, "A direction-indicating color schlieren system," *AIAA J.*, vol. 8, p. 2282, 1970.
- [10] D. G. Falconer, "Optical processing of bubble chamber photographs," *Appl. Opt.*, vol. 5, p. 1966.
- [11] J. W. Goodman, *Introduction to Fourier Optics*. New York: McGraw-Hill, 1968.

Francis T. S. Yu (M'66-SM'80), photograph and biography not available at the time of publication.

H. M. Mueller, photograph and biography not available at the time of publication.

SECTION XXIII

White-Light Talbot Interferometer

REAL-TIME COLOR-CODING OF DEPTH USING A WHITE-LIGHT TALBOT INTERFEROMETER

S. JUTAMULIA, T.W. LIN and F.T.S. YU

Department of Electrical Engineering, The Pennsylvania State University, University Park, PA 16802, USA

Received 5 December 1985; revised manuscript received 4 February 1986

A method for real-time color-coding of depth using a white-light Talbot interferometer is presented. Based on the fact that the Talbot planes of a grating are formed at different distances for different colors, the topographical structure of a surface can be color-coded in real-time. Experimental results are provided to verify the proposed method.

1. Introduction

The technique of depth sensing has become an important issue for advanced industrial inspection [1]. Generally, the depth measurement can be undertaken optically by means of interferometry [2] and moiré effect [3] for small and large depth variations, respectively. However, these methods only provide relative depth information. Methods based on the Fresnel diffraction theory providing absolute depth information have been presented recently [4,5]. In these methods, the depth information is recovered from the distance-modulated Talbot image of a grating with coherent processing. A white-light processor is then applied to display the information in pseudocolor [5].

The white-light processor has been used for color coding in many ways. Besides the exploitation of its excellent low-noise performance [6], the generation of color fringes in the Talbot interferometer [7] has been utilized to encode phase information [8]. When a grating is illuminated by a collimated monochromatic light, an image of the grating will be formed at the multiples of a certain distance. This phenomenon is known as Talbot effect [7]. By means of a white-light illumination, the color Talbot images are generated at different distances. In other words, the color of the Talbot image contains length information. If a surface is exposed to reflect the Talbot image, the depth information of the surface is surely encoded in the color of the Talbot image at the observation plane.

Therefore, a direct color-coding of depth can be achieved by using a white-light Talbot interferometer. The present method will provide a real-time color-coding of depth without using liquid crystal light valve and TV camera system as in the previous method [5].

2. Principle of operation

Theoretical description of the Talbot effect has been presented in a great detail in the literature [7]. This section is essentially devoted to give a theoretical concept for the special application concerned with the color-coding of depth.

Consider that a monochromatic plane wave is incident on a Ronchi grating. The field behind this grating is

$$u(x, y; 0) = \sum_{n=-\infty}^{\infty} A_n \exp(2\pi i n x / d), \quad (1)$$

where d is the period of the grating, A_n is the n th coefficient of the Fourier series. The angular plane wave spectrum at the grating is given by the Fourier transform of eq. (1) as

$$\tilde{u}(\nu, \mu; 0) = \sum A_n \delta(\nu - n/d) \delta(\mu). \quad (2)$$

The propagation of the angular plane wave spec-

trum is formulated by the Rayleigh-Sommerfeld-Debye (RSD) theory as [7]

$$\bar{u}(\nu, \mu; z) = \bar{u}(\nu, \mu; 0) \exp[2\pi i(1 - \lambda^2(\nu^2 + \mu^2))^{1/2} z / \lambda]. \quad (3)$$

Correspondingly, the angular plane wave spectrum at a distance z from the grating becomes

$$\bar{u}(\nu, \mu; z) = \sum A_n \delta(\nu - n/d) \delta(\mu) \times \exp[2\pi i(1 - \lambda^2 n^2/d^2)^{1/2} z / \lambda], \quad (4)$$

and the optical field can be expressed as

$$u(x, y; z) = \sum A_n \exp(2\pi i n x / d) \times \exp[2\pi i(1 - \lambda^2 n^2/d^2)^{1/2} z / \lambda]. \quad (5)$$

Assuming that the grating is rough enough such that $d \gg |\lambda|$, one can approximate that

$$(1 - \lambda^2 n^2/d^2)^{1/2} = 1 - \frac{1}{2} \lambda^2 n^2 / d^2. \quad (6)$$

Eq. (5) then becomes

$$u(x, y; z) = \exp(2\pi i z / \lambda) \times \sum A_n \exp(2\pi i n x / d) \exp(-i\pi n^2 \lambda z / d^2). \quad (7)$$

Consider that an identical grating is placed at a distance z from the first grating. The amplitude transmittance of this grating can be expressed as

$$G(x, y) = \sum_{m=-\infty}^{\infty} A_m \exp(2\pi i m x / d). \quad (8)$$

After passing through the second grating, the field behind this grating becomes

$$p(x, y; z) = u(x, y; z) G(x, y). \quad (9)$$

And the total intensity is

$$P = \iint |p(x, y; z)|^2 dx dy. \quad (10)$$

According to the Parseval theorem, the total intensity can also be expressed as

$$P = \iint |\bar{p}(\nu, \mu; z)|^2 d\nu d\mu. \quad (11)$$

where $\bar{p}(\nu, \mu, z)$ is the Fourier transform of $p(x, y; z)$, and can be expressed as

$$p(\nu, \mu; z) = \bar{u}(\nu, \mu; z) * \bar{G}(\nu, \mu), \quad (12)$$

where $*$ denotes a convolution operation and $\bar{G}(\nu, \mu)$ is the Fourier transform of $G(x, y)$. By substituting eq. (4) with the approximation of eq. (6) and the Fourier transform of eq. (8) into eq. (12), it yields

$$\bar{p}(\nu, \mu; z) = \exp(2\pi i z / \lambda) \times \sum_n \sum_m A_n \exp(-i\pi n^2 \lambda z / d^2) \times A_m \delta(\nu - (n - m)/d) \delta(\mu). \quad (13)$$

Neglecting the unimportant phase factor, $\exp(2\pi i z / \lambda)$, the total intensity becomes

$$P = \iint \left| \sum_n \sum_m A_n A_m \exp(-i\pi n^2 \lambda z / d^2) \times \delta(\nu - (n - m)/d) \delta(\mu) \right|^2 d\nu d\mu. \quad (14)$$

It is apparent from this equation that the total intensity P is maximum when

$$z = z_T = k 2d^2 / \lambda. \quad (15)$$

where k is an integer. This condition is known as Talbot distance.

In order to illustrate eq. (14) more clearly, a model of cosine grating is applied. The amplitude transmittance of a cosine grating is

$$C(x, y) = 1 + \frac{1}{2} \exp(2\pi i x / d) + \frac{1}{2} \exp(-2\pi i x / d). \quad (16)$$

This equation can be expressed in the form of eq. (1) where

$$A_0 = 1, \quad A_1 = A_{-1} = \frac{1}{2}; \\ A_n = 0, \quad \text{for } |n| = 1, \quad n \neq 0. \quad (17)$$

With the same approximation applied on eq. (8), the total intensity becomes

$$P = c + \cos(\pi \lambda z / d^2), \quad (18)$$

where c is an arbitrary constant. It is apparent again from eq. (18) that the total intensity P is maximum when

$$z = z_T = k 2d^2 / \lambda.$$

The distance z_T is again the Talbot distance as stated previously in eq. (14). Therefore, the strongest color observed indicates the distance between two gratings.

3. Experimental setup

An optical setup can be constructed to conduct the depth measurement as shown in fig. 1. A white-light point source is collimated by an achromatic lens L_1 to illuminate the first grating G_1 . Every monochromatic light contained in the white-light possesses Talbot plane at different distance from G_1 . These Talbot planes are imaged on a test surface by lens L_2 . Since the surface is not flat, a colorful grating image is formed on the test surface. The grating image has the same period for all the colors. These colors are corresponding to the topographical structure of the surface. For the surface element closer to the G_1 , a red color is observed, and for the surface element farther away from the G_1 , a blue or violet color ap-

pears. To extract the color of the grating image, the test surface is then imaged by lens L_3 through a beam splitter (BS) on the second grating G_2 . The back side of G_2 is covered with a diffuser to make the output observable.

4. Experimental verification

In practice, the test surface usually has a low reflectivity that is difficult to collect the reflected light. This drawback would restrict the method only applicable to the test surface with a high reflectivity. In order to verify the proposed method, a mirror-like surface was used. In the first experiment, a surface consisting of two different depths was tested. The side projection of the surface is depicted in fig. 2(a). Fig. 2(b) shows the color-coded image of the test surface. Moiré fringes are shown in the picture due to the improper alignment between the orientations of two gratings. Nevertheless, the moiré fringes did not

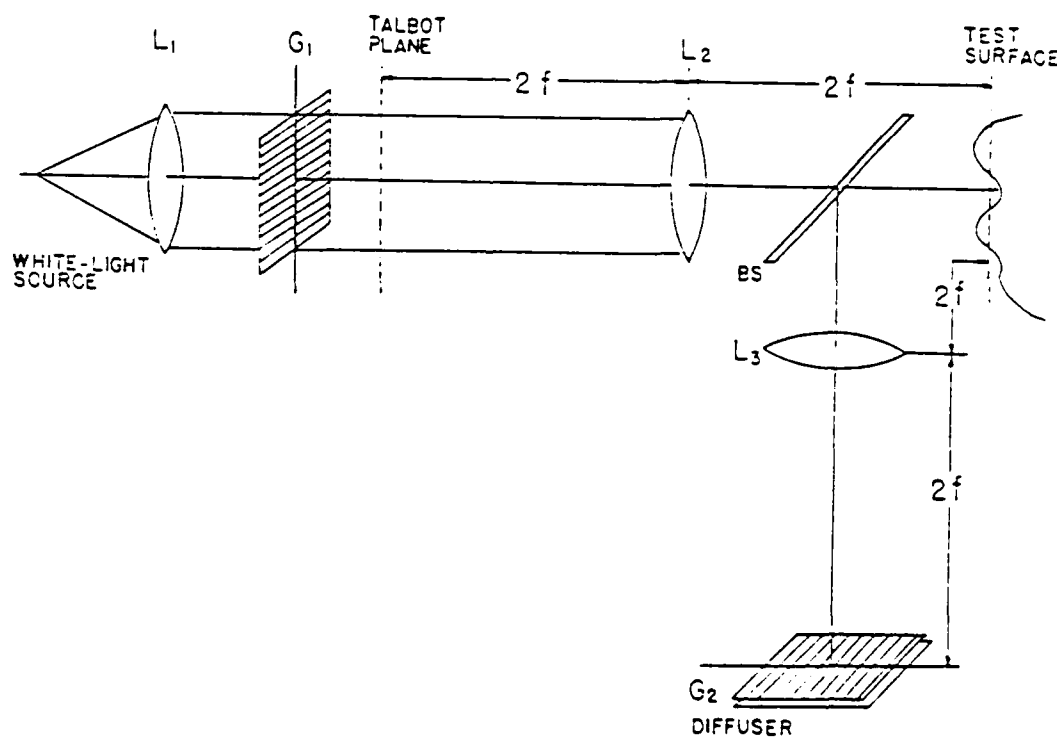


Fig. 1. Experimental setup for real-time depth color-coding using a white-light Talbot interferometer.

affect the color coding. It should be noted that the fringes were blue in the upper part of the picture, and were orange in the lower part. According to the experimental setup as shown in fig. 1, where a 100 lines/inch Ronchi grating and an imaging lens with 380 mm focal length were used, the blue color corresponded to a distance of 773.4 mm from grating G_1 , and the orange color corresponded to a distance of 770.7 mm from G_1 . Therefore, the depth difference was 2.7 mm. This agreed with the real structure of the test surface as shown in fig. 2(a).

Another experiment where a concave mirror was used as a test surface has also been conducted. The

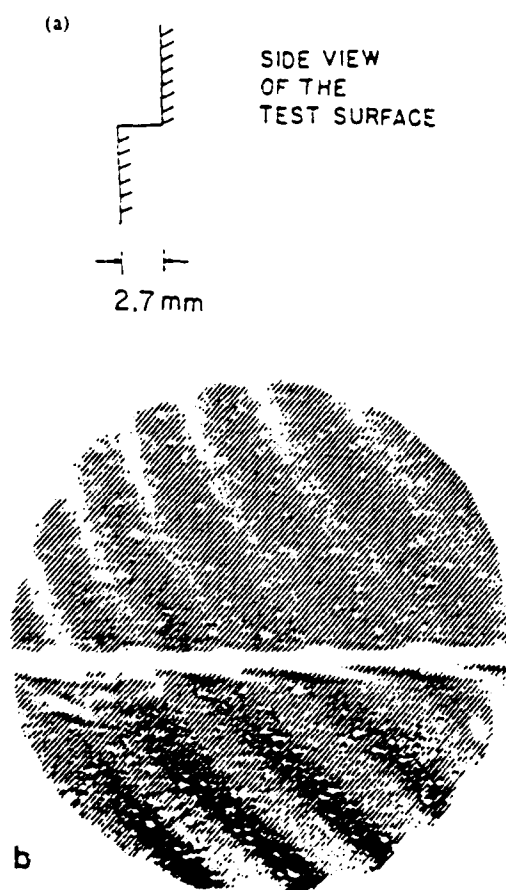


Fig. 2. (a) Side projection of a test surface. (b) Black-and-white picture of the color-coded image of the test surface. Fringes were blue and orange in the upper and lower parts, respectively.

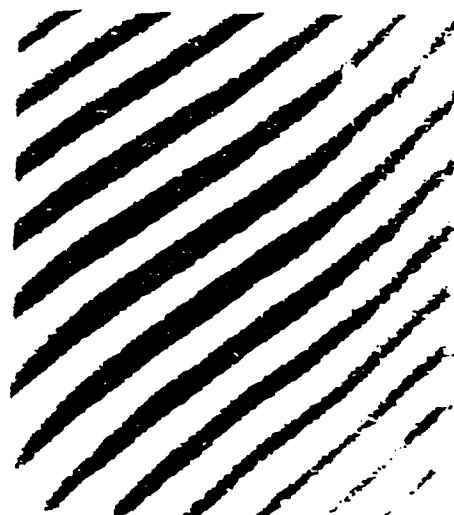


Fig. 3. Black-and-white picture of the experimental results of alignment color-coding. The color of the moiré fringes was gradually changed from red at the left upper corner to blue at the right lower corner.

combination of L_2 and the concave mirror forms the image of the Talbot plane of grating G_1 around the position of the second grating G_2 . In this case, the concave mirror provides the focusing and L_3 can be left out. If the concave mirror is correctly aligned, the moiré pattern observed at the back of G_2 will be a single color. However, if the concave mirror is tilted, the moiré pattern will consist of gradually varying color. Fig. 3 shows an experimental result when the concave mirror is slightly tilted. It was observed that the color of the moiré pattern was gradually changed from red at the left upper corner to blue at the right lower corner.

5. Theoretical restrictions

The encoding color is produced by overlapping the second grating and the surface image. Although the Talbot images of different colors are produced on the test surface, the contrast is too low that the color is difficult to be detected directly. By placing the second grating on the image of test surface, a color moiré fringe pattern having larger fringe distance and

better contrast can be observed. If the second grating is aligned perfectly with the first grating, the moiré fringes disappear and a color pattern corresponding to the topographical structure of the test surface will be produced. It is understandable that the finest element of the test surface to be encoded equals to the period of the gratings.

If the system is correctly focused for one object distance, surface elements somewhat closer or farther away may still be imaged satisfactorily. This range of satisfactory imaging is called the depth of field. By considering that the blur circle due to defocus must be smaller than a grating period, the acceptable depth of field could be defined [5] as

$$l < d/(N.A.), \quad (21)$$

where (N.A.) is the numerical aperture of the system, d is the period of the grating used.

6. Conclusion

We shall conclude that the topographical structure of a surface can be encoded in color based on the Talbot effect. Due to the different distance of the surface element to the first grating, the Talbot images with different color at the surface elements are observed. The contrast of the color is enhanced by

imaging the test surface onto the second identical grating. The color is produced correspondingly to the distance between the test surface and the first grating. Therefore, the topographical structure of a surface can be encoded in color. This method could be useful for machine vision or instant inspection.

Acknowledgement

This research is supported by U.S. Air Force Office of Scientific Research grant AFOSR-83-0140.

References

- [1] T.C. Strand, *Opt. Eng.* 24 (1985) 033.
- [2] W.R.J. Funnell, *Appl. Optics* 20 (1981) 3245.
- [3] J.C. Perrin and A. Thomas, *Appl. Optics* 18 (1979) 563.
- [4] P. Chavel and T.C. Strand, *AlP Conf. Proc.* 65 (1980) 431.
- [5] J.R. Leger and M.A. Snyder, *Appl. Optics* 23 (1984) 1655.
- [6] F.T.S. Yu, *White-light optical signal processing* (Physikalisches Institut der Universität, Erlangen, 1975). (Wiley Interscience, New York, 1985).
- [7] A.W. Lohmann, *Optical information processing* (Physikalisches Institut der Universität, Erlangen, 1975).
- [8] S. Jutamulia, T.W. Lin and F.T.S. Yu, *J. Optics (Paris)*, in press.

ELECTRICAL ENGINEERING DEPARTMENT, PENNSYLVANIA STATE UNIVERSITY
University Park, Pennsylvania

COLOR VISUALIZATION OF PHASE OBJECT USING TALBOT INTERFEROMETER

S. JUTAMULIA, T. W. LIN and F. T. S. YU

MOTS CLES :

Codage couleurs
Visualisation de la phase
Traitement en lumière blanche

KEY WORDS :

Color coding
Phase visualization
White-light processing

Codage en couleurs des objets de phase par interférométrie de Talbot

RÉSUMÉ : On présente une méthode de codage en couleurs d'un objet de phase par les franges de Talbot. Si on éclaire un réseau par un faisceau de lumière blanche collimatée, la distance de l'image de Talbot variera pour différentes couleurs. En plaçant un réseau identique à une certaine distance de l'image de Talbot réelle ou virtuelle, on sélectionne une de ces couleurs. Une représentation en couleurs d'un objet de phase placé entre deux réseaux peut être ainsi obtenue par filtrage spatial. La teinte traduit la dérivée première spatiale de la phase.

SUMMARY : A method of color visualization of a phase object based on Talbot effect is presented. If a grating is illuminated with a collimated white-light, the distance of the Talbot image will differ for different color. By placing an identical grating at a certain distance of negative or positive Talbot image, a single color output is extracted. A color visualization of a phase object placed between two gratings can be performed by a first-order spatial filtering. The hue is related to the first derivative of the phase distribution.

I. — INTRODUCTION

A phase object can be observed by using phase contrast method [1]. The irradiance of the image produced by phase contrast method is directly proportional to the phase distribution of the object, if the phase is small compared to unity [1]. On the other hand, the irradiance of the image produced by the Schlieren method [2] or differential shearing interference microscopy [3] is, however, proportional to the first derivative of the phase distribution. The analogy between the interference of two wavefronts and the Moiré effect leads to the detection of phase object by using two gratings [4]. The image of the phase object formed by these two successive gratings is equivalent to multiple-shearing interference and that can be reduced to triple-shearing or double-shearing interference by the addition of proper spatial filtering [5].

The irradiance variation of a single-color fringe pattern may be traced by photodetector to provide a precise information of phase variation. However, the color-coding of phase variation may give a better visual perception and fast interpretation for human than an irradiance variation does. The advantages of color processing have been described in detail elsewhere [6]. It is indeed an old idea to encode phase information in color, as one can look back to the Schlieren method [6, 7]. Another example of

quantitative color coding of a phase object was shown recently by Wu and Yu [8]. In their method, the color indicating the phase distribution is formed by a mixture of two colors. The hue is directly related to the phase distribution.

The method of color visualization of phase object described in this paper is based upon the Talbot effect [9]. The hue is proportional to the first derivative of the phase distribution. The generation of color Moiré fringes in the Talbot interferometer using two gratings has been pointed out by Lohmann and Silva [4, 5, 9]. Nevertheless, the color visualization of phase object based on the Talbot effect has not been proposed or performed yet.

II. — THEORY

Theoretical description of the Talbot effect has been presented in a great detail in the literature [9]. This section is essentially devoted to give a theoretical concept for the special application of color coding. The Talbot effect is also known as Fourier imaging or self-imaging. If a grating is illuminated by a collimated monochromatic light, an image of the grating is formed at multiples of a distance $z = 2d^2/\lambda$, where d is the grating period and λ is the illumination wave-

length. The negative images of the grating are formed at the distances: d^2/λ , $3d^2/\lambda$, $5d^2/\lambda$, etc.

A complete theory demonstrating that the Talbot interferometer produces an image proportional to the derivative of a phase object has been presented by Silva [5]. This theory is applied further to study the color coding of a phase object in this section. The schematic diagram of the optical setup is shown in figure 1. A white-light point source is positioned at the front focus of an achromatic lens L_1 . After lens L_1 a collimated white-light is produced to illuminate the first Ronchi grating G_1 . The second identical grating G_2 is separated from G_1 by a distance $(z_1 + z_2)$. The phase object to be studied is placed at plane P_1 somewhere between two gratings. The distances of each of the gratings and the object plane P_1 are z_1 and z_2 , respectively. P_2 is the spatial filtering plane, and P_3 is the observation plane.

Consider a collimated white-light incident on the Ronchi grating G_1 . Since white-light contains many wavelengths, for each of these wavelengths the field behind this grating can be expressed as

$$u(x, y; z_1) = \exp(-ikz_1) \sum_{n=-\infty}^{\infty} c_n \exp(2\pi i n x/d), \quad (1)$$

where Fourier series denotes the grating G_1 of period d . After propagating a distance z_1 and passing through the object, the field just after the object plane $z = 0$ is

$$u(x, y; 0) = \exp(-ikz_1) \sum_{n=-\infty}^{\infty} c_n u_0(x, y) \times \exp\{ik[nx\lambda d - z_1[1 - (n\lambda/d)^2]^{1/2}]\}, \quad (2)$$

where $u_0(x, y)$ is the two-dimensional object transmittance function. Eq. (2) is obtained directly from Fresnel diffraction integral. For simplicity, the concept of angular spectrum is applied. And the angular spectrum of Eq. (2) can be written as

$$\tilde{u}(v, \mu; 0) = \iint_{-\infty}^{\infty} u(x, y; 0) \times \exp[-2\pi i(vx + \mu y)] dv d\mu. \quad (3)$$

As the diffracted wave of phase object propagates a distance z_2 , the angular spectrum of the field at the plane just prior to G_2 can be expressed as

$$\tilde{u}(v, \mu; z_2) = \exp(-ikz_2) \sum_{n=-\infty}^{\infty} c_n \tilde{u}_0(v - n/d, \mu) \times \exp\{ik[z_2[1 - (n\lambda/d)^2]^{1/2} - z_2[1 - \lambda^2(v^2 + \mu^2)]^{1/2}]\}, \quad (4)$$

where $\tilde{u}_0(v, \mu)$ is the angular spectrum of the object. The field just after grating G_2 is

$$u(x, y; z_2) = u(x, y; z_2) \sum_{m=-\infty}^{\infty} c_m \exp(i\pi m) \times \exp(2\pi i m x/d). \quad (5)$$

The factor $\exp(i\pi m)$ is due to the half-a-period shift of G_2 with respect to G_1 . In the Fourier domain Eq. (5) becomes a convolution of the form

$$\tilde{u}(v, \mu; z_2) = \exp(-ikz_2) \sum_{n=-\infty}^{\infty} \sum_{m=-\infty}^{\infty} c_n c_m \exp(i\pi m) \times \tilde{u}_0(v - (n+m)/d, \mu) \exp\{ik[z_2[1 - (n\lambda/d)^2]^{1/2} + z_2[1 - \lambda^2[(v-m/d)^2 + \mu^2]]^{1/2}]\}. \quad (6)$$

The angular spectrum of the field at the observation plane becomes

$$\tilde{v}(v, \mu) = \sum_{n=-\infty}^{\infty} \sum_{m=-\infty}^{\infty} c_n c_m \exp(i\pi m) \times \tilde{u}_0(v - (n+m)/d, \mu) \times \exp\{ik[z_2 \lambda^2 v m d - \frac{z_1}{2}(n\lambda/d)^2 - \frac{z_2}{2}(m\lambda/d)^2]\}. \quad (7)$$

The field at the observation plane is the Fourier transform of Eq. (7), that is

$$v(x, y) = \sum_{n=-\infty}^{\infty} \sum_{m=-\infty}^{\infty} c_n c_m u_0\left(x + \frac{z_2 \lambda}{d}, y\right) \times \exp\left\{2\pi i \left[\frac{m}{2} + \frac{\lambda}{2d^2} \{z_2(m^2 + 2nm) - z_1 n^2\} + \frac{\lambda}{d}(n+m)\right]\right\}. \quad (8)$$

By a certain spatial filtering, only the first order of Eq. (7) is passed through a slit placed at plane P_2 , while other terms are stopped. In other words, we filter the $n-m=1$ term. Since $c_m = c_n = 0$ for even m and n , all the terms in Eq. (8) vanish except those of $m=0$; $n=1$ and $m=1$; $n=0$. By the first-order spatial filtering, the field at the observation plane becomes

$$v(x, y) = c_0 c_1 \exp\left(2\pi i \frac{y}{d}\right) \times \left[u_0(x, y) \exp\left\{2\pi i \left(\frac{-z_1 \lambda}{2d^2}\right)\right\} - u_0\left(x - \frac{z_2 \lambda}{d}, y\right) \times \exp\left\{2\pi i \left(\frac{z_2 \lambda}{2d^2}\right)\right\} \right]. \quad (9)$$

If the first grating is illuminated by a monochromatic plane wave, and the distance of two gratings satisfies the Talbot distance that is $z_1 + z_2 = 2Md^2/\lambda$, Eq. (9) then reduces to

$$v(x, y) = c_0 c_1 \exp\left\{2\pi i \left(\frac{x}{d} - \frac{z_1 \lambda}{2d^2}\right)\right\} \times \left[u_0(x, y) - u_0\left(x - \frac{z_2 \lambda}{d}, y\right) \exp\left\{2\pi i \frac{(z_1 - z_2) \lambda}{2d^2}\right\} \right]. \quad (10)$$

This is a result derived by Silva to encode the first derivative of a phase object in varying irradiance [5]. However, instead of irradiance coding, Eq. (9) could

be applied further for color coding of the first derivative of a phase object by means of white-light illumination.

For the color coding, the second grating G_2 is now placed at a distance of the first blue negative Talbot image, that is $z_1 + z_2 = d_2/\lambda_b$. λ_b stands for the blue wavelength. The blue color output at the observation plane is then

$$v(x, y) = -c_0 c_1 \exp \left\{ 2\pi i \left(\frac{x}{d} - \frac{z_1 \lambda_b}{2d^2} \right) \right\} \times \left[u_0(x, y) + u_0 \left(x + \frac{z_2 \lambda_b}{d}, y \right) \exp \left\{ \frac{2\pi i (z_1 + z_2) \lambda}{2d^2} \right\} \right]. \quad (11)$$

Considering the phase object with amplitude of unity, it is seen that high intensity blue color appears if the phase difference of $u_0(x, y)$ and $u_0 \left(x + \frac{z_2 \lambda_b}{d}, y \right)$ equals to zero. Since only the intensity is observed, the phase factor can be neglected so that the irradiance at the observation plane will be

$$|v(x, y)|^2 = c_0^2 c_1^2 \left| u_0(x, y) - u_0 \left(x + \frac{z_2 \lambda}{d}, y \right) \times \exp \left\{ 2\pi i (z_1 + z_2) \frac{\lambda}{2d^2} \right\} \right|^2. \quad (12)$$

By substituting $(z_1 + z_2) = d^2/\lambda_b$, it yields

$$|v(x, y)|^2 = c_0^2 c_1^2 \left| u_0(x, y) - u_0 \left(x + \frac{z_2 \lambda}{d}, y \right) \times \exp \left\{ 2\pi i \left(\frac{\lambda}{\lambda_b} \right) \right\} \right|^2. \quad (13)$$

It is apparent from Eq. (13) that any wavelength for which the phase difference is not 2π passes the second grating to some extent. However the color with wavelength λ will appear as the dominant color at the observation plane if the phase difference of $u_0(x, y)$ and $u_0 \left(x + \frac{z_2 \lambda}{d}, y \right) \exp \left\{ 2\pi i \left(\frac{\lambda}{\lambda_b} \right) \right\}$ is π . Let

the phase difference of $u_0(x, y)$ and $u_0 \left(x + \frac{z_2 \lambda}{d}, y \right)$ be denoted by $\Delta\phi'$, the relation of λ and $\Delta\phi'$ is

$$\Delta\phi' = \pi \left(1 - \frac{\lambda}{\lambda_b} \right). \quad (14)$$

It should be noted that the shear $z_2 \lambda/d$ varies due to different wavelength λ . Assume the phase changes linearly within the shear $z_2 \lambda/d$. The phase difference of $u_0(x, y)$ and $u_0 \left(x + \frac{z_2 \lambda}{d}, y \right)$, $\Delta\phi'$, can be normalized to the phase difference of $u_0(x, y)$ and $u_0 \left(x + \frac{z_2 \lambda_b}{d}, y \right)$, $\Delta\phi$, by the geometrical relation

$$\Delta\phi = \frac{\lambda_b}{\lambda} \cdot \Delta\phi'. \quad (15)$$

Substitution of Eq. (14) into Eq. (15) yields

$$\Delta\phi = \pi \left(\frac{\lambda_b}{\lambda} - 1 \right). \quad (16)$$

If z_2 is small enough, $\Delta\phi$ will be proportional to the first derivative of the phase object in the direction perpendicular to the grating.

The phase difference $\Delta\phi$ is determined from the hue produced at the observation plane as following: deep red ($\lambda = 700$ nm) \rightarrow red ($\lambda = 630$ nm) \rightarrow yellow ($\lambda = 575$ nm) \rightarrow green ($\lambda = 530$ nm) \rightarrow blue ($\lambda = 480$ nm) \rightarrow violet ($\lambda = 400$ nm) corresponds to $-57^\circ \rightarrow -43^\circ \rightarrow -30^\circ \rightarrow -17^\circ \rightarrow 0^\circ \rightarrow 36^\circ$. It is shown that the well-defined phase information is limited within a range. Outside the range of $-57^\circ \leq \Delta\phi \leq 36^\circ$, $\Delta\phi$ is represented by a mixture of several colors which is difficult to be interpreted. In fact, it is still possible to predict the hue of $\Delta\phi$ outside the available range by using computer analysis. However, the use of a computer will lose the simplicity of the method. It is obvious that the distance of two gratings can be calibrated to give any color as the background color. Accordingly, a different color code will be obtained.

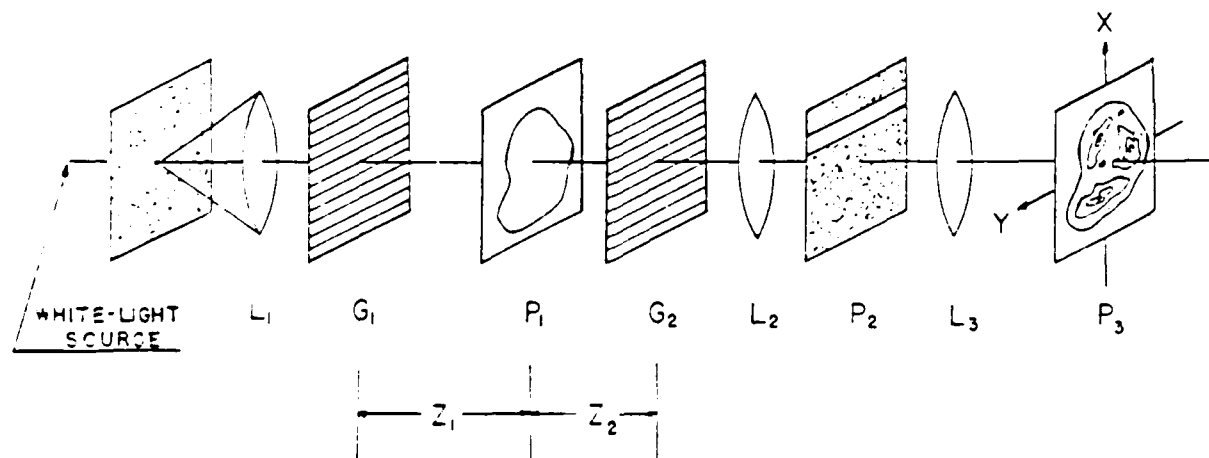


FIG. 1 — Schematic diagram of optical setup

III. EXPERIMENTAL DEMONSTRATIONS

The experiment was conducted using the setup shown in *figure 1*. Two identical glass Ronchi gratings of period $d = 0.23$ mm were separated by a distance $z_1 + z_2 \approx 11$ cm. These gratings were precisely aligned such that no Moire fringes were produced. As a transparent phase object is inserted between two gratings, a color pattern corresponding to the first derivative of the phase object is observable at the plane P_3 .

The experimental results are shown in *figure 2*. *Figure 2(a)* shows the blue background adjusted for $z_1 + z_2 \approx 11$ cm. This pure blue background color is obtained by first-order spatial filtering with a slit. When a piece of plastic was used as a tested object, a color pattern was observed as shown in *figure 2(b)*. The observed colors consist of yellow, green, blue and violet. This indicates that the shearing phase difference are within 36° , i.e., $|\Delta\phi| \leq 36^\circ$. A wedge constructed by two pieces of glass plate filled with water was also used as a tested object. Since the wedge has a constant derivative, it should produce only a single color. However, if the wedge is tilted with respect to the x axis, the shear $z_2 \lambda / d$ varies as z_2 is changed. Because the shear varies while the derivative of wedge is maintained as another constant, different shearing interference results are obtained for different position x . Consequently color bands are produced at the observation plane. This can be seen in *figure 2(c)*. Two color bands, yellow and green, were observed in this particular result.

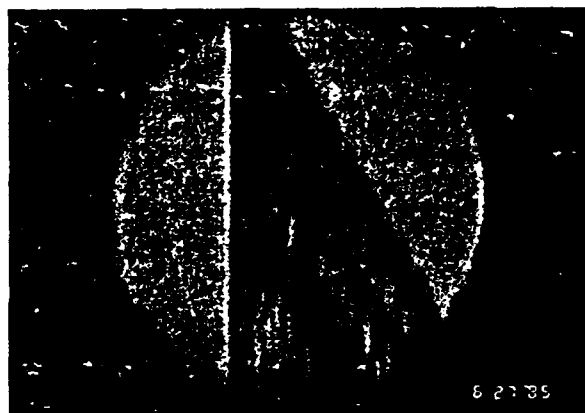
IV. CONCLUSION

An alternative method for color visualization of a phase object is presented in this paper. The first derivative of the object transmittance function is encoded in color. The phase object to be studied is placed between two gratings separated by half of a Talbot distance. By means of a collimated white-light source and a first-order spatial filtering, the color-coded phase pattern of the studied object can be generated. This color-coded phase pattern is found to be related to the first derivative of the phase distribution in the tested object.

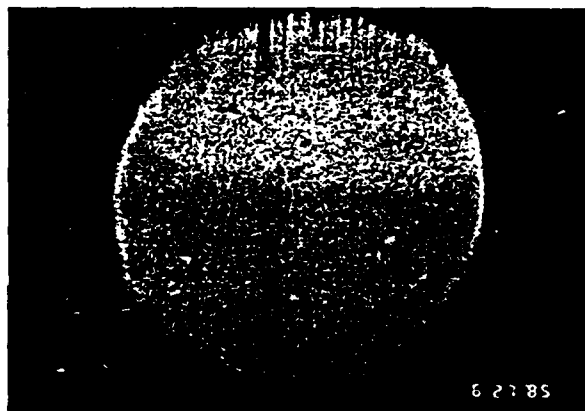
It is noted that the present method suffers from the fact that the visualized phase information is only definable in a limited range. Nevertheless, it provides distinct results for phase object having small variation as shown in the experiment. Furthermore, the color-coded phase pattern gives a better visual perception for human in real-time.

ACKNOWLEDGEMENTS

S. Jutamulia wishes to thank Professor T. Asakura of Hokkaido University, Japan, for some discussions on this topic when he was there. This research is supported by U.S. Air Force Office of Scientific Research grant AFOSR-83-0140.



a)



b)



c)

FIG. 2 — Color pictures of the experimental results observed: (a) Adjusted pure blue background, (b) color-coded phase pattern of a piece of plastic showing yellow, green, blue and violet colors, and (c) color-coded phase pattern of a tilted wedge showing a yellow band in the upper part and a green band in the lower part.

REFERENCES

- [1] BORN (M.) and WOLF (E.). — *Principle of Optics* (Pergamon, New York, 1975) 5th ed.
- [2] DE VELIS (J. B.) and REYNOLDS (G. O.). — *Theory and Application of Holograph* (Addison Wesley, Reading, 1967).
- [3] FRANCON (M.). — *Progress in Microscopy* (Pergamon, New York, 1961).
- [4] LOHMANN (A. W.) and SILVA (D. E.). « An Interferometer Based on the Talbot Effect », *Opt. Commun.* 2 (1971) 413.
- [5] SILVA (D. E.). — « Talbot Interferometer for Radial and Lateral Derivatives », *Appl. Opt.* 11 (1972) 2613.
- [6] YU (F. T. S.). — *White-Light Optical Signal Processing* (John Wiley & Son, New York, 1985).
- [7] WEINBERG (F. J.). — *Optics of Flames* (Butterworths, Washington, 1963).
- [8] WU (S. T.) and YU (F. T. S.). — « Visualization of Color Coded Phase Variation with Incoherent Optical Processing Technique », *J. Opt.* 13 (1982) 52.
- [9] LOHMANN (A. W.). — *Optical Information Processing* (Physikalisches Institut der Universität, Erlangen, 1978).

(Manuscript received in July 29, 1985.)

SECTION XXIV

Cross Spectral Density Analysis

An analysis of white-light processing system based on cross-spectral
density function

X. J. Lu and F. T. S. Yu

Electrical Engineering Department

The Pennsylvania State University

University Park, PA 16802

Abstract

An analysis of a white-light optical processing system is presented based on the cross-spectral density function. A plane-by-plane analysis of the cross spectral density function is given, including the effects of source size and grating frequency. The degree of coherence in the Fourier plane is examined in detail, and an explanation of the fan-shaped deblurring filter based on this analysis is also given.

I. Introduction

There has been interest in optical image processing using incoherent source. In the past decade a number of optical processing systems using a white-light source have been proposed^{1,2}. In a white-light processing system a prism or a grating is used to disperse the light into rainbow colors providing a high temporal coherence at certain regions so that coherent processing becomes possible. The operation carried out in the white-light system is in fact an approximate coherent operation.

In the conventional approach to analyzing a white-light processing system, coherent methods are adapted to describe the quasi-complex amplitude. The system is analyzed for a given wavelength, then the coherence requirement for a particular optical operation is determined.³

Recently several studies have been performed using the cross spectral density function to analyze an incoherent optical system. Sudol and Thompson⁴ used the cross spectral density function to explain the Lau effect, which is generated by two identical gratings in an incoherent system. The technique was extended by Cartwright⁵ to analyze an incoherent optical system.

In this paper the cross spectral density function is used to study a grating-based white light optical system, analyzing plane by plane from the source to the output. The cross spectral density function is used to derive the degree of coherence at the pupil (Fourier) plane and to examine the fan-shaped deblurring filter.

II. Propagation of Cross Spectral Density Function

The cross spectral density function may be thought of as a correlation between the Fourier components of the light oscillations at two points in a wavefield. If $v(\vec{r} + \frac{1}{2} \Delta \vec{r}, \nu)$ and $v(\vec{r} - \frac{1}{2} \Delta \vec{r}, \nu')$ are the fluctuations of the optical wavefield at $Q_1(\vec{r} + \frac{1}{2} \Delta \vec{r})$ and $Q_2(\vec{r} - \frac{1}{2} \Delta \vec{r})$ with optical frequencies ν and ν' , respectively, the cross spectral density function, $W(\vec{r}, \Delta \vec{r}, \nu)$ is defined by⁶

$$W(\vec{r}, \Delta \vec{r}, \nu) \delta(\nu - \nu') = \langle v(\vec{r} + \frac{1}{2} \Delta \vec{r}, \nu) v^*(\vec{r} - \frac{1}{2} \Delta \vec{r}, \nu) \rangle \quad (1)$$

and

$$W(\vec{r}, \Delta \vec{r}, \nu) = \int_{-\infty}^{\infty} \Gamma(\vec{r}, \Delta \vec{r}, \tau) e^{i2\pi\nu\tau} d\tau \quad (2)$$

where \vec{r} denotes the position vector, the sharp brackets denote ensemble average, the asterisk superscript indicates complex conjugate, and $\Gamma(\vec{r}, \Delta \vec{r}, \tau)$ is the mutual coherence function.

With reference to paraxial approximation, the propagation of the cross spectral density function from one plane to the other in Fraunhofer region can be written as

$$W'(\vec{r}', \Delta \vec{r}', \nu) = \frac{e^{-i \frac{2\pi}{\lambda z} \vec{r}' \cdot \Delta \vec{r}'}}{(\lambda z)^4} \iint W(\vec{r}, \Delta \vec{r}, \nu) e^{-i \frac{2\pi}{\lambda z} (\Delta \vec{r}' \cdot \vec{r} + \Delta \vec{r} \cdot \vec{r}')} d\Delta \vec{r} d\vec{r} \quad (3)$$

where $W(\)$ and $W'(\)$ are the cross spectral functions defined in the first and the second plane, respectively, z is the propagation distance, and λ is the wavelength of the light source.

The white light system to be studied is shown in Fig. 1. The source plane, P_0 , contains the incoherent light source. The input plane, P_1 , contains the object transparency in contact with a grating. Plane P_2 is the pupil plane where filters may be placed to perform the desired optical processing operations. Finally, the processed image is obtained at the output plane, P_3 .

From Eq. (3), the cross spectral density function propagating from plane P_0 to plane P_1 would be

$$W_1(\vec{r}_1, \Delta\vec{r}_1, \nu) = \frac{1}{(\lambda f)^4} \iint_{-\infty}^{\infty} W_0(\vec{r}_0, \Delta\vec{r}_0, \nu) e^{-i \frac{2\pi}{\lambda f} (\Delta\vec{r}_1 \cdot \vec{r}_0 + \Delta\vec{r}_0 \cdot \vec{r}_1)} d\Delta\vec{r}_0 d\vec{r}_0, \quad (4)$$

where f is the focal length of all the lenses, L_0 , L_1 and L_2 . For an incoherent source in plane P_0 with radiance distribution $I(\vec{r}_0, \nu)$, the cross spectral density function is assumed to be

$$W_0(\vec{r}_0, \Delta\vec{r}_0, \nu) = A(\nu) \cdot I_\nu(\vec{r}_0) \delta(\Delta\vec{r}_0), \quad (5)$$

and the intensity distribution of the source can be written as

$$I_0(\vec{r}_0) = \int_0^\infty W_0(\vec{r}_0, 0, \nu) d\nu = I_\nu(\vec{r}_0) \int_0^\infty A(\nu) d\nu \quad (6)$$

By substituting Eqs. (5) and (6), Eq.(4) becomes

$$W_1(\vec{r}_1, \Delta\vec{r}_1, \nu) = \frac{A(\nu)}{(\lambda f)^4} \int_0^\infty I_\nu(\vec{r}_0) e^{-i \frac{2\pi}{\lambda f} \vec{r}_0 \cdot \Delta\vec{r}_1} d\vec{r}_0, \quad (7)$$

The overall intensity distribution incident at the input plane, P_1 , is

$$I_1(\vec{r}_1) = \int_0^\infty W_1(\vec{r}_1, \Delta\vec{r}_1, \nu) d\nu$$

$$= \int_0^\infty \frac{A(\nu)}{(\lambda f)^4} d\nu \int_{-\infty}^\infty I_\nu(\vec{r}_0) e^{-i \frac{2\pi}{\lambda f} \vec{r}_0 \cdot \Delta\vec{r}_1} d\vec{r}_0 \quad (8)$$

Immediately after the object transparency and grating, the cross spectral density function can also be written as

$$W_1'(\vec{r}_1, \Delta\vec{r}_1, \nu) = t(\vec{r}_1 + \frac{1}{2} \Delta\vec{r}_1) t^*(\vec{r}_1 - \frac{1}{2} \Delta\vec{r}_1) g_1(\vec{r}_1 + \frac{1}{2} \Delta\vec{r}_1)$$

$$g_1^*(\vec{r}_1 - \frac{1}{2} \Delta\vec{r}_1) W_1(\vec{r}_1, \Delta\vec{r}_1, \nu) \quad (9)$$

where $t(\)$ and $g_1(\)$ represent the complex amplitude transmittances of the object transparency and the grating, respectively.

Similarly, the cross spectral density function at the pupil plane P_2 , is found to be

$$W_2(\vec{r}_2, \Delta\vec{r}_2, \nu) = \frac{1}{(\lambda f)^4} \iint_{-\infty}^\infty W_1'(\vec{r}_1, \Delta\vec{r}_1, \nu) e^{-i \frac{2\pi}{\lambda f} (\Delta\vec{r}_2 \cdot \vec{r}_1 + \Delta\vec{r}_1 \cdot \vec{r}_2)} d\Delta\vec{r}_1 d\vec{r}_1$$

$$= \frac{1}{(\lambda f)^4} \iint_{-\infty}^\infty t(\vec{r}_1 + \frac{1}{2} \Delta\vec{r}_1) t^*(\vec{r}_1 - \frac{1}{2} \Delta\vec{r}_1) e^{-i \frac{2\pi}{\lambda f} (\Delta\vec{r}_2 \cdot \vec{r}_1 + \Delta\vec{r}_1 \cdot \vec{r}_2)} d\Delta\vec{r}_1 d\vec{r}_1$$

$$\cdot \iint_{-\infty}^\infty g_1(\vec{r}_1 + \frac{1}{2} \Delta\vec{r}_1) g_1^*(\vec{r}_1 - \frac{1}{2} \Delta\vec{r}_1) e^{-i \frac{2\pi}{\lambda f} (\Delta\vec{r}_2 \cdot \vec{r}_1 + \Delta\vec{r}_1 \cdot \vec{r}_2)} d\Delta\vec{r}_1 d\vec{r}_1$$

$$\cdot \iint_{-\infty}^\infty W_1(\vec{r}_1, \Delta\vec{r}_1, \nu) e^{-i \frac{2\pi}{\lambda f} (\Delta\vec{r}_2 \cdot \vec{r}_1 + \Delta\vec{r}_1 \cdot \vec{r}_2)} d\Delta\vec{r}_1 d\vec{r}_1 \quad (10)$$

where $*$ denotes convolution. By Substituting Eq. (7) into the Eq. (10) yields

$$W_2(\vec{r}_2, \Delta\vec{r}_2, \nu) = \frac{1}{(\lambda f)^4} A(\nu) I_\nu(-\vec{r}_2) \delta(\Delta\vec{r}_2) * T\left(\frac{\vec{r}_2}{\lambda f}, \frac{\Delta\vec{r}_2}{\lambda f}\right) * G\left(\frac{\vec{r}_2}{\lambda f}, \frac{\Delta\vec{r}_2}{\lambda f}\right) \quad (11)$$

where

$$T\left(\frac{\vec{r}_2}{\lambda f}, \frac{\Delta\vec{r}_2}{\lambda f}\right) = \iint_{-\infty}^{\infty} t(\vec{r}_1 + \frac{1}{2} \Delta\vec{r}_1) t^*(\vec{r}_1 - \frac{1}{2} \Delta\vec{r}_1) e^{-i \frac{2\pi}{\lambda f} (\Delta\vec{r}_2 \cdot \vec{r}_1 + \Delta\vec{r}_1 \cdot \vec{r}_2)} d\Delta\vec{r}_1 d\vec{r}_1 \quad (12a)$$

$$G\left(\frac{\vec{r}_2}{\lambda f}, \frac{\Delta\vec{r}_2}{\lambda f}\right) = \iint_{-\infty}^{\infty} g_1(\vec{r}_1 + \frac{1}{2} \Delta\vec{r}_1) g_1^*(\vec{r}_1 - \frac{1}{2} \Delta\vec{r}_1) e^{-i \frac{2\pi}{\lambda f} (\Delta\vec{r}_2 \cdot \vec{r}_1 + \Delta\vec{r}_1 \cdot \vec{r}_2)} d\Delta\vec{r}_1 d\vec{r}_1 \quad (12b)$$

are the correlation function of the aperture $t(\vec{r}_1)$ and the grating $g_1(\vec{r}_1)$, respectively.

At plane P_3 , the cross spectral density function would be

$$\begin{aligned} W_3(\vec{r}_3, \Delta\vec{r}_3, \nu) &= \frac{1}{(\lambda f)^8} \iint_{-\infty}^{\infty} A(\nu) I_\nu(-\vec{r}_2) \delta(\Delta\vec{r}_2) e^{-i \frac{2\pi}{\lambda f} (\Delta\vec{r}_3 \cdot \vec{r}_2 + \Delta\vec{r}_2 \cdot \vec{r}_3)} d\Delta\vec{r}_2 d\vec{r}_2 \\ &\times \iint_{-\infty}^{\infty} T\left(\frac{\vec{r}_2}{\lambda f}, \frac{\Delta\vec{r}_2}{\lambda f}\right) e^{-i \frac{2\pi}{\lambda f} (\Delta\vec{r}_3 \cdot \vec{r}_2 + \Delta\vec{r}_2 \cdot \vec{r}_3)} d\Delta\vec{r}_2 d\vec{r}_2 \\ &\times \iint_{-\infty}^{\infty} G\left(\frac{\vec{r}_2}{\lambda f}, \frac{\Delta\vec{r}_2}{\lambda f}\right) e^{-i \frac{2\pi}{\lambda f} (\Delta\vec{r}_3 \cdot \vec{r}_2 + \Delta\vec{r}_2 \cdot \vec{r}_3)} d\Delta\vec{r}_2 d\vec{r}_2 \quad (13) \end{aligned}$$

The first integral may be written as $A(\nu) C\left(\frac{\Delta\vec{r}_3}{\lambda f}\right)$ where

$$C\left(\frac{\Delta \vec{r}_3}{\lambda f}\right) = \iint_{-\infty}^{\infty} I_v(-\vec{r}_2) e^{-i \frac{2\pi}{\lambda f} \Delta \vec{r}_3 \cdot \vec{r}_2} d\vec{r}_2.$$

If we let $\Delta \vec{r}_3 = 0$, then $C\left(\frac{\Delta \vec{r}_3}{\lambda f}\right)$ is a constant C_0 . The second and third integrals of Eq. (13) are recognized as the inverse Fourier transforms of Eqs. (12a) and (12b). By letting $\Delta \vec{r}_3 = 0$, the cross spectral density function can be shown as

$$W_3(\vec{r}_3, 0, v) = C_0 A(v) t^2(-\vec{r}_3) g_1^2(-\vec{r}_3). \quad (14)$$

The output intensity distribution is therefore,

$$I_3(\vec{r}_3) = B t^2(-\vec{r}_3) g_1^2(-\vec{r}_3) \quad (15)$$

where $B = C_0 \int_{v_{\min}}^{v_{\max}} A(v) dv$. It is apparent that the output intensity

distribution is the image of the object transparency modulated by the grating.

We now examine the pupil plane, P_2 , using Eq. (11). For our analysis we will assume that the radiance distribution of the light source is uniform over a circular disk of diameter d_s , that is $I_s(\vec{r}_s) = I_s \text{ circ}\left(\frac{\vec{r}_s}{d_s/2}\right)$, and that the frequency factor, $A(v)$ is a constant over the visible light range (v_{\min}, v_{\max}).

The grating used in the white-light processing system can be either a sinusoidal amplitude grating, a sinusoidal phase grating, or a Ronchi grating. Table 1 shows the amplitude and intensity transmittance functions and the correlation functions of the three gratings. Although the

high diffraction efficiency, we will use the sinusoidal amplitude grating to simplify the analysis.

The correlation function of the grating, $\Delta \vec{r}_2 = 0$, is

$$G_1\left(\frac{\vec{r}_2}{\lambda f}, 0\right) = \frac{1}{4} \left\{ \delta\left(\frac{\vec{r}_2}{\lambda f}\right) + \frac{1}{4} \left[\delta\left(\frac{x_2}{\lambda f}, \frac{y_2}{\lambda f} - \frac{1}{h}\right) + \delta\left(\frac{x_2}{\lambda f}, \frac{y_2}{\lambda f} + \frac{1}{h}\right) \right] \right\} \quad (16)$$

where $1/h$ is the spatial frequency of the grating. In order to get some physical insight, consider an object transparency which is a rectangular aperture, $t(\vec{r}_1) = \text{rect}\left(\frac{x_1}{L_x}\right)\text{rect}\left(\frac{y_1}{L_y}\right)$. Since the dimensions of the aperture, L_x and L_y , are much larger than the diameter of the light source, d_0 , from eq. (12), we have,

$$T\left(\frac{\vec{r}_2}{\lambda f}, \frac{\Delta \vec{r}_2}{\lambda f}\right) = \delta\left(\frac{\vec{r}_2}{\lambda f}, \frac{\Delta \vec{r}_2}{\lambda f}\right) \quad (17)$$

by substituting Eq. (16) and (17) into Eq. (11), we obtained the following result:

$$W_2\left(\frac{\vec{r}_2}{\lambda f}, 0, v\right) = \frac{1}{4} A(v) \left\{ I_v(-\vec{r}_2) + \frac{1}{4} I_v\left(-x_2, -y_2 - \frac{\lambda f}{h}\right) + \frac{1}{4} I_v\left(-x_2, -y_2 + \frac{\lambda f}{h}\right) \right\}$$

Thus, the intensity distribution in plane P_2 is

$$I_2(\vec{r}_2) = \frac{1}{4} I_0(-\vec{r}_2) + \frac{A^2 I_s}{16} \int_{v_{\min}}^{v_{\max}} \text{sinc}\left(\frac{v}{v_{\max}}\right) \text{sinc}\left(\frac{v}{v_{\max}}\right) dv$$

$$+ \frac{A^2 I_s}{16} \int_{v_{\min}}^{v_{\max}} \text{sinc}\left(\frac{v}{v_{\max}}\right) \text{sinc}\left(\frac{v}{v_{\max}}\right) dv$$

AD-A179 489 WHITE-LIGHT OPTICAL INFORMATION PROCESSING AND
HOLOGRAPHY(U) PENNSYLVANIA STATE UNIV UNIVERSITY PARK
DEPT OF ELECTRICAL ENGINEERING F T YU 23 JAN 87
UNCLASSIFIED AFOSR-TR-87-0456 AFOSR-83-0140 F/B 20/6

WHITE-LIGHT OPTICAL INFORMATION PROCESSING AND
HOLOGRAPHY(U) PENNSYLVANIA STATE UNIV UNIVERSITY PARK
DEPT OF ELECTRICAL ENGINEERING F T YU 23 JAN 87
AFOSR-TR-87-0456 AFOSR-83-0140 F/B 20/6

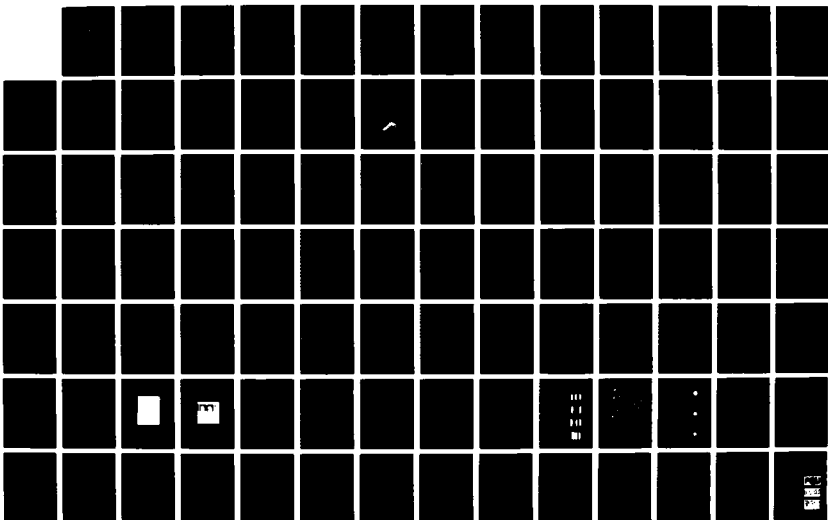
3/4/

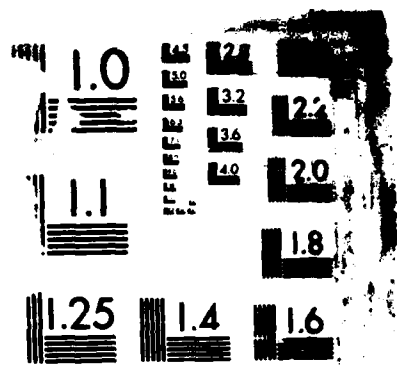
UNCLASSIFIED

F T YU 23 JAN 87

F/G 20/6

ML





MI

Figure 2(a) depicts this intensity distribution. It consists of an image of the white light source at the origin plus one first-order distribution which is dispersed in the y_2 direction with respect to wavelength.

In reality the first-order distribution does not have a constant width over the dispersed wavelengths as shown in Fig. 2(a). The diameter of the light spot increases with wavelength. Two main factors cause this effect. Axial chromatic aberration of the lens brings light of different wavelengths to different focal points on the optical axis. Thus if plane P_2 is the blue focal plane, the red spot will be out of focus and appear somewhat larger than the blue spot.

The second factor is that the focal surface is spherical with radius f rather than plane. Again if plane P_2 is at the focal point of the blue spot, the red spot is out of focus and hence somewhat larger. Referring to the geometry of Fig. 3(a), the two effects give a red spot of diameter

$$d_r = d_o + \frac{D}{f} \left[1 - \left(\frac{\lambda_r}{h} \right)^2 \right]^{-1/2} (\Delta l_1 + \Delta l_2) \quad (20)$$

where d_o is the diameter of the blue spot (which is the same as the diameter of the white light source), D is the diameter of the lens or the aperture in the input plane, λ_r is red wavelength, Δl_1 is the distance between red and blue focal planes due to chromatic aberration, and $\Delta l_2 = \frac{\lambda_r \Delta \lambda_{rb} f}{h^2}$, and $\Delta \lambda_{rb}$ is the bandwidth (from red to blue).

Consider a numeric example where the condenser is a single lens with a large relative aperture and Δl_1 is a few millimeters. If $D/f = 1/10$, $f = 381$ mm, $\lambda_r = 5461 \text{ \AA}$, $\Delta \lambda_{rb} = 2 \times 10^{-4}$ mm, $h = 1/136$ mm, $d_o = 0.50$ mm, and $\Delta l_1 = 3.0$ mm, then

$$d_r = 0.50 \text{ mm} + 0.30 \text{ mm} + 0.089 \text{ mm} = 0.89 \text{ mm}.$$

We see that the axial chromatic aberration is an important factor in providing the coma-like distribution. In our example the effect of the spherical field departure is somewhat smaller but would become significant if a higher frequency grating is used. The intensity distribution derived from Eq. (19) and Eq. (20) is shown in Fig. 2(b) in a 3-D computer graphics plot.

We now examine the bandwidth of optical wavelengths at any point in the first-order diffracted distribution. Suppose there are two distinguishable circular distributions $I_{\nu_1}(0, -y_2 + \frac{\lambda_1 f}{h})$ and $I_{\nu_2}(0, -y_2 + \frac{\lambda_2 f}{h})$ with the same diameter d_0 but different optical frequencies ν_1 and ν_2 .

Referring to Fig. 3(b) the circles intersect at $(x_2, \frac{\lambda f}{h})$ and $(-x_2, \frac{\lambda f}{h})$. One can have

$$\Delta\lambda = \lambda_2 - \lambda_1 = \frac{h}{f} \sqrt{d_0^2 - 4x_2^2} \quad (21)$$

where $\Delta\lambda$ is the bandwidth of light incident at the points $(x_2, \frac{\lambda f}{h})$ and $(-x_2, \frac{\lambda f}{h})$. At the point $(0, \frac{\lambda f}{h})$ the bandwidth is

$$\Delta\lambda = \frac{h}{f} d_0. \quad (22)$$

Thus the bandwidth is proportional to the diameter of the light source and inversely proportional to the grating frequency and the focal length of the lens. We note that, the bandwidth decreases as it move away from the y_2 axis.

A quasi-monochromatic light source is obtained by placing a pin hole of diameter d_1 in the first-order diffraction intensity distribution at

point $(0, \frac{\lambda f}{h})$. The bandwidth of this secondary source is

$$\Delta\lambda = \frac{h}{f} (d_0 + d_1) \quad (23)$$

We stress that, Eq. (23) corrects the corresponding equation in an earlier publication in which $\Delta\lambda = \frac{h}{f} d_1$ was used.

The diameters of both the primary source and the pin hole affect the bandwidth of the secondary source. As a numeric example consider $f = 380$

mm, $h = \frac{1}{136}$ mm, $d_0 = 0.5$ mm, and $d_1 = 0.5$ mm. At any point on the y_2 axis the inherent bandwidth (due to the primary source) is about 100Å. Over the secondary source pin hole, however, the bandwidth is about 200Å.

III. Coherence at the Fourier Plane

We now examine the complex degree of coherence in the first-order diffraction in the Fourier plane, P_2 . The complex degree of spectral coherence is the normalized cross spectral density function and is defined as

$$\mu(\vec{r}, \Delta\vec{r}, \nu) = \frac{W(\vec{r}, \Delta\vec{r}, \nu)}{[W(\vec{r} + \frac{1}{2}\Delta\vec{r}, 0, \nu)W(\vec{r} - \frac{1}{2}\Delta\vec{r}, 0, \nu)]^{1/2}} \quad (24)$$

and the complex degree of coherence is defined by

$$\gamma(\vec{r}, \Delta\vec{r}, \tau) = \frac{\Gamma(\vec{r}, \Delta\vec{r}, \tau)}{[I(\vec{r} + \frac{1}{2}\Delta\vec{r})I(\vec{r} - \frac{1}{2}\Delta\vec{r})]^{1/2}} \quad (25)$$

where $I(\vec{r}')$ is the intensity at \vec{r}' , given by

$$I(\vec{r}') = \Gamma(\vec{r}', 0, 0) = \int_0^\infty W(\vec{r}', 0, \nu) d\nu \quad .$$

Since the light is separated into its component frequencies at the

plane P_2 , for a small area $(\Delta x, \Delta y)$ around a point $(x_2 = 0, y_2 = \frac{\lambda f}{h})$ and $\Delta \nu$ is small compared to the mid-band frequency, $\bar{\nu}$, that is $\Delta \bar{\nu} \ll \nu$. If $W(\vec{r}, \Delta \vec{r}, \nu)$ is assumed to be constant over the bandwidth, then Eq. (25) becomes

$$\gamma(\vec{r}, \Delta \vec{r}, \tau) = \mu(\vec{r}, \Delta \vec{r}, \bar{\nu}) e^{-i2\pi \bar{\nu} \tau} \text{sinc}(\tau \Delta \nu), \quad (26)$$

where the magnitude of the complex degree of coherence, $|\gamma(\vec{r}, \Delta \vec{r}, \tau)|$, gives the visibility of interference fringes at some point Q_3 in P_3 plane, due light traveling from points $Q (\vec{r}_1 + \frac{1}{2} \Delta \vec{r})$ and $Q (\vec{r}_2 - \frac{1}{2} \Delta \vec{r})$ at P_2 , where τ is the difference in travel times. From the $\text{sinc}(\tau \Delta \nu)$ envelope in Eq. (26) we see that visibility fringes can be observed only if $\tau < \frac{1}{\Delta \nu}$.

Yu et al⁹ recently proposed a two-beam interference technique to measure the degree of coherence in the Fourier plane of a white light processor. A slit of width d_s is placed in the P_1 plane in contact with and oriented perpendicular to the grating. The amplitude transmittance of

the slit is $t(\vec{r}_1) = \text{rect}(\frac{x_1}{d_s}) \text{rect}(\frac{y_1}{L_y})$, where $d_s \ll L_y$. Then

$$T(\frac{\vec{r}_2}{\lambda f}, \frac{\Delta \vec{r}_2}{\lambda f}) = \delta(\frac{y_2}{\lambda f}, \frac{\Delta y_2}{\lambda f}) d_s^2 \text{Sinc}[\frac{d_s}{\lambda f} (x_2 + \frac{\Delta x_2}{2})] \text{Sinc}[\frac{d_s}{\lambda f} (x_2 - \frac{\Delta x_2}{2})]. \quad (27)$$

For the grating we consider only the first order diffracted term at $y_2 = \frac{\lambda f}{h}$ and $x_2 = 0$; i.e.,

$$G_1(\frac{\vec{r}_2}{\lambda f}, \frac{\Delta \vec{r}_2}{\lambda f}) = \frac{1}{i6} \delta(\frac{x_2}{\lambda f}, \frac{\Delta x_2}{\lambda f}) \delta(\frac{y_2}{\lambda f} - \frac{1}{h}, \frac{\Delta y_2}{\lambda f}). \quad (28)$$

The cross spectral density function (for the circular disk source) can be evaluated from Eq. (11), i.e.,

$$W_2(\vec{r}_2, \Delta\vec{r}_2, \nu) = \frac{1}{16} d_s^2 A(\nu) I_s \text{circ}\left(\frac{2\sqrt{x_2^2 + (y_2 - \frac{\lambda f}{h})^2}}{d_o}\right) \delta(\Delta y_2) \\ * \text{Sinc}\left(\frac{d_s}{\lambda f}(x_2 + \frac{\Delta x_2}{2})\right) \text{Sinc}\left(\frac{d_s}{\lambda f}(x_2 - \frac{\Delta x_2}{2})\right). \quad (29)$$

For $\Delta\vec{r}_2 = 0$, it reduces to

$$W_2(\vec{r}_2, 0, \nu) = \frac{1}{16} d_s^2 A(\nu) I_s \text{circ}\left(\frac{2\sqrt{x_2^2 + (y_2 - \frac{\lambda f}{h})^2}}{d_o}\right) * [\text{Sinc}(\frac{d_s}{\lambda f} x_2)]^2. \quad (30)$$

We now analyse the complex degree of coherence around a given wavelength, λ_o , between two points that are symmetric about the y_2 axis at

$y_2 = \frac{\lambda_o f}{h}$. Eq. (29) and (30) can be rewritten as

$$W_2(x_2, 0, \nu_o) = \frac{1}{16} d_s^2 A(\nu_o) I_s \int_{-\frac{d_o}{2}}^{\frac{d_o}{2}} [\text{Sinc}(\frac{d_s}{\lambda_o f}(x_2 - \xi))]^2 d\xi \quad (31)$$

and

$$W_2(\vec{r}_2, 0, \nu_o) = \frac{1}{16} d_s^2 A(\nu_o) I_s \text{rect}\left(\frac{x_2}{c_o}\right) * [\text{Sinc}(\frac{d_s}{\lambda_o f} x_2)]^2. \quad (32)$$

Notice that $W_2(x_2, 0, \nu_o)$ is symmetric about the y_2 axis, i.e. $W_2(x_2, 0, \nu_o) = W_2(-x_2, 0, \nu_o)$. The complex degree of spectral coherence at symmetric points

with respect to $x_2 = 0$, $y_2 = \frac{\lambda_o f}{h}$ is (from Eq. (24))

$$\mu'(\vec{r}, \Delta\vec{r}, \nu_0) = \mu(\Delta x_2, \nu_0) \Big|_{x_2 = 0; y_2 = \frac{\lambda_0 f}{h}}$$

$$= \frac{\int_{-\frac{d_0}{2}}^{\frac{d_0}{2}} \text{Sinc}\left(\frac{d_s}{\lambda_0 f}(\xi - x_2)\right) \text{Sinc}\left(\frac{d_s}{\lambda_0 f}(\xi + x_2)\right) d\xi}{\int_{-\frac{d_0}{2}}^{\frac{d_0}{2}} [\text{Sinc}\left(\frac{d_s}{\lambda_0 f}(x_2 - \xi)\right)]^2 d\xi}, \quad (33)$$

where the two symmetric points are $(x_2, \frac{\lambda_0 f}{h})$ and $(-x_2, \frac{\lambda_0 f}{h})$.

Since the light is separated into narrowband frequencies in the first-order diffraction region at P_2 plane, Eqs. (26) (33) would be used to get the complex degree of coherence at the symmetric points: i.e.

$$\gamma(x_2, -x_2, \tau) = \mu'(x_2, -x_2, \nu_0) e^{-i2\pi\nu_0\tau} \text{Sinc}(\tau\Delta\nu). \quad (34)$$

It is apparent from Eq. (34) that μ' and γ are functions of the source size d_0 , and the width, d_s , of the slit in the P_1 plane. The factor $\mu'(x_2, -x_2, \nu_0)$ of Eq. (34) represents the spatial coherence between the two symmetric points, while the $\text{sinc}(\tau\Delta\nu)$ factor represents the temporal coherence. The main range of $\mu'(x_2, -x_2, \nu_0)$ can be defined, from Eq. (33), as

$$\Delta x_2 = 2 x_2 = 2 \frac{\lambda_0 f}{c_s}. \quad (35)$$

This is in fact the width of the intensity distribution from Eq. (32) when

$d_0 \ll \frac{\lambda_0 f}{c_s}$. The frequency bandwidth $\Delta\nu$ of Eq. (34) corresponds to the

bandwidth of Eq. (22) and is given by $\Delta\nu = \frac{h c_0}{f \lambda_0^2} c$, where c is the velocity of light propagation.

Now consider the interference in the P_3 plane of light from the two points $(x_{20}, \frac{\lambda_0 f}{h})$ and $(-x_{20}, \frac{\lambda_0 f}{h})$ in the P_2 plane. The visibility of fringes produced is equal to $|\gamma(x_{20}, -x_{20}, \tau)|$, where τ is the time difference for light traveling to the observation point $(x_{30}, 0)$ in the P_3 plane. Referring to Fig. 4, we see that

$$\tau = \frac{2x_{20}x_{30}}{cf\sqrt{1+(x_{20}/f)^2}} = \frac{2x_{20}x_{30}}{cf}, \quad (36)$$

and the fringe visibility is

$$|\gamma| = \left| \mu'(x_2, -x_2, v_0) \text{sinc}\left(\frac{h d_0}{(\lambda_0 f)^2} d_\lambda x_{30}\right) \right|, \quad (37)$$

where $d_\lambda = 2x_{20}$, is the separation between the two points $(x_{20}, \frac{\lambda_0 f}{h})$ and $(-x_{20}, \frac{\lambda_0 f}{h})$.

In the interference experiment carried out by Yu et al⁹, a pair of slanted slits is placed in the P_2 plane symmetrically about the y_2 axis to produce an interference pattern in plane P_3 . For a given $y_2 = \frac{\lambda_0 f}{h}$, the pair of points in the two slits corresponds to the wavelength λ_0 . In order for all pairs of points at different wavelengths to produce interference fringes with the same period and intensity, the angle of inclination of the slits should be

$$\epsilon = \tan^{-1}\left(\frac{h d_{\lambda_0}}{2 \lambda_0 f}\right) \quad (38)$$

where d_{λ_0} is the mean separation of the slits at the mean wavelength, λ_0 . Eq. (38) agrees with the corresponding equation given in a previous paper⁹. However, in the experiment a larger angle was used to accommodate the increase in spot size as given in Eq. (20). A more detail explanation of the inclination angle will be given in the next section.

On the other hand, suppose that the slit in the P_1 plane is placed parallel to the grating rulings. In this case the amplitude transmittance of the slit is $t'(r_1^{\rightarrow}) = \text{rect}(\frac{1}{L_x})\text{rect}(\frac{1}{d_p})$, where $d_p \ll L_x$. Following a procedure similar to that used to develop Eq. (33), the complex degree of spectral coherence can be shown as,

$$\mu'(\frac{\lambda_0 f}{h} + \frac{\Delta y_2}{z}, \frac{\lambda_0 f}{h} - \frac{\Delta y_2}{z}, \nu_0) = \frac{\int_{-\frac{d_0}{2}}^{\frac{d_0}{2}} \text{Sinc}(\frac{d_p}{\lambda_0 f}(\frac{\Delta y_2}{2} - \xi)) \text{Sinc}(\frac{d_p}{\lambda_0 f}(\frac{\Delta y_2}{2} + \xi)) d\xi}{\int_{-\frac{d_0}{2}}^{\frac{d_0}{2}} [\text{Sinc}(\frac{d_p}{\lambda_0 f}(\frac{\Delta y_2}{2} - \xi))]^2 d\xi}, \quad (39)$$

and the degree of coherence (i.e., the visibility) is

$$|\gamma| = \left| \mu'(\frac{\lambda_0 f}{h} + \frac{\Delta y_2}{z}, \frac{\lambda_0 f}{h} - \frac{\Delta y_2}{z}, \nu_0) \text{Sinc}(\tau' \Delta \nu) \right|, \quad (40)$$

where

$$\tau' = \frac{\Delta y_2 y_{30}}{cf[1 + (\frac{\lambda_0}{h})^2]} = \frac{\Delta y_2 y_{30}}{cf}. \quad (41)$$

By substituting Eq. (41) into Eq. (40) and considering

$$\Delta \nu = \frac{hc}{f \lambda_0^2} (d_0 + \Delta y), \text{ we get}$$

$$|\gamma| = \left| \mu' \left(\frac{\lambda_o f}{h} + \frac{\Delta y_2}{2}, \frac{\lambda_o f}{h} - \frac{\Delta y_2}{2}, v_o \right) \text{Sinc} \left(\frac{h \Delta y_2 (d_o + \Delta y_2)}{(\lambda_o f)^2} y_{30} \right) \right|. \quad (42)$$

Now if a pair of parallel slits is placed parallel to the x_2 axis and

centered at $y_2 = \frac{\lambda_o f}{h}$, a set of fringes can be observed in plane P_3 . These fringes will be perpendicular to those formed by the system with the slit perpendicular to the grating in the P_1 plane and the pair of slanted slits in the P_2 plane.

Fig. 5 and Fig. 6 show some numerical results obtained from Eqs. (37) and Eq. (42) respectively. Fig. 5 shows the degree of coherence as a function of the mean slit separation d_{λ_o} for various values of source size. The degree of coherence is averaged over $x_3 = 0.5, 1.0, 1.5, 2.0$, and 2.5, for the comparison with the results obtained experimentally.

Since the period of the fringes is large (for example of $d_{\lambda_o} = 0.6$ mm, the period is 0.69 mm), the visibility measured is in fact an average value.

Comparing the theoretical analysis in Fig. 5 with the experimental results given in Fig. 5 of the previous paper⁹, the common features are: $|\gamma|$ decreases as d_{λ_o} increases and some of the zeros of $|\gamma|$ move toward the origin as d_o becomes larger. The major differences between the theoretical and experimental results are: (1) the first zero of the theoretical curve ($d_{\lambda_o} = 0.52$ mm) is at a smaller mean slit separation than that of the experimental curve ($d_{\lambda_o} = 1.5$ mm); (2) for large d_{λ_o} the theoretical value of $|\gamma|$ is less than the experimental value (for example 0.27 versus about 0.4 for $d_{\lambda_o} = 2.05$ mm with $d_s = 0.6$ mm and $d_o = 0.4$ mm); and (3) the theoretical curve has more zero points.

It is considered a possibility that if more observations are taken, the experimental curves would have more zero points and would more closely match the theoretical curves. Another factor which may account for the difference is the assumption that the source is separable into luminance and frequency factors and has uniform luminance over a circular disk. In fact a square source was utilized in the experiment.

The degree of coherence for the system with parallel slits is shown in Fig. 6 as a function of slit separation for various source sizes. Its value is significant only in the main lobe of the curve.

IV. Fan-Shaped Deblurring Filter

In this section we present an analysis of the smear deblurring method using a fan-shaped filter with a white light system as proposed and performed by Chao et al¹⁰.

It is well known that the point spread function of a linear blur process is a line segment. In a white light system, however, the smear point spread function can be regarded as a set of single point spread functions acting like a grating with amplitude transmittance function

$$h(x_1, y_1) = \text{rect}\left(\frac{x_1}{a}\right)g(y_1) \quad (43)$$

where a is the smear length and $g(y_1)$ represents a sinusoidal amplitude grating. The corresponding transfer function is

$$\begin{aligned} H\left(\frac{x_2}{\lambda f}, \frac{y_2}{\lambda f}\right) &= B\delta(y_2)\text{Sinc}\left(\frac{a}{\lambda f} x_2\right) * \left[\delta(x_2, y_2) + \frac{1}{2} \delta\left(x_2, y_2 - \frac{\lambda f}{h}\right) \right. \\ &\quad \left. + \frac{1}{2} \delta\left(x_2, y_2 + \frac{\lambda f}{h}\right)\right] . \end{aligned} \quad (44)$$

Considering only the first-order-diffracted term at $y_2 = \frac{\lambda f}{h}$, we get

$$H'\left(\frac{x_2}{\lambda f}\right) \bigg|_{y_2 = \frac{\lambda f}{h}} = \frac{B}{2} \text{Sinc}\left(\frac{a}{\lambda f} x_2\right) \quad (45)$$

where B is a proportionality constant. Notice that the width of H' is given by $\Delta x_2 = 2 \frac{\lambda f}{a}$ and is proportional to the wavelength. Thus over a range of wavelengths the filter takes a fan shape.

To get the cross spectral density function, the correlation functions of $\text{rect}\left(\frac{x_1}{a}\right)$ and $g(y_1)$ are expressed as

$$\tau_h(\frac{\vec{r}_2}{\lambda f}, \frac{\Delta \vec{r}_2}{\lambda f}) = a^2 \delta(\frac{y_2}{\lambda f}, \frac{\Delta y_2}{\lambda f}) \text{Sinc}(\frac{a}{\lambda f}(x_2 + \frac{\Delta x_2}{2})) \text{Sinc}(\frac{a}{\lambda f}(x_2 - \frac{\Delta x_2}{2}))$$

and

$$G'_h(\frac{\vec{r}_2}{\lambda f}, \frac{\Delta \vec{r}_2}{\lambda f}) = \frac{1}{16} \delta(\frac{x_2}{\lambda f}, \frac{\Delta x_2}{\lambda f}) \delta(\frac{y_2}{\lambda f} - \frac{1}{h}, \frac{\Delta y_2}{\lambda f}) \quad (46)$$

Following the same procedure as from Eq. (27) to Eq. (32) the cross spectral density function is

$$W_h(\vec{r}_2, 0, v_0) = \frac{1}{16} a^2 A(v_0) I_s \text{rect}(\frac{x_2}{c_0}) * [\text{Sinc}(\frac{a}{\lambda_0 f} x_2)]^2 \quad (47)$$

Since the function $\text{rect}(\frac{x_2}{c_0})$ can be regarded as a δ function for $d_0 \ll \frac{\lambda_0 f}{a}$,

the comparison of Eq. (47) with Eq. (45) yields

$$W_h \propto [H']^2 \quad (48)$$

Fig. 7 shows W_h as a function of x_2 calculated using Eq. (48) for a given value of a and various values of source size d_0 . A curve of $[\text{sinc}(\frac{a}{\lambda_0 f} x_2)]^2$ is also shown for comparison. The difference between the $(\text{sinc})^2$ and the convolution curves is less than 10% if $d_0 \leq \frac{2}{3} \frac{\lambda_0 f}{a}$.

Given a smear length $a = 0.5$ mm and $\lambda_0 = 5461 \text{ \AA}$, the corresponding source size depends on f , for example, $f=380$ mm, $d_0 \leq 0.28$ mm and $f=1000$ mm $d_0 \leq 0.73$ mm.

If the 10% error is acceptable for a deblurring process, then the diameter of the white light source should be

$$d_0 \leq \frac{2}{3} \frac{\lambda_0 f}{a} \quad (49)$$

Then an inverse filter $1/H'$ centered at $x_2 = 0$ and $y_2 = \frac{\lambda_0 f}{a}$ in the P_2

plane can be used for deblurring at the wavelength λ_0 . Over the range of visible wavelengths a fan type filter is implemented. Substituting

$d_{\lambda_0} = 2 \frac{\lambda_0 f}{a}$ into Eq. (40) the angle of inclination is

$$\theta = \tan^{-1}(h/a) . \quad (50)$$

However, this expression must be modified to account for the increase in spot size due to axial chromatic aberration and the spherical focal surface. Applying Eq. (20) we get

$$\theta' = \tan^{-1}\left(\frac{h}{a} + \Delta d_{\lambda} \frac{h}{\Delta \lambda f}\right) \quad (51)$$

where

$$\Delta d_{\lambda} = \frac{D}{f} \left[1 - \left(\frac{\lambda_r}{h}\right)^2\right]^{-1/2} \left[\Delta \ell_1 + \frac{\lambda_r \Delta \lambda f}{h^2}\right] . \quad (52)$$

From the numerical example of Section II, we obtain $\theta = 35'$ and $\theta' = 3^\circ$.

Thus $h/a \ll \Delta d_{\lambda} \frac{h}{\Delta \lambda f}$, and the angle of inclination is determined mainly by

the parameters of the white light system (the axial chromatic aberration in this example) and not the smear length a .

V. Conclusion

The cross spectral density function has been used to analyze a white-light optical processing system with a grating in the input plane. The propagation of the cross spectral density function from the source plane to the output plane was examined in detail and used to derive the complex degree of coherence and intensity distribution under certain assumptions about the white light source. A theoretical explanation of the fan-shaped filter for deblurring a color smeared object has also been presented. Good agreement between the theoretical and experimental results indicates that the cross spectral density function is a useful tool in the study of interference phenomena in a white-light system. We acknowledge the support of the U.S. Air Force Office of Scientific Research grant AFOSR-83-1040.

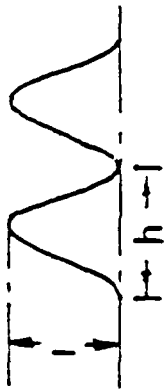
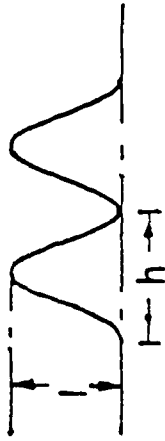
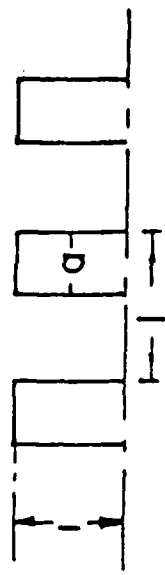
References

1. F. T. S. Yu and J. L. Horner, "Optical processing of photographic images," Opt. Eng., 20, 666 (1981).
2. W. T. Rhodes and A. A. Sawchuck, "Incoherent optical processing," in Optical Information Processing - Fundamentals, S. H. Lee, Ed. (Springer, New York, 1981), p. 69.
3. F. T. S. Yu, Optical Information Processing (Wiley-Interscience, New York, 1983).
4. R. Sudol and B. J. Thompson, "Lau effect: theory and experiment" Appl. Opt., 20, 1107 (1981).
5. S. Cartwright, "Incoherent optical processing: a coherence theory approach," Appl. Opt., 23, 318 (1984).
6. L. Mandel and E. Wolf, "Spectral coherence and the concept of cross-spectral purity," J. Opt. Soc. Am., 66, 529 (1976).
7. E. Wolf, "Coherence and radiometry," J. Opt. Soc. Am. 68, 6 (1978).
8. X. J. Lu, "Pseudocolor encoding with a white-light processing system," Opt. Commun., 48, 13 (1983).
9. F. T. S. Yu, F. K. Hsu and T. H. Chao, "Coherence measurement of a grating-based white-light optical signal processor," App. Opt. 23, 333 (1984).
10. T. H. Chao, S. L. Zhuang and F. T. S. Yu, "Broad spectral band color image deblurring," Appl. Opt., 22, 1037 (1983).
11. M. Born and E. Wolf, Principles of Optics (Pergamon, New York, 1975), Chap. 10.

Figure Captions

- Fig. 1. White-light optical processing system.
- Fig. 2. (a) One of the first order intensity distributions in the pupil plane. (b) Computer-calculated 3-D graphics representing corrected distribution of (a).
- Fig. 3. (a) Chromatic aberration at the first order intensity distribution in the pupil plane P_2 .
(b) Overlapping of two first order diffracted color spots.
- Fig. 4. Schematic diagram showing the path difference in the interference of a pair of slanted slits.
- Fig. 5. Degree of coherence $|\gamma|$ in x_2 direction as a function of mean slit separation d_{λ_0} for various values of source size d_0 .
- Fig. 6. Degree of coherence $|\gamma|$ in y_2 direction as a function of parallel slit separation d_{λ_0} for various values of source size d_0 .
- Fig. 7. Convolution factor of the cross-spectral density function shown in Eq. (68) for various source sizes d_0 and an additional curve of $[\text{Sinc}(\frac{a}{\lambda_0 f} x_2)]^2$ for comparison.

Table 1

Amplitude sinusoidal grating	Phase sinusoidal grating	Ronchi grating
 $g_1 = \frac{1}{2} \left(1 + \cos 2\pi \frac{y}{h} \right)$ $g \cdot g^* = \frac{1}{4} \left(1 + \cos 2\pi \frac{y + \frac{y}{2}}{h} \right) \left(1 + \cos 2\pi \frac{y - \frac{y}{2}}{h} \right)$ $G_1 = \frac{1}{4} \delta \left(\frac{y}{\lambda f}, \frac{y}{\lambda f} \right) + \frac{1}{16} \left[\delta \left(\frac{y}{\lambda f} - \frac{1}{h}, \frac{y}{\lambda f} \right) + \delta \left(\frac{y}{\lambda f} + \frac{1}{h}, \frac{y}{\lambda f} \right) \right] + \frac{1}{16} \left[\delta \left(\frac{y}{\lambda f}, \frac{y}{\lambda f} - \frac{2}{h} \right) + \delta \left(\frac{y}{\lambda f}, \frac{y}{\lambda f} + \frac{2}{h} \right) \right] + \frac{1}{8} \left[\delta \left(\frac{y}{\lambda f} - \frac{1}{2h}, \frac{y}{\lambda f} - \frac{1}{h} \right) + \delta \left(\frac{y}{\lambda f} + \frac{1}{2h}, \frac{y}{\lambda f} - \frac{1}{h} \right) \right] + \delta \left(\frac{y}{\lambda f} - \frac{1}{h}, \frac{y}{\lambda f} + \frac{1}{h} \right) + \delta \left(\frac{y}{\lambda f} + \frac{1}{h}, \frac{y}{\lambda f} + \frac{1}{h} \right)$	 $g_2 = \exp \left\{ \frac{A}{2} \sin 2\pi \frac{y}{h} \right\}$ $g \cdot g^* = \sum_{m,n} J_m \left(\frac{A}{2} \right) J_n \left(\frac{A}{2} \right) e^{-i 2\pi \frac{m-n}{h} y} e^{i 2\pi \frac{m+n}{2h} y}$ $G_2 = \sum_{m,n} J_m \left(\frac{A}{2} \right) J_n \left(\frac{A}{2} \right) \delta \left(\frac{y}{\lambda f} - \frac{m+n}{2h}, \frac{y}{\lambda f} + \frac{m-n}{h} \right)$	 $g_3 = \sum_n \text{Sinc} \left(\frac{na}{x} \right) e^{i 2\pi n y / x}$ $g \cdot g^* = \sum_{m,n} \text{Sinc} \left(\frac{ma}{x} \right) \text{Sinc} \left(\frac{na}{x} \right) e^{i 2\pi \frac{m+n}{x} y} e^{i 2\pi \frac{m-n}{2x} y}$ $G_3 = \sum_{m,n} \text{Sinc} \left(\frac{ma}{x} \right) \text{Sinc} \left(\frac{na}{x} \right) \delta \left(\frac{y}{\lambda f} - \frac{m+n}{2x}, \frac{y}{\lambda f} - \frac{m-n}{x} \right)$

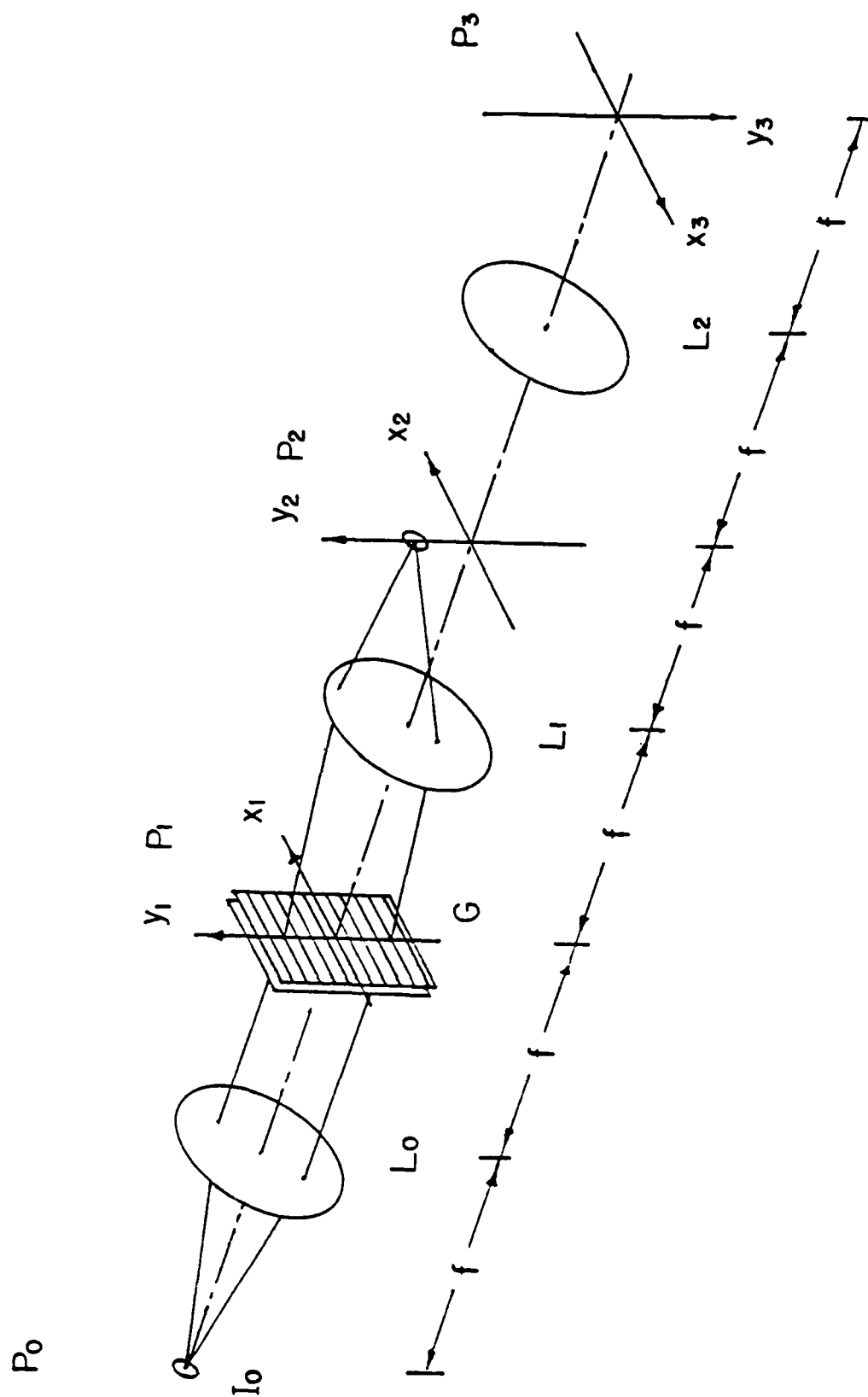
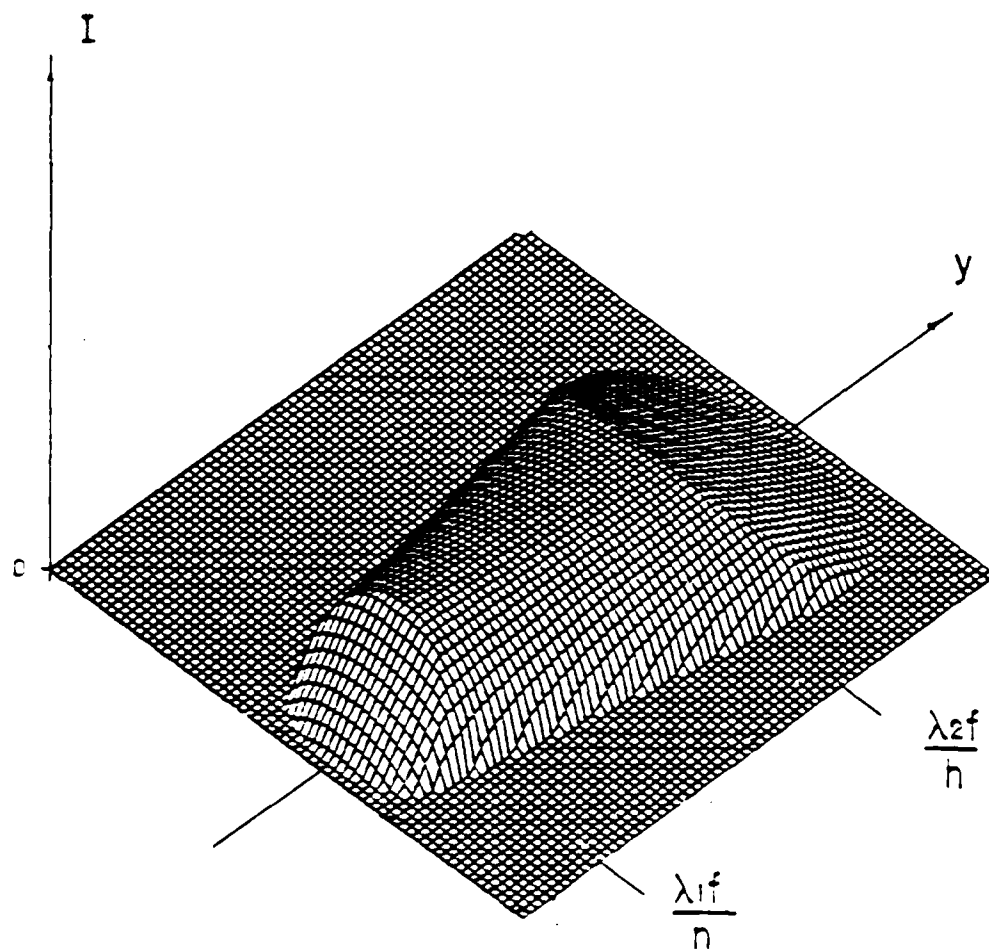
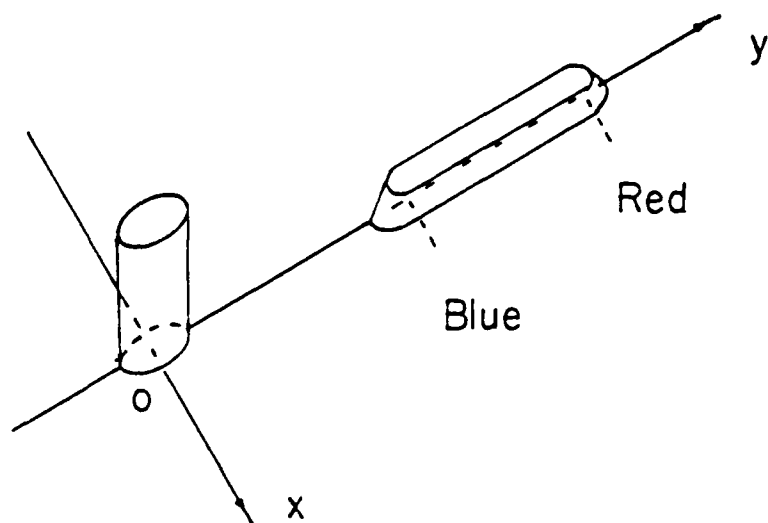


Fig 1



3-D INTENSITY DISTRIBUTION

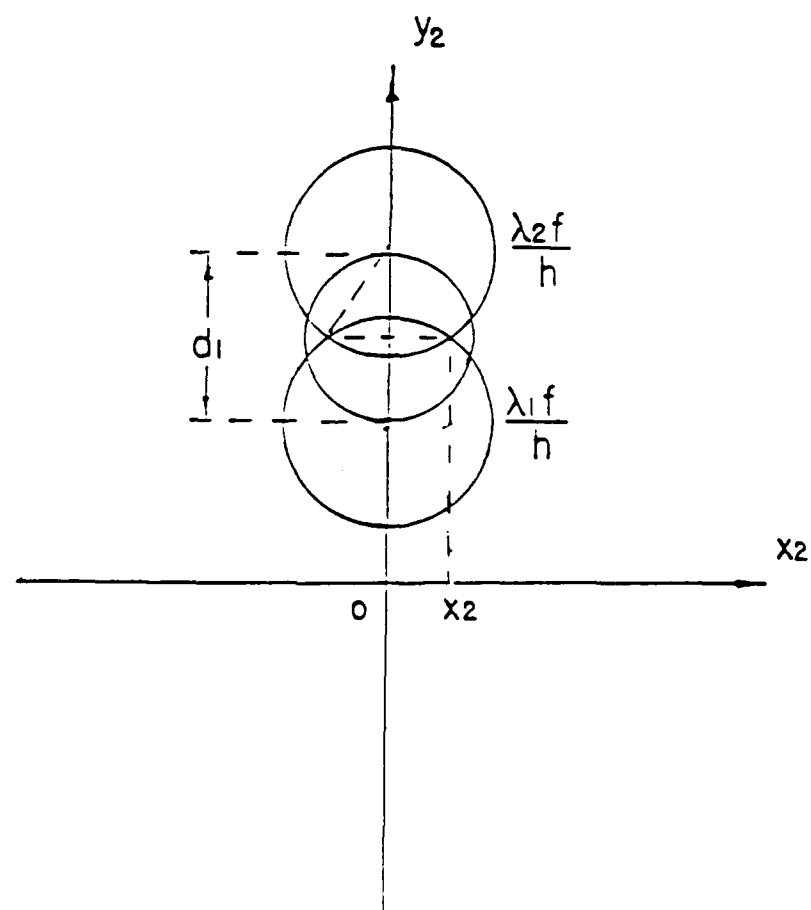
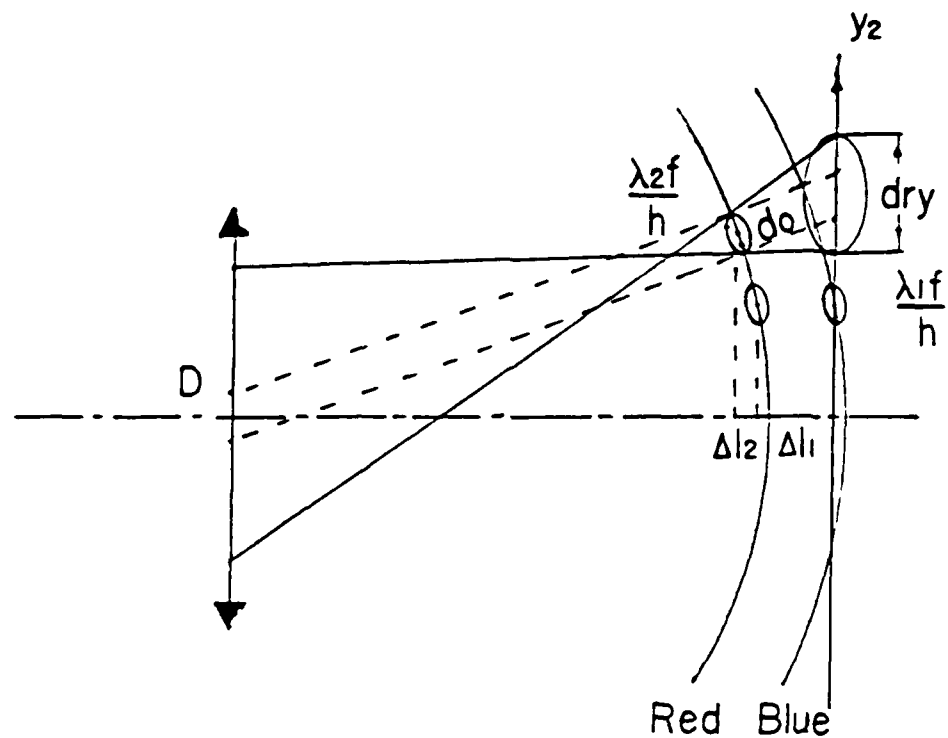
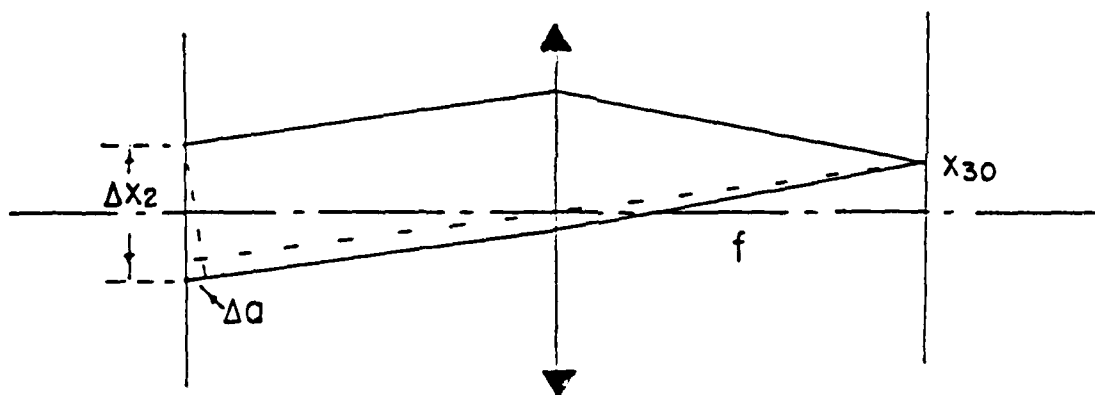
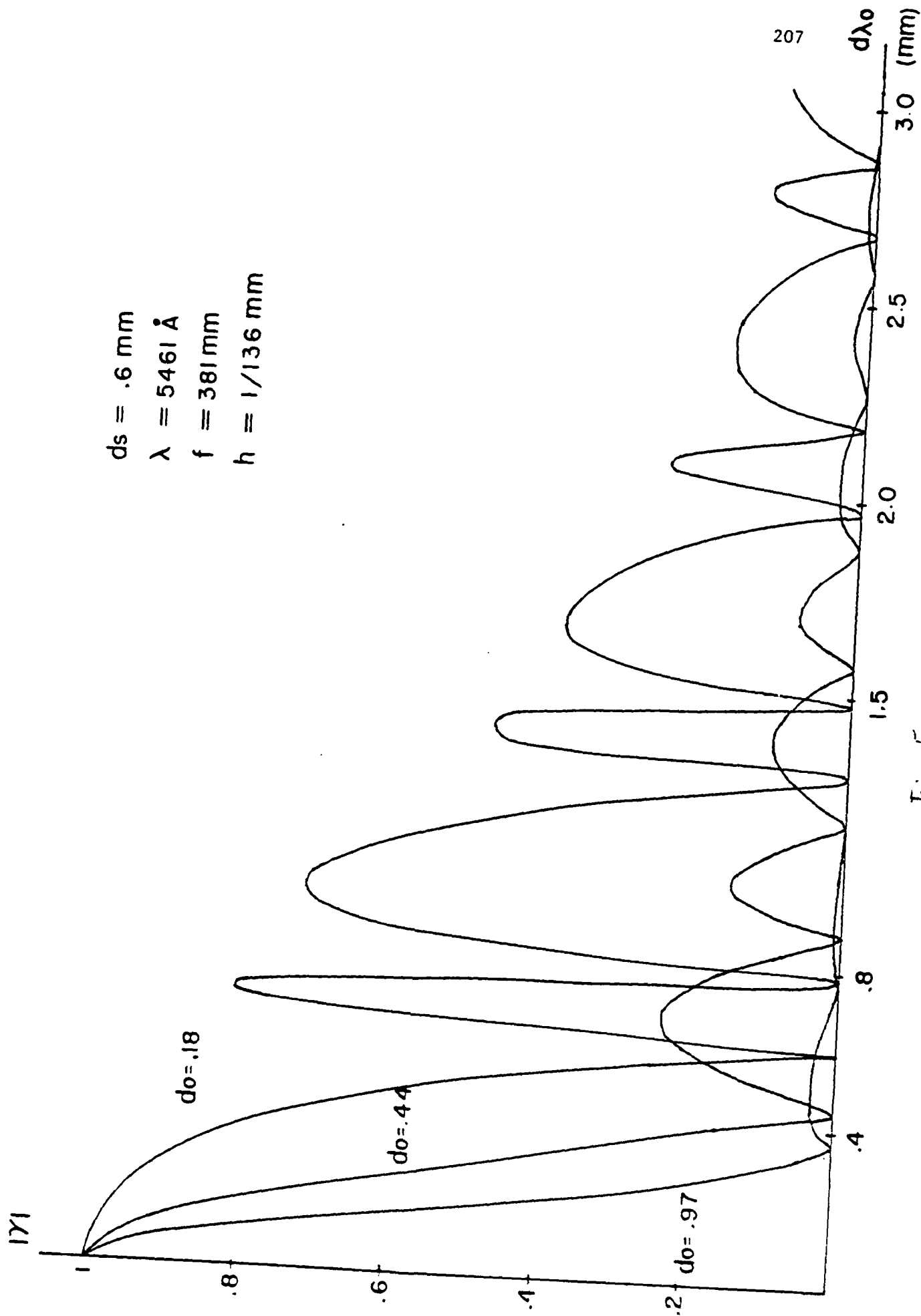


Fig. 3





$ds = .6$ mm
 $\lambda = 5461$ Å
 $f = 381$ mm
 $h = 1/136$ mm

Fig 5

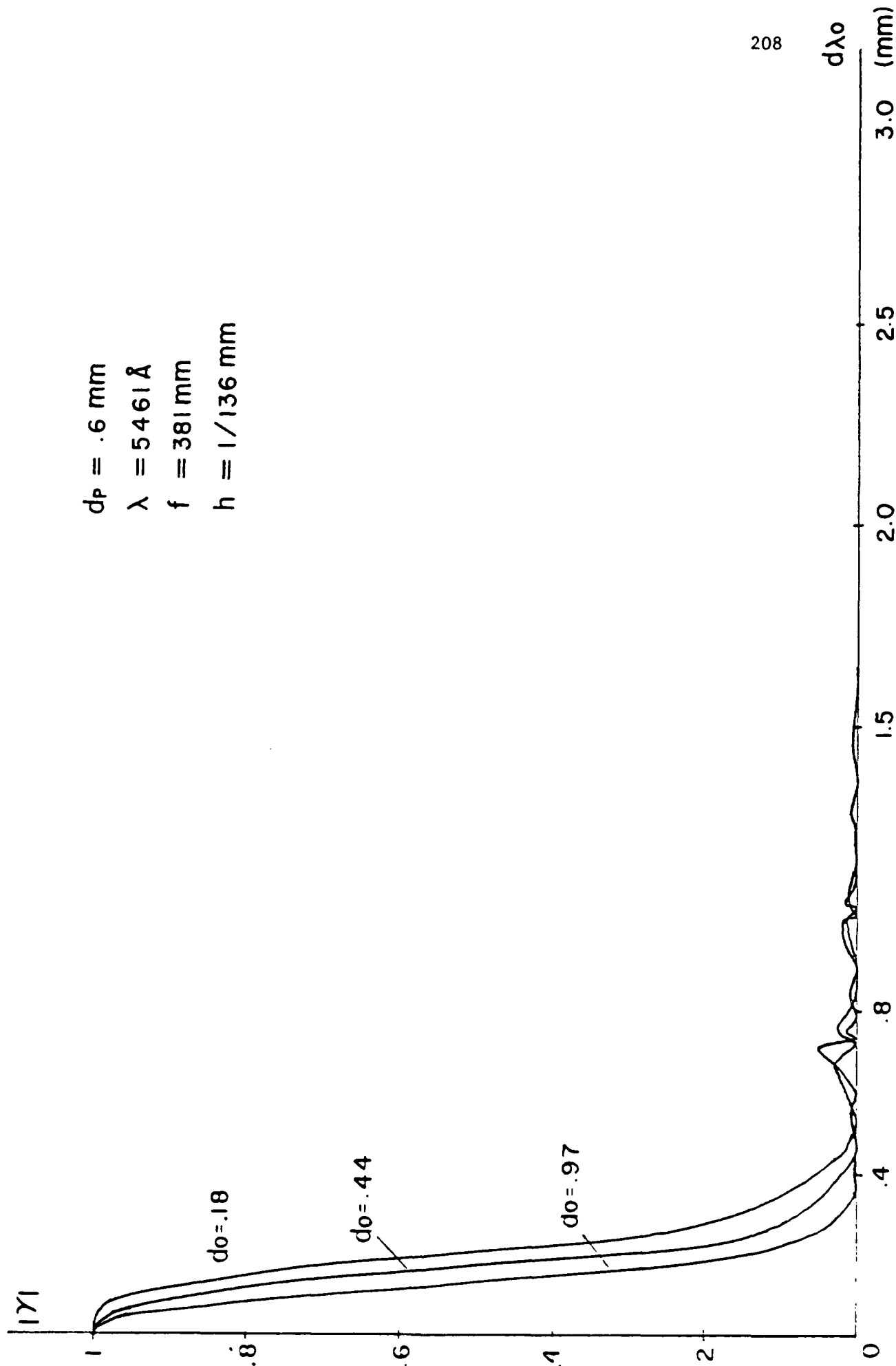


Fig. 6

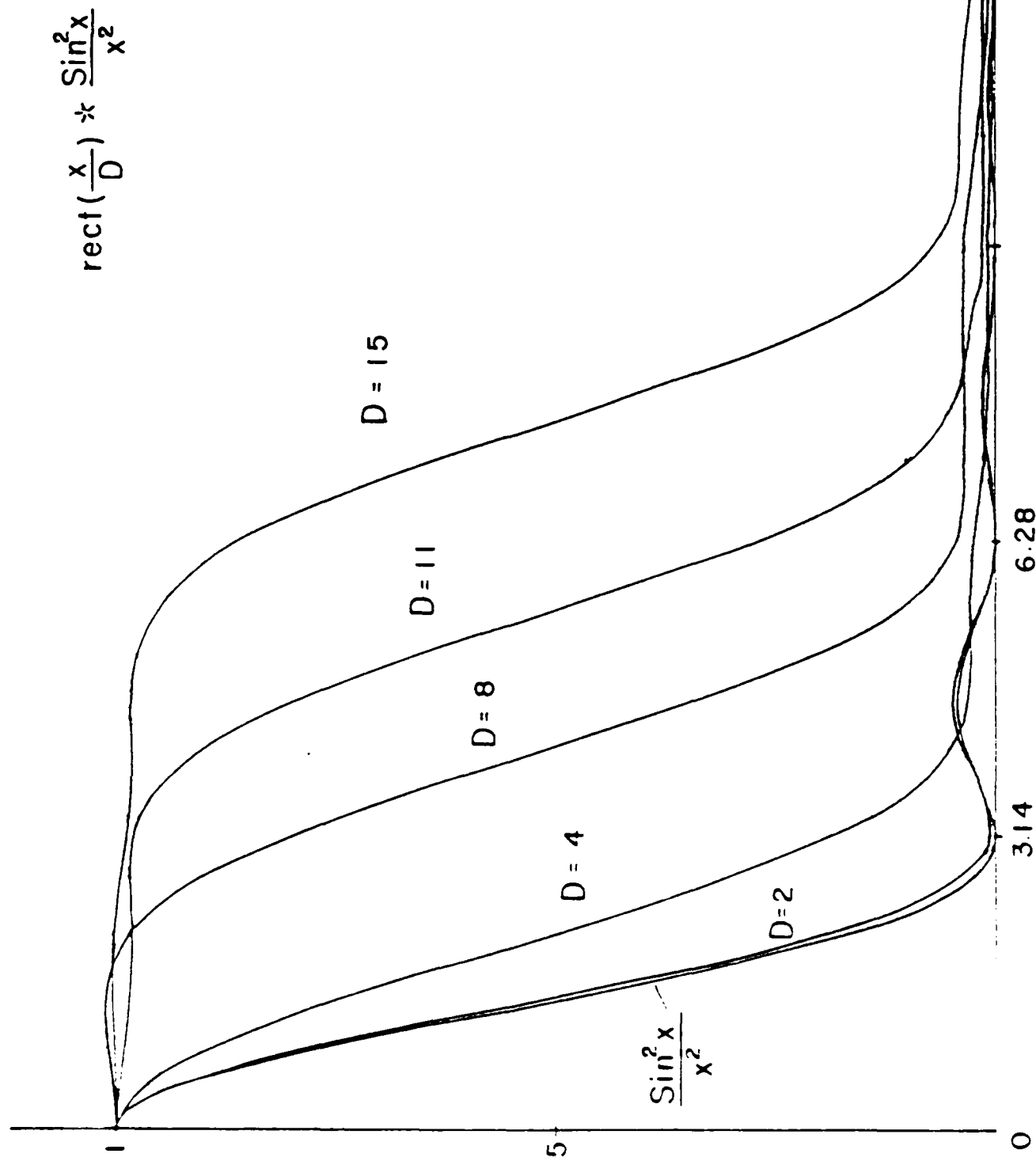


Fig. 7

SECTION XXV

Computer Generated Filter in White-Light Processor

Color Image Processing with CGH Filters in a
White Light Optical System

Michael S. Dymek* and Francis T.S. Yu

The Pennsylvania State University, Department of
Electrical Engineering, 121 Electrical Engineering
East, University Park, Pennsylvania 16802

*When this work was done, both authors were with
The Pennsylvania State University. Mr. Dymek is
now with Martin Marietta Laboratories,
1450 S. Rolling Rd., Baltimore, Maryland 21227.

Abstract

Computer simulation and experimental results
of computer-generated hologram (CGH) spatial filters
applied to the deblurring of color images in a

dispersed white light optical processor are presented. Significant performance can be achieved with moderate resolution images and 1-D processing operations. Color smear and multi-band filter/signal spectrum size mismatch limit applications involving large space-band-width images and/or 2-D processing operations with the dispersed system configuration. The flexibility of the CGH spatial filter fabrication technique, combined with the added processing dimension of wavelength and the inherent ability to reduce coherent artifact noise, make this processing scheme attractive for many image processing applications.

Introduction

Color image processing with Fourier plane spatial filters in a dispersed white light optical system¹ has been demonstrated to have the advantages of reduced coherent artifact noise, reduced cost, and relaxed conditions for the processing environment when compared to strictly coherent systems. The added dimension of wavelength may provide a more "natural"

display of output images for human observation or it may provide added flexibility for the discrimination of objects in pattern recognition systems. The white light system² utilizes a set of band-by-band spatial frequency filters to process quasi-2-D spectra and has been applied to complex color signal detection, smeared color image deblurring, color image subtraction, and spatial frequency and density pseudo-color encoding.

Applications requiring the realization of complex functions in the spatial filters present two major difficulties for the dispersed white light processing scheme. First, the complex processing operations require a significant degree of coherence to be maintained in the system, which is difficult to achieve while still maintaining sufficient light energy for processing. This problem has been partially overcome for some processing applications through the clever use of source encoding techniques. Second, the patterns contained in the complex spatial filter bands must be matched in scale to their corresponding wavelength bands of the dispersed Fourier spectra. Interferometric recording and thin

film deposition³ have both been used to fabricate these complex spatial filters, but are considered too time-consuming or too costly for most applications. An alternative, which is the subject of this paper, utilizes the maturing computer-generated hologram (CGH) technology⁴⁻⁷ for the fabrication of the complex multi-band filters.⁸

We will present analysis of the characteristics exhibited by the CGH filters, which are unique to the dispersed white light processor. The range of wavelengths processed by each filter band has the most significant effect on 1-D processing performance, while similar effects can be expected for 2-D processing operations as well. The effects on processing performance due to color smearing are similar to those produced by white light illumination of conventional holograms, but can be substantially reduced by minimizing the spatial width of each filter band. Computer simulation and experimental results, using the processing example of linearly smeared color image deblurring, demonstrate the processing performance achievable with the proposed CGH multi-band filter

concept. The feasibility of using phase-only CGH filters⁹ in the white light processor is also demonstrated. At the same time, limitations of the technique become apparent when applied to the processing of color images having substantial baseband energy along the dispersion axis.

Mathematical Formulation

The color image processor using computer-generated spatial filters is based on the dispersed white light optical processor discussed in previous papers.¹⁻³ The optical arrangement for the system is depicted in Fig. 1. A collimated beam of white light is produced from an arc lamp source through a pinhole spatial filter. The color image to be processed, usually in the form of a color transparency, having transmittance $s(x,y;\lambda)$, is placed in contact with a diffraction grating having transmittance $t_g(x)$ in plane P_1 . Ideally, the grating must have both high and uniform diffraction efficiency throughout the range of wavelengths to be processed. The combined transmittance at the input plane is

$$s(x,y)t_g(x) = s(x,y)[1 + \cos p_0 x], \quad (1)$$

where p_0 is the angular spatial frequency of the grating and it is understood that the input color image transmittance depends on wavelength. The signal spectrum is assumed bandlimited according to

the description

$$S(p,q) = \begin{cases} \iint s(x,y) \exp[-i(px+qy)] dx dy & \text{for } |p| < p_{\max} \\ & \text{and } |q| < q_{\max} \\ 0 & \text{otherwise.} \end{cases} \quad (2)$$

An achromatic transform lens, L_1 , placed one focal length behind the input plane produces the two dimensional Fourier transform at the spatial frequency plane P_2 . The complex light distribution at P_2 is described by

$$E(p,q) = C_1 \iint s(x,y) [1 + \cos p_0 x] \exp[-i(px+qy)] dx dy d\lambda, \quad (3)$$

where the integration is performed over the input spatial domain and the spectral band of the light source, (p,q) represents the angular spatial frequency coordinate system, and C_1 is a complex constant.

The color spectra in the first order diffraction term of the spatial frequency plane are

dispersed so that they may be operated upon by a multi-band spatial filter. In general, the band-by-band filter can be described by

$$H(p, q) = C \sum_{j=1}^N H_j(q) \text{rect}[q/(2q_{j\max})] \text{rect}[(p-p_j)/2(\Delta p_j)], \quad (4a)$$

and

$$H_j(q) = |H_j(q)| \exp[i\phi_j(q)], \quad (4b)$$

where the first factor, $H_j(q)$ in the summation represents the complex spatial filter for one-dimensional processing in the j th wavelength band; the second factor represents the spatial frequency window over which the j th filter operates, with $q_{j\max}$ equal to the maximum angular spatial frequency along the processing direction passed through the j th filter band; the third factor represents the extent, $[2(\Delta p_j)]$, of the j th filter band along the dispersion axis, where p_j is the angular spatial frequency corresponding to the j th band center wavelength, λ_j .

The light distribution immediately behind the spatial frequency plane can be described as the product

of the signal spectrum and the spatial filter transmittance or

$$E_2(p,q) = C \iiint s(x,y) [1 + \cos p_0 x] \exp[-i(px+qy)] dx dy d\lambda$$

$$\times \prod_{j=1}^N \{ \pm H_j(q) \text{rect}[q/2q_{j\max}] \text{rect}[(p-p_j)/2(\Delta p_j)] \}.$$

(5)

A second achromatic transform lens, L_2 , produces the Fourier transform of the filtered spectrum at the output image plane, P_3 , and is given by

$$E(x,y) = K_1 \iiint E_2(p,q) \exp[-i(px+qy)] dp dq d\lambda, \quad (6)$$

where K_1 is a complex constant; the integration is over the spatial frequency plane and the spectral band of the light source; the dependence of the output image light distribution on λ is understood and the symbolic representation is left out for brevity.

In this paper we will assume that the multi-band filter is a computer generated hologram filter, which

realizes a desired complex filter function, by way of the detour-phase effect, in the first order diffraction term of the output plane. The grating-like CGH filter transmittance within a single band, can be described as

$$H(\alpha, \beta) = \sum_{m,n} |H(md, nd)| \text{rect}[\alpha - md/a_{mn}] \text{rect}[\beta - nd - P_{mn}/b_{mn}], \quad (7)$$

where, for the m th rectangular sample cell, a_{mn} is the height along the α -direction, b_{mn} is the width along the β -direction, d is the spatial sampling period, $H(md, nd)$ is the sampled filter function value, and P_{mn} is the shift proportional to the sampled phase term, $\phi(md, nd)$; (α, β) represent the spatial coordinates corresponding to the spatial frequency plane, where $\alpha = (\lambda f/2\pi)p$ and $\beta = (\lambda f/2\pi)q$.

Since the desired output image appears in the neighborhood of the first order diffraction term, in order to avoid aliasing, the criterion for choosing the value of d for a given wavelength is

$$d/\lambda f < 1/W, \quad (8)$$

where W is the width of the output image and f is the focal length of the second transform lens.

More thorough analyses of CGH spatial filters in monochromatic optical systems are presented by other authors.^{4-7,9} Here we will concentrate on the requirements for and the effects due to the application of CGH filters to the dispersed white light processor. For simplicity, we will consider 1-D processing operations and, initially, input images having zero spatial frequency content along the dispersion, (p) , axis. This case produces a Fourier transform in plane P_2 which is vanishingly narrow along the p -direction for a single wavelength.

1-D Processing

In order to produce overlapping color output images for the entire range of processing wavelengths, the value of d should be inversely proportional to the wavelength at each value of α . In the multi-band filtering scheme, the

filter function and the value of d are constant as a function of α , within each band. This constraint models the realistic limitations of filter generation techniques. For each band in the filter, a continuous range of wavelength-scaled signal spectra are passed, causing corresponding filter/signal spectrum size mismatch.

Two different effects emerge from this mismatch when the multi-band filter is realized by CGH techniques. First, and most obvious, is that incorrect values of amplitude and phase may be imparted at most spatial frequency values where the signal spectrum wavelength differs from the design wavelength of the filter band. This problem may be less severe for filter functions which change slowly along the processing axis. The effect on processing performance depends strongly on the characteristics of the filter function, but, in general, the effect is most severe at higher spatial frequencies. Results of computer simulations of this effect for the linear deblurring operation will be presented later.

The second effect caused by the size mismatch is color smear due to the dispersion of the multi-colored diffracted output images coming from a single filter band. The smear is also present with multi-band filters generated using interferometric techniques and is similar to the effect produced by illuminating a conventional hologram with a white light source. In general, the spectral bandwidth, $\Delta\lambda_j$ ($j=1,2,3,\dots,N$), of the j th filter band must satisfy the condition

$$\sum_{j=1}^N \Delta\lambda_j < (\lambda_{\max} - \lambda_{\min}), \quad (9)$$

where N is the total number of discrete filter bands and λ_{\min} and λ_{\max} are the minimum and maximum wavelengths to be processed in the system.

Consider one extreme case where

$$\sum_{j=1}^N \Delta\lambda_j = (\lambda_{\max} - \lambda_{\min}), \quad (10)$$

which implies that the j th and $(j+1)$ th filter bands

are adjacent with no "blank" space between them. All the light energy present in the first order term, within the spatial frequency range of the filter, is processed. However, this case also allows the greatest amount of color smear in the output image.

A general expression for the smearing length in the output due to the j th filter band is given by

$$l_{\lambda j} = \Delta \lambda_j f / d_j , \quad (11)$$

where f is the focal length of the second transform lens and d_j is the CGH sampling period within the j th filter band, centered at wavelength λ_j . Equations (8) and (11) indicate the tradeoff that exists between the smearing length and the maximum spatial extent of the output image along the processing axis. A wider output image requires a smaller CGH filter sampling period to avoid aliasing, but the smaller sampling period produces a longer smearing length. Rapidly varying filter functions also require a smaller sampling period to provide accurate sampling, but again causing a longer smearing length.

In the second extreme case, for which $\Delta\lambda_j = 0$, the smearing length approaches zero by using extremely narrow filter bands, spaced relatively far apart. However, this scheme wastes processing light energy and requires very high resolution in the CGH filter fabrication technique.

Two other effects on processing performance were found to be quite significant and will be analyzed here. Of the various misalignment problems normally encountered with the multi-band CGH filter scheme, the most annoying is rotational misalignment of the filter in the spatial frequency plane. The outlines of the dispersed signal spectra and a rotationally misaligned multi-band CGH filter are shown in Fig. 2(a) with an enlarged view in Fig. 2(b). The pivot of rotation is chosen at the spatial center of the filter, $(\alpha, \beta) = (\alpha_p, 0)$, and the angle of rotation, ϵ , with respect to the processing axis, β . The signal spectrum, $S(\alpha, \beta)$, passes through a rotated CGH filter producing a light distribution given by

$$F(\alpha, \beta) = S(\alpha, \beta)H(\alpha', \beta') \quad (12)$$

where (α', β') represent the filter coordinate system centered at $(\alpha, \beta) = (\alpha_p, 0)$ and rotated counter-clockwise through an angle θ .

Consider first, the filter band centered at the pivot point as shown in Fig. 2(b). Since the grating-like structure of the CGH filter has been rotated from the signal spectrum processing axis, the resulting image in the first order output diffraction term will be centered along an axis, y' , which is rotated by angle θ from y . Assuming that for each wavelength, the signal spectrum has energy only along the processing axis, some of the higher spatial frequency information may pass through one or more filter bands other than the corresponding design wavelength band. For design wavelength, λ_i , spectrum energy will pass through the i th filter band up to a value of β given by

$$|\beta_{ri}| = \Delta\alpha_i' / \sin\theta, \quad (13)$$

where $\Delta\lambda_i'$ is the halfwidth of the i th filter band. The remaining i th spectrum energy will pass through the $(i+1, 2, \dots)$ th filter bands, causing another type of smearing in the output image, due to the different cell periods in different filter bands. This discrete type of smearing due to filter rotation increases as the value of θ increases and as the difference between spectrum wavelength and filter band design wavelength, λ_i , increases.

A second effect caused by rotational filter misalignment is the mismatch between the filter function and the signal spectrum. The phase change imparted by the CGH filter is independent of the actual cell period, provided the period is uniform throughout the filter (band). In those regions of the i th signal spectrum which pass through the $(i+1, 2, \dots)$ th filter bands, the cell period uniformity is disturbed, causing phase distortion in the output image.

In filter bands away from the pivot point, the lateral shift due to filter rotation is given

by

$$\Delta a_k = (a_k - a_p)(1 - \cos \theta) \quad (14)(a)$$

$$\Delta b_k = (a_k - a_p) \sin \theta, \quad (14)(b)$$

where a_k is the location along the a -axis of the properly aligned k th filter band center and a_p is the location along the a -axis of the pivot point. For small values of θ , the additional color smear due to this lateral shift may be insignificant compared to the error caused by filter/signal spectrum lateral mismatch along the processing axis.

2-D Processing

The final section of analysis will deal with the more physically realistic case of 2-D signal spectra, i.e., spectra containing baseband energy along the dispersion axis, p , as well as the processing axis, q . Previous analysis of the dispersed white light processor assumed that the width of each filter band was equal to the spatial frequency extent of the signal spectrum having the same wavelength as the filter band design wavelength. The present discussion

extends that analysis to account for signal spectra having spatial frequency content along the dispersion axis that "spills over" into more than one filter band.

Consider the 2-D spectrum with wavelength, $\lambda_i' = (\lambda_i + \Delta\lambda)$, horizontally centered within the i th filter band, H_i , as shown in Fig. 3. The range of signal spectrum angular spatial frequencies passing through H_i is given by

$$\begin{aligned}\Delta p_{ih} &= \Delta p_i - \Delta p_i' \\ &= (1 - \Delta\lambda / \Delta\lambda_i) \Delta p_i\end{aligned}\tag{15}(a)$$

$$\begin{aligned}\Delta p_{il} &= \Delta p_i + \Delta p_i' \\ &= (1 + \Delta\lambda / \Delta\lambda_i) \Delta p_i,\end{aligned}\tag{15}(b)$$

where Δp_i is the angular spatial frequency halfwidth of the i th filter band, $\Delta p_i'$ is the spatial frequency displacement from the center of the i th filter band of the spectrum having wavelength λ_i' , and $\Delta\lambda_i$ is the wavelength halfwidth of the i th filter band. Restating, Δp_{ih} is the range of spatial frequencies

passing through the i th band on the large p side and Δp_{i1} is the range on the small p side.

Two significant causes of error arise from the λ_i ' signal spectrum energy that extends beyond the i th filter band and into the $(i+1, 2, \dots)$ th bands: (1) the difference in CGH filter cell period for different filter bands, and (2) the filter/signal spectrum band size mismatch outside the i th filter band. The first error results in a smearing effect acting upon the higher spatial frequencies for a given wavelength. This smear is different than that discussed earlier in that the high spatial frequency information is smeared along the y output axis with respect to the low spatial frequency information for a single wavelength. An expression for the high frequency smearing length in the output image is given approximately by

$$\Delta l_{hf} = \lambda_i f [2\Delta p_i / p_0 d_i], \quad (16)$$

where d_i is the i th band CGH filter cell period and $2\Delta p_i$ is the difference between the maximum and minimum spatial frequencies of the i th baseband spectrum.

The second source of error, filter/signal spectrum size mismatch, produces an effect similar to the size mismatch discussed earlier for the 1-D spectra case. Although the effect on performance is strongly dependent on the characteristics of the filter and signal spectrum functions, the degradation is certainly more severe for higher spatial frequencies. The performance of the dispersed white light processor when operating on color images having 2-D baseband spectra is probably the most significant limitation of the processing scheme. Quality is improved by increasing the value of p_0 , the frequency of the input plane diffraction grating. But this possible solution is limited by the quality of available optical components and aberrations in the system.¹²

Computer Simulation and Experimental Results

An extensive computer program was written to simulate the processing performance of the multi-band CGH filters in a dispersed white light optical system. The results presented here use the processing example of linearly smeared color image deblurring, although little modification is needed to incorporate any operator selected 1-D processing operation. The simulator utilizes commercially available FFT subroutines to compute the Fourier transform of a linearly smeared color input image for a large number of wavelength values. The program simulates the operation of the CGH filter by sampling the product of the CGH filter band transmittance and the dispersed signal spectra, inverse Fourier transforming, and incoherently summing the multi-colored output images. A 1-D slice of the output image was considered, in order to conserve computer time.

The concept of linearly smeared image deblurring has been discussed by others^{10,11} and will only be

summarized here. The spectrum of a point image that has been linearly smeared over a distance Δy is described in one dimension by

$$G(q) = \Delta y \sin(q\Delta y/2)/(q\Delta y/2). \quad (17)$$

The corresponding inverse spatial filter is proportional to $1/G(q)$ or

$$H(q) = q\Delta y/2/[\sin(q\Delta y/2)]. \quad (18)$$

Since this function contains infinite poles, it cannot be physically realized, although an approximate realization, with some degree of restoration error, is possible. The approximation to Eqn. (18) used throughout the remainder of this work results from clipping the large magnitude values to a normalized maximum value, computed from the product of the number of magnitude quantization levels and the minimum magnitude of the filter function, $H(\phi)$.

Initially, a large set of parameters (e.g., filter band spectral bandwidth, amplitude quantization, cell duty cycle, lateral filter translation, etc.)

describing the CGH filters were varied to produce many simulation results. We found, though, that two parameters were most significant. First, the spectral bandwidth of a given filter band had the greatest effect on performance of the CGH filter system. The curves in Fig. 4(a) depict the output irradiance versus output spatial coordinate near the first order diffraction, resulting from a CGH filter band with 64 amplitude quantization levels (i.e., 6 bits) and designed for an input image blur length of 0.5 mm. As the spectral bandwidth of the filter band grows from 0 nm to 10 nm, the width of the deblurred first order image increases as well, though it still remains a fraction of the input blur length.

The second significant CGH filter parameter was found to be amplitude quantization. A surprisingly good result is shown in Fig. 4(b), for which phase-only CGH filters were used for the deblurring operation. Significant deblurring of the color input image is achieved, for values of filter band spectral bandwidth up to 20 nanometers. Interpreting these simulation results in terms of

CGH filter geometry, we could predict significant deblurring performance for a phase-only CGH filter having as few as 20 filter bands, with uniform spectral width, covering the visible wavelength range from 400nm to 700nm. These results for the multi-band phase-only filters applied in the dispersed white light processor enhance the results of others⁹ who have shown good processing performance achieved with phase-only filters in monochromatic optical processors.

Figures 5(a) and 5(b) summarize the performance of the simulated multi-band CGH filter system for phase-only, as well as 8 and 64 amplitude quantization levels over the range of filter band spectral bandwidth from 0 to 50 nm. The plotted measure of performance is (input blur width)/(deblurred 3dB width) for the curves in Fig. 5(a), which indicate that excellent deblurring performance (factor of 5) can be achieved with a moderate number (>8) of filter amplitude quantization levels, up to 10 nm spectral bandwidths, or with phase-only filtering up to 5 nm bandwidths. Significant deblurring (factor of 2) can still be achieved with any value of amplitude quantization

for filter bands covering 15-20 nm.

In Fig. 5(b), the plotted measure of performance is (total irradiance contained within the deblurred 3dB points)/(total irradiance within the first order output term). Although the shape of these curves would, in general, depend on the exact processing operation, for linear deblurring, the ability of the processor to collect light energy into the deblurred 3dB region tends to increase with few quantization levels as the filter bandwidth increases, while it decreases slightly for many quantization levels. Within the filter band spectral bandwidth of interest, at least 60% of the total first order output irradiance is within the deblurred 3dB points for non-phase-only filters and at least 40% for phase-only filters. (In retrospect, one of the authors (MSD) regrets not having collected appropriate simulation data for calculation of a Horner-like efficiency.⁹⁾)

Several phase-only multi-band deblurring filters were fabricated and tested in a dispersed white light optical processor. Results of experiments

using binary and continuous-tone linearly smeared color input images are presented in Figs. 6 and 7, respectively. In both experiments a xenon arc lamp served as the source of white light with pinhole spatial filtering providing an effective source diameter of $75\mu\text{m}$ and Fourier transform lenses with 381mm focal lengths were used for processing. Output images were recorded on Kodak Ektachrome 200 ASA film.

The phase-only CGH spatial filter pattern was plotted on a Tektronix 4662 digital plotter and photographically reduced onto Kodak Technical Pan Film, followed by chemical developing using the R-10 bleaching process. With an input plane diffraction grating frequency of 120 lp/mm , the maximum spatial dimension of the spatial filter along the dispersion axis was 13.7 mm , assuming processing wavelengths in the range from 400 nm to 700 nm , and the maximum spatial frequency along the processing axis was 20 lp/mm . The CGH filter cell period ranged between 0.018 mm and 0.031 mm , with an average duty cycle of 0.25 , while the filters were designed for a 0.5 mm blur length.

Figure 6 shows a black-and-white photograph of the color output plane light distribution for the deblurring operation performed on a binary slit test image. The photo shows the zero-order output image (essentially a copy of the smeared input image) surrounded by the first order images, which have been deblurred by approximately a factor of 3. In the original color recording, a yellow-orange color present in the zero-order image is due to residual dye in the filter after bleaching. The first order deblurred images appear almost completely white, because their relatively high irradiance has saturated the color recording material. Experimental results agree quite well with computer simulation results in this example. The color smearing caused by baseband spatial frequency energy along the dispersion axis is evident at the two ends of the slit and around some fiber-like noise near the center.

Figure 7 shows a black-and-white photo of the color output for the case of a linearly smeared, continuous-tone color input image. The zero-order term on the left side is again essentially a copy

of the input image, with the higher order terms surrounding it. Since this input image produces all of the possible error-causing effects in the first-order output image, including those due to film nonlinearity during recording of the smeared input image, it can be considered a worst-case input image. However, the first-order image on the right side still shows evidence of successful deblurring, especially at the shirt buttons, the arms, and the "V" at the shirt collar. Barely visible are small yellow designs scattered throughout the red shirt, which also show evidence of deblurring. The region of the head in the image (brightness in the face and darkness in the hair) manifests the effect of non-linear transmittance vs. exposure characteristics of the film used to record the smeared input image. Although this example does not represent an ideal test of the multi-band CGH filter system, it does represent a possible situation in a practical application of the technique. Further work must also be directed to more faithful color reproduction in the processed image.

Conclusions

This paper has presented computer simulations and experimental demonstrations of multi-band CGH spatial filters applied to color image processing in a dispersed white light system. Significant processing performance can be achieved for 1-D processing operations and color input images with moderate space-bandwidth products. The CGH spatial filter fabrication technique adds flexibility to a color image processor which already possesses the advantages of reduced coherent artifact noise, low cost, and reduced sensitivity to the processing environment, when compared to coherent (laser-based) systems.

Analysis of several types of color smear occurring at the output due to characteristics of the CGH system were presented. In addition to rotational alignment of the multi-band filter, the parameter which most effects processing performance is the filter band spectral bandwidth. We calculate that good performance for 1-D operations can be expected from filter bands with up to 10 nm bandwidths along

the dispersion axis, in the visible range of wavelengths. Phase-only CGH filters were also shown via both simulation and experiment to achieve significant performance in the dispersed white light processor. The effect of filter/color spectra size mismatch will be significant with 2-D images. Further work is needed to devise multi-band CGH filters which can process inputs having large space bandwidth products and to retain faithful image colors at the system output.

The authors would like to acknowledge partial support from AFOSR grant #83-0140.

References

- 1 F.T.S. Yu, Optical Information Processing
(John Wiley and Sons, New York, 1983).
- 2 F.T.S. Yu and J.L. Horner, "Optical Processing
of Photographic Images," Opt. Eng. 20, 666 (1981).
- 3 T.H. Chao, S.L. Zhuang, S.Z. Mao and F.T.S. Yu,
"Broad Spectral Band Color Image Deblurring,"
Appl. Opt. 22, 1439 (1983).
- 4 A.W. Lohmann and D.P. Paris, "Computer Generated
Spatial Filters for Coherent Optical Data
Processing," Appl. Opt. 7, 651 (1968).
- 5 W-H. Lee, "Computer-Generated Holograms: Techniques
and Applications," Progr. Opt. 16, E. Wolf, ed.,
North-Holland, Amsterdam (1978).
- 6 D. Casasent, "Computer Generated Holograms in
Pattern Recognition: A Review," Opt. Eng. 24,
724 (1985).

- 7 S.M. Arnold, "Electron Beam Fabrication of Computer-Generated Holograms," Opt. Eng. 24, 803 (1985).
- 8 M.S. Dymek, "Color Image Processing with Computer Generated Spatial Filters in a Dispersed White Light Optical System," PhD Thesis, Department of Electrical Engineering, The Pennsylvania State University, University Park, Pennsylvania (1985).
- 9 J.L. Horner and P.D. Gianino, "Phase-Only Matched Filtering," Appl. Opt. 23, 812 (1984).
- 10 T.H. Chao, S.L. Zhuang, S.Z. Mao, and F.T.S. Yu, "Broad Spectral Band Color Image Deblurring," Appl. Opt. 22, 1439 (1983).
- 11 J. Tsujiuchi, T. Honda, and T. Fukaya, "Restoration of Blurred Photographic Images by Holography," Opt. Commun. 1, 379 (1970).
- 12 P.D. Gianino, C.L. Woods and F.T.S. Yu, "Computer Simulation of White-Light Correlator Performance," Abstract TH9, Opt. Soc. Amer. Annual Mtg.,

Washington, D.C. (1985).

Figure Captions

Fig. 1. Optical arrangement for the dispersed white light processor using multi-band CGH spatial filters.

Fig. 2. Rotational misalignment of CGH filter;
(a) outlines of rotated filter and dispersed color spectra, (b) rotated filter bands near pivot point.

Fig. 3. Two-dimensional signal spectrum extending over more than one filter band.

Fig. 4. Deblurred output irradiance vs. spatial coordinate for (a) 64 levels of filter amplitude quantization and three values of filter band spectral bandwidth, and (b) phase-only filter and four values of spectral bandwidth.

Fig. 5. Deblurring performance vs. filter band spectral bandwidth for phase-only, 8-level, and 64-level amplitude quantization; performance measure is (a) input blur width/deblurred 3dB width and (b) total 3dB irradiance/total first order irradiance.

Fig. 6. Black & white photo of color output light distribution for binary slit input. Zero-order term is in center surrounded by first-order deblurred terms. Input blur width is indicated as Δy .

Fig. 7. Black & white photo of the color output light distribution for a linearly smeared, continuous-tone color input image. Zero-order term is left of the deblurred first-order term. Input blur width is indicated as Δy .

Fig. 6. Black & white photo of color output light distribution for binary slit input. Zero-order term is in center surrounded by first-order deblurred terms. Input blur width is indicated as Δy .

Fig. 7. Black & white photo of the color output light distribution for a linearly smeared, continuous-tone color input image. Zero-order term is left of the deblurred first-order term. Input blur width is indicated as Δy .

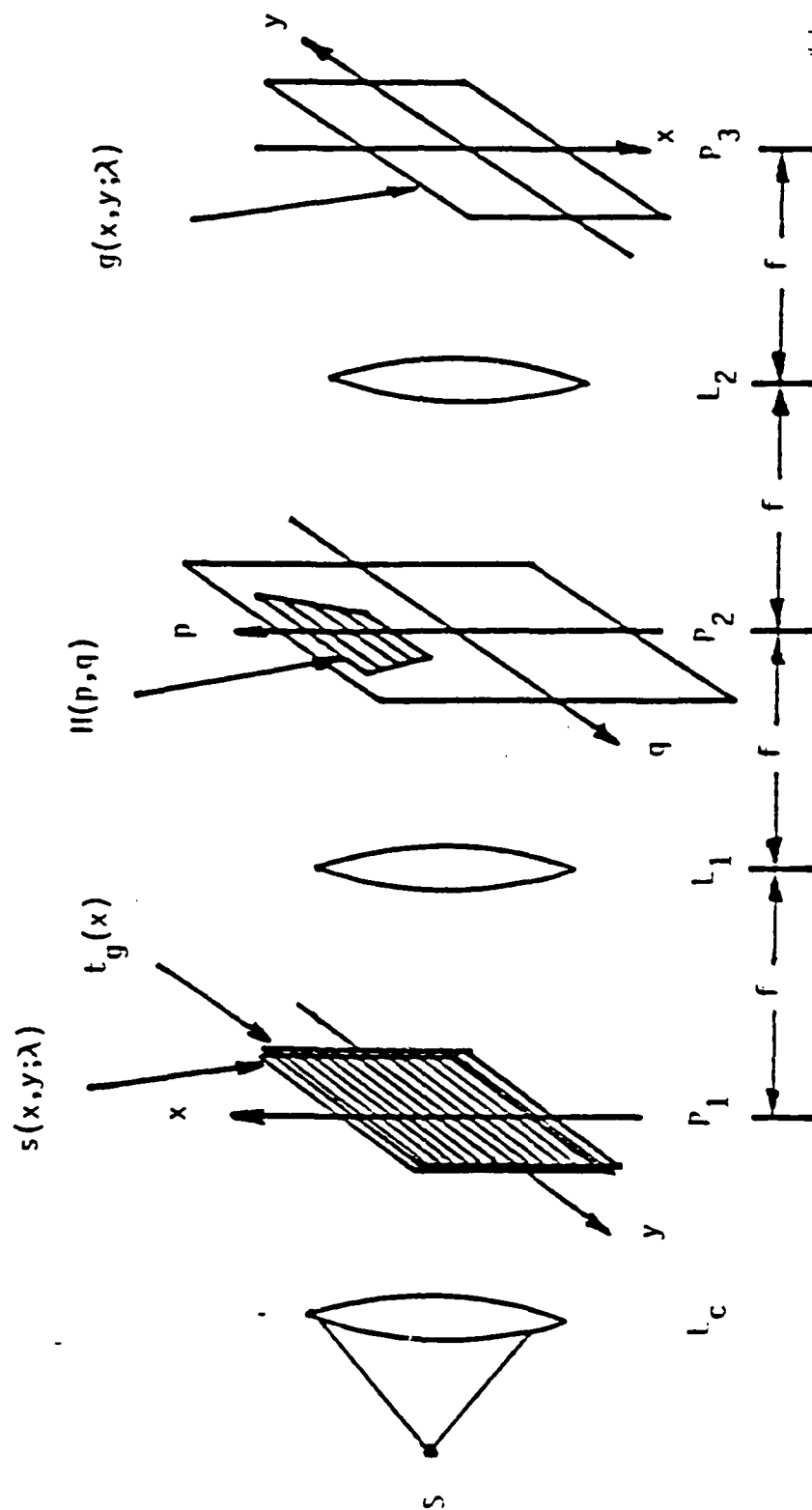


Fig. 1. Optical arrangement for the dispersed white light processor using multi-band CGH spatial filters.

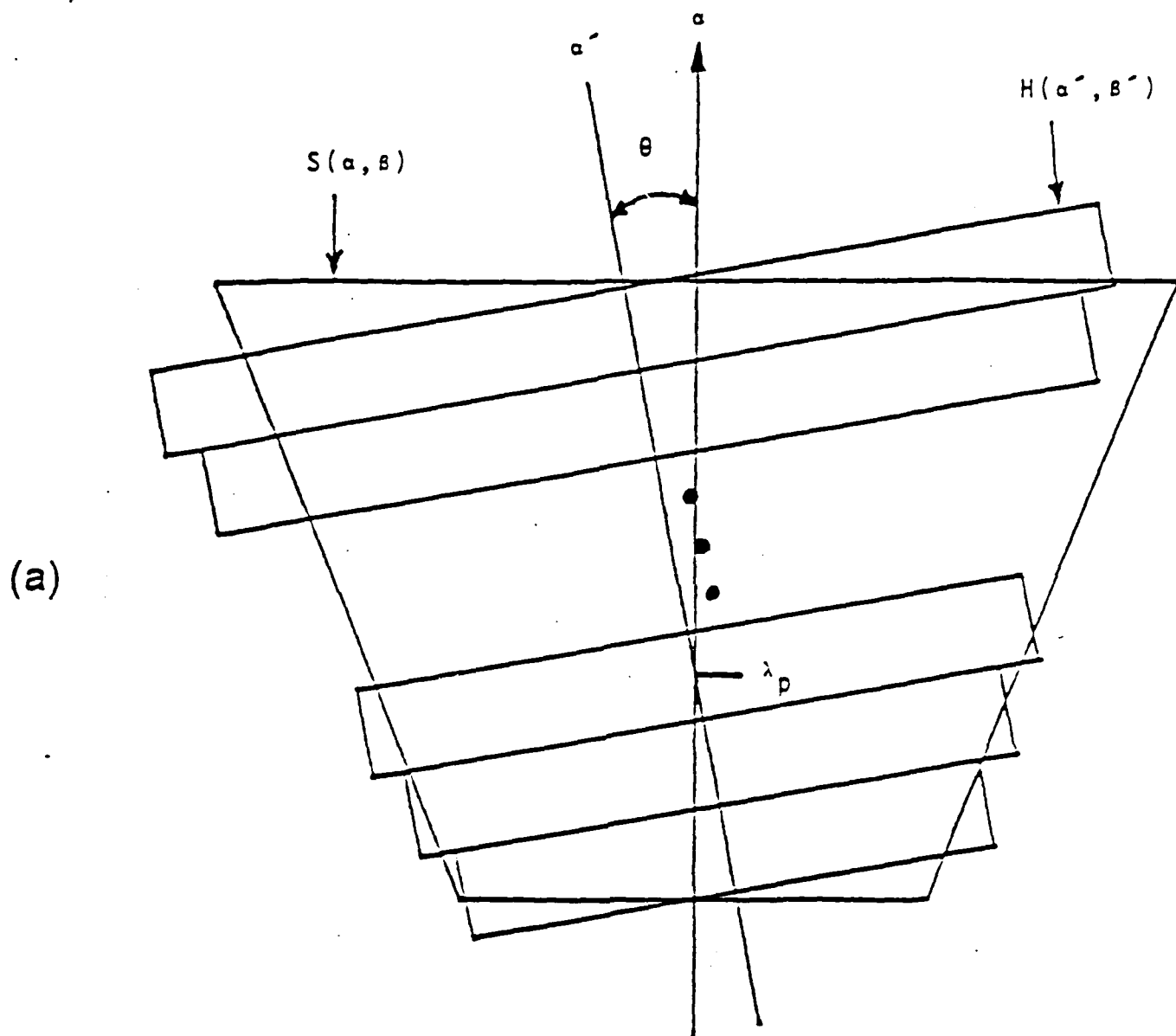


Fig. 2. Rotational misalignment of CGH filter;
 (a) outlines of rotated filter and dispersed color
 spectra, (b) rotated filter bands near pivot point.

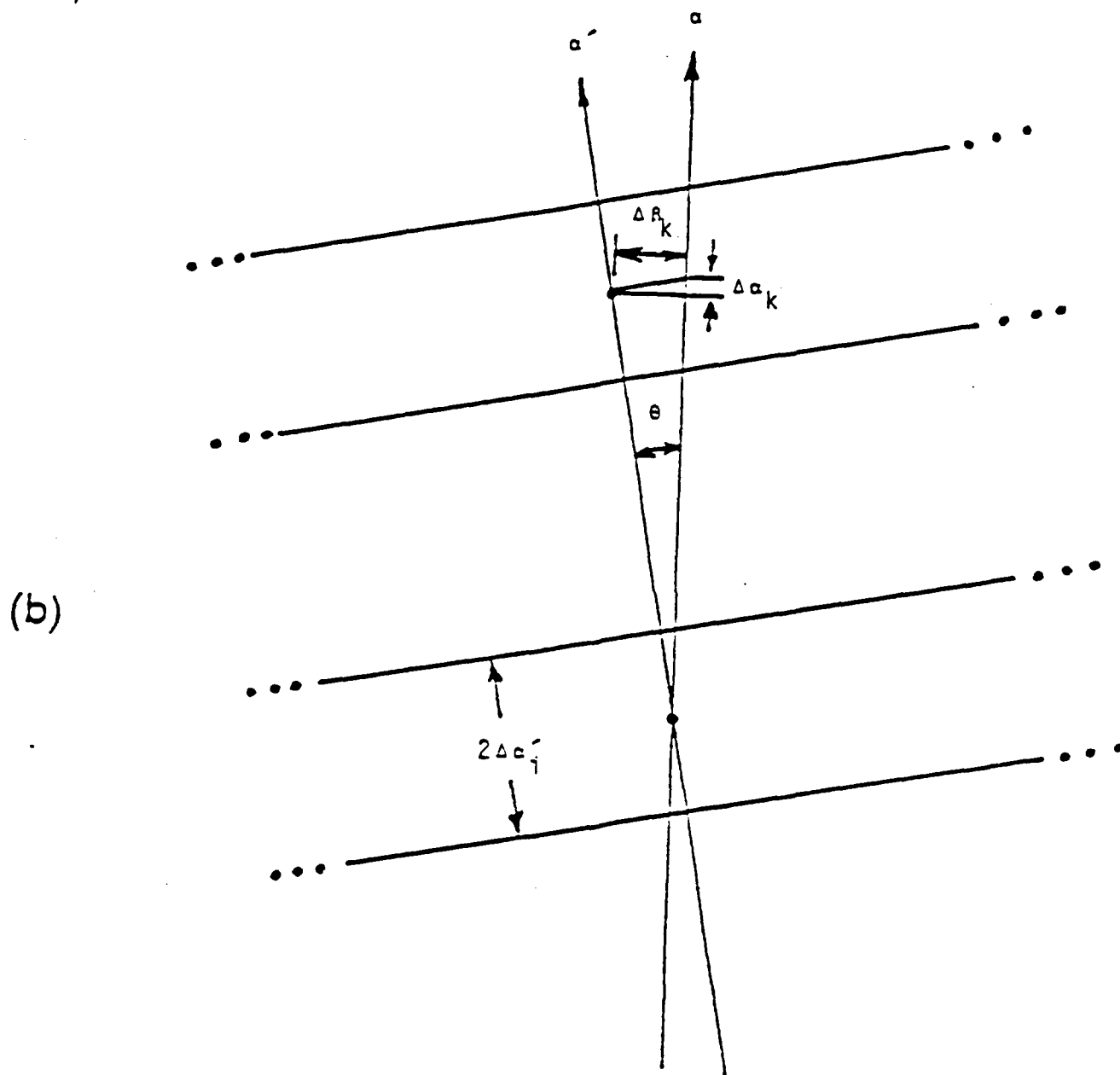


Fig. 2. Rotational misalignment of CGH filter;
 (a) outlines of rotated filter and dispersed color
 spectra, (b) rotated filter bands near pivot points.

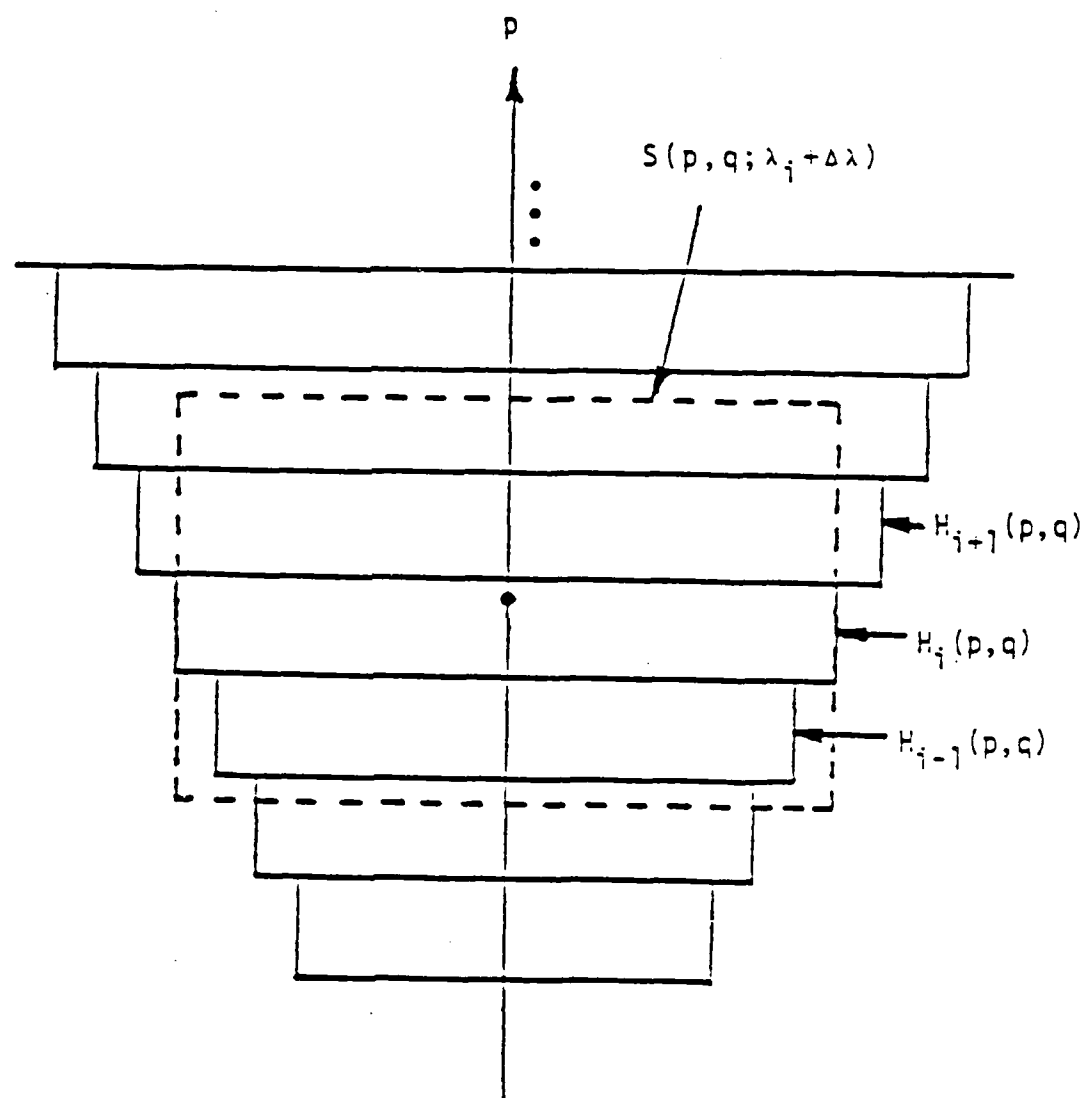


Fig. 3. Two-dimensional signal spectrum extending over more than one filter band.

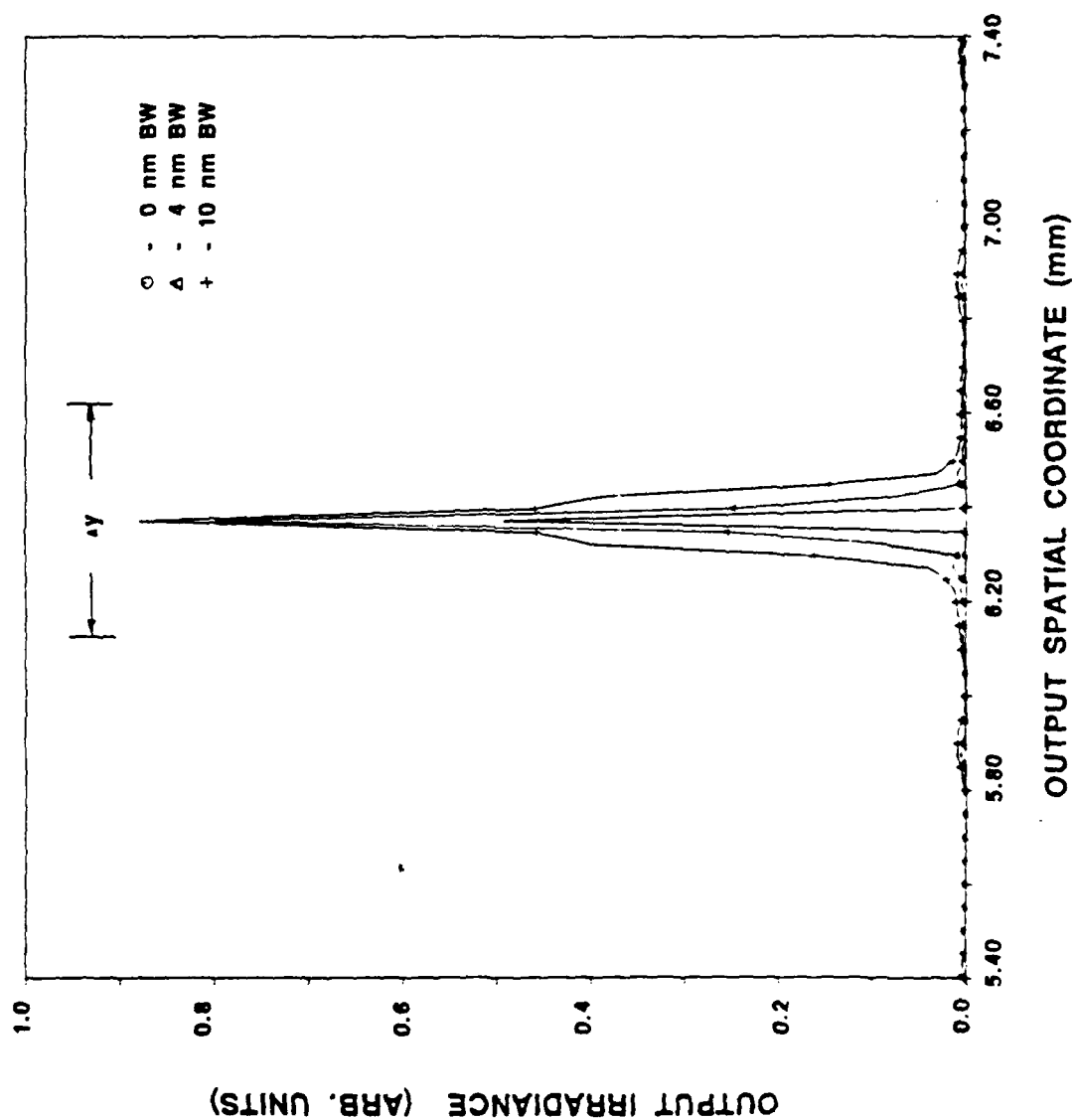


Fig. 4. Deblurred output irradiance vs. spatial coordinate for (a) 64 levels of filter amplitude quantization and three values of filter band spectral bandwidth, and (b) phase-only filter and four values of spectral bandwidth.

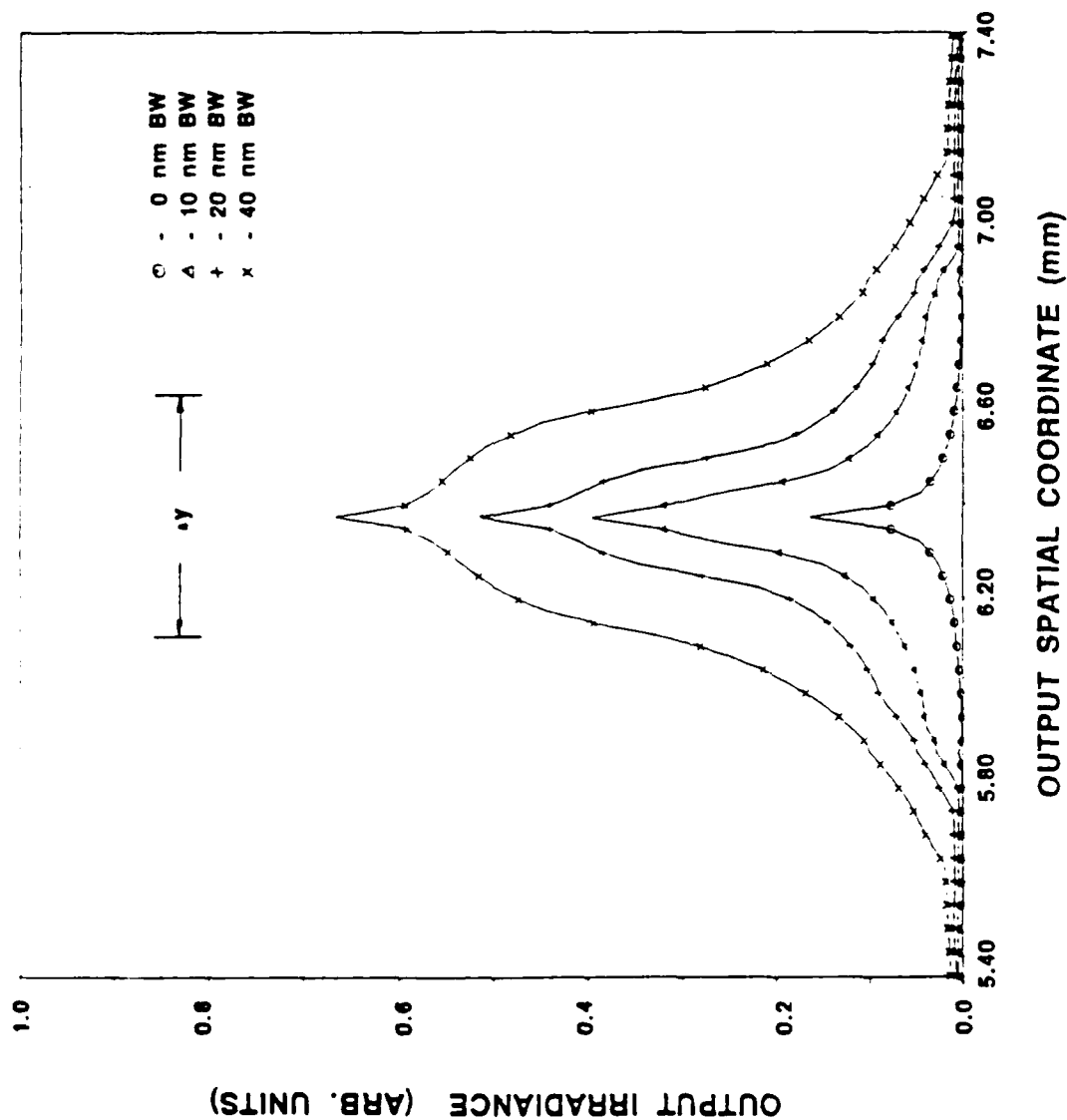
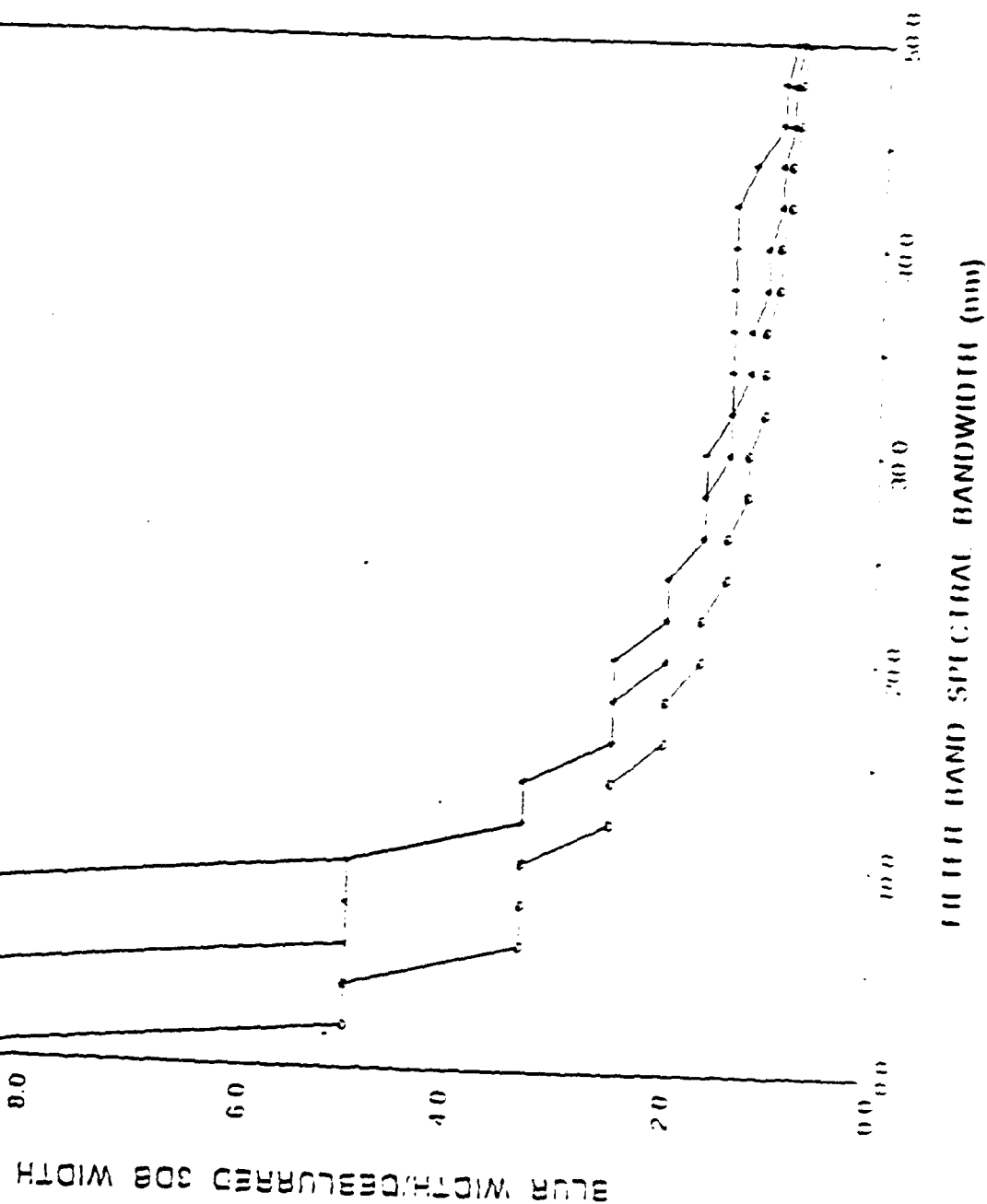


Fig. 4. Deblurred output irradiance vs. spatial coordinate for (a) 64 levels of filter amplitude quantization and three values of filter band spectral bandwidth, and (b) phase-only filter and four values of spectral bandwidth.

○ PHASE ONLY
 ▲ 8 QUANTIZATION LEVELS
 + 64 QUANTIZATION LEVELS



(a)

Fig. 5. Deblurring performance vs. filter band spectral bandwidth for phase only, 8 level, and 64 level amplitude quantization; performance measure is (a) input blur width/deblurred 3dB width and (b) total 3dB irradiance (total first order irradiance)

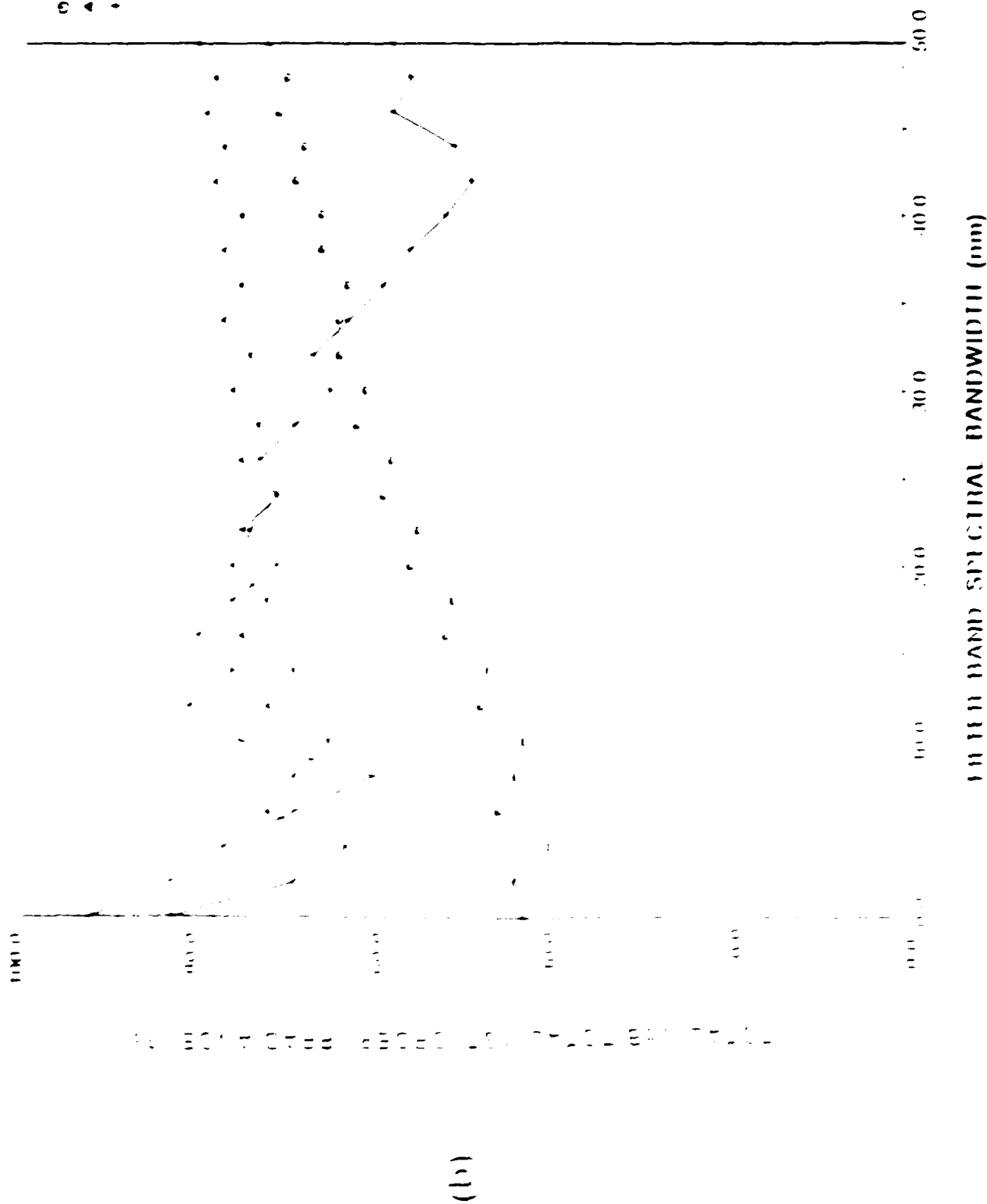


Fig. 5. Debblurring performance vs. filter band spectral bandwidth for phase-only, 8-level, and 64-level amplitude quantization; performance measure is (a) input blur width/deblurred 3dB width and (b) total 3dB irradiance/total first order irradiance.



Fig. 7. Black & white photo of the color output & ant distribution for a linearly created, non-subtractive color image. Zero-order term is left of the colorized three-order term.

SECTION XXVI

Holographic Tomography

II. — ANALOG RECORDING AND RECONSTRUCTION SYSTEMS

Holographic techniques are important not only to display interesting object fields but also to serve as an image processing tool in optical systems.⁶ In the present method the hologram generated will be utilized to display sequential projections of the studied object field optically. It will also serve as a processing tool to collect the projected data for computer post-processing.

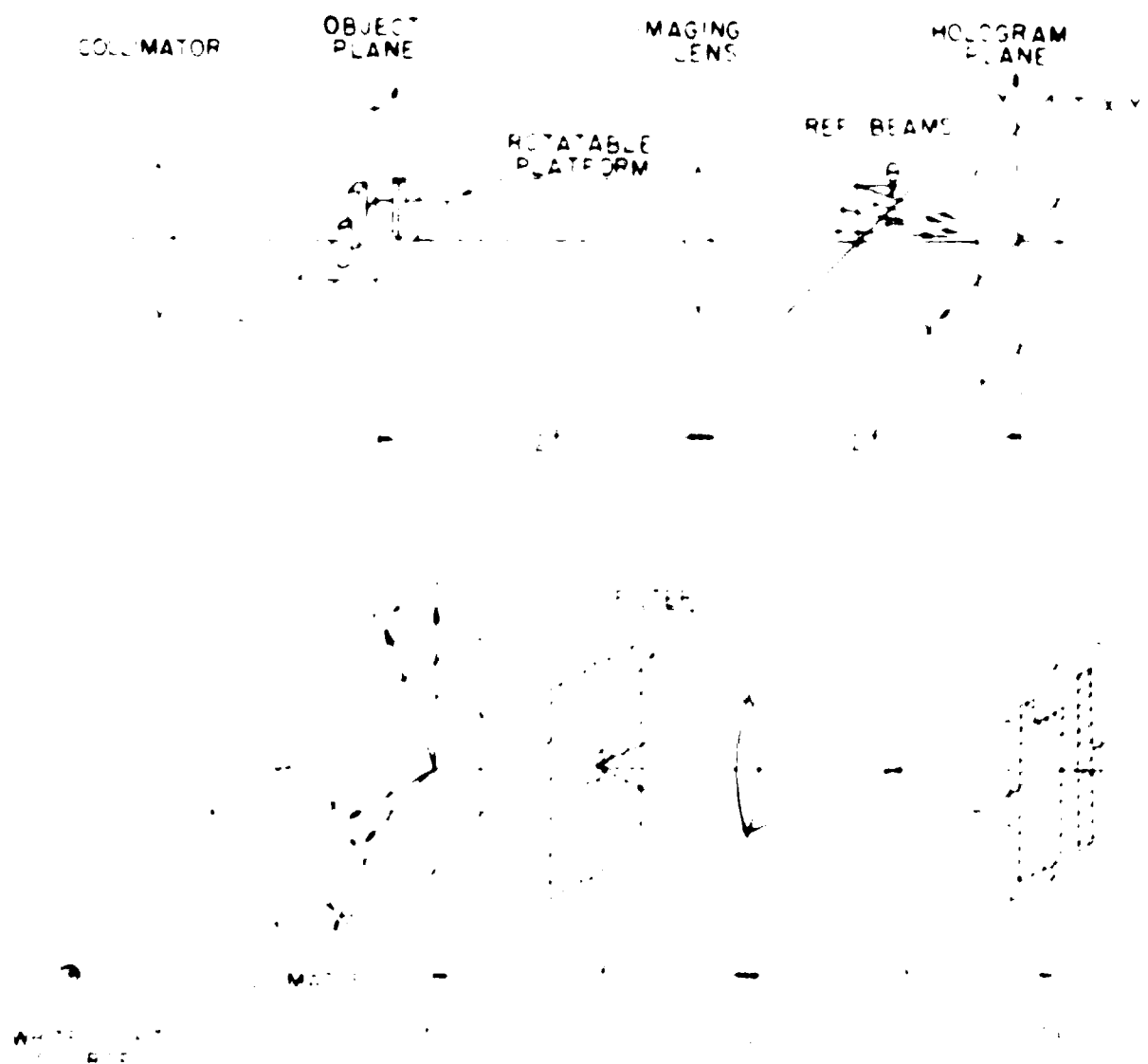
As shown in Fig. 1, a projection hologram can be synthesized by imaging the object field onto a holographic plate or film with a reference beam. To be at an angle θ with the optic axis. As the object field is oriented in different directions, the corresponding projected data can be multiplexed onto the plate or holographic plate by changing the angle θ of the reference beam sequentially. The corresponding data can be recorded on the plate. Assuming that the multiplexed hologram

is linearly recorded, the amplitude transmittance can be written as

$$T(x, y) = K_1 + K_2 \sum_{\theta} \exp \left\{ i \left[\frac{2\pi}{\lambda} (x \sin \theta + y \sin \theta) + \frac{2\pi}{\lambda} z \right] \right\} \quad (1)$$

where $\theta = \theta_1, \theta_2, \dots, \theta_N$ is the projected signal, K_1 and K_2 are arbitrary constants, θ is the oblique angle of the reference beam. The subscript θ denotes different directions and are used for sequential oriented field. If, in superimposing this recording process, twice the beam θ_1 is used as object distance such that the projected data recorded in the hologram will be the exact duplicate of the object with coordinates reversed.

After finishing the recording process, the multiplexed hologram can be inserted in the system shown in Fig. 2. The transmitted light produces in this system the recorded hologram and the reconstructed image.



rear side by a conjugate reference beam at an oblique angle, θ . Since twice the focal length is used again in this system, the real images which correspond to the different projectional views, i.e., $S_n(x_n, y_n)$, will be reimaged onto the observation plane, P_1 . In order to perform a sequential reconstruction for each projectional view, a mask can be employed between the hologram and the imaging lens to filter out the d_0 term and other unwanted terms. In this manner, by rotating the hologram in different orientations, the corresponding projectional views will be reconstructed on the observation plane sequentially.

In addition to the immediate play back, an image sensing device such as 1-D CCD array can be used to collect the projection data for post-processing, as depicted in figure 3. This computer post-processing will be discussed in greater detail in the next section. It is noted that any slice of the object field (horizontal cross section) can be reconstructed with this post-processing by placing the image sensing device at a chosen position. In other words, a 3-D reconstructed image of the object field can be realized by applying a 2-D image sensing device across the observation plane.

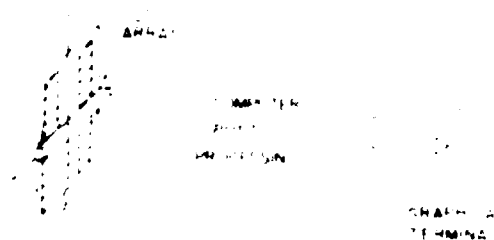


FIGURE 3. Post-processing setup.

III. DIGITAL RECONSTRUCTION OF THE OBJECT FIELD

The digital reconstruction of the object field is performed by the following steps:

$$f(x, y) = \sum_{n=1}^N S_n(x_n, y_n) \exp(i\phi_n)$$

where $f(x, y)$ is the object field, $S_n(x_n, y_n)$ is the

projectional view of the object field, ϕ_n is the phase of the projectional view, N is the number of projectional views, x_n and y_n are the coordinates of the projectional view, x and y are the coordinates of the object field, $f(x, y)$ is the reconstructed object field, $S_n(x_n, y_n)$ is the projectional view of the object field, ϕ_n is the phase of the projectional view, N is the number of projectional views, x_n and y_n are the coordinates of the projectional view, x and y are the coordinates of the object field, $f(x, y)$ is the reconstructed object field.

The digital reconstruction of the object field is performed by the following steps:

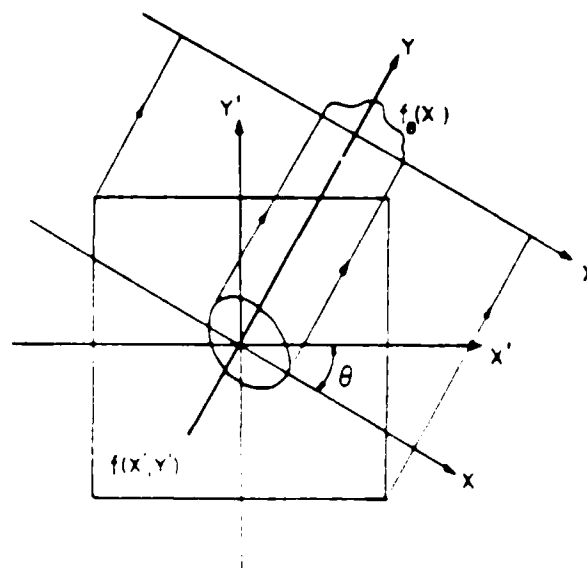


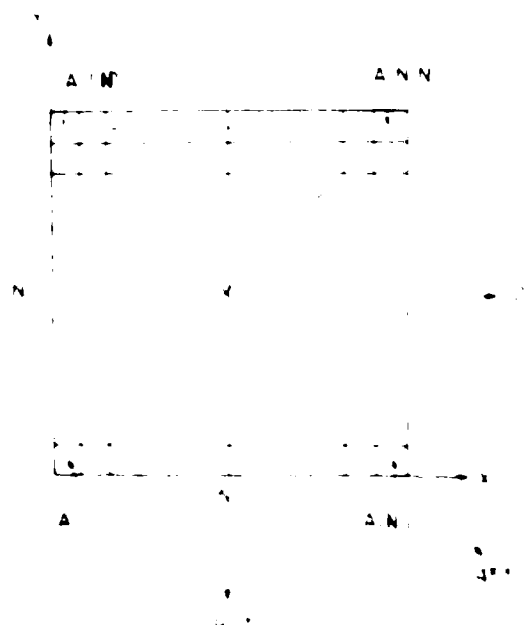
FIGURE 4. Geometric relationship between the object field and the projectional view.

logic OR operation in binary case. Let us assume that

- 1) when a light ray is being blocked by any object
- 2) otherwise

13

where 1 and 0 are logic states. In performing the reconstruction digitally, $N \times N$ sample points are designated to the object field as depicted in figure 5.



for a particular projected slice. Therefore, the image of this particular slice can be represented by

$$f(x', y') \cong \sum_{x=1}^N \sum_{y=1}^N A(x, y), \quad (4)$$

where $A(x, y)$ is again defined as in Eq. (3), and $f(x', y')$ is the reconstructed image of the chosen slice. As parallel light beam passes through this slice at certain angle θ , the projected data $P_\theta(\xi)$ is determined. The relation between the state of reconstructing pixels and the projected data can be written generally as

$$P_\theta(\xi_k) = \bigcup_{x=m}^n \bigcup_{y=p}^q A(x, y), \quad (5)$$

where parameters m, n, p , and q change with respect to the projecting angle θ . K denotes the different scanning rays. Obviously, if the projection for a particular ray is dark, i.e., $P_\theta(\xi_0) = 1$, it indicates that the scanning ray is blocked by at least one object in the field. Hence, the reconstructing pixels along this particular ray are designated by logic state "1". On the contrary, those pixels corresponding to lighted projection, i.e., $P_\theta(\xi_0) = 0$, will be permanently designated by logic state "0" regardless of other projected data from different angles. With these logic operations, the state of each pixel, $A(x, y)$, can be determined from projected data, $P_\theta(\xi)$. In other words, the back-projection process is performed logically after the projected data being fed to the computer by image sensing device. Therefore, the slice image, $f(x', y')$, can be estimated by Eq. (4). Obviously, a better reconstruction of the image may be expected as the number of projected angle employed is increased. We will discuss the relation between accuracy of reconstructed images and the quantity of projected directions in a later section.

In order to perform the reconstruction for any number and any direction of projections, the principle of the algorithm adapted to express the coordinates of reconstructed image pixels from the corresponding projection data is illustrated as follows.

First, four standard projected directions are selected, i.e., $0^\circ, 45^\circ, 90^\circ$, and 135° , as shown in figure 5.

(1) When $\theta = 0^\circ$ (or 90°), the relation between projected data and pixels is directly obtained from Eq. (5).

For $\theta = 0^\circ$, scanning rays are parallel with y -axis,

$$P_{0^\circ}(\xi_k) = \bigcup_{y=1}^N A(x, y), \quad (6)$$

where K denotes different scanning rays with the value from 1 to N . For $\theta = 90^\circ$, scanning rays are parallel with x -axis,

$$P_{90^\circ}(\xi_k) = \bigcup_{x=1}^N A(x, y), \quad (7)$$

When $\theta = 45^\circ$, the scanning rays are parallel with the line $y = x$. The scanning rays are numbered from 1 to N , and the number of pixels along each ray is designated by m, n, p , and q . The scanning rays are parallel with the line $y = x$, and the scanning rays are numbered from 1 to N .

ever, if we divide the whole field into two parts by its diagonals (see fig. 5), the relation between the reconstructed pixels and the projected data can be generally represented by

$$P_\theta(\xi_k) = \bigcup_{x=m}^n A(x, y), \quad (8)$$

with parameters m, n changes as follows:

A) When $\theta = 45^\circ$,

a) as the location of different scanning ray goes from the left edge ($A(1, 1)$) to the diagonal (the line from $A(1, N)$ to $A(N, 1)$), the corresponding parameters are

$$m = 1 \\ n = K,$$

where

$$K = 1, 2, \dots, N$$

The coordinate x changes with x as the following expression

$$x = n - x + 1, \quad (9)$$

b) as the location of different scanning ray goes continuously from the center to the right edge ($A(N, N)$), the corresponding parameters are

$$m = K - N + 1 \\ n = N$$

and

$$x = K - x + 1, \quad (10)$$

where

$$K = N + 1, N + 2, \dots, 2N - 1$$

B) When $\theta = 135^\circ$,

a) similarly, as the location of different scanning ray goes from $A(1, N)$ to the diagonal (the line from $A(1, 1)$ to $A(N, N)$), the corresponding parameters are

$$m = 1 \\ n = K$$

and

$$x = N - K + N, \quad (11)$$

where

$$K = 1, 2, \dots, N$$

b) as the scanning ray goes forward from the center to the right edge ($A(N, N)$), the corresponding parameters are

$$m = K - N + 1 \\ n = N$$

and

$$x = K - x + 1, \quad (12)$$

where

$$K = N + 1, N + 2, \dots, 2N - 1$$

After realizing the relations between the reconstructed pixels and the projected data in these four particular directions, we can generalize the whole process into multidirectional projecting case by the concept of coordinate transformation.

2. Multidirectional Projections.

For simplicity, a new coordinate system, (x_1, y_1) , is assigned with the origin O_1 coincides with the center of the field as shown in figure 6. As the field rotates an angle α , the coordinates of each pixel, within the objects, will change differently in different quadrants. However, these new coordinates can be calculated through the rotation of coordinates with respect to angle α . The new coordinates so obtained can be translated back to the original coordinate system (x, y) . In this case, we can get another four directional projections, i.e., $\alpha + 45^\circ + \alpha$, $90^\circ + \alpha$, and $135^\circ + \alpha$. With this procedure repeated, we can have any number of projected data processed and a better reconstruction can be achieved.

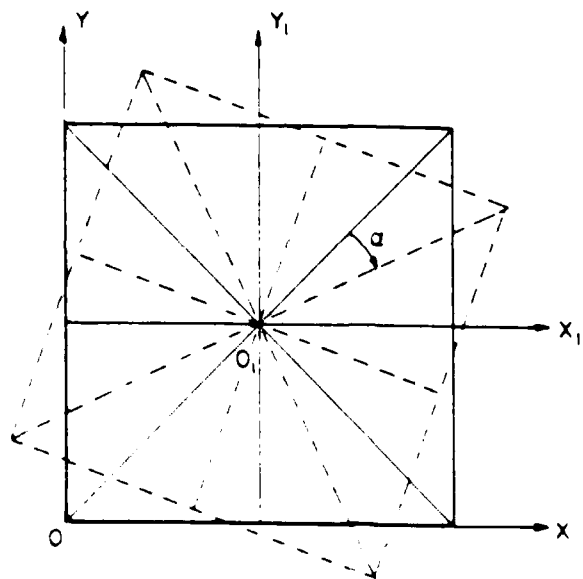


Fig. 6. Schematic diagram of coordinate rotation for multidirectional projections.

IV. — EXPERIMENTAL PROCEDURES AND RESULTS

As described in the previous sections, the method proposed utilizes optical holographic technique to record the projection data and to perform the analog reconstruction of the studied object field. In this part of the experiment, a 50 mW He-Ne laser is used as a light source. Two achromatic lenses L_1 and L_2 are used for collimation and imaging respectively (see fig. 1). The objects are fixed on a rotatable platform so that the angle of projection can be changed throughout the recording process. The reference beams are introduced at a fixed angle with respect to the optical

axis. However, the orientation can be changed continuously on a plane perpendicular to the axis as desired.

In the reconstruction process, the multiplexed hologram is oriented perpendicular to the optical axis to give the different directional projected views of the object field. Figure 7 shows four different views of the reconstructed image from the multiplexed hologram generated by a sample object field.

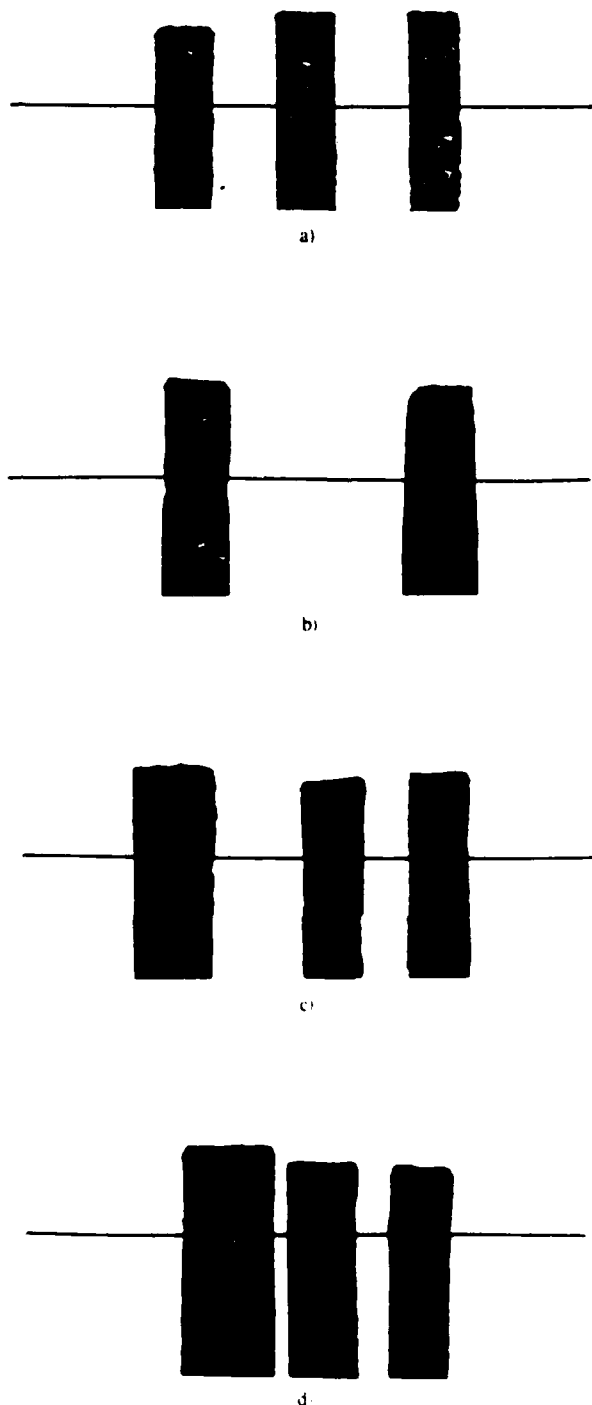
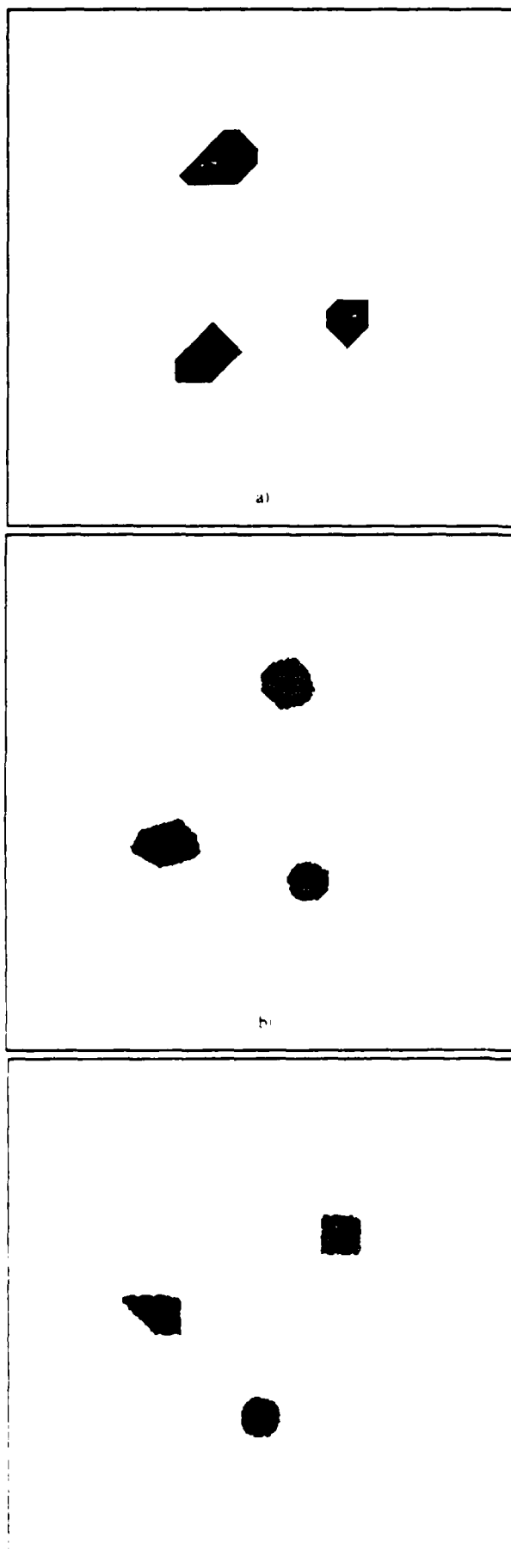


Fig. 7. Four different views of the reconstructed image from the multiplexed hologram. The bars in (a), (b), (c), and (d) represent the reconstructed image of the object field from the multiplexed hologram at 45° , 90° , and 135° respectively.



As an image sensing device is employed behind the observation plane and the multiplexed hologram is oriented, a series of projection data are available for the post-processing. By means of the algorithm described in previous section, results generated from different number of projected directions are shown in *figure 8*. From this figure and the original cross section shown in *figure 9*, we see that the shapes and the locations of the objects in the field are well defined.

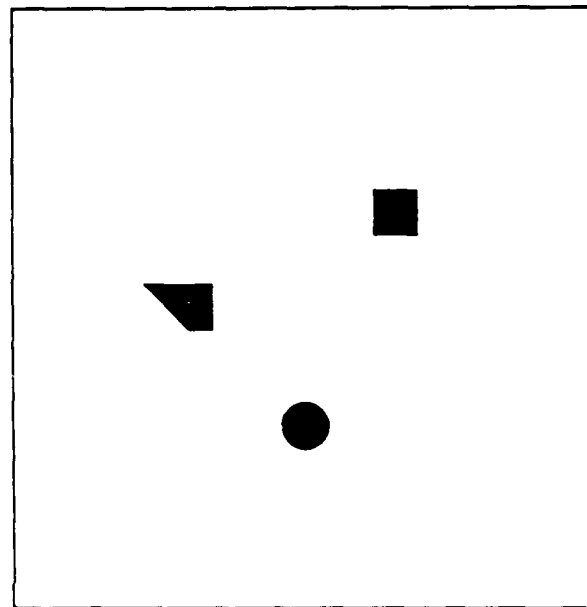


FIG. 9 — The original cross section for the sample slice of the object field

It is noted that there are two major factors effecting the performance of this digital reconstruction: namely, the number of the selected projection angles and the number of the sampling points chosen to represent the object field. From *figure 8*, we see that the reconstructed image is approaching the cross section of original object field as the number of projections increased. Practically, since a set of four equally divided directions is chosen as standard projecting directions in the algorithm, the multidirectional cases are selected by rotating these four directions simultaneously with the same angle. In this manner, the restoration accuracy can be foreseen as depicted in *figure 10* as the number of scanning angle increased. *Figure 11* also shows results of a cylindrical object in the center of field for different number of scanning angles. Obviously, the number of sampling points chosen to represent the object field also plays a very important role. As the complexity of object field increases, more sampling points are needed to reconstruct a finer image.

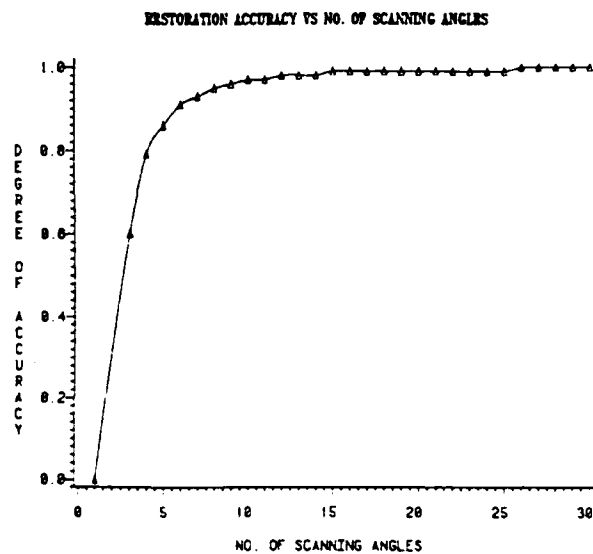


FIG. 10. — Reconstruction accuracy vs. the number of scanning directions.

V. — CONCLUSION

In this paper, we have developed a holographic tomography concept by which a 3-D complex field may be studied and reconstructed from 2-D projected data. A particular case of some opaque objects in a 3-D field is discussed as a preliminary application of this concept. The holographic multiplexing technique provides a series of projected data for tomographic reconstruction. With the algorithm used in computer post-processing, the image of a chosen slice in the studied field can be reconstructed from its one-dimensional projected data. The relative locations and the shapes of the objects inside the field are well defined by the reconstructed image. It is noted in this particular case, the principle used in the algorithm is much more suitable for convex object fields. This limitation arises from the fact that the projected data are the silhouettes of opaque objects. However, the ultimate objective is the study of 3-D complex fields. Hopefully, with the aid of holographic concept, some advantages such as reduction in computational procedures, may be achieved as compared with conventional tomographic techniques.

We acknowledge the support of the U.S. Air Force Office of Scientific Research grant AFOSR-83-0140.

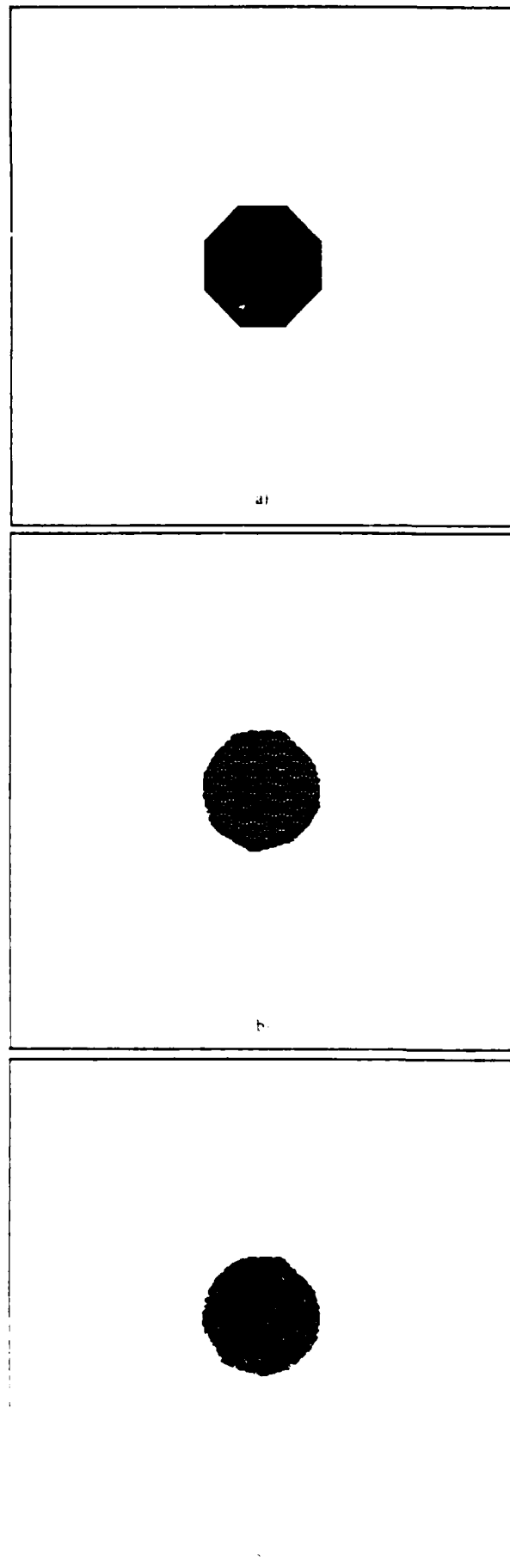


FIG. 11. — Reconstruction of a circular object with the number of scanning directions of 4, 8 and 12. (a), (b) and (c) represent the reconstructed results respectively.

REFERENCES

- [1] SWEENEY (D. W.) and VEST (C. M.) — « Reconstruction of Three-Dimensional Refractive Index Fields from Multi-directional Interferometric Data », *Appl. Opt.*, 12, 2649 (1973).
- [2] PRIKRYL (I.) and VEST (C. M.) — « Holographic Interferometry of Transparent Media using Light Scattered by Embedded Test Objects », *Appl. Opt.*, 21, 2554 (1982).
- [3] RAY SNYDER and LAMBERTUS HESSELINK — « Optical Tomography for Flow Visualization of the Density Field Around a Revolving Helicopter Rotor Blade », *Appl. Opt.*, 23, 1985 (1984).
- [4] BENNETT (K.) and BYER (R. L.) — « Optical Tomography: Experimental Verification of Noise Theories », *Opt. Eng.*, 23(1) (1984).
- [5] HARRISON (H.), BARRETT (J.) and WILLIAMS (S. J.) — « Aerial Reconstructions: Methods for Transaxial Tomography », *Proc. of the IEEE*, 65, 89 (1977).
- [6] F. T. S. YU — *Optical Tomography*, Elsevier, Wiley Interscience, New York, 1985.

Manuscript received November 1985

SECTION XXVII

Medical Imaging with White-Light

PSEUDOCOLOR ENCODING OF MEDICAL IMAGES WITH WHITE LIGHT

B.M. Palmer, K.K. Shung, F.T.S. Yu*

Bioengineering Program

*Department of Electrical Engineering
Pennsylvania State University
University Park, Pa. 16802

ABSTRACT: Color enhancement of medical images has been shown to be effective in increasing the perceived dynamic range of the images and thereby the diagnostic value of those images. An analog pseudocoloring technique based upon Fourier optics has been used in our laboratory to encode images obtained from such modalities as conventional X-ray, Ultrasound and CT. Emphasis is placed on the production of pseudocolored images mapped into the "heated-object" scale by way of primary intensity functions which are based on color matching principles and realized by film non-linearity properties. A final phase relief transparency contains the information required to produce the color scale when used as the input signal to the white-light optical processor.

KEYWORDS: Pseudocolor, white-light

INTRODUCTION: The effectiveness of a medical image can be measured as a clinician's ability to make a positive diagnosis from the image. Part of that ability depends on the image's dynamic range, which includes not only the signal-to-noise ratio of the technique, but also the manner in which the image is displayed. A measure of the human eye's ability to recognize important information from a display modality is called the perceived dynamic range (PDR). By modifying the display system to increase the PDR, the overall diagnostic effectiveness can be improved.

It has been experimentally shown that displaying images in color increases the PDR due to the human eye's higher sensitivity to color contrasts (1). Because of the many color scales available, the following criteria for an optimal scale have been suggested: 1) the scale must possess a natural order of intensities; 2) it must be averageable such that a non-homogeneous region can be displayed and an average intensity easily deduced and 3) the scale must have a linear intensity mapping according to human eye perception.

A color scale which meets these requirements and provides the highest PDR is the so called "heated-object" scale (HOS), which is based upon the wavelength distribution of radiation emitted from a Plankian blackbody. The intensity of the signal to be displayed can be interpreted as a temperature of a blackbody emitter and the

corresponding color assigned

White-light optical systems have been used for pseudocolor encoding [2]. With the proper input image provided, these systems can produce a color enhanced image mapped into the HSI. In this paper, the process used to produce the input image and the fundamental concepts of the white light process will be described.

FILM ENCODING The information encoded onto the input image is based upon color matching principles. These principles are common to the idea that any perceived color produced from a wavelength distribution like that from a blackbody can be simulated by the proper addition of three primary colors. By using the technique of color matching, the HSI can be simulated by the appropriate intensity functions of the primary colors.

Figure 1 shows the relative intensity functions of three primary colors required to map a grey scale image into the HSI. Linearization of the scale, such that there is a constant ratio of just-noticeable-differences in the color scale to those in the grey, has been achieved experimentally. Color scale production has also been modeled, but it has been strongly suggested that a more accurate model of color perception would be necessary to analytically produce a full range linearized scale.

The intensity functions can be realized analogly by utilizing the full range of the Transmittance-Exposure curve (figure 2). By a two-step process, positive transparencies can be produced whose transmittance functions closely approximate the required color intensity functions. The information from all three positive transparencies can be encoded onto one photographic film needed for subsequent optical processing.

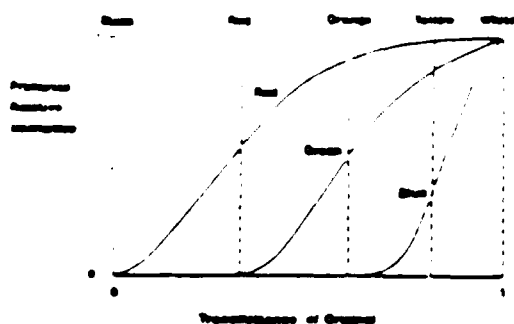


Figure 1. Color Intensity Functions for the Three Primary Colors for Production of HSI

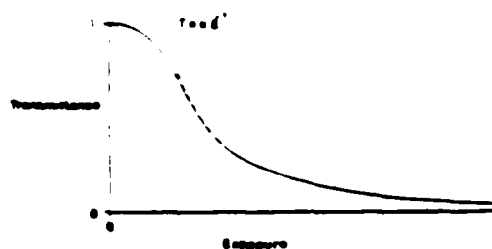


Figure 2. Transmittance-Exposure Curve for Film

The encoding is performed by exposing each transparency onto black and white film through a sampling grating (40 lines per mm) at specific azimuthal angles (figure 3). The angles were chosen to minimize exposure saturation and Moire fringe interference. This final transparency has an intensity transmittance which can be written as:

$$T(x,y) = K \left\{ T(x,y)[1+\cos(px)] + T(x,y)[1+\cos(qy)] + T(x,y)[1+\cos(xp/\sqrt{2})][1+\cos(yq/\sqrt{2})] \right\}^{-\gamma}$$

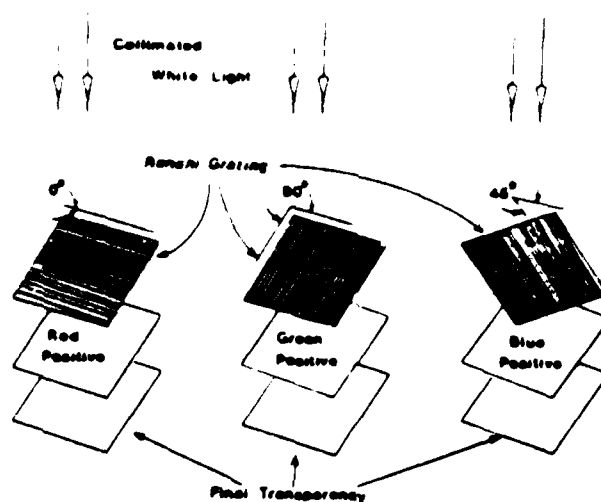


Figure 3: Film Encoding for Optical Processing.

OPTICAL PROCESSOR: By bleaching the encoded transparency, a phase relief object is produced, which can be written as:

$$T(x,y) = \exp[i\Phi(x,y)]$$

$$\Phi(x,y) = K' \left\{ T(x,y)[1+\cos(px)] + T(x,y)[1+\cos(qy)] + T(x,y)[1+\cos(xp/\sqrt{2})][1+\cos(yq/\sqrt{2})] \right\}$$

If this film is placed at the input plane of the white-light processor (figure 4) then the complex light distribution for every wavelength at the Fourier Plane will be determined by the Fourier transformation:

$$S(a,b) = \iint [1+i\Phi(x,y)-1/2\Phi(x,y)+...] \exp[-i2\pi(ax+by)/\lambda f] dx dy$$

where the input exponential has been expanded and f is the focal length of the Fourier Lens.

By blocking all but the first order terms and color filtering the appropriate smears in the Fourier plane the complex light field passed is given by:

$$S(a,b) = S(a - \frac{\lambda f}{2\pi} p, b) + S(a, b - \frac{\lambda f}{2\pi} q) + S(a - \frac{\lambda f}{2\pi} p, b - \frac{\lambda f}{2\pi} q)$$

Another Fourier Transformation is required to produce an output image whose irradiance is resolved as:

$$I(x,y) = T_A^2(-x,-y) + T_C^2(-x,-y) + T_D^2(-x,-y)$$

which is the superposition of the three primary intensity functions encoded on the input plane and now properly colored to produce the image in the HOS.

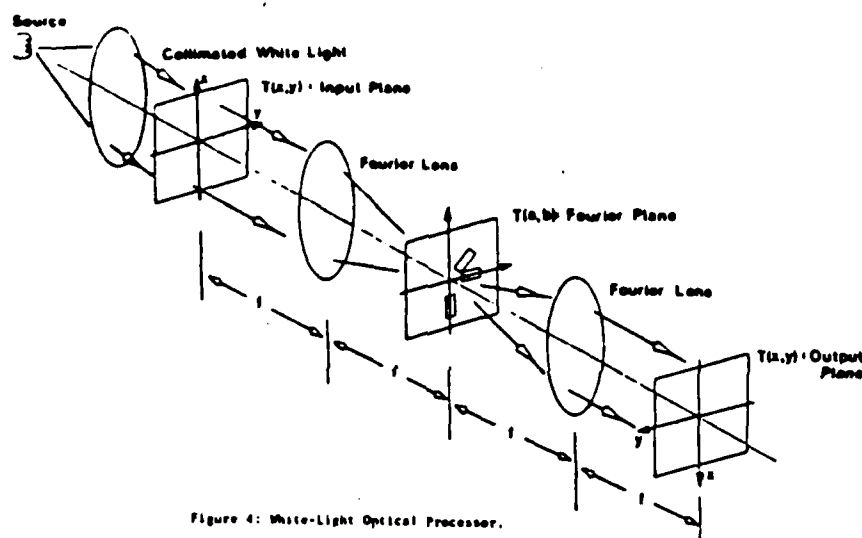


Figure 4: White-Light Optical Processor.

RESULTS AND DISCUSSION: Grey scale X-ray, CT and Ultrasonic images have been successfully encoded into the HOS utilizing this technique in our laboratory. We are now in the process of assessing the clinical efficacy of this technique. The cost associated with this approach in producing a pseudocolor image from a grey scale image is apparently less than the digital approach, however, it is also much less flexible. Therefore, whether this technique can replace the digital technique remains to be seen.

REFERENCES:

- 1) S.M. Pizer and J.B. Zimmerman, "Color Display in Ultrasonography," *Ultrasound Med. Biol.*, 9, 331, 1983.
- 2) F.T.S. Yu, K.K. Shung, X.X. Chen, "A White-Light Pseudocolor Encoder for Diagnostic Imaging," *IEEE Trans. BME-32*, 3, 1985.

SECTION XXVIII

Dual-Aperture Sampling with White-Light

Fringe visibility of dual-aperture sampling with partially coherent illumination

F. T. S. Yu and Y. W. Zhang

The effect on fringe visibility of a dual-aperture imaging system produced by two mutually partially coherent point sources is studied. The two mutually partially coherent point sources are generated by an original extended incoherent source. The problem formulation is developed from the partial coherence theory of Wolf. The results show that the fringe visibility is affected by the spectral bandwidth, source size, sampling aperture size, as well as the defocused distance of the imaging system. These results are quite consistent with the Thompson's predictions of Young's experiment.

I. Introduction

The earliest investigation of the subject of partial coherence may be that of Verdet¹ who in 1865 studied the region of coherence for light from an extended source. Some of the more important developments of partial coherence theory are those due to Van Cittert² in 1934 and Zernike³ in 1938. They determined the degree of coherence for light disturbances at any two points on a screen illuminated by an extended light source. However, it was Wolf's mutual coherence function⁴ in 1957 that made a broader scope of applications possible for coherence theory. In addition, it was the two-beam interferometric technique of Thompson and Wolf^{5,6} that provided a practical measurement technique of the degree of coherence.

Recently, Thompson and Sudol⁷ addressed the problem of finite-aperture effects in the measurement of the degree of coherence. They presented a 1-D analysis showing that the fringe visibility of a two-beam interferogram can be predicted by the convolution of two finite apertures under illumination. They have developed simple formulas to gain insight for the application of the theory. More recently, Marathay and Pollock⁸ generalized the study of Thompson and Sudol elegantly by utilizing a 2-D approach. Their analyses^{7,8} have shown that the effect of aperture size becomes predominant in the neighborhood of the zeros of the coherence or in regions where the coherence function is rapidly changing. While Thompson and

Sudol⁷ and Marathay and Pollock⁸ intended to point out that there is no separation of apertures for which the fringes disappear completely due to finite size of the aperture, we shall analyze the decrease of the fringe visibility due to the spectral bandwidth, source size, sampling aperture size, and defocused distance by following a similar approach.^{7,8}

In this paper we shall study the effects of fringe visibility under partially coherent illumination. Two mutually partially coherent point sources derived by an extended incoherent source are imaged by a dual-aperture imaging system to produce interference fringes. We shall utilize a partial coherence theory to analyze a dual-aperture imaging system under partially coherent illumination.

II. Problem Formulation

The layout of the system under consideration is depicted in Fig. 1. It shows that a diffused surface is illuminated by a collimated partially coherent light at the object plane of a double-aperture imaging system. The imaging lens of Fig. 1 is assumed very thin so that the pair of sampling apertures, which are touching the lens, can be located at either the entrance or exit pupil.

In the problem formulation, we assumed that a linear extended incoherent source is utilized. If the intensity distribution of the source is $\gamma(\theta)$, then, for a given wavelength λ , the mutual intensity function in a 1-D form arriving at the object plane P_1 would be⁴

$$\Gamma(\xi_1, \xi_2; \lambda) = \int_{-\theta_0}^{\theta_0} \gamma(\theta) \exp[-ik(\xi_1 - \xi_2)\theta] d\theta, \quad (1)$$

where

$$\theta_0 = \frac{\Delta s/2}{[(D_1/2)^2 + f_1^2]^{1/2}} \quad (2)$$

is the source divergent angle, D_1 is the diameter of the

The authors are with Pennsylvania State University, Electrical Engineering Department, University Park, Pennsylvania 16802.

Received 22 January 1986.

0003-6935/86/183191-06\$02.00/0.

© 1986 Optical Society of America.

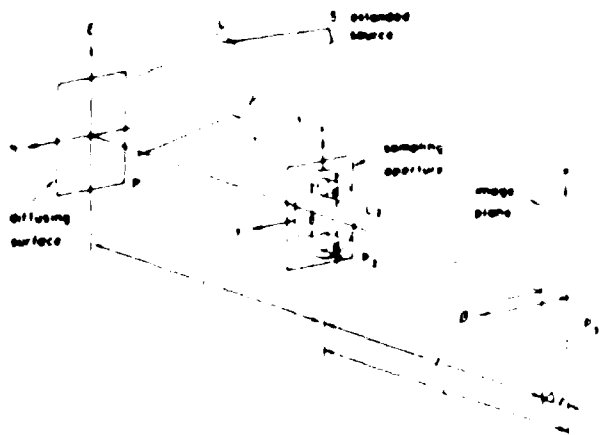


Fig. 1 Dual-aperture imaging system with partially coherent illumination. L_1 , collimating lens; L_2 , imaging lens; P_1 , object plane; P_3 , output plane.

collimating lens L_1 , f_1 is the focal length of L_1 , and $k = 2\pi/\lambda$.

If we assume that the diffused complex light field from the object plane P_1 is $t(\xi)$, the mutual intensity function reflected from diffused object at P_1 would be

$$\Gamma'(\xi_1, \xi_2; \lambda) = \Gamma(\xi_1, \xi_2; \lambda) t(\xi_1) t^*(\xi_2), \quad (3)$$

where the superscript asterisk denotes the complex conjugate. Due to the Fresnel diffraction from P_1 to P_2 , the mutual intensity function at the front of the sampling apertures would be

$$\Gamma(x_1, x_2; \lambda) = \frac{1}{\lambda^2 f^2} \iint \Gamma'(\xi_1, \xi_2; \lambda) \times \exp\left\{-i \frac{k}{2f} [(x_1 - \xi_1)^2 - (x_2 - \xi_2)^2]\right\} d\xi_1 d\xi_2, \quad (4)$$

The mutual intensity function immediately behind the image lens would be

$$\Gamma'(x_1, x_2; \lambda) = \Gamma(x_1, x_2; \lambda) T(x_1) T^*(x_2), \quad (5)$$

where

$$T(x) = \begin{cases} \exp\left(i \frac{k}{2f} x^2\right), & \frac{D}{2} - \frac{d}{2} \leq |x| \leq \frac{D}{2} + \frac{d}{2}, \\ 0, & \text{otherwise,} \end{cases} \quad (6)$$

f is the focal length of the imaging lens L_2 . Therefore, the output mutual intensity function at P_3 would be

$$\Gamma(a_1, a_2; \lambda) = \frac{1}{\lambda^2 L^2} \iint \Gamma'(x_1, x_2; \lambda) \times \exp\left\{-i \frac{k}{2L} [(a_1 - x_1)^2 - (a_2 - x_2)^2]\right\} dx_1 dx_2. \quad (7)$$

It is apparent that the corresponding intensity distribution due to λ at P_3 can be written as

$$I(a) = \frac{1}{\lambda^2 L^2} \iint \iint \Gamma(a_1, a_2; \lambda) \Gamma^*(a_1, a_2; \lambda) \times \exp\left\{-i \frac{k}{2L} [(a_1 - x_1)^2 - (a_2 - x_2)^2]\right\} \times d\xi_1 d\xi_2 dx_1 dx_2. \quad (8)$$

We are now in a position to raise a fundamental issue to what extent would the visibility of the output interference fringes be affected by the degree of coherence of the illumination? To answer this question we shall utilize the general formulation of Eq. (8) to determine the effects.

III. Effect under Temporally Partially Coherent Illumination

We shall first determine the effect under temporally partial coherent illumination. To do so, we let the light source S be a point (i.e., $\Delta s = 0$) but with finite bandwidth (i.e., $\Delta\lambda \neq 0$). Thus the overall output image irradiance at P_3 would be

$$I(a) = \int_{\lambda_0 - \Delta\lambda/2}^{\lambda_0 + \Delta\lambda/2} I(a; \lambda) d\lambda, \quad (9)$$

where λ_0 is the center wavelength of the light source, and $\Delta\lambda$ is its spectral bandwidth.

The light field within the sampling aperture with radius d can be kept coherence if $|t(\xi, \eta) t^*(\xi, \eta)|$ has a shape and size similar to the Airy spot produced by the aperture. However, in this paper we shall discuss a special case where the dual aperture is illuminated by two mutually partially coherent point sources.

Let us now take two arbitrary object points at P_1 with separation equals to the Airy spot projected into the source plane, i.e.,

$$t(\xi) = \delta(\xi - \xi_0) + \delta(\xi + \xi_0), \quad (10)$$

where

$$\xi_0 = \frac{1.22\lambda}{\sin\phi}, \quad (11)$$

$$\sin\phi = \frac{d}{[f^2 + (D/2)^2]^{1/2}}, \quad (12)$$

and the magnification of the Airy spot is assumed unity.

We note that ξ_0 could be another value rather than the Airy spot in the following analysis, but the Airy spot would be important if an extended object at P_1 is considered. By substituting the above equations into Eq. (8), we show that

$$I(a; \lambda) = A(a; \lambda) A^*(a; \lambda), \quad (13)$$

where

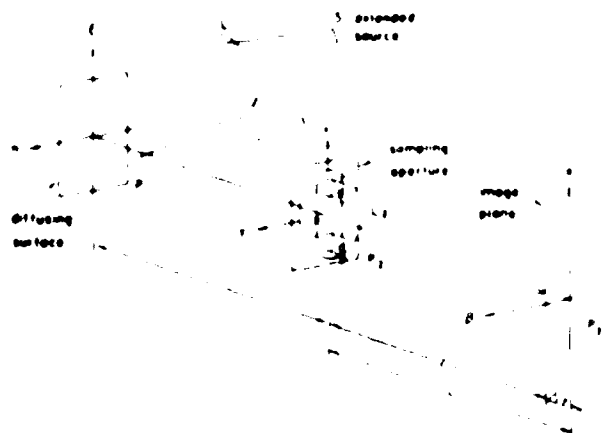


Fig. 1 Dual-aperture imaging system with partially coherent illumination. L_1 , collimating lens; L_2 , imaging lens; P_1 , object plane; P_3 , output plane

collimating lens L_1 , f_1 is the focal length of L_1 , and $k = 2\pi/\lambda$.

If we assume that the diffused complex light field from the object plane P_1 is $t(\xi)$, the mutual intensity function reflected from diffused object at P_1 would be

$$\Gamma'(\xi_1, \xi_2; \lambda) = \Gamma(\xi_1, \xi_2; \lambda) t(\xi_1) t^*(\xi_2), \quad (3)$$

where the superscript asterisk denotes the complex conjugate. Due to the Fresnel diffraction from P_1 to P_2 , the mutual intensity function at the front of the sampling apertures would be

$$\Gamma(x_1, x_2; \lambda) = \frac{1}{\lambda^2 f^2} \iint \Gamma'(\xi_1, \xi_2; \lambda) \times \exp\left\{-i \frac{k}{2f} [(x_1 - \xi_1)^2 - (x_2 - \xi_2)^2]\right\} d\xi_1 d\xi_2, \quad (4)$$

The mutual intensity function immediately behind the image lens would be

$$\Gamma'(x_1, x_2; \lambda) = \Gamma(x_1, x_2; \lambda) T(x_1) T^*(x_2), \quad (5)$$

where

$$T(x) = \begin{cases} \exp\left(i \frac{k}{2f} x^2\right), & \frac{D}{2} - \frac{d}{2} \leq |x| \leq \frac{D}{2} + \frac{d}{2}, \\ 0, & \text{otherwise,} \end{cases} \quad (6)$$

f is the focal length of the imaging lens L_2 . Therefore, the output mutual intensity function at P_3 would be

$$\Gamma(\alpha_1, \alpha_2; \lambda) = \frac{1}{\lambda^2 L^2} \iint \Gamma'(x_1, x_2; \lambda) \times \exp\left\{-i \frac{k}{2L} [(\alpha_1 - x_1)^2 - (\alpha_2 - x_2)^2]\right\} dx_1 dx_2. \quad (7)$$

It is apparent that the corresponding intensity distribution due to λ at P_3 can be written as

$$I(\alpha; \lambda) = \frac{1}{\lambda^2 L^2} \iint \left| \Gamma(\xi_1, \xi_2; \lambda) t(\xi_1) t^*(\xi_2) \right| \times \exp\left\{-i \frac{k}{2} \left[(x_1 - \xi_1)^2 - (x_2 - \xi_2)^2 \right] \right. \\ \left. - i \frac{k}{2} \left[(\alpha_1 - x_1)^2 - (\alpha_2 - x_2)^2 \right] \right\} \\ \times d\xi_1 d\xi_2 dx_1 dx_2, \quad (8)$$

We are now in a position to raise a fundamental issue: to what extent would the visibility of the output interference fringes be affected by the degree of coherence of the illumination? To answer this question we shall utilize the general formulation of Eq. (8) to determine the effects.

III. Effect under Temporally Partially Coherent Illumination

We shall first determine the effect under temporally partial coherent illumination. To do so, we let the light source S be a point (i.e., $\Delta s = 0$) but with finite bandwidth (i.e., $\Delta\lambda \neq 0$). Thus the overall output image irradiance at P_3 would be

$$I(\alpha) = \int_{\lambda_0 - \Delta\lambda/2}^{\lambda_0 + \Delta\lambda/2} I(\alpha; \lambda) d\lambda, \quad (9)$$

where λ_0 is the center wavelength of the light source, and $\Delta\lambda$ is its spectral bandwidth.

The light field within the sampling aperture with radius d can be kept coherence if $|t(\xi, \eta) t^*(\xi, \eta)|$ has a shape and size similar to the Airy spot produced by the aperture. However, in this paper we shall discuss a special case where the dual aperture is illuminated by two mutually partially coherent point sources.

Let us now take two arbitrary object points at P_1 with separation equals to the Airy spot projected into the source plane, i.e.,

$$t(\xi) = \delta(\xi - \xi_0) + \delta(\xi + \xi_0), \quad (10)$$

where

$$\xi_0 \approx \frac{1.22\lambda}{\sin\phi}, \quad (11)$$

$$\sin\phi = \frac{d}{[f^2 + (D/2)^2]^{1/2}}, \quad (12)$$

and the magnification of the Airy spot is assumed unity.

We note that ξ_0 could be another value rather than the Airy spot in the following analysis, but the Airy spot would be important if an extended object at P_1 is considered. By substituting the above equations into Eq. (8), we show that

$$I(\alpha; \lambda) = A(\alpha; \lambda) A^*(\alpha; \lambda), \quad (13)$$

where

$$A(\alpha; \lambda) \triangleq \frac{1}{\lambda^2 i L} \left\{ \exp \left[-i \frac{k}{2} \left(\left(\frac{1}{l} + \frac{1}{L} - \frac{1}{f} \right) x_1^2 + \left(\frac{\xi_0^2}{l} + \frac{\alpha^2}{L} \right) \right) \right] \exp \left[i k \left(\frac{\xi_0}{l} + \frac{\alpha}{L} \right) x_1 \right] + \exp \left[-i k \left(\frac{\xi_0}{l} + \frac{\alpha}{L} \right) x_1 \right] \right\} dx_1 \quad (14)$$

Since the output plane P_3 is assumed at some distance Δz away from the imaging plane, i.e., $\Delta z \ll z$, the Gaussian lens formula would still be a good approximation for the analysis, i.e.,

$$\frac{1}{l} + \frac{1}{L} - \frac{1}{f} \approx 0$$

Thus Eq. (14) can be written as

$$A(\alpha; \lambda) = A_1(\alpha; \lambda) + A_2(\alpha; \lambda), \quad (15)$$

where

$$A_1(\alpha; \lambda) \triangleq \frac{\exp \left[-i \frac{k}{2} \left(\frac{\alpha^2}{L} + \frac{\xi_0^2}{l} \right) \right]}{\lambda^2 i L} \left\{ \left(\int_{-\frac{D}{2} - \frac{d}{2}}^{-\frac{D}{2} + \frac{d}{2}} + \int_{\frac{D}{2} - \frac{d}{2}}^{\frac{D}{2} + \frac{d}{2}} \right) \times \exp \left[i k \left(\frac{\alpha}{L} + \frac{\xi_0}{l} \right) x_1 \right] dx_1 \right. \\ \left. - \frac{4 \exp \left[-i \frac{k}{2} \left(\frac{\alpha^2}{L} + \frac{\xi_0^2}{l} \right) \right]}{2\pi \lambda (l\alpha + L\xi_0)} \times \sin \left[k \left(\frac{\alpha}{L} + \frac{\xi_0}{l} \right) \frac{d}{2} \right] \cos \left[k \left(\frac{\alpha}{L} + \frac{\xi_0}{l} \right) \frac{D}{2} \right] \right\} \quad (16)$$

$$A_2(\alpha; \lambda) \triangleq \frac{\exp \left[-i \frac{k}{2} \left(\frac{\alpha^2}{L} + \frac{\xi_0^2}{l} \right) \right]}{\lambda^2 i L} \left\{ \left(\int_{-\frac{D}{2} - \frac{d}{2}}^{-\frac{D}{2} + \frac{d}{2}} + \int_{\frac{D}{2} - \frac{d}{2}}^{\frac{D}{2} + \frac{d}{2}} \right) \times \exp \left[i k \left(\frac{\alpha}{L} - \frac{\xi_0}{l} \right) x_1 \right] dx_1 \right. \\ \left. - \frac{4 \exp \left[-i \frac{k}{2} \left(\frac{\alpha^2}{L} + \frac{\xi_0^2}{l} \right) \right]}{2\pi \lambda (l\alpha - L\xi_0)} \times \sin \left[k \left(\frac{\alpha}{L} - \frac{\xi_0}{l} \right) \frac{d}{2} \right] \cos \left[k \left(\frac{\alpha}{L} - \frac{\xi_0}{l} \right) \frac{D}{2} \right] \right\} \quad (17)$$

With reference to Eqs. (15), (16), and (17), Eq. (13) can be written in terms of those quantities:

$$I(\alpha; \lambda) = |A_1(\alpha; \lambda)|^2 + |A_2(\alpha; \lambda)|^2 + A_1(\alpha; \lambda) A_2^*(\alpha; \lambda) + A_1^*(\alpha; \lambda) A_2(\alpha; \lambda). \quad (18)$$

The overall output image irradiance at P_3 can be written as

$$I(\alpha) = I_1(\alpha) + I_2(\alpha) + I_3(\alpha), \quad (19)$$

where

$$I_1(\alpha) \triangleq \frac{4}{\pi^2 (l\alpha + L\xi_0)^2} \int_{\lambda_0 - \Delta\lambda}^{\lambda_0 + \Delta\lambda} \frac{1}{\lambda^2} \sin^2 \left[\frac{\pi d (l\alpha + L\xi_0)}{\lambda L} \right] \times \cos^2 \left[\frac{\pi D (l\alpha + L\xi_0)}{\lambda L} \right] d\lambda, \quad (20)$$

$$I_2(\alpha) \triangleq \frac{4}{\pi^2 (l\alpha - L\xi_0)^2} \int_{\lambda_0 - \Delta\lambda}^{\lambda_0 + \Delta\lambda} \frac{1}{\lambda^2} \sin^2 \left[\frac{\pi d (l\alpha - L\xi_0)}{\lambda L} \right] \times \cos^2 \left[\frac{\pi D (l\alpha - L\xi_0)}{\lambda L} \right] d\lambda, \quad (21)$$

$$I_3(\alpha) \triangleq \frac{4}{\pi^2 (\lambda^2 \alpha^2 - L^2 \xi_0^2)} \int_{\lambda_0 - \Delta\lambda}^{\lambda_0 + \Delta\lambda} \frac{1}{\lambda^2} \sin^2 \left[\frac{\pi d (l\alpha + L\xi_0)}{\lambda L} \right] \times \sin^2 \left[\frac{\pi d (l\alpha - L\xi_0)}{\lambda L} \right] \cos \left[\frac{\pi D (l\alpha + L\xi_0)}{\lambda L} \right] \cos \left[\frac{\pi D (l\alpha - L\xi_0)}{\lambda L} \right] d\lambda. \quad (22)$$

It is now apparent that the fringe visibility as defined,

$$V(\alpha) \triangleq \frac{I_{\max}(\alpha) - I_{\min}(\alpha)}{I_{\max}(\alpha) + I_{\min}(\alpha)}, \quad (23)$$

can be written as (see Appendix)

$$V(\alpha) = \left\{ (l\alpha - L\xi_0)^2 \operatorname{sinc}^2 \left[\frac{2d(l\alpha + L\xi_0)\Delta\lambda}{lL\lambda_0^2} \right] + (l\alpha + L\xi_0)^2 \operatorname{sinc}^2 \left[\frac{2d(l\alpha - L\xi_0)\Delta\lambda}{lL\lambda_0^2} \right] \right\} / 2(l^2\alpha^2 + L^2\xi_0^2). \quad (24)$$

Figure 2 shows plots of fringe visibility as a function of α for various spectral bandwidths of the light source. From this figure, we see that the visibility decreases as the spectral bandwidth of the light source increases, which is quite consistent with Thompson's prediction. Figure 3 shows the effect of fringe visibility due to sampling aperture size. Thus we see that the visibility decreases as the aperture size increases. Figure 4

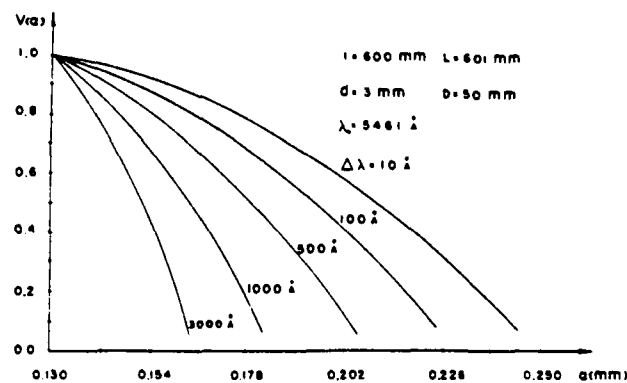


Fig. 2. Effect of fringe visibility due spectral bandwidth $\Delta\lambda$ of the light source under temporally partially coherent illumination.

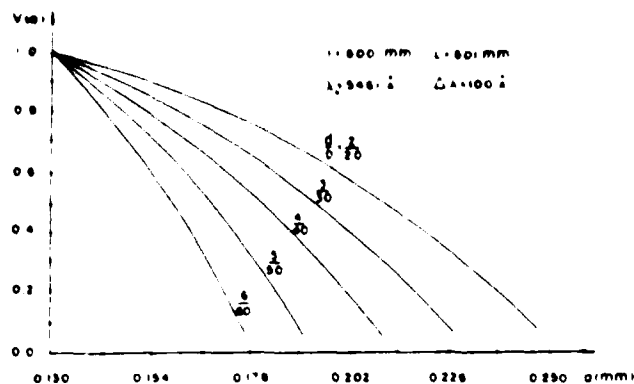


Fig. 3. Effect of fringe visibility due to sampling aperture size d under temporally partially coherent illumination.

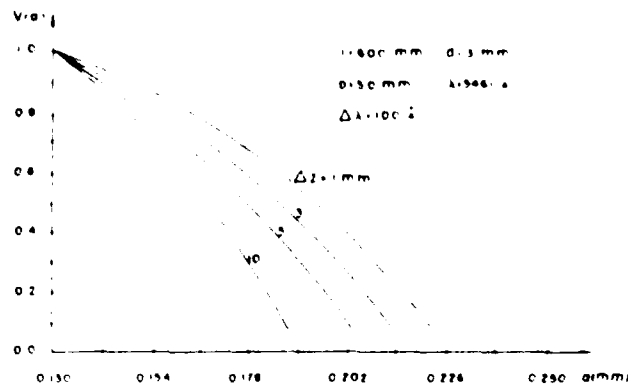


Fig. 4. Effect of fringe visibility due to defocused distance Δz under temporally partially coherent illumination.

shows the effect due to deviation of Δz (i.e., defocused distance). This figure shows that the fringe visibility decreases as the defocused distance Δz increases.

IV. Effect under Spatially Partially Coherent Illumination

We shall now consider the effect due to spatially coherent illumination. In this case, we assume that the light source is temporally coherent but with finite extension (i.e., $\Delta\lambda = 0$ and $\Delta s \neq 0$). The source irradiance may be written as

$$\gamma(\theta) = \begin{cases} 1, & |\theta| \leq \theta_0 \\ 0, & \text{otherwise.} \end{cases} \quad (25)$$

where θ_0 is the source divergent angle.

By letting $\lambda = \lambda_0$, the quantity of $A(\alpha; \lambda_0)$ can be derived from Eq. (8), i.e.,

$$A(\alpha; \lambda_0) = \frac{1}{\lambda^2 L} \int \exp(-ik_0 \xi_1 \theta) [\delta(\xi_1 - \xi_0) + \delta(\xi_1 + \xi_0)] \\ \times \exp\left\{-\frac{ik_0}{2} \left[\frac{(x_1 \xi_1)^2}{l} - \frac{x_1^2}{l} + \frac{(\alpha - x_1)^2}{L} \right]\right\} d\xi_1 dx_1, \quad (26)$$

which can be written as

$$A(\alpha; \lambda_0) = \frac{4 \exp\left[-i \frac{k_0}{2} \left(\frac{\alpha^2}{L} + \frac{\xi_0^2}{l} \right)\right]}{2\pi \lambda_0 (l\alpha + L\xi_0)} \sin\left[k_0 \left(\frac{\alpha}{L} + \frac{\xi_0}{l} \right) \frac{d}{2}\right] \\ \times \cos\left[k_0 \left(\frac{\alpha}{L} + \frac{\xi_0}{l} \right) \frac{D}{2}\right] \exp[-ik_0 \xi_0 \theta] \\ + \frac{4 \exp\left[-i \frac{k_0}{2} \left(\frac{\alpha^2}{L} + \frac{\xi_0^2}{l} \right)\right]}{2\pi \lambda_0 (l\alpha - L\xi_0)} \sin\left[k_0 \left(\frac{\alpha}{L} - \frac{\xi_0}{l} \right) \frac{d}{2}\right] \\ \times \cos\left[k_0 \left(\frac{\alpha}{L} - \frac{\xi_0}{l} \right) \frac{D}{2}\right] \exp(ik_0 \xi_0 \theta), \quad (27)$$

where $k_0 = 2\pi/\lambda_0$, and λ_0 is the wavelength of the light source. Thus the overall output image irradiance at P_0 would be

$$I(\alpha) = \int_{-\theta_0}^{\theta_0} |A(\alpha; \lambda_0)|^2 d\theta \\ = \left\{ \frac{4}{\lambda_0^2 \pi^2 (l\alpha + L\xi_0)^2} \sin^2\left[k_0 \left(\frac{\alpha}{L} + \frac{\xi_0}{l} \right) \frac{d}{2}\right] \cos^2\left[k_0 \left(\frac{\alpha}{L} + \frac{\xi_0}{l} \right) \frac{D}{2}\right] \right. \\ + \frac{4}{\lambda_0^2 \pi^2 (l\alpha - L\xi_0)^2} \sin^2\left[k_0 \left(\frac{\alpha}{L} - \frac{\xi_0}{l} \right) \frac{d}{2}\right] \cos^2\left[k_0 \left(\frac{\alpha}{L} - \frac{\xi_0}{l} \right) \frac{D}{2}\right] \\ + \frac{8}{\lambda_0^2 \pi^2 (l^2 \alpha^2 - L^2 \xi_0^2)} \sin\left[k_0 \left(\frac{\alpha}{L} + \frac{\xi_0}{l} \right) \frac{d}{2}\right] \cos\left[k_0 \left(\frac{\alpha}{L} + \frac{\xi_0}{l} \right) \frac{D}{2}\right] \\ \times \sin\left[k_0 \left(\frac{\alpha}{L} - \frac{\xi_0}{l} \right) \frac{d}{2}\right] \cos\left[k_0 \left(\frac{\alpha}{L} - \frac{\xi_0}{l} \right) \frac{D}{2}\right] \left. \right\} \text{sinc}\left(\frac{4\xi_0 \theta_0}{\lambda_0}\right) 2\theta_0. \quad (28)$$

As similar to the foregoing temporally partially coherent source, the effect of the fringe visibility due to the spatially partially coherent illumination can be evaluated from the above equation.

Figures 5-7 show the plots of visibility as a function of distance α for various values of source size Δs , sampling aperture size d , and defocused distance Δz , respectively. From these figures, we notice that the visibility decreases as the source size increases, the sampling aperture enlarges, and Δz increases. Although the variation of the fringe visibility due to an extended source behaves in a similar manner as the bandwidth variation, the effect due to increasing bandwidth (i.e., $\Delta\lambda$) is more sensitive, as can be seen from Figs. 2 and 5. In terms of the sampling aperture size (i.e., d), we have seen that the effect on fringe visibility is not much different for the two cases. However, fringe visibility is more sensitive to aperture size d than to the separation D . As for the changes of defocus distance Δz , the effect on the fringe visibility has generally behaved similarly for both cases.

Finally we stress that the results that we have obtained, using two mutually partially coherent point sources, are quite consistent with the two-beam interference measurement of Thompson.^{5,6}

$$\begin{aligned}
& - \frac{d}{\left(\frac{2\pi ad}{L} + \frac{2\pi aD}{l} \right)} \\
& \cdot \left[\sin \left(\frac{2\pi ad}{L} + \frac{2\pi aD}{l} \right) \frac{1}{(\lambda_0 + \Delta\lambda)} - \sin \left(\frac{2\pi ad}{L} \right. \right. \\
& \left. \left. + \frac{2\pi aD}{l} \right) \frac{1}{(\lambda_0 - \Delta\lambda)} \right] \\
& - \frac{d}{\left(\frac{2\pi ad}{l} - \frac{2\pi \xi_0 D}{L} \right)} \cdot \left[\sin \left(\frac{2\pi ad}{l} - \frac{2\pi \xi_0 D}{L} \right) \frac{1}{(\lambda_0 + \Delta\lambda)} \right. \\
& \left. - \sin \left(\frac{2\pi ad}{l} - \frac{2\pi \xi_0 D}{L} \right) \frac{1}{(\lambda_0 - \Delta\lambda)} \right] - \frac{d}{\left(\frac{2\pi ad}{l} + \frac{2\pi \xi_0 D}{L} \right)} \\
& \cdot \left[\sin \left(\frac{2\pi ad}{l} + \frac{2\pi \xi_0 D}{L} \right) \frac{1}{(\lambda_0 + \Delta\lambda)} \right. \\
& \left. - \sin \left(\frac{2\pi ad}{l} + \frac{2\pi \xi_0 D}{L} \right) \frac{1}{(\lambda_0 - \Delta\lambda)} \right] \Bigg\}. \quad (A3)
\end{aligned}$$

If we assume that $D \gg d$, the quantity of $I_3(\alpha)$ is much smaller than $I_1(\alpha)$ and $I_2(\alpha)$. Thus $I_3(\alpha)$ can generally be neglected, and $I_1(\alpha)$ and $I_2(\alpha)$ can be further simplified as

$$\begin{aligned}
I_1(\alpha) = & \frac{lL}{\pi^3(l\alpha + L\xi_0)^3d} \left\{ \frac{\pi d(l\alpha + L\xi_0)}{lL(\lambda_0 - \Delta\lambda)} - \frac{\pi d(l\alpha + L\xi_0)}{lL(\lambda_0 + \Delta\lambda)} \right. \\
& \left. + \frac{1}{2} \sin \left[\frac{2\pi d(l\alpha + L\xi_0)}{lL(\lambda_0 + \Delta\lambda)} \right] - \frac{1}{2} \sin \left[\frac{2\pi d(l\alpha + L\xi_0)}{lL(\lambda_0 - \Delta\lambda)} \right] \right\}. \quad (A4)
\end{aligned}$$

$$\begin{aligned}
I_2(\alpha) = & \frac{lL}{\pi^3(l\alpha - L\xi_0)^3d} \left\{ \frac{\pi d(l\alpha - L\xi_0)}{lL(\lambda_0 - \Delta\lambda)} - \frac{\pi d(l\alpha - L\xi_0)}{lL(\lambda_0 + \Delta\lambda)} \right. \\
& \left. + \frac{1}{2} \sin \left[\frac{2\pi d(l\alpha - L\xi_0)}{lL(\lambda_0 + \Delta\lambda)} \right] - \frac{1}{2} \sin \left[\frac{2\pi d(l\alpha - L\xi_0)}{lL(\lambda_0 - \Delta\lambda)} \right] \right\}. \quad (A5)
\end{aligned}$$

By expanding $1/(\lambda_0 + \Delta\lambda)$ and $1/(\lambda_0 - \Delta\lambda)$ in binominal series and neglecting the higher-order terms of $(\Delta\lambda)^2$, the output image irradiance can be written as

$$\begin{aligned}
I(\alpha) \approx I_1(\alpha) + I_2(\alpha) = & \frac{2\Delta\lambda}{\pi^2(l\alpha + L\xi_0)^2\lambda_0^2} \\
& \times \left\{ 1 + \operatorname{sinc} \left[\frac{2d(l\alpha + L\xi_0)\Delta\lambda}{lL\lambda_0^2} \right] \cos \left[\frac{2\pi d(l\alpha + L\xi_0)}{lL\lambda_0} \right] \right\} \\
& + \frac{2\Delta\lambda}{\pi^2(l\alpha - L\xi_0)^2\lambda_0^2} \left\{ 1 + \operatorname{sinc} \left[\frac{2d(l\alpha - L\xi_0)\Delta\lambda}{lL\lambda_0^2} \right] \right. \\
& \left. \cdot \cos \left[\frac{2\pi d(l\alpha - L\xi_0)}{lL\lambda_0} \right] \right\}. \quad (A6)
\end{aligned}$$

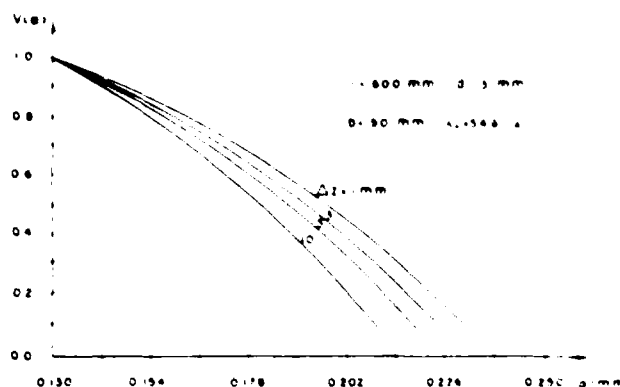


Fig. 7. Effect of fringe visibility due to defocused distance Δz under spatially partially coherent illumination.

Thus the corresponding fringe visibility can be written as

$$\begin{aligned}
V(\alpha) = & \left\{ (l\alpha - L\xi_0)^2 \operatorname{sinc} \left[\frac{2d(l\alpha + L\xi_0)\Delta\lambda}{lL\lambda_0^2} \right] \right. \\
& \left. + (l\alpha + L\xi_0)^2 \operatorname{sinc} \left[\frac{2d(l\alpha - L\xi_0)\Delta\lambda}{lL\lambda_0^2} \right] \right\} / 2(l^2\alpha^2 + L^2\xi_0^2). \quad (A7)
\end{aligned}$$

We acknowledge the support of the U.S. Air Force Office of Scientific Research AFOSR grant 83-0140.

References

1. E. Verdet, *Interferences en General*, Vol. 5/6, *Lecons d'Opt. Phys.* (L'Imprimerie Imperiale, Paris, 1869), 1, p. 106.
2. P. H. Van Cittert, "Die Wahrscheinliche Schwingungsverteilung in einer von einer lichtquelle direkt Oden Mittels einer linse," *Physica* 1, 201 (1934).
3. F. Zernike, "The Concept of Degrees of Coherence and Its Application to Optical Problems," *Physica* 5, 785 (1938).
4. M. Born and E. Wolf, *Principles of Optics* (Pergamon, New York, 1964), pp. 499-508.
5. B. J. Thompson and E. Wolf, "Two-Beam Interference with Partially Coherent Light," *J. Opt. Soc. Am.* 47, 895 (1957).
6. B. J. Thompson, "Illustration of the Phase Change in Two-Beam Interference with Partially Coherent Light," *J. Opt. Soc. Am.* 48, 95 (1958).
7. B. J. Thompson and R. Sudol, "Finite Aperture Effects in the Measurement of the Degree of Coherence," *J. Opt. Soc. Am.* A 1, 598 (1984).
8. A. S. Marathay and D. B. Pollock, "Young's Interference Fringes with Finite-Size Sampling Apertures," *J. Opt. Soc. Am.* A 1, 1057 (1984).

SECTION A-13

LDTV Processing with white light

Reprinted from Applied Optics, Vol. 25, Page 3324, October 1, 1986
Copyright © 1986 by the Optical Society of America and reprinted by permission of the copyright owner.

Experimental application of low-cost liquid crystal TV to white-light optical signal processing

Francis T. S. Yu, S. Jutamulia, and X. L. Huang

Electrical Engineering Department, Pennsylvania State University, University Park, Pennsylvania 16802.

Received 3 June 1986.

Sponsored by Hua-Kuang Liu, Jet Propulsion Laboratory. 0003-6935/86/193324-03\$02.00/0.

© 1986 Optical Society of America.

Optical processing has made significant progress in the last two decades. However, an existing drawback of optical processing is the requirement of an input transparency that eventually sacrifices real-time processing capability. The extremely expensive spatial light modulators such as liquid crystal light valve (LCLV), microchannel spatial light modulator (MSLM), and magnetooptic device (MOD) have been successfully produced and applied to real-time optical processing. On the other hand, low-cost (<\$150) commercially available flat screen transmission-type liquid crystal television (LCTV) can be modified and used as a spatial light modulator in a real-time optical signal processor. Applications of the LCTV to real-time pattern recognition using a coherent optical correlator have been shown by Liu *et al.*¹ and Gregory.² A study of the performance of the LCTV has also been reported by McEwan *et al.*³ Recently, Young⁴

reported coherent edge enhancement using the LCTV, and Tai⁵ has also shown the high optical quality of the LCTV. In this Communication, we shall report other applications of the LCTV to white-light optical processing.

The basic experimental setup is depicted in Fig. 1, where the display panel of the LCTV is put in a liquid gate. A prefiltering aperture is included to remove the higher-order spatial frequencies associated with the inherent grating

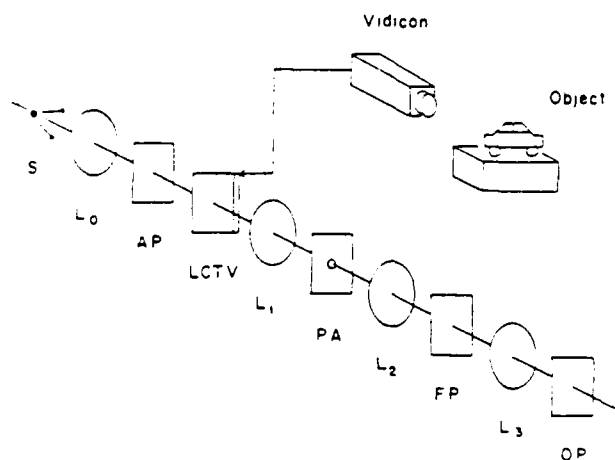


Fig. 1. Basic experimental setup: S, white-light source; L_0 , collimator; AP, additional polarizer; LCTV, liquid crystal television display; L_1 , Fourier transform lens; PA, prefiltering aperture; L_2 , imaging lens; FP, enlarged Fourier transform plane; L_3 , Fourier transform lens; OP, output plane.



(a)



(b)



(c)

Fig. 2. (a) Input pattern displayed on the LCTV screen; (b) filtered image of the input pattern; (c) filtered image of the input pattern.

AD-A179 489

WHITE-LIGHT OPTICAL INFORMATION PROCESSING AND
HOLOGRAPHY(U) PENNSYLVANIA STATE UNIV UNIVERSITY PARK
DEPT OF ELECTRICAL ENGINEERING F T YU 23 JAN 87

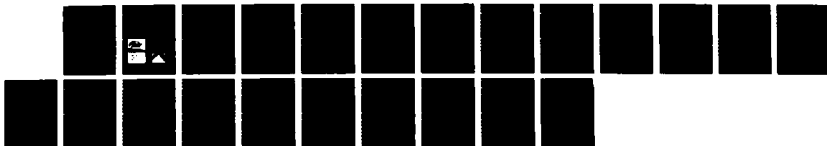
4/4

UNCLASSIFIED

AFOSR-TR-87-0456 AFOSR-83-0140

F/G 20/6

NL





M1

structure of the LCTV. Lens L_2 is added to enlarge the Fourier transform to simplify spatial filtering.

An input pattern is displayed on the LCTV based on a scanning process; however, due to the sufficiently long relaxation time of the pixels, the input pattern is actually a partially spatially coherent image. The Fourier spectra of a grating input was observed clearly. However, it is not illustrated in this Communication, since it has been shown by Liu *et al.*¹ Thus it is evident that the Fourier transform can be effectively performed.

Lewis⁶ had reported real-time coherent optical edge enhancement using an expensive Hughes LCLV. However, the low-cost LCTV can be employed to provide the same result. Young⁴ showed some results of the edge enhancement of a 2-D pattern using laser. The edge enhancement of a 2-D pattern using a white-light processor is shown in Fig. 2. Figure 2(a) illustrates the input pattern as displayed on the LCTV. A high-pass spatial filter is placed on the enlarged Fourier transform plane (FP) to generate an edge enhanced image. The corresponding result is shown in Fig. 2(b). The edge enhanced image obtained using laser illumination is provided in Fig. 2(c) for comparison. We note that the coherent artifact noise shown in Fig. 2(c) has been removed in the white-light processing as shown in Fig. 2(b). Another experiment of edge enhancement using a 3-D object is also demonstrated in Fig. 3. A small toy car is viewed with a remote vidicon and displayed on the LCTV as shown in Fig. 3(a). The corresponding edge enhanced image is shown in Fig. 3(b).

Another application of the LCTV to white-light processing has also been studied. An input pattern shown in Fig. 4(a) is used to demonstrate spatial color encoding. At the enlarged Fourier transform plane the vertically diffracted light passes

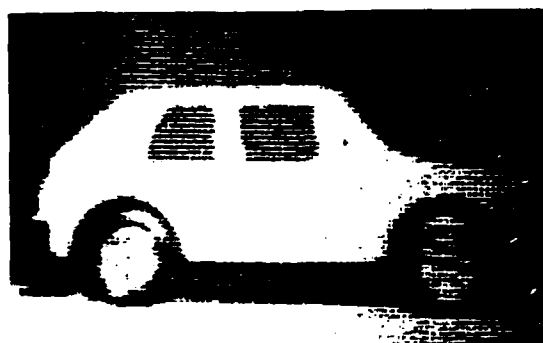
through a green color filter. In the same manner, the horizontally diffracted light passes through a red filter at the enlarged Fourier transform plane. Therefore, a red triangle and green background would be obtained. This method is commonly used in the archival storage of color films.⁷ The color-coded experimental result using a white-light source is shown in the black-and-white picture in Fig. 4(b). The result has good color separation.

Summarizing: Applications of a low-cost commercially available flat screen transmission-type LCTV to real-time elementary white-light optical signal processing have been studied. Although the picture is displayed on the LCTV based on a scanning process, the sufficiently long relaxation time of the pixels provide a partially spatially coherent input image. Thus real-time optical signal processing can be carried out using the LCTV instead of other extremely expensive light modulators. However, the LCTV has such drawbacks as low resolution and contrast. We like to stress that the LCTV is low in cost, and with further improvements the LCTV should be very useful for not only coherent but also white-light optical signal processing.

We acknowledge the support by U.S. Air Force Office of Scientific Research grant AFOSR-83-0140.

References

1. H. K. Liu, J. A. Davis, and R. A. Lilly, "Optical-Data-Processing Properties of a Liquid-Crystal Television Spatial Light Modulator," *Opt. Lett.* 10, 635 (1985).
2. D. A. Gregory, "Real-Time Pattern Recognition Using a Modified Liquid Crystal Television in a Coherent Optical Correlator," *Appl. Opt.* 25, 467 (1986).

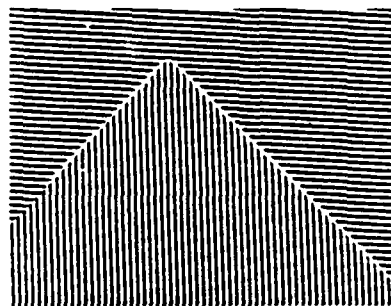


(a)



(b)

Fig. 3. (a) Input pattern of a toy car which is displayed on the LCTV. (b) Edge enhanced image of (a) using a white-light processor.



(a)



(b)

Fig. 4. (a) Input pattern used for spatial color encoding. (b) Black-and-white picture of the color encoded result where the triangle was red and the background green.

3. J. A. McEwan, A. D. Fisher, P. D. Rolsma, and J. N. Lee, "Optical-Processing Characteristics of a Low-Cost Liquid Crystal Display Device." *J. Opt. Soc. Am. A* 2(13), 8 (1985).
4. M. Young, "Low-Cost LCD Video Display for Optical Processing," *Appl. Opt.* 25, 1024 (1986).
5. A. M. Tai, "Low-Cost LCD Spatial Light Modulator with High Optical Quality," *Appl. Opt.* 25, 1380 (1986).
6. R. W. Lewis, "Real-Time Coherent Optical Edge Enhancement," *Appl. Opt.* 17, 161 (1978).
7. F. T. S. Yu, X. X. Chen, and S. L. Zhuang, "Progress Report on Archival Storage of Color Films Utilizing a White-Light Processing Technique." *J. Opt. Paris* 16, 59 (1985).

SECTION XXX

Computer Generated Tricolor Sampling

DEPARTMENT OF ELECTRICAL ENGINEERING
The Pennsylvania State University, University Park, PA 16802

Computer Generated Linear Tricolor Sampling Pattern and its Application

FRANCIS T. S. Yu, XIN-XIANG CHEN, KATHLEEN E. McCLURE

MOTS CLÉS :

Réseau échantillonneur
Conception par ordinateur
Restitution des couleurs
Traitement d'image

KEY WORDS :

Computer generated sampling pattern
Color image retrieval
Image processing

SUMMARY : A one-step method for recording color information on a monochrome transparency using a linear tricolor sampling pattern is proposed. It is shown that the method avoids color-cross-talk, moiré fringes, and marginal resolution loss. The linear tricolor sampling pattern is described in detail as well as a method for computer generating the tricolor grating. Color images retrieved using the grating show that the method is a viable alternative to previous three step encoding methods.

Description et utilisation d'un réseau échantillonneur trichromatique créé par ordinateur

RÉSUMÉ : On propose une méthode qui permet d'enregistrer les couleurs d'un coup sur une émulsion noir et blanc, en utilisant un réseau échantillonneur trichromatique. On montre que la méthode évite l'intermodulation des couleurs, les phénomènes de moiré et minimise les pertes de résolution. Le réseau échantillonneur linéaire est décrit ainsi qu'une méthode pour générer le réseau trichromatique par ordinateur. Les résultats expérimentaux montrent que cette méthode est une alternative envisageable à la précédente méthode de codage en trois étapes.

1. — INTRODUCTION

Industries which rely on the archival storage of color images have long been plagued with the problem of color fading. The cause of this fading is the instability of the organic dyes used in color films. In an effort to avoid color fading, numerous methods of diffraction color photography have been proposed. In 1969, P. F. Mueller [1] proposed a one-step method of color image retrieval using a tricolor grid screen to encode on a monochrome transparency. The image was retrieved using three quasi-monochromatic light sources. This method successfully avoided the cross-product spectra by using limiting apertures in the Fourier plane, but these apertures also caused some marginal resolution loss. In addition, due to the non-linearity of color film, the overlapping elements of the tricolor grid screen resulted in unavoidable color-cross-talk.

Several similar methods of archival storage have been subsequently reported by Macovski, Grousion,

Kinany, and Yu [2-4]. In recent articles, Yu *et al.* [5] have demonstrated a white-light method for archival storage of color information on a monochrome transparency. Each of the three primary colors of an image were modulated into separate positions by three diffraction gratings of different frequencies or azimuthal orientations. The image was retrieved by passing the three primary image spectra through wide band spatial filters and recombining them to form a color image.

In the present paper, we propose a one-step method for recording color information on a monochrome transparency using a linear tricolor sampling pattern. Since the sampling pattern is linear, both moiré fringes and color-cross-talk are avoided. In addition, broad band spatial filters can be used for decoding, thus avoiding marginal resolution loss. In the following sections, we will describe the linear tricolor sampling pattern in detail as well as discuss a method for constructing the grating using computer generated plots. We will then demonstrate the application of the tricolor grating to both color archival storage and color image retrieval and discuss its unique merits.

II. — THEORY

A method has been suggested for generating a tricolor sampling pattern by sequential exposures of sampling gratings [1] as shown in figure 1. By using white-light illumination the tricolor grating sampled the respective three-color information of the color transparency onto the photographic film.

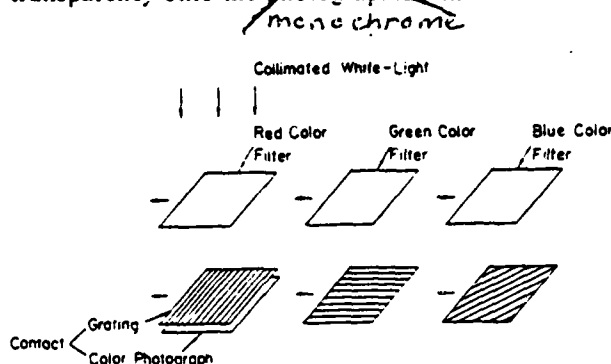


FIG. 1. — Generating a tricolor grating by sequential exposures of sampling gratings.

We now discuss the encoding procedure in more detail. For simplicity, a bicolor grid is illustrated rather than a tricolor grating. Let region 1-2-3-4 be $g_0(x, y)$, as shown in figure 2, and the grating function $g(x, y)$ be written as

$$g(x, y) = \sum \sum g_0(x + md_1, y + nd_2), \quad (1)$$

where d_1 and d_2 are the periods in the x and y directions respectively.

The complex amplitude transmittance of the bicolor grid can be described by the following equation:

$$t(x, y, \lambda) = \sum \sum C_{mn}(\lambda) \exp[i(2\pi/\lambda f)(mx_0 x + n\beta_0 y)], \quad (2)$$

where f is the focal length, and $C_{mn}(\lambda)$ are the double Fourier coefficients in terms of wavelength λ described by

$$C_{mn}(\lambda) = \frac{1}{d_1 d_2} \int_{-d_1/2}^{d_1/2} \int_{-d_2/2}^{d_2/2} g_0(x, y) \times \exp[-i(2\pi/\lambda f)(mx_0 x + n\beta_0 y)] dx dy, \quad (3)$$

$$C_{mn}(g) = \frac{1}{d_1 d_2} \int_{-d_1/2}^{d_1/2} \int_{-d_2/2}^{d_2/2} [A(g) \exp[-i(2\pi/\lambda f)(mx_0(x - a_1/2) - n\beta_0(y - a_2/2))] - [A(g) - \Delta A(g)] \exp[-i(2\pi/\lambda f)(mx_0(x - a_1/2) - n\beta_0(y - a_2/2))]] dx dy$$

$$= \begin{cases} K_m(g) [A(g) - \Delta A(g)] & n = 0 \\ K_n(g) \Delta A(g) & m = 0 \end{cases} \quad (5)$$

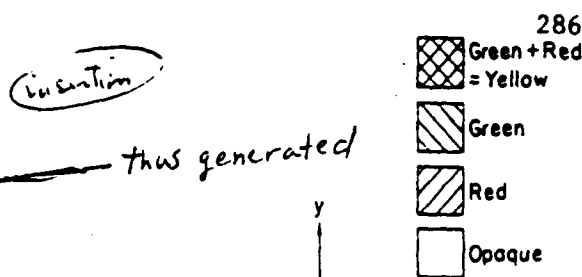


FIG. 2. — A bicolor grid demonstrating color-cross-talk.

x and y are the linear spatial coordinates of the Fourier plane, and the respective angular spatial frequencies, p_0 and q_0 , can be written as

$$p_0 = (2\pi/\lambda f) x_0 = 2\pi/d_1, \quad (4)$$

$$q_0 = (2\pi/\lambda f) \beta_0 = 2\pi/d_2.$$

Let the amplitude of the green light passed by the nonoverlapping region 0-5-2-6 be $A(g)$, the red light passed by the nonoverlapping region 0-7-4-8 be $A(r)$, and the amplitude of light passed by the region 0-6-3-7, which is the overlapping of green and red, be $A(y)$. Then due to the nonlinearity of photographic film, the amplitude of light passed by the region 0-6-3-7 is not equal to $A(g)$ plus $A(r)$, but is instead equal to $A(g) - \Delta A(g)$ plus $A(r) - \Delta A(r)$. Illumination by collimated white-light results in

and

$$C_{mn}(r) = \frac{1}{d_1 d_2} \int_{-a_1/2}^{a_1/2} \int_{-a_2/2}^{a_2/2} \{ A(r) \exp[-i(2\pi/\lambda_r f)(mx_0(x + a_1/2) + n\beta_0(y - a_2/2))] + \\ + [A(r) - \Delta A(r)] \exp[-i(2\pi/\lambda_r f)(mx_0(x - a_1/2) + n\beta_0(y - a_2/2))] \} dx dy \\ = \begin{cases} K_n(r) [A(r) - \Delta A(r)] & m = 0 \\ K_m(r) \Delta A(r) & n = 0. \end{cases} \quad (6)$$

where $K_x(\lambda)$ are complex constants with index m or n , and we have assumed that $a_1 = (1/2) d_1$, $a_2 = (1/2) d_2$.

Taking a two-dimensional Fourier transform of $t(x, y, \lambda)$, we have

$$\hat{T}(\alpha, \beta, \lambda) = \sum_m \sum_n C_{mn}(\lambda) \delta(\alpha - m\lambda_r f d_1) \delta(\beta - n\lambda_r f d_2). \quad (7)$$

The distribution of spectra in the α direction of the Fourier plane can be written as

$$\hat{T}(\alpha, \lambda_r) = \sum_n K_n(\lambda_r) [A(\lambda_r) - \Delta A(\lambda_r)] \delta(\alpha - m\lambda_r f d_1). \quad (8)$$

and

$$\hat{T}(\alpha, \lambda_r) = \sum_m K_m(r) \Delta A(r) \delta(\alpha - m\lambda_r f d_1). \quad (9)$$

Similarly, the distribution of spectra in the β direction of the Fourier plane can be written as

$$\hat{T}(\beta, \lambda_r) = \sum_n K_n(\lambda_r) \Delta A(\lambda_r) \delta(\beta - n\lambda_r f d_2). \quad (10)$$

and

$$\hat{T}(\beta, \lambda_r) = \sum_m K_m(r) [A(r) - \Delta A(r)] \delta(\beta - n\lambda_r f d_2). \quad (11)$$

From Eqs. (8) to (11), we conclude that there are not only the spectra of the green-color-grating but also the spectra of the red-color-grating on the α -axis of the Fourier plane. Furthermore, the size of the light source and the color smear cause the n th order of both spectra to overlap resulting in color-cross-talk (i.e., two colors can not be distinguished). Color-cross-talk also occurs on the β -axis. To avoid the effects of color-cross-talk, we propose a new type of sampling pattern from which three distinguishable spectra will result.

Figure 3 shows the constitution of a linear tricolor sampling pattern (LTSP). The basic idea is that no color cells overlap, so that we avoid the effects of the nonlinearity of the film. The red color periodic pattern, which is independent of the y direction, has the period, d_r , in the x direction. The green pattern has the period, d_g , in the x direction, and the period, d_y , in the y

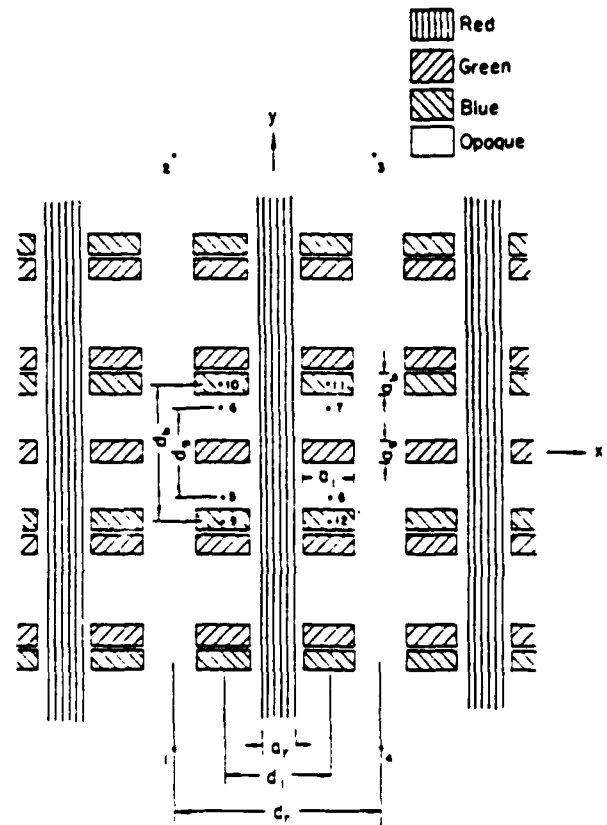


FIG. 3. A linear tricolor sampling pattern (LTSP).

direction. The blue pattern has the same period, d_b , in the x direction, as the green one, and the period, d_y , in y direction. The sizes of the transparent cells of red, green, and blue color are a_r by y , a_g by a_y , and a_b by a_y , respectively. The relative dimensions of the parameters are

$$d_r = 2 d_1, \quad d_1 \geq a_1 - a_r, \\ 3 d_g = 2 d_b, \quad d_g \geq 2(a_g - a_b). \quad (12)$$

The LTSP function $g(x, y)$ can be written as

$$g(x, y) = g_r(x, y) + g_g(x, y) + g_b(x, y) \\ = \sum_m \sum_n [g_{r0}(x - md_r) + g_{g0}(x - md_g, y - nd_y) + g_{b0}(x - md_b, y - nd_y)]. \quad (13)$$

where $g_{r0}(x)$ = region 1-2-3-4, $g_{g0}(x, y)$ = region 5-6-7-8, and $g_{b0}(x, y)$ = region 9-10-11-12 (see fig. 3).

We employ Eqs. (2) and (3), and recalculate $C_{mn}(\lambda)$. Illumination by collimated white-light results in

$$\begin{aligned} C_{mn}(r) &= \frac{1}{d_r} \int_{-a_r/2}^{a_r/2} A(r) \exp[-i(2\pi/\lambda_r f)(mx_0 x)] dx \\ &= (a_r/d_r) A(r) \text{sinc}(ma_r/d_r) \\ &= K_{mn}(r) A(r). \end{aligned}$$

$$\begin{aligned} C_{mn}(g) &= \frac{1}{d_1 d_g} \int_{-a_1/2}^{a_1/2} \int_{-a_g/2}^{a_g/2} A(g) \exp[-i(2\pi/\lambda_g f)[mx_1(x - y)]] dx dy \\ &= (a_1 a_g/d_1 d_g) A(g) \exp(i\pi ma_1/d_1) \text{sinc}(ma_1/d_1) \text{sinc}(n a_g/d_g) \\ &= K_{mn}(g) A(g). \end{aligned}$$

$$\begin{aligned} C_{mn}(b) &= \frac{1}{d_1 d_b} \int_{-a_1/2}^{a_1/2} \int_{-a_b/2}^{a_b/2} A(b) \exp[-i(2\pi/\lambda_b f)[mx_1(x - y)]] dx dy \\ &= (a_1 a_b/d_1 d_b) A(b) \exp(i\pi ma_1/d_1) \text{sinc}(ma_1/d_1) \times \\ &\quad \times \exp(i\pi na_b/d_b) \text{sinc}(na_b/d_b) \\ &= K_{mn}(b) A(b). \end{aligned}$$

where $K_{mn}(r)$, $K_{mn}(g)$, and $K_{mn}(b)$ are complex constants, and x and y are the linear spatial coordinates. The respective angular spatial frequencies p_0 , p_1 , q_1 , and q_2 can be written as

$$\begin{aligned} p_0 &= (2\pi/\lambda f) x_0 = 2\pi/d_r \\ p_1 &= (2\pi/\lambda f) x_1 = 2\pi/d_1 \\ q_1 &= (2\pi/\lambda f) \beta_1 = 2\pi/d_g \\ q_2 &= (2\pi/\lambda f) \beta_2 = 2\pi/d_b. \end{aligned}$$

The Fourier transform of $t(x, y, \lambda)$ can be written as

$$\hat{T}(x, \beta, \lambda) = \sum \sum \sum C_{mn}(\lambda) \delta(x - mx_0) \delta(\beta - n\beta_1). \quad (17)$$

In the x direction of the Fourier plane,

$$\begin{aligned} \hat{T}(x, \lambda) &= \sum [K_{mn}(r) A(r) \delta(x - mx_0) - \\ &\quad - K_{mn}(g) A(g) \delta(x - mx_1) \\ &\quad - K_{mn}(b) A(b) \delta(x - mx_1)]. \end{aligned} \quad (18)$$

It is noted that the first order spectra of the green color pattern and the blue color pattern are located at twice the distance of the red one in the x direction because $x_1 = 2x_0$. At the same time, on the β -axis of the Fourier plane, we have

$$\begin{aligned} \hat{T}(\beta, \lambda) &= \sum [K_{mn}(g) A(g) \delta(\beta - n\beta_1) \\ &\quad - K_{mn}(b) A(b) \delta(\beta - n\beta_2)]. \end{aligned} \quad (19)$$

The first order spectrum of the green color pattern appears at 3/2 the distance of the blue one on the β axis because $\beta_1 = (3/2)\beta_2$.

Thus we have shown that with the LTSP we can obtain a set of distinguishable first order spectra on the Fourier plane, and both the moiré effect and the color-cross-talk effect can be avoided.

III. — COMPUTER GENERATING LTSP

In principle, it is possible to realize the one-step-encoding technique by using the linear tricolor sampling pattern (LTSP) from the preceding discussions.

Now we will propose a method for computer generating the LTSP. In addition, some special features of the one-step-encoding technique will be discussed.

To construct an LTSP, we first use a computer plotter to generate a large diagram of the LTSP, which we then reduce the diagram into a 35 mm color transparency by means of a photographic method. We can divide the LTSP into three parts, i.e., the red-color-sampling-pattern, the green-color-sampling-pattern, and the blue-color-sampling-pattern. Thus, we are able to use a computer to generate three diagrams individually in black and white corresponding to the three color-sampling-patterns. During the reducing process, by using a special mark to fix these diagrams at their exact position, the LTSP can be obtained by exposing a color transparency through the corresponding red, green, and blue primary color filters. The flowchart of the procedure for generating the LTSP is shown in figure 4.

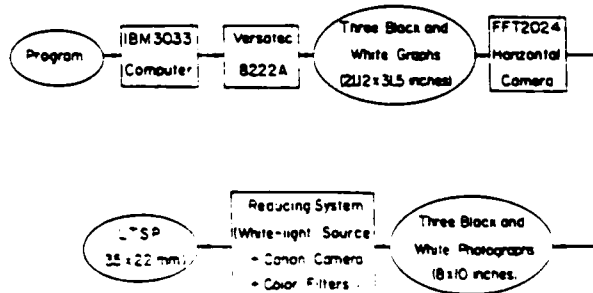


FIG. 4 — A flowchart of the procedure for generating the LTSP

The Versatec 8222A electrostatic plotter was used to generate black and white diagrams of the three sampling patterns. The writing instrument is a double row of plotting nibs past which the plotting paper moves. Each nib is 0.005 inches in diameter and the two rows are offset by 0.0025 inches, forming a relatively smooth and continuous plot. The plotting surface is 21.12 inches wide and 72.00 inches long. Referring to Eq. (12) and figure 3, we have $d_1 \geq 4$ pixels if $a_1 = a_2 = 1$ pixel. Due to the overlap of two adjacent dots, d_1 is taken to be 8 pixels so that $d_2 = 12$ pixels. Because the actual width of useful paper is 21.12 inches on the Versatec 8222A plotter, we have 4224 pixels in the x-direction. After leaving space for the special marks, for example 128×2 pixels, $4224 - 128 \times 2 = 3968$ pixels remain. Thus, we can draw $3968/12 \approx 330$ lines for the blue-color-sampling-pattern, and $3968/8 \approx 496$ lines for the green-color-sampling-pattern in the x direction. After reducing to a 35 mm transparency, the sampling frequencies are $330/22 \approx 15$ (lines/mm) and $496/22 \approx 22.5$ (lines/mm) respectively. Similarly, if $a_1 = 1$ pixel and $d_1 = 12$ pixels, we can draw 525 lines in the y-direction (corresponding to 6300 pixels, i.e., 31.5 inches long). Then the red-color-sampling-pattern frequency is approximately equivalent to $525/35 \approx 15$ (lines/mm).

Although sampling frequencies of 15 lines/mm and 22.5 lines/mm are low, they are satisfactory for evaluating the potential for a one-step-encoding technique. To achieve higher sampling frequencies, we can use instruments which possess very fine output, such as a Microdensitometer. For example, the PDS model 1010 Microdensitometer is able to resolve the pixel position information with a resolution of 1μ . With a spacing of 12μ , the sampling frequency is expected to be about 80 lines/mm.

Diffraction efficiency is one of the most important considerations when constructing the LTSP. Theoretically, the thin rectangle shape amplitude transmittance grating possesses the maximum diffraction efficiency with $\eta_{\max} \approx 10\%$ [6]. However, the differences of the colors and the sampling patterns may cause the efficiency of the LTSP to be less than the maximum. The diffraction efficiency can be increased by optimizing the sampling pattern parameters and by optimizing the length of exposure to each color-sampling-pattern during grating construction.

In finding the optimal sampling pattern parameters we investigate the effects of the sampling frequencies and the sizes of the transparent cells. Recalling Eqs. (14) to (16), the diffracted wave amplitudes are the Fourier coefficients, $C_{mn}(\lambda)$. The mn (th) order diffraction efficiency is defined by

$$\eta_{mn} = C_{mn}(\lambda) C_{mn}^*(\lambda), \quad (20)$$

where $*$ denotes the complex conjugate. For the red-sampling-pattern we are interested in the $mn = 10$ order and for the green and blue-sampling-patterns we are interested in the $mn = 01$ order. Figure 5 shows the curves of diffraction efficiency versus a/d as calculated from Eq. (20). These curves show that the diffraction efficiency improves as the cell size is increased and the period is decreased.

The second method for improving the diffraction efficiency of the LTSP is by finding the optimal length

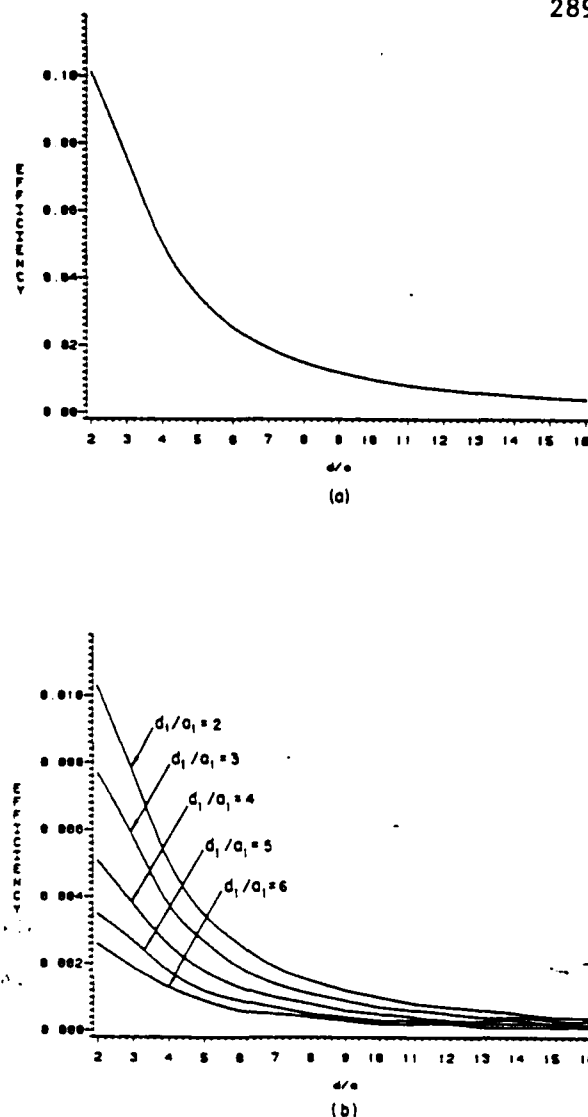


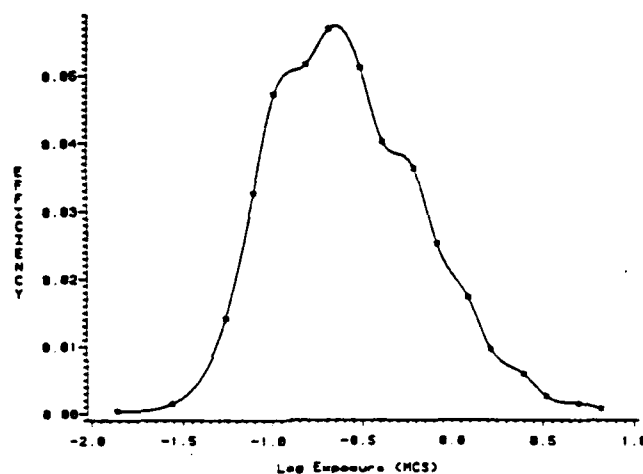
FIG. 5. — Diffraction efficiency versus a/d .
(a) Red-sampling-pattern.
(b) Green and blue sampling-patterns.

of exposure to each color-sampling-pattern when recording the grating. Figures 6(a), (b), and (c) show the empirical exposure versus efficiency curves for each of the three color-sampling-patterns recorded on Kodak 2483 color film. These curves show where the optimal exposure values occur. In practice, we do not have access to equipment that would enable us to realize the optimal sampling pattern shape. However, we do follow the optimal exposure times from figure 6 in recording the grating.

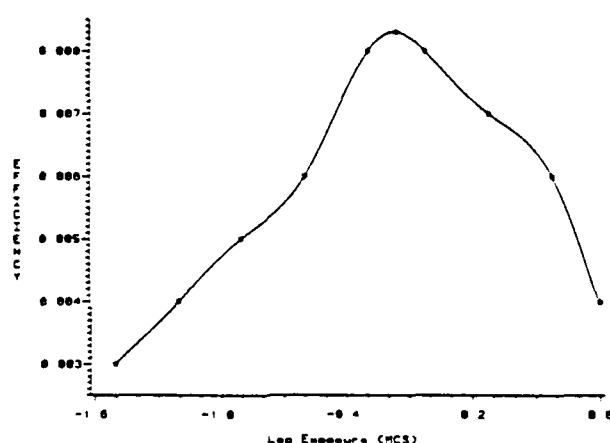
A second consideration in recording the LTSP is the color balance of the retrieved color image. It is known that the exposure, E , of an encoded film is defined by

$$E = IT \quad (21)$$

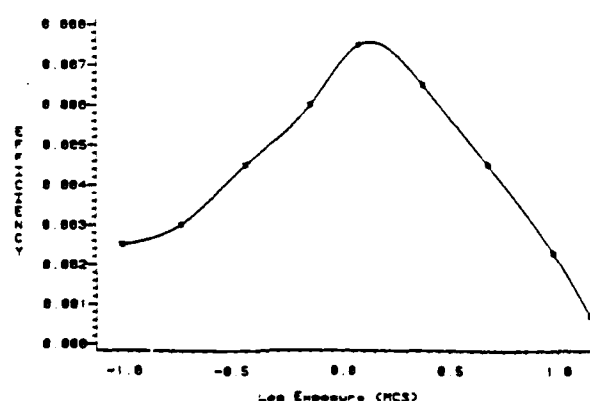
where T is the duration of the exposure and I is the



(a)



(b)



(c)

FIG. 6. — Diffraction efficiency versus exposure.
 (a) Red-sampling-pattern
 (b) Green-sampling-pattern
 (c) Blue-sampling-pattern

intensity incident on the encoded film. In three step encoding we controlled color balance by adjusting the length of exposure, T , for each color encoded. However, for one-step encoding, T is the same for all three colors and the color balance now depends only on the variation of I with respect to λ . The incident intensity is dependent upon the intensity of light transmitted by the LTSP which is dependent on the length of exposure to each color-sampling-pattern during grating construction. Thus we must choose whether to optimize color balance or grating efficiency when choosing the exposure times for recording the grating. However, the color balance of the retrieved color image can also be adjusted by using neutral density filters at the Fourier plane. With this in mind and considering the difficulties in realizing the optimal sampling-pattern for maximum efficiency, we choose exposure times that maximize the diffraction efficiency of the grating.

A final consideration when recording the LTSP is the film. A high resolution film is best, and we choose Kodak 2483 color film which has a cut off spatial frequency of 200 lines/mm.

IV. — APPLICATIONS AND RESULTS

One step color archival storage can be achieved using the contact printing method illustrated in figure 7. Kodak AHU 5460 Microfilm was chosen as the film to be encoded because its spectral response matches that of the tricolor grating and it is a high resolution film. The film was encoded by bringing it into contact with the grating and exposing it to the object transparency. To increase the diffraction efficiency, the encoded film was bleached after development. Figure 8 shows the original transparency, a picture of two football players which contains the

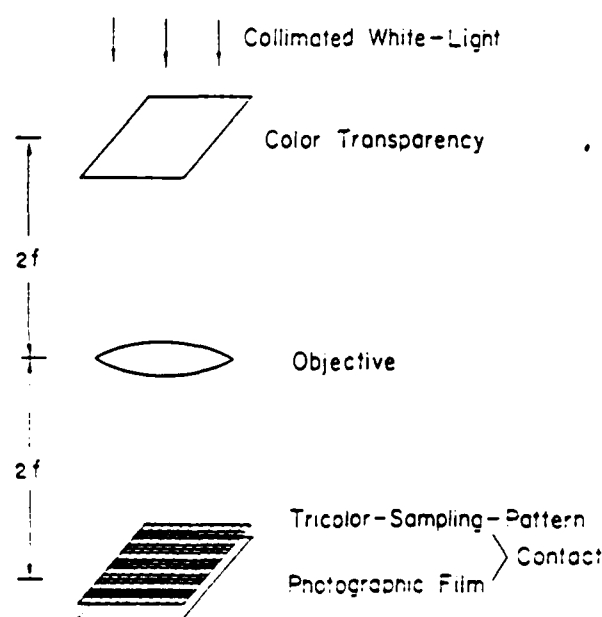


FIG. 7. — One-step encoding

Original

FIG. 8 — Original color picture of two football players.

Retrieved

FIG. 9 — Color picture of two football players retrieved from the one-step encoded monochrome transparency.

primary colors. Figure 9 is a picture of the image retrieved from the encoded transparency.

The tricolor grating can be used for color image retrieval by mounting the grating on a glass slide and placing the slide in the focal plane of a camera as shown in figure 10. When the black and white film is loaded in the camera and the camera back closed, the film and grating emulsions are brought into contact

to obtain a contact print. To prevent scratching the film against the grating, the camera back is left open, and the room darkened, when advancing the film. The method could be further simplified by devising a spring mechanism in the camera which would hold the films in contact during exposure and release them when the film is advanced. In this manner the camera back could remain closed throughout the encoding

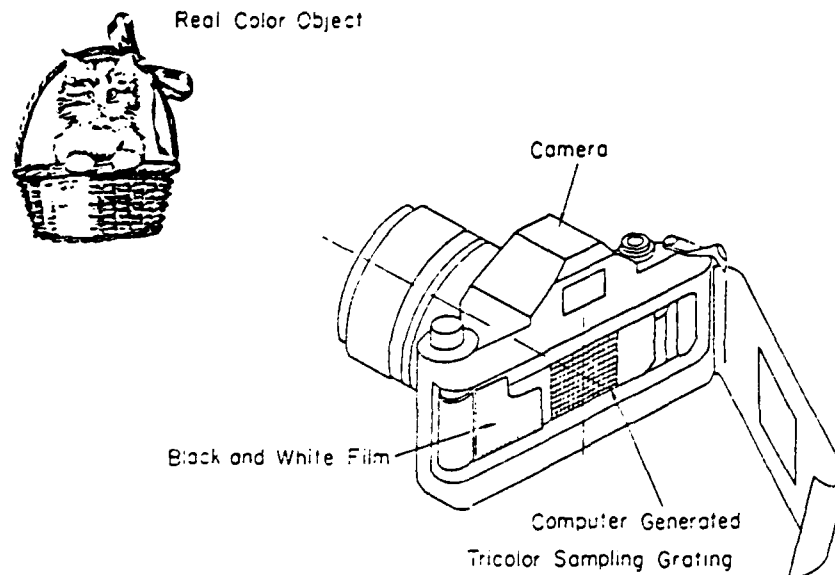


FIG. 10. Color image encoding on the black and white film using the LTSP mounted in a camera.

process. Figure 11 is a picture of the object, a toy lion, used to demonstrate color image retrieval and figure 12 is the retrieved color image. Here again, Kodak 5460 Microfilm was encoded and the developed film was bleached to increase efficiency.

Examining the results, one sees that the color in the retrieved images is very close to the original. However, some resolution is lost in the retrieved image. Increasing the sampling frequency of the sampling pattern would increase the resolution of the retrieved image as well as enrich the color. One additional advantage of the tricolor grating is that since the color cells do not overlap, the dynamic range of exposure is greatly expanded.

FIG. 11. Color picture of a toy lion

V. — CONCLUSION

We have discussed a linear tricolor sampling pattern (LTSP) for recording color information on a monochrome transparency. The grating has no overlapping color cells so that color-cross-talk and moiré fringes are avoided. In addition, since the system uses white-light and broad band spatial filters for decoding, marginal resolution loss is avoided. A method for constructing LTSP using computer generated plots of the sampling pattern has been presented with special attention paid to maximizing the diffraction efficiency. Results obtained with the LTSP have remarkably good color although some loss of resolution is suffered. Increasing the sampling frequency would avoid resolution loss as well as enrich the color of the retrieved image.

ACKNOWLEDGEMENT

We acknowledge the support of the U.S. Air Force Office of Scientific Research
Grant AFOSR-83-1040.

FIG. 12. Color picture of a toy lion retrieved from the camera encoded monochrome transparency

9

REFERENCES

- [1] MUELLER (P. Y.) — *Appl. Opt.*, 1969, 8, 2051
- [2] MACOVSKI (A.) — *Appl. Opt.*, 1972, 11, 416
- [3] GROSSEON (R.) and KINASY (R. J.) — *J. Opt.*, 1978, 9, 333
- [4] YU (F. T. S.) — *Appl. Opt.*, 1980, 19, 2457
- [5] YU (F. T. S.), CHEN (X. X.) and ZHANG (S. L.) — *J. Opt.*, 1985, 16, 59
- [6] MAGNUSSEN (R.) and GAYLORD (T. K.) — *Opt. Comm.*, 1979, 28, 1

Manuscript received in June 17, 1986.

SECTION XXXI

Concluding Remarks

XXXI. Concluding Remarks

In this research, we have developed a white-light optical signal processor for complex data processing. The coherence requirement is analyzed through the partial coherence theory of Wolf. We have shown that the white-light signal processor is capable of processing the signal in complex amplitude as a coherent image processor; at the same time the processor is capable of suppressing artifact noise as an incoherent processor.

To alleviate the spatial coherence constraint of a physical light source, a source encoding concept is developed so that the optical processing can be carried out with an extended source. To remove the constraint of the temporal coherence of a white-light source, we utilize an image sampling grating to improve the degree of temporal coherence in the Fourier plane so that the image can be processed in complex amplitude. We have also demonstrated that the white-light optical processor is very economical and easy to operate, in contrast with coherent counterparts. We have shown that the white-light optical processor would offer a broader range of application to many scientific imageries.

In this report, we have summarised some of the advances in deblurring, subtraction, color retrieval, and pseudocolor encoding can be easily carried out by the proposed white-light optical signal processor.

In spite of the flexibility of digital processing, optical methods offer the advantage of capacity, color, simplicity, and cost effectiveness. Instead of confronting each other, we can expect a gradual merging of the optical and digital techniques. The continued development of optical-digital interfaces and various electro-optics devices will lead to

a fruitful result: hybrid optical digital image processing techniques, utilizing the strengths of both processing operations. Furthermore, I believe that white-light optical signal processing is at the threshold of widespread application. I hope that this will serve a basic foundation, already established in part, to help guide interested readers toward various imaginative signal processing applications.

SECTION XXXII

List of Publications Resulting from AFOSR Support

XXXII. LIST OF PUBLICATIONS RESULTING FROM AFOSR SUPPORT

1. S. T. Wu and F. T. S. Yu, "Source Encoding for Image Subtraction," Optics Letters, Vol. 6, pp. 452-454, September, 1981.
2. F. T. S. Yu and J. L. Horner, "Optical Processing of Photographic Images," Optical Engineering, Vol. 20, pp. 666-676, September-October 1981.
3. F. T. S. Yu, "Partially Coherent Optical Processing of Images," SPIE Proceedings on "Processing Images and Data from Optical Sensors," Vol. 292, pp. 2-8, 1982.
4. F. T. S. Yu and J. L. Horner, "Review of Optical Processing of Images," SPIE Proceedings on Processing Images and Data from Optical Sensors," Vol. 292, pp. 9-24, 1982.
5. F. T. S. Yu, S. L. Zhuang and T. H. Chao, "Color Photographic-Image Deblurring by White-Light Processing Technique," Journal of Optics, Vol. 13, pp. 57-61, March-April, 1982.
6. S. T. Wu and F. T. S. Yu, "Image Subtraction with Encoded Extended Incoherent Source," Applied Optics, Vol. 20, pp. 4082-4088, December 1981.
7. F. T. S. Yu, S. L. Zhuang and S. T. Wu, "Source Encoding for Partial Coherent Optical Processing," Applied Physics, Vol. B27, pp. 99-104, February 1982.
8. S. T. Wu and F. T. S. Yu, "Visualization of Color Coded Phase Object Variation with Incoherent Optical Processing Technique," Journal of Optics, Vol. 13, pp. 111-114, May-June, 1982.
9. S. L. Zhuang and F. T. S. Yu, "Coherence Requirement for Partially Coherent Optical Information Processing," Applied Optics, Vol. 21, pp. 2587-2595, July 1982.
10. F. T. S. Yu and S. T. Wu, "Color Image Subtraction with Encoded Extended Incoherent Source," Journal of Optics, 13, 183 (1982).
11. S. L. Zhuang and F. T. S. Yu, "Apparent Transfer Function for Partially Coherent Optical Information Processing," Applied Physics, B28, 359-366, August, 1982.
12. Y. W. Zhang, W. G. Zhu, and F. T. S. Yu, "Rainbow Holographic Aberrations and Bandwidth Requirements," Applied Optics, 22, 164 (1983).
13. F. T. S. Yu, X. X. Chen, and S. L. Zhuang, "Progress Report on Archival Storage of Color Films with White-Light Processing Technique," submitted to Applied Optics.
14. T. H. Chao, S. L. Zhuang, S. Z. Mao and F. T. S. Yu, "Broad Spectral Band Color Image Deblurring," Applied Optics, 22, 1439 (1983).
15. F. T. S. Yu, Optical Information Processing, Wiley-Interscience, N.Y., 1983.

16. F. T. S. Yu, "Source Encoding, Signal Sampling and Filtering for White-Light Signal Processing," Proceedings of 10th International Optical Computer Conference, pp. 111-116, April 6-8, 1983.
17. X. J. Lu and F. T. S. Yu, "Restoration of Out-of-Focused Color Photographic Images," Optics Communications, Vol. 46, pp. 278-833, July (1983).
18. C. Warde, H. J. Caulfield, F. T. S. Yu and J. E. Ludman, "Real-Time Joint Spectral-Spatial Matched Filtering," Optics Communications, Vol. 49, pp. 241-244, March (1984).
19. F. T. S. Yu, "Source Encoding, Signal Sampling and Spectral Band Filtering for Partially Coherent Optical Signal Processing," Journal of Optics, Vol. 14, pp. 173-178, July-August (1983).
20. F. T. S. Yu, "Recent Advances in White-Light Optical Signal Processing," Conference on Laser and Electro-Optics, Cleo '83 Technical Digest, pp. 28-30, May (1983).
21. F. T. S. Yu, X. X. Chen and T. H. Chao, "Density Pseudocolor Encoding with Three Primary Colors," Journal of Optics, Vol. 15, pp. 55-58, March-April (1984).
22. F. T. S. Yu, S. L. Zhang and K. S. Shaik, "Noise Performance of a White-Light Optical Signal Processor: Part I, Temporally Partially Coherent Illumination, Journal of the Optical Society of America A, Vol. 1, pp. 489-494, May (1984).
23. F. T. S. Yu, F. K. Hsu and T. H. Chao, "Coherence Measurement of a Grating-Based White-Light Optical Signal Processor," Applied Optics, Vol. 23, pp. 333-340, January (1984).
24. F. T. S. Yu, "Advances in White-Light Optical Signal Processing," Proceedings on Optical Information Processing Conference II, NASA CP-2303 Conference publication, pp. 53-69, August (1983).
25. S. L. Zhuang, "Coherence Requirements, Transfer Functions and Noise Performance of a Partially Coherent Optical Processor," Ph.D. Dissertation, Pennsylvania State University, University Park, PA, 1983.
26. T. H. Chao, "A Grating-Based White-Light Optical Signal Processor," Ph.D. Dissertation, Pennsylvania State University, University Park, PA, 1983.

27. X. J. Lu, "Pseudocolor Encoding with White-Light Processing System," Optics Communications, pp. 13-16, November (1983).
28. J. E. Ludman, B. Javidi, F. T. S. Yu, H. J. Caulfield and C. Warde, "Real-Time Colored-Pattern Recognition," SPIE Proceedings of Spatial Light Modulators and Applications, Vol. 465, pp. 143-149, January 1984.
29. F. T. S. Yu, X. X. Chen and S. L. Zhuang, "Progress Report on Archival Storage of Color Films Utilizing a White-Light Processing Technique," Journal of Optics, Vol. 16, pp. 59-61, January-February (1985).
30. F. T. S. Yu, T. N. Lin and K. B. Xu, "White-Light Optical Speech Spectrogram Generation," Applied Optics, Vol. 24, pp. 836-841, March (1985).
31. F. T. S. Yu and G. W. Petersen, "A Low-Cost High-Quality Pseudocolor Encoder for Remote Sensing Applications," submitted to Photogrammetric Engineering and Remote Sensing.
32. B. Javidi and F. T. S. Yu, "Optics at Pennsylvania State University," Optical Engineering, Vol. 23, SR, pp. 068-071, May/June (1984).
33. F. T. S. Yu, X. J. Lu and M. F. Cao, "Applications of Magneto-Optic Spatial Light Modulator to White-Light Optical Processing," Applied Optics, Vol. 23, pp. 4100-4104, November (1984).
34. F. T. S. Yu and X. X. Chen, "Solar Optical Processing," Optics Communications, Vol. 51, pp. 377-381, October (1984).
35. F. T. S. Yu and H. Mueller, "A Low-Cost White-Light Optical Processor," IEEE Transaction of Education, Vol. E-28, pp. 131-137, August (1985).
36. F. T. S. Yu, "Recent Advances in White-Light Image Processing," ICO-13 Conference Digest on "Optics in Modern Science and Technology," pp. 412-413, August (1984).
37. F. T. S. Yu and X. X. Chen, "A Low-Cost White-Light Pseudocolor Encoder for Astronomical Imaging Applications," International Conference on "Progress in Optical Physics," Melbourne, Australia, August 15-17, 1984.
38. F. T. S. Yu, L. N. Zheng and F. K. Hsu, "Noise Measurement of a White-Light Optical Signal Processor," Applied Optics, Vol. 24, pp. 173-176, January (1985).
39. H. M. Mueller, "A Low-Cost White-Light Optical Processor," M.S. Dissertation, Pennsylvania State University, University Park, PA, 1984.
40. F. T. S. Yu and F. K. Hsu, "White-Light Fourier Holography," Optics Communications, Vol. 52, pp. 384-386, January (1985).

41. F. T. S. Yu and F. K. Hsu, "Generation of Broadband Fourier Holograms," SPIE Proceedings on "Application of Holography," Vol. 523, p.p. 319-323, January (1985).
42. F. T. S. Yu, White-Light Optical Signal Processing, Wiley-interscience, Ny, May 1985.
43. F. T. S. Yu, "Garden of White-Light Optical Signal Processing," Optics News, Vol. 11, pp. 5-8, May (1985)(invited).
44. F. K. Hsu, "White-Light Fourier Transform Holography," M. S. Dissertation, Pennsylvania State University, University Park, PA., 1985.
45. M. S. Dymek, "Color Image Processing with Computer-Generated Spatial Filters in a Dispersed White-Light Optical System," Ph.D. Dissertation, Pennsylvania State University, University Park, PA, 1985.
46. F. T. S. Yu and G. W. Peterson, "Generating False-Color Composites with a White-Light Optical Processor, Photogramm, Eng. and Remote Sensing, Vol. 52, pp. 367-371, March (1985).
47. S. Jutamulia, T. W. Lin and F. T. S. Yu, "Real-Time Color-Coding of Depth Using a White-Light Talbot Interferometer", Opt. Commun., Vol. 58, pp. 78-82, May (1986).
48. S. Jutamulia, T. W. Lin and F. T. S. Yu, "Color Visualization of Phase Object Using Talbot Interferometer", J. Opt., Vol. 17, pp. 129-133, May/June (1986).
49. X. J. Lin and F.T.S. Yu, "Analysis of White-Light Processing System Based on Cross Spectral Density Function", Submitted to J. Opt. Soc. Am.
50. M. S. Dymek and F. T. S. Yu, "Color Image Processing with CGH Filters in a White-Light Optical System", Appl. Opt. (in press).
51. F. T. S. Yu, L. N. Zheng and T. W. Lin, "Holographic Tomography in Determining the Structure of Three Dimensional Object Fields", J. Opt., Vol. 17, pp. 97-104, March/April (1986).
52. B. M. Palmer, K. K. Shung and F. T. S. Yu, "Pseudocolor Encoding of Medical Images with White Light", IEEE Proceedings of 12th Annual Northeast Bioengineering, pp. 83-86, March (1986).
53. F. T. S. Yu and Y. W. Zhang, "Fringe Visibility of Dual-Aperture Sampling with partially Coherent Illumination", Applied Optics Vol. 25, pp. 3191-3196, September (1986).
54. F. T. S. Yu, S. Jutamulia and X. L. Huang, "Experimental Application of Low-Cost Liquid Crystal TV to White-Light Optical Signal Processing", Applied Optics, Vol. 25, pp. 3324-3326, October (1986).

55. F. T. S. Yu, X. X. Chen and K. E. McClure", Computer Generated Linear Tricolor Sampling Pattern and its Application", Journal of Optics, Vol. 17, (1987) (in press).
56. F. T. S. Yu, "Garden of White-Light Optical Signal Processing", Proceeding of the International Conference on Laser '85, pp. 77-85, Fed. C. P. Wang, SIT Press, December 1985, (invited).
57. F. T. S. Yu and J. E. Ludman, "A Microcomputer Based Programmable Optical Correlator for Automatic Pattern Recognition and Identification", Optics Letters, Vol. 11, pp. 395-397, June 1986.
58. F. T. S. Yu and S. Jutamulia, "Application of White-Light Processing to Interferometric Studies", SPIE Proceedings on Optical Testing and Metrology, Vol. 661, pp. 9-15, June (1986) (invited)
59. G. Gheen, "A Study of the Performance and Processing Capabilities of a Grating-Based White-Light Optical Processor", Ph.D. Dissertation, Pennsylvania State University, University Park, PA. 1986.
60. F. T. S. Yu, "Principle of Optical Processing with Partially Coherent Light", In Progress in Optics, Vol. 23, Fed. E. Wolf, North-Holland Physics Publishing, Amsterdam, The Netherlands, 1986.

END

5-87

DTIC